I. R. IRAN

ISSN: 2423-7167
e-ISSN: 1735-9244

# International Journal of Engineering

Journal Homepage: www.ije.ir

MERC

## TRANSACTIONS C: ASPECTS

Volume 36, Number 03, March 2023

*Materials and Energy Research Center*

**In the Name of God**

# *INTERNATIONAL JOURNAL OF ENGINEERING*
# *Transactions C: Aspects*



**DISCLAIMER**

The publication of papers in International Journal of Engineering does not imply that the editorial board, reviewers or publisher accept, approve or endorse the data and conclusions of authors.


**I**nternational **J**ournal of **E**ngineering *Transactions A: Basics* (ISSN 1728-1431) (EISSN 1735-9244)
**I**nternational **J**ournal of **E**ngineering *Transactions B: Applications* (ISSN 1728-144X) (EISSN 1735-9244)
**I**nternational **J**ournal of **E**ngineering *Transactions C: Aspects* (ISSN 2423-7167) (EISSN 1735-9244)
Web Sites: www.ije.ir & www.ijeir.info E-mails: ije.editor8@gmail.com, Tel: (+9821) 88771578, Fax: (+9821) 88773352
Materials and Energy Research Center (MERC)

ISSN: 2423-7167, e-ISSN: 1735-9244

**International Journal of Engineering, Volume 36, Number 03, March 2023**

## CONTENTS

### Transactions C: Aspects

ISSN: 2423-7167, e-ISSN: 1735-9244

**International Journal of Engineering, Volume 36, Number 03, March 2023**

International Journal of Engineering

Journal Homepage: www.ije.ir

# Design and Simulation of a Novel Hetero-junction Bipolar Transistor with Gate-Controlled Current Gain

A. Hoonan Mehrabani, A. Fattah*, E. Rahimi

*Electrical Engineering Department, Shahrood University of Technology, Shahrood, Iran*

*PAPER INFO*

*Paper history:*
Received 28 January 2022
Received in revised form 13 October 2022
Accepted 03 November 2022

*Keywords*:
*Current Gain*
*Hetero-junction Bipolar Transistor*
*Gate-Controlled*
*SiGe*
*Silvaco*

*ABSTRACT*

A new structure for SiGe Hetero-junction Bipolar transistor (HBT) is designed and simulated using Silvaco simulator. The considered extra terminal gives the ability to control the transistor's current gain. By applying voltage to the gate terminal, the base effective width would be controlled. Decrement of the Base width yields to the carrier recombination rate reduction, let the emitted electrons to have higher chance to reach the collector. Considering extra terminal have two approaches. One is to improve the current gain of the transistor by applying a constant voltage to the gate and the other is to modify the characteristics of the transistor in such a way that the current gain became optimized. The current gain of the transistor without any gate voltage is about 50V, which increases to 750 for high and 50,000 for low collector currents with the gate voltage variation consideration. In addition, our final proposed gate-controlled HBT with a large gate over the base and collector has the breakdown voltage of 8V and the cut-off frequency of about 11 GHz. The maximum FoM of 1200 is achieved using the proposed structure.

***doi**: 10.5829/ije.2023.36.03c.01*

## 1. INTRODUCTION

In semiconductor technology, both bipolar and field effect transistors are required for various analog and digital applications. In fact, these two technologies are complementary. Bipolar Complementary Metal-Oxide Semiconductor (BiCMOS) technology uses both types of transistors to take their advantages to build more complex and convenient circuits [1, 2]. Although there are many innovations in the design and fabrication of new transistor structures such as carbon nanotube field effect transistors (CNTFET) [2, 3] and QCA structures [4]. It is predicted that the electronics industry will move towards the use of these devices, but there is still a need to use bipolar transistors in a lot of high power or high frequency applications [5]. In Radio Frequency (RF) applications, BJTs are superior to field effect ones [6], but in terms of the number of in-chip transistors, MOSFET transistors are superior. In BJTs, the current gain (β) is one of the most important parameters [7], which is determined during the design and fabrication processes and the manufacturing technology, which may change with factors such as temperature and affect the circuit operation. There is also a great desire to increase or control this parameter using different techniques [8].

Considering the suggestion to add another terminal to BJTs, which is called gate; it is possible to change the current gain of a bipolar transistor. The above device is made in two conventional CMOS technologies [9]. To increase the gain of bipolar transistors, heterogeneous junction is used in Base-Emitter contact [10]. As the integration of two types of transistors on a chip is challenging [11], bipolar transistors based on SOI have been studied and built because of the fact that they are used in system-on-chip (SoC) structures [12-15]. According to the applied bias voltage, it is possible to increase the gain of the transistor by the application a constant voltage to the gate terminal [16]. Due to the application of Heterojunction Bipolar Transistor (HBT) structure, the final proposed structure is expected to have higher speed and efficiency compared to the conventional bipolar junction transistors (BJTs) [17].

A hybrid-mode device based on a standard sub-micrometer CMOS technology is presented as a

*Corresponding Author Institutional Email: a.fattah@shahroodut.ac.ir (A. Fattah)

Please cite this article as: A. Hoonan Mehrabani, A. Fattah, E. Rahimi, Design and Simulation of a Novel Hetero-junction Bipolar Transistor with Gate-Controlled Current Gain, ***International Journal of Engineering, Transactions C: Aspects,*** Vol. 36, No. 03, (2023) 433-440

MOSFET in which the gate and the well are internally connected to form the base of a lateral BJT. At low collector current levels, lateral bipolar action with a current gain higher than 1000 is achieved [18]. Moreover, a CMOS-compatible gate-controlled lateral BJT (GC-LBJT) is fabricated with a conventional 90 nm CMOS technology for RF applications. The Emitter injection efficiency and the doping profile of P-well were optimized by properly controlling source, drain, and well implants. Consequently, the GC-LBJT with the Gate length of 0.15μm would achieve a current gain over than 2000 and $f_T/f_{max}$ ratio of about 17/19, which compare to previously reported LBJT, yield to the improvements of 1000%, 200%, and 60% in current gain, $f_T$ and $f_{max}$, respectively [19].

Bipolar devices are widely used in the nuclear reactor control systems, and the radiation effects are challenging in their operation. The lateral PNP BJT is a radiation-sensitive structure in bipolar integrated devices. Its degradation under irradiation is the primary cause for functional failures of these devices. It is useful to estimate the radiation response of the transistors to find better design strategies for radiation hardness. Three kinds of gate-controlled lateral PNP transistors (GCL-PNPs) with different base widths and doping concentrations are specially designed to explore base current degradation induced by reactor neutrons and gamma rays. Dependence on base width and doping concentration of the degradation is analyzed in this work and the results are beneficial to radiation-hardening design of the lateral PNP BJT [20].

## 2. NEW DEVICE STRUCTURE

Controlling the current gain of a bipolar structure using the gate terminal has been discussed for BJTs and not for a HBT structure in previous investigations. This work studies the effect of adding the gate terminal to a SiGe HBT which has not been previously discussed. Figure 1 shows the structure of a 1-um width HBT transistor with a base made of SiGe in Silvaco software. To implement this structure, the Atlas environment of Silvaco software has been used. This novel structure is a bipolar transistor which has four terminals. In the upper part of the transistor, like MOSFETs, there is a $SiO_2$ insulation layer between the gate and substrate. The length of the transistor is considered as 2 microns and physical width of the base is 300 nanometers. Furthermore, the oxide thickness is equal to 100 nm and the space of 50 nm is provided between the terminals of the transistor to prevent them from affecting each other. In addition, the gate plate, which is placed on the oxide, covers about half of the base and part of the collector. The collector, base and emitter widths are 0.85, 0.3 and 0.85 microns, respectively.

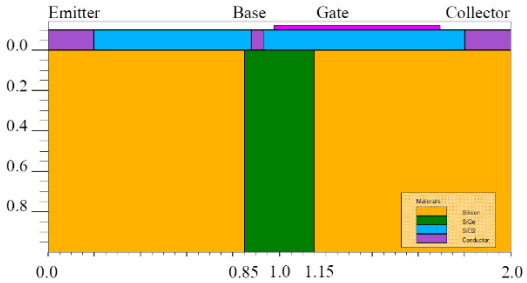


**Figure 1.** Structure of the proposed HBT transistor

The doping distribution of different regions of the transistor is shown in Figure 2. This transistor is an n-p-n type and the doping of the collector, base and emitter regions are $1\times10^{15}$, $3\times10^{16}$ and $5\times10^{18}$ $cm^{-3}$, respectively. Compare to a BJT, it is possible to increase the base doping to have a higher $f_T$, without any degradation in current gain value. To have ohmic contacts, $n^+$ and $p^+$ regions are used beneath the surface to make connection with the collector and the base metals.

## 3. SILVACO SIMULATIONS

In this article, all the simulations have been performed using Silvaco device simulator in order to investigate the electrical behavior of the proposed structure. The sizes and doping levels of the structure are optimized to reach the optimum performance point.

The gate contact in the proposed structure controls the base width, through which the transistor current gain will be controlled. When the Gate voltage is zero, there are no changes in the base width and the transistor current gain totally depends on doping values, thicknesses and dimensions. On the other hand, by applying a positive voltage on the gate contact, an inversion region would be formed under the gate. As a result, a portion of the p-base region will be converted to an n-region, merges to the collector part. In the proposed transistor, the gate length is designed to cover half of the base width. It is important to note that there is not any MOS structure in the proposed transistor design because the gate covers a part of the p-base region.

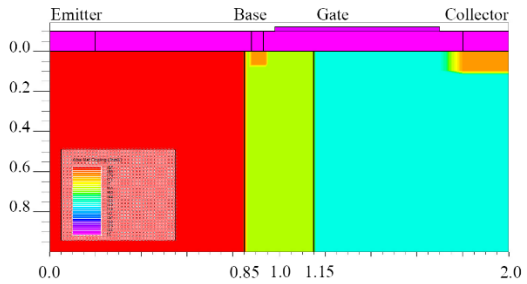


**Figure 2.** Doping distribution of the structure in Silvaco

As the gate position and its length have a major effect on the transistor characterization, we have considered them as two variable parameters in our simulations. By increasing the gate length, its capacitance with the substrate increases which yield to the absorption of carriers transporting from base to the collector to the $SiO_2$ layer beneath and forming a path with lower resistance for the passing carriers. This point tends to a lower base resistance, higher cut-off frequency and much more current gain. The gate length increases up to the point where it affects the functionality of the base and collector contacts.

**3. 1. Gate Position** In this simulation, to find the appropriate location of the gate and its optimized size, the device is simulated without gate and the currents of base and collector are measured. The profile of current density of the device due to the application of 3V collector voltage and 650mV base voltage is shown in Figure 3. In this case, the current path is at all depths of the device and the electrons path is determined by the collector and emitter terminals voltages and the non-uniform internal electrical field of the collector-emitter junction.

Figure 4 demonstrates the base and collector currents in terms of the base-emitter voltage while the emitter is grounded. According to this curves, it is obvious that the collector current is a coefficient of the base current and by dividing the collector current to the base one at each point, the value of β would be calculated. The obtained β for this transistor is 50, which is acceptable and the structure can be used to investigate the effect of adding gate to the device.

To add the gate terminal to this structure, a layer of silicon oxide is considered. Figures 5 to 8 implies the current density profiles for four different modes of gate location and size. Also, Table 1 summarized the device specifications in these modes. Considering the obtained results, the multiplication of β and break down voltage as the figure of merit (FoM) of the structure, increases about 70% using gate in our structure. Moreover, using a large gate on collector yields to an improvement of about 175% and 200% for the cut-off frequency and β values,

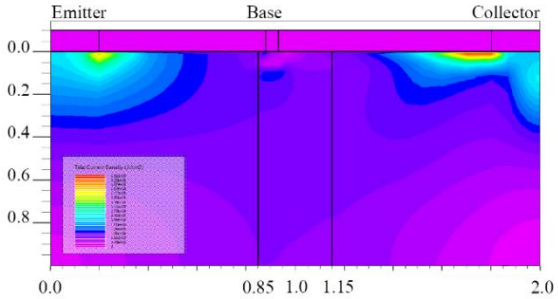


**Figure 3.** Device currents density without considering the Gate voltage

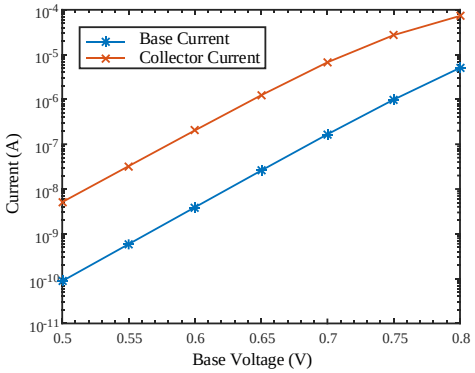


**Figure 4.** Base and Collector currents without applying the Gate voltage

respectively; while the break down voltage at the worst case has the degradation of about 38%. As the large gate condition has the most FoM and $f_T$ values, it is selected as the final proposed structure.

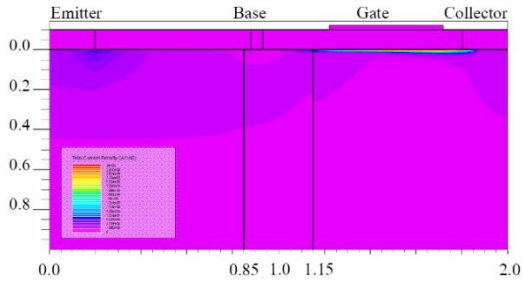


**Figure 5.** Device current density with gate on collector

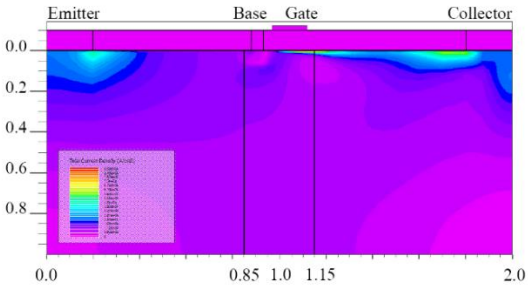


**Figure 6.** Device current density with gate on base

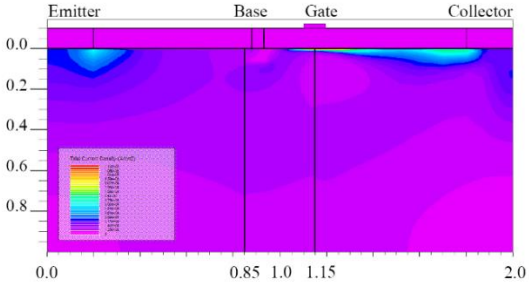


**Figure 7.** Device current density with small Gate

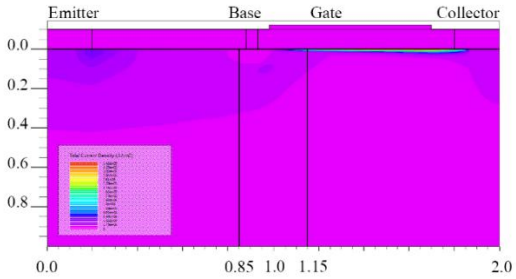


**Figure 8.** Device current density with large Gate

**TABLE 1.** Device characteristics in different modes for Gate dimensions and location

| Parameter | Without Gate | Gate on Collector | Gate on Base | Small Gate | Large Gate |
|---|---|---|---|---|---|
| **Collector current (μA)** | 1 | 2 | 1.5 | 1.5 | 3 |
| **Base current (μA)** | 0.02 | 0.02 | 0.02 | 0.02 | 0.02 |
| **Current gain (β)** | 50 | 100 | 75 | 75 | 150 |
| **Break down voltage ($V_A$)** | 13 | 11 | 10 | 10 | 8 |
| **Cut-off frequency (GHz)** | 4 | 7.6 | 6.7 | 7.1 | 11 |
| **FoM** | 650 | 1100 | 750 | 750 | 1200 |

Figure 9 shows the β values for all 5 different modes of gate location and size. As is apparent, with increment in base voltage, all the gain curves decreases. As the base voltage increases, the collector current tends to be saturated and the $I_C/I_B$ ratio decreases. Among the modes, the large gate one has the most values of current gain as the inversion layer formation caused by voltage application to the gate forms a path for the carriers to reach the collector with the minimum resistivity.

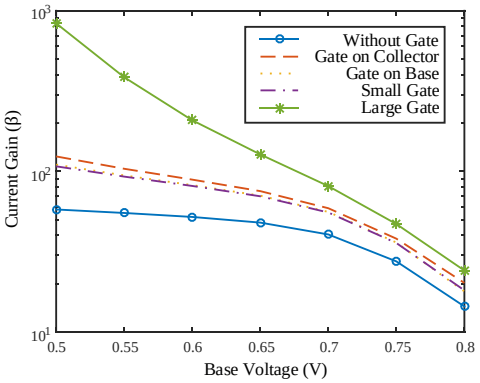


**Figure 9.** Variation of β versus base voltage for different gate modes

**3. 2. Oxide Capacitance** Another way to increase the efficiency of the gate functionality in our proposed device is to enhance the gate-oxide capacitance, which is similar to the MOS one in a field effect transistor. Considering the relation of $C_{ox} = \varepsilon \frac{A}{d}$ , there are generally three methods to increase the oxide capacitance. Enlarging the surface of oxide area, reducing its thickness or substituting the oxide with a higher permittivity one. Figure 10 demonstrates the β values as a function of the base voltage for all three modes of without gate, with a 3V biased gate and oxide relative permittivity of 3.9 and 15.

Another important and effective factor is the thickness of the insulator under the gate plate. Figure 11 shows the current gain of the transistor as a function of gate voltage for different thicknesses of $SiO_2$. As the thickness increases, formation of the inversion layer needs a higher voltage, tends to the decrement of collector current and as a result the current gain degradation. Consequently, the thickness of 50 nm is selected for the gate oxide in our analysis and simulations.

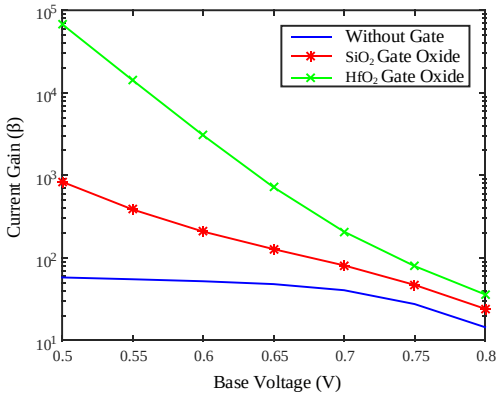


**Figure 10.** Values of β as a function of the base voltage

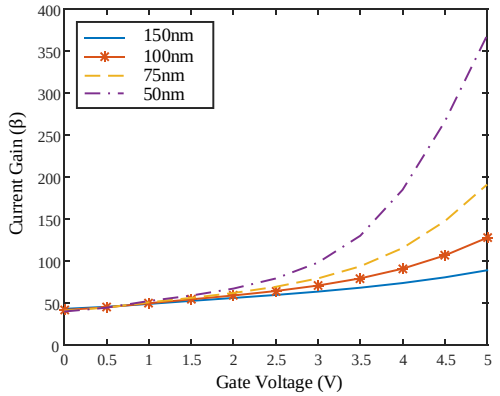


**Figure 11.** Current gain varations as a function of the gate voltage for different oxide thicknesses

Considering these methods for improving the device performance, the value of β is improved about 15 times more for large collector currents and even much higher than the mentioned value for low collector currents. Finally, the value of β measured at 650 mV of base voltage is increased from 50 to 750, which by changing the gate voltage from 0 to 5V, the desired gain within this range is achievable.

## 4. TRANSISTOR OPERATION ANALYSIS

In comparison with Si BJTs, HBTs show better performance in terms of emitter injection efficiency, base resistance, base-emitter capacitance, and cutoff frequency. They also offer good linearity, low phase noise and high power efficiency. In the proposed structure, high injection efficiency is obtained by using SiGe material with a smaller energy band gap for the base than Si, which is used as the emitter material. The large energy band-gap of emitter blocks injection of holes from the base. Therefore, the doping concentration in the base and emitter can be adjusted over a wide range with a little effect on injection efficiency, tends to higher current gain values in comparison with BJTs, without degrading the early voltage ($V_A$) value.

In the HBT conventional structure, due to the uniform distribution of impurities, the electric field is also uniform in space charge region. Figure 12 shows this uniform field at the base and collector junctions. The green area is the base which is made of SiGe and the yellow area on the right corresponds to the collector.

Similar to the previous figure, the electric field distribution at the base-emitter junction by the application of 5V to the considered gate is depicted in Figure 13. Here, due to the application of positive voltage to the gate and the accumulation of electrons under the oxide, a vertical field is created from top to bottom. The field intensity depends on the capacitor value and the applied voltage to the gate. Finally, by the interaction of these two fields, one with the direction from top to bottom and the other from the collector to the base, a non-uniform field would be created. The direction of this field

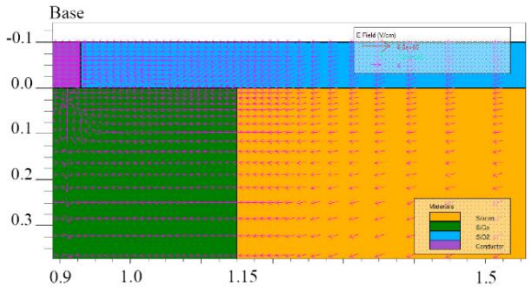


**Figure 12.** Direction of electric field distribution at the junction of Base and Collector

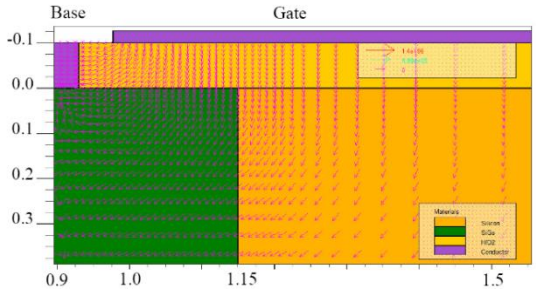


**Figure 13.** Non-uniform field distribusion at the junction of Base and Collector after the positive voltage application to the Gate

is from the collector to the base in the lower parts of the device and from the top to the bottom and inclined towards the base in the upper regions. This causes the electrons in the base to be attracted to the collector.

As the positive voltage is applied to the gate, electrons in the base region, similar to a MOSFET, accumulate below the gate oxide and create an inversion layer. As a result, the effective width of the base reduces just after applying the positive voltage to the gate and therefore, the current gain would increase. Moreover, Figure 14 implies the value of β as a function of the gate voltage, where the transistor is in the active region and the base voltage is 600mV.

**4. 1. Breakdown Voltage** Figure 15 shows the current-voltage characteristic of the transistor as a voltage of 5V is applied to the gate terminal. To find the breakdown voltage of the collector-base junction, the collector voltage is swiped from 0 to 10V for a constant current of 1nA at the base terminal. This increment in voltage should be continued until an abrupt change in the collector current occurs at the collector voltage of 8V.

**4. 2. Cut-off Frequency** In a bipolar transistor, the cut-off frequency is mostly related to the base width and its doping level; so the smaller the base width, the higher the cut-off frequency of the transistor. As in a bipolar

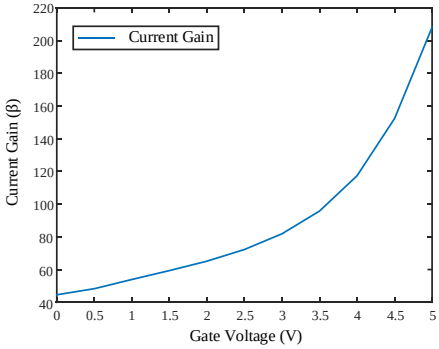


**Figure 14.** Values of β versus the gate voltage

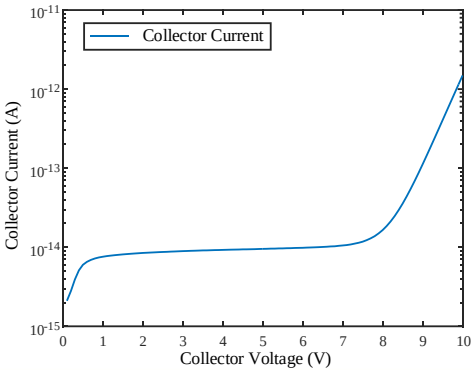


**Figure 15.** Collector-Base reverse breakdown voltage determination

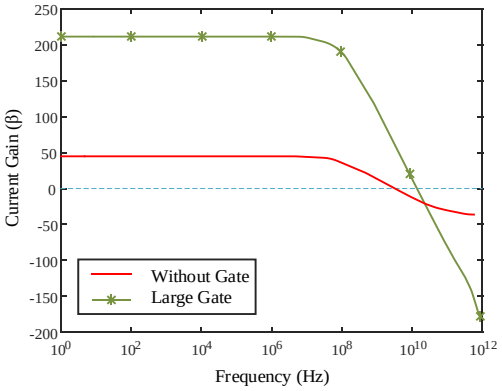


**Figure 17.** Values of β versuss frequency before and after consideration of the gate in the structure

transistor, the cut-off frequency is inversely related to the passage time of the carriers from the emitter to the collector. In addition, short base width yields to its smaller resistance which tends to a faster transistor operation.

Figure 16 shows the electrons accumulation under the gate plate in the base region due to the application of positive voltage to the gate. Here, a voltage of 5 volts is applied to the gate, and due to the accumulation of carriers, the electrons injected from the emitter go through the path under gate to reach the collector.

Considering no voltage application to the gate, the base width is the same as the actual value, which is defined according to the dimensions of the device. Considering this point in Figure 17, the 4 GHz cut-off frequency would be increased to 11 GHz after applying 5 volts to the gate terminal. Therefore, considering a large gate for the structure would improve not only the current gain but also the cut-off frequency.

Table 2 represents the comparison between different reports on the gain controlling of bipolar transistors. It should be noted that the β value for high currents is 750. Because in most articles, the value of β is reported for low collector currents, here the values of β, which corresponds to the base current of five μA at the base voltage of 500 mV, has been reported. Considering the product of current gain and break down voltage as the FoM of each transistor, our structure has the most value.

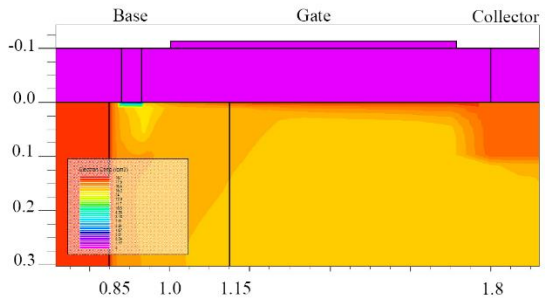


**Figure 16.** The electrons concentration in the structure due to the application of positive voltage to the gate

**TABLE 2.** Comparison table of the results with previous articles

| Reference | Structure | Current gain (β) | Cut-off frequency (GHz) | Break down voltage (V) |
|---|---|---|---|---|
| **[14]** | Lateral bipolar | 30 | 20 | 8.2 |
| **[19]** | Combined with MOS | 250 | 13 | 45.2 |
| **[7]** | Combined with MOS | 10000 | 0.1 | - |
| **[21]** | Lateral bipolar | 1600 | 13 | 5 |
| **[8]** | Controlling the Base width | 2000 | 25 | 5.7 |
| **[22]** | Strained Si/SiGe HBT | 2900 | 500 | - |
| **[23]** | InP based HBT | 126 | 5.4 | - |
| **This research (Large Gate)** | Gate-controlled gain | 50000 | 11 | 8 |

## 5. CONCLUSION

In this research, a new HBT structure with Gate-controlled gain is proposed and simulated by Silvaco software. The simulations were performed with SiGe Base on both conventional bipolar and Gate-controlled structures. In addition, the effect of the gate position and length on its performance are investigated and the appropriate location and dimension were determined. The simulations imply that the current gain of the transistor is acceptable, as for the gate voltage of zero, the gain of the transistor is about 50 and with the gate voltage increment to 5V, it reaches to 750 for high and even up to 50,000 for low collector currents. This

transistor also has a reasonable breakdown voltage and cut-off frequency which are about 8V and 11GHz, respectively, as the voltage is applied to the gate.

## 6. REFERENCES


1. Hashimoto T., Nonaka Y., Tominari T., Fujiwara H., Tokunaga K., Arai M., Wada S., Udo T., Seto M., Miura M. and Shimamoto H., "Direction to improve SiGe BiCMOS Technology featureing 200-GHz SiGe HBT and 80-nm GAT CMOS" in ***IEEE International Electron Devices Meeting*** (2003), 5.5.1-5.5.4. DOI: 10.1109/IEDM.2003.1269182.
2. Karimi G. R. and Shirazi S. G., "Ballistic (n, 0) Carbon Nanotube Field Effect Transistors\' I-V Characteristics: A Comparison of n=3a+1 and n=3a+2", ***International Journal of Engineering, Transactions A: Basics***, Vol. 30, No. 4, (2017), 516-522, DOI: 10.5829/idosi.ije.2017.30.04a.09.
3. Dixit A. and Gupta N., "A Compact Model of Gate Capacitance in Ballistic Gate-All-Around Carbon Nanotube Field Effect Transistors", ***International Journal of Engineering, Transactions A: Basics***, Vol. 34, No. 7, (2021), 1718-1724, DOI: 10.5829/IJE.2021.34.07A.16.
4. Chakrabarty R., Roy S., Pathak T., and Kumar Mandal M., "Design of Area Efficient Single Bit Comparator Circuit using Quantum dot Cellular Automata and its Digital Logic Gates Realization", ***International Journal of Engineering, Transactions C: Aspects***, Vol. 34, No. 12, (2021), 2672-2678, DOI: 10.5829/ije.2021.34.12c.13.
5. Freeman G., Jagannathan B., Shwu-Jen J., Jae-Sung R., Stricker A. D., Ahlgren. D. C. and Subbanna S., "Transistor design and application considerations for> 200-GHz SiGe HBTs", ***IEEE Transactions on Electron Devices***, Vol. 50, No. 3, (2003), 645-655, DOI: 10.1109/TED.2003.810467.
6. Washio K., "SiGe HBT and BiCMOS technologies for optical transmission and wireless communication systems", ***IEEE Transactions on Electron Devices***, Vol. 50, No. 3, (2003), 656-668, DOI: 10.1109/TED.2003.810484.
7. Zhixin Y., Deen M. J. and Malhi D. S., "Gate-Controlled Lateral PNP BJT: Characteristics, Modeling and Circuit Applications", ***IEEE Transactions on Electron Devices***, Vol. 44, No. 1, (1997), 118-128, DOI: 10.1109/16.555443.
8. Hosseini S. E. and Goodarzi Dehrizi H., "A new BJT-transistor with ability of controlling current gain", in ***International Multi-Conference on Systems, Signals & Devices*** (2012), 1-4, DOI: 10.1109/SSD.2012.6198085.
9. Huang T.-H. and Chen. M.-J., "Empirical modelling for Gate-controlled Collector current of lateral bipolar transistors in an n-MOSFET structure", ***Solid-state Electronics***, Vol. 38, No. 1, (1995), 115-119, DOI: 10.1016/0038-1101(94)E0037-F.
10. Fregonese S., Avenier G., Maneux C., Chantre A. and Zimmer T., "A Compact Model for SiGe HBT on Thin-Film SOI", ***IEEE Transactions on Electron Devices***, Vol. 53, No. 2, (2006), 296-303, DOI: 10.1109/TED.2005.862237.
11. Sun I. -S., Tung M., Ng W., Kanekiyo K, Kobayashi T., Mochizuki H., Toita M., Imai H., Ishikawa A., Tamura S., and Takasuka K., "Lateral High-Speed Bipolar Transistors on SOI for RF SoC Applications," ***IEEE Transactions on Electron Devices***, Vol. 52, No. 7, (2005), 1376-1382, DOI: 10.1109/TED.2005.850676.
12. Matsuzawa A., "RF-SoC-Expectations and Required Conditions", ***IEEE Transactions on Microwave Theory and Technology***, Vol. 50, No. 1, (2002), 245-253, DOI: 10.1109/22.981277.
13. Rodder M., and Antoniadis. D A, "Silicon-on-insulator bipolar transistors", ***IEEE Electron Device Letters***, Vol. 4, No. 6, (1983), 193-195, DOI: 10.1109/EDL.1983.25701.
14. Shahidi G. G., Tang D. D., Davari B., Taur Y., McFarland P., Jenkins K., Danner D., Rodriguez M., Megdanis A., Petrillo E., Polcari M. and Ning T. H., "A novel high-performance lateral bipolar on SOI", in ***International Electron Devices Meeting*** (1991), 663-666, DOI: 10.1109/IEDM.1991.235335.
15. Li X., Yang J., Fleetwood D. M., Liu C., Wei Y., Barnaby H. J. and Galloway K. F., "Hydrogen soaking, displacement damage effects, and charge yield in Gated lateral bipolar junction transistors", ***IEEE Transactions on Nuclear Science***, Vol. 65, No. 6, (2018), 1271-1276, DOI: 10.1109/TNS.2018.2837032.
16. Sturm J. C., McVittie J. P., Gibbons J. F. and Pfeiffer L., "A lateral silicon-on-insulator bipolar transistor with a selfaligned Base contact", ***IEEE Electron Device Letters***, Vol. 8, No. 3, (1987), 104-106, DOI: 10.1109/EDL.1987.26567.
17. Jin D., Zhao X., Zhang W., Wang X., Hu R. and Fu O., "Novel superjunction Collector power SiGe HBTs with high thermal stability" in 12th IEEE International Conference on Solid-State and Integrated Circuit Technology, (2014), 1-3, DOI: 10.1109/ICSICT.2014.7021540.
18. Verdonckt-Vandebroek S., Wong S. S., Woo J. C. S., and Ko P. K., "High-gain lateral bipolar action in a MOSFET structure", ***IEEE Transactions on Electron Devices***, Vol. 38, No.11, (1991), 2487-2496, DOI: 10.1109/16.97413.
19. Chen S. M., Fang Y. K., Yeh W. K., Lee I. C. and Chiang Y. T., "A high current gain Gate-controlled lateral bipolar junction transistor with 90 nm CMOS technology for future RF SoC applications", ***Solid-State Electronics***, Vol. 52, No. 8, (2008), 1140-1144, DOI: 10.1016/j.sse.2008.06.003.
20. Wang C., Chen W., Jin X., Liu Y. and Yang. S., "Dependence on Base width and doping concentration of current degradation in Gate-controlled lateral pnp bipolar transistors exposed to reactor neutrons and gamma rays", ***Energy Procedia***, Vol. 127, (2017), 110-119, 10.1016/j.egypro.2017.08.119.
21. Homayoni F., Hosseini S. E. and Baedi J., "A high gain lateral BJT on thin film silicon substrate", in ***IEEE International Conference of Electron Devices and Solid-State Circuits,*** (2009), 278-281, DOI: 10.1109/EDSSC.2009.5394267.
22. Wen J., Wei J., Song Q., Wang G., Zhou C., Wang W., "Design and Simulation of Strained Si/SiGe HBT Architecture with Uniaxially-stressed Collector" in ***International Symposium on Devices, Circuits and Systems*** (2021), 1-4, DOI: 10.1109/ISDCS52006.2021.9397921.
23. Jena M. R., Panda A. K. and Dash G. N., "Cap-layer and charge sheet effect in InP based pnp δ-doped heterojunction bipolar transistor", ***Microsystem Technologies***, Vol. 27, No. 11, (2021), 4035-4040, DOI: 10.1007/s00542-020-04764-2.

Persian Abstract

**چکیده**

ساختار جدیدی برای ترانزیستور دوقطبی اتصال هترو (HBT) مبتنی بر SiGe با استفاده از شبیه‌ساز Silvaco طراحی و شبیه سازی شده است. پایه اضافی در نظر گرفته شده برای این ساختار قابلیت کنترل بهره جریان ترانزیستور را بدست می‌دهد که در نتیجه آن با اعمال ولتاژ به ترمینال گیت، عرض موثر بیس کنترل می‌شود. کاهش عرض بیس منجر به کاهش نرخ بازترکیب حامل‌ها شده و به الکترون‌های پخش شده اجازه می‌دهد شانس بیشتری برای رسیدن به کلکتور داشته باشند. لحاظ کردن پایه اضافی دو رویکرد را در نظر دارد. یکی بهبود بهره جریان ترانزیستور با اعمال ولتاژ ثابت به گیت و دیگری اصلاح ویژگی‌های ترانزیستور بگونه‌ای که بهره جریان بهینه شود. بهره جریان ترانزیستور بدون اعمال ولتاژ گیت حدود ۵۰ است که با در نظر گرفتن تغییرات ولتاژ گیت تا ۷۵۰ برای جریان های کلکتور زیاد و ۵۰۰۰۰ برای جریان های کلکتور کم، افزایش می‌یابد. علاوه بر این، ساختار HBT کنترل شده با گیت پیشنهادی ما با یک گیت بزرگ روی بیس و کلکتور دارای ولتاژ شکست ۸ ولت و فرکانس قطع حدود ۱۱ گیگاهرتز است. همچنین حداکثر ضریب شایستگی ۱۲۰۰ با استفاده از ساختار پیشنهادی به دست می‌آید.

International Journal of Engineering

Journal Homepage: www.ije.ir

# Performance Evaluation of Weighted Feedback Based UPQC under Various Power Quality Issues

K. Bhavya*[a], P. V. V. Rama Rao[b], L. Ravi Srinivas[c]

[a] *Department of Electrical & Electronics Engineering, JNTUK, Kakinada, India*
[b] *Department of Electrical & Electronics Engineering, Maturi Venkata Subba Rao (M.V.S.R) Engineering College, Hyderabad, India*
[c] *Department of Electrical & Electronics Engineering, Gudlavalleru Engineering College, Gudlavalleru, India*

*PAPER INFO*

*Paper history:*
Received 09 February 2022
Received in revised form 17 March 2022
Accepted 23 September 2022

*Keywords*:
*Unified Power Quality Conditioner*
*Weighted Feedback Algorithm*
*Fault Conditions*
*Voltage Source Converter*

*ABSTRACT*

Power efficiency is one of the big issues in the energy sector today. It becomes much more critical with the advent of sophisticated and complex systems, whose output is highly dependent on the efficiency of the power supply. Electronic systems are extremely vulnerable to disturbances, so industrial loads are less tolerant to power quality issues like voltage dips, voltage sags, voltage flickers, harmonics, and load unbalance, among others. For custom power applications, a variety of highly modular controllers that take advantage of newly available power electronics components are currently on the market. This paper introduces the concept of a unified power quality conditioner based on the VSC theorem, which is used to increase power quality. Capacitor banks, a series-active filter, and a shunt active filter make up the model. Negative-sequence current and harmonics are primarily compensated by series-active and shunt-active filters, while capacitor banks are used to compensate the reactive power of power frequency. This paper also includes using a weighted feedback algorithm to manage the PCC parameters as well as the UPQC performance. The proposed architecture has been put through its paces with a variety of distributed systems and fault scenarios. The entire framework was designed and analyzed with the help of MATLAB simulink and code.

***doi**: 10.5829/ije.2023.36.03c.02*

**NOMENCLATURE**

| Symbols | Meaning | Symbols | Meaning |
|---|---|---|---|
| $\beta$ | Angle of voltage | $V_i$ | Series voltage |
| $I_s$ | Specified load power factor | $V_0$ | Output voltage |
| $P_a$ | Active power | $V_s$ | Voltage sag |
| $R_a$ | Reactive power | $W_n$ | Randomized weight |
| $V_A$ | Apparent voltage | $W_{new}$ | new weight |
| $V_{inj}$ | Injected voltage | $W_{old}$ | old weight |

## 1. INTRODUCTION

A power quality issue is a phenomenon that occurs in end-use equipment loss due to nonstandard voltage, current, or frequency. As power electronics-based devices used to improve the power efficiency in distribution networks, modeling and simulation of conventional power conditioner is an important concern [1, 2]. UPQC plays an important role in ensuring the device's proper function. In addition to artificial intelligence-based control schemes, traditional control schemes are commonly used. In addition, some sophisticated mathematical techniques in general, and the wavelet transform in particular, are used to improve power [3] efficiency. There are many research papers based on the applications of fuzzy logic, expert systems, neural networks, and genetic algorithms available in power efficiency. The ANN (Artificial Neural Network)-

*Corresponding Author Email: bhavya.eee.08@gmail.com
(K. Bhavya)

Please cite this article as: K. Bhavya, P. V. V. Rama Rao, L. Ravi Srinivas, Performance Evaluation of Weighted Feedback Based UPQC under Various Power Quality Issues, ***International Journal of Engineering, Transactions C: Aspects,*** Vol. 36, No. 03, (2023) 441-449

based controller is intended for current managing of the shunt-active power filter and was qualified offline by means of data from the proportional-integral regulator. A fully digital controller based on the TMS320F2812 DSP platform is also proposed, which can be used for both comparison generation and control. In another effort, the use of fuzzy logic (FL) [4] inside a micro grid energy infrastructure based on the most recent power conditioning tools systems, such as the Unified Power Quality Conditioner, was proposed (UPQC). Similarly, to coordinate the action of the UPQC's sequence and shunt VSIs, a linear quadratic regulator (LQR) regulation technique [5] entrenched with the ANN is worn. In an additional improvement, a wavelet transform-based control algorithm for UPQC is proposed to repress harmonics in the current and voltage sags. Following that, some authors stress the use of UPQC [6] with a fuzzy logic controller (FLC) and an artificial neural network (ANN) controller on top of the traditional proportional-integral (PI) controller to improve power efficiency. The fortitude of voltage references for series-active power filters was also carried out using a sturdy three-phase optical phase locked loop (PLL) method and a fuzzy regulator. Khadkikar [7] also used the particle swarm optimization (PSO) approach to find the answer to the objective function extracted for minimizing UPQC's actual power injection and constraints. Through using PSO-based data for various voltage sag settings, adaptive neuro fuzzy inference systems were used to get the proposed technique for minimal real power injection with UPQC online. Gravitational search algorithm is used here for power optimization in stability and power quality improvement which depends on the law of gravity and motion. Anwar et al. [8] proposed a technique for current load enhancement using gravitational search algorithm. In this study, gravitational search algorithm focused on optimizing the power quality. However, it exhibits heavy computational overhead for large volume of parameters. Bat algorithm-based power quality improvement is also emerged for investigating power quality issues. Bat algorithm is one of the optimization algorithms proposed by Xin et al. [9]; which was brought from the idea of pulse rate and frequency changes of bats when they were searching for prey. Alam and Arya [10] proposed a steady state linear filter based on bat algorithm for improving power quality in distributed network. Even though bat-based techniques have some advantages in terms of speed, accuracy and execution. However, low exploration is one of main drawback of this algorithm that leads to premature convergence. Ant colony-based optimization is also used previous to sort out the power quality issues which is based on the idea of cooperation and adaptation. Tiwari and Dubey [11] proposed an active power filter based on ant colony algorithm. The work adapted this algorithm to compensate harmonics. However, theoretical analysis of this algorithm if found to be difficult. Although convergence is guaranteed, time taken to achieve the convergence is unpredictable. Many research has been emerged for the power quality issues [10, 12-14], most of the paper focused only on basic functionality features. They cannot cop up with the power quality improvements efficiently. The key goal of this proposed scheme is to increase power efficiency by using a weighted feedback technique to compensate for voltage sag and eliminate harmonics in the distribution network.

The below is how the article is structured: The suggested method is introduced in section I, and the centralized power efficiency conditioner is explained in section II. The topic of the weighted feedback algorithm is covered in section III. The execution of the simulation and discussion of the effects are covered in section IV. The results taken from the proposed work are discussed in section V.

## 2. UNIFIED POWER QUALITY CONDITIONER

The UPQC is a custom power unit that is used in electrical power delivery systems to increase the power efficiency by eliminating various fault conditions such as power fluctuations, various voltage disturbances and many more. Basically, UPQC has 2 insulator-based converters, one converter is placed in series while the other converter is in common DC bus. Present harmonics may be cancelled, reactive power compensated, voltage harmonics eliminated, voltage control improved, voltage and current imbalances corrected, voltage sag or swell corrected, and voltage interruptions avoided using UPQC. Shunt and sequence compensators are also used in UPQC. Present disturbances are cancelled using a shunt compensator, while voltage disturbances are cancelled using a sequence compensator. The shunt compensator could be attached to the series compensator on either side. The aim of a shunt compensator is to attain strictly balanced sinusoidal source currents in phase by way of the supply voltages at the specified magnitude and frequency. Series compensation, on the other side, injects voltage to keep the terminal [1-3] voltage at the defined amount and frequency. Shunt and series compensation is done with voltage source inverters. Both voltage source inverters are powered by a single DC connection capacitor, as can be seen. Using injection transformers, one of the voltage source inverters is connected in parallel to the AC grid, while the other is connected in sequence. The shunt compensation circuit [4] is made up of a parallel connected inverter and its control circuit. The series compensation circuit, on the other hand, is formed by connecting the inverter in series with the appropriate control circuit. The DC capacitor voltage must be at least 150 percent of the maximum line-line supply voltage for the UPQC to work properly. The shunt

compensation [5-7] circuit is made up of a parallel-connected inverter and its control circuit. The series compensation circuit, on the other side, is formed by connecting an inverter in series with a suitable control circuit. The DC capacitor voltage must be at least 150 percent of the maximum line-line supply voltage in order for the UPQC to work properly. The block diagra, of UPQC to PCC is shown in Figure 1.

The expression for the injected voltage of UPQC can be given as follows [8, 10, 11]:

$$V_{inj}^2 = V_0^2 s^2 + 2V_0^2(1-s)(1-\cos\beta) \quad (1)$$

where $V_{inj}$ is the injected voltage by UPQC, $V_0$is the output voltage, $\beta$ is the angle of voltage.
The expression for the apparent power of UPQC can be given as follows:

$$V_A - UPQC = V_0 I_0\left(Q_1(\theta, s, \beta) + Q_2(\theta, \beta)\right) + I_0^2 Q_2^2(\theta, \beta)Z \quad (2)$$

The source voltage of UPQC is used as a reference and is calculated as follows:

$$V_{in}\angle\theta = V_p\angle\beta + V_{ph}\angle\delta \quad (3)$$

It is important to note that for a power factor of considered load and voltage sag necessity, the amount and phase angles of Vp must be re-soluted in order to remain the load voltage at its rated assessment. For Vp, there are an endless number of possibilities.
The expression for load current can be given as follows:

$$I_{in}\angle\theta + I_c\angle\delta = I_{ph}\angle\delta - \theta \quad (4)$$

The angle Ø denotes the load current's (Iph) lagging angle with reference to Vph. Assuming that only the active portion of the load current is supplied by the power supply with $\delta = 0$. The reactive load current portion is ideally the current $I_C$. The suffix "ph" stands for load variables, while "in" stands for supply variables. Suffixes 1 and 2 signify two points in order for UPQC to take place, on the opposite side of the power source.

$$V_{in} = V_{ph1} = V_{in1} = V_0 \quad (5)$$

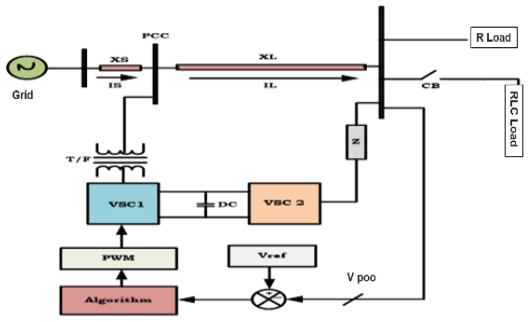


**Figure 1.** Block Diagram of Unified Power Quality Conditioner connected to PCC

The SLCVC current is supplied by $I_{C1}$ in that case, with position of +90; the power factor is presumed to be lagging in progress of the supply voltage. The amount of supply voltage has decreased to $V_{in2}$ in stage 2, requiring the UPQC to work to restore $V_{ph2}$ to its new scale ($|V_{ph1}| = |V_{ph2}|$). This is accomplished by introducing the series voltage $V_{inj}$, and the load voltage is obtained by choosing between 0 and 90, along with the required magnitude of $V_{inj}$.

$$I_{in}cos\beta = I_{ph2}cos\theta \quad (6)$$

The load reactive control is injected if the both of the active filters are still active. Surprisingly, for a specified load power factor, this sagging voltage causes the angle to equal, and thus $I_{S2} = I_{L2}$ can be deduced.

$$I_{s2} = I_{L2} = I_0 \quad (7)$$

The load's active power demand is constant and equal to the source's active power demand:

$$V_s I_s = V_L I_L cos\emptyset \quad (8)$$

In the condition of voltage sag, where $|V_{S2}|<|V_{S1}|$ and s is the voltage sag per unit, then

$$V_{s2} = (1-s)V_{s1} = (1-s)V_0 \quad (9)$$

In a voltage sag, $V_{S1}I_{S1} = V_{L2}I_{L2}$ and $V_{S1}I_{S1} = V_{L2}I_{L2}$ are used to sustain a steady active power.

$$I_{s2} = \frac{V_0 I_L cos\emptyset}{V_0(1-s)} \quad (10)$$

$$I_{s2} = \frac{I_L cos\emptyset}{(1-s)} \quad (11)$$

$$V_{L2}sin \propto = V_{inj}sin\gamma \quad (12)$$

$$V_{L2}cos \propto = V_{s2} + V_{inj}cos\gamma \quad (13)$$

Combining the above equations, it can be attained that,

$$V_{inj}^2 = V_0^2 s^2 + 2V_0^2(1-s)(1-\cos\alpha) \quad (14)$$

The expression for apparent power can be given as follows:

$$V_{inj}I_{s2} = V_0 I_0 cos\emptyset \frac{\sqrt{s^2+2(1-s)(1-cos\alpha)}}{(1-s)} \quad (15)$$

$$I_{c2}cos\alpha = I_{L2} + V_{inj}\sin(\emptyset - \alpha) \quad (16)$$

There by the model for apparent power can be given as follows:

$$I_{c2}V_{L2} + I_{c2}^2 Z = I_{L2}(V_0 \frac{\sin(\emptyset-\propto)}{cos\propto} + I_{L2}\frac{\sin(\emptyset-\propto)^2}{cos\propto}Z) \quad (17)$$

The expression for the total apparent power can be given as follows:

$$V_A - UPQC = V_0 I_0\left(Q_1(\theta, s, \beta) + Q_2(\theta, \beta)\right) + I_0^2 Q_2^2(\theta, \beta)Z \quad (18)$$

$$Q_1(\theta, s, \beta) = \cos\theta \frac{\sqrt{s^2+2(1-s)(1-cos\beta)}}{(1-s)} \quad (19)$$

$$Q_2(\theta, \beta) = \frac{\sin(\emptyset-\beta)}{\cos\beta} \quad (20)$$

When Ø=α, $I_{S2} = I_{L2}$ and $I_{C2} = 0$, the minimum VA is obtained. The optimal injected voltage under these conditions is given by:

$$V_{inj} = V_0\sqrt{s^2 + 2(1-s)(1-cos\emptyset)} \quad (21)$$

Also the expression for advance angle for voltage can be given as follows:

$$sin\gamma = \frac{\sqrt{1-cos^2\alpha}}{\sqrt{s^2+2(1-s)(1-cos\emptyset)}} \quad (22)$$

## 3. WEIGHTED FEEDBACK ALGORITHM

When a system's outputs are redirected back as inputs as part of a cause-and-effect chain that forms a circuit or loop, this is referred to as feedback. The device is said to feedback on itself in this case. The feedback weighted link is a type of network in which nodes' connections form a directed graph in a temporal order. This enables it to behave in a temporally complex manner. These are feed forward networks that can process variable length sequences of inputs by using their internal state (memory). The term "feedback weighted relation" is loosely applied to two broad groups of networks with a common general structure, one with finite impulse and the other with infinite impulse. The action in both types of networks is temporal hierarchical. An infinite impulse-based feedback network is a guided cyclic graph that cannot be unrolled and restored with a purely feed forward system, while a finite impulse feedback system is a directed acyclic diagram that can be unrolled and replaced with a strictly feed forward system. The output of each point is calculated by some non-linear function of the sum of its inputs, and the "signal" at each relation is a real number. Edges are the term for the contacts. In most cases, the weight of inputs and edges changes as learning progresses. The signal intensity at a link is increased or decreased depending on the weight [10, 12-14]. Systems are trained by analyzing instances, each of which includes a known "input" and "effect," creating probability-weighted relations among the two, and storing them within the net's information structure. The discrepancy among the network's processed yield and a target yield is normally used to train a device [15-20]. This is the mistake. The system then updates its weighted correlations using this error value and a learning law. For each adjustment, the system can generate output that is more and more close to the target output. The instruction will be terminated based on such conditions after a reasonable amount of these changes [9, 21-26] have been made. Models do not always converge to a single solution, for a variety of reasons [27, 28]. For example, depending on the cost function and the model, local minima may occur. Second, when starting far from any local minimum, the optimization process cannot guarantee convergence [29-32]. Third, certain approaches become inefficient when dealing with vast amounts of data or criteria [33]. The following are the steps that have been followed in weighted feedback algorithm.

- Randomize weight ($w_n$) for estimation of $x_i$, $y_j$, and $z_k$, where n is the amount of NBCC in the sample with a lot of space.
- Ra's optimal goal must be defined.
- Predictive models should be entered.
- If the predicted output for the cutting combination $x_i$, $y_j$, and $z_k \geq R_a$, then new weight becomes $W_{new} = (R_a W_{old})/xiyjzk$
- If not then $W_{new} = W_{old}$
- Go to step 3 and end the training.

The proposed weighted feedback algorithm as shown in Figure 2 is used to manage the PCC parameters as well as UPQC output. The performance of the proposed algorithm is compared with other state-of-the-art algorithms such as gravitational search algorithm (GSA), the BAT algorithm, and the ANT colony algorithm. From the comparative analysis, we observed that the proposed weighted feedback algorithm performs well than the other algorithms.

## 4. RESULTS AND DISCUSSION

The proposed power system was simulated with UPQC and tested with different test cases such as load switching, fault incidence, and control with four algorithms: weighted feedback algorithm, gravitational search algorithm, ant colony optimization algorithm, and BAT algorithm.

### 4. 1. With Fault Condition in the Power System

At t=0.1s to t=0.65s, the LLL fault was introduced into the system, and different UPQC algorithms were tested.

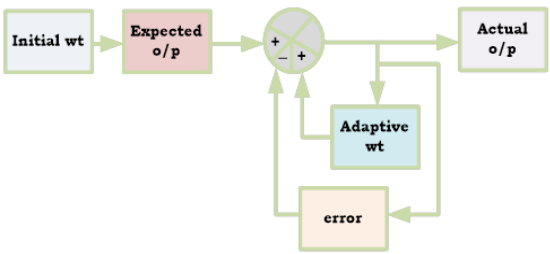


**Figure 2.** Block Diagram of weighted feedback algorithm

**4. 2. Weighted Feedback Algorithm** The UPQC was implemented using the weighted feedback algorithm, and the waveform below depicts PCC parameters such as voltage, current, active strength, reactive power, and power factor under faulted conditions with UPQC. The PCC parameters of the power system under faulted condition with UPQC and WFA is shown in Figure 3.

The voltage has remained almost unchanged, the current has increased to 1.5 times the rated value, the active power has increased to 1.5 times the rated value, and the reactive power has decreased to almost zero.

**4. 3. Gravitational Search Algorithm** For the unified power quality conditioner, the Gravitational Search Algorithm was used, and the waveform below displays the PCC parameters under faulted conditions with UPQC. The PCC parameters of the power system under faulted condition with UPQC and GSA is shown in Figure 4.

The voltage has remained nearly constant, although the current has increased to 1.566 times the rated value, the active power has increased to 1.6 times the rated value, and the reactive power has decreased to nearly zero.

Table 1 shows the perfromance of various algortihms based UPQC under faulted condition in terms of various parameters like voltage, current, active power, reactive power and power factor at the point of common coupling.

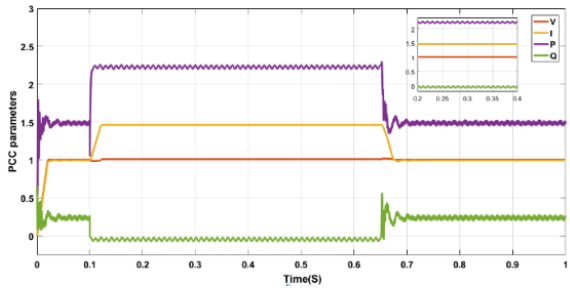


**Figure 3.** PCC Parameters of power system under faulted condition with UPQC and WFA

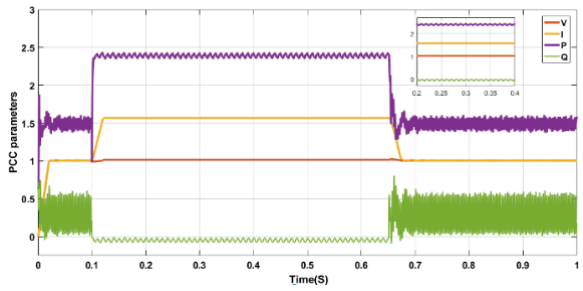


**Figure 4.** PCC Parameters of power system under faulted condition with UPQC and GSA

**TABLE 1.** PCC Parameters with fault, DVR, GSA, BAT, ANT algorithms

| Parameters | Without facts devices | Weighted feedback | GSA | BAT | ANT |
|---|---|---|---|---|---|
| Voltage | 0.256pu | 1.00pu | 0.99pu | 0.98pu | 0.98pu |
| Current | 25.9pu | 1.466pu | 1.566pu | 1.664pu | 1.706pu |
| Active power | 10pu | 2.25pu | 2.43pu | 2.6pu | 2.66pu |
| Reactive power | 0pu | 0pu | 0pu | 0pu | 0pu |
| Power factor | 0.99pu | 1.00pu | 0.999pu | 0.99pu | 0.99pu |

**4. 4. With Wind Based Synchronous Generator** At t=0.1s to t=0.65s, the wind turbine-based synchronous generator was attached to the grid, and various algorithms for UPQC were tested.

**4. 5. Weighted Feedback Algorithm** The weighted feedback algorithm was used to apply the UPQC, and the waveform in Figure 5 shows PCC parameters including voltage, current, active intensity, reactive capacity, and power factor under sudden turbine switching conditions with UPQC.

The voltage has remained almost constant, although the current has increased to 1.1 times the rated value, active power has increased to 1.6 times the rated value, and reactive power has increased to nearly 0.4. It shows smaller ripples during the transition condition but with lesser magnitude.

**4. 6. Gravitational Search Algorithm** For the UPQC, the gravitational search algorithm was used, and the waveform in Figure 6 below displays the PCC parameters for a wind turbine-based synchronous generator connected to the UPQC.

The voltage has remained almost constant, although the current has increased to 1.15 times the rated value, active power has increased to 1.7 times the rated value, and reactive power has increased to nearly 0.5. It shows higher ripples during the transition condition when compared to weighted feedback algorithm.

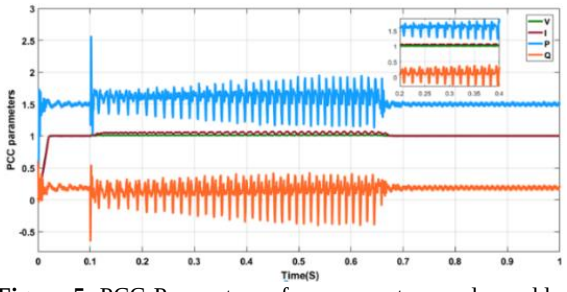


**Figure 5.** PCC Parameters of power system under sudden switching condition with UPQC and WFA

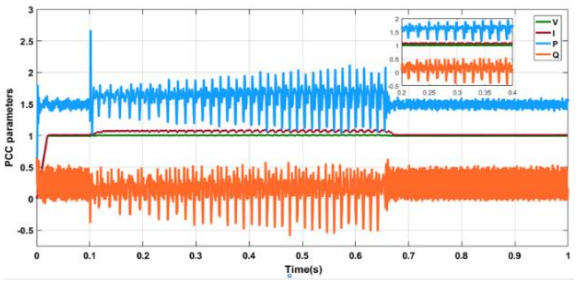


**Figure 6.** PCC Parameters of power system under sudden switching condition with UPQC and GSA

The efficiency of various algorithms-based UPQC in terms of voltage, current, active power, reactive power, and power factor when the turbine is unexpectedly turned on is seen in the Table 2 where weighted feedback algorithms outperforms other algorithms.

**4. 7. With Wind Based Induction Generator** At t=0.1s to t=0.65s, a wind turbine-based induction generator was attached to the grid, and various algorithms for UPQC were tested.

**4. 8. Weighted Feedback Algorithm** The waveform in Figure 7 shows PCC parameters such as voltage, current, active rpm, reactive capacity, and power factor with UPQC using the weighted feedback algorithm under sudden turbine switching conditions.

The voltage has remained virtually constant although the current has increased to 1.25 times the rated value, active power has increased to 1.2 times the rated value,

**TABLE 2.** PCC Parameters with synchronous generator, DVR, GSA, BAT, ANT algorithms

| Parameter | Without Facts | Weighted feedback | GSA | BAT | ANT |
|---|---|---|---|---|---|
| Voltage | 0.98pu | 1.02pu | 1.01pu | 1.009pu | 1.003pu |
| Current | 1.249pu | 1.05pu | 1.09pu | 1.11pu | 1.2pu |
| Active power | 1.81pu | 1.8pu | 1.9pu | 2.01pu | 2.35pu |
| Reactive power | 0.4pu | 0.35pu | 0.51pu | 0.57pu | 0.41pu |
| Power factor | 0.98pu | 0.99pu | 0.98pu | 0.975pu | 0.971pu |

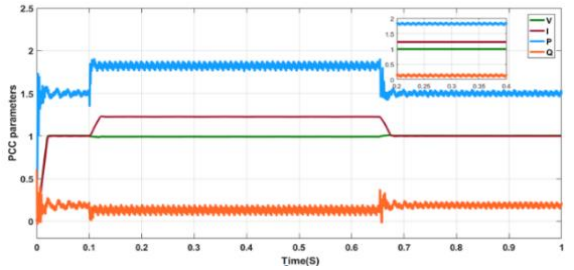


**Figure 7.** PCC Parameters of power system under sudden switching condition with UPQC and WFA

and reactive power has increased to approximately 0.2. It shows smaller ripples of lesser magnitude during the transition state.

**4. 9. Gravitational Search Algorithm** The Weighted Feedback Algorithm was used for the UPQC, and the waveform in Figure 8 shows the PCC parameters with the UPQC connected to a wind turbine-based induction generator. The voltage has remained almost constant although the current has increased to 1.37 times the rated value, active power has increased to 1.7 times the rated value, and reactive power has increased to 0.42. It has more ripples during the transition process than the weighted feedback algorithm.

Table 3 summarized the performance of different algorithms-based UPQC in terms of voltage, current, active power, reactive power, and power factor when the turbine is turned on suddenly. From the analysis, it is observed that the weighted feedback outperforms other algorithms.

**4. 10. With RLC (Resistive, Inductive, and Capacitive) load** The RLC load has been connected to the system at t=0.1s to t=0.65s and various algorithms have been tested for UPQC.

**4. 11. Weighted Feedback Algorithm** For the UPQC, the Weighted Feedback Algorithm was used, and the waveform below displays the PCC parameters with the RL load connected to the UPQC. The PCC parameters of the power system under faulted condition with UPQC and WFA is shown in Figure 9.

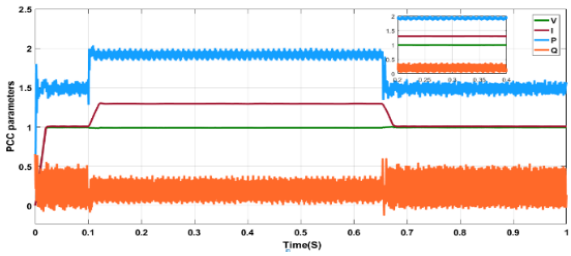


**Figure 8.** PCC Parameters of power system under sudden switching condition with UPQC and GSA

**TABLE 3.** PCC Parameters with induction generator, DVR, GSA, BAT, ANT algorithms

| Parameter | Without Facts | Weighted feedback | GSA | BAT | ANT |
|---|---|---|---|---|---|
| Voltage | 0.935pu | 0.992pu | 0.989pu | 0.987pu | 0.965pu |
| Current | 2pu | 1.225pu | 1.297pu | 1.315pu | 1.362pu |
| Active Power | 2.4pu | 1.88pu | 2.01pu | 2.025pu | 2.1pu |
| Reactive Power | 1.5pu | 0.2pu | 0.36pu | 0.39pu | 0.18pu |
| Power factor | 0.5pu | 0.996pu | 0.994pu | 0.993pu | 0.996pu |

While the current has increased to 1.01 times the rated value, active power has increased to 1.05 times the rated value, and reactive power has increased to approximately 0.2, the voltage has remained relatively unchanged.

**4. 12. Gravitational Search Algorithm** The gravitational search Algorithm has been used for the UPQC and below waveform in Figure 10 shows the PCC parameters with connection of RLC load with UPQC.

While the current has increased to 1.01 times the rated value, active power has increased to 1.1 times the rated value, and reactive power has increased to 0.47, the voltage has remained nearly unchanged. During the transformation phase, it has more ripples than the weighted feedback algorithm.

From Table 4, we came to know that the weighted feedback algorithm is comparatively better than the other algorithms in terms of voltage, current, active power, reactive power, and power factor.

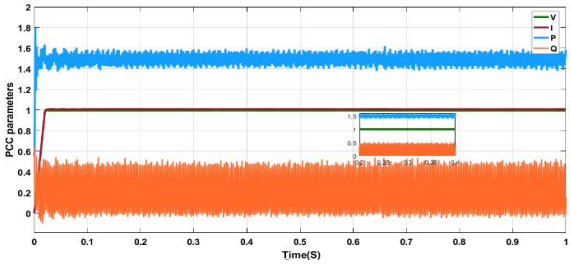


**Figure 9.** PCC Parameters of power system under sudden switching condition with UPQC and WFA

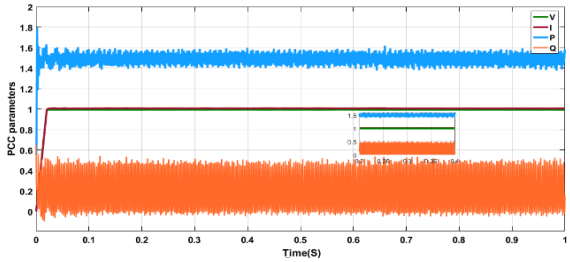


**Figure 10.** PCC Parameters of power system under sudden switching condition with UPQC and GSA

**TABLE 4.** PCC Parameters with RLC load, DVR, GSA, BAT, ANT algorithms

| Parameter | Without Facts | Weighted feedback | GSA | BAT | ANT |
|---|---|---|---|---|---|
| Voltage | 0.998pu | 1pu | 0.996pu | 0.996pu | 0.995pu |
| Current | 1.018pu | 1pu | 1.01pu | 1.015pu | 1.025pu |
| Active power | 1.526pu | 1.54pu | 1.58pu | 1.61pu | 1.85pu |
| Reactive power | 0.0001pu | 0.22pu | 0.5pu | 0.51pu | 0.36pu |
| Power factor | 0.999pu | 0.99pu | 0.98pu | 0.979pu | 0.97pu |

## 5. CONCLUSION

In this article, the idea of a unified power quality conditioner based on the VSC theorem is explored and designed. The PCC parameters as well as the UPQC output are managed using a weighted feedback algorithm in this article. In addition to UPQC, three other algorithms, namely the gravitational search algorithm, the BAT algorithm, and the ANT colony algorithm, were investigated. In addition, a comparison of all four algorithms for UPQC has been made in terms of voltage, current, active power, reactive power, and power factor, with the weighted feedback algorithm outperforming the others under different test conditions. The proposed system is implemented in MATLAB Simulink and the performance of the whole system is evaluated under various operating procedures. The model is further tested for PCC parameters against various conditions. By observing the waveforms, the proposed model proves that the weighted feedback based UPSC is efficient for power quality improvement. As part of the future work, we plan to investigate the performance of the proposed model by combining several algorithms in addition to the abovementioned algorithms.

## 6. REFERENCES

1. Fagundes, S.M. and Mezaroba, M., "Reactive power flow control of a dual unified power quality conditioner", in IECON 2016-42nd Annual Conference of the IEEE Industrial Electronics Society, IEEE., (2016), 1156-1161.
2. Sindhu, S., Sindhu, M. and Nambiar, T.P., "Implementation of photovoltaic integrated unified power conditioner for power quality enhancement", in 2016 IEEE International Conference on Power Electronics, Drives and Energy Systems (PEDES), IEEE., (2016), 1-6.
3. Swain, S.D., Ray, P.K. and Mohanty, K.B., "Improvement of power quality using a robust hybrid series active power filter", ***IEEE Transactions on Power Electronics***, Vol. 32, No. 5, (2016), 3490-3498. https://doi.org/10.1109/tpel.2016.2586525
4. Soukhtekouhi, M.R., Hamzeh, M. and Iman-Eini, H., "Performance improvement of unified power quality conditioner under various load, source, and line conditions using a new control method", in 2020 11th Power Electronics, Drive Systems, and Technologies Conference (PEDSTC), IEEE., (2020), 1-6.
5. Gupta, N., "Artificial neural network and synchrosqueezing wavelet transform based control of power quality events in distributed system integrated with distributed generation sources", ***International Transactions on Electrical Energy Systems***, Vol. 31, No. 10, (2021), e12824.
6. Farooqi, A., Othman, M.M., Abidin, A.F., Sulaiman, S.I. and Radzi, M.A.M., "Mitigation of power quality problems using series active filter in a microgrid system", ***International Journal of Power Electronics and Drive Systems***, Vol. 10, No. 4, (2019), 2245.
7. Khadkikar, V., "Enhancing electric power quality using upqc: A comprehensive overview", ***IEEE Transactions on Power Electronics***, Vol. 27, No. 5, (2011), 2284-2297.
8. Siddiqui, A.A., Deb, T. and Singh, M., "Improved gravitational search algorithm for loadability enhancement of transmission

lines using upfc", ***International Journal of System Assurance Engineering and Management***, Vol. 5, No. 3, (2014), 444-449. doi: 10.1109/INDICON.2015.7443412.

9. Xin, Q., Wang, C., Chen, C.-Y., Yang, G. and Chen, L., "Robust vibration control based on rigid-body state observer for modular joints", ***Machines***, Vol. 9, No. 9, (2021), 194.
10. Alam, S.J. and Arya, S.R., "Control of upqc based on steady state linear kalman filter for compensation of power quality problems", ***Chinese Journal of Electrical Engineering***, Vol. 6, No. 2, (2020), 52-65.
11. Tiwari, A.K. and Dubey, S.P., "Ant colony optimization based hybrid active power filter for harmonic compensation", in 2016 International Conference on Electrical, Electronics, and Optimization Techniques (ICEEOT), IEEE., (2016), 777-782.
12. Chandrakala Devi, S., Singh, B. and Devassy, S., "Modified generalised integrator based control strategy for solar pv fed upqc enabling power quality improvement", ***IET Generation, Transmission & Distribution***, Vol. 14, No. 16, (2020), 3127-3138. https://doi.org/10.1049/iet-gtd.2019.1939
13. Errouissi, R., Shareef, H. and Awwad, F., "Disturbance observer-based control for three-phase grid-tied inverter with lcl filter", ***IEEE Transactions on Industry Applications***, Vol. 57, No. 5, (2021), 5411-5424. doi: 10.1109/TIA.2021.3088391.
14. Errouissi, R., Shareef, H. and Wahyudie, A., "A novel design of pr controller with antiwindup scheme for single-phase interconnected pv systems", ***IEEE Transactions on Industry Applications***, Vol. 57, No. 5, (2021), 5461-5475. doi: 10.1109/TIA.2021.3094490.
15. Aiswarya, M., Ilango, K., Manitha, P. and Nair, M.G., "Simulation analysis of modified dc bus voltage control algorithm for power quality improvement on distributed generation systems", in 2014 Power and Energy Systems: Towards Sustainable Energy, IEEE., (2014), 1-5.
16. Hagh, M.T. and Sabahi, M., "A single phase unified power quality conditioner (upqc)", in 2016 IEEE international conference on power system technology (POWERCON), IEEE., (2016), 1-4.
17. Vijayasamundiswary, S. and Baskaran, J., "A novel approach to nine switch unified power quality conditioner for power quality improvement", in 2017 International Conference on Innovative Research In Electrical Sciences (IICIRES), IEEE., (2017), 1-5.
18. Sinku, R.K., "Study of unified power quality conditioner for power quality improvement", (2015),
19. Silas, S., Rajsingh, E.B. and Issac, T., "Wasf—weighted average based subjective feedback system for e-healthcare services", in 2016 2nd International Conference on Next Generation Computing Technologies (NGCT), IEEE., (2016), 35-39.
20. Zhao, J., Liao, X., Wang, S. and Chi, K.T., "Kernel least mean square with single feedback", ***IEEE Signal Processing Letters***, Vol. 22, No. 7, (2014), 953-957.
21. Sharma, N. and Mishra, S., "A new approach for efficient siso equalizer with modified least mean square algorithm", in 2017 International Conference on Innovations in Information, Embedded and Communication Systems (ICIIECS), IEEE., (2017), 1-6.
22. Paramanik, S., Sarker, K., Chatterjee, D. and Goswami, S., "Smart grid power quality improvement using modified upqc", in 2019 Devices for Integrated Circuit (DevIC), IEEE., (2019), 356-360.
23. Bhosale, S.S., Bhosale, Y., Chavan, U.M. and Malvekar, S.A., "Power quality improvement by using upqc: A review", in 2018 International conference on control, power, communication and computing technologies (ICCPCCT), IEEE., (2018), 375-380.
24. Bueno-Contreras, H., Ramos, G.A. and Costa-Castelló, R., "Power quality improvement through a upqc and a resonant observer-based mimo control strategy", ***Energies***, Vol. 14, No. 21, (2021), 6938.
25. Rajendran, M., "Comparison of various control strategies for upqc to mitigate pq issues", ***Journal of The Institution of Engineers (India): Series B***, Vol. 102, No. 1, (2021), 19-29.
26. Ramos, G.A., Ruget, R.I. and Costa-Castelló, R., "Robust repetitive control of power inverters for standalone operation in dg systems", ***IEEE Transactions on Energy Conversion***, Vol. 35, No. 1, (2019), 237-247.
27. Sundarabalan, C.K., Puttagunta, Y. and Vignesh, V., "Fuel cell integrated unified power quality conditioner for voltage and current reparation in four-wire distribution grid", ***IET Smart Grid***, Vol. 2, No. 1, (2019), 60-68. https://doi.org/10.1049/iet-stg.2018.0148
28. Akagi, H., Kanazawa, Y. and Nabae, A., "Instantaneous reactive power compensators comprising switching devices without energy storage components", ***IEEE Transactions on Industry Applications***, Vol., No. 3, (1984), 625-630.
29. Hassanpour, H. and Ehsanian, M., "Fast grid voltage synchronization using modified fll in single-phase grid-connected power systems", ***International Journal of Engineering, Transactions C: Aspects,*** Vol. 34, No. 6, (2021), 1430-1437. doi: 10.5829/ije.2021.34.06c.06.
30. Ahmadi, M., Sharafi, P., Mousavi, M.H. and Veysi, F., "Power quality improvement in microgrids using statcom under unbalanced voltage conditions", ***International Journal of Engineering, Transactions C: Aspects,*** Vol. 34, No. 6, (2021), 1455-1467. doi: 10.5829/ije.2021.34.06c.09.
31. Gupta, P. and Pandey, R., "Dual output voltage differencing buffered amplifier based active-c multiphase sinusoidal oscillator", ***International Journal of Engineering, Transactions C: Aspects,*** Vol. 34, No. 6, (2021), 1438-1444. doi: 10.5829/ije.2021.34.06c.07.
32. Basit, M.A., Dilshad, S., Badar, R. and Sami ur Rehman, S.M., "Limitations, challenges, and solution approaches in grid-connected renewable energy systems", ***International Journal of Energy Research***, Vol. 44, No. 6, (2020), 4132-4162. doi: 10.1002/er.5033.
33. Mallesham, G. and Siva Kumar, C., Power quality improvement of weak hybrid pemfc and scig grid using upqc, in Advances in decision sciences, image processing, security and computer vision. 2020, Springer.406-413.

Persian Abstract

**چکیده**

بهره وری انرژی یکی از مسائل مهم در بخش انرژی امروزه است. با ظهور سیستم های پیچیده، که خروجی آنها به شدت به کارایی منبع تغذیه بستگی دارد، بسیار حیاتی تر می شود. سیستم های الکترونیکی به شدت در برابر اختلالات آسیب پذیر هستند، بنابراین بارهای صنعتی نسبت به مسائل کیفیت توان مانند افت ولتاژ، کاهش ولتاژ، سوسو زدن ولتاژ، هارمونیک ها و عدم تعادل بار و غیره تحمل کمتری دارند. برای کاربردهای برق سفارشی، انواع مختلفی از کنترلرهای بسیار ماژولار که از قطعات الکترونیکی قدرت جدید در دسترس بهره می برند، در حال حاضر در بازار هستند. این مقاله مفهوم یک تهویه کننده کیفیت توان یکپارچه را بر اساس قضیه VSC معرفی می کند که برای افزایش کیفیت توان استفاده می شود. بانک های خازن، فیلتر سری فعال و فیلتر فعال شنت مدل را تشکیل می دهند. جریان و هارمونیک های دنباله منفی در درجه اول توسط فیلترهای فعال سری و شنت فعال جبران می شوند، در حالی که از بانک های خازن برای جبران توان راکتیو فرکانس توان استفاده می شود. این مقاله همچنین شامل استفاده از یک الگوریتم بازخورد وزنی برای مدیریت پارامترهای PCC و همچنین عملکرد UPQC است. معماری پیشنهادی با انواع سیستم های توزیع شده و سناریوهای خطا در مراحل خود قرار گرفته است. کل فریم ورک با کمک شبیه‌لینک و کد MATLAB طراحی و تحلیل شد.

International Journal of Engineering

Journal Homepage: www.ije.ir

# Experimental Investigation of the Effects of using Waste Rubber Ash on Mechanical Properties of Plain Concrete

H. Nikkhah, H. R. Tavakoli*, N. Fallah

*Department of Civil Engineering, Babol Noshirvani University of Technology, Babol, Iran*

*P A P E R I N F O*

*Paper history:*
Received 18 April 2022
Received in revised form 29 October 2022
Accepted 03 November 2022

*Keywords*:
*Tire Rubber Ash*
*Mechanical Properties*
*Compressive Strength*
*Elasticity Modulus*
*Bending Strength*

*A B S T R A C T*

In this study, the effects of using rubber ash on the mechanical properties of plain concrete were experimentally investigated. The main purpose of this study was to determine the proper fraction of rubber ash to be utilized in concrete by investigating the mechanical properties of concrete such as elasticity modulus, compressive strength, tensile strength, bending strength, and fresh concrete slump. Four different fractions of rubber ash (2.5, 5, 7.5 and 10% of cement weight) were added to the concrete mixture. Based on the results achieved from the tests conducted on the specimens, it could be deduced that adding rubber ash to concrete considerably increased compressive and bending strength and reduced the slump flow. It also increased tensile strength and elasticity modulus at a lower level.

***doi**: 10.5829/ije.2023.36.03c.03*

**NOMENCLATURE**

| | |
|---|---|
| TRA | Tire Rubber Ash |

## 1. INTRODUCTION

For several years, concrete has been known as a compatible material that is generally used in the construction industry. Concrete has some weaknesses like its brittle nature that limits its usage in some conditions. There have also been some concerns about the coexistence of concrete with nature and its environmental impacts. For this reason, many attempts have been made at making durable concrete with no need for repair and rehabilitation with the lowest environmental impacts [1-3].

Today, the development of the auto industries in the world has increased the production of tires and rubbers and has led to a tremendous increase in the utilization of polymeric materials. The low decomposition rate and failure in the recycling process of tire rubber have been a huge problem for the environment. Thus, it is necessary to use optimally these wastes [4].

Direct replacement of the rubber in the concrete as fine or coarse aggregates is one of the solutions proposed by researchers [5, 6]. It was found that if the materials are produced in smaller sizes, the bonds they make with other phases around them would be much stronger than when they are produced in larger sizes [7]. However, the results from previous studies indicate the fact that the direct use of rubber will severely reduce the strength of the concrete [8-14].

Al-Akhras and Smadi [15] added tire rubber ash (TRA) as filler in the concrete mortar. By conducting some tests, they resolved that by adding TRA, the air content of the mortar reduces, both primary and secondary setting times of concrete increase, and its resistance against freeze-thaw cycles increases as well. They declared that the reason for such improvement in the mortar properties is due to the filling role of rubber ash and the considerable amount of silica in this material.

In addition, Tavakoli and Rahimpour [16] investigated the influence of rubber ash on shotcrete concrete. The results of their research indicated that the tensile strength of concrete is simultaneously increased by increasing the content of rubber ash. The presence of

* Corresponding author, E-mail address: tavakoli@nit.ac.ir
(H. Tavakoli)

Please cite this article as: H. Nikkhah, H. R. Tavakoli, N. Fallah, Experimental Investigation of the Effects of using Waste Rubber Ash on Mechanical Properties of Plain Concrete, ***International Journal of Engineering, Transactions C: Aspects,*** Vol. 36, No. 03, (2023) 450-456

sulfone links make the silica network more orderly and increase the cement matrix strength. According to their results, the high fineness of rubber ash and its filler role causes an increase in concrete strength [17].

It is worth mentioning that in Tavakoli et al. [16]'s research, the effect of rubber ash on the durability of concrete containing rubber ash (with soda solution and salt ink for 70 days) was investigated, and the results showed that the durability of concrete containing rubber ash is good.

Senin et al. [18] investigated and compared the physical and chemical properties of rubber ash and sand. By comparing the results obtained from the Scanning Electron Microscope (SEM) test, they declared that the surface of rubber ash is more irregular than sand and this improves the cement matrix. Furthermore, rubber ash has nano dimensions that properly fill the voids in the mortar of the concrete. Generally, they concluded that the rubber ash is a proper replacement for sand in the concrete.

Although there have been several investigations on the effects of TRA on the properties of concrete; to the authors' knowledge, there have been no experimental studies made to investigate the mechanical properties of concrete specimens with different percentages of rubber ash used as filler.

Four different percentages of cement weight were selected for adding TRA to the concrete mixture (2.5, 5, 7.5, and 10%). In this study, while two other percentages were only used for the compressive strength test (15% and 20%) to determine the optimum percentage of TRA in concrete. Tests were carried out on fresh concrete as well as cubic, cylindrical and rectangular specimens and slump-flow, elasticity modulus, compressive strength, tensile strength, and bending strength were analyzed. Some valuable results were obtained from the analysis.

## 2. EXPERIMENTAL STUDY

### 2. 1. Materials

**2. 1. 1. Cement** In this study, ordinary type 2 Portland cement was used. Table 1 presents the primary properties of this material.

**2. 1. 2. Aggregates** For this test, a coarse aggregate with a maximum dimension of 12.5 mm and fine aggregate with a maximum dimension of 4.75 mm and sand equivalent (SE) of 96%, and a fineness modulus of 3.1 was adopted. The gradation curves for coarse and fine aggregates are depicted in Figure 1 and are both in the range of the ASTM standard [19]. In addition, the water absorption capacity of the aggregates is shown in Table 1.

**TABLE 1.** Physical and mechanical properties of cement, aggregates, rubber ash

| Analysis | Results |
|---|---|
| Setting time (min) of OPC cement | Initial time – 120<br>Final time – 230 |
| Compressive strength (MPa) of OPC cement | 3 Days – 24<br>7 Days – 34<br>28 Days – 43 |
| Water absorption of coarse aggregate | 0.5% |
| Water absorption of fine aggregate | 0.5% |
| Water absorption of rubber ash | 0.3% |

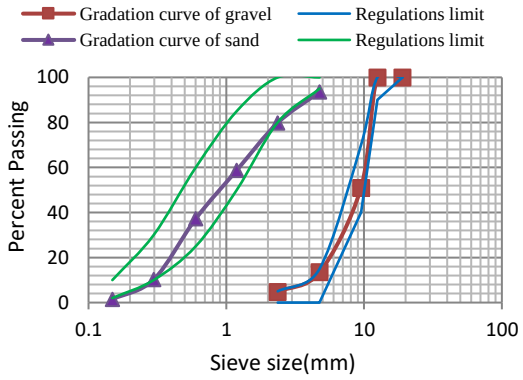


**Figure 1.** Gradation curve for used gravel and sand

**2. 1. 3. Waste Tire Rubber Ash** This is a black material with a relative density of 0.455. The first step in this study was to determine the optimum temperature at which rubber should be burned. This was necessitated by the fact that there are few studies about waste tire rubber ash as an additive in concrete. For this purpose, the compressive test was conducted on 28-day cubic specimens containing rubber ashes that were burnt at temperatures from 350 to 900°C, and from the results, the optimum temperature was obtained.

**2. 2. Mixture Proportions** A concrete mix design with a water to cement ratio of 0.61 was obtained and based on ACI C211 guideline, rubber ash was added as an additive to concrete with the fractions of 2.5, 5, 7.5, and 10% of cement weight, respectively (Table 2). The fractions of 15% and 20% were only tested under the compressive strength test.

**2. 3. Specimens Properties** For conducting compressive tests, fifteen cubic concrete specimens with a cross-section of 100x100mm were fabricated. In addition, fifteen other cylindrical specimens with a

**TABLE 2.** Mixing proportions of concrete (kg/m$^3$)

| Design name | Tire rubber ash (Percent of cement weight) | Cement | Water | Gravel | Sand |
|---|---|---|---|---|---|
| Ref | - | 363 | 222 | 924 | 1000 |
| TRA2.5 | 2.5% | 363 | 222 | 924 | 1000 |
| TRA5 | 5% | 363 | 222 | 924 | 1000 |
| TRA7.5 | 7.5% | 363 | 222 | 924 | 1000 |
| TRA10 | 10% | 363 | 222 | 924 | 1000 |
| TRA15 | 15% | 363 | 222 | 924 | 1000 |
| TRA20 | 20% | 363 | 222 | 924 | 1000 |

diameter of 150 mm and a height of 300 mm were made for the tensile strength test (Figure 2).

To evaluate the bending strength parameter, fifteen unreinforced concrete specimens with a cross-section of 100x100 mm and a height of 840 mm were fabricated. Table 3 describes the number and the type of specimens used for each test.

**2. 4. Loading Program and Apparatus** To conduct the compressive test, 21 cubic specimens were applied to compressive loading according to the ASTM C39 standard. As 7 different mix designs were selected for this study, each mix design was tested three times and from the average of the results, the amount of compressive strength was obtained. The loading apparatus used for the compressive strength test in this study is presented in Figure 3.

**TABLE 3.** Details and properties of the test specimens.

| Type of test | Number of specimens | Shape of specimen | Dimension (mm) |
|---|---|---|---|
| Compressive strength | 21 | Cubic | 100x100x100 |
| Tensile strength | 15 | cylindrical | 300x150 |
| Bending strength | 15 | Grooved beam | 100x100x840 |
| Temperature determination of TRA | 9 | Cubic | 100x100x100 |

**Figure 2.** The process of making cubic specimens for compressive tests

For the tensile strength test, the Brazilian tensile strength test was conducted on 15 cylindrical specimens according to ASTM C496. The loading apparatus and tested specimens for this test are depicted in Figure 4.

UTM[1] as completely depicted in Figure 5 is the loading apparatus used for the bending strength test. According to the ASTM C78 standard, 15 grooved concrete beam specimens were applied to bending loading.

## 3. DISCUSSION AND RESULTS

**3. 1. Ash FTIR Analysis** The FTIR spectrum of concrete with rubber as is illustrated in Figure 6. Results from FTIR spectroscopic tests showed the presence of a sulfone peak in the concrete containing rubber ash.

**3. 2. Slump** The slump-flow test was conducted on fresh concrete for different mix designs according to ASTM C143 standard. Figure 7 indicates the effect of

**Figure 3.** Loading apparatus for the compressive strength test

**Figure 4.** Loading apparatus and specimens for the tensile strength test

[1] Hydraulic Universal Testing Machine

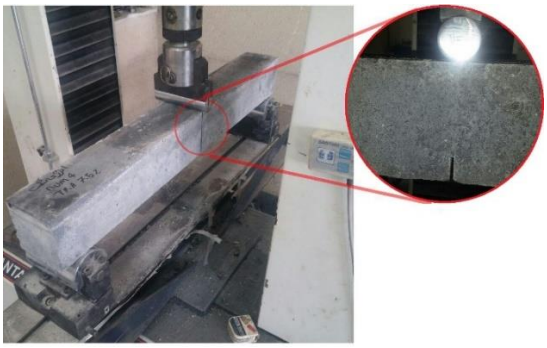

**Figure 5.** Test setup of bending strength test (Universal testing machine)

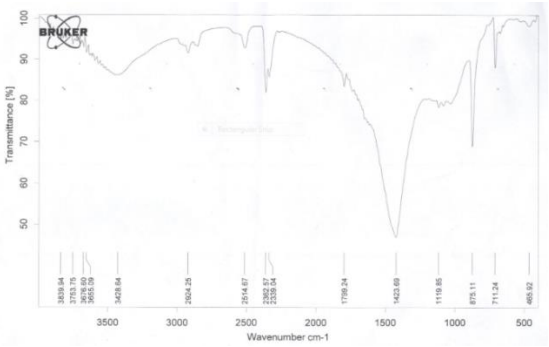


**Figure 6.** FTIR Images of spectrometric test of concrete with rubber ash

adding rubber ash on the slump of fresh concrete. It could be claimed from the obtained values that the slump of fresh concrete is reduced by increasing the percentage of rubber ash. The slump for the reference mix design was 110 mm but for concrete containing 10% rubber ash, it was measured to be about 30 mm.

For concrete mix designs of TRA2.5, TRA5, TRA7.5, and TRA10, the reduced percentage of a slump than reference mix design is equal to 18, 32, 45, and 73%, respectively. The reason for this increment in the slump amount is due to fine particles of rubber ash, its higher specific surface, and its filler role in concrete. The chemical properties of rubber ash are such that it could result in severe adhesion in the concrete.

**3. 3. Elasticity Modulus** The elasticity modulus test was conducted on concrete cylindrical specimens with dimensions of 150x300 mm by the installation of a strain gauge on them. Since human errors could be involved during the calculation of choral elasticity modulus, secant elasticity modulus has also been calculated for all mix designs. The results obtained from this test are indicated in Figure 8.

The results obtained from the elasticity modulus test indicated that by increasing the rubber ash content in the specimens, the modulus of elasticity would have an ascending trend such that for a specimen with 10% rubber ash, the choral elasticity modulus would increase up to 14% and secant elasticity modulus would also increase up to 15% than the Ref mix design.

**3. 4. Compressive Strength** In this study, the compressive strength of concrete is presented as the determinative parameter. Therefore, two more fractions (15% and 20%) of rubber ash were tested in this section for a comprehensive result and to reach an optimum percent of rubber ash in concrete. The test was conducted on cubic specimens of 100 mm with two setting periods of 7 and 28 days. Figure 9 indicates the obtained average values for the compressive strength of different fractions of rubber ash. By increasing the rubber ash up to 15% and 20%, the compressive strength will have a descending trend. The obtained amounts of compressive strength for both 7 and 28-day specimens and every mix design are listed in Table 4.

For the different fractions of rubber ash from 2.5 to 20%, the amount of increase in compressive strength compared to the Ref mix design for specimens of 7 days was 6.6, 13, 22, 38, 20, and 13% and for specimens of 28 days were 8, 16, 22, 35, 21.5 and 9%, respectively. The reason for this increase in compressive strength is that the fine particles of rubber ash fill the voids between aggregates. Furthermore, these particles have silica in

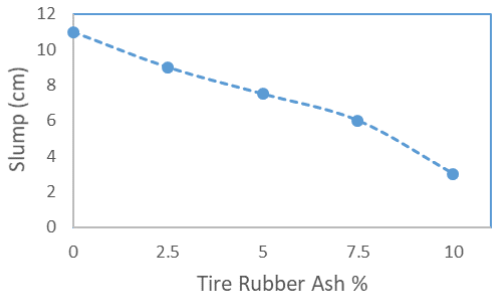


**Figure 7.** The slump of fresh concrete based on the rubber ash percentage

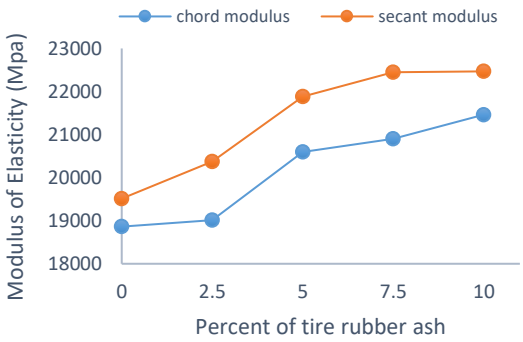


**Figure 8.** Secant and choral modulus for different percentages of rubber ash

**TABLE 4.** Compressive strength of 7 and 28-day specimens.

| Mix design | 7-day compressive strength (Mpa) | 28-day compressive strength (Mpa) |
|---|---|---|
| Ref | 21.95 | 31.26 |
| TRA2.5 | 23.4 | 33.79 |
| TRA5 | 24.78 | 36.21 |
| TRA7.5 | 26.72 | 38.33 |
| TRA10 | 30.32 | 42.2 |
| TRA15 | 26.3 | 38 |
| TRA20 | 24.8 | 34.1 |

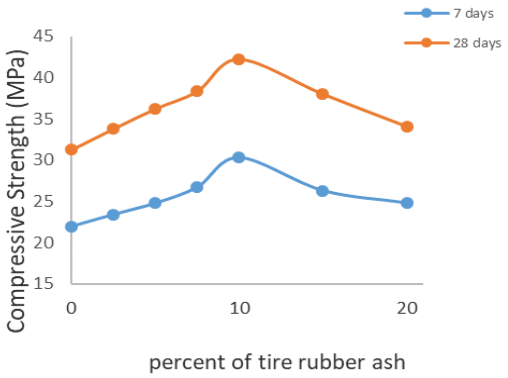


**Figure 9.** Compressive strength of specimens containing different percentages of rubber ash

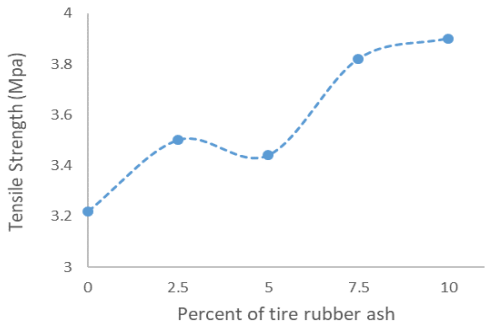


**Figure 10.** Tensile strength for halving the samples containing different percentages of rubber ash

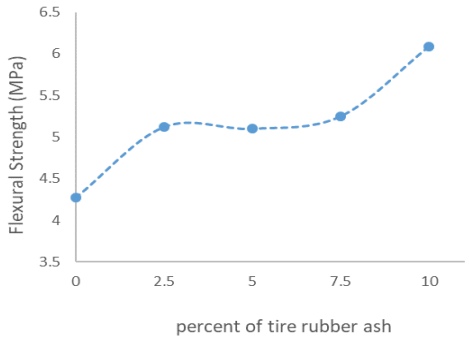


**Figure 11.** Bending strength for different percentages of rubber ash

their chemical compound which increases the strength of concrete as well. However, by increasing the rubber ash by over 10%, the gap between aggregates would increase more than the normal size thereby causing the concrete's transition zone to become weak and thus, resulting to lower compressive strength.

**3. 5. Tensile Strength** Brazilian tensile strength test was conducted on 28-day cylindrical specimens (150 × 300 mm) and the results obtained from this test are depicted in Figure 10. As demonstrated in the diagram, the tensile strength of the specimens increased with the increase of rubber ash. As for TRA10, the tensile strength of the concrete increased up to 21% than the to mix design.

By increasing the percentage of rubber ash, the transition zone of the concrete will be improved causing the tensile strength of the specimens to increase. Adding rubber ash to a concrete mixture also prevents cracks and micro-cracks propagation and as a result, concrete would be promoted against tensile strength.

**3. 6. Bending Strength** The bending strength test was conducted on beam specimens with dimensions 100× 100× 500mm based on ASTM C293. Figure 11 indicates the effects of adding different fractions of rubber ash on the flexural strength of unreinforced beam specimens. When up to 10% of rubber ash was added to the concrete, the bending strength of the concrete increased from 4.27 to 6.09 Mpa.

By increasing the rubber ash in concrete specimens up to 2.5, 5, 7.5, and 10%, the bending strength of the concrete increased to 20, 19.5, 23, and 42%, respectively compared to reference mix design. The increase in bending strength of the specimens is due to the co-operation of the physical and chemical properties of rubber ash such that the physical properties of this material cause the existing voids in the concrete to be filled. Thus, it results in denser concrete with a strong transition zone. Furthermore, the chemical properties of rubber ash are due to the presence of silica. This is the main factor responsible for the increase in concrete strength as well as the creation of Sulfone bonds in concrete, causing the regularity of the silica network and increasing the matrix strength of the cement.

## 4. CONCLUSION

In this study, experimental evaluations were performed to evaluate the effects of adding waste tire rubber ash to

concrete by measuring the mechanical properties of the specimens. Based on the results obtained, the following conclusions can be drawn:

Increasing the percentage of rubber ash, leads to a lower slump for fresh concrete. As for the TRA 10% mix design, there would be a decrease of up to 73% in the slump.

The choral and secant elasticity modulus of the concrete will have ascending trend by increasing the rubber ash content such that by adding 10% rubber ash to concrete, the choral elasticity modulus increased up to 14%, and the Secant elasticity modulus increased up to 15%.

During setting periods of 7 and 28 days, the compressive strength of the specimens increased by increasing the content of rubber ash up to 10%. However, by increasing the rubber ash by more than 10%, the concrete strength would have a descending trend. It can be stated that 10% of rubber ash is the optimum amount of rubber ash that shows the best performance of concrete.

The bending strength of the concrete indicates an ascending trend by increasing the rubber ash content such that by increasing TRA up to 10%, the bending strength of concrete increases up to 42% more than the Ref mix design.

## 5. ACKNOWLEDGMENTS

This research was funded by the Babol Noshirvani University of Technology under Grant No. BUT/388011/1401.

## 6. REFERENCES

1. Darwin, D., Mindess, S. and Young, J., *Concrete*. 2003, Prentice-Hall, Upper Saddle River, NJ.
2. Tavakoli, H., Mahmoudi, S., Goltabar, A. and Jalali, P., "Experimental evaluation of the effects of reverse cyclic loading rate on the mechanical behavior of reinforced scc beams", ***Construction and Building Materials***, Vol. 131, (2017), 254-266. https://doi.org/10.1016/j.conbuildmat.2016.11.043
3. Aiello, M.A. and Leuzzi, F., "Waste tyre rubberized concrete: Properties at fresh and hardened state", ***Waste Management***, Vol. 30, No. 8-9, (2010), 1696-1704. https://doi.org/10.1016/j.wasman.2010.02.005
4. Nehdi, M. and Khan, A., "Cementitious composites containing recycled tire rubber: An overview of engineering properties and potential applications", ***Cement, Concrete and Aggregates***, Vol. 23, No. 1, (2001), 3-10.
5. Yilmaz, A. and Degirmenci, N., "Possibility of using waste tire rubber and fly ash with portland cement as construction materials", ***Waste Management***, Vol. 29, No. 5, (2009), 1541-1546. https://doi.org/10.1016/j.wasman.2008.11.002
6. Gupta, T., Chaudhary, S. and Sharma, R.K., "Assessment of mechanical and durability properties of concrete containing waste rubber tire as fine aggregate", ***Construction and Building Materials***, Vol. 73, (2014), 562-574. https://doi.org/10.1016/j.conbuildmat.2014.09.102
7. Oriakhi, C.O., "Polymer nanocomposition approach to advanced materials", ***Journal of Chemical Education***, Vol. 77, No. 9, (2000), 1138. https://doi.org/10.1021/ed077p1138
8. Siringi, G.M., "Properties of concrete with tire derived aggregate and crumb rubber as a ligthweight substitute for mineral aggregates in the concrete mix", (2012). Ph.D. Dossertations, University of Texas, USA.
9. Khatib, Z.K. and Bayomy, F.M., "Rubberized portland cement concrete", ***Journal of Materials in Civil Engineering***, Vol. 11, No. 3, (1999), 206-213. https://doi.org/10.1061/(ASCE)0899-1561(1999)11:3(206)
10. Turatsinze, A., Bonnet, S. and Granju, J.-L., "Mechanical characterisation of cement-based mortar incorporating rubber aggregates from recycled worn tyres", ***Building and Environment***, Vol. 40, No. 2, (2005), 221-226. https://doi.org/10.1016/j.buildenv.2004.05.012
11. Li, G., Garrick, G., Eggers, J., Abadie, C., Stubblefield, M.A. and Pang, S.-S., "Waste tire fiber modified concrete", ***Composites Part B: Engineering***, Vol. 35, No. 4, (2004), 305-312. https://doi.org/10.1016/j.compositesb.2004.01.002
12. Yung, W.H., Yung, L.C. and Hua, L.H., "A study of the durability properties of waste tire rubber applied to self-compacting concrete", ***Construction and Building Materials***, Vol. 41, (2013), 665-672. https://doi.org/10.1016/j.conbuildmat.2012.11.019
13. Li, L., Ruan, S. and Zeng, L., "Mechanical properties and constitutive equations of concrete containing a low volume of tire rubber particles", ***Construction and Building Materials***, Vol. 70, (2014), 291-308. https://doi.org/10.1016/j.conbuildmat.2014.07.105
14. Richardson, A.E., Coventry, K.A. and Ward, G., "Freeze/thaw protection of concrete with optimum rubber crumb content", ***Journal of Cleaner Production***, Vol. 23, No. 1, (2012), 96-103. https://doi.org/10.1016/j.jclepro.2011.10.013
15. Al-Akhras, N.M. and Smadi, M.M., "Properties of tire rubber ash mortar", ***Cement and Concrete Composites***, Vol. 26, No. 7, (2004), 821-826. https://doi.org/10.1016/j.cemconcomp.2004.01.004
16. Tavakoli, H. and Rahimipour, M., "Effect of ash tires on mechanical properties and durability of concrete shotcrete and comparison with concrete shotcrete containing nano-silica", (2015).
17. Pavia, D.L., Lampman, G.M., Kriz, G.S. and Vyvyan, J.A., "Introduction to spectroscopy, Cengage learning, (2014).
18. Senin, M.S., Shahidan, S., Leman, A.S. and Hannan, N.I.R.R., "Analysis of physical properties and mineralogical of pyrolysis tires rubber ash compared natural sand in concrete material", in IOP Conference Series: Materials Science and Engineering, IOP Publishing. Vol. 160, (2016), 012053.
19. Conshohocken, P., "Astm international", Atanasova, B., Langlois, D., Nicklaus, S., Chabanet, C. et Etiévant, P, (2004).

Persian Abstract

**چکیده**

در این مطالعه اثرات استفاده از خاکستر لاستیک بر خواص مکانیکی بتن به صورت تجربی بررسی شد. هدف اصلی این مطالعه تعیین مقدار مناسب خاکستر لاستیک مورد استفاده در بتن، با بررسی خواص مکانیکی بتن مانند مدول الاستیسیته، مقاومت فشاری، مقاومت کششی، مقاومت خمشی و اسلامپ بتن تازه بود. چهار بخش مختلف خاکستر لاستیک (۲.۵٪، ۵٪، ۷.۵٪ و ۱۰٪ بر اساس وزن سیمان) به مخلوط بتن اضافه شد. بر اساس نتایجی که از آزمایش بر روی نمونه ها به‌دست‌آمد، می‌توان استنباط کرد که افزودن خاکستر لاستیک به بتن به طور قابل‌توجهی باعث افزایش مقاومت فشاری و خمشی بتن شد و اسلامپ بتن را نیز کاهش داد. همچنین مقاومت کششی و مدول الاستیسیته با افزایش میزان خاکستر لاستیک در بتن در سطح پایین تری افزایش یافت.

International Journal of Engineering

Journal Homepage: www.ije.ir

# Performance Assessment of Ductile Detailing Code-Based Reinforced Concrete Special Moment Resisting Frames

S. Chiluka*, P. Oggu

*Department of Civil Engineering, Vardhaman College of Engineering, Hyderabad, Telangana, India*

*PAPER INFO*

*Paper history:*
Received 08 July 2022
Received in revised from 24 October 2022
Accepted 28 October 2022

*Keywords*:
*Seismic Performance*
*Ductile Detailing*
*Pushover Analysis*
*Cost-benefit Analysis*

*ABSTRACT*

Reinforced concrete (RC) buildings make up the majority of Indian building stocks. Structural elements of these buildings are often designed limited to non-ductile detailing. With a very low building replacement rate, many Indian buildings are vulnerable to earthquakes and pose a significant risk to lives, properties and economic activities. This paper examines the effectiveness of ductile-detailing in mitigating the seismic collapse risk by analyzing the behaviour of a four-storey RC Special Moment Resisting Frame (RC SMRF) using the latest codes of ductile detailing. It also aims to quantify the impact of lateral force resisting system detailing on the performance and cost of RC SMRF buildings and its benefits. The present study emphasizes the effect of ductile detailing on three fundamental aspects of the structure – safety, stability and economy. Two four-storeyed building models – one without ductile detailing and the other with ductile detailing are designed and then analyzed using non-linear static analysis. The results of this study represent the behaviour of ductile-detailed and non-ductile-detailed buildings in terms of pushover curves, and hinge behaviour and identify the mode of final failure. In extension to that, a cost-benefit analysis is done to study the benefits of ductile detailing with the increased cost. The marginal increase in initial cost associated with ductile detailing is significantly outweighed by the resulting savings in the repair and downtime costs during the service life of the building.

***doi**: 10.5829/ije.2023.36.03c.04*

## 1. INTRODUCTION

A severe earthquake is one of the most destructive phenomena of nature. It is impossible to predict an earthquake, as it causes a severe damage to the structure. The damage to a structure can be reduced by providing a proper design. In order to provide a proper design, it is required to estimate the actual loads (i.e., dead load, live load, wall load, floor load, floor finish load, seismic load, wind load etc.) hitting the structure accurately. Among all other loads, lateral dynamic loads due to wind and seismic forces generally exhibit the highest degree of uncertainty and causes more damage to the structure which is to be eliminated by a proper design. In seismic zones, structures when subjected to an earthquake, structure experiences more amount of the seismic energy in axial directions. In order to withstand and absorb the energy, structure should have to produce more plastic deformations which can be possible by adopting ductile materials. Previous works on performance evaluation of structure considering non-ductile detailing and ductile detailing, in terms of capacity, damage, response reduction factor and drift done using static non-linear analysis and fragility analysis for estimation of the post damage yielding behaviour of structure where studies have shown that the design will reduce the damage in the structure significantly and design code is recommending a higher response reduction factor value, due to which the member size decreases and lead the structure to have more damage compared to the ductile detailed structures, thus 'R' need to be defined [1]. IS code recommending a higher 'R'-value than the actual, which is potentially dangerous. The actual value of 'R' is expected to be even lower than IS recommendations, due to structural

*Corresponding Author Institutional Email: chsathwik555@gmail.com (S. Chiluka)

Please cite this article as: S. Chiluka, P. Oggu, Performance Assessment of Ductile Detailing Code-Based Reinforced Concrete Special Moment Resisting Frames, ***International Journal of Engineering, Transactions C: Aspects,*** Vol. 36, No. 03, (2023) 457-464

irregularity leading to minor to moderate torsional effects, lack of quality control during the construction, and not following the ductile detailing requirements exactly as per the guidelines [2]. Other studies explore the current ACI seismic design code for moderate seismic hazard and cost-benefits of various levels of ductile connection detailing requirements are reviewed for steel buildings in the United States resulting in increased rates for improved ductility, and thus lower member forces, in the response of the structure [3]. Modal pushover analysis provides accurate results for low rise structures and consecutive pushover analysis provides more efficient results for high-rise and mid-rise frames [4]. Pushover analysis is used to predict potential weak areas by tracking the sequence of damages of each member in the structure and determining the weak joints. Finally, concluded that the values obtained using both the codes are the same. It is observed for the same loading conditions using ACI code displacement along Y direction increases compared to IS code [5]. The performance of a structure depends on the loads acting on the structure**,** based on the loads acting, type of analysis is adopted. Generally, base shear for seismic design is two times higher than gravity load design [6]. Seismic evaluation of a structure can be done by using pushover analysis [7-9]. Effect of ductile detailing influences the stability and strength of the structure [10, 11]. Vulnerability of a high-rise structure under seismic load can be evaluated using fragility curves following performance-based approach [12]. Exact behaviour of beam-column joint with ductile detailed and non-ductile detailed can be evaluated by applying reverse cyclic quasi-static stress till failure [13]. The process of evaluation of a structure due to seismic loading can be performed by pushover analysis which is used in this study and when a structure subjected to imposed loading can be performed by modal pushover analysis [14-18].

### 1. 1. IS 13920-2016 Code Recommendations

Latest code for ductile detailing of structure is IS 13920-2016 recommends to adopt ductile detailing in medium and high seismic zones in the structure. Those recommendations are:

Seismic Zone -II can be made as ordinary moment resisting frame (OMRF). Ductile detailing can be adopted for seismic Zone-III with above five stories in height; for seismic Zone-IV and Zone-V, ductile detailing is mandatory. It recommends to use a minimum of M20 grade of concrete. It recommends to use M25 or more grade of concrete in the case of the structural height exceeds 15 meters in Zone – III, IV, V; use Fe415 or less grade of steel; use Fe500 or more if change in length of the member is more than 14.5%; recommends to adopt strong column-weak beam design concept.

The scope of the study is limited to a low to mid-rise RC frame structure. Two models (i) Structure without ductile detailing (Model-I); (ii) Structure with ductile detailing (Model-II) are modelled and analysed under seismic Zone IV condition. Seismic analysis is done using non-linear static analysis (i.e., pushover analysis) using ETABS software. Soil-structure interaction is not taken into consideration which means foundation design and analysis is neglected. Cost estimation is done using CSi Detail and MS Excel software tools. This study has significant importance in the current scenario of existing buildings in India. It deals with the importance of ductile detailing in RC buildings with the current design practice and presents a cost comparison with cost-benefit analysis. Main objectives to be carried out in this paper includes, the study on the behaviour of a ductile detailed structure over the non-ductile detailed structure using pushover analysis as per new code, assessment on the exact behaviour of the structure using pushover curves and finally, to perform cost-benefit analysis.

## 2. MODELING AND DESIGN OF RC FRAMES

In this study, two different models are considered, one is without ductile detailing and other is with ductile detailing and the comparative study is done to assess the performances of both the models (Figure 1). The modeling, analysis and the design are performed using software tools i.e., CSi ETABS and CSi Detail.

Assumed building parameters (Table 1), seismic parameters (Table 2) are provided below, and the building is assumed with a live load of 1.5 kN/m$^2$ on terrace and 3 kN/m$^2$ on typical floors, along with that wall loads are also taken as 4.9 kN/m$^2$ on terrace and 14.7 kN/m$^2$ on typical floors (values obtained based on the manual calculations done considering the material unit weight) respectively.

After analysing the structures using linear approach, both the RC frames are designed and its design section properties are as follows – (i) Structure without ductile detailing (Model-I) – Beam 350 mm X 400 mm, Column 400 mm X 450 mm, Slab 130 mm, (ii) Structure with

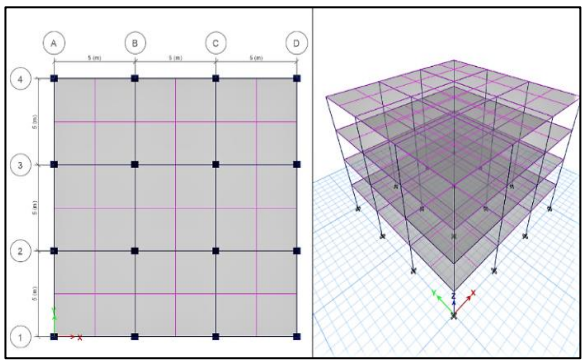


**Figure 1.** Plan and rendered view of model

ductile detailing (Model-II) – Beam 350 mm X 450 mm, Column-I 600 mm X 650 mm, Column-II 550 mm X 550 mm, Slab 130 mm.

After analyzing the frames based on the above assumed parameters, it is designed following three different code provisions in which for Model-I (Structure without ductile detailing) is designed using IS 456: 2000 + IS 1893: 2016 and Model-II Structure with ductile detailing) is designed using IS 456: 2000 + IS 1893: 2016 + IS 13920: 2016. The design output values of both the models which includes material properties (Tables 3 and 4).

## 3. PERFORMANCE ASSESSMENT ON THE DESIGNED MODELS

To identify the maximum extent of failure of structures, new models have created with the designed properties obtained from linear approach and those new models are analyzed using pushover analysis with *displacement coefficient method*.

**TABLE 1.** Building parameters

| Size of the plot | 15 m X 15 m |
|---|---|
| Storey height | 3 m |
| Total number of stories | G + 3 |

**TABLE 2.** Seismic parameters

| Zone | IV |
|---|---|
| Zone value | 0.24 |
| Site soil type | II (medium) |
| Importance factor | 1.5 |
| Response reduction factor | 5 |
| Time period along X and Y | 0.4835 sec |

**TABLE 3.** Designed material properties of Model-I

| Element | Grade of concrete | Main reinforcement | Secondary reinforcement | Cover |
|---|---|---|---|---|
| Beam | M25 | Fe500 | Fe415 | 25 mm |
| Column | M30 | Fe500 | Fe415 | 40 mm |
| Slab | M25 | Fe500 | Fe415 | 20 mm |

**TABLE 4.** Designed material properties of Model-II

| Element | Grade of concrete | Main reinforcement | Secondary reinforcement | Cover |
|---|---|---|---|---|
| Beam | M25 | Fe500 | Fe415 | 25 mm |
| Column | M30 | Fe500 | Fe415 | 40 mm |
| Slab | M25 | Fe500 | Fe415 | 20 mm |

Pushover analysis is generally used to estimate forces and displacements of the structure; sequence of failure of an element and its effects over the stability of entire frame; it identifies the critical regions where inelastic deformations are expected to be high; performance of the structure can be assessed on studying the pushover curves which includes capacity-demand curve, hinge responses; condition of hinges explains the severity of the entire structure; hinges forms in three stages namely IO- immediate occupancy, LS- life safety, CP- collapse prevention (Figure 2).

In order to assess the performance of both the Models, new models are created in ETABS using the designed properties which were obtained first using linear approach are considered as inputs and created new models including reinforcement details using section designer in ETABS and analyzed using pushover analysis. The below mentioned figures (Figures 3 and 4) represents the cross-section details of beams and columns in both the models, which are used in creating new models.

The models are assigned with hinges in beams and columns near the either ends of the element. For beams assign hinges based on the code ASCE 41-17 under table 10-7 (concrete flexure beams) with M3 degree of freedom along Push X and Push Y. For columns assign hinges based on the code ASCE 41-13 under table 10-8(concrete columns) with P-M2-M3 interaction under flexure/shear failure condition along Push X and Push Y.

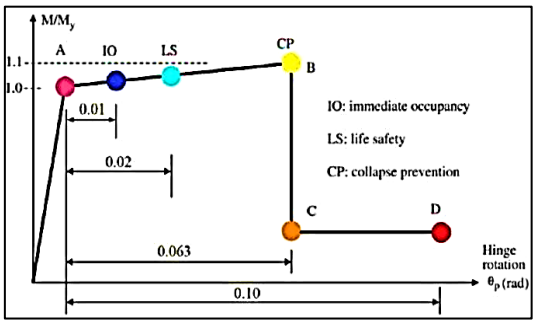


**Figure 2.** Behaviour of plastic hinge under pushover analysis

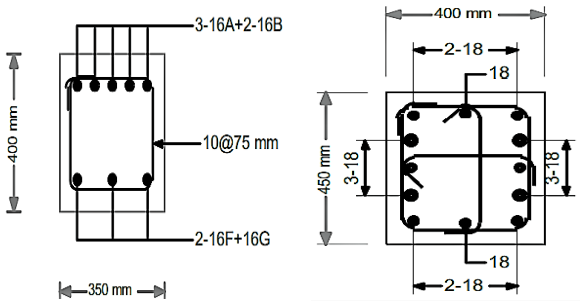


**Figure 3.** Designed section details of beams and columns in Model-I

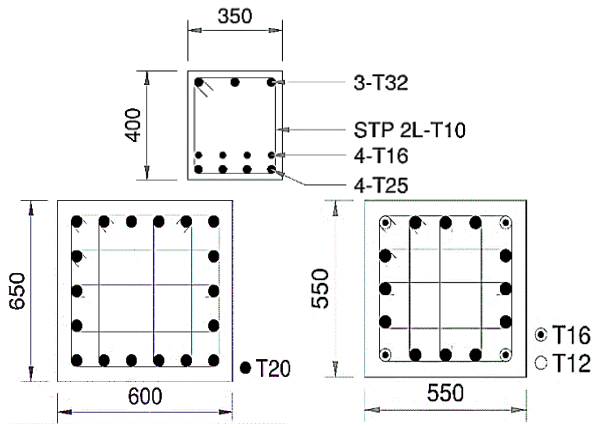


**Figure 4.** Designed section details of beams, columns in Model-II

**3. 1. Hinge Formations in Model-I** After pushover analysis on Model-I, the target displacement is observed to be 151 mm (Figure 5), the formation of hinges at this point are considered, which indicates that such amount of deformation occurs due to future earthquake (Figure 6).

**3. 2. Hinge Formations in Model-II** After pushover analysis on Model-II, the target displacement is observed to be 117 mm (Figure 7), the formations of hinges at this point are considered, which indicates that such amount of deformation occurs due to future earthquake (Figure 8).

## 4. COST-BENEFIT ANALYSIS OF RC FRAMES

A cost-benefit analysis is a process used to gauge the benefits of a decision or taking action minus the costs related to taking that action. Cost-benefit analysis is an economic analysis which gives you an outlook of changes in cost and the benefit which arises from it. The cost-benefit analysis may be applicable for both the new as well as old projects. It is based on an accepted social principle that is on individual preference. Based on the structural drawings obtained from the analysis and design configurations, the estimation and costing will be done to identify where actually the cost is getting fluctuated concerning each other and the major benefits of using ductile detailing are also pointed out. In depth analysis is carried out to find how and where the amount is getting increased compared to a conventional RC frame.

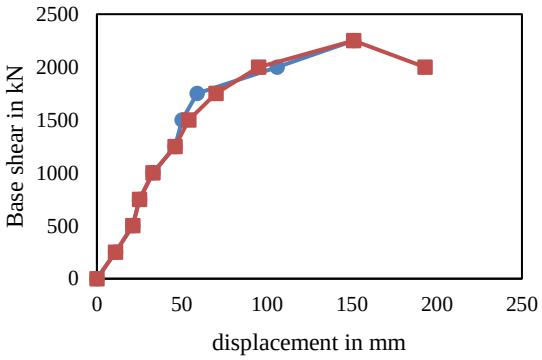


*Blue line indicates – Bilinear FD
*Red line indicates – Capacity curve
*Target displacement is noted to be 151 mm

**Figure 5.** Capacity-demand curve in Model-I

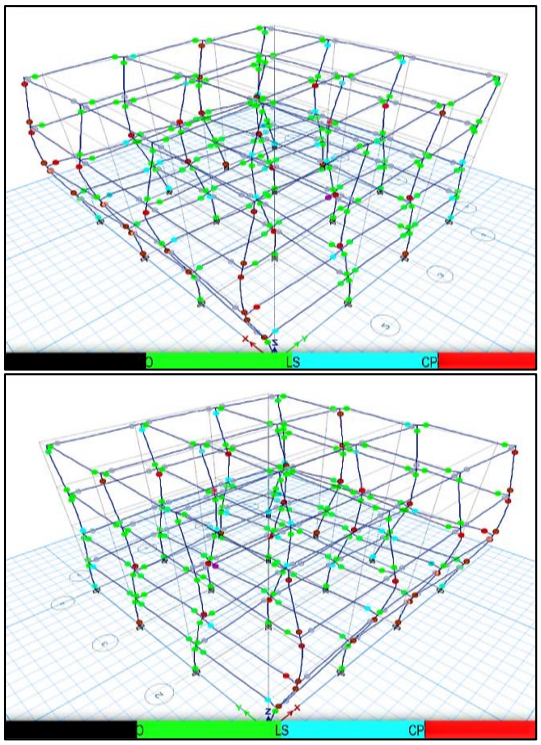


**Figure 6.** Maximum target displacement and hinge response at that point

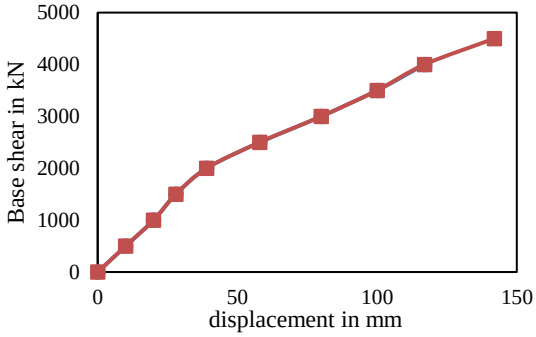


*Blue line indicates – Bilinear FD
*Red line indicates – Capacity curve
*Target displacement is noted to be 117 mm

**Figure 7.** Capacity-demand curve in Model-II

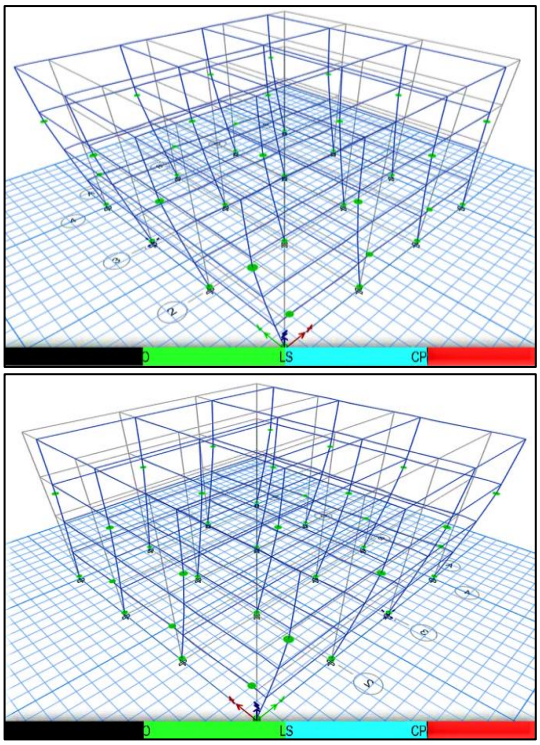


**Figure 8.** Maximum target displacement and hinge response at that point

The main objective of cost-benefit analysis is to identify and compare the cost increase in ductile detailed building to non-ductile detailed building. In this study, the cost difference is investigated for structural components specifically. The quantity and cost estimation are limited to beams, columns and slabs only. Indirect costs such as electrification charges, sanitary charges are not included because those remain almost the same for both buildings. Labour charges and their wages are also considered and computed accordingly. The cost for 1kg of steel is taken as 56/- INR, cost for 1 $m^3$ of concrete is taken as 3800/- INR and is taken based on 'Standard Schedule of Rates' given by Telangana state I&CAD department, India, 2021.

The complete quantity and cost comparison is given in Tables 5 and 6. Benefits of using ductile detailing can be stated after estimating the whole cost of construction of both the models.

Labour wages are estimated and computed based on the quantity of materials such as concrete and steel occurred in different RCC works such as column, beams, slab work (Table 5).

Wages of labour are differentiated based on labour category, such as skilled labour and unskilled labour. Mason and blacksmith come under skilled labours whereas Mazdoor, Beldar, Mistri, Bisti comes under unskilled labours. Based on Indian conditions expected

**TABLE 5.** Quantity estimation comparison between the Models

| S. No | Quantity | Structural element | Quantity in Model-I | Quantity in Model-II |
|---|---|---|---|---|
| 1. | Concrete (in $m^3$) | Slab | 117.00 | 179.84 |
| | | Beam | 100.80 | 25.62 |
| | | Column | 60.48 | 98.47 |
| 2. | Steel Rebar (in kg) | Slab | 8,549.00 | 11,231.36 |
| | | Beam | 14,050.00 | 10,436.53 |
| | | Column | 10,426.00 | 23,288.51 |

**TABLE 6.** Cost comparison between the models

| S. No | Material Type | Cost for Model-I | Cost for Model-II | Remarks |
|---|---|---|---|---|
| 1 | Concrete | 10,69,560/- | 14,70,135/- | **37.45%** |
| 2 | Steel Rebar | 18,49,456/- | 25,54,310/- | **38.11%** |
| 3 | Total Cost | 29,19,016/- | 39,87,695/- | **36.60%** |

Note: The costs of the materials for both the Models are estimated in INR (Indian Rupee).

out-turn of a labour per day (8 hours of work), for RCC work is 3.00 cum per mason. Labour requirement for different works in Indian condition is shown below in Table 7.

Expected wages of labour are taken from "Building material prices and wages of labour a statistical compendium 2014 – National buildings organisation, Government of India" based on it, labour wages for (i) Mason – 500 INR, (ii) Unskilled labour Male – 350 INR, (iii) Unskilled labour Female – 300 INR. The above-mentioned wages are computed with reference to a city lies in seismic Zone-IV. With reference to the above-mentioned labour charges, total cost incurred in ductile detailed and non-ductile detailed are computed as follows:

Benefit-cost ratio is evaluated to verify whether benefits over weighs cost or not (Figure 9).

**TABLE 7.** Labour requirement for out-turn

| Type of work | Labour type | Labour per day |
|---|---|---|
| RCC work (for 2.83 cum) | Beldar | 2 |
| | Mazdoor | 3 |
| | Bhisti | 1.5 |
| | Mason | 0.5 |
| Reinforcement work (for 1 quintal) | Blacksmith | 1 |
| | Beldar | 1 |

**TABLE 8.** Total labour wages during construction

| Type of work | Labour type | Total labour wages in Model-I (in INR) | Total labour wages in Model-II (in INR) |
|---|---|---|---|
| Column | Mason | 20,000 | 32,500 |
| | Unskilled labour (Male) | 28,000 | 45,400 |
| | Unskilled labour (Female) | 24,000 | 39,000 |
| Beam | Mason | 33,000 | 9,000 |
| | Unskilled labour (Male) | 46,200 | 12,600 |
| | Unskilled labour (Female) | 39,600 | 10,800 |
| Slab | Mason | 39,000 | 60,000 |
| | Unskilled labour (Male) | 54,600 | 84,000 |
| | Unskilled labour (Female) | 46,800 | 72,000 |
| **TOTAL COST** | | **3,31,200** | **3,65,300** |

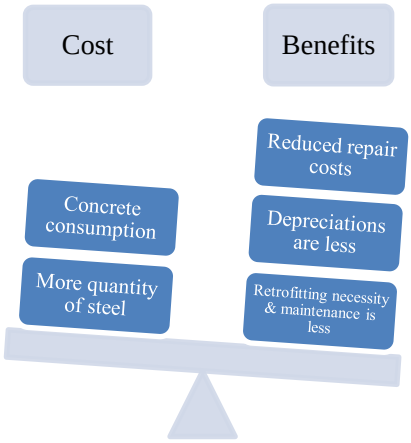


**Figure 9.** Chart representing benefit-cost ratio of Model-II

## 5. RESULTS AND DISCUSSION

### 5. 1. Pushover Analysis Results Comparison

**5. 1. Capacity-demand Curves** Model-I exhibits a maximum target displacement of 155.63 mm at 2289.89 KN base shear (Figure 10), but has a capability to exhibit non-linearity up to 220.45 mm at2068.35 KN base force. Model-II exhibits a maximum target displacement of 117 mm at 4307.82 KN base shear but has a capability to exhibit non-linearity up to 162.54 mm at 3769.53 KN base force.

**5. 2. Base Shear vs Displacement Curves** It is noted that a maximum inelastic displacement of 275.14 mm at 2512.56 kN base shear in Model-I and a maximum inelastic displacement of 329.14 mm at 6612.51 kN base shear. This result says that the capacity of Model-II (Figure 11) is more as it experiences more inelastic deformations by absorbing more amount of base shear compared to Model-I.

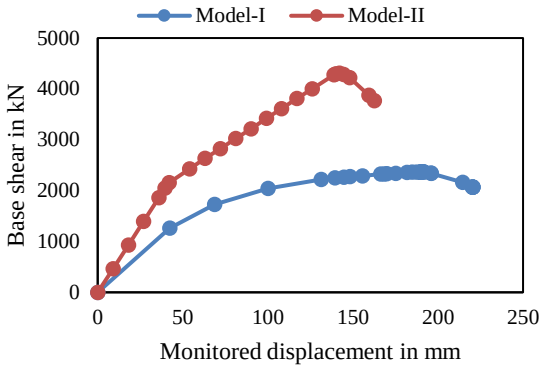


**Figure 10.** Capacity-demand curve

**5. 3. Storey Displacement** Model-I exhibits a maximum displacement of 42.448 mm at 12 m height, it is clear that storey drift increases from base of the structure at an average increasing rate of 43.446 %.

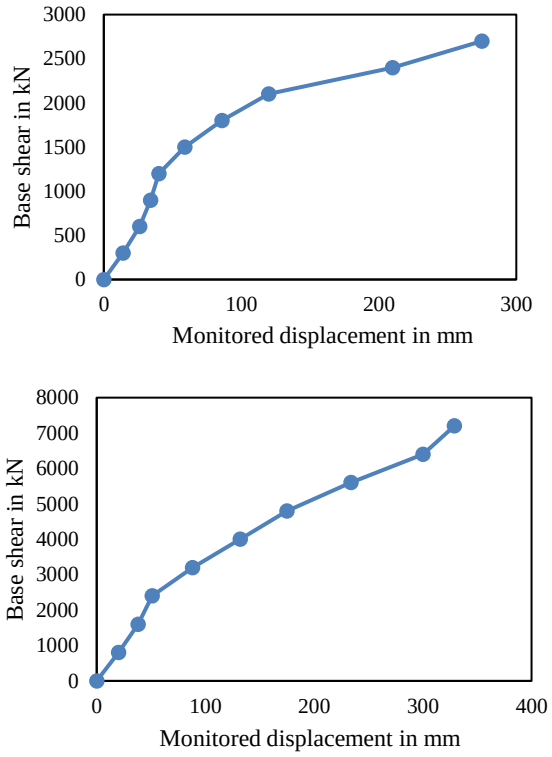


**Figure 11.** Base shear vs monitored displacement curves in Model-I and Model-II

Model-II exhibits a maximum displacement of 9.024 mm at 12 m height, it is clear that storey drift increases from base of the structure at an average increasing rate of 56.968 %. As Model-II has ductile detailing and confinement of steel is more, so it exhibited less storey displacement (Figure 12).

## 6. SUMMARY AND CONCLUSIONS

From the hinge responses obtained from pushover curves, in non-ductile detailed structure, the performance of this model says that it has less capacity and resistance against seismic load and its target displacement is 151 mm which means that the structure experiences such displacement under future earthquake. Whereas, in ductile detailed structure, target displacement is 117 mm and less hinges are formed which are in the limits (none exceeded collapse prevention stage), and hinge response says that the structure can safely carry the future seismic load. Maximum inelastic displacement of 329.14 mm at 6612.51 kN base shear is recorded in ductile detailed structure, where non-ductile detailed has experienced 275.14 mm at 2512.56 kN base shear which says that ductile detailed structure has high ability to take absorb forces acting due to seismic excitation. Since lateral ties, stirrups are used more near the supports in Model-II to enhance the stiffness of the structure in column and beams resulting in strong-column weak-beam mechanism and usage of low-grade of steel in ductile detailed structure has increased the ductile nature of the structure resulting in more plastic deformations, which is a desirable property.Further, a maximum storey displacement of 42.44 mm is observed in non-ductile detailed structure, whereas a maximum of 9.02 mm is observed in ductile detailed structure. Ductile detailed structure has 78.74% less displacement compared to non-ductile detailed structure. Ductile detailed structure is more flexible than structure without ductile detailing. It is possible to create “no sudden collapse (brittle failure)” using ductile detailing. Occupants will have sufficient warning before its final failure. Plastic deformations will be more and energy will get dissipated uniformly reducing the impact of seismic effect on the structure.

Further, it was also observed that the structure with ductile detailing has increased its cost by 36.60% compared to structure with non-ductile detailing, due to a greater number of steel bars in ductile detailed structure. Rebar count is more in Model-II with an increased value of 38.11% and it is mainly due to confinement of reinforcement in beams. As the grade of steel in Model-II is restricted to Fe415, a greater number of bars are used to enhance the lateral stability of the structure, due to which geometry is required more, which reflected in more quantity of concrete consumption in Model-II with an increased rate of 37.4%. As lateral ties, stirrups are more used more near the supports in ductile detailed structure to enhance the stiffness of the structure. Labour wages estimation between both the Models have shown minimal difference in its cost, therefore labour wages difference is not much effective. Benefit-cost ratio is high in ductile detailed structure and benefits exceeds over cost, and it was found that the marginal initial cost increase associated with ductile detailing is considerably outweighed by the resulting savings in the repair and downtime costs and concludes that it is economical.

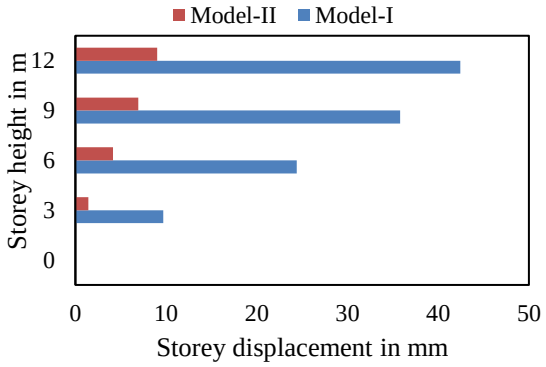


**Figure 12.** Maximum storey displacement

## 7. REFERENCES

1. Goud, S.S. and Kumar, R.P., "Seismic design provisions for ductile detailed reinforced concrete structures", in 15th Symposium on Earthquake Engineering (15SEE), (2014).
2. Mondal, A., Ghosh, S. and Reddy, G., "Performance-based evaluation of the response reduction factor for ductile rc frames", ***Engineering Structures***, Vol. 56, (2013), 1808-1819. https://doi.org/10.1016/j.engstruct.2013.07.038
3. Batt, D.P. and Odeh, D.J., "A discussion and analysis of ductile detailing requirements for seismic design in moderate seismic regions", in Structures Congress 2005: Metropolis and Beyond. (2005), 1-9.
4. Alvi, A.A., "A comparative view on the enhancements of pushover analysis methods for estimating seismic demands", ***International Research Journal of Engineering and Technology***, Vo. 8, No. 2, (2021), 2075-2080.
5. Ahiwale, D.D., Khartode, R.R. and Raut, K.V., "Seismic response for rc frames on sloping ground using pushover analysis", ***Journal of Structural Engineering and Management***, Vol. 7, No. 1, (2020), 1-10.
6. Abdullah, M. and Kulkarni, P., "Behaviour of multi-storey rc building under seismic load using pushover analysis", in IOP Conference Series: Materials Science and Engineering, IOP Publishing. Vol. 1197, (2021), 012012.
7. Sadjadi, R., Kianoush, M. and Talebi, S., "Seismic performance of reinforced concrete moment resisting frames", ***Engineering Structures***, Vol. 29, No. 9, (2007), 2365-2380. https://doi.org/10.1016/j.engstruct.2006.11.029
8. Kavitha, R., Sundarraja, M., Vinodhini, C., Dinakaran, E., Aswinkumar, A. and Princy, A.J., "Analysis of seismic performance of reinforced concrete framed structure", in IOP Conference Series: Materials Science and Engineering, IOP Publishing. Vol. 1145, (2021), 012077.

9. Sullivan, T.J., Saborio-Romano, D., O'Reilly, G.J., Welch, D.P. and Landi, L., "Simplified pushover analysis of moment resisting frame structures", ***Journal of Earthquake Engineering***, Vol. 25, No. 4, (2021), 621-648. https://doi.org/10.1080/13632469.2018.1528911

10. Shah, A.H., Sharma, U.K., Kamath, P., Bhargava, P., Reddy, G. and Singh, T., "Effect of ductile detailing on the performance of a reinforced concrete building frame subjected to earthquake and fire", ***Journal of Performance of Constructed Facilities***, Vol. 30, No. 5, (2016), 04016035. https://doi.org/10.1061/(ASCE)CF.1943-5509.0000881

11. Liel, A.B., Haselton, C.B. and Deierlein, G.G., "Seismic collapse safety of reinforced concrete buildings. Ii: Comparative assessment of nonductile and ductile moment frames", ***Journal of Structural Engineering***, Vol. 137, No. 4, (2011), 492-502. https://doi.org/10.1061/(ASCE)ST.1943-541X.0000275

12. Nair, S., Hemalatha, G. and Stephen, E., "Seismic vulnerability studies of a g+ 17 storey building in abu dhabi-uae using fragility curves", ***International Journal of Engineering, Transactions B: Applications***, Vol. 34, No. 5, (2021), 1167-1175. doi: 10.5829/IJE.2021.34.05B.10.

13. Ravikumar, S. and Kothandaraman, S., "Experimental study on performance of ductile and non-ductile reinforced concrete exterior beam-column joint", ***International Journal of Engineering, Transactions A: Basics***, Vol. 35, No. 7, (2022), 1237-1245. doi: 10.5829/IJE.2022.35.07A.03.

14. Asgari, M. and Tariverdilo, S., "Investigating the seismic response of structural walls using nonlinear static and incremental dynamic analyses", ***International Journal of Engineering, Transactions B: Applications***, Vol. 30, No. 11, (2017), 1691-1699. doi: 10.5829/ije.2017.30.11b.09.

15. Kiran, K. and Noroozinejad Farsangi, E., "Blast demand estimation of rc-moment-resisting frames using a proposed multi-modal adaptive pushover analysis procedure", ***International Journal of Engineering, Transactions A: Basics***, Vol. 34, No. 1, (2021), 46-55. doi: 10.5829/IJE.2021.34.01A.06.

16. Oggu, P. and Pithadiya, M., "Influence of real ground motion records in performance assessment of rc buildings", ***International Journal of Engineering, Transactions C: Aspects***, Vol. 32, No. 12, (2019), 1745-1752. doi: 10.5829/IJE.2019.32.12C.07.

17. Oggu, P., Gopikrishna, K. and Sewaiwar, S., "Seismic assessment of existing gravity load-designed rc framed building: A case study from warangal, india", ***SN Applied Sciences***, Vol. 2, No., (2020), 1-13. doi: 10.1007/s42452-020-2690-7.

18. Oggu, P., Gopikrishna, K. and Jha, S., "Importance of 'daf'in evaluating structural adequacy of gravity-load designed rc buildings", ***Materials Today: Proceedings***, Vol. 32, (2020), 810-818. https://doi.org/10.1016/j.matpr.2020.04.018

## Persian Abstract

**چکیده**

ساختمان های بتن آرمه (RC)اکثریت ساختمان های هند را تشکیل می دهند. عناصر سازه ای این ساختمان ها اغلب محدود به جزئیات غیر شکل پذیر طراحی می شوند. با نرخ بسیار پایین تعویض ساختمان، بسیاری از ساختمان های هندی در برابر زلزله آسیب پذیر هستند و خطرات قابل توجهی برای جان، اموال و فعالیت های اقتصادی به همراه دارند. این مقاله اثربخشی جزئیات شکل پذیر را در کاهش خطر فروپاشی لرزه ای با تجزیه و تحلیل رفتار یک قاب چهار طبقه مقاوم در برابر ممان ویژه RC (RC SMRF) با استفاده از آخرین کدهای جزئیات انعطاف پذیر بررسی می کند. همچنین هدف آن تعیین کمیت تأثیر سیستم مقاوم در برابر نیروی جانبی بر روی عملکرد و هزینه ساختمان‌های RC SMRF و مزایای آن است. مطالعه حاضر بر تأثیر جزئیات شکل پذیر بر سه جنبه اساسی سازه – ایمنی، پایداری و اقتصاد تأکید دارد. دو مدل ساختمان چهار طبقه – یکی بدون جزئیات شکل پذیر و دیگری با جزئیات شکل پذیر طراحی شده و سپس با استفاده از تحلیل استاتیکی غیر خطی مورد تجزیه و تحلیل قرار می گیرند. نتایج این مطالعه نشان دهنده رفتار ساختمان‌های با جزئیات شکل‌پذیر و غیر شکل‌پذیر از نظر منحنی‌های فشار آور و رفتار لولا و شناسایی حالت شکست نهایی است. در بسط آن، یک تحلیل هزینه–فایده برای مطالعه مزایای جزئیات شکل پذیر با افزایش هزینه انجام می شود. افزایش حاشیه ای در هزینه اولیه مرتبط با جزئیات شکل پذیر به طور قابل توجهی با صرفه جویی در هزینه های تعمیر و خرابی در طول عمر ساختمان جبران می شود.

International Journal of Engineering

Journal Homepage: www.ije.ir

# Assessing Potential Performance of GPS and Galileo in context of Broadcast Precise Orbits and Clock Corrections

D. Kuna*, P. Naveen Kumar

*Advanced GNSS Research Laboratory, Department of ECE, University College of Engineering, Osmania University, Telangana, India*

*PAPER INFO*

*Paper history:*
Received 13 August 2022
Received in revised form 17 October 2022
Accepted 18 October 2022

*Keywords*:
*GPS*
*Galileo*
*Broadcast and Precise Ephemerides*
*Satellite Visibility*
*Horizontal Accuracy*

*ABSTRACT*

The global navigation satellite system (GNSS) is becoming a vital positioning technology across various services. The ephemeris quality is one of the factors that directly impact the user's position accuracy. Some applications, such as investigations into Earth's crustal dynamics, need more precise ephemeris data than broadcast ephemeris. Several institutions, such as the international GNSS service (IGS), have developed precise orbital services to enable these applications. Unfortunately, data rates for such precise orbits are often confined to 15 minutes. In this paper, in order to generate precise ephemeris with the broadcast sampling period, the well-known Lagrange interpolation method is used. Furthermore, a comparative GPS and Galileo position analysis corresponding to the broadcast and precise ephemeris over a typical day in September 2021 is presented. To get insight into comparative positioning analysis over Hyderabad Station, the ENU (East-North-Up) directional errors, satellite visibility and horizontal accuracy parameters are considered. Based on the numerical analysis, standalone Galileo has similar capabilities to GPS, and it can be used in Multi-GNSS over India and its surrounding areas. This work may help in the development of single- or dual-frequency GNSS receivers for civilian navigation services.

***doi**: 10.5829/ije.2023.36.03c.05*

## 1. INTRODUCTION

The GNSS consist of the GPS, GLONASS, Galileo and Compass systems with global coverage. Currently, the GPS, Glonass and Compass are fully operational and enable autonomous geo-spatial positioning. They are also being gradually modernized. The European Space Agency (ESA) and the European Union (EU) are also working on Galileo, which is the latest civilian-controlled GNSS [1]. Galileo is a more appropriate system for safety-critical applications for civilian users than existing satellite navigation systems. Galileo comprises of 30 MEO (Medium Earth Orbit) satellites constellation. Currently, 22 satellites are operational and are visible from India at different times. Currently, it is not yet fully operational, but the initial services were started in December 2016[1]. Galileo is expected to introduce new modernization elements other than GPS and GLONASS in soon[2]. Because Galileo is still in its early stages with initial services, it is more important to evaluate its performance with existing constellations. Characterizing the Clock and Ephemeris errors of the GNSSs is a key part of validating the assumptions for such integrity evaluation of GNSS Safety-of-Life (SoL) augmentation systems. In the past few years, there haven't been many studies that used both ground-based and space-based GNSS observational data. Some researchers are analysing Galileo's absolute positioning performance in navigation [2, 3]. With ample research demonstrating the benefits of Galileo in multi-GNSS environments in various geographical regions [4-8], there has been a lack of study to demonstrate the performance of Galileo in India, especially with mass-market GNSS receivers. However, very little research on Galileo's performance evaluation over India has been reported [9]. There are also some studies mainly focusing on the accuracy of navigation systems related to multiple GNSS components [10-13]. In this research work, an attempt

*Corresponding Author Institutional Email: devadaskuna@osmania.ac.in (D. Kuna)

[1] https://www.gsc-europa.eu/system-status/Constellation-Information
[2] https://en.wikipedia.org/wiki/Galileo(satellite_navigation)#cite_note-2

Please cite this article as: D. Kuna, P. Naveen Kumar, Assessing Potential Performance of GPS and Galileo in context of Broadcast Precise Orbits and Clock Corrections, ***International Journal of Engineering, Transactions C: Aspects,*** Vol. 36, No. 03, (2023) 465-472

has been made to enhance position accuracy using integrated ground- and space-based observations. This paper examines the impact of broadcast and precise ephemerides on GPS and Galileo observations over Hyderabad station.

The structure of the paper is as follows: Following the introduction, section 2 provides a brief description of the research approach, focusing on the Lagrange interpolation algorithm used to analyze Galileo and GPS navigation data. Section 3 outlines the results and discussions based on the cases studied. The GPS and Galileo data sets are used, and some issues with precise and broadcast data are identified. The characterization of the observed horizontal accuracy is addressed and discussed in the ENU reference frame, in which the mean and the 50th and 95th percentiles are measured. The paper concludes with final remarks.

## 2. METHODOLOGY

A highly sensitive multi-GNSS Novatel triple-frequency GPStation-6 receiver with GPS-703-GGG choke ring antenna is used to test the performance of Standalone Galileo and GPS. This was mounted at the Advanced GNSS Research Laboratory (AGRL), Department of Electronics and Communication Engineering, Osmania University, Hyderabad, India. The linear combination positioning solutions of Galileo E1/E5a and GPS L1/L5 observables in receiver independent exchange format (RINEX) files are acquired at 30-second intervals over a 24-hour period. In this paper, the GPS and Galileo satellite positions and satellite clock corrections related to broadcast ephemeris and precise IGS site products are compared. Moreover, the standalone Galileo and GPS' position accuracy capabilities corresponding to both orbital data are also evaluated.

**2. 1. Lagrange's Interpolation** The GNSS satellites transmit a broadcast ephemeris (BE) composed of Keplerian elements as a navigation message. It enables orbit information to be calculated at any time over a two-hour validity period. Its orbital precision is around 3 m, and its satellite clock accuracy is about 7 ns. The orbit and clock inaccuracies of BE products determine their single-point-positioning (SPP) accuracy. For accurate positioning on the Earth, the precise orbit of GNSS satellites must be known. In contrast to broadcast orbits, precise satellite orbits or precise ephemeris (PE) are more accurate [14]. It is derived directly from the post-mission precise orbital services, specifically IGS [15]. This information contains the precise three-dimensional (3D) positions for all GNSS satellites as well as the satellite clock corrections, which are generally reported in an standard product-3 (SP3) formatted file. Thus, a Keplerian calculation is not necessary to obtain precise satellite orbits [16]. The satellite orbits and the clock corrections provided by IGS are far more accurate than the broadcast orbits, which are 5 cm and 0.1 ns, respectively [17]. Broadcast ephemerides are useful for visibility analysis, observation data quality control, and relative navigation despite their lower accuracy.

The precise IGS orbits are usually available for every 15-minute interval of time. With the interpolation technique, it is possible to obtain precise orbital coordinates with the broadcast sample period [18]. Interpolation is a mathematical technique for deriving new data points from a discrete set of previously known data points. In addition, it facilitates determining the accuracy of broadcast coordinates by comparing them with interpolated precise coordinates [19]. The well-known Lagrange Interpolation has often been used to generate the interpolated PE measurements, in particular for GPS satellites [20, 21]. The Lagrange method is better than Newton's because it can be used with values that are not evenly spaced [22]. The Lagrange formulae (Equations (1) to (4)) are used to determine the value of a mathematical function at any intermediate value of the independent variable.

Let $f_0$, $f_1$, $f_2$, …, $f_n$ be the value of the specific data at time $t_0$, $t_1$, $t_2$, …, $t_n$. An approximation of $f_1$given by $p(t)$, at any time $t$ is given by [23]:

$$p(t) = a_0 f_0 + a_1 f_1 + a_2 f_2 + \cdots + a_n f_n = \sum_{j=1}^{n} a_i f_i \quad (1)$$

where:

$$a_i = \frac{(t-t_0)(t-t_1).....(t-t_{i-1})(t-t_{i+1}).....(t-t_n)}{(t_i-t_0)(t_i-t_1).....(t_i-t_{i-1})(t_i-t_{i+1}).....(t-t_n)} \quad (2)$$

Because $a_i$ coefficient is a function of $t$, it is also known as $L_i(t)$ which stands for Lagrange operator. Now, in Equation (2) we can replace $t$ with $t_0$, $t_1$, $t_2$, …, $t_n$

$$a_i = L_i(t) = \begin{cases} 1, & for\ t = t_i \\ 0, & otherwise \end{cases} \quad (3)$$

Going back to Equation 1 and substituting again $t$ by $t_0$, $t_1$ ,$t_2$, …,$t_n$, we get:

$$p(t_0) = f_0, p(t_1) = f_1, p(t_2) = f_2, \ldots, p(t_n) = f_n \quad (4)$$

After obtaining the precise interpolated results, the BE and PE measurements are evaluated by comparing satellite ECEF (Earth-Centered-Earth-Fixed) coordinates and clock parameters.

**2. 2. User Position Analysis** As users are interested primarily in the positioning accuracy of GNSS, the user's position is expressed as latitude (ϕ), longitude (λ), and height/altitude (h) values in a spherical coordinate system (LLA). Generally, a rectangular coordinate system, like ENU is the best to use to quantify position errors in local topo-centric coordinates. The E and N axes are parallel to the orientation of the receiver's latitude and longitude, respectively. On the other hand, the up-axis is perpendicular to both of these axes in the

upward direction. To get ENU coordinates, firstly, the conversion between LLA and ECEF coordinates is achieved by using Equation 5. Kuna et al. [24] mentioned formulae are used to get ENU coordinates.

$$\begin{aligned} X &= (\frac{a}{\chi} + h)\cos\phi\cos\lambda \\ Y &= (\frac{a}{\chi} + h)\cos\phi\sin\lambda \\ Z &= (\frac{a(1-e^2)}{\chi} + h)\cos\phi\cos\lambda \end{aligned} \quad (5)$$

where $\chi = \sqrt{1 - e^2 sin^2\phi}$ here '$a$' and '$e$' are the semi-major axis and eccentricity of the ellipsoid respectively. Here, the earth's surface is approximated by an ellipsoid with '$a$' and the flattening '$f$' parameters.

In order to illustrate the systematic error behavior of estimated two-dimensional (2D) user position estimation (which includes east and north dimensions), it will be displayed in a 'scatter plot'. Furthermore, the most popular static 2D position accuracy parameters of GNSS are DRMS (Distance Root Mean Square) and CEP (Circular Error Probability). Here, the radius of a circle is centred at the true position and the position solutions with their associated probability ranges are presented in a scatter plot. Equations in Table 1 represent GNSS static position accuracy measurements, with the standard deviation calculated by computing Equation (6). It is used to figure out the standard deviation of all directional errors after the ENU coordinates have been estimated.

$$\sigma_x = \sqrt{\frac{\sum_{i=1}^{n}(x_i - \bar{x})^2}{n-1}} \quad (6)$$

where $x_i$ is the east component of an estimated $i^{th}$ position sample, $\bar{x}$ be the average measurement of a static position in the east direction. Similar expressions may well be defined for north (y) and up (z) coordinates [25].

## 3. RESULTS AND DISCUSSION

The article discusses a comparative evaluation based on the satellite and user positions of the standalone GPS and Galileo systems over a low-latitude station. In addition to this, the formal analysis of the orbit accuracy and satellite clock corrections corresponding to BE and PE measurements is presented. The results of data analysis are presented below for individual constellations. The first section examines standalone GPS observations, and the second section examines standalone Galileo observations. At the time of this observation, GPS consisted of 30 satellites, whereas Galileo only had a total of 22 satellites. Instead of examining each satellite, relative to satellite availability at the observation site, GPS pseudorandom noise (PRN) 24 (G24) and Galileo PRN 7 (E7) are considered. It is noticed that the G24 satellite has a less stable block IIF Cesium atomic clock, whereas E7 satellite uses very stable passive hydrogen masers. These two satellite measurements are used to compare orbital accuracy and clock corrections.

**TABLE 1.** Static positioning horizontal accuracy (2D) measures [20]

| Accuracy Parameters | Equation | Probability |
|---|---|---|
| CEP | $0.62\,\sigma_x + 0.56\,\sigma_y$ | 50% |
| DRMS | $\sqrt{(\sigma_x^2 + \sigma_y^2)}$ | 65% |
| 2DRMS | $2\sqrt{(\sigma_x^2 + \sigma_y^2)}$ | 95% |

**3. 1. Standalone GPS** During GPS week 2177 on September 30, 2021, over the observed station, the G24 has a vicinity period between 00:00:00 and 08:05:12, which corresponds to GPS time between 345600 and 374730 seconds. So, the BE and PE measurements are shown along with the G24 satellite's orbits and clock corrections during the aforementioned time period.

**3. 1. 1. Lagrange Interpolation Results** Figure 1 illustrates the similar orbital behavior of the G24 for both precise and interpolated ECEF measurements. In this figure, the y-axis denotes the GPS satellite position data samples, while the x-axis represents the amount of time that the GPS satellite was visible. The SP3 data file's X, Y, and Z coordinates with 5 minutes sample period for the GPS satellite in the ECEF coordinate system are signified as a dotted line (Figure 1(a)). By interpolation, 289 number of initial samples are increased to 3853 samples. Figure 1(b) represents smoothed interpolated path of XYZ coordinates of GPS satellite with increased time samples for every 30 seconds along the X axis. It reveal the behaviour of the interpolation algorithm, but not the accuracy of the coordinates. In three TOWC (Time of Week Count) periods, there were discontinuities between 351000 and 351480 seconds, 357000 and 358080 seconds, and 367800 and 368280 seconds are observed. In UTC (Coordinated Universal Time) (hrs:min:sec), the discontinuities are 01:29:42 (hrs:min:sec) to 01:37:42 (hrs:min:sec), 03:09:42 (hrs:min:sec) to 03:27:42 (hrs:min:sec), and then 06:09:42 (hrs:min:sec) to 06:17:42 (hrs:min:sec). There are several reasons for this kind of discontinuities usually occurs, but primarily due to BE's updating.

Figure 2 (a-c) illustrates the variation in computed broadcast coordinates and interpolated precise ECEF coordinates of the G24 satellite. It is noticed that the X, Y and Z coordinates using BE and PE overlap each other; the differences are minor. Figure 2(d) shows a comparison between both ECEF coordinates related to BE and PE, during the satellite vicinity period. In view of the all-estimated satellite ECEF coordinates, the difference between BE and PE is in the 4 metre range only. On Figure 3(a), the orientation of the G24 satellite is illustrated in relation to its elevation angle. This

satellite with zero elevation has been observed at TOWC between 374760 and 432000 seconds, corresponding to UTC times between 05:05:42 (hrs:min:sec) and 19:55:42 (hrs:min:sec). As part of this observation, it was noted that the G24 had orientation between lower (<10°) and higher (>50°) elevations. The G24 satellite clock corrections related to BE are overlaid on those for PE (Figure 3(b)). Also, a similar pattern of discontinuities is seen in Figure 3(b). The clock discontinuities are the difference between the current and prior broadcast ephemeris sets' clock offsets. The BE-PE clock corrections difference is detailed in Figure 3(c), and it is nearly 3 picoseconds or 300 nanoseconds.

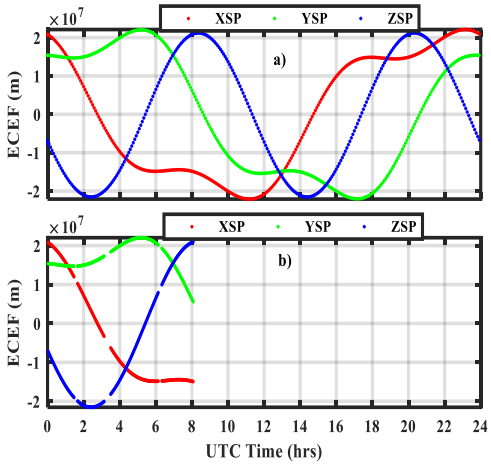


**Figure 1.** The GPS PRN-24 satellite precise ECEF orbit coordinates derived from a) SP3 file and b) Lagrange interpolated

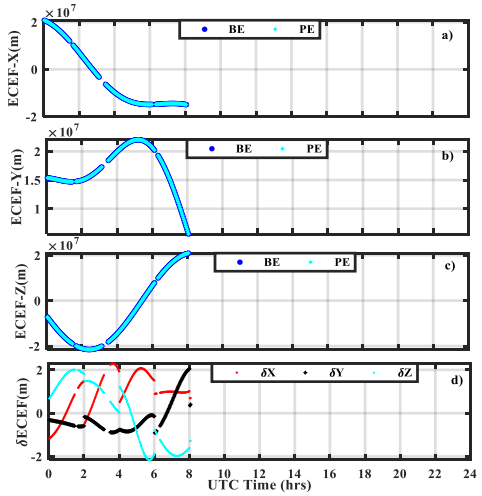


**Figure 1.** Variation of GPS PRN-24 satellite Broadcast and Precise ECEF a) X-directional b) Y-directional c) Z-directional coordinates and d) Comparison of BE and PE ECEF coordinates during satellite vicinity period

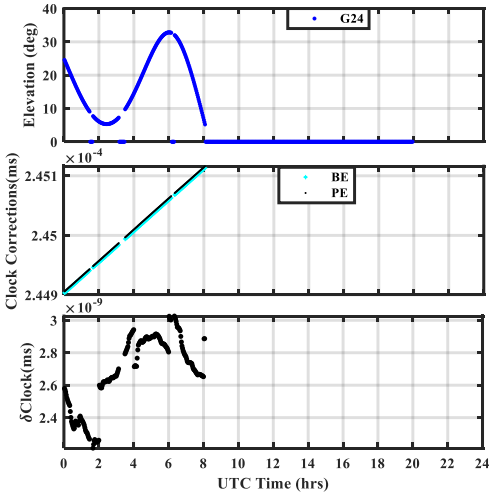


**Figure 2.** Variation of GPS PRN-24 satellite a) Elevation angle (degrees) b) Comparative variation and c) Deviation between BE and PE Clock corrections corresponding to UTC time

**3. 1. 2. User Position Analysis Corresponding to BE and PE** In order to quantify the accuracy of the BE and PE measurements, the user position is computed using the Least Squares (LS) Algorithm, based on both orbital measurements [26]. Figure 4 depicts a scatter plot of the user position latitude and longitudinal variations. It is found that the user positions corresponding to BE and PE are aligned more than 70% of the time, and only a small percentage of user positions are deflected from the reference position. Over a typical day, the receiver tracks a maximum of 12–6 GPS L1, L2, and L5 compatible frequency satellites at the observed location, for a total of 30 satellites. Because the L5 band has only 16 GPS satellites, 9-1 GPS (L1, L5) satellites are visible from the observed location on the observed day, as shown in Figure 5(a). Here, Figure 5 (b-d) shows the variation of estimated ENU coordinates of the user's position based on GPS BE and PE measurements. Table 2 summarized the calculated mean and standard deviation for ENU directional errors related to both BE and PE. In the case of PE-based ENU errors, east errors are much more deviated (mean = 13.97) compared to north (mean = 7.99) and up errors (mean = 4.90). For the GPS, the horizontal accuracy parameters are shown in Table 1, with respective percentile confidence regions. The CEP, DRMS, and 2DRMS for BE and PE measurements were 16.82 m, 20.48 m, 40.96 m, and 13.09 m, 16.10 m, and 32.20 m, respectively, throughout the observed day.

**3. 2. Standalone Galileo** During GPS week 2177 on September 30, 2021, over the observed station, the E24 has a vicinity period of between 05:21:00 and

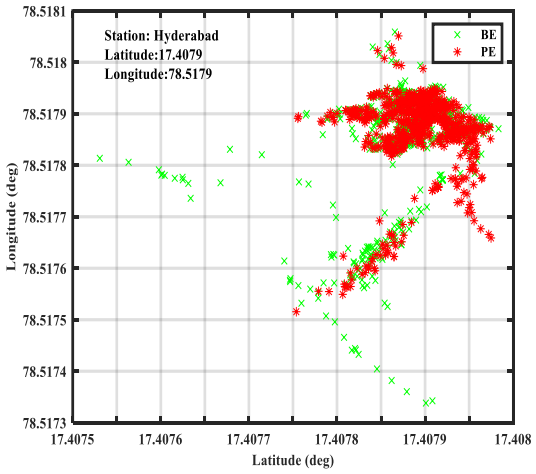


**Figure 4.** Scatter Plot of Estimated Latitude and Longitudinal variations of standalone GPS on 30 September 2021

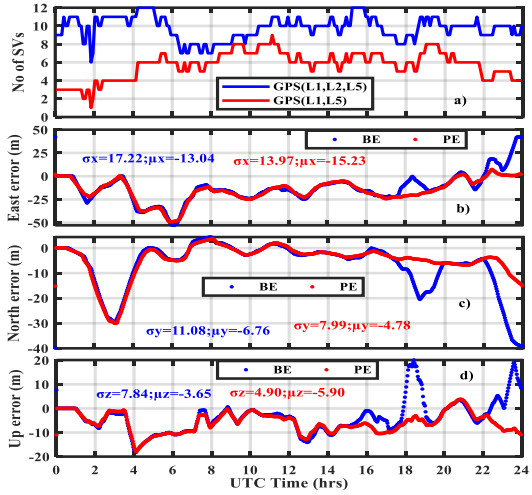


**Figure 3.** Variations of a) GPS dual and triple frequency Satellite visibility and Comparative variation of BE and PE user position in b) East, c) North and d) Up coordinates (m) with respective standard deviation (m) and mean (m)

16:36:42, which corresponds to GPS time between 364920 and 405420 seconds. So, the orbits of the E24 satellite and the clock corrections for BE and PE measurements are shown during the time period mentioned above.

**3. 2. 1. Lagrange Interpolation Results** Figure 6 (a-b) shows the E7's orbital behaviour for both precise and interpolated ECEF measurements. In contrast to G24 ECEF coordinates, no discontinuities were detected in E7 satellite coordinates with respect to UTC.

There are several reasons for this, because the GPS system, which use atomic frequency standards like those of block IIR rubidium, IIF cesium, and GPS III rubidium clocks, seems to have a greater proportion of satellites with greater clock noise than Galileo, which employs predominantly highly stable passive hydrogen masers. This drastically reduces Galileo's error rate by decreasing clock prediction error. Secondly, the shortened update period of the orbit information for on-board Galileo satellites provides a significantly higher upload rate of the broadcast navigation data compared to GPS, hence reducing orbit and clock extrapolation errors [8]. This feature of Galileo may be helpful in highly sensitive GNSS applications. Figures 7 (a-c) show how E7 satellite ECEF coordinates change over time. The marginal comparisons of BE and PE satellite coordinates have similar variations and appear to mostly overlap each other. Even the difference is insubstantial, as shown in Figure 7(d).

In view of the all estimated satellite ECEF coordinates, the difference between BE and PE is in the 4 meter range which is quite similar to GPS. On Figure 8a, the orientation of the G24 satellite is illustrated in relation to its elevation angle. The E24 satellite is visible over a minimum 2-hour period with a high elevation angle (>60°). Figure 8b shows the Clock Corrections for BE and PE, which appear to be overlapped on each other. The BE-PE clock corrections difference is detailed in Figure 8c and it ranges approximately to 3ns. It indicates that the clock correction parameters related to BE and PE are quite similar for observed E7 satellite.

**3. 2. 2. User Position Analysis Corresponding to BE and PE** The scatter plot of user position latitude and longitudinal variation is depicted in Figure 9. There are substantial variations in positioning solutions, and they are widely scattered relative to a fixed receiver reference position. On a typical day, the receiver observes a

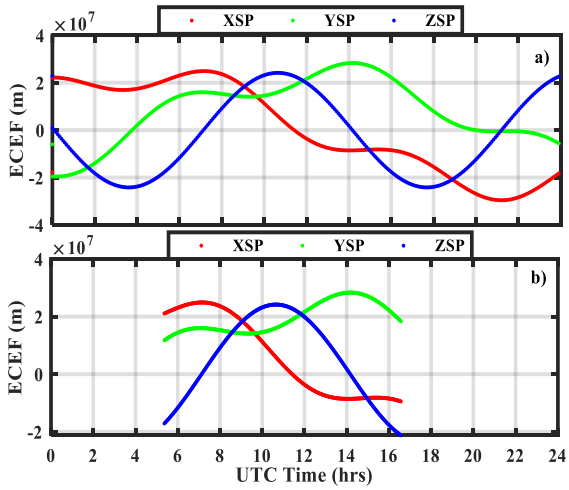


**Figure 6.** Plot of Galileo PRN-E7 satellite precise ECEF orbit coordinates derived from a) SP3 file and b) Lagrange interpolated

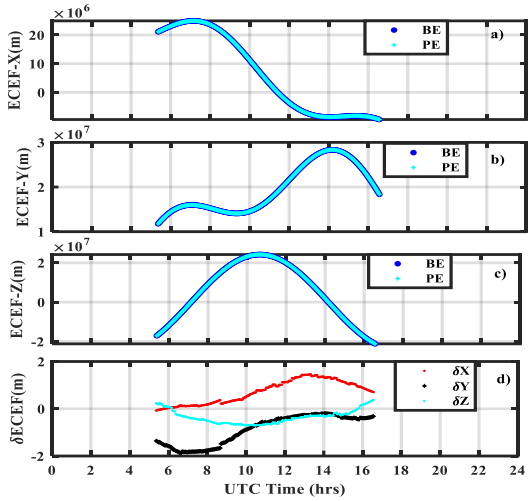


**Figure 74.** Variation of Galileo PRN-E7 satellite Broadcast and Precise ECEF a) X-directional b) Y-directional c) Z-directional coordinates and d) Comparison of BE and PE ECEF coordinates during satellite vicinity period

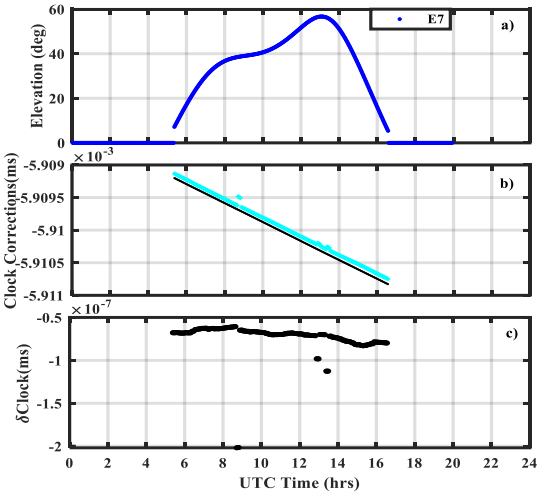


**Figure 8.** Variation of Galileo PRN-E7 satellite a) Elevation angle (degrees) b) Comparative variation and c) Deviation between BE and PE Clock corrections corresponding to UTC time

maximum of 9 and a minimum of 5 satellites, out of the 22 deployed Galileo satellites, as illustrated in Figure 10 (a). Figure 10 (b-d) depicts the estimated ENU coordinates of user position, mean, and standard deviation for the BE and PE orbits of the Galileo constellation. In the case of PE-related ENU directional errors, Table 2 reveals that the east error (mean = 14.30 m) is significantly more deviated (similar to GPS) than the north and up directional errors (mean = -1.99 m and -5.42 m, respectively). Table 3 contains the standard deviation values for positional errors. For Galileo, the standard deviation of east, north, and up computations employing PE measurements are 69%, 62%, and 77% more precise than with BE measurements, respectively. In contrast, the standard deviations of east, north, and up directional errors for GPS PE measurements are 18%, 27%, and 37% more accurate than BE measures, respectively. Table 4 shows the 2D horizontal position precision characteristics. During the observed day, the CEP, DRMS, and 2DRMS with respective percentile confidence areas for Galileo BE and PE measurements are 12.13 m, 16.22 m, 32.45 m and 3.86 m, 5.01 m, 10.03 m. The Galileo has a more precise horizontal accuracy than GPS, whose 95th percentile value is approximately three times greater at 32.20 m compared to 10.30 m.

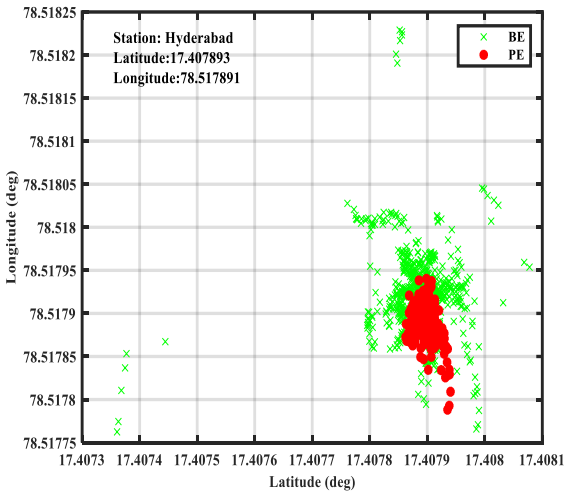


**Figure 9.** Scatter Plot of Estimated Latitude and Longitudinal variations of standalone Galileo on 30 September 2021

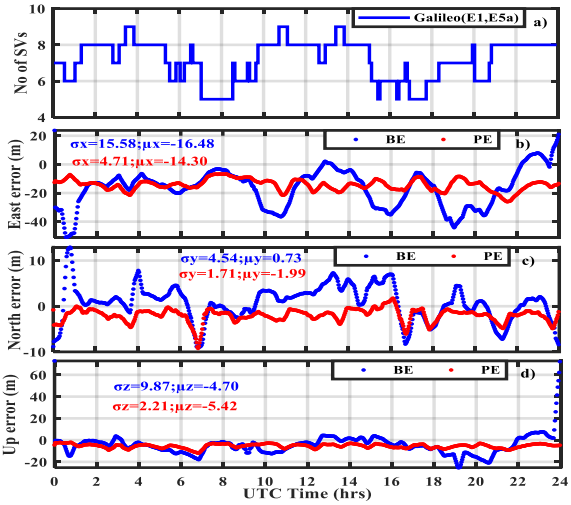


**Figure 5.** Variations of a) Galileo dual frequency Satellite visibility and Comparative variation of BE and PE user position in b) East, c) North and d) Up coordinates (m) with respective standard deviation (m) and mean (m)

**TABLE 2.** Mean of the East, North and Up directional errors (m) for Standalone GPS and Galileo on 30 September 2021 (DOY-273)

| Constellation | Measurements | Mean (m) | | |
|---|---|---|---|---|
| | | East | North | Up |
| Standalone GPS | BE | -13.04 | -6.76 | -3.65 |
| | PE | -15.23 | -4.78 | -5.90 |
| Standalone Galileo | BE | -16.48 | 0.73 | -4.70 |
| | PE | -14.30 | -1.99 | -5.42 |

**TABLE 3. S**tandard deviations in the ENU coordinate system for Standalone GPS and Galileo on 30 September 2021 (DOY-273)

| Constellation | Measurements | Standard Deviation(m) | | |
|---|---|---|---|---|
| | | East | North | Up |
| Standalone GPS | BE | 17.22 | 11.08 | 7.84 |
| | PE | 13.97 | 7.99 | 4.90 |
| Standalone Galileo | BE | 15.58 | 4.54 | 9.87 |
| | PE | 4.71 | 1.71 | 2.21 |

**TABLE 4.** The Horizontal precision estimation parameters as CEP, DRMS, and 2DRMS values for Standalone GPS and Galileo on 30 September 2021 (DOY-273)

| Constellation | Measurements | CEP (m) | DRMS (m) | 2DRMS (m) |
|---|---|---|---|---|
| Standalone GPS | BE | 16.82 | 20.48 | 40.96 |
| | PE | 13.09 | 16.10 | 32.20 |
| Standalone Galileo | BE | 12.13 | 16.22 | 32.45 |
| | PE | 3.86 | 5.01 | 10.03 |

## 4. CONCLUSIONS

The performance of SPP is evaluated in order to assess the GPS and Galileo satellites' precise and broadcast measurements as well as clock offsets over a low latitude station. During the observation period, the E7 satellite has a better clock offset of 3 ns than the G24 satellite (300 ns) with BE and PE measurements. It is noticed that Galileo outperforms GPS with more L1-L5 satellite visibility and a high update rate of navigation messages over the observation period. The numerical results show that the GPS north, east, and vertical components typically improve about 63%, 15%, and 13%, while Galileo improves by 41%, 14%, and 38% corresponding to PE measurements. The PE measures improve CEP and 2DRMS values by 68% and 69% for Galileo and 22% and 21% for GPS, respectively. During the observations, it was observed that the Galileo offers better accuracy than the GPS with PE measurements and low clock offset error. This kind of analysis is useful for future research with regional and global constellations in low-latitude areas.

## 5. ACKNOWLEDGMENT

The authors would like to convey their sincerest gratitude to IGS for supplying GNSS data and products [http://igscb.jpl.nasa.gov] and for making data globally accessible. The authors would like to thank, AGRL, Department of Electronics and Communication Engineering of Osmania University College of Engineering for providing the facilities to carry out this research work.

## 6. REFERENCES

1. Kaplan, E.D. and Hegarty, C., "Understanding gps/gnss: Principles and applications, Artech house, (2017).
2. Hadas, T., Kazmierski, K. and Sośnica, K., "Performance of galileo-only dual-frequency absolute positioning using the fully serviceable galileo constellation", ***GPS Solutions***, Vol. 23, No. 4, (2019), 108. doi. https:// doi. org/ 10. 1007/s10291- 019- 0900-9
3. Gonçalvesa, J.A., Magalhãesa, A. and Bastosa, L., "Galileo performance assessment for aerial navigation", (2021).
4. Supriadi, S., Abadi, P. and Prabowo, D., "Preliminary result of galileo performance on gbas in indonesia", in AIP Conference Proceedings, AIP Publishing LLC. Vol. 2226, (2020), 060002.
5. Basile, F., Moore, T. and Hill, C., "Analysis on the potential performance of gps and galileo precise point positioning using simulated real-time products", ***The Journal of Navigation***, Vol. 72, No. 1, (2019), 19-33. doi: 10.1017/S0373463318000577.
6. Rouch, C., Ramos, A., Bonhoure, B., Suard, N. and Laurichesse, D., "Galileo/gps performance comparison since galileo initial services declaration in december 2016", in Proceedings of the 32nd International Technical Meeting of the Satellite Division of The Institute of Navigation (ION GNSS+ 2019), (2019), 1124-1133.
7. Yin, X., Chai, H., Xiang, M. and Du, Z., "Modelling and assessment of galileo and galileo/gps velocity determination with stand-alone receiver", ***The Journal of Navigation***, Vol. 74, No. 4, (2021), 901-913.
8. Carlin, L., Hauschild, A. and Montenbruck, O., "Precise point positioning with gps and galileo broadcast ephemerides", ***GPS Solutions***, Vol. 25, No. 2, (2021), 77.
9. Kuna, D. and Perumalla, N.K., Investigating the positioning capability of gps and galileo constellations over indian sub-continent, in Communication and intelligent systems: Proceedings of iccis 2021. 2022, Springer.829-842.
10. Valizadeh, A. and Hamidi, H., "Improvement of navigation accuracy using tightly coupled kalman filter", ***International Journal of Engineering, Transactions B: Applications***, Vol. 30, No. 2, (2017), 215-223. doi: 10.5829/idosi.ije.2017.30.02b.08.
11. El Abdellaoui, L., Zbitou, J., Errkik, A., Zahraoui, I. and Sanchez Mediavilla, A., "New low cost printed antenna cpw-fed for global positioning system, personal communication system and worldwide interoperability for microwave access band

applications", ***International Journal of Engineering, Transactions B: Applications***, Vol. 29, No. 8, (2016), 1056-1061. doi: 10.5829/idosi.ije.2016.29.08b.04.

12. Voosoghi, B. and Rastbood, A., "Fixing of cycle slips in dual-frequency gps phase observables using discrete wavelet transforms", ***International Journal of Engineering, Transactions A: Basics***, Vol. 21, No. 1, (2008), 9-26.
13. Sridher, T., Sarma, A. and Naveen Kumar, P., "Performance evaluation of onboard wi-fi module antennas in terms of orientation and position for iot applications", ***International Journal of Engineering, Transactions A: Basics***, Vol. 35, No. 10, (2022), 1918-1928. doi: 10.5829/ije.2022.35.10a.11.
14. Warren, D.L. and Raquet, J.F., "Broadcast vs. Precise gps ephemerides: A historical perspective", ***GPS Solutions***, Vol. 7, No., (2003), 151-156. doi.
15. Johnston, G., Neilan, R., Craddock, A., Dach, R., Meertens, C. and Rizos, C., "The international gnss service 2018 update", in EGU General Assembly Conference Abstracts. Vol., No. Issue, (2018), 19675.
16. Bhatta, B., "Global navigation satellite systems: Insights into gps, glonass, galileo, compass, and others, BS Publications, (2010).
17. Greenspan, R., Parkinson, B., Spilker, J., Axelrad, P. and Enge, P., "The global positioning system: Theory and applications", Washington, DC: AIAA Progress in Aeronautics and Astronautics BW Parkinson, JJ Spilker, Jr., P. Axelrad, P. Enge, editors.(1996): 187, Vol. 218, No., (1996).
18. Remondi, B.W., "Computing satellite velocity using the broadcast ephemeris", ***GPS Solutions***, Vol. 8, No. 3, (2004), 181-183.
19. Weisstein, E.W., "Lagrange interpolating polynomial", https://mathworld. wolfram. com/, (2004).
20. Schenewerk, M., "A brief review of basic gps orbit interpolation strategies", ***GPS Solutions***, Vol. 6, No. 4, (2003), 265-267.
21. Schueler, T., "On the interpolation of sp3 orbit files", ***I***fEN Technical IFEN-TropAC-TN–002–01. Institute of Geodesy and Navigation, University of Federal Armed Forces, Munich, (1998).
22. Horemuž, M. and Andersson, J.V., "Polynomial interpolation of gps satellite coordinates", ***GPS Solutions***, Vol. 10, (2006), 67-72.
23. Spiegel, M. and Liu, J., "Mathematical handbook of formulas and tables mcgraw-hill", ***New York***, (1999).
24. Kuna, D., Santhosh, N. and Perumalla, N.K., "Preliminary analysis of standalone galileo and navic in the context of positioning performance for low latitude region", ***Procedia Computer Science***, Vol. 171, (2020), 225-234.
25. El-Rabbany, A., "Introduction to gps: The global positioning system, Artech house, (2002).
26. Mosavi, M.R., Azarshahi, S., Emamgholipour, I. and Abedi, A.A., "Least squares techniques for gps receivers positioning filter using pseudo-range and carrier phase measurements", ***Iranian Journal of Electrical & Electronic Engineering***, Vol. 10, No. 1, (2014), 18-26.

## Persian Abstract

**چکیده**

سیستم ماهواره ای ناوبری جهانی ( (GNSSدر حال تبدیل شدن به یک فناوری موقعیت یابی حیاتی در سرویس های مختلف است. کیفیت ephemeris یکی از عواملی است که مستقیماً بر دقت موقعیت کاربر تأثیر می گذارد. برخی از برنامه ها، مانند تحقیقات در مورد پویایی پوسته زمین، به داده های زودگذر دقیق تری نسبت به گذراهای پخش شده نیاز دارند. چندین مؤسسه، مانند سرویس بین المللی GNSS (IGS)، خدمات مداری دقیقی را برای فعال کردن این برنامه ها توسعه داده اند. متأسفانه، نرخ داده برای چنین مدارهای دقیقی اغلب به ۱۵ دقیقه محدود می شود. در این مقاله، به منظور تولید ابطال دقیق با دوره نمونه‌برداری پخش، از روش درون یابی معروف لاگرانژ استفاده شده است. علاوه بر این، یک تجزیه و تحلیل موقعیت GPS و گالیله مقایسه ای مربوط به پخش و قطعی دقیق در یک روز معمولی در سپتامبر ۲۰۲۱ ارائه شده است. برای به دست آوردن بینش در مورد تجزیه و تحلیل موقعیت یابی مقایسه ای بر روی ایستگاه حیدرآباد، خطاهای جهت ) ENUشرق-شمال-بالا)، دید ماهواره و پارامترهای دقت افقی در نظر گرفته شده است. بر اساس تجزیه و تحلیل عددی، گالیله مستقل دارای قابلیت های مشابه با GPS است و می توان از آن در Multi-GNSS در هند و مناطق اطراف آن استفاده کرد. این کار ممکن است به توسعه گیرنده‌های GNSS تک فرکانس یا دو فرکانس برای خدمات ناوبری غیرنظامی کمک کند.

International Journal of Engineering

Journal Homepage: www.ije.ir

# Compaction Quality Control of Coarse-grained Soils Using Dynamic Penetration Test Results through Correlation with Relative Compaction Percentages

S. M. S. Ghorashi[a], M. Khodaparast*[a], M. Khodajooyan Qomi[b]

[a] *University of Qom, Faculty of Engineering, Civil Engineering Department, Qom, Iran*
[b] *Isfahan University of Technology, Faculty of Civil Engineering, Isfahan, Iran*

*PAPER INFO*

*Paper history:*
Received 19 August 2022
Received in revised form 09 November 2022
Accepted 12 Novemeber 2022

*Keywords*:
*Dynamic Penetration Test*
*Dynamic Penetrometer of Light*
*Dynamic Penetrometer of Medium*
*Dynamic Cone Resistance*
*Relative Compaction*
*Coarse-grained Soils*

*ABSTRACT*

In this study, in order to control the compaction quality of the coarse-grained soils used in sub-base and base layers of several road construction projects, the dynamic penetration test (DPT) has been conducted on 50 locations using both dynamic penetrometer of light (DPL) and dynamic penetrometer of medium (DPM). First, in order to obtain the results independently from the penetrometer type, the dynamic cone resistance ($q_d$) values were calculated in each location based on hammer blows of both DPL and DPM. Next, the average values of $q_d$ obtained by both the penetrometers, were correlated with the percentages of relative compaction ($RC$) in the same location obtained by performing the sand cone test on location and modified proctor test in laboratory. Accordingly, it was extracted a power correlation between the $q_d$ values and $RC$ percentages, with the determination coefficient ($R^2$) of about 0.64. Then, for considering the effect of soil grains size using the median particle size ($D_{50}$), a more accurate power correlation was obtained which as a result, the $R^2$ value enhanced to 0.89. Furthermore, in order to consider the soil vertical stresses caused by depth of testing as well as obtaining a normalized relationship, the $q_d$ values were divided by the vertical stresses and correlated with the $RC$ percentages. Afterwards, regarding the effect of soils grains size and also their gradation properties, this time by using the dimensionless coefficients of uniformity ($Cu$) and curvature ($Cc$), it was extracted an other normalized power correlation. The results showed that the $R^2$ value enhanced from about 0.49 to 0.92.

***doi***: *10.5829/ije.2023.36.03c.06*

## 1. INTRODUCTION

Dynamic penetration test (DPT) is one of the in-situ tests which is employed for estimating the resistive properties of soils. DPT is an economical and simple method for assessing and determining the strength of the soil layers in civil projects. In this test, the dynamic energy resulting from a hammer drop with a specific weight and height, causes the penetration of a rod with conical tip into the ground, and the number of hammer blows needed for a specific penetration of cone is a criterion for evaluating the materials compaction. In each step of cone penetration, typically the number of blows for penetration of 10 and 20 cm, is recorded as $N_{10}$ and $N_{20}$, respectively. The NF P94-105 [1], BS 5930 [2], EN ISO 22476-2 [3] and ASTM D6951/D6951-09 [4] are among the accepted standards.

In addition to the number of blows achieved by DPT, the dynamic penetration index (DPI) or dynamic cone penetration index (DCPI) which is usually presented in the unit of millimeters/blow, explains the penetration depth of cone's tip into the soil for every hammer blow. Generally with increasing the strength or toughness of the soil materials, the number of blows for a specific penetration is increased, and consequently the DPI value is decreased.

Other way for using the DPT results, is calculating of the dynamic cone resistance ( $q_d$ ). Sanglerat [5] assumed that the penetration of cone into soil is similar to a driven pile and accordingly, showed that the $q_d$ is calculated as follows:

*Corresponding Author Institutional Email: khodaparast@qom.ac.ir
(M. Khodaparast)

Please cite this article as: S. M. S. Ghorashi, M. Khodaparast, M. Khodajooyan Qomi, Compaction Quality Control of Coarse-grained Soils Using Dynamic Penetration Test Results through Correlation with Relative Compaction Percentages, ***International Journal of Engineering, Transactions C: Aspects,*** Vol. 36, No. 03, (2023) 473-480

$$q_d = \frac{m}{m+m'}.(\frac{mgh}{Ae}) \quad (1)$$

where $A$ is cross-section area of the cone, $e$ is the average of cone penetration in each blow (the DPI can also be used instead of $e$), $h$ is the height of hammer drop, $m$ is hammer mass, $m'$ is total mass of penetrometer (except hammer) and $g$ is gravity acceleration.

In Some standards, Equation (1) is also suggested [3], and just instead of $e$, the values of $0.1/N_{10}$ (e.g. DPL and DPM) and $0.2/N_{20}$ (such as $DPH_B$) are substituted. As shown in Equation (1), the advantage of using the $q_d$ parameter is that it has less dependence to the type of chosen penetrometer due to consider the value of penetrometer energy, the cone geometry and the penetrometer mass [6].

One of the important factors that can be effective on the results of all penetration tests, is the vertical stress emanated from the overburden of soil mass which increases with an increase in depth. Increasing the vertical stress and consequently, increasing the lateral pressure on the cone's penetrometer will affect the results of the test, but its effect varies in different soils. Accordingly, some studies that the penetration test results should be corrected for different depths. Also, in the standard penetration test (SPT) which is used significantly in literature [7, 8]. This correction is referred to as overburden correction [9]. In DPT such as SPT, the existence of overburden stresses can affect the results obtained by the test. Lee et al. [10] introduced the normalized parameter of dynamic cone resistance ($q_{d,n}$) to eliminate the effect of vertical stress and its lateral pressure. Also, other important factor can affect on DPT results is while the DPT is carried out in a hand excavated pit [11].

As mentioned before, simple equipments have been used in DPT, hence this test is considered as a inexpensive, simple and fast method. Due to the mentioned advantages, this test is a common favored test in everyday application to identify the important physical and strength parameters in different soils. Accordingly, this test has been used in various studies for different purposes, including the estimation of density and unit weight [12-14], relative density [15-17], shear strength and its related parameters [10, 18, 19], etc.

In order to use the DPT results and their relation with geotechnical properties of fine-grained soils, various studies have been conducted, especially in compaction quality control of the soils layers in road projects [20, 21]. This is while that the majority of previous studies on DPT results and their relation with compaction control of coarse-grained soil layers, have been performed on physical models made in laboratory [22-25]. In these studies, DPT is mainly carried out on a physical model with limited dimensions. While in the mentioned studies, it has been tried to keep the dimension of the models to be close to the real conditions in a location, but due to problem of the model boundary effects on the test results in physical models, the results of DPT in these models significantly differ from the test results in location. Therefore, using the DPT in a location with realistic conditions makes the results have been more exact, compared to the tests performed in a physical model made in laboratory.

So far, in the field of compaction quality control of coarse-grained soil layers, various studies have been performed in location using DPT and other tests like California bearing ratio (CBR) test [26-28]. These studies mainly show the relationship between DPI and CBR values. But studies about the relation of DPT results and *RC* values, are scarce in location with coarse-grained soils.

Jayawickrama et al. [29] studied the *RC* of coarse-grained soils using the dynamic cone penetrometer (DCP) test (a lightweight kind of DPT). The tests were conducted on a range of granular materials that have been used as backfills and embedment for buried structures, including thermoplastic pipes. Jayawickrama et al. [29] conducted a series of DCP tests according to ASTM D2321 Classes I and II. Accordingly, they showed the profiles of DCP blows count with respect to the penetration depth of penetrometer in different granular soil, for two methods of soil compaction, including an impact rammer and a vibratory plate compactor. Results showed that for a given soil, the DCP blows count per penetration depth in impact rammer has been significantly higher than the vibratory plate compactor which means that the soils reach a higher compaction quality. Finally, the researchers suggested to present the data in the form of DCP blow count profiles per penetration depth, which then can used as the basis to compare between different soils, compaction equipments, and levels of compaction energy.

As mentioned before, in the field of compaction quality control of soil layers, studies that can explain the relationship between DPT results and relative compaction (*RC*) of the coarse-grained soil layers as an index of the compaction control, are scant in a location with realistic conditions. However, the coarse-grained soils are widely used in different parts of road construction projects, including subgrade, sub-base and base. On other hand, the parameter of *RC* is a good dimensionless index for the compaction quality control of soil layers and hence it has a global application. So, obtaining a appropriate correlation between the DPT results and *RC* values, can be used as a quick and non-destructive way to control the compaction quality of road layers compared to the time-consuming methods with high degree of destruction such as conventional methods of *RC* determination. It should be noted that the operation of *RC* determination of soil is normally carried out by in-

situ tests and through digging holes on the road materials such as sand cone test and using the standard or modified proctor testing in laboratory. The mentioned tests are time-consuming and expensive, and it is necessary to perform the tests many times to control the compaction quality of road layers.

In this paper, first the DPT is conducted using both dynamic penetrometer of light (DPL) and dynamic penetrometer of medium (DPM) and the results are converted to $q_d$ values and presented a reasonably accurate relationships between the mentioned values and the percentages of *RC* in different kinds of coarse-grained soils with different gradation. Also, the other relationships are extracted by considering the effect of grains size and gradation properties of the soils. The structure of the paper includes, definition of the DPT and its kinds and standards, a brief reviewing of the studies related to DPT, reviewing of the studies related to the present study, the necessity, innovation and scope of this study (*Introduction section*), specifications of the construction road projects in terms of geology, coarse-grained soils used, different types of the tests performed (*Material and Method section*), explanation of the results obtained by the all the tests, presentation of correlations and discussion about them (*Results and Discussions*), a brief explanation of the present study and results and classification of all the correlation obtained by this study (*Conclusion section*). Figure 1 presents the flowchart of the research methodology.

## 2. MATERIALS AND METHODS

The material studied in this paper, are coarse-grained soils used for sub-base and base layers of several road construction projects in two cities of Qom and Asaluyeh in Iran. Qom is a city in Qom province and in terms of geological divisions, is located in the central part of Iranian plateau, and has a hot and dry climate (desert climate). According to studies, this city has generally four alluvial layers. Layer 1 includes fill soils and surficial alluviums, and usually has less than 15 m thickness. Layer 2 has medium to coarse-grained alluviums with thickness ranging from 5 to 52 m. Layer 3 consists of a thick aquifer, which is composed of fine-grained and medium-grained alluviums, and is thickest layer along the central area of Qom and along the Qomrood river, with 250 m thickness, and the lowest thickness of the layer in the south-east area of Qom, with 95 m thickness. Layer 4 as the bedrock, is made of marlstone and limestone marl. Asaluyeh city is a port of Bushehr province and in terms of geological divisions, it is located in the Zagros structural zone (External Zagros) and on the Arabian basement. This city has a hot and humid climate, and its average elevation from the sea level, is about 5 m. The surface of this area mainly consists of alluvial deposits. This area includes the Mishan formation (grey marls, clay limestone and claystone), Aghajari formation (brown to grey sandstone, gypsum, cream to red marls, siltstone), Bakhtyari formation (conglomerate, sandstone, limestone, clayey marl, siltstone, claystone), Asmari formation (brown to cream limestone, cream marls associated with fossil), Guri formation (sandstone, limestone, lime marl), and Surmeh formation (dolomitic lime, dolomite, clay limestone). Figure 2 shows the situation of mentioned projects.

Table 1 summarized the specification of coarse-grained soils studied in this paper. The soils classification is according to ASTM D2487 (Unified soil classification system) [30]. As stated in Table 1, for each type of soil, the locations where the sand cone tests and DPT tests using both types of DPL and DPM has been conducted, are mentioned. Moreover, in this study, two types of SW soil with different gradation were used, which are stated as SW1 and SW2 in Table 1. As is illustrated in Figure 3, each location where all the tests are performed (DPL, DPM and sand cone test), comprises a small circular area with 50 cm diameter, so that the soil conditions remain identical for all the tests. In addition to specifications of the mentioned soil in Table 1, the gradation curves of this materials are presented in Figure 4.

The Conventional dynamic penetrometers which are usually used in engineering projects include light-type penetrometers (e.g. DPL and DCP), and medium-type penetrometer (e.g. DPM). These penetrometers because of their low costs, simplicity to work and their lighter

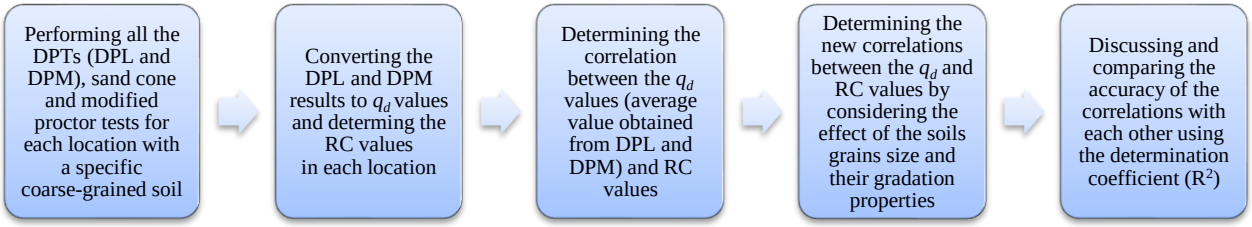


**Figure 1.** Flowchart of the research methodology

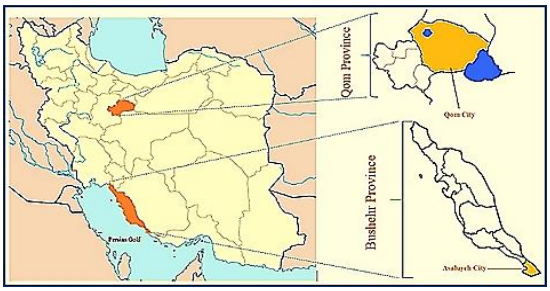


**Figure 2.** The situation of the road construction projects in this study

weight are employed in various projects compared to their heavier types such as heavy (DPH) and super heavy (DPSH) penetrometers, especially in road construction projects, which it is not required to investigate the resistance parameters in high depths. In this research, to perform the DPT in each location both the DPL and DPM according to EN ISO 22476-2 [3] is performed. Table 2 summarized the specification of penetrometers used in this study. Figure 5 depicts their schematic and penetrating cone.

**TABLE 1.** The specifictaions of soils used and number of the locations for all the tests in each soil type

| Number of locations for all the tests | Soil type | $D_{50}$ (mm) | Coefficient of Uniformity ($Cu$) | Coefficient of Curvature ($Cc$) | Plasticity Index (%) |
|---|---|---|---|---|---|
| 9 | GW | 4.8 | 52.3 | 1.62 | - |
| 9 | SW1 | 3.5 | 38.57 | 1.244 | - |
| 14 | SW2 | 3.6 | 34.37 | 1.63 | - |
| 6 | GW-GC | 5.2 | 11.67 | 2.14 | 5.7 |
| 12 | SP | 3.1 | 16.67 | 0.96 | 10.1 |

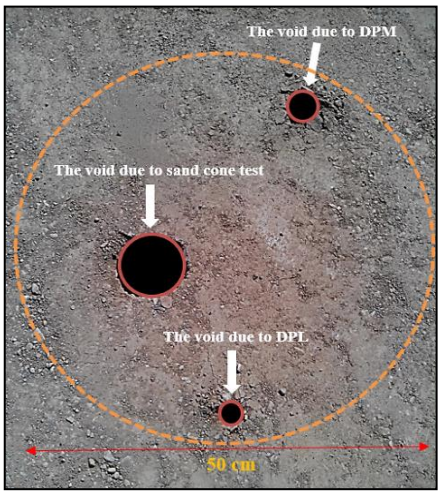


**Figure 3.** The situation and void types due to the tests conducting for each location

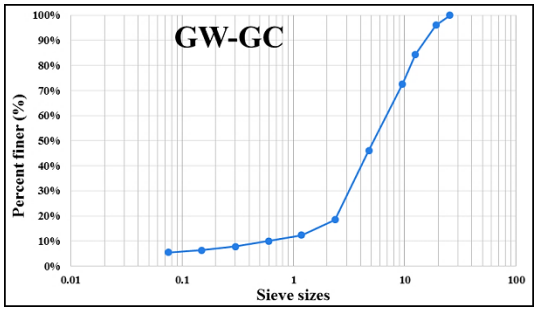


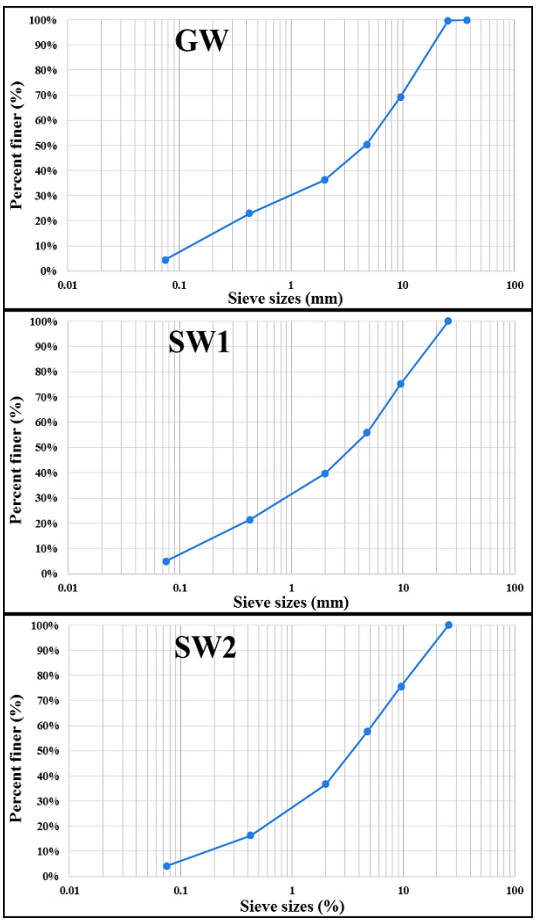

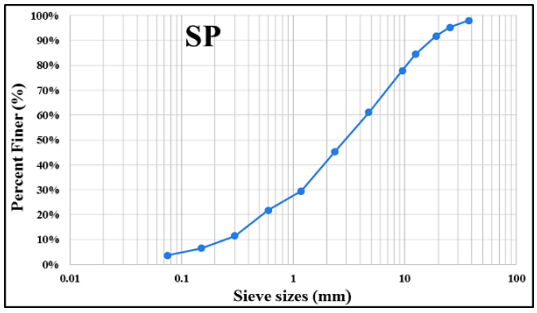


**Figure 4.** The gradation curves of coarse-grained materials used in the layers of road projects

**TABLE 2.** The specifications of penetrometers used in this study

| Penetrometer | DPL | DPM |
|---|---|---|
| Hammer mass (kg) | 10 | 30 |
| Drop height (mm) | 500 | 500 |
| Cone diameter (mm) | 35.7 | 43.7 |
| Angle of cone's tip (degree) | 90 | 90 |
| Cross-section area of cone ($cm^2$) | 10 | 15 |
| Specific work for each blow($kJ/m^2$) | 49 | 98 |

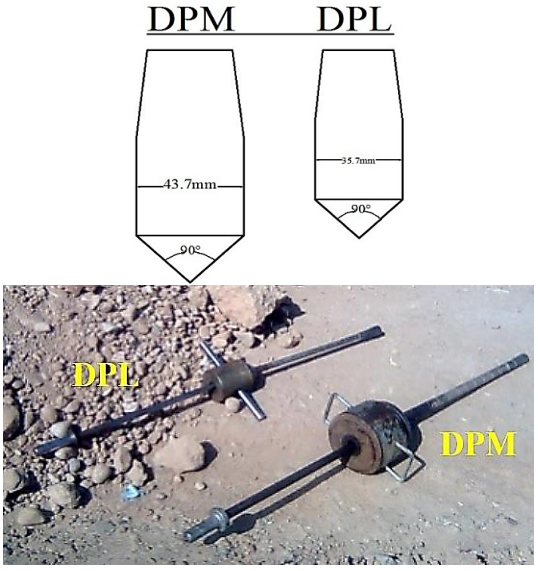


**Figure 5.** The Penetrometers used in this study (up) and their cone specifications (down)

In addition to perform the DPT in each location, to calculate the *RC* percentage of road layers in the studied soils, the sand cone test was performed to obtain the soil dry unit weight ($\gamma_{d(field)}$) modified compaction test in laboratory according to ASTM D1557-12 [31] in order to determine the maximum dry unit weight of the soil ($\gamma_{d(\max)}$). So, according to above-mentioned, the percentage of *RC* is obtained as follows:

$$RC(\%) = \frac{\gamma_{d(field)}}{\gamma_{d(\max)}} \times 100 \quad (2)$$

## 3. RESULTS AND DISCUSSION

After conducting the DPTs (both the DPL and DPM) in each location with each coarse-grained soils mentioned in this study, the hammer blows resulting from each mentioned test is converted to the $q_d$ values obtained from Equation (1). The variation of $q_d$ values resulting from DPM against the DPL is shown in Figure 6. As is evident, the $q_d$ values of DPM vary linearly with respect to DPL values and with a very high determination coefficient ($R^2$=0.9927). This means that the difference of $q_d$ values resulting from both the tests is very small. Therefore, it can be concluded that the results of the tests are independent of the penetrometer type.

It should be noted that because in the present study, it was used both the DPL and DPM according to valid standards [3], investigating the results repeatability obtained from these tests, has been neglected.

Also, in a study performed using both the DPL and DPM, Khodaparast et al. [20] observed that more than 70% of the tests results, have the variation coefficient of less than 10% and more than 95% of them have the variation coefficient of less than 30%. These low values of variation coefficient show that the investigation of the results repeatability obtained from these tests (both the DPL and DPM) is negligible. It is noticeable that due to superficial depth of the tests (DPL and DPM) in this study, as well as the larger diameter of the penetrating cone compared to the penetrating rod, the friction between the rod and soil is almost ineffective [5, 32, 33] [6, 36, 37]. Therefore, the effect of the friction on $q_d$ values has been neglected.

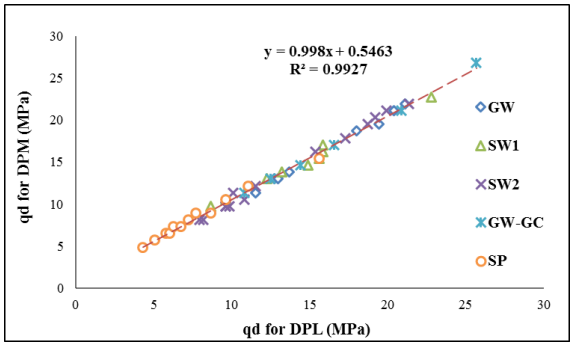


**Figure 6.** The relationship between the variations of DPM and DPL results

**3. 1. Correlations Between the DPT results and *RC* Percentages of the Soils** After obtaining the $q_d$ values, and the proximity of DPL and DPM values to each other, and proving the independence of these values from the penetrometer type, it was used the average $q_d$ value of DPL and DPM as the final value of $q_d$. As mentioned before, according to Equation (2), the *RC* percentages for each location with a given soil, are calculated using the values obtained from dry unit weight in location and maximum dry unit weight in laboratory. Now, in the following, a relationship is presented by fitting a power curve between the final values of $q_d$ and *RC* percentages as shown in Figure 7. By increasing the $q_d$ value, the *RC* percentage increases, i.e. the soil with higher compaction shows more resistance against the penetration of penetrometer, and therefore, for a given penetration, more blows are required. Also, this result is confirmed by Jayawickrama et al. [29]. Moreover, it has been shown other relationship on the same plot, the $\frac{q_d}{D_{50}}$ versus *RC* percentages. It is clear that by dividing the $q_d$ values by $D_{50}$ (median particle size of soil), in fact, it has been considered the size effect of soil grains on the $q_d$ values. As is shown in Figure 7, by considering the $D_{50}$ of coarse-grained soils considered in this study, a desired correlation is achieved. As a result the $R^2$ values are enhanced from about 0.64 to 0.89, and consequently, the accuracy of the correlation is much better and more acceptable compared to the prior state (while $D_{50}$ is not considered). Lee et al. [34] also used the parameter of $D_{50}$ to consider the grains size effect of sandy soils on DPT results (i.e. DPI values) and as a result they reached the accurate correlations.

In the following, in order to normalize the $q_d$ values and obtain a better correlation compared to previous states, and also to consider the overburden weight or depth of conducting DPTs, it is achieved a relationship by creating the correlation between the values of $\frac{q_d}{\gamma z}$ and *RC* percentages, as is shown in Figure 8(a). The $\gamma$, is the unit weight of soil in each location, and *z*, is the overburden depth or the penetration depth of penetrometer cone in DPT. Also in Figure 8(b), other relationship is presented to consider the gradation and size effects of soil particles. According to Figure 8(b), to keep the correlation values dimensionless, this time, two dimensionless parameters are used to determine the correlation, namely, the uniformity (*Cu*) and curvature (*Cc*) coefficients of gradation curves of the soils. Therefore, this time, a relationship between $\frac{q_d}{\gamma z.Cu.\sqrt{Cc}}$ and *RC* percentages is presented. By comparing the correlations shown in Figures 8(a) and 8(b), it can be concluded that considering the *Cu* and *Cc* values, has a great impact on the $R^2$ and consequently, the accuracy of obtained correlation. Therefore, the $R^2$ value increases from about 0.49 to 0.92. This means that by considering the *Cu* and *Cc* values as coefficients for considering the gradation properties and size effects of coarse-grained soils, it can be reached from a low-accuracy correlation to a high-accuracy and valid correlation. This can be used for controlling the compaction quality of coarse-grained soils used in road layers.

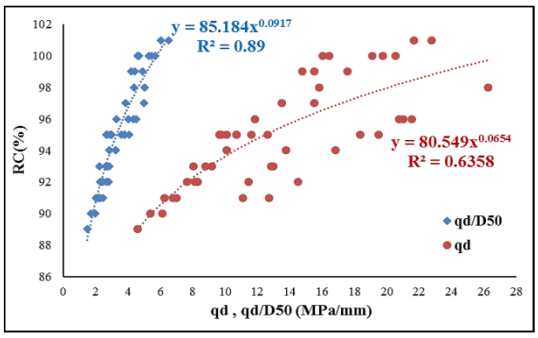


**Figure 7.** The correlation of $q_d$ and $\frac{q_d}{D_{50}}$ values with the percentage of soils RC

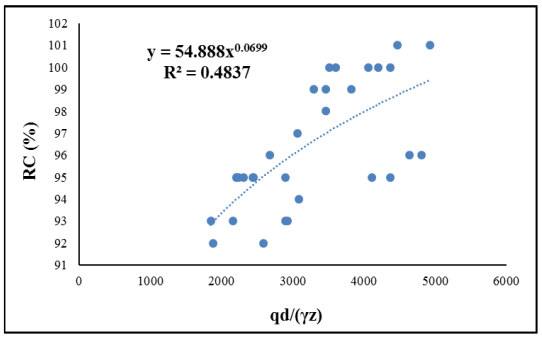


(a)

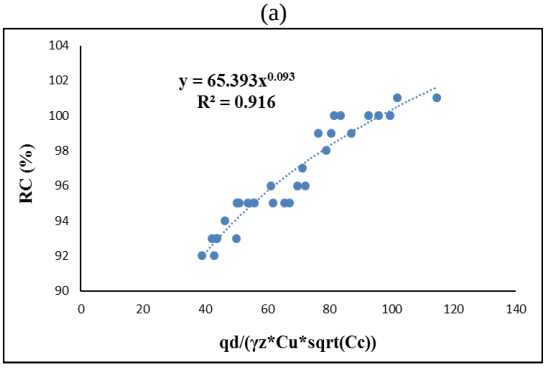


(b)

**Figure 8.** The correlation of $\frac{q_d}{\gamma z}$ (a), and $\frac{q_d}{\gamma z.Cu.\sqrt{Cc}}$ (b), with the percentage of soils RC

## 4. CONCLUSION

In this paper, for controlling the compaction of coarse-grained soil layers which are mainly used in different parts of road layers, five common types of the soils, including GW, SW with two different types of gradation (SW1 and SW2), GW-GC and SP, have been used in sub-base and base layers of several road construction projects in Iran. In each location, both the DPL and DPM were conducted and the results obtained from these tests were converted to $q_d$ values to make the results insensitive to penetrometer type. In addition to the DPT, the sand cone test was carried out in location and modified proctor test was carried in laboratory to determine the *RC* in each location. Then, a series of correlations was presented between the $q_d$, $\frac{q_d}{D_{50}}$, $\frac{q_d}{\gamma z}$, $\frac{q_d}{\gamma z.Cu.\sqrt{Cc}}$ values and *RC* percentages as follows:

- The correlation between $q_d$ and *RC* percentages:

$$RC = 80.549 q_d^{\,0.0654} \quad (R^2 = 0.6358) \tag{3}$$

- The correlation between $\frac{q_d}{D_{50}}$ and *RC* percentages:

$$RC = 85.184\left(\frac{q_d}{D_{50}}\right)^{0.0917} \quad (R^2 = 0.89) \tag{4}$$

- The correlation between $\frac{q_d}{\gamma z}$ and *RC* percentages:

$$RC = 54.888\left(\frac{q_d}{\gamma z}\right)^{0.0699} \quad (R^2 = 0.4837) \tag{5}$$

- The correlation between $\frac{q_d}{\gamma z.Cu.\sqrt{Cc}}$ and *RC* percentages:

$$RC = 65.393\left(\frac{q_d}{\gamma z.Cu.\sqrt{Cc}}\right)^{0.093} \quad (R^2 = 0.916) \tag{6}$$

The results obtained from the above correlations, show that the parameters of $D_{50}$, *Cu* and *Cc* can play a significant role in creating more accurate correlations and as a result, they cause the compaction quality control of the coarse-grained soils be more exact.

It should be noted that the parameters of *Cu* and *Cc* due to obtain a normalized correlation (see Equation (6)) with highest accuracy and considering the effect of soils grains size and their gradation properties in form of dimensionless, are more appropriate than $D_{50}$ parameter.

## 5. REFERENCES


1. P94-105, N., Grounds: Investigation and testing, measuring compaction quality. Method using variable energy dynamic penetrometer - penetrometer calibration principle and method - processing results-interpretation. 2012: Paris: Association Française de Normalisation (AFNOR).
2. Standard, B., "5930, 1981. Code of practice for site investigations", ***British Standards Institution, London***, Vol. 147, (1981).
3. ISO, E., "22476-2 2005: Geotechnical investigation and testing–field testing–part 2: Dynamic probing", ***CEN, Brussels***, (2005).
4. ASTM, Standard test method for use of the dynamic cone penetrometer in shallow pavement applications. 2003.
5. Sanglerat, G., "The penetrometer and soil exploration development in geotechnical engineering vol. 1", ***Amsterdam The Netherland***, (1972).
6. Butcher, A., McElmeel, K. and Powell, J., "Dynamic probing and its use in clay soils", in Proceedings of the international conference on Advances in site investigation practice,(Craig C.(eds)). Thomas Telford, London. (1996), 383-395.
7. Arshid, M.U., "Knowledge based prediction of standard penetration resistance of soil using geotechnical database", ***Civil Engineering Journal***, Vol. 7, (2021), 1-2. http://dx.doi.org/10.28991/CEJ-SP2021-07-01
8. Khodaparast, M., Rajabi, A.M. and Derakhshan, M., "Development of practical correlations between cone penetration resistance and spt values for various types of soils", ***Iranian Journal of Science and Technology, Transactions of Civil Engineering***, Vol. 44, (2020), 471-481. https://doi.org/10.1007/s40996-019-00319-2
9. Liao, S.S. and Whitman, R.V., "Overburden correction factors for spt in sand", ***Journal of Geotechnical Engineering***, Vol. 112, No. 3, (1986), 373-377. https://doi.org/10.1061/(ASCE)0733-9410(1987)113:3(283)
10. Lee, J.-S., Kim, S.Y., Hong, W.-T. and Byun, Y.-H., "Assessing subgrade strength using an instrumented dynamic cone penetrometer", ***Soils and Foundations***, Vol. 59, No. 4, (2019), 930-941. doi. https://doi.org/10.1016/j.sandf.2019.03.005
11. Ghorashi, S., Khodaparast, M. and Rajabi, A., "Evaluation of dynamic probing testing effect in hand excavated pit on test results using numerical modeling", ***International Journal of Engineering, Transactions B: Applications***, Vol. 33, No. 8, (2020), 1553-1559. https://doi.org/10.5829/ije.2020.33.08b.13
12. Salgado, R. and Yoon, S., "Dynamic cone penetration test (dcpt) for subgrade assessment", ***Joint Transportation Research Program***, (2003), 73.
13. Hamid, A.M., Al-Amoudi, O.S.B. and Aiban, S.A., "Assessing the effect of density and water level on the degree of compaction of sand using dynamic cone penetration test", ***Arabian Journal for Science and Engineering***, Vol. 44, (2019), 4921-4930. https://doi.org/10.1007/s13369-018-3641-0
14. Chennarapu, H., Garala, T.K., Chennareddy, R., Balunaini, U. and Venkata Narasimha Reddy, G., "Compaction quality control of earth fills using dynamic cone penetrometer", ***Journal of Construction Engineering and Management***, Vol. 144, No. 9, (2018), 04018086. https://doi.org/10.1061/ (ASCE) CO.1943-7862.0001530
15. Lin, L., Li, S., Liu, X. and Chen, W., "Prediction of relative density of carbonate soil by way of a dynamic cone penetration test", ***Géotechnique Letters***, Vol. 9, No. 2, (2019), 154-160. https://doi.org/10.1680/jgele.18.00165
16. MacRobert, C., Bernstein, G. and Nchabeleng, M., "Dynamic cone penetrometer (DCP) relative density correlations for sands", (2019). http://dx.doi.org/10.28927/SR.422201
17. Lin, L., Li, S., Sun, L., Li, T. and Yin, J., "Assessing relative density of carbonate granular soil via dynamic cone penetration field and model tests", ***Marine Georesources & Geotechnology***, Vol. 39, No. 12, (2021), 1472-1480. https://doi.org/10.1080/1064119X.2020.1850950

18. Fakher, A., Khodaparast, M. and Jones, C., "The use of the mackintosh probe for site investigation in soft soils", ***Quarterly Journal of Engineering Geology and Hydrogeology***, Vol. 39, No. 2, (2006), 189-196. https://doi.org/10.1144/1470-9236-05-039
19. Kim, S.Y. and Lee, J.-S., "Energy correction of dynamic cone penetration index for reliable evaluation of shear strength in frozen sand–silt mixtures", ***Acta Geotechnica***, Vol. 15, (2020), 947-961. https://doi.org/10.1007/s11440-019-00812-y
20. Khodaparast, M., Rajabi, A. and Mohammadi, M., "The new empirical formula based on dynamic probing test results in fine cohesive soils", ***International Journal of Civil Engineering***, Vol. 13, No. 2, (2015), 105-113. https://doi.org/10.22068/IJCE.13.2.105
21. Zhang, J., Yao, Y., Zheng, J., Huang, X. and Lan, T., "Measurement of degree of compaction of fine-grained soil subgrade using light dynamic penetrometer", ***Advances in Civil Engineering***, Vol. 2018, (2018). https://doi.org/10.1155/2018/1364868
22. Ampadu, S.I. and Arthur, T.D., "The dynamic cone penetrometer in compaction verification on a model road pavement", ***Geotechnical Testing Journal***, Vol. 29, No. 1, (2006). http://dx.doi.org/10.1520/GTJ12306
23. Mohammadi, S., Nikoudel, M., Rahimi, H. and Khamehchiyan, M., "Application of the dynamic cone penetrometer (DCP) for determination of the engineering parameters of sandy soils", ***Engineering Geology***, Vol. 101, No. 3-4, (2008), 195-203. http://dx.doi.org/10.1016/j.enggeo.2008.05.006
24. Mansour, M., Samieh, A. and El-Deen, A.N., "Use of lightweight dynamic cone penetrometer for compaction control of cohesionless soils", ***GEOMATE Journal***, Vol. 17, No. 64, (2019), 115-122. https://doi.org/10.21660/2019.64.82998
25. Mohajerani, A., Nguyen, B.T., Wang, Z., Antequera, M., Sohanpal, J., Conte, J.S., Yap, W.J., Malliaras, I. and Gao, X., "A practical technique for the compaction control of sand in road construction: Using a dynamic lightweight cone penetrometer", ***Road Materials and Pavement Design***, Vol. 22, No. 1, (2021), 200-214. https://doi.org/10.1080/14680629.2019.1634123
26. Livneh, M., "Validation of correlations between a number of penetration tests and in situ california bearing ratio tests", ***Transportation Research Record***, Vol. 1219, (1989), 56-67. https://onlinepubs.trb.org/Onlinepubs/trr/1989/1219/1219-006.pdf
27. Smith, R. and Pratt, D., "A field study of in situ california bearing ratio and dynamic cone penetrometer testing for road subgrade investigations", ***Australian Road Research***, Vol. 13, No. 4, (1983). http://worldcat.org/issn/00050164
28. Thives, L.P. and Trichês, G., "Methodology of layers' compaction control through dynamic cone penetrometer (DCP)", ***Arabian Journal of Geosciences***, Vol. 15, No. 13, (2022), 1224. https://doi.org/10.1007/s12517-022-10468-w
29. Jayawickrama, P.W., Amarasiri, A.L. and Regino, P.E., "Use of dynamic cone penetrometer to control compaction of granular fill", ***Transportation Research Record***, Vol. 1736, No. 1, (2000), 71-80. http://dx.doi.org/10.3141/1736-10
30. Testing, A.S.f. and Materials, "Astm d2487-17e1: Standard practice for classification of soils for engineering purposes (unified soil classification system), ASTM. (2017).
31. Astm, D., "Standard test method for laboratory compaction characteristics of soil using modified effort (d1557)", ***ASTM, West Conshohocken, Pennsylvania, USA***, (2012). doi.
32. Stefanoff, G., Sanglerat, G., Bergdahl, U. and Melzer, K., "Dynamic probing (dp): International reference test procedure", in International Symposium on penetration testing; ISOPT-1. 1. (1988), 53-70.
33. Meardi, G., "Discussion: The correlation of cone size in the dynamic cone penetration test with the standard penetration test", ***Géotechnique***, Vol. 21, No. 2, (1971), 184-190. https://doi.org/10.1680/geot.1971.21.2.184
34. Lee, C., Kim, K.-S., Woo, W. and Lee, W., "Soil stiffness gauge (SSG) and dynamic cone penetrometer (DCP) tests for estimating engineering properties of weathered sandy soils in korea", ***Engineering Geology***, Vol. 169, (2014), 91-99. http://dx.doi.org/10.1016/j.enggeo.2013.11.010


## Persian Abstract


**چکیده**

در این پژوهش، به منظور کنترل کیفیت تراکم خاک های درشت دانه، آزمون نفوذسنجی دینامیکی (DPT) با استفاده از هر دو کاوشگر دینامیکی نوع سبک (DPL) و متوسط (DPM) در ۵۰ محل در لایه های اساس و زیراساس چند پروژه راه سازی استفاده شده است. در این خصوص ابتدا در هر محل، بر اساس تعداد ضربات چکش مخروط هر دو کاوشگر DPL و DPM، مقادیر مقاومت دینامیکی مخروط ( $q_d$ ) جهت مستقل شدن نتایج به دست آمده از نوع کاوشگر، محاسبه شده اند. سپس متوسط مقادیر $q_d$ به دست آمده از هر دو نفوذسنج با درصدهای تراکم نسبی ($RC$) در همان محل که با استفاده از انجام آزمایش مخروط ماسه درمحل و آزمون تراکم اصلاح شده در آزمایشگاه، به دست آمده اند، مرتبط شدند. بر این اساس، یک رابطه همبستگی توانی با ضریب تعیین ($R^2$) حدود ۰/٦٤ استخراج شد. سپس با در نظرگرفتن تاثیر اندازه دانه های خاک با استفاده از شاخص اندازه میانی ذرات ($D_{50}$)، رابطه ای با دقت بالاتر به دست آمده که مقدار $R^2$ به ۰/۸۹ ارتقا یافته است. به علاوه، به جهت درنظر گرفتن تنش های عمودی ناشی از عمق انجام آزمون و همچنین به دست آوردن یک رابطه نرمال شده و بی بعد، مقادیر $q_d$ بر تنش های عمودی تقسیم شدند و با درصدهای تراکم مرتبط شدند. پس از آن، به منظور درنظر گرفتن تاثیر اندازه دانه های خاک ها و همچنین دانه بندی آنها، با استفاده از پارامترهای بی بعد ضریب یکنواختی ($Cu$) و انحنا ($Cc$) یک رابطه توانی نرمال شده و بی بعد دیگر استخراج شد. نتایج نشان داد که مقدار $R^2$ از حدود ۰/٤۹ به مقدار ۰/۹۲ افزایش یافته است.

International Journal of Engineering

Journal Homepage: www.ije.ir

# Viscosity Analysis of Water-based Copper Oxide Nanofluids

J. Singh*[a], R. Kumar[b], H. Kumar[b], M. Gupta[c]

[a] *Dr. SSB UICET, Panjab University, Chandigarh, India*
[b] *Department of Mechanical Engineering, UIET, Panjab University, Chandigarh, India*
[c] *Department of Mechanical Engineering, GJUST, Hissar, Haryana, India*

*PAPER INFO*

*Paper history:*
Received 16 October 2022
Received in revised form 17 November 2022
Accepted 18 November 2022

*Keywords*:
*Viscosity*
*Temperature*
*Nanofluid*
*Analysis of Variance*
*Concentration*
*Contour and Surface Plots*

*ABSTRACT*

In this paper, the effects of weight concentration of nanoparticles and temperature on the viscosity of water-based copper oxide nanofluids have been studied experimentally using analysis of variance (ANOVA)-based two-factor three-level ($2^3$) factorial design. The results show that a maximum increase of 23.12% in viscosity is observed at 30°C temperature as the weight concentration of nanoparticles increases from 0.03 to 0.3wt.%. Whereas the temperature increases from 30 to 60°C, the viscosity decreases up to 46.19% in the case of 0.3wt.% nanofluid. Temperature is found to be more dominant than the concentration of nanoparticles. The optimum value of viscosity (0.513 mPa.s) is found at concentrations of 0.1wt.% and 60°C temperature with an 18.72% enhancement in viscosity as compared to the base fluid. The experimental and model values of viscosity have been compared with the predictions of the proposed equation for viscosity. The experimentally measured results are found near the proposed results whereas the model underestimates the viscosity in the case of all nanofluids. The maximum underestimation of 25.92 % was observed in the case of 0.3wt.% nanofluid at 60°C temperature.

***doi**: 10.5829/ije.2023.36.03c.07*

**NOMENCLATURE**

| | | | |
|---|---|---|---|
| DW | Distilled water | **Greek Symbols** | |
| CuO | Copper oxide | $\rho$ | Density (kg/m$^3$) |
| XRD | X-ray Diffraction | $\mu$ | Viscosity (mPa.s) |
| FESEM | Field Emission Scanning Electron Microscopy | $\tau$ | Temperature (°C) |
| DRV | Deviation from the reference value | $\varphi$ | Concentration of nanoparticles |
| d | Average particle diameter | $\lambda$ | wavelength |
| $w$ | Weight | $\beta$ | full-width half-max. of diffraction peak |
| $R^2$ | R Squared | $\kappa$ | Debye Scherrer's constant |
| $R^2$ (adj.) | Adjusted R Squared | $\theta$ | Bragg's Diffraction angle |
| $R^2$ (pred.) | Predicted R Squared | **Subscripts** | |
| Adj.SS | Adjusted sum of squares | *np* | nanoparticle |
| Adj.MS | Adjusted mean sum of squares | *nf* | nanofluid |
| DF | Degree of freedom | *bf* | Base fluid |

## 1. INTRODUCTION

These days nanofluids have been used to enhance the heat transfer rate in thermal industries. Nanofluids are the homogeneous suspensions of nanoparticles in conventional base fluids. But with an increase in the concentration of nanoparticles in the base fluid, the viscosity also increases, which further increases the pumping power required, which is not favorable [1-3]. This may be because of the increased chances of sedimentation and agglomeration.

*Corresponding Author Institutional Email: jodhsingh@pu.ac.in
(J. Singh)

Please cite this article as: J. Singh, R. Kumar, H. Kumar, M. Gupta, Viscosity Analysis of Water-based Copper Oxide Nanofluids, ***International Journal of Engineering, Transactions C: Aspects,*** Vol. 36, No. 03, (2023) 481-489

Gautam and Chudasama [4] found 22% thermal efficiency at a particle concentration of 0.2 wt.% for MWCNT nanofluids. Further increases in concentration lead to decreased thermal conductivity and increased pumping power. Adibi et al. [5] reported that the effective viscosity and thermal conductivity of nanofluid are more than those of base fluid. With the addition of nanoparticles, the friction factor was raised to 42% and the mean Nusselt number increased. Shiravi et al. [6] reported an enhancement of 40.7% in heat transfer at a mass concentration of 0.21% at a constant Reynold number for carbon-based nanofluids. The friction factor was increased by increasing particle concentration and decreasing the Reynolds number. The same trend was reported by Davarnejad and Mohammadi Ardehali [7].

Most of the models for viscosity are valid for small fractions of concentrations but Shahriari et al. [8] proposed a model for particle concentration up to 11 vol.%. Shahriari et al. [9] studied different models to estimate the thermal conductivity and viscosity of nanofluids. They reported that viscosity models showed more influence on the transfer the than thermal conductivity model. Equation (1) represents the Einstein model [3] that is mostly used by Davarnejad and Kheiri [10] and Ebrahimi et al. [11]. This model is used in the present study for the estimation of viscosity.

$$\mu_{nf} = (1 + 2.5 \times \varphi)\mu_{bf} \quad (1)$$

$$\varphi = [wnp \div (wnp + wbf)] \times 100 \quad (2)$$

A brief summary of other related research work is summarized in Table 1.

**TABLE 1.** Summary table of the related literature review

| Nano-fluid | Main finding | Reference |
|---|---|---|
| CuO/ EG | Viscosity increased by 23% with the increase the in the concentration of nanoparticles ($\varphi$) from 1 to 4 vol.%. Viscosity was decreased by 80% when the temperature ($\tau$) was increased from 293K to 353K. | [12] |
| Cu-$SiO_2$/ (Glycerin-water) | An enhancement of 50.3% in viscosity was observed when $\varphi$ was increased by 1% at a constant $\tau$ of 80°C. Viscosity varied directly with $\varphi$ and indirectly with $\tau$. | [13] |
| $Al_2O_3$-CuO/ Water | With the addition of surfactant < 0.2 wt.%, no change in viscosity was observed but a significant increase was observed when surfactant was added beyond this limit. The optimum $\varphi$ of 0.005 wt.% was obtained. | [14] |
| CuO-$TiO_2$/ Water | The maximum viscosity of 1.74 mPasec was obtained at $\varphi$ = 1 vo1% and $\tau$ = 25°C. Significant enhancement was observed in viscosity with the increase in $\varphi$ but an increase in temperature showed an adverse effect. | [15] |
| $Al_2O_3$-CuO/ (Water- EG) | Hybrid nanofluids were prepared at different particle ratios ($Al_2O_3$-CuO), i.e., 20:80,40:60,50:50 and 60:40. The particle ratio of 20:80 showed the lowest viscosity at a temperature of 70°C. A significant reduction in viscosity with an increase in $\tau$ was reported in all cases. | [16] |
| $TiO_2$-CuO/ EG | Enhancement of 80% and 17% was observed in viscosity and thermal conductivity respectively at $\varphi$ = 2 vol.% and $\tau$ = 40.4°C. Viscosity decreased with an increase in temperature. | [17] |
| MWCNT/Water | Viscosity was decreased by 7.9% when the $\tau$ was increased from 30°C to 70°C. It was increased when $\varphi$ was increased up to 0.9 vol.% with temperature ranging from 30-70°C. | [18] |
| Ag-MgO (50:50)/ Water | Viscosity was underestimated by the models used. Viscosity varied directly with the $\varphi$ and values deviated from model values up to 10% with nanofluids having $\varphi$ = 2 wt.%. | [19] |
| $SiO_2$/ Water | Viscosity was decreased by 44.89% when the $\tau$ was changed from 25 to 30°C at a lower $\varphi$ = 0.075 vol.%. With the increase in $\tau$ from 35 to 40°C the viscosity decreased by 18.85%. However, with the further increase in $\tau$ beyond 40°C viscosity became independent of concentration ($\varphi$ ). | [20] |

It is observed from the literature review that the concentration of the nanoparticles is the key parameter that affects the viscosity of the nanofluids. The addition of nanoparticles increases the thermal conductivity of nanofluid as well as the power that is required for pumping due to the enhanced viscosity [3]. The viscosity is directly proportional to particle concentration but varies inversely with the temperature. The nanofluids should achieve the highest thermal conductivity with the lowest possible concentrations of nanoparticles [10].

Most of the studies available in the literature are focused on the heat transfer characteristics of nanofluids using viscosity as one of the parameters. The number of research articles that evaluated heat transfer is significantly higher as compared to articles on viscosity and other properties of nanofluids [21]. There are few papers related to the investigation of the viscosity of CuO-based mono- nanofluids whereas studies based on the hybrid nanofluids containing CuO as one of the materials are more in number.

This motivates the authors to carry out the present work. Temperature and weight concentration of nanoparticles have been selected as factors to study their effects on the viscosity of prepared nanofluids by using ANOVA based on $2^3$ factorial design. Viscosity was measured experimentally using a viscometer (Rheolab QC) and compared with the model values and values given by the correlation that is proposed for the viscosity. This analysis and correlation will help researchers and

scientists to carry out further research in this area. Figure 1 depicts the layout of the present study.

## 2. MATERIALS AND METHODS

CuO nanoparticles (50 nm) were purchased from Nanoshel Company, Willmington United States and distilled water (DW) was obtained from the departmental lab of Dr. SSB UICET, PU, Chandigarh. Nanoparticles were nearly spherical and black with 99.9 % purity. The material was characterized and confirmed by using X-ray Diffraction (PAN analytical Xpert Pro-XRD) and Field Emission Scanning Electron Microscopy (HITACHI, H-7500-FESEM) methods. The results are presented in Figure 2(a and b). The peaks in the XRD report indicate the good crystallinity of CuO nanoparticles and agreed with that of monoclinic CuO as per the literature (JCPDS, File No. 01-080-1916). When compared with the published results, it has been observed that similar results have been reported by other researchers discussed in literature [22-25]. Khallili et al. [26] used Debay Scherrer Equation (3) to calculate the average size of the nanoparticles.

$$d = (k \times \lambda) \div (\beta \times \cos\theta) \quad (3)$$

The average particle size in the present study comes out to be 48.3 nm when $k$, $\lambda$, $\theta$, and $\beta$ are taken as 0.94, 1.54 Å, 17.6, and 0.172° respectively as per the XRD report. The calculated size is very close to the size (50nm) that was claimed by the supplier. FESEM result demonstrates the structure of CuO nanoparticles. Figure 2(b) shows that nanoparticles are nearly spherical and cylindrical in shape and are found in form of clusters. However, the supplier claimed the nanoparticles to be nearly spherical. The deformation in the shape may result from the agglomeration of nanoparticles.

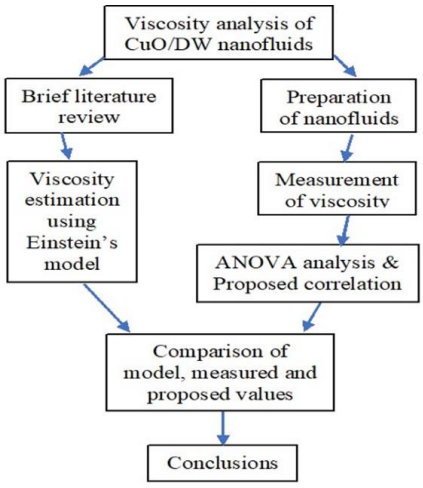


**Figure 1.** The layout of the present study

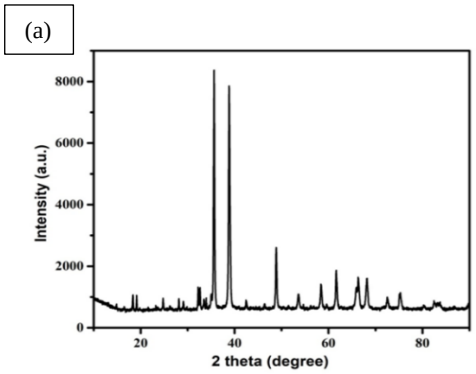


**Figure 1(a).** XRD pattern of CuO nanoparticles

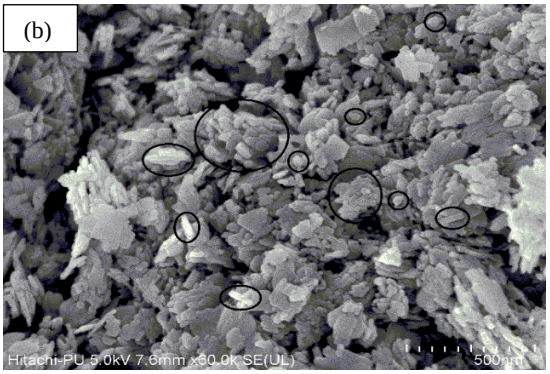


**Figure 2(b).** FESEM image of CuO nanoparticles

Nanofluids were prepared using a two-step method. Nanoparticles were measured by electronic balance (Sartorius BSA 224S-CW) and dispersed in DW to get different weight concentrations of 0.03, 0.1, and 0.3%. These mixtures were stirred for one hour using a magnetic stirrer (Heidolph's MR Hei-Tec.) to break down the clusters followed by ultrasonication using an ultrasonicator (Bandelin DT 255 H) for two hours to get stable and homogeneous nanofluids.

Table 2 contains the selected factors with their levels and Table 3 represents the different combinations of the factors as per the factorial design.

## 3. RESULTS AND DISCUSSION

The viscometer (Rheolab QC) was validated, by measuring the viscosity of DW at different temperatures

**TABLE 2**. Selected factors with their levels

| Factors \ Levels | Low | Medium | High |
|---|---|---|---|
| φ (wt%) | 0.03 | 0.1 | 0.3 |
| τ (°C) | 30 | 45 | 60 |

**TABLE 3.** Combination of factors as experimental sets

| Experimental sets | Concentration φ (wt%) | Temperature τ (°C) |
|---|---|---|
| 1 | 0.03 | 30 |
| 2 | 0.1 | 30 |
| 3 | 0.3 | 30 |
| 4 | 0.03 | 45 |
| 5 | 0.1 | 45 |
| 6 | 0.3 | 45 |
| 7 | 0.03 | 60 |
| 8 | 0.1 | 60 |
| 9 | 0.3 | 60 |

(30, 45, and 60°C) before the actual experiment. Each measurement was performed three times and mean values were considered. Table 4 compares the results for validation of the viscometer and their deviation from the reference values [27, 28]. It is observed that measured values are near the standard results with deviations varying from 2.5-8.3%. Thus, the viscometer was validated and used for nanofluids at different experimental sets as shown in Table 3. The results have been drawn graphically in Figure 3 (a and b).

The net increase in viscosity is observed in the case of prepared nanofluids when compared with base fluid. This increase is because of the addition of nanoparticles in the case of nanofluids which goes on increasing with an increase in particle concentration. The enhancement of viscosity varies from 15.49 to 38.68% for the given range of concentration (0.03-0.3%) and temperature (30°C-60°C) when compared with that of DW. The maximum enhancement is found at a high level of weight concentration (0.3%) and low level of temperature (30°C) whereas, minimum enhancement is found at a low level of weight concentration (0.03%) and high level of temperature (60°C). When the weight concentration was increased from 0.03 to 0.3%, the viscosity increased by 23.12, 19.09, and 16.41% at 30, 45, and 60°C, respectively. This increase in viscosity may be due to a direct influence on the fluid's internal shear stress, which is imposed by an increase in concentration [14, 15, 29]. Viscosity is reduced at a higher temperature. With an increase in temperature from 30 to 60°C the viscosity is decreased by 43.09, 43.61, and 46.19% at a weight concentration of 0.03, 0.1, and 0.3%, respectively. However, the maximum reduction of 44.5% is found in the case of base fluid with this increase in temperature. The reason behind the decreasing viscosity with increased temperature may be the weak adhesion forces between particles and molecules [12, 29, 30].

The intermolecular forces decrease with the increase in temperature; hence, the resistance to flow, i.e., viscosity, is decreased. Figure 3(a and b) shows the direct relationship of viscosity with the concentration of nanoparticles and the indirect relationship with temperature i.e., viscosity decreases with an increase in temperature.

**TABLE 4.** Measured viscosity of DW and deviation from reference values

| Temperature (°C) | Measured (mPa.s) | A.Nagashima (mPa.s) [27] | Databook (mPa.s) [28] | DRV (%) [27] | DRV (%) [28] |
|---|---|---|---|---|---|
| 30 | 0.7786 | 0.79844 | 0.8300 | 2.5 | 6.2 |
| 45 | 0.5623 | 0.60052 | 0.60825 | 6.4 | 7.6 |
| 60 | 0.4321 | 0.46601 | 0.4710 | 7.3 | 8.3 |

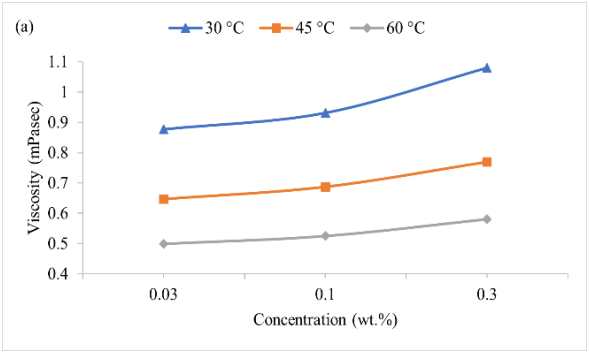


**Figure 3(a).** Variation of viscosity with concentration

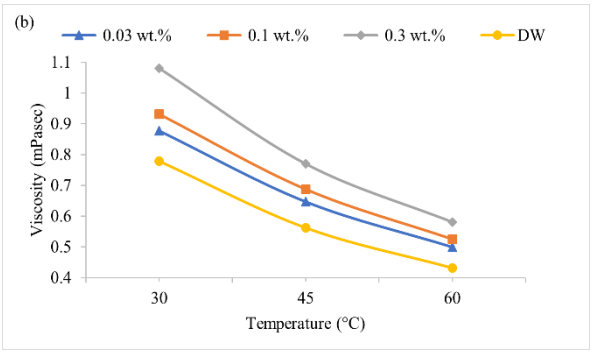


**Figure 3(b).** Variation of viscosity with temperature

**3. 1. ANOVA Analysis** ANOVA was performed using MINITAB 17 to understand how the selected parameters i.e., the concentration of nanoparticles (x) and temperature (y), respond to the viscosity of CuO/DW nanofluids. To study the effects of parameters on the viscosity of CuO/DW nanofluid, an ANOVA-based $2^3$ factorial design has been used. The following Table 5 presents the summary of the regression analysis and information regarding the significance of the model using constants and coefficients of the proposed equation.

**TABLE 5.** Results obtained from software for ANOVA and regression

| Source | DF | Adj SSx10$^{-3}$ | Adj MSx10$^{-3}$ | F-Value | P-Value | Significance |
|---|---|---|---|---|---|---|
| Regression | 3 | 307.5 | 102.5 | 107.5 | 0.000 | Significant |
| φ (wt.%) | 1 | 11.22 | 11.22 | 11.78 | 0.019 | Significant |
| τ (°C) | 1 | 76.90 | 76.90 | 80.69 | 0.000 | Significant |
| 2-Way (φ.τ) | 1 | 4.0 | 4.0 | 4.20 | 0.096 | Not significant |
| Error | 5 | 4.765 | 0.953 | | | |
| Total | 8 | 312.3 | | | | |

| MODEL SUMMARY | | | |
|---|---|---|---|
| S | R-sq ($R^2$) | R-sq (adj.) | R-sq (Pred.) |
| 0.030872 | 98.47% | 97.56% | 91.36% |

| Regression Coefficients | | | |
|---|---|---|---|
| Constant | φ | τ | φ.τ |
| 1.2059 | 1.175 | -0.01210 | -0.01505 |

After analyzing the different values (P-value, F-value, $R^2$, $R^2$(adj.), and $R^2$(pred.), it may be concluded that the present model is a significant, fit, and valid model that contains only significant factors. The values of $R^2$, $R^2$(adj.), and $R^2$(pred.) are near 100% which proves the model to be a good fit model and ensures its validity. Small P-values and the least difference between $R^2$ and $R^2$(adj.) indicates the absence of any insignificant factor [31, 32].

Figure 4 shows that the main effects of parameters are significant but interactive effects are insignificant. The trends of the main effects in Figure 4 are the same as shown in Figure 3(a and b). Moreover, the slope of the temperature line in Figure 4 indicates that temperature is more significant or dominant than the concentration of nanoparticles.

**3. 2. Response Optimization and Proposed Equation** The response is optimized using the experimentally obtained data to minimize the viscosity of the nanofluid to improve its rheological characteristics. The fit optimum value as predicted by the software for the present model is 0.513 mPa.s with a confidence interval of 95%. The predicted value is close to the actual experimental value of 0.525 mPa.s. So, optimum viscosity (0.513 mPa.s) with 18.72% enhancement is observed at a medium level of A and a high level of B (i.e., 0.1% and 60°C). Based on ANOVA analysis of the experimental data, Equation (4) is proposed for estimating the viscosity of nanofluid under the given conditions of the present work. The proposed equation is valid for the ranges of $0.03 \le \varphi \le 0.3$ wt.% and $30 \le \tau \le 60$ °C.

$$\mu_{nf} = 1.259 + 1.5 \times (\varphi) - 0.0121 \times (\tau) - 0.01505 \times (\varphi) \times (\tau) \quad (4)$$

The high value of $R^2$ (98.47%) indicates the high precision of the equation and proves the equation to be acceptable for the given range of factors in the present work.

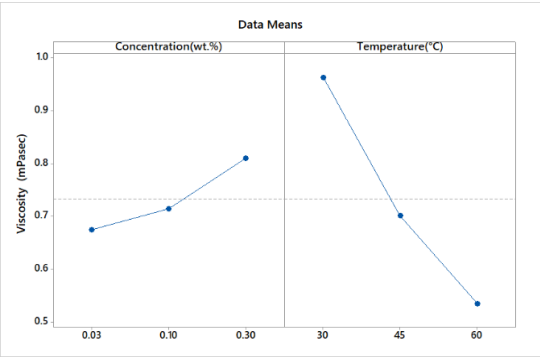


**Figure 2.** Main effects of the parameters on viscosity

**3. 3. Contour and Surface Plots** The selected factors' effects on nanofluids' viscosity are shown in Figure 5(a and b). In a contour plot, viscosity is represented as contours having different colors. As the temperature increases, the contour's color changes from dark green to dark blue. This shows the decreasing trend of viscosity with rising temperature. The surface plot shows the relationship between viscosity, concentration, and temperature. The surface plot shows that viscosity has an increasing and decreasing trend with concentration and temperature respectively. Viscosity is maximum at the lowest temperature and highest

concentration. The lowest value of viscosity is found at the highest temperature and lowest concentration. The peaks and valleys in the surface correspond to the combination of concentration and temperature that produce the local maximum and minimum thermal conductivity. The trends of the plots in Figure 5(a and b) comply with the graphs in Figures 3 and 4. Plots show that viscosity increases with an increase in concentration at a constant temperature but decreases with an increase in temperature at a constant concentration.

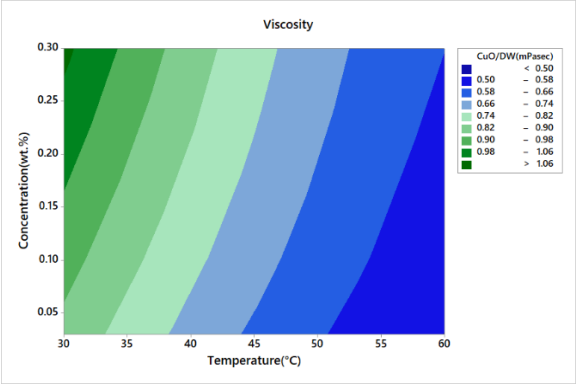


**Figure 5 (a)**. Contour plot showing the effects of factors on viscosity

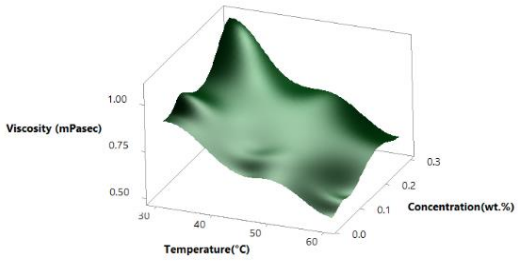


**Figure 5 (b).** Surface plot showing the relation between the factors and viscosity

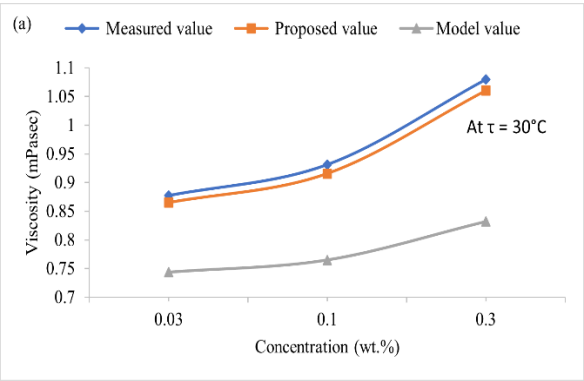


**Figure 6 (a).** Viscosity versus concentration at 30°C

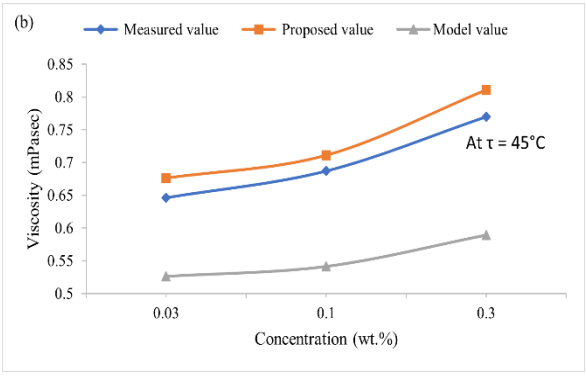


**Figure 6 (b).** Viscosity versus concentration at 45°C

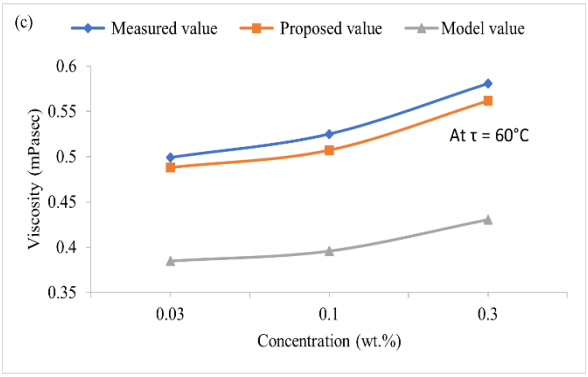


**Figure 6(c).** Viscosity versus concentration at 60°C

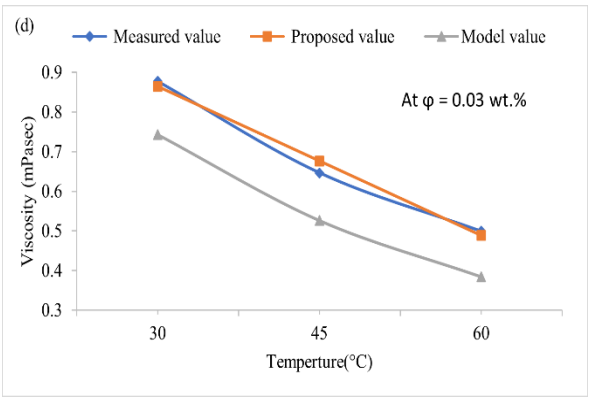


**Figure 6(d).** Viscosity versus temperature at 0.03 wt.%

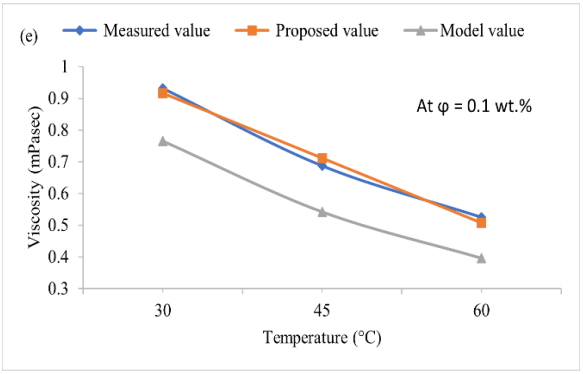


**Figure 6(e).** Viscosity versus temperature at 0.1 wt.%

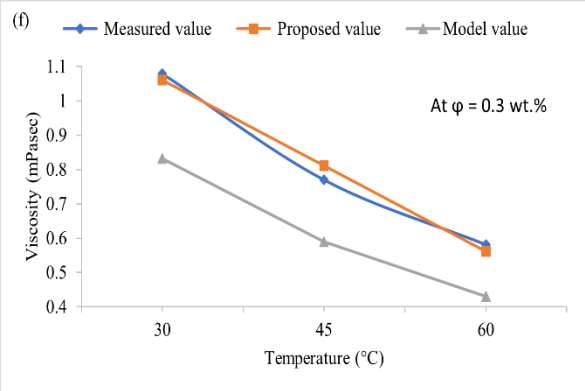


**Figure 6(f).** Viscosity versus temperature at 0.3 wt.%

**3. 4. Comparison of Results** The proposed Equation (4) and Einstein model Equation (1) have been used to calculate the viscosity under the same conditions which are used to determine viscosity experimentally. A comparison among measured proposed, and model values have been made and presented graphically in Figure 6(a-f). It is observed that the modal underestimates the viscosity as the model values are on the lower side in all the cases. The overall underestimation by the model varies from 15.24 to 25.92%. The amount of underestimation is increased with an increase in the weight concentration of nanoparticles and temperature. The maximum underestimation is observed at 0.3 wt.% and 60°C. Whereas minimum underestimation is observed at 0.03 wt.% and 30°C.

The model used is empirical and does not include the effects of factors like the shape and size of nanoparticles etc. and various mechanisms that influence the viscosity. This underestimation by the model may be attributed to such reasons. However, the values found from the proposed Equation (4) are close to the experimentally measured values. This proves the accuracy and validity of the proposed equation for the given set of conditions.

## 4. CONCLUSION

Effects of weight concentration of nanoparticles and temperature on the viscosity of prepared nanofluids were studied using ANOVA-based $2^3$ factorial design. The following conclusions are drawn from the present study:

1. The viscosity of nanofluids is more than base fluid i.e., DW in all the cases. It shows a direct relationship with the concentration of nanoparticles but varies indirectly with temperature.
2. The net enhancement in viscosity varied from 15.49 to 38.68% in nanofluids when compared with that of DW. The maximum value is observed at a high level of concentration of nanoparticles (0.3 wt.%) and a low level of temperature (30°C) whereas, whereas minimum enhancement is observed at a low level of concentration of nanoparticles (0.03 wt.%) and high level of temperature (60°C).
3. With the increase in the concentration of nanoparticles from 0.03 to 0.3 wt.%, the viscosity is increased by 23.12, 19.09, and 16.41 % at 30, 45, and 60°C respectively.
4. With the increase in temperature from 30 to 60°C the viscosity is decreased by 43.09, 43.61, and 46.19% at concentrations of 0.03, 0.1, and 0.3 wt.% respectively. However, the maximum reduction of 44.5% is found in the case of DW.
5. The 18.72% enhancement in viscosity has been noticed at the optimum conditions i.e., a medium level of concentration and a high level of temperature (i.e., 0.1% and 60°C).
6. The model underestimates the viscosity. The maximum 25.92% underestimation is observed at a concentration of 0.3 wt.% and 60°C whereas the minimum 15.24% underestimation is found at a concentration of 0.03 wt.% and 30°C.
7. The results of the proposed correlation are very close to the experimental findings. The high value of $R^2$ (98.47 %) indicates the high precision of the equation and proves the equation to be acceptable for the given range of factors in the present work.

## 5. REFERENCES

1. Ismail, I.A., Yusoff, M.Z., Ismail, F.B. and Gunnasegaran, P., "Heat transfer enhancement with nanofluids: A review on recent applications and experiments", in AIP Conference Proceedings, AIP Publishing LLC. Vol. 2035, (2018), 040006.
2. Devendiran, D.K. and Amirtham, V.A., "A review on preparation, characterization, properties and applications of nanofluids", ***Renewable and Sustainable Energy Reviews***, Vol. 60, (2016), 21-40. https://doi.org/10.1016/J.RSER.2016.01.055
3. Einstein, A., "Eine neue bestimmung der moleküldimensionen", ETH Zurich, (1905),
4. Gautam, P. and Chudasama, M., "An experimental investigation of parabolic trough collector using industrial-grade multiwall carbon nanotube (MWCNT)-$H_2O$ based nanofluid", ***International Journal of Engineering, Transactions A: Basics***, Vol. 35, No. 1, (2022), 112-120. https://doi.org/10.5829/ije.2022.35.01a.10
5. Adibi, T., Razavi, S.E. and Adibi, O., "A characteristic-based numerical simulation of water-titanium dioxide nano-fluid in closed domains", ***International Journal of Engineering, Transactions A: Basics***, Vol. 33, No. 1, (2020), 158-163. https://doi.org/10.5829/ije.2020.33.01a.18
6. Shiravi, A.H., Shafiee, M., Firoozzadeh, M., Bostani, H. and Bozorgmehrian, M., "Experimental study on convective heat transfer and entropy generation of carbon black nanofluid turbulent flow in a helical coiled heat exchanger", ***Journal of Thermal Analysis and Calorimetry***, Vol. 145, (2021), 597-607. https://doi.org/10.1007/s10973-020-09729-1
7. Mohammadi Ardehali, R. and Davarnejad, R., "Modeling of $TiO_2$-water nanofluid effect on heat transfer and pressure drop",

***International Journal of Engineering, Transactions B: Applications***, Vol. 27, No. 2, (2014), 195-202. https://doi.org/10.5829/IDOSI.IJE.2014.27.02B.04

8. Shahriari, A., Jahantigh, N. and Rakani, F., "Providing an analytical model in determining nanofluids", ***International Journal of Engineering, Transactions C: Aspects***, Vol. 30, No. 12, (2017), 1919-1924. https://doi.org/10.5829/ije.2017.30.12c.14
9. Shahriari, A., Jahantigh, N. and Rakani, F., "Assessment of particle-size and temperature effect of nanofluid on heat transfer adopting lattice boltzmann model", ***International Journal of Engineering, Transactions A: Basics***, Vol. 31, No. 10, (2018), 1749-1759. https://doi.org/10.5829/ije.2018.31.10a.18
10. Kheiri, M. and Davarnejad, R., "Numerical comparison of turbulent heat transfer and flow characteristics of $SiO_2$/water nanofluid within helically corrugated tubes and plain tube", ***International Journal of Engineering, Transactions A: Basics,*** Vol. 28, No. 10, (2015), 1408-1414. https://doi.org/10.5829/idosi.ije.2015.28.10a.02
11. Akbarzade, S., Sedighi, K., Farhadi, M. and Ebrahimi, M., "Experimental investigation of force convection heat transfer in a car radiator filled with $SiO_2$-water nanofluid", ***International Journal of Engineering, Transactions B: Applications***, Vol. 27, No. 2, (2014), 333-340. https://doi.org/10.5829/idosi.ije.2014.27.02b.17
12. Bhat, A.Y. and Qayoum, A., "Viscosity of cuo nanofluids: Experimental investigation and modelling with FFBP-ANN", ***Thermochimica Acta***, Vol. 714, (2022), 179267. https://doi.org/10.1016/j.tca.2022.179267
13. Lahari, M.C., Sai, P.S.T., Sharma, K. and Narayanaswamy, K., "Thermal conductivity and viscosity of glycerine-water based cu-$SiO_2$ hybrid nanofluids", ***Materials Today: Proceedings***, Vol. 66, (2022), 1823-1829. https://doi.org/10.1016/j.matpr.2022.05.284
14. Ma, M., Zhai, Y., Yao, P., Li, Y. and Wang, H., "Effect of surfactant on the rheological behavior and thermophysical properties of hybrid nanofluids", ***Powder Technology***, Vol. 379, (2021), 373-383. https://doi.org/10.1016/j.powtec.2020.10.089
15. Asadi, A., Alarifi, I.M. and Foong, L.K., "An experimental study on characterization, stability and dynamic viscosity of cuo-$TiO_2$/water hybrid nanofluid", ***Journal of Molecular Liquids***, Vol. 307, (2020), 112987. https://doi.org/10.1016/j.molliq.2020.112987
16. Wanatasanappan, V.V., Abdullah, M. and Gunnasegaran, P., "Thermophysical properties of al2o3-cuo hybrid nanofluid at different nanoparticle mixture ratio: An experimental approach", ***Journal of Molecular Liquids***, Vol. 313, (2020), 113458. https://doi.org/10.1016/j.molliq.2020.113458
17. Akilu, S., Baheta, A.T. and Sharma, K., "Experimental measurements of thermal conductivity and viscosity of ethylene glycol-based hybrid nanofluid with $TiO_2$-CuO/C inclusions", ***Journal of Molecular Liquids***, Vol. 246, No., (2017), 396-405. https://doi.org/10.1016/J.MOLLIQ.2017.09.017
18. Thakur, M., Gangacharyulu, D. and Singh, G., "An experimental study on thermophysical properties of multiwalled carbon nanotubes (research note)", ***International Journal of Engineering, Transactions B: Applications***, Vol. 30, No. 8, (2017), 1223-1230. https://doi.org/10.5829/ije.2017.30.08b.15
19. Esfe, M.H., Arani, A.A.A., Rezaie, M., Yan, W.-M. and Karimipour, A., "Experimental determination of thermal conductivity and dynamic viscosity of Ag–MgO/water hybrid nanofluid", ***International Communications in Heat and Mass Transfer***, Vol. 66, (2015), 189-195. https://doi.org/10.1016/j.icheatmasstransfer.2015.06.003
20. Jamshidi, N., Farhadi, M., Ganji, D. and Sedighi, K., "Experimental investigation on the viscosity of nanofluids", ***International Journal of Engineering Transactions B: Applications,***, Vol. 25, No. 3, (2012), 201-209. https://doi.org/10.5829/idosi.ije.2012.25.03b.07
21. Babar, H. and Ali, H.M., "Towards hybrid nanofluids: Preparation, thermophysical properties, applications, and challenges", ***Journal of Molecular Liquids***, Vol. 281, (2019), 598-633. https://doi.org/10.1016/J.MOLLIQ.2019.02.102
22. Kayani, Z.N., Umer, M., Riaz, S. and Naseem, S., "Characterization of copper oxide nanoparticles fabricated by the sol–gel method", ***Journal of Electronic Materials***, Vol. 44, (2015), 3704-3709. https://doi.org/10.1007/s11664-015-3867-5
23. Arun, K., Batra, A., Krishna, A., Bhat, K., Aggarwal, M. and Francis, P.J., "Surfactant free hydrothermal synthesis of copper oxide nanoparticles", ***American Journal of Materials Science***, Vol. 5, No. 3A, (2015), 36-38. https://doi.org/10.5923/s.materials.201502.06
24. Radhakrishnan, A.A. and Beena, B.B., "Structural and optical absorption analysis of CuO nanoparticles", ***Indian Journal of Advances in Chemical Science***, Vol. 2, No. 2, (2014), 158-161. http://www.ijacskros.com/artcles/IJACS-M64.pdf
25. Khatun, N., Santra, S.K., Banerjee, A. and Patel, B.K., "Nano cuo catalyzed cross dehydrogenative coupling (CDC) of aldehydes to anhydrides", ***European Journal of Organic Chemistry***, Vol. 2015, No. 6, (2015), 1309-1313. https://doi.org/10.1002/ejoc.201403508
26. Khalili, R., "Preparation and characterization of polyaniline/$Sb_2O_3$ nanocomposite and its application to removal of Pb(ii) from aqueous media", ***International Journal of Engineering, Transactions B: Applications***, Vol. 27, No. 2, (2014), 239-246. https://doi.org/10.5829/idosi.ije.2014.27.02b.08
27. Ramires, M.L., Nieto de Castro, C.A., Nagasaka, Y., Nagashima, A., Assael, M.J. and Wakeham, W.A., "Standard reference data for the thermal conductivity of water", ***Journal of Physical and Chemical Reference Data***, Vol. 24, No. 3, (1995), 1377-1381. https://doi.org/10.1063/1.555963
28. Levenspiel, O., "Engineering flow and heat exchange, Springer, (2014).
29. Williams, W., Buongiorno, J. and Hu, L.-W., "Experimental investigation of turbulent convective heat transfer and pressure loss of alumina/water and zirconia/water nanoparticle colloids (nanofluids) in horizontal tubes", ***Journal of heat transfer***, Vol. 130, No. 4, (2008). http://dx.doi.org/10.1115/1.2818775
30. Kole, M. and Dey, T., "Role of interfacial layer and clustering on the effective thermal conductivity of CuO–gear oil nanofluids", ***Experimental thermal and fluid science***, Vol. 35, No. 7, (2011), 1490-1495. https://doi.org/10.1016/J.EXPTHERMFLUSCI.2011.06.010
31. Rostamian, H. and Lotfollahi, M.N., "New functionality for energy parameter of redlich-kwong equation of state for density calculation of pure carbon dioxide and ethane in liquid, vapor and supercritical phases", ***Periodica Polytechnica Chemical Engineering***, Vol. 60, No. 2, (2016), 93-97. https://dx.doi.org/10.3311/ppch.8221
32. LotfizadehDehkordi, B., Ghadimi, A. and Metselaar, H.S., "Box–behnken experimental design for investigation of stability and thermal conductivity of $TiO_2$ nanofluids", ***Journal of Nanoparticle Research***, Vol. 15, (2013), 1-9. doi. http://dx.doi.org/10.1007/s11051-012-1369-4

Persian Abstract

**چکیده**

در این مقاله، اثرات غلظت وزنی نانوذرات و دما بر ویسکوزیته نانوسیالات اکسید مس مبتنی بر آب با استفاده از طرح فاکتوریل دو عاملی سه سطحی (23) مبتنی بر تحلیل واریانس (ANOVA)به صورت تجربی مورد بررسی قرار گرفته است. نتایج نشان می دهد که با افزایش غلظت وزنی نانوذرات از ۰.۰۳ به ۰.۳ وزنی، حداکثر افزایش ۲۳.۱۲ درصد در ویسکوزیته در دمای ۳۰ درجه سانتی گراد مشاهده می شود. در حالی که دما از ۳۰ تا ٦۰ درجه سانتی گراد افزایش می یابد، ویسکوزیته در مورد نانوسیال ۰.۳ درصد وزنی تا ٤٦.۱۹ درصد کاهش می یابد. دما غالبتر از غلظت نانوذرات است. مقدار بهینه ویسکوزیته ۰.٥۱۳ mPa.s در غلظت‌های ۰.۱ درصد وزنی و دمای ٦۰ درجه سانتی‌گراد با افزایش ۱۸.۷۲ درصدی ویسکوزیته در مقایسه با سیال پایه یافت می‌شود. مقادیر تجربی و مدل ویسکوزیته با پیش‌بینی‌های معادله پیشنهادی برای ویسکوزیته مقایسه شده است. نتایج اندازه‌گیری‌شده تجربی در نزدیکی نتایج پیشنهادی یافت می‌شوند در حالی که مدل ویسکوزیته را در مورد همه نانوسیال‌ها دست‌کم می‌گیرد. حداکثر کمترین برآورد ۲٥.۹۲ درصد در مورد نانوسیال ۰.۳ درصد وزنی در دمای ٦۰ درجه سانتی گراد مشاهده شد.

International Journal of Engineering

Journal Homepage: www.ije.ir

# Variations of Organic Loading Rate on Tofu Wastewater Degradation using Upflow Anaerobic Sludge Blanket Reactor by Modified Stover-Kincannon Model

F. Batubara[a], M. Turmuzi[a], I. Irvan[a], N. Yanqoritha*[b]

[a] *Department of Chemical Engineering, Universitas Sumatera Utara, Jalan Almamater Kampus USU, Medan, Indonesia*
[b] *Department of Industrial Engineering, Universitas Prima Indonesia, Medan, Indonesia*

*PAPER INFO*

*Paper history:*
Received 26 February 2022
Received in revised form 17 November 2022
Accepted 22 November 2022

*Keywords*:
*Organic Loading Rate*
*Tofu Wastewater*
*Hybrid Upflow Anaerobic Sludge Blanket Reactor*
*Modified Stover-Kincannon Model*

*ABSTRACT*

This research aims to examine the varians of organic loading rate (OLR) on degradation of tofu wastewater using the hybrid upflow anaerobic sludge blanket (hybrid UASB) reactor using the modified kinetic model of Stover Kincannon. This reactor was operated at OLRs variation of 1.5-12 kg COD $m^{-3}$ $d^{-1}$ and HRT of 12 - 24 hours for 328 days. Higher COD removal efficiency of 86.41% and biogas production of 7700 mL were achieved at OLR 4.8 kg COD $m^{-3}$ $d^{-1}$ and HRT 24 hours on 140 days. Modified Stover-Kincannon model was observed and matched data sets were obtained. The kinetic values of model obtained at HRT variations, the parameters $K_B$ and $\mu_{max}$ were 3.7, 12.97, 2.42 $mgL^{-1}$ $d^{-1}$ and 0.59, 9.41, 0.014 $mgL^{-1}$ $d^{-1}$, respectively. This model was a plot of the inverse of the removal rate, versus inverse of the total loading rate resulted in a straight line. It showed that the Stover-Kincannon Model is the rate of substrate removal was affected by the organic load rate (OLR) that flowed into the hybrid UASB reactor.

***doi***: *10.5829/ije.2023.36.03c.08*

## 1. INTRODUCTION

Many cases of industrial and domestic wastewater contain high COD, which should be treated in a wastewater treatment system before being discharged into water bodies. The wastewater treatment plant (WWTP) system is one of the most important factors influencing the improvement of environmental conditions. The excess sludge from the WWTP was referred to as sewage sludge, which was the main waste accounts for an average of 3% of the volume of treated wastewater [1, 2]. Tofu industry wastewater is one of the liquid wastes that has a high organic load content, one of which has a high concentration of chemical oxygen demand (COD) [3, 4], this amount exceeds the maximum level set by the Indonesian government, which is 100 $mgL^{-1}$ for COD and 200 $mgL^{-1}$ for total suspended solid (TSS) [5]. Indonesia has a tofu industry with more than 84,000 units and an annual production capacity of more than 2.56 million tons. Industrial wastewater from tofu involves a TSS concentration of more than 1000 $mgL^{-1}$ and a chemical oxygen demand (COD) of 5000–8000 $mgL^{-1}$. Waste water production can be up to 40–43 times larger for every kg of soybeans used to make tofu [4, 6].

An alternative method for lowering COD and creating biogas is anaerobic decomposition. Due to the comparatively high processing costs, many tofu industries in Indonesia continue to dispose of untreated liquid effluent. Tofu industry costs must be reduced by enhanced waste treatment [3, 7-11]. The anaerobic process has an economic advantage in which the sludge produced is low so it does not need to pay for the handling of sludge caused by anaerobic reactors which is an immediate economic benefit [8, 12-15]. Anaerobic biomass fermentation accompanied by methane production needs a long time, so organic waste requires a proper anaerobic digester [16, 17]. Processing of the anaerobic system is divided into a suspension system, attached and a combination of them. Anaerobic processing of the suspension system has been widely

*Corresponding Author Institutional Email: nyimasyanqoritha@unprimdn.ac.id (N. Yanqoritha)

Please cite this article as: F. Batubara, M. Turmuzi, I. Irvan, N. Yanqoritha, Variations of Organic Loading Rate on Tofu Wastewater Degradation using Upflow Anaerobic Sludge Blanket Reactor by Modified Stover-Kincannon Model, ***International Journal of Engineering, Transactions C: Aspects,*** Vol. 36, No. 03, (2023) 490-496

proven using UASB reactor. The UASB reactor is able to work for high load rates, high biomass concentrations and is very good for separating solids and liquids. The UASB reactor was developed by combining the attached system as a medium for the growth of microorganisms. This system is carried out on one reactor that is the hybrid UASB reactor [18, 19]. The hybrid UASB reactor is an attractive technology for the treatment of industrial wastewater from sago, tofu, refineries, starch and dairy industries. The hybrid UASB reactor was able to effectively remove up to 95% COD and produces biogas [8, 20]. The effect of OLR on degradation of wastewater in the hybrid UASB reactor using PVC as attached media showed 85.57% COD removal, day 171 at OLR 5.2 kg COD $m^{-3}$ $d^{-1}$ [21]. In the processing of refinery wastewater, the removal of organic load is obtained about 87.35% [22]. OLR was a parameter that, under operational circumstances, may have an impact on the state of the process and needed to be regulated [1, 20, 21]. The hybrid UASB reator at OLR 8.9 kg COD $m^{-3}$ $d^{-1}$ is able to remove up to 93% COD to treat dairy industrial wastewater [23]. The COD removal efficiency was found to be more than 95% at a 24-hour constant hydraulic retention time (HRT). The hybrid UASB reactor was reasonable, environmentally friendly and sustainable to handle refinery washing [24]. The hybrid reactor had a role as an additional processing stage is more significant in low HRT and rising flow velocity so that it could maintain biomass and contribute to improved granulation [25]. HRT is a significant main operating parameter because it contributes to the performance of the bioreactor as well [26-28]. Based on the biochemistry and microbiology of anaerobic processes, kinetic studies provide a rational basis for process analysis, control and design. Upflow system kinetics studies on COD removal are needed to determine the kinetics of bacterial growth. Kinetic model is an analytical approach to describe specific parameters for monitoring system performance. Kinetic models are currently being developed to help design and optimize processes for upflow and hybrid anaerobic reactors [1, 17, 21, 29, 30]. The kinetic model is also considered feasible and suitable for approaches on removal performance, prediction of effluent concentrations and optimization of biological processes [31]. Nevertheless, there are still very few studies related to the study of kinetic parameters for the process in the hybrid UASB reactor and there is no tofu industry that uses a treatment system for wastewater from tofu manufacture. This study aims to investigate the rate of change of the substrate using a modified Stover-Kincannon kinetic model due to the effect of OLR on the hybrid UASB reactor for handling tofu liquid waste. So that in the future the hybrid UASB reactor can become a reference as a good performance in the tofu industrial process wastewater treatment. Although, it requires a burdensome cost for the tofu factory industry and it is a task for the local government so that the tofu industrial wastewater treatment must still be carried out as a healthy environmental consideration.

## 2. MATERIALS AND METHODS

**2. 1 Hybrid UASB Reactor** Figure 1 is a lab-scale hybrid UASB reactor, which was designed like previous studies [3, 8, 32]. The hybrid UASB reactor consists of 3 parts, namely suspended sludge blanket, attached media and gas liquid solid separator (GLSS). The hybrid UASB reactor system is a combination of a suspended system and an anaerobic fixed film (Figure 1) [33], which is a hybrid wastewater treatment process with a fixed film attached system (supporting medium) providing a surface as an embedded medium in the biofilm to support the growth of anaerobic microorganisms. Wastewater as feed flows upward through the sludge layer and dissolved pollutants are absorbed by the biofilm, so decomposition occured. The hybrid UASB reactor was made of acrylic with a height ratio for suspended media and attached media of 1:1, each medium height of 80 cm. Suspended media is 3 inches in diameter and embedded media is 4 inches in diameter. The capacity of the reactor is 8.6 liters and the use of bioballs as attached media. Tofu wastewater was fed by a pristaltic pump to the hybrid UASB reactor as an upflow system to GLSS. Then it flowed continuously as a process that come out through the outlet as effluent to the clarifier and biogas to the biogas outlet. Biogas was collected into the reservoir via the gas flow. Bioball media was a media system to support the growth of microorganisms as a media attached to a UASB hybrid reactor. GLSS in the reactor to separate flue gas, liquid and solid when feed movement occured.

**2. 2. Tofu Wastewater as Influent** Tofu wastewater was processed from the tofu industry in the

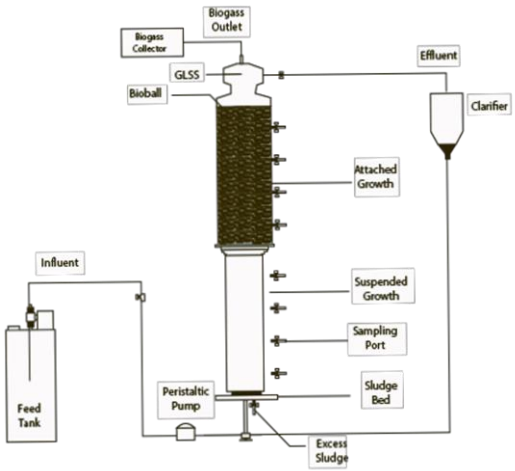


**Figure 1.** Schematic diagram of the Hybrid UASB reactor

city of Medan, Indonesia. Industrial wastewater tofu contained chemical oxygen demand 60000 $mgL^{-1}$ and pH 3-4. To prevent pH fluctuations, $NaHCO_3$ was added and $K_2HPO_4$ to tofu wastewater. Tofu industrial wastewater is fed as inlet by a pristaltic pump, the system moves upward through the suspended and attached medium. The system media is attached as a filter used in this study were 167 bioballs, diameter of about 4 cm, specific area 230 $m^2/m^3$, cavity porosity of 0.92. Process water as outlet at the top reactor connected to clarifier as a waste tank. The reactor is equipped with a gas liquid-solid separator (GLSS) to separate the rising effluent due to the movement of the feed.

**2. 3. Analytical Procedure** Daily checks are made of the variables that influence the process, such as pH and temperature, biogas, COD, the flow rate (Q), HRT, Treated and untreated samples were analyzed for pH, COD, Total Suspended Solids (TSS), volatile suspended solid (VSS), volatile fatty acid (VFA) and alkalinity according to the Standard Method of Water and Wastewater Inspection. The closed reflux titrimetric approach was used to monitor COD. VFA and alkalinity were also assessed using titrimetry. All samples were filtered before analysis utilizing a 0.45 mm filter to remove suspended matters. Homogeneous samples were filtered with filter media that had been weighed. The residue retained on the filter media was dried in a temperature range of 103 °C to 105°C to constant weight. The increase in weight indicates (TSS). Furthermore, the filter media from the TSS test were tested for (VSS) analysis at a temperature of 550 $^0$C. Observation of VSS to determine the number of microbes because the seeding is considered complete if the concentration of VSS > 3000 mg $L^{-1}$; this indicates an increase in microbial biomass. The whole determination was operated in accordance to APHA Standard Methods [34].

**2. 4. Reactor Operation** The acclimatization process at HRT 12, 18, 24 hours, the flow rate (Q) was in the range of 5.9-11.97 mL per minute and the flow rate increased (Vup) 0.08-0.17 m $h^{-1}$. The acclimatization process was carried out so that microorganisms adapt to the tofu industrial wastewater to be processed. The seeding treatment was carried out simultaneously with the acclimatization process after 7 days, with variations in concentration from the lowest to a concentration of 100% of tofu industrial wastewater (25, 50, 75, 100%). $NaHCO_3$ was added as a buffer to maintain pH 6.5-7. The wastewater from the tofu industry is channeled by a peristaltic pump to the hybrid UASB reactor with an upflow system.

**2. 5. Modified Stover-Kincannon Model** The Stover-Kincannon model was the most suitable model in determining kinetic evaluation. The parameters obtained in this model were very important for estimating the efficiency and performance of a bioreactor system. Therefore, it can be applied to large-scale industrial bioreactors. Model of Stover-Kincannon is used for determining the rate of change of substrate concentration which is stated in Equation (1) [17, 35-40].

$$\frac{dS}{dt} = \frac{Q(S_o - S_e)}{V} = \frac{\mu\left(\frac{QS_o}{V}\right)_{max}}{K_B + \left(\frac{QS_o}{V}\right)} \quad (1)$$

$$V\left(\frac{dS}{dt}\right) = QS_o - QS_e \quad (2)$$

Equation (3) is achieved by substituting Equation (1) into Equation (2):

$$V\left[\frac{\mu max\ (\frac{Q\,So}{V})}{K_B + (\frac{Q\,So}{V})}\right] = QSo - QSe \quad (3)$$

The concentration of effluent substrate is measured by Equation (4).

$$S_e = S_o - \frac{\mu max\ So}{K_B + (\frac{Q\,So}{V})} \quad (4)$$

where, So and Se are the influent and efluent substrate concentration (mg $L^{-1}$) respectively. μmax, $K_B$, V and Q are the maximum rate of substrate utilization (mg $L^{-1}$ $d^{-1}$), the saturation constant (mg $L^{-1}d^{-1}$), the reactor volume (L) and the flow rate (L $d^{-1}$), respectively [17, 35-40].

$$\left[\frac{dS}{dt}\right]^{-1} = \frac{V}{Q(S_0 - S_e)} = \frac{K_B}{\mu_{max}}\frac{V}{Q\,S_0} + \frac{1}{\mu_{max}} \quad (5)$$

Input and output substrate concentrations, respectively, are So and Se (measured in mg $L^{-1}$). Maximum substrate consumption rate (mg $L^{-1}$ $d^{-1}$), saturation constant (mg $L^{-1}$ $d^{-1}$), reactor volume (L), and flow rate (L $d^{-1}$), are represented by max, $K_B$, V, and Q, respectively.

## 3. RESULTS AND DISCUSSIONS

**3. 1. Hybrid UASB Reactor Performance** The removal of the substrate depends on the load rate in the bioreactor system design that will produce biogas where the volume of the load rate is related to the mass of methanogens immobilized [8]. In this study amount of OLR fed into the reactor was based on the values of HRT (24, 18 and 12h). The OLR of the hybrid UASB reactor were varied from 1.5 to 12 kg COD $m^{-3}$ $d^{-1}$ for 328 days.

Substrate removal and biogas production at different OLRs during the process are shown in Figure 2. The highest efficiency of removal COD was 86.41% at OLR 4.8 kg COD $m^{-3}$ $d^{-1}$ and produced the highest biogas.

The process was carried out for 328 days with the influent pH range kept stable between 6.5 - 7.5 by the addition of $NaHCO_3$. Anaerobic bioreactor process in the hydrolysis phase and microorganism acidogenesis is able to work optimally in the pH range 5.5-7, and microorganisms in the methanogenesis phase are able to

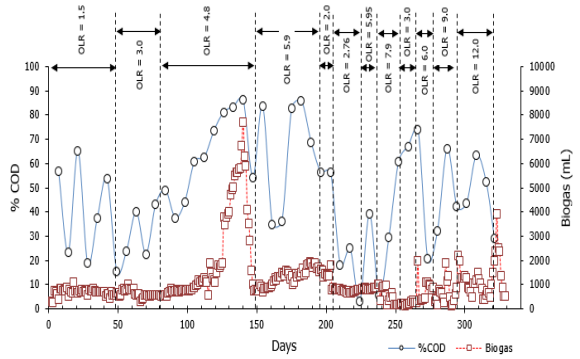


**Figure 2.** Relationship between % COD and biogas on OLRs

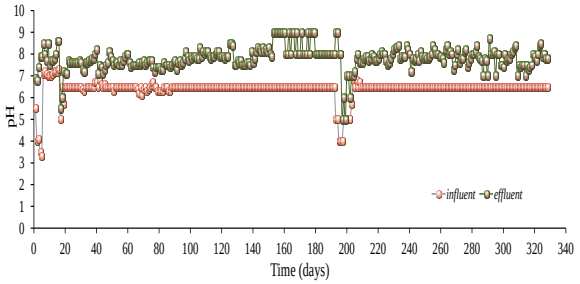


**Figure 3.** Values of influent pH and values of effluent pH on time

work optimally in the range of pH 6.5 - 8.0 [41] and the methanogen process can work optimally in the range of pH 6.5 -8.2 [42]. Figure 2. and Figure 3. indicated that COD removal and biogas production are highest at pH 7.6 at OLR 4.8 kg COD $m^{-3}$ $d^{-1}$. This shows the OLR 4.8 kg COD $m^{-3}$ $d^{-1}$ and HRT 24 h have the optimum contact time in degrading organic compounds in the Hybrid UASB reactor and the process pH shows more active metanogenic microorganisms. Increased production of biogas and efficiency of COD are influenced by the OLR in the appropriate range. Increased organic loads provide modified granular structures and loss of stability. Hence the increased OLR causes a decrease in volatile solid and biogas production [19, 43, 44]. Excessive OLR levels can cause system instability. Therefore, the level of organic loading that grows must be in the right range so as to increase the rate of biogas production [42-44].

**3. 2. Performance of The Kinetic Model of Stover-Kincannon** Substrate utilization rate is shown as a function of organic loading rate on the Stover-Kincannon model. Figure 4. shows a linear regression curve between the rate of organic load and the rate of substrate removal at HRT 24 h. Kinetic constants ($K_B$ = $\mu_{max}$ x b) are saturation constants and μmax is the maximum rate of substrate utilization and μmax is the maximum rate of substrate utilization ($\mu_{max}$ = 1/a). Figures 4, 5 and 6 indicate plot of COD loading V/QSo versus COD removal rate V/(Q (So-Se)) of hybrid reactor UASB. From Figure 4. slope and intercept of a best line ($R^2$ = 0.9704), constant of kinetic for COD removal in the hybrid reactor of UASB were determined as $\mu_{max}$ = 0.59 mg $L^{-1}$ $d^{-1}$ and $K_B$ = 3.7 mg $L^{-1}$ $d^{-1}$, respectively.

Therefore organic loading rate (OLR) in reactor hybrid UASB takes the following form:

$$\frac{Q(So-Se)}{V} = \left[\frac{0.59\,(\frac{Q\,So}{V})}{3.7+(\frac{Q\,So}{V})}\right] \quad (6)$$

And effluent substrate of reactor hybrid UASB could be predicted by rearranging Equation (6):

$$S_e = S_o - \left[\frac{0.59\,So}{3.7+(\frac{Q\,So}{V})}\right] \quad (7)$$

Figure 5 shows a linear regression curve between the rate of organic load and the rate of substrate removal in HRT 18 h. From Figure 5, the slope and intercept of a best line ($R^2$ = 0.9425), constant of kinetic for COD removal in hybrid UASB reactor were determined as μmax = 9.41 mg $L^{-1}$ $d^{-1}$ and $K_B$ = 12.97 mg $L^{-1}$ $d^{-1}$, respectively. Therefore organic loading rate (OLR) in hybrid UASB reactor takes the following form:

$$\frac{Q(So-Se)}{V} = \left[\frac{9.41\,(\frac{Q\,So}{V})}{12.97+(\frac{Q\,So}{V})}\right] \quad (8)$$

And effluent substrate of reactor hybrid UASB could be predicted by rearranging Equation (9):

$$S_e = S_o - \left[\frac{9.41\,So}{12.97+(\frac{Q\,So}{V})}\right] \quad (9)$$

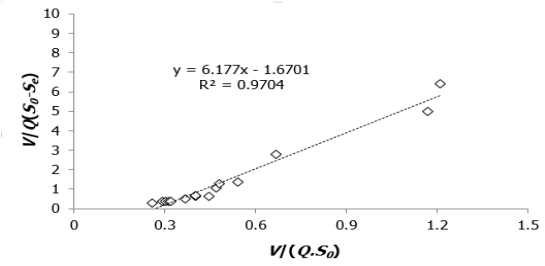


**Figure 4.** Plots of substrate removal for COD removal at HRT 24 h

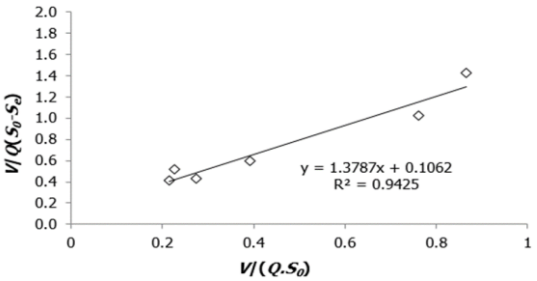


**Figure 5.** Plots of substrate removal for COD removal at HRT 18 h

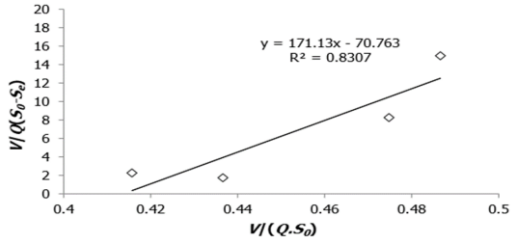


**Figure 6.** Plots of substrate removal for COD removal at HRT 12 h

Figure 6 shows a linear regression curve between the rate of organic load and the rate of substrate removal in HRT 12 h. From Figure 6 the slope and intercept of a best line ($R^2$ = 0.8307), constant of kinetic for COD removal in the hybrid UASB reactor were determined as μmax = 0.014 mg $L^{-1}$ $d^{-1}$ and $K_B$ = 2.42 mg $L^{-1}$ $d^{-1}$, respectively. Therefore, organic loading rate (OLR) in the hybrid UASB reactor takes the following form:

$$\frac{Q(So - Se)}{V} = \left[\frac{0.014\ (\frac{Q\ So}{V})}{2.42 + (\frac{Q\ So}{V})}\right] \quad (10)$$

And effluent substrate of hybrid UASB reactor could be predicted by rearranging Equation (10).

$$S_e = S_o - \left[\frac{0.014\ So}{2.42 + (\frac{Q\ So}{V})}\right] \quad (11)$$

Calculations of the above kinetic parameters to predict kinetic parameters in the hybrid UASB reactor. The model of Stover-Kincannon can be said that the substrate removal rate is influenced by the organic load rate (OLR) that enters the hybrid UASB reactor. The compatibility of the Stover Kincannon model for each HRT is shown by the regression coefficient ($R^2$). Which is the best performance shown in Figure 4 ($R^2$ = 0.9704). This is much different when compared to the pulp and paper industrial wastewater treatment using hybrid UASB reactor, namely $R^2$ = 0.4994 [21]. Therefore, it can be said that the hybrid UASB reactor for treating tofu wastewater at HRT 24 h can be applied to industrial scale.

## 4. CONCLUSION

The OLR is one of the parameters that influences the wastewater treatment process in the bioreactor. Process control is related to loading rate. Therefore the loading rates must be pressed up in order to reduce the size of the reactor so that monitor and control are more critical.

Increased efficiency of COD removal and biogas production were influenced by the level of suitability of the organic load (OLR) in the reactor process. The optimum process was shown in OLR 4.8 kg COD $m^{-3}d^{-1}$ and HRT 24 hours in the hybrid UASB reactor where these conditions resulted in the highest COD removal efficiency and biogas production, namely 86.41% and 7700 mL. Modified Stover-Kincannon model was observed and matched data sets were obtained. The kinetic values of model obtained of HRT variations (12, 18, 24h), the parameters $K_B$ and $\mu_{max}$ were 3.7, 12.97, 2.42 $mgL^{-1}$ $d^{-1}$ and 0.59, 9.41, 0.014 $mgL^{-1}$ $d^{-1}$, respectively. This model was a plot of the inverse of the removal rate, versus inverse of the total loading rate resulted a straight line. This shows that model kinetic of Stover-Kincannon is the rate of substrate removal that is affected by the organic load rate (OLR) that enters the hybrid UASB reactor.

## 5. REFERENCES


1 Jurczyk, Ł., Koc-Jurczyk, J.and Balawejder, M. "Quantitative dynamics of chosen bacteria phylla in wastewater treatment plants excess sludge after ozone treatment" ***Journal of Ecology Engineering***, Vol. 20, No. 3, (2019), 204-213. doi: 10.12911/22998993/99784.

2 Abdollahzadeh, E. and Bonakdarpour, B. "The Study of Organic Removal Efficiency and Membrane Fouling in a Submerged Membrane Bioreactor Treating Vegetable Oil Wastewater" ***International Journal of Engineering, Transactions C: Aspetcs,*** Vol. 29, No. 12, (2016), 1642-1649. doi: 10.5829/idosi.ije.2016.29.12c.02.

3 Yanqoritha, N., Turmuzi, M. and Derlini. "Acclimatization process of tofu wastewater on hybrid upflow anaerobic sludge blanket reactor using polyvinyl chloride rings as a growth medium" In AIP Conference Proceedings, Vol. 1840, No. 1, (2017), p. 110013. https://doi.org/10.1063/1.4982343.

4 Faisal, M., Gani, A., Mulana, F. and Daimon, H. "Treatment and Utilization of Industrial Tofu Waste in Indonesia." ***Asian Journal of Chemistry,*** Vol. 28, No. 3, (2016), 501-507. doi: 10.14233/ajchem.2016.19372.

5 Kambuaya, B. "Baku Mutu Air Limbah bagi Usaha atau Pengolahan Kedelai" Jakarta: Ministry of Environmental (in Indonesia), (2014).

6 Indriyati, J. P. dan Susanto, "Biological processing performance of tofu liquid wastes" ***Jurnal Teknologi Lingkungan***, Vol. 13, No. 2, (2012), 159-166.

7 Mufarida, N., N., A. and Abidin, A., A. "The Innovation of Tofu Waste Liquid Biogas Reactor Technology as an Alternative Energy Resource" ***Waste Technology,*** Vol. 9, No. 1, (2021), 20-24. doi: http://dx.doi.org/10.14710/wastech.9.1.20-24

8 Yanqoritha, N., Turmuzi, M., Irvan, Fatimah, and Derlini. "The Effect of Organic Loading Rate Variation on Digestion of Tofu Wastewater using PVC Rings as Growth Media in a Hybrid UASB Reactor" ***Oriental Journal Chemistry***, Vol. 34, No. 3, (2018), 1653-1657. doi: 10.13005/ojc/340361.

9 Adisasmito, S., Rasrendra, C. B., Chandra, H., and Gunartono, M. A. "Anaerobic reactor for Indonesian tofu wastewater treatment" ***International Journal of Engineeringn & Technology,*** Vol. 7, No. 3, (2018), 30-32, doi: 10.14419/ijet.v7i3.26.17456.

10 Li, L., Guo, X. P., Zhao, T. N., Liu, L. and Li, T. Y. "Identifying the key environmental factors and bacterial communities in humification and their relationships during green waste composting." ***Applied Ecology and Environmental Research,*** Vol. 19, No. 1, (2021), 45-62. doi: 10.15666/aeer/1901_045062.

11 Effendi, H., Seroja, R., and Hariyadi, S. "Response surface method application in tofu production liquid waste treatment" ***Indonesian Journal of Chemistry,*** Vol. 19, No. 2, (2019), 298-304. doi: 10.22146/ijc.31693.

12 Kleerebezem, R., Joosse, B., Rozendal, R. and Loosdrecht, M. C. M. V. "Anaerobic digestion without biogas" ***Reviews in Environmental Science and Bio/Technology,*** Vol. 14, No. 4, (2015), 787-801. doi: 10.1007/s11157-015-9374-6.

13 Beegle, J., R. and Borole, A. P. , "Energy production from waste: Evaluation of anaerobic digestion and bioelectrochemical systems based on energy efficiency and economic factors" ***Renewable and Sustainable Energy Reviews,*** Vol. 96, (2018), 343-351, doi: 10.1016/j.rser.2018.07.057.

14 Shrestha, B., Hernandez, R., Fortela, D., L., B., Sharp, W., Chistoserdov, A., Gang, D., Revellame, E., Holmes, W. and Zappi, M., E. "A review of pretreatment methods to enhance solids reduction during anaerobic digestion of municipal wastewater sludges and the resulting digester performance: implications to future urban biorefineries" ***Applied Sciences,*** Vol. 10, No. 24, (2020) 1-28. doi: 10.3390/app10249141.

15 BPPT, Development of Planning and Policy Support for Improving the Potential Production of Biogas as Renewable Energy in Indonesia'a Tofu Industries. 2013: Renewable Energy-Efficiency Energy Partnership (REEEP) Environmental Technology Centre, The Agency for the Assessment and Application of Technology, Indonesia.

16 Hidayat, Y. A., Kiranamahsa, S. and Zamal, M. A. "A study of plastic waste management effectiveness in Indonesia industries." ***AIMS Energy,*** Vol. 7, No. 3, (2019), 350-370. doi: 10.3934/ENERGY.2019.3.350.

17 Gnanapragasam, G., Arutchelvan, V., Soundari, L. and Maneeshkumar, C., S. "Evaluation of kinetic models for tearing textile dyeing wastewater using UASB reactor." ***IOSR Journal of Biotechnology and Biochemistry,*** Vol. 03, No. 04, (2017), 57-65. doi: 10.9790/264x-03045765.

18 Akulshin, A., Shcherbakov, V. I., Kuznetsova, N. V., Bienkowski, N. and Shchukina, T. V. "Biogas uninterrupted production process intensification" ***Journal Applied Engineering Science,*** Vol. 15, No. 4, (2017), 471-473. doi: 10.5937/jaes15-15453.

19 Babaee, A. and Shayegan, J. "Effect of Organic Loading Rates (OLR) on Production of Methane from Anaerobic Digestion of Vegetables Waste" World Renewable Energy Congress 2011, Bioenergy Technology Linköping, Sweden, (2011), 411. doi: http://dx.doi.org/10.3384/ecp11057411.

20 Govindaradjane, S., Sundararajan, T., Sivasankaran, M. A., and Kumar, V. N., "Performance and Kinetics of a HUASB reactor for treating tapioca-based starch industrial waste stream." ***International Journal of Engineering and Advanced Technology***, Vol. 2 No. 4, (2013), 105-110.

21 Hemalatha, D. and Keerthinarayana, S. "Kinetic modelling of hybrid upflow anaerobic sludge blanket reactor in treatment of pulp and paper mill wastewater" ***Indian Journal Chemical Technology***, Vol. 24, No. 3, (2017), 352-357.

22 Li, Y. F., Abraham, C., Nelson, M. C., Chen, P. H., Graf, J. and Yu, J. "Effect of organic loading on the microbiota in a temperature-phased anaerobic digestion (TPAD) system co-digesting dairy manure and waste whey", ***Applied Microbiology Biotechnology,*** Vol. 99, No. 20, (2015), 8777-8792. doi: 10.1007/s00253-015-6738-3.

23 Gomes D. R. S., Papa, L.G., Cichello, G.C.V. Belançon, D., Pozzi, E.G., Balieiro, J.C.C., Monterrey-Quintero, E.S., Tommaso, G. "Effect of enzymatic pretreatment and increasing the organic loading rate of lipid-rich wastewater treated in a hybrid UASB reactor" ***Desalination,*** Vol. 279, No. 1-3, (2011), 96-103. doi: 10.1016/j.desal.2011.05.067.

24 Thiyagu, R. and Sivarajan, P. "Influence of organic loading rate in acclimatization phase of hybrid upflow anaerobic sludge blanket (UASB) reactor treating distillery spent wash" ***Nature Environment and Pollution Technology,*** Vol. 17, No. 1, (2018), 223-227.

25 Zinatizadeh, A. A., Mohammadi, P., Mirghorayshi, M., Ibrahim, S., Younesi, H. and Mohamed, A. R. "An anaerobic hybrid bioreactor of granular and immobilized biomass for anaerobic digestion (AD) and dark fermentation (DF) of palm oil mill effluent: Mass transfer evaluation in granular sludge and role of internal packing" ***Biomass and Bioenergy,*** Vol. 103, (2017), 1-10, doi: 10.1016/j.biombioe.2017.05.006.

26 Jiang, M., Westerholm, M., Qiao, W. Wandera, S. M. and Dong, R. "High rate anaerobic digestion of swine wastewater in an anaerobic membrane bioreactor" ***Energy,*** Vol. 193, (2020), 116783. doi: 10.1016/j.energy.2019.116783.

27 Ghasemian, P., Abdollahzadeh Sharghi, E. and Davarpanah, L. "The influence of short values of hydraulic and sludge retention time on performance of a membrane bioreactor treating sunflower oil refinery wastewater" ***International Journal of Engineering, Transactions A: Basics,*** Vol. 30, No. 10, (2017), 1417-1424. doi: 10.5829/ije.2017.30.10a.01.

28 Meng, F., Zhang, S., Oh, Y., Zhou, Z., Shin, H. S. and Chae, S. R.. "Fouling in membrane bioreactors: An updated review" ***Water Research,*** Vol. 114, (2017), 151-180. doi: 10.1016/j.watres.2017.02.006.

29 Abyar, H., Younesi, H., Bahramifar, N., Zinatizadeh, A. A. and Amini, M. "Kinetic evaluation and process analysis of COD and nitrogen removal in UAASB bioreactor" ***Journal of the Taiwan Institute of Chemical Engineers,*** Vol. 78, No. 11, (2017), 272-281. doi: 10.1016/j.jtice.2017.06.014.

30 Jafarzadeh, M. T., Mehrdadi, N. and Hashemian, S. J. "Kinetic constants of anaerobic hybrid reactor treating petrochemical waste" A***sian Journal of Chemistry***, Vol. 21, No. 3, (2009), 1672-1684.

31 Wu, X., Yang, Y., Wu, G., Mao, J. and Zhou, T. "Simulation and optimization of a coking wastewater biological treatment process by activated sludge models (ASM)" ***Journal of Environmental Management,*** Vol. 165, (2016) 235-242. doi: 10.1016/j.jenvman.2015.09.041.

32 Hassan, S. R., Zwain, H. M. and Dahlan, I. "Development of Anaerobic Reactor for Industrial Wastewater Treatment : An Overview Present Stage and Future Prospects" ***Journal of Advanced Scientific Research***, Vol. 4, No. 1, (2013), 7-12.

33 APHA (American Public Health Association, Washington, DC) *Standard Methods for the Examination of Water and Wastewater*. Washington, DC, 2012.

34 Narasimha, G. and Saigopal, D. "Impact of indigenous microorganisms on soil microbial and enzyme activities Related papers Changes in soil enzyme activities under the influence of sugar industry effluents Maddela Naga Raju Influence of organic manure on soil microbial and enzyme activities" ***Archives of Applied Science Research*** Vol. 4, No. 2, (2012) 1065-1073. [Online].Available:www.scholarsresearchlibrary.com

35 Wang, T., Li, C. and Zhu, G. "Performance, process kinetics and functional microbial community of biocatalyzed electrolysis-assisted anaerobic baffled reactor treating carbohydrate-containing wastewater" ***The Royal Society of Chemistry***, Vol. 8, No. 72, (2018), 41150-41162, Doi: 10.1039/c8ra08590k.

36 Xiu-lan, Z., qiong Li, B., Jiu-pai, Ni, J. and De-ti Xie. "Effect of four crop straws on transformation of organic matter during sewage sludge composting" ***Journal Integrative Agriculture,*** Vol. 15, No. 1, (2016), 232-240, doi: 10.1016/S2095-3119(14)60954-0.

37 Tchobanoglous, G., Franklin I. Burton & David Stensel, H. "Wastewater Engineering Treatment and Reuse", McGraw Hill Series Companies, Inc., 2003.

38 Azbar, N., Tutuk, F. and Keskin, T. "Biodegradation performance of an anaerobic hybrid reactor treating olive mill effluent under various organic loading rates" ***International Biodeterioration & Biodegradation***, Vol. 63, No. 6, (2009), 690-698. doi: 10.1016/j.ibiod.2009.02.009.

39 Speece, Richard E. "Anaerobic biotechnology" ***Environmental Science & Technology***, Vol. 17, No. 9, (1983), 417A.

40 Najafpour, G. D., A. A. L. Zinatizadeh, A. R. Mohamed, M. Hasnain Isa, and H. Nasrollahzadeh. "High-rate anaerobic digestion of palm oil mill effluent in an upflow anaerobic sludge-fixed film bioreactor" ***Process Biochemistry***, Vol. 41, No. 2, (2006), 370-379. https://doi.org/10.1016/j.procbio.2005.06.031

41 Adebayo, A., Jekayinfa, S., and Linke, B. "Effects of Organic Loading Rate on Biogas Yield in a Continuously Stirred Tank Reactor Experiment at Mesophilic Temperature" ***British Journal of Applied Science & Technology,*** Vol. 11, No. 4, (2015), 1-9. doi: 10.9734/bjast/2015/18040.

42 Sun, M.T., Fan, X.L., Zhao, X.X., Fu, S.F., He, S., Manasa, M.R.K. and Guo, R.B. "Effects of organic loading rate on biogas production from macroalgae: Performance and microbial community structure" ***Bioresource Technology,*** Vol. 235, (2017), 292-300. doi: 10.1016/j.biortech.2017.03.075.

43 Zinatizadeh, A. A. L., A. R. Mohamed, A. Z. Abdullah, M. D. Mashitah, M. Hasnain Isa, and G. D. Najafpour, "Process modeling and analysis of palm oil mill effluent treatment in an up-flow anaerobic sludge fixed film bioreactor using response surface methodology (RSM)", ***Water Research***, Vol. 40, No. 17 (2006),3193-3208. https://doi.org/10.1016/j.watres.2006.07.005

44 Zinatizadeh, A. A. L., A. R. Mohamed, G. D. Najafpour, M. Hasnain Isa, and H. Nasrollahzadeh. "Kinetic evaluation of palm oil mill effluent digestion in a high rate up-flow anaerobic sludge fixed film bioreactor", ***Process Biochemistry***, Vol. 41, No. 5 (2006), 1038-1046. https://doi.org/10.1016/j.procbio.2005.11.011

## Persian Abstract

**چکیده**

هدف این تحقیق بررسی متغیرهای نرخ بارگذاری آلی (OLR) در تصفیه فاضلاب توفو با استفاده از راکتور لجن بی‌هوازی هیبریدی با جریان بالا (Hybrid UASB) با استفاده از مدل سینتیک اصلاح‌شده Stover Kincannon است. این راکتور با تغییرات OLR 1.5-12 کیلوگرم $COD\ m^{-3}\ d^{-1}$ و HRT 12 تا ۲٤ ساعت به مدت ۳۲۸ روز کار می کرد. راندمان حذف COD بالاتر ۸٦.٤۱٪ و تولید بیوگاز ۷۷۰۰ میلی لیتر در OLR 4.8 کیلوگرم $COD\ m^{-3}\ d^{-1}$ و HRT 24 ساعته در ۱٤۰ روز به دست آمد. مدل اصلاح شده استوور-کینکنن مشاهده شد و مجموعه داده های منطبق به دست آمد. مقادیر جنبشی مدل به دست آمده در تغییرات HRT، پارامترهای $K_B$ و $\mu max$ به ترتیب ۳.۷، ۱۲.۹۷، ۲.٤۲ $mgL^{-1}\ d^{-1}$ و ۰.۵۹، ۹.٤۱، ۰.۰۱٤ $mgL^{-1}\ d^{-1}$ بود. این مدل نمودار معکوس نرخ حذف بود، در مقابل معکوس نرخ بارگذاری کل منجر به یک خط مستقیم شد. نشان داد که مدل استوور-کینکنن نرخ حذف بستر تحت تأثیر نرخ بار آلی (OLR)است که به راکتور هیبریدی UASB جریان می‌یابد.

International Journal of Engineering

Journal Homepage: www.ije.ir

# Improving the Position Accuracy of Rover Receiver using Differential Positioning in Indian Regional Navigation Satellite System

K. Madhu Krishna*, P. Naveen Kumar

*Advanced GNSS Research Laboratory, Department of ECE, University College of Engineering, Osmania University, Hyderabad, India*

*P A P E R I N F O*

*Paper history:*
Received 19 August 2022
Received in revised form 21 October 2022
Accepted 03 November 2022

*Keywords*:
*NavIC*
*Differential IRNSS*
*Positional Accuracy*
*Differential Corrections*

*A B S T R A C T*

Navigation with Indian Constellation (NavIC) is the Indian Regional Navigation Satellite System (IRNSS) developed by Indian Space Research Organization (ISRO) to provide the position and navigation services for Indian region. NavIC or IRNSS is individual satellite constellation which has seven satellites covering the Indian subcontinent. Accuracy of NavIC standalone is insufficient in certain applications such as civil aviation. To improve the position accuracy performance of NavIC system, differential positioning technique is utilized. In this paper, differential positioning is carried out, considering two IGS (IRNSS-GPS-SBAS) receivers (one as reference station and the other as rover), which are capable of receiving IRNSS signals from 7 satellites, GPS signals from 12 satellites, SBAS signals from 2 satellites. Here, NavIC constellation alone is considered for the analysis. The differential positioning is carried out using the pseudorange measurements on L5 (1176.45 MHz), S1 (2492.028 MHz) and dual (L5 and S1 both) and accuracies are compared in terms of the statistical parameters Circular Error Probability (CEP), Distance Root Mean Square (DRMS), 2DRMS (twice the DRMS). The improvement in the horizontal accuracy (2DRMS) of the rover using pseudorange measurements on L5 is observed to be 78.81%, on S1 it is 69.14 % and using dual frequency (L5 and S1 both) it is 80.73% when compared to NavIC standalone.

***doi**: 10.5829/ije.2023.36.03c.09*

**NOMENCLATURE**

| | | | |
|---|---|---|---|
| $t_s$ | Time at which the signal departed from the satellite | $t_r$ | Time at which the signal is received at the receiver |
| c | Speed of light | $\rho$ | Pseudorange |
| r | Geometric range | $\Delta\rho$ | pseudorange error, |
| $\delta t_r$ | Receiver clock error | $\delta t_s$ | Satellite clock error |
| I | Ionospheric delay | T | Tropospheric delay |
| $\varepsilon$ | Other errors like receiver noise, multipath and antenna delay | $(x_s, y_s, z_s)$ | Satellite position |
| $(x_r, y_r, z_r)$ | Receiver position | $\hat{\rho}_r$ | corrected pseudorange |
| $\sigma_x$, $\sigma_y$ | Standard deviations of east and north components of the user position error | | |

## 1. INTRODUCTION

Standalone accuracy of NavIC system is insufficient in certain applications such as civil aviation. To improve the accuracy one of the methods is to accurately estimate the NavIC errors such as ionospheric error (as it is the most dominating error in satellite navigation applications) using appropriate models [1, 2]. This method may not provide sufficient accuracy in case of standalone receivers [3]. Differential positioning is the technique used to provide better accuracy for certain applications when compared to standalone accuracy of NavIC system [4]. A typical Differential IRNSS architecture is shown in Figure 1. Differential IRNSS consists of a reference receiver which is located at a well surveyed location. This system also consists of one or more rover receivers. The reference receiver and differential correction processing equipment together are called the reference station [5]. Satellite range measurement is affected by different errors. Some of them are slowly varying error

*Corresponding Author Institutional Email: kmadhukrishna@osmania.ac.in (K. Madhu Krishna)

Please cite this article as: K. Madhu Krishna, P. Naveen Kumar, Improving the Position Accuracy of Rover Receiver using Differential Positioning in IRNSS, ***International Journal of Engineering, Transactions C: Aspects,*** Vol. 36, No. 03, (2023) 497-504

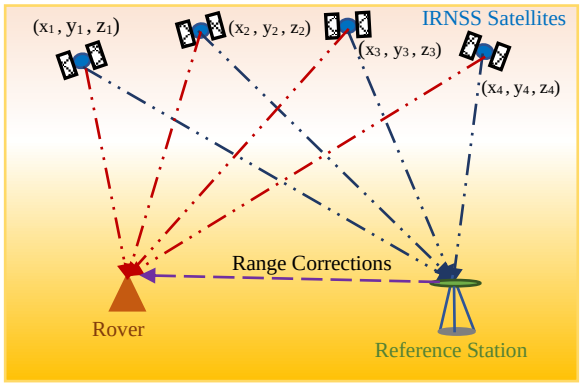


**Figure 1.** Differential IRNSS Architecture

components which are estimated by reference station [6]. Reference station also computes the range corrections for each IRNSS satellite in view. These corrections are called differential corrections. Differential corrections are transmitted to the rover receivers. The differential corrections are estimated by taking the difference between the pseudorange measurement and true range [7]. When both the receivers are nearby (within the vicinity of the reference station), they are affected by the errors which are common to both the receivers. These common errors can be eliminated completely or reduced by transmitting the differential corrections from the reference station to the rover receiver [8-10]. The ephemeris error and satellite clock error can be eliminated completely. The atmospheric errors such as ionospheric error and tropospheric error can be reduced [11, 12]. There will not be any change in the errors such as multipath error and receiver noise. Using these corrections, the rover accuracy is much improved. The improved accuracy is attained when the same set of satellites which are visible at the reference receiver are also visible at the rover receiver [4, 13].

## 2 CALCULATION OF PSEUDORANGE CORRECTIONS

The raw pseudorange can be measured by multiplying the speed of light c with the signal propagation time.

$$\rho = (t_r - t_s) * c \quad (1)$$

where $t_s$ is the time at which the signal departed from the satellite and $t_r$ is the time at which the signal is received at the receiver [14, 15].

The pseudorange measurement is affected by different errors such as ionospheric delay, tropospheric delay, satellite ephemeris error, receiver clock error and multipath.

The pseudorange measurement at the receiver can be represented as follows:

$$\rho = r + \Delta\rho = r + c * (\delta t_r - \delta t_s) + I + T + \varepsilon \quad (2)$$

where $r$ is the geometric range, $\Delta\rho$ is the pseudorange error, $\delta tr$, $\delta ts$ are the receiver clock error and the satellite clock error respectively, $I$ is the ionospheric delay, $T$ is the tropospheric delay, $\varepsilon$ the other errors like receiver noise, multipath and antenna delay [16, 17].

The geometric range $r$, can also be expressed by the following equation:

$$r = ((x_s - x_r)^2 + ((y_s - y_r)^2 + ((z_s - z_r)^2)^{0.5} \quad (3)$$

where $(x_s, y_s, z_s)$ is the satellite position and $(x_r, y_r, z_r)$ is the receiver position [18].

At the reference station the pseudorange corrections are computed as follows:

$$\Delta\rho = \rho - r \quad (4)$$

The corrected pseudoranges $\hat{\rho}_r$ at the rover for each epoch of observation is written as follows:

$$\hat{\rho}_r = \rho_r + \Delta\rho \quad (5)$$

If same set of satellites are visible at both the receivers, then the satellite clock error is identical and can be completely eliminated. The errors $\delta I$, $\delta T, \delta\varepsilon$ are negligible when the distance between the reference station and the mobile receiver is small [4, 18].

For the estimation of rover position at the mobile receiver these corrected pseudoranges are applied. This leads to the improvement in the mobile user position.

NavIC receivers here are dual frequency receivers. The frequencies used are L5 (1176.45 MHz) and S1 (2492.028 MHz). The pseudoranges on L5 and S1 are used for computing differential corrections and compare the positional accuracies.

## 3 ACCURACY MEASURES IN 2D

When the IRNSS data logged over the time, the measured positions are disseminated over an area because of the measurement error. These distributed points are called scatter plot, which is used to characterize accuracy of IRNSS receiver. The area within which the estimated parameters are likely to be is the confidence region [9, 10, 19]. The performance of IRNSS is statistically quantified by analyzing the confidence region. The probability with which the solution will be within the specified accuracy is described with the confidence region with certain radius [20].

### 3. 1. Distance Root Mean Square (DRMS)

DRMS is a number which signifies 2D accuracy of the NavIC receiver. To calculate the DRMS of horizontal position accuracy, the standard errors (σ) from the known position in the directions of the coordinate axis are

required. DRMS refers to the radius of a circle in which 65% of the values occur [19, 21].

DRMS can be expressed as follows:

$$DRMS = \sqrt{\sigma_x^2 + \sigma_y^2} \quad (6)$$

where $\sigma_x$ and $\sigma_y$ are the standard deviations of east and north components of the user position error.

**3. 2. Circular Error Probability (CEP)** CEP is defined to be the radius of circle with center as the true position, containing the position estimate with probability of 50% [19].

CEP can be expressed as follows:

$$CEP = 0.62\sigma_x + 0.56\sigma_y \quad (7)$$

2DRMS is twice the DRMS of the horizontal position errors [20].

## 4 RESULTS AND DISCUSSION

Differential IRNSS consists two receivers, a reference station and a rover receiver. The two IGS (IRNSS-GPS-SBAS) receivers are considered (one receiver as a reference station and the other as a rover receiver) which are located at Advanced GNSS Research Laboratory (AGRL), Department of Electronics and Communication Engineering, University College of Engineering (UCE), Osmania University (OU), Hyderabad. These receivers are capable of receiving IRNSS signals from 7 satellites, GPS signals from 12 satellites, SBAS signals from 2 satellites. The two receivers' antennas are separated with a distance of 1.4 m. All the data from the receivers are obtained by considering the receivers to be static. The data obtained from both receivers are of the same date and time (i.e. on 15 September 2019 for 24 hours duration).

The receivers' proprietary data is converted to the Receiver Independent Exchange (RINEX) and Comma-Separated Values (CSV) formats. The reference receiver is set at a well surveyed location (the coordinates are 17.407°, 78.517°, 450 m). To get the reference receiver coordinates (surveyed location), the user coordinates in *(x, y, z)* are estimated for the duration of a week and averaged. These coordinates are then converted to latitude, longitude and height, which are used as reference station coordinates for computation of differential corrections.

**4. 1. Differential IRNSS Corrections** Differential IRNSS corrections are computed at reference station using the Equation (4) by taking the difference between the pseudoranges (obtained from IGS Receiver) and the true range. True range is computed using the Equation (3). The corrections are computed for satellites with PRN 2, 3, 4, 5, 6 ,7 (i.e. 6 satellites) with respect to time, individually. These corrections are applied at the rover station to improve the accuracy of the receiver.

The position accuracy using differential IRNSS is analyzed by considering the psuedoranges on L5, S1 and dual frequency (L5 and S1).

**4. 2. Differential IRNSS Considering the Pseudoranges on L5** The pseudoranges on L5 are utilized for improving the horizontal accuracy of the rover. The pseudoranges on L5 are obtained from IGS receivers in CSV file format.

**4. 2. 1. Position of Rover before and after Applying Corrections** The position of rover receiver in Latitude, Longitude and Height (LLH) before applying corrections and after applying corrections is plotted as shown in Figure 2. Latitude, Longitude and Height are plotted here for the duration of 24 hours.

**4. 2. 2. Rover Accuracy without Applying Corrections** Accuracy of standalone IRNSS (using pseudoranges on L5) is plotted by considering east error on x-axis and north error on y-axis in meters. An East-North-Up (ENU) system is used to represent the IRNSS accuracy in terms of east error and north error in meters. The east error and north error are considered to represent the horizontal position error. The data considered is of 24 hrs duration. Accuracy is plotted with the horizontal accuracy parameters CEP, DRMS, 2DRMS. Figure 3 describes the horizontal accuracy plot with CEP, DRMS and 2DRMS values.

For standalone IRNSS, the CEP value is observed to be 5.31 m, which contain the position estimates with probability of 50%. The DRMS value observed is 7.36 m, which is radius of circle with the position estimates with the probability of 65%. The 2DRMS is twice the DRMS value and is observed to be 14.72 m, which is

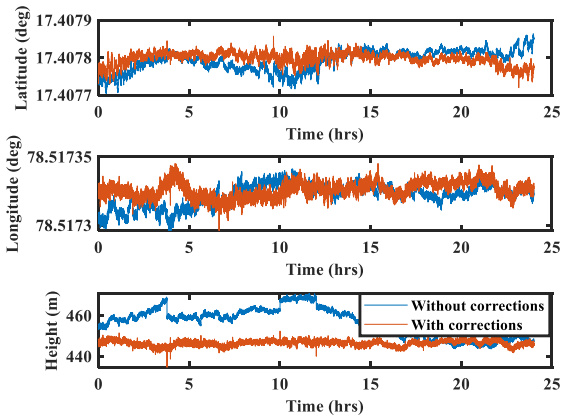


**Figure 2.** Rover position (LLH) (on L5) before and after applying corrections

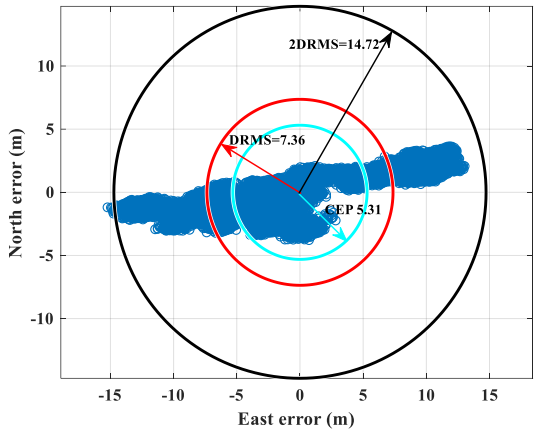


**Figure 3.** Rover receiver radial error CEP, DRMS and 2DRMS estimated over 24 hours before corrections (on L5)

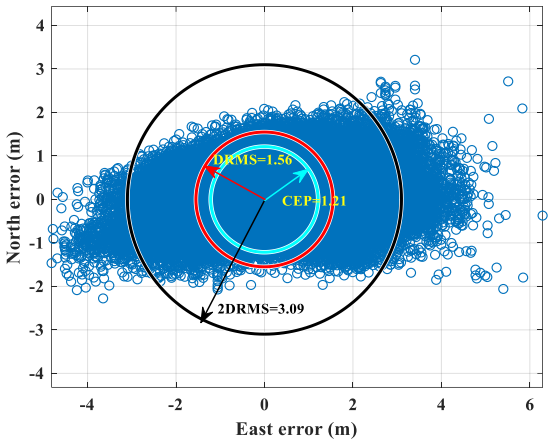


**Figure 4.** Rover receiver radial error CEP, DRMS and 2DRMS estimated over 24 hours with corrections (on L5)

radius of circle with the position estimates with a probability of 95%.

### 4. 2. 3. Rover Accuracy after Applying Corrections

Accuracy of IRNSS (using pseudoranges on L5) with corrections is plotted (Figure 4) by considering east error on x-axis and north error on y-axis in meters. When the corrections applied to rover, the 50% of the position fix errors which does not exceed respective CEP value. The radius of the confidence region 1.21 m matches the accuracy of receiver's position fix in horizontal plane with 50 % probability of estimation. The DRMS value observed is 1.56 m, which is radius of circle with the position estimates with the probability of 65%. The 2DRMS is twice the DRMS value and is observed to be 3.09 m, which is radius of circle with the position estimates with a probability of 95%.

Table 1 gives the comparison of standalone IRNSS and Differential IRNSS positional accuracies. The accuracy parameters are CEP, DRMS and 2DRMS. It is observed that there is an improvement in the accuracy when differential positioning technique is used. The percentage improvement in the accuracy observed is to be 77.21 and 78.81%. The percentage improvement in the accuracy parameter 2DRMS is the same as DRMS improvement.

**TABLE 1.** Accuracy parameters of rover receiver estimated over 24 hours for standalone and differential IRNSS and the percentage improvement in accuracy (on L5)

| Accuracy Parameters | Standalone (without Corrections) | Differential (with corrections) | % improvement in accuracy |
|---|---|---|---|
| CEP (50%) | 5.31 m | 1.21 m | 77.21 % |
| DRMS (65%) | 7.36 m | 1.56 m | 78.81 % |
| 2DRMS (95%) | 14.72 m | 3.1 m | 78.81 % |

The histogram plot and Gaussian distribution of the standalone IRNSS and differential IRNSS rover accuracy on L5 signal in terms of East error and North error in meters are shown in Figure 5. The Gaussian distribution with respective mean values and standard deviation values are represented in Figure 5 (a to d). The mean values for standalone and differential IRNSS accuracy plots are approximately zero for east error and north error in both cases. The standard deviation (STD) values for standalone east error and north error are 7.19 and 1.58, respectively and for differential IRNSS, east error and north error, they are 1.42 and 0.59, respectively. In Figure 5 (a, b) the error values are distributed widely from -10 m to 10 m when compared to Figure 5 (c, d) which are distributed from -5m to 5 m which is narrow, respectively for east error plot. For North error plot, the Gaussian distribution is from -4 m to 4 m when compared to and -2 m to 2 m which is narrow and are confined to zero for

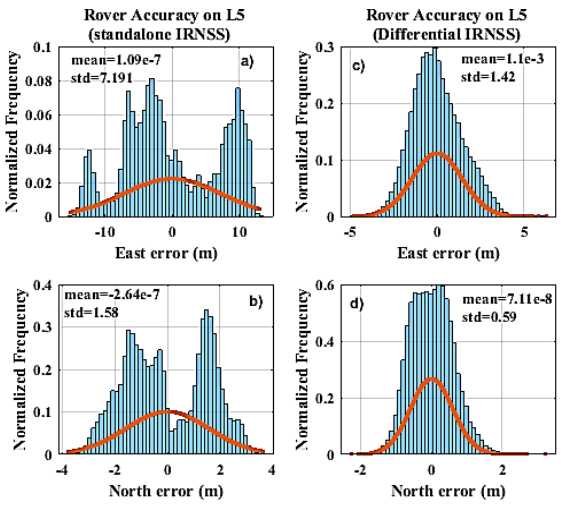


**Figure 5.** Histogram plot and Gaussian Distribution of IRNSS standalone and differential rover accuracy on L5

differential IRNSS. It is observed that the accuracy in case of differential IRNSS is improved when compared to standalone IRNSS rover accuracy.

**4. 3. Differential IRNSS Considering the Pseudoranges on S1** The pseudoranges on S1 are utilized for the improvement in the horizontal accuracy of the rover. The pseudoranges on S1 are obtained from IGS receivers in CSV file format.

**4. 3. 1. Position of Rover before and after Applying Corrections** The position of rover receiver in Latitude, Longitude and Height (LLH) before applying corrections and after applying corrections is plotted as shown in Figure 6. Latitude, Longitude and Height are plotted here are by considering for the duration of 24 hours.

**4. 3. 2. Rover Accuracy without Corrections** Accuracy of standalone IRNSS (using pseudoranges on S1) is plotted by considering east error on x-axis and north error on y-axis in meters. Figure 7 describes the horizontal accuracy plot (radial error) with CEP, DRMS and 2DRMS values. For standalone IRNSS, the CEP, DRMS, 2DRMS values observed to be 3.86 m, 5.38 m, 10.76 m, respectively.

**4. 3. 3. Rover Accuracy after Applying Corrections** Accuracy of IRNSS (using pseudoranges on S1) with corrections is plotted (Figure 8) by considering east error on x-axis and north error on y-axis in meters. When the corrections applied to rover, the CEP, DRMS, 2DRMS are observed to be 1.31 m, 1.66 m, 3.32 m, respectively. The horizontal accuracy parameter 2DRMS is 10.76 m and is improved to 3.32 m after applying corrections.

The comparison of standalone IRNSS and Differential IRNSS positional accuracies on S1 is represented in Table 2**.** It is observed that there is an improvement in the accuracy when differential position is used.

The accuracy parameters CEP and DRMS, the percentage improvement in the accuracy observed is to be 66.06 % and 69.14 %. The percentage improvement in the accuracy parameter 2DRMS is same as DRMS improvement.

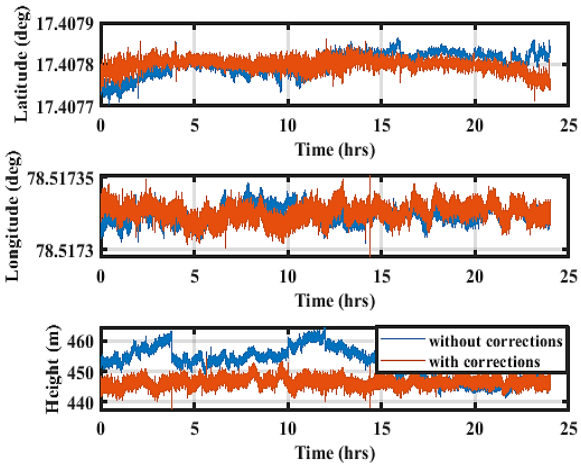


**Figure 6.** Rover position (LLH) (on S1) before and after applying corrections

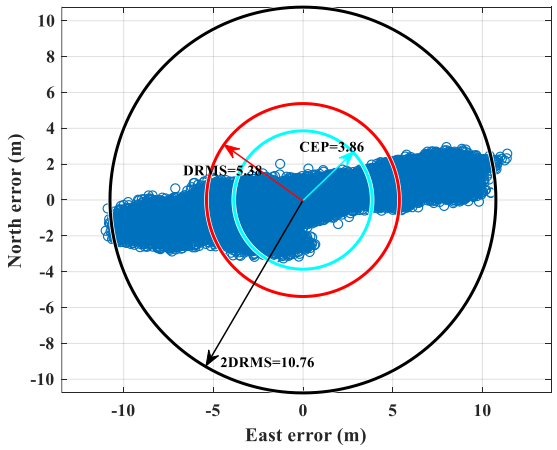


**Figure 7.** Rover receiver radial error CEP, DRMS and 2DRMS estimated over 24 hours without corrections (on S1)

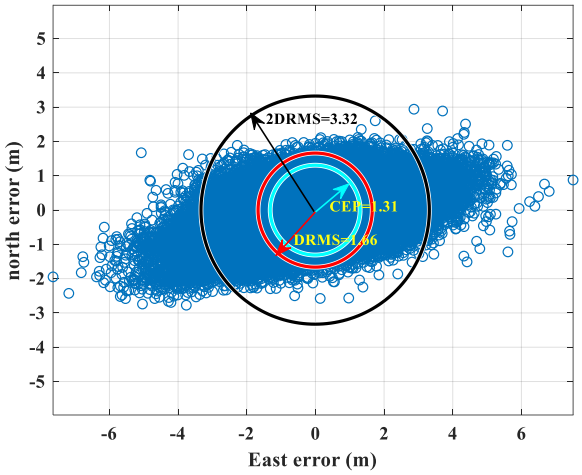


**Figure 8.** Rover receiver radial error CEP, DRMS and 2DRMS estimated over 24 hours with corrections (on S1)

**TABLE 2.** Accuracy parameters of rover receiver estimated over 24 hours for standalone and differential with percentage improvement in accuracy (on S1)

| Accuracy Parameters | Standalone (without Corrections) | Differential (with corrections) | % improvement in accuracy |
|---|---|---|---|
| CEP (50%) | 3.86 m | 1.31 m | 66.06 % |
| DRMS (65%) | 5.38 m | 1.66 m | 69.14 % |
| 2DRMS (95%) | 10.76 m | 3.32 m | 69.14 % |

The histogram plot and Gaussian distribution of the standalone IRNSS and differential IRNSS rover accuracy on S1 signal in terms of East error and North error in meters are shown in Figure 9. The Gaussian distribution with respective mean values and standard deviation values are represented in Figure 9 for the accuracy plots on signal S1. The mean values for standalone and differential accuracy plots are approximately zero for east error and north error. The standard deviation (STD) values for standalone east error and north error are 5.26 and 1.1, respectively and for differential IRNSS, east error and north error they are 1.52 and 0.65, respectively. In Figure 9 (a, b) the error values are distributed widely from -10 m to 10 m when compared to Figure 9 (c, d) which are distributed from -5m to 5 m which is narrow, respectively for east error plot. For North error plot the Gaussian distribution is from -2 m to 2 m in both cases but most of the error values are confined to zero for Differential IRNSS. It is observed that the accuracy in case of differential IRNSS is improved when compared to standalone IRNSS rover accuracy.

**4. 4. Differential IRNSS Considering the Combined Pseudoranges on L5 and S1 (Dual Frequency)** The pseudoranges on L5 and S1 (dual) are utilized together for the improvement of the horizontal accuracy of the rover.

**4. 4. 1. Position of Rover before and after Applying Corrections** The position of rover receiver in Latitude, Longitude and Height (LLH) before applying corrections and after applying corrections is plotted as shown in Figure 10. Latitude, Longitude and Height are plotted here for the duration of 24 hours.

**4. 4. 2. Rover Accuracy without Corrections** Accuracy of standalone IRNSS (using pseudoranges on L5 and S1 both) is plotted by considering east error on x-axis and north error on y-axis in meters. Figure 11 describes the horizontal accuracy plot with CEP, DRMS and 2DRMS values. For standalone IRNSS, the CEP, DRMS, 2DRMS values observed to be 4.51 m, 6.28 m, 12.57 m, respectively.

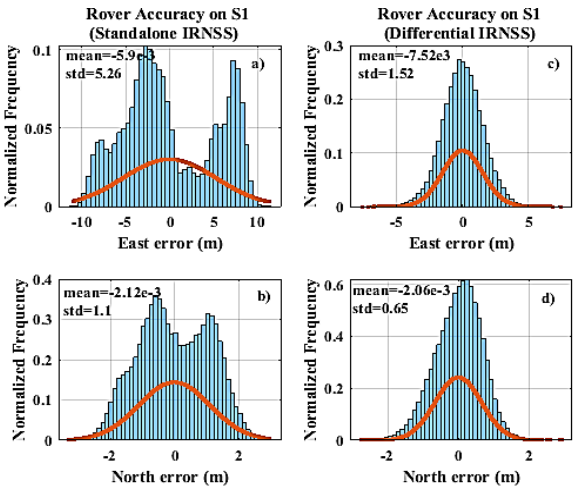


**Figure 9.** Histogram plot and Gaussian Distribution of NavIC standalone and differential rover accuracy on S1

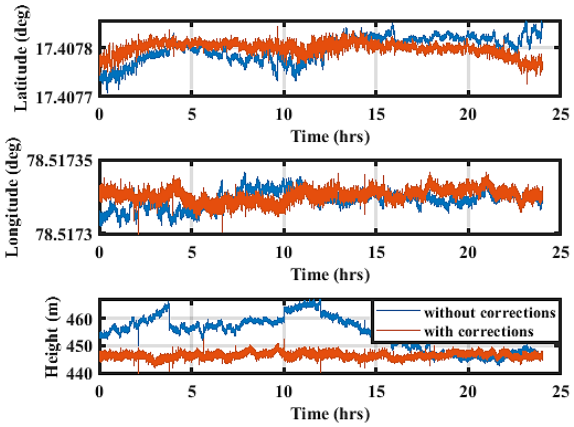


**Figure 10.** Rover position (LLH) (dual) before and after applying corrections

**4. 4. 3. Rover Accuracy after Applying Corrections** Accuracy of IRNSS (using pseudoranges on L5 and S1 both) with corrections is plotted (Figure 12) by considering east error on x-axis and north error on y-axis in meters. When the corrections applied to rover, the CEP, DRMS, 2DRMS are observed to be 0.95 m, 1.21 m, 2.41 m, respectively. The horizontal accuracy parameter 2DRMS was 10.76 m and is improved to 2.41 m after applying corrections.

The comparison of IRNSS standalone and Differential IRNSS positional accuracies on L5 and S1 both (dual frequency) is represented in Table 3. It is observed that there is an improvement in the accuracy

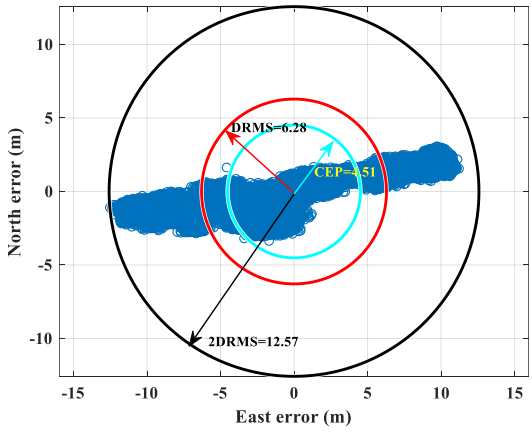


**Figure 11.** Rover receiver radial error CEP, DRMS and 2DRMS estimated over 24 hours without corrections (combined)

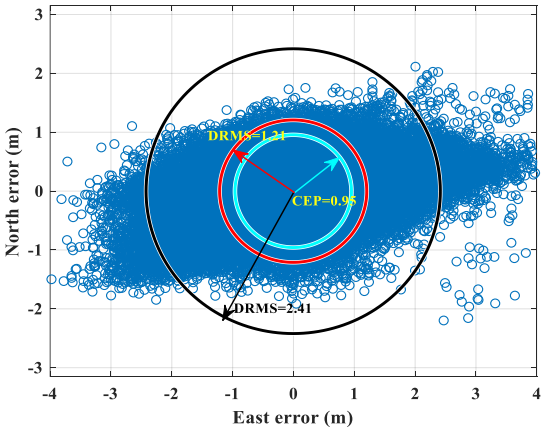


**Figure 12.** Rover receiver radial error CEP, DRMS and 2DRMS estimated over 24 hours with corrections (dual)

**TABLE 3.** Accuracy parameters of rover receiver estimated over 24 hours for standalone and differential with percentage improvement in accuracy (dual frequency)

| Accuracy Parameters | Standalone (without Corrections) | Differential (with corrections) | % improvement in accuracy |
|---|---|---|---|
| CEP (50%) | 4.51 m | 0.95 m | 78.93 % |
| DRMS (65%) | 6.28 m | 1.21 m | 80.73 % |
| 2DRMS (95%) | 12.57 m | 2.41 m | 80.73 % |

when differential position is used. The accuracy parameters CEP and DRMS. The percentage improvement in the accuracy observed is to be 78.93 % and 80.73 %. The percentage improvement in the accuracy parameter 2DRMS is the same as DRMS improvement.

The histogram plot and Gaussian distribution of the standalone IRNSS and differential IRNSS rover accuracy on dual frequency (L5 and S1) signals in terms of East error and North error in meters are shown in Figure 13.

The Gaussian distribution with respective mean values and standard deviation values are represented in Figure 13 for the accuracy plots on dual frequency signal. The mean values for standalone and differential IRNSS accuracy plots are approximately zero for east error and north error. The standard deviation (STD) values for standalone east error and north error are 6.15 and 1.3, respectively and for differential IRNSS, east error and north error they are 1.1 and 0.49, respectively. In Figure 13 (a, b) the east error and north error values are distributed widely from -10 m to 10 m and -2 m to 2 m, repectively, for standalone IRNSS, when compared to the Figure 13 (c, d) the east error and north errors are distributed from -2m to 2 m and -1 m to 1 m, which is narrow and are confined to zero for Differential IRNSS. It is observed that the accuracy in case of differential IRNSS is improved when compared to standalone IRNSS rover accuracy.

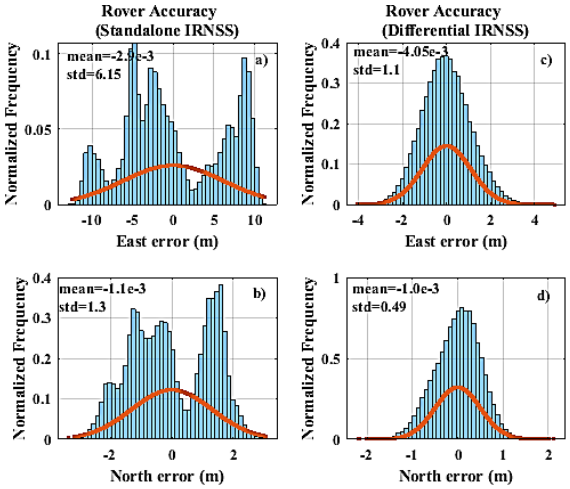


**Figure 13.** Histogram plot and Gaussian Distribution of NavIC standalone and differential rover accuracy on L5 and S1 (dual frequency)

## 5 CONCLUSIONS

Differential positioning is to improve the position accuracy of the rover receiver which is in the vicinity of the reference station. It is useful in certain applications where precise position accuracy is required. Here, the position accuracy on L5, S1 and dual frequency (L5 and S1) are analyzed and compared. Differential position accuracy improvement of 78.81 %, 69.14 % and 80.73 % in 2DMRS horizontal accuracy are observed on L5, S1 and dual frequency (both L5 and S1). The highest improvement in accuracy observed is 80.73 % which is when the rover receiver is in dual frequency mode.

## 6. REFERENCES

1. Devireddy, K., Narsetty, S., Ramavath, A.K. and Perumalla, N.K., "Validation of the iri-2016 model with indian navic data for future navigation applications", ***IET Radar, Sonar & Navigation***, Vol. 15, No. 1, (2021), 37-50. https://doi.org/10.1049/rsn2.12013
2. Kumar, D.K.P.N., "Performance evaluation of global ionospheric models with indian regional navigation data over low latitude station during low solar activity year 2017", ***Performance Evaluation***, Vol. 114, (2021), 279-295. doi: 10.2528/PIERC21053101.
3. Kuna, D., Santhosh, N. and Perumalla, N.K., "Preliminary analysis of standalone galileo and navic in the context of positioning performance for low latitude region", ***Procedia Computer Science***, Vol. 171, (2020), 225-234. https://doi.org/10.1016/j.procs.2020.04.024
4. Seeber, G., *Satellite geodesy.-2-nd edition*. 2003, Berlin, New York: Walter de Gruyter.
5. Kaplan, E.D. and Hegarty, C., "Understanding gps/gnss: Principles and applications, Artech house, (2017).
6. Parveen, S.N. and Siddaiahx, P., "Position error calculations for irnss system using pseudo range method"
7. Madhu Krishna, K., Naveen Kumar, P. and Naraiah, R., "Prediction of differential gps corrections using ar and arma

models", in Advances in Decision Sciences, Image Processing, Security and Computer Vision: International Conference on Emerging Trends in Engineering (ICETE), Vol. 2, Springer. (2020), 290-298.

8. Misra, P. and Enge, P., "Global positioning system: Signals, measurements & performance", ***IEEE Aerospace and Electronic Systems Magazine***, Vol. 17, No. 10, (2002), 36-37.
9. Sridher, T., Sarma, A. and Naveen Kumar, P., "Performance evaluation of onboard wi-fi module antennas in terms of orientation and position for iot applications", ***International Journal of Engineering, Transactions A: Basics***, Vol. 35, No. 10, (2022), 1918-1928. https://doi.org/10.5829/IJE.2022.35.10A.11
10. Voosoghi, B. and Rastbood, A., "Fixing of cycle slips in dual-frequency gps phase observables using discrete wavelet transforms", ***International Journal of Engineering, Transactions B: Applications***, Vol. 21, No. 1, (2008), 9-26. https://www.ije.ir/article_71682_de8ea1357a2674c6d302e93172faa394.pdf
11. Devireddy, K., Abedin, N.U., Kuna, D. and Kumar, P.N., "Analysis of various parameters of l5 and s1 navic signals over low latitude region", ***Procedia Computer Science***, Vol. 171, (2020), 2704-2712. https://doi.org/10.1016/j.procs.2020.04.293
12. Sharma, A., Gurav, O., Bose, A., Gaikwad, H., Chavan, G., Santra, A., Kamble, S. and Vhatkar, R., "Potential of irnss/navic l5 signals for ionospheric studies", ***Advances in Space Research***, Vol. 63, No. 10, (2019), 3131-3138. https://doi.org/10.1016/j.asr.2019.01.029
13. Althaf, A. and Hablani, H.B., "Static baseline estimation using navic pseudoranges: A long-term study", ***IETE Technical Review***, Vol. 39, No. 4, (2022), 827-837. https://doi.org/10.1080/02564602.2021.1912660
14. Mingqin, S. and Xiuping, S., "Study on differential gps positioning methods", ***Hangzhou, China: IEEE***, (2015).
15. Krishna, K.S. and Ratnam, D.V., "Determination of navic differential code biases using gps and navic observations", ***Geodesy and Geodynamics***, Vol. 11, No. 2, (2020), 97-105. https://doi.org/10.1016/j.geog.2020.01.001
16. Naveen Kumar, P., Sarma, A.D. and Supraja Reddy, A., "Modelling of ionospheric time delay of global positioning system (GPS) signals using taylor series expansion for gps aided geo augmented navigation applications", ***IET Radar, Sonar & Navigation***, Vol. 8, No. 9, (2014), 1081-1090. https://doi.org/10.1049/iet-rsn.2013.0351
17. Sundara, R.R. and Raju, G., *Estimation of indian regional navigation satellite system receiver's position accuracy in terms of statistical parameters*. 2022, SAE Technical Paper.
18. Shukla, A., Thakkar, P. and Ganatra, A., "Navic carrier-phase based relative positioning using l5 single frequency measurements", in 4th International Conference on Science, Technology and Management (ICSTM). Vol. 4, (2017), 134-139.
19. Chin, G.Y., *Two-dimensional measures of accuracy in navigational systems*. 1987, United States. Dept. of Transportation. Office of Research and Special Programs.
20. Kuna, D., Perumalla, N.K. and Anil Kumar, R., "Positioning parameters for stand-alone and hybrid modes of the indian navic system: Preliminary analysis", in Advances in Decision Sciences, Image Processing, Security and Computer Vision: International Conference on Emerging Trends in Engineering (ICETE), Vol. 2, Springer., (2020), 299-306.
21. Specht, M., "Statistical distribution analysis of navigation positioning system errors—issue of the empirical sample size", ***Sensors***, Vol. 20, No. 24, (2020), 7144.

## Persian Abstract

**چکیده**

ناوبری با صورت فلکی هند (NavIC)سیستم ماهواره ای ناوبری منطقه ای هند (IRNSS)است که توسط سازمان تحقیقات فضایی هند (ISRO)برای ارائه موقعیت و خدمات ناوبری برای منطقه هند توسعه یافته است. NavIC یا IRNSS یک صورت فلکی ماهواره ای است که دارای هفت ماهواره است که شبه قاره هند را پوشش می دهد. دقت NavIC مستقل در برخی کاربردها مانند هوانوردی غیرنظامی کافی نیست. برای بهبود عملکرد دقت موقعیت سیستم NavIC، از تکنیک موقعیت‌یابی دیفرانسیل استفاده می‌شود. در این مقاله، موقعیت یابی دیفرانسیل با در نظر گرفتن دو گیرنده (IGS IRNSS-GPS-SBAS)یکی به عنوان ایستگاه مرجع و دیگری به عنوان کاوشگر انجام شده است که قادر به دریافت سیگنال IRNSS از ۷ ماهواره، سیگنال GPS از ۱۲ ماهواره، سیگنال SBAS از ۲ ماهواره. در اینجا، صورت فلکی NavIC به تنهایی برای تحلیل در نظر گرفته شده است. موقعیت‌یابی دیفرانسیل با استفاده از اندازه‌گیری‌های شبه درL5 1176.45 مگاهرتز، ) 2492.028S1مگاهرتز و دوگانه (L5 و S1 هر دو) انجام می‌شود و دقت‌ها از نظر پارامترهای آماری احتمال خطای دایره‌ای (CEP)*، میانگین ریشه فاصله مقایسه می‌شوند. مربع (DRMS)، ۲ DRMSدو برابر .(DRMS) بهبود دقت افقی ۲ (DRMS)مربع نورد با استفاده از اندازه‌گیری‌های شبه L5در 78.81 درصد، S1در 69.14 درصد و با استفاده از فرکانس دوگانه (L5 و S1 هر دو) ۸۰.۷۳ درصد در مقایسه با NavIC مستقل است.

International Journal of Engineering

Journal Homepage: www.ije.ir

# Improving the Accuracy of Brain Tumor Identification in Magnetic Resonanceaging using Super-pixel and Fast Primal Dual Algorithm

M. Emadi*[a], Z. Jafarian Dehkordi[b], M. Iranpour Mobarakeh[c]

[a] *Faculty of Electrical Engineering, Mobarakeh Branch, Islamic Azad University, Mobarakeh, Isfahan, Iran*
[b] *Faculty of Software Engineering, Najaf Abad Branch, Islamic Azad University, Najaf Abad, Isfahan, Iran*
[c] *Department of Computer Engineering and IT, Payam Noor University, Tehran, Iran*

*PAPER INFO*

*Paper history:*
Received 15 March 2022
Received in revised form 25 November 2022
Accepted 28 November 2022

*Keywords*:
*Brain Tumor Identification*
*Fast Primal Dual Algorithm*
*Markov Random Fields*
*MRI Imaging*
*Segmentation*

*ABSTRACT*

Brain tumors are one of the most common causes of death that have been widely investigated by scholars in research areas, including care and prevention. Despite various empirical studies on the brain tumor segmentatin, there is still a need for further investigation. This fact is more needed in the automatic methods of brain tumors detection. In the present study, a new method for improving brain tumor segmentation accuracy based on super-pixel and fast primal dual (PD) algorithms has been proposed. The proposed method detects brain tumor tissue in Flair-MRI imaging in BRATS2012 dataset. This method detects the primary borders of tumors using a super-pixel algorithm, and improves brain tumor borders using fast PD in Markov random field optimization. Then, post-processing processes are used to delete white brain areas. Finally, an active contour algorithm was employed to display tumor area. Different experiments were carried on the proposed method and qualitative and quantitative criteria such as dice similarity measure, accuracy and F-measure were used for evaluation. The obtained results showed the efficiency of the proposed method, such that in the accuracy and sensitivity of 86.59 and 88.57% and F1-Measure 86.37 were obtained, respectively.

***doi**: 10.5829/ije.2023.36.03c.10*

**NOMENCLATURE**

| | | | |
|---|---|---|---|
| $BR$ | $V$ | MRF | Marcov Random Field |
| E | Energy function | LGG | Low Graid Gliomas |
| $x_p$ | Label belonged to object p | $T_P$ | Is a tumor and tumor has been identified |
| $c_p(x_p)$ | Potential function | $F_N$ | Is a tumor and tumor has not been identified |
| $d(x_p.x_q)$ | Distance measure | $F_P$ | Is not a tumor and tumor has been identified |
| $w_{pq}$ | Weight is considered for each binary cost function | $T_N$ | Is not a tumor and tumor has not been identified |

## 1. INTRODUCTION

Since timely diagnosis and proper therapy in cancers patients increase the improvement and lifetime of patients, image processing can be used as a decision-making tool by physicians for early cancer identification. In the 21st century, empirical studies on cancer have been changed into a common research effort. Based on the statistics, the international agency for research on cancer (2022) has estimated that there are 25 million people suffering from cancer [1-3]. Also, the American Cancer Society (2022) has reported that heart diseases have been officially replaced by cancer, such has been the main death factor. People's survival for each type of cancer is 63% on average [4-6]. Cancer is detected based on interfering methods such as surgery, radiotherapy and chemotherapy. As studies revealed, using new computer technologies, such as image processing mechanisms have been successful in the processes related to cancers identification and segmentation [7-9]. During the

*Corresponding Author Email: emadi.mehran49@gmail.com
(M. Emadi)

Please cite this article as: M. Emadi, Z. Jafarian Dehkordi, M. Iranpour Mobarakeh, Improving the Accuracy of Brain Tumor Identification in Magnetic Resonanceaging using Super-pixel and Fast Primal Dual Algorithm, ***International Journal of Engineering, Transactions C: Aspects,*** Vol. 36, No. 03, (2023) 505-512

computations and processes related to tumor exact segmentation in brain tumor scanned images, it can be referred to some challenges, such as hardy in distinguishing tumor tissue and the tissue of cysts of the main tissue of the human brain, three-dimensional tumor tissue surrounded a wide part of the brain (but two-dimension images have been used in the processing system), and the lack of the probability of diagnosing the depth of tumor and diagnosing three-dimension area of tumor [10]. It seems that one of the challenges existing in tumor diagnosis is low accuracy since satisfactory results have been obtained by using the fast PD algorithm in similar or other studies [11]. Fast PD is a Markov random field optimizing algorithmthat attempts to solve an alternative problem instead of solving the main optimization problem. It occurs in an optimal repetitive process; therefore, good results are expected. Considering the title of the paper, the main purpose of the study is to integrate fast PD algorithms to identify cancer regions as well as increase the accuracy of tumor diagnosis in MRI images. Cobzas et al. [12] presented a fully automatic method based on superpixel algorithm. Kircher et al. [13] have presented tumor identification and localization based on statistical features and classification of support vector machine in images (FLAIR). Buchbender et al. [14] presented a new method to detect brain tumors in MR images by using convolutional neural network and Atsu thresholding. Roy and Bandyopadhyay [15] presented a new method in tumor segmentation using deep neural network technology coupled with imaging strategy using nanoparticles. Rehman et al. [16], provided an overview of MRI image segmentation methods in brain tumor diagnosis. Padlia and Sharma [17] presented a new method based on convolutional neural network. Vijh et al. [18] have used Generative Adversarial Networks with Transfer Learning. Akbari and Emadi [19] proposed imaging with nano-particles through neural networks molecular technology with FPCNN feedback pulses. Using previous imaging algorithms, they achieved a higher-level imaging which is very helpful for tumor diagnosis in images .Working on brain tumors in PET/MRI images, Harouni et al. [20] presented a fuzzy neural c-mean algorithm-based artificial neural network of PNFCM. Their purpose was segmenting tumor, white matter, gray matter and skull based on MRI features. Chattopadhyay and Maitra [21] used symmetrical analysis of brain images computed the ratio of tumors in right and left hemispheres and segmented growing region with labeling components connected to the diagnosis area. They attempted to distinguish brain from neck skin, bone and ventricle as well as distinguish brain regions from head skin and tumor tissue pathology from natural tissue in brain MRI images [22]. Bauer et al. [23] studied brain tumor extracted by MRI using mathematical image reconstruction. In this regard, they achieved a support vector machine to compute tumors growing region in cancer growth trend. Sharma and Meghrajani [24] have used support vector machine for localizing cancer tumor growing region. Their study's unique feature was automatically combining divide the area of tumor and then, tumor contour based purification. The important feature of their work was using fuzzy patterns to diagnose and purify tumor area and its growth areas. Eberlin et al. [25] worked on brain tumor classifying in human. They classified various tissue groups in brain MRI images, including cerebrospinal fluid and white and gray matters. The outmost part of their study was organizer mapping and vector match. Sayed et al. [26] prposed combination of tissue segmentation and neural networks to diagnose brain tumor identificationis. They also achieved good results in TMRI identification brain tumor by changing gray surface of the image to a colored space image and image factor labeled by tumor clustering measure in order to identify the exact size of tumors and their area. Damodharan and Raghavan [27] investigated an algorithm comprised of the brain and segmentation of diagnosis measure of brain tumors. They computed tumor segmentation in 2D and 3D brain MRI images with different brightness level in tumor and non-tumor areas. Menze et al. [28] used learning and convolution algorithms to investigate imaging data analysis machine of MRI. They reported that it is possible to diagnose cancer tumors hidden in human brain mass in brain MRI images using deep learning and CNN-based prediction segmentation method. Kamnitsas et al. [29] investigated an algorithm comprised of the brain and segmentation of diagnosis measure of brain tumors. They computed tumor segmentation in 2D and 3D brain MRI images with different brightness level in tumor and non-tumor areas. Shenbagarajan et al. [30] studied deep learning and convolution algorithms to investigate imaging data analysis machine of MRI. They reported that it is possible to diagnose cancer tumors hidden in human brain mass in brain MRI images using deep learning and CNN-based prediction segmentation method. Chandra and Rao [31] proposed segmentation algorithm and area-based brain tumor segmentation method to classify cancer areas in brain to diagnose brain tumors. They used Livewire G-wire structural algorithm based on generalized multi-dimensional diagram formula. The feature of their method was exact segmentation of tumor areas even in noisy images. Havaei et al. [32] proposed a genetic algorithm-based method for brain tumor segmentation. In this study, they considered the number of genetic algorithm genes as a contain value. Then, the tumor susceptible areas identified by the algorithm were adjusted with learning training phase. After adjustment, the number of the algorithm genes changes and the previous stages were reiterated if tumor area was out of the identified area. Reiteration continues till reaching a favorable level of segmentation. The proposed method

has been tested on the images collected by Ishikawa [33] used a CNN- based method for brain tumor segmentation. In this study carried on MRI images with high and low grands, a new architecture of CNN has been employed for brain tumor identification and segmentation. In this architecture, the images are entered in parallel in 2 outputs to convolution filters. Under such conditions, the filters of on input have large size and the filters of the second input have small size. In the second stage, pooling operations is done on the images filtered by large filters to double the images of this input with the size of the second input images. In the next stage, the filtered images are integrated with a maximum rule to generate the single and final image and enter into fully connected neural network.

## 2. MARKOV RANDOM FIELD

One of the issues that is highly considered in machine vision and pattern identification and can be formalized is discrete labelling, and most problems can be stated in the form of discrete MRF. As a result, optimization problems in MRF are critical and have received considerable attention from researchers in recent years [34]. In other words, MRF optimization can be stated as follows: V objects exist in the problem space. In other words, these objects are the graph G's heads. The edges of this graph shown by indicate the relationship between these objects or graph heads. In this problem, a set of discrete labels also given. The main purpose is to consider a label for each objective or V graph heads. If $x_p$ which is a label is given to object p ($x_p$ a label belonged to object p), a cost based on potential function $c_{\mathrm{p}}(x_p)$ should be paid. In other words, when $x_p$ label is selected on the object p, single cost should be paid based on the potential function of $c_{\mathrm{p}}(x_p)$. While if two related and dependent objects of p and q are given the labels of $x_p$،$x_q$, respectively. Another cost should be paid which is shown by binary cost function of d($x_p . x_q$). Notably, two single and binary cost functions of $c_{\mathrm{p}}(x_p)$، d($x_p . x_q$) are of the specified conditions of the problem and are considered as input. The main purpose is to select labels such that the leas cost is paid. According to the aforementioned, labelling should be performed such that the total of MRF potentials are minimized or MRF energy is minimized. That is, the purpose of problem solving is to minimize Equation (1):

$$\mathrm{E} = \arg\ \min \sum_{p\in \cup} c_p(x_p) + \sum_{(p.q)\in \Sigma} w_{pq} d(x_p . x_q) \qquad (1)$$

In Equation (1), a $w_{pq}$ weight is considered for each binary cost function of $d(x_p . x_q)$. This weight is applied for scaling (high or low) the binary potential functions for each edge. With respect to the popularity of MRFs, it seems that MRF optimization problems is a vital issue. In this regard, researchers have had many attempts for their optimization. This problem has not been so important up to now since all MRFs have been considered by convex energy functions. Now, if MRFs energy functions are not convex and their number of local minimums is high, their optimization is very hard. The main reason of MRF hard optimization is the convex characteristic of MRF related functions [35]. It should be noted that most of the functions considered in this study for optimization and minimization are also non-convex; therefore, it is hard to optimize them. Notably, the hardy and complexity of MRF optimization problem does not depend on single functions of $c_p(x_p)$. In other words, the main hardy in optimization is on binary functions of $d(x_p . x_q)$ such that each function of $d(x_p . x_q)$ is a sub-unit. MRFs can be optimized in multi-phrase time functions. For example, an overall optimizer is computed [36]. More simply, if each binary potential function of $d(x_p . x_q)$ is considered only a distance function (distance measure), optimization problem will be very hard. If a distance measure is considered for $d(x_p . x_q)$, NP optimization problem will be hard. If there is no primary assumption for $d(x_p . x_q)$ functions, there is no guarantee and only one local min can be given in output [18]. In MRF algorithm optimization, it is aimed to control MRF energies as much as possible and create an approximately optimal solution. As shown in Figure 1, vertical axis indicates the complexity of MRF problem and horizontal axis indicates binary function of MRF. Further, the complexity and hardness have been shown based on the considered function. Ideally, it is sought to select a global function for optimizing $d(x_p . x_q)$. That is, moving toward right side reaches to better choices on the horizontal axis and of course, its ability to propose an optimal solution is maintained. In other words, rapid responses are reached in the lowest possible point. Optimization problem and the algorithm presented should be big enough on the horizontal axis; that is, MRF in more general functions of $d(x_p . x_q)$ should be presented. In other words, the employed binary functions of $d(x_p . x_q)$ should be generalizable as much as possible while it should be placed in the lowest point in the vertical axis. The optimum state is to move under the dotted line as shown in Figure 1. The aim of this research is to make a binary cost function of $d(x_p . x_q)$ such that it is arbitrary, generalizable and is not in local minimums as much as possible and finally, overall minimums are appeared in output.

## 3.PROPOSED METHOD

The proposed method for tumor segmentation in FLAIR images without Tu-Deg-FPD is based on fast PD

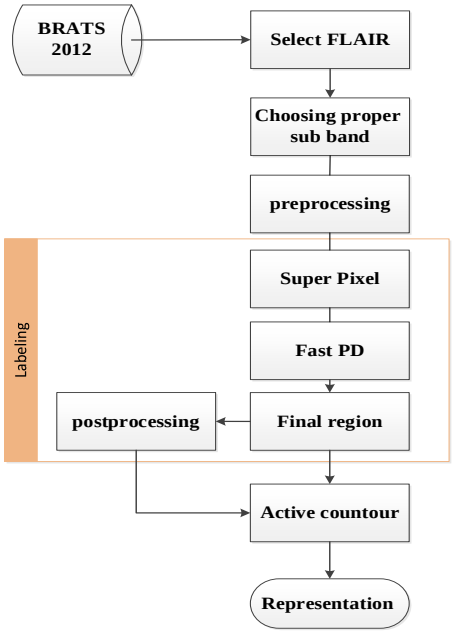


**Figure 1.** The block diagram of Tu-Seg-FPD

optimization for Markov random fields. After selecting the appropriate processing band with 3D Slicer 4.8.1 Software, the selected image is entered into the fast PD algorithm via appropriate pre-processors such as high-pass filters to optimize random fields. Figure 1 depicts the proposed method's block diagram. The database used in this research is BRATS2012. This database has 10 LGG (low graid glioma) patients. In LGG type brain tumor patients, the tumor is going through its hidden growth period and sometimes it can cause superficial paralysis in people. Also, there are 20 high graid gliuma HGG patients in this database, which usually results from the transformation of a LGG.

**3. 1. Pre-processing** A Butterworth low-pass filter was used during pre-processing. High-frequency portions of the image, such as the edges and corners, are sharpened by this filter, making it easier to discriminate between the tumor and other parts of the brain.

**3. 2. Fast PD Algorithm** The idea of discrete MRF can be defined as segmentation with the concept of labeling pixels. In Markov random fields, choosing labels with the lowest possible cost or with the smallest possible cost function is the main objective. According to the aforementioned, labeling should be carried out in a way that minimizes the total MRF potentials or the MRF energy.According to the aforementioned, labeling should be performed in a manner that minimizes the total MRF potentials or the MRF energy. Primal dual optimization is presented as a new fast PD method by to improve MRF. It is comparable to an expansion approach that ends with a set of graphs. In this method, MRF efficiency is significantly increased. In the method, the generalized relations between the number of paths and gaps of primal-dual allocated by primal MRF its and dual are proved. Fast PD, in fact, is a combined optimization problem and has a high efficiency with respect to the importance of computational efficacy in machine vision applications (due to the nature of MRF in segmentation). In spite of the high efficacy, fast PD also minimize MRF energy considerably. In general, the main purpose of fast PD algorithm is to present a solution for MRF problem optimization. Figure 2 shows fast PD algorithm with its inputs.

To employ fast PD algorithm for segmentation, there is a need of regulating its parameters. These parameters have been identified based on the number of considered areas segmentation, label weight, the weight of edges among the labelled nodes and distance measure (metric measure is considered). Figure 3 shows the output of the algorithm.

After labelling Markov random fields by fast PD algorithm in a fully optimal manner, they should be changed into binary images in one stage to use active contour algorithm. In this stage, white areas of brain membrane are identified as tumor if the proposed pre-processing does not perform on the algorithm. This important fact highly appears in Low Grade Gliomas

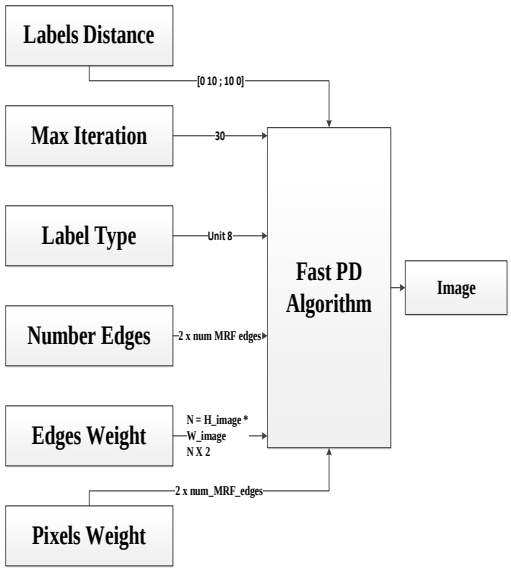


**Figure 2.** Fast PD Algorithm

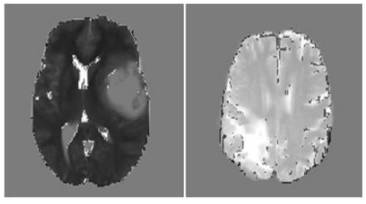

**Figure 3.** An Example of fast PD Algorithm outputs

(LGG) images. Low Grade Gliomas are brain tumors that originate from glial cells, which support and nourish neurons in the brain. Figure 4 shows an example of these outputs. Figure 5 shows most of areas existing in the image including brain tissue and skull. To complete pre-processing process through applying fast PD algorithm, pre-processing at one stage is performed through morphological functions. The employed pre-processing process is erosion and non-tumor areas are removed after using the method. Figure 5 shows the results obtained by pre-processing process.

## 4. RESULT ANALYSIS

The applied purpose of implementing the proposed Tu-Seg-FDP is to exactly identify the brain tumor tissue in Flair-MRI images. The proposed method is based on MRF random fields optimization through fast PD algorithm. To segment tumor area and depict it, active contour-based method has been used. In the following, the obtained results are discussed.

**4. 1. Database** In this study, BRATS2012 database has been used [20]. In this study, only FIAIR images have been used to test the proposed algorithm. FIAIR images have been used due to high resolution of tumor area in white areas of the brain. These areas are identified as tumor areas by most of algorithms. FIAIR images in BRATS2012 database has a size of 240*240 and a spectrum of 155. In fact, these images are read by the software before using MATLAB Software in different formats.

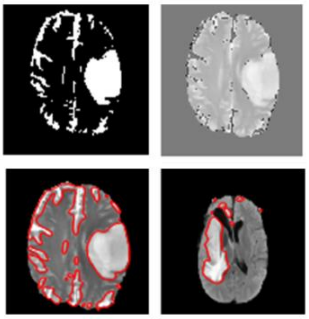

**Figure 4.** The output of tumor segmentation and identification without pre-processing with binary images after applying fast PD algorithm

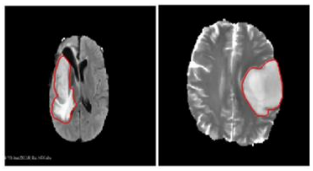

**Figure 5.** Segmentation output after pre-processing

**4. 2. Analysis of Distance Measure** With respect to the aforementioned discussion, the best function in distance measures id metric and distance functions. However, regarding segmentation, the obtained results revealed that fixed distance has the best outcome. In other words, segmentation by fixed distance measure has better results. Figure 6 shows the results obtained by identifying tumor in different distance states. As shown in the figure, when the fixed distance and $d = 1000I_2$, there is no identification. According to the obtained results, the best state is $d = 10I_2$ .

**4. 3. Analysis of Kernel Dimension** Morphological operators were used to remove the white area of the brain membrane after segmentation in the fast PD algorithm in MRF. Operators are disappearing. The size and type of erosion operators window are critical. In terms of the importance of the tumor issue and the area that needs to be filled, the best type of window is a square window.

The white areas of the brain membrane are typically smaller in size than the tumor area, and this is true for LGG and HGG tumor images. Figure 7 depicts an HGG image with kernel sizes 7 and 11. As illustrated in Figure 8, the kernel size of 7*7 produced the best results.

**4. 3. Analysis of Kernel Dimension** Morphological operators were used to remove the white area of the brain membrane after segmentation in the fast PD algorithm in MRF. Operators are disappearing. The size and type of erosion operators window are critical. In terms of the importance of the tumor issue and the area that needs to be filled, the best type of window is a square window. The white areas of the brain membrane are typically smaller in size than the tumor area, and this is true for LGG and HGG tumor images. Figure 7 depicts an HGG image with kernel sizes 7 and 11. As illustrated in Figure 8, the kernel size of 7*7 produced the best results.

**4. 4. Analysis of Energy in Active Contour** The main goal of active contour is to minimize and reduce energy of edge detection. The primary framework in this

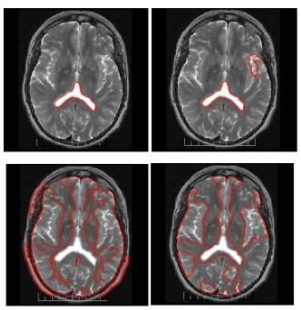

**Figure 6.** The results obtained by applying different distance functions in different distance states of a. $10I_2$, b. $100I_2$, c. $1000I_2$, d. $10000I_2$

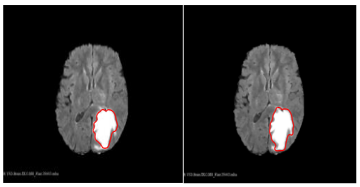

**Figure 7.** The HGG images with two values of 0.15 and 0.20

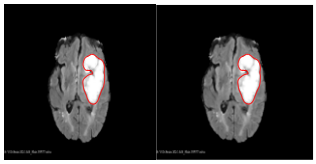

**Figure 8.** The HGG image with the kernel size of 7*7

algorithm is a narrow line. This line is drawn around the considered area in the image using a specific function, namely the energy function. By reducing the energy amount in the function, the narrow line depicted on the image under processing approaches the edges of the considered areas in the image. The closer the narrow line gets to the area being processed, the less energy function there will be. This trend continues till the line is inserted on the considered area edges. This parameter can be intangibly perceived by hanging the weight of P function variable manually used for the energy such that tumor borders are displaced significantly. Notably, in HGG images with higher weighting values, better results have been obtained. While, in LGG images, the weight should be small as much as possible. After various experiments, the best P value for HGG and LGG have been reported 0.15 and 0.05, respectively. Figure 8 shows HGG images with two values of 0.15 and 0.20.

**4. 5. Quantitative Analysis** F1-measure measure has been employed to analyze and prove the proposed method. This measure is obtained by Equation (2) [37].

$$\text{F1\_Measure}=\frac{2*TN}{2*TP+FP+FN} \quad (2)$$

In Equation (2), TP is a tumor and tumor has been identified. FN is a tumor and tumor has not been identified. FP is not a tumor and tumor has been identified. TN is not a tumor and tumor has not been identified.

**4. 6. Accuracy and Sensitivity** In accuracy test of algorithm, the proposed algorithm is analyzed by two measures of accuracy and sensitivity. The accuracy and sensitivity are computed by the parameters shown in Table 1. The accuracy and sensitivity index are formulated in Equations (3) and (4), respectively [38].

$$accuracy=\frac{TP+TN}{TP+FN+FP+TN}\ 100\% \quad (3)$$

$$Sensitivity=recall=\frac{TP}{TP+FN}\times 100\% \quad (4)$$

Tabel 1, shows the result of proposed method for brain tumor segmentaion. F1-measure, accuracy and sensitivity for 30 FLAIR image of BRATS2012 dataset were segmented. Also mean, standard deviation STD and confidence interval of measured value are represnted.

**TABLE 1.** The algorithm accuracy analysis

| No. | Accuracy(%) | Sensitivity(%) | F1(%) |
|---|---|---|---|
| 1 | 85.11 | 89.00 | 87.01 |
| 2 | 97.53 | 88.35 | 92.71 |
| 3 | 83.38 | 90.31 | 86.71 |
| 4 | 85.31 | 92.23 | 88.64 |
| 5 | 91.59 | 85.11 | 88.23 |
| 6 | 92.31 | 81.83 | 86.75 |
| 7 | 87.33 | 89.17 | 88.24 |
| 8 | 95.43 | 78.35 | 86.05 |
| 9 | 89.11 | 84.48 | 86.73 |
| 10 | 88.18 | 83.03 | 85.53 |
| 11 | 95..31 | 93.14 | 94.21 |
| 12 | 88.81 | 88.73 | 88.77 |
| 13 | 89.58 | 89.30 | 89.44 |
| 14 | 97.96 | 90.18 | 93.91 |
| 15 | 85.43 | 78.18 | 81.64 |
| 16 | 78.93 | 77.83 | 78.38 |
| 17 | 79.81 | 82.14 | 80.96 |
| 18 | 88.88 | 92.14 | 90.48 |
| 19 | 77.63 | 83.69 | 80.55 |
| 20 | 73.54 | 79.14 | 76.24 |
| 21 | 93.91 | 89.34 | 91.57 |
| 22 | 93.42 | 89.34 | 91.33 |
| 23 | 84.10 | 87.14 | 85.59 |
| 24 | 87.43 | 90.14 | 88.76 |
| 25 | 81.34 | 82.50 | 81.92 |
| 26 | 87.16 | 82.60 | 84.82 |
| 27 | 85.31 | 90.86 | 88.00 |
| 28 | 83.35 | 83.65 | 83.50 |
| 29 | 80.77 | 84.14 | 82.42 |
| 30 | 84.11 | 80.50 | 82.27 |
| mean | 86.59 | 88.57 | 86.37 |
| STD | 4.589 | 4.624 | 4.61 |
| Confidence interval | [86.63 92.5] | [84.47 93.87] | [83.52 94.00] |

The best accuracy value is 97.96 while the mean is 86.59. the STD and confidence interval for accurcay claim the results are acceptable. Also in F1-measure and Sensitivity mean values are 88.87 and 86.37, respectively. The same as accuracy STD and confidence interval of these criteria shows that the results are proper and also acceptable.

## 5. CONCLUSION

The purpose of the present study was to improve the accuracy of brain tumor segmentation in magnetic resonance imaging. The proposed method was based on markov random field and fast primal dual optimization algorithm. The FLAIR image in BRATS2012 MRI dataset were used for evaluating the segmentation results. In the proposed method first the imgae is clusterd using super pixel algorithm forr finding the ealy region and edges of tumor, then fast PD algorithms used for optimizing the Markov random fields to find the edge of tumor area in FLAIR images. In the proposed method post-processing stage add to final stage for improve tumor edge displayed in active contour algorithm. Various tests were carried on the proposed method. Qualitative evaluation shows the edge of tumor in proposed method are fined accurately. Also quantitative measures such as F1-measure, accuracy and sensitivity were used to evaluate and claim the Qualitative evaluation. Quantitative results fr 30 images of data set shows the superiority of proposed markov random field and fast primal dual optimization for segmetation.

## 6. REFERENCES


1. Stewart, B. and Wild, C.P., "International agency for research on cancer", ***World Cancer Report***, Vol. 2014, (2014).
2. Mustaqeem, A., Javed, A. and Fatima, T., "An efficient brain tumor detection algorithm using watershed & thresholding based segmentation", ***International Journal of Image, Graphics and Signal Processing***, Vol. 4, No. 10, (2012), 34. doi: 10.5815/ijigsp.2012.10.05.
3. Karimi, M., Harouni, M., Jazi, E.I., Nasr, A. and Azizi, N., Improving monitoring and controlling parameters for alzheimer's patients based on iomt, in Prognostic models in healthcare: Ai and statistical approaches. 2022, Springer.213-237.
4. Islami, F., Guerra, C.E., Minihan, A., Yabroff, K.R., Fedewa, S.A., Sloan, K., Wiedt, T.L., Thomson, B., Siegel, R.L. and Nargis, N., "American cancer society's report on the status of cancer disparities in the united states, 2021", ***CA: a Cancer Journal for Clinicians***, Vol. 72, No. 2, (2022), 112-143.
5. Siddharth, D., Saini, D. and Singh, P., "An efficient approach for edge detection technique using kalman filter with artificial neural network", ***International Journal of Engineering, Transactions C: Aspects***, Vol. 34, No. 12, (2021), 2604-2610. doi: 10.5829/IJE.2021.34.12C.04.
6. Pourafzal, A., Fereidunian, A. and Safarihamid, K., "Chaotic time series recognition: A deep learning model inspired by complex systems characteristics", ***International Journal of Engineering, Transactions A: Basics***, Vol. 36, No. 1, (2023), 1-9. doi: 10.5829/ije.2023.36.01a.01.
7. Rehman, A., Harouni, M., Karimi, M., Saba, T., Bahaj, S.A. and Awan, M.J., "Microscopic retinal blood vessels detection and segmentation using support vector machine and k-nearest neighbors", ***Microscopy Research and Technique***, Vol. 85, No. 5, (2022), 1899-1914. doi: 10.1002/jemt.24051.
8. Karimi, M., Harouni, M. and Rafieipour, S., Automated medical image analysis in digital mammography, in Artificial intelligence and internet of things. 2021, CRC Press.85-116.
9. Harouni, M., Karimi, M., Nasr, A., Mahmoudi, H. and Arab Najafabadi, Z., Health monitoring methods in heart diseases based on data mining approach: A directional review, in Prognostic models in healthcare: Ai and statistical approaches. 2022, Springer.115-159.
10. Nasiri, J. and Shakibian, H., "Probabilistic twin support vector machine for solving unclassifiable region problem", ***International Journal of Engineering, Transactions A: Basics***, Vol. 35, No. 1, (2022), 1-13. doi: 10.5829/ije.2022.35.01a.01.
11. Noori, Y., Teymourtash, A.R. and Zafarmand, B., "Use of random vortex method in simulating non-newtonian fluid flow in a t-junction for various reynolds numbers and power-law indexes", ***International Journal of Engineering, Transactions B: Applications***, Vol. 35, No. 5, (2022), 954-966. doi: 10.5829/ije.2022.35.05b.11.
12. Cobzas, D., Birkbeck, N., Schmidt, M., Jagersand, M. and Murtha, A., "3d variational brain tumor segmentation using a high dimensional feature set", in 2007 IEEE 11th international conference on computer vision, IEEE., (2007), 1-8.
13. Kircher, M.F., De La Zerda, A., Jokerst, J.V., Zavaleta, C.L., Kempen, P.J., Mittra, E., Pitter, K., Huang, R., Campos, C. and Habte, F., "A brain tumor molecular imaging strategy using a new triple-modality mri-photoacoustic-raman nanoparticle", ***Nature Medicine***, Vol. 18, No. 5, (2012), 829-834. https://doi.org/10.1038/nm.2721
14. Buchbender, C., Heusner, T.A., Lauenstein, T.C., Bockisch, A. and Antoch, G., "Oncologic pet/mri, part 1: Tumors of the brain, head and neck, chest, abdomen, and pelvis", ***Journal of Nuclear Medicine***, Vol. 53, No. 6, (2012), 928-938. doi: 10.2967/jnumed.112.105338.
15. Roy, S. and Bandyopadhyay, S.K., "Detection and quantification of brain tumor from mri of brain and it's symmetric analysis", ***International Journal of Information and Communication Technology Research***, Vol. 2, No. 6, (2012).
16. Rehman, Z.U., Naqvi, S.S., Khan, T.M., Khan, M.A. and Bashir, T., "Fully automated multi-parametric brain tumour segmentation using superpixel based classification", ***Expert Systems with Applications***, Vol. 118, (2019), 598-613. doi: 10.1016/j.eswa.2018.10.040.
17. Padlia, M. and Sharma, J., "Fractional sobel filter based brain tumor detection and segmentation using statistical features and svm", in Nanoelectronics, Circuits and Communication Systems: Proceeding of NCCS 2017, Springer., (2019), 161-175.
18. Vijh, S., Sharma, S. and Gaurav, P., "Brain tumor segmentation using otsu embedded adaptive particle swarm optimization method and convolutional neural network", ***Data Visualization and Knowledge Engineering: Spotting Data Points with Artificial Intelligence***, (2020), 171-194.
19. Akbari, E. and Emadi, M., "Detection of brain tumors from magnetic resonance imaging by combining superpixel methods and relevance vector machines classification (RVM)", ***Journal of Intelligent Procedures in Electrical Technology***, Vol. 9, No. 36, (2019), 33-42.
20. Harouni, M., Karimi, M. and Rafieipour, S., "Precise segmentation techniques in various medical images", ***Artificial***

***Intelligence and Internet of Things***, (2021), 117-166. doi: 10.1201/9781003097204-6.

21. Chattopadhyay, A. and Maitra, M., "Mri-based brain tumor image detection using cnn based deep learning method", ***Neuroscience Informatics***, (2022), 100060. doi: 10.1016/j.neuri.2022.100060.
22. Yaqub, M., Jinchao, F., Ahmed, S., Arshid, K., Bilal, M.A., Akhter, M.P. and Zia, M.S., "Gan-tl: Generative adversarial networks with transfer learning for mri reconstruction", ***Applied Sciences***, Vol. 12, No. 17, (2022), 8841. doi: 10.3390/app12178841.
23. Bauer, S., Wiest, R., Nolte, L.-P. and Reyes, M., "A survey of mri-based medical image analysis for brain tumor studies", ***Physics in Medicine & Biology***, Vol. 58, No. 13, (2013), R97. doi: 10.1088/0031-9155/58/13/R97.
24. Sharma, Y. and Meghrajani, Y.K., "Brain tumor extraction from mri image using mathematical morphological reconstruction", in 2014 2nd International Conference on Emerging Technology Trends in Electronics, Communication and Networking, IEEE., (2014), 1-4.
25. Eberlin, L.S., Norton, I., Orringer, D., Dunn, I.F., Liu, X., Ide, J.L., Jarmusch, A.K., Ligon, K.L., Jolesz, F.A. and Golby, A.J., "Ambient mass spectrometry for the intraoperative molecular diagnosis of human brain tumors", ***Proceedings of the National Academy of Sciences***, Vol. 110, No. 5, (2013), 1611-1616. doi: 10.1073/pnas.1215687110.
26. El-Sayed, A., Mohsen, H.M., Revett, K. and Salem, A.-B.M., "Computer-aided diagnosis of human brain tumor through mri: A survey and a new algorithm", ***Expert Systems with Applications***, Vol. 41, No. 11, (2014), 5526-5545. doi: 10.1016/j.eswa.2014.01.021.
27. Damodharan, S. and Raghavan, D., "Combining tissue segmentation and neural network for brain tumor detection", ***International Arab Journal of Information Technology***, Vol. 12, No. 1, (2015).
28. Menze, B.H., Jakab, A., Bauer, S., Kalpathy-Cramer, J., Farahani, K., Kirby, J., Burren, Y., Porz, N., Slotboom, J. and Wiest, R., "The multimodal brain tumor image segmentation benchmark (BRATS)", ***IEEE Transactions on Medical Imaging***, Vol. 34, No. 10, (2014), 1993-2024. doi: 10.1109/TMI.2014.2377694.
29. Kamnitsas, K., Ledig, C., Newcombe, V.F., Simpson, J.P., Kane, A.D., Menon, D.K., Rueckert, D. and Glocker, B., "Efficient multi-scale 3d cnn with fully connected crf for accurate brain lesion segmentation", ***Medical Image Analysis***, Vol. 36, No., (2017), 61-78. doi: 10.1016/j.media.2016.10.004.
30. Shenbagarajan, A., Ramalingam, V., Balasubramanian, C. and Palanivel, S., "Tumor diagnosis in mri brain image using acm segmentation and ann-lm classification techniques", ***Indian Journal of Science and Technology***, Vol. 9, No. 1, (2016), 1-12. doi: 10.17485/ijst/2016/v9i1/78766.
31. Chandra, G.R. and Rao, K.R.H., "Tumor detection in brain using genetic algorithm", ***Procedia Computer Science***, Vol. 79, (2016), 449-457.
32. Havaei, M., Davy, A., Warde-Farley, D., Biard, A., Courville, A., Bengio, Y., Pal, C., Jodoin, P.-M. and Larochelle, H., "Brain tumor segmentation with deep neural networks", ***Medical Image Analysis***, Vol. 35, (2017), 18-31. doi: 10.1016/j.media.2016.05.004.
33. Ishikawa, H., "Exact optimization for markov random fields with convex priors", ***IEEE Transactions on Pattern analysis and Machine Intelligence***, Vol. 25, No. 10, (2003), 1333-1336. doi.
34. Komodakis, N., "Image completion using global optimization", in 2006 IEEE Computer Society Conference on Computer Vision and Pattern Recognition (CVPR'06), IEEE. Vol. 1, (2006), 442-452.
35. Komodakis, N. and Tziritas, G., "A new framework for approximate labeling via graph cuts", in Tenth IEEE International Conference on Computer Vision (ICCV'05) Volume 1, IEEE. Vol. 2, (2005), 1018-1025.
36. Smii, B., "Markov random fields model and applications to image processing", ***AIMS Math***, Vol. 7, (2022), 4459-4471. doi: 10.3934/math.2022248.
37. Hamamci, A. and Unal, G., "Multimodal brain tumor segmentation using the tumor-cut method on the brats dataset", ***Proc MICCAI-BraTS***, Vol., No., (2012), 19-23.
38. Aziz, K., Saripan, M., Saad, F., Abdullah, R. and Waeleh, N., "A markov random field approach for ct image lung classification using image processing", ***Radiation Physics and Chemistry***, Vol. 200, (2022), 110440. doi: 10.1016/j.radphyschem.2022.110440.

## Persian Abstract

**چکیده**

تومورهای مغزی یکی از شایع ترین علل مرگ و میر هستند که به طور گسترده توسط محققان در زمینه های تحقیقاتی از جمله مراقبت و پیشگیری مورد بررسی قرار گرفته است. علیرغم مطالعات تجربی مختلف بر روی قطعه بندی تومور مغزی، هنوز نیاز به تحقیقات بیشتر وجود دارد. این واقعیت در روش های خودکار تشخیص تومورهای مغزی بیشتر مطرح است. در این مقاله، روش جدیدی برای بهبود دقت تقسیم‌بندی تومور مغزی بر اساس الگوریتم‌های سوپرپیکسل و پریمال دوگانه سریع (PD) ارائه شده است. روش پیشنهادی بافت تومور مغز را در تصویربرداری Flair-MRI در مجموعه داده BRATS2012 شبیه سازی شده است. این روش مرزهای اولیه تومورها را با استفاده از یک الگوریتم سوپرپیکسل شناسایی می‌کند و با استفاده از PD سریع در بهینه‌سازی میدان تصادفی مارکوف، مرزهای تومور مغزی را بهبود می‌بخشد. سپس از فرآیندهای پس پردازش برای حذف نواحی سفید مغز استفاده شده و در نهایت از یک الگوریتم کانتور فعال برای نمایش ناحیه تومور استفاده شده است. آزمایش‌های مختلفی بر روی روش پیشنهادی انجام شده است و از معیارهای کمی و کیفی مانند اندازه‌گیری شباهت تاس، دقت و اندازه‌گیری F1 برای ارزیابی استفاده شده است.نتایج به‌دست‌آمده نشان‌دهنده کارایی روش پیشنهادی بود، به‌طوری که در دقت و حساسیت به ترتیب ۸۶/۵۹ و ۸۸/۵۷ درصد و F1-Measure 37/86 به‌دست آمدند.

International Journal of Engineering

Journal Homepage: www.ije.ir

# Growth Media Optimization for Production of Alkaline Protease from Industrial Wastewater using *Bacillus subtilis* PTCC 1254

Z. Jafari[a], G. Najafpour Darzi*[a], H. Zare[b]

[a] *Biotechnology Research Laboratory, Faculty of Chemical Engineering, Babol Noshirvani University of Technology, Babol, Iran*
[b] *Department of Chemical Engineering, Buein Zahra Technical University, Buein Zahra, Qazvin, Iran*

*PAPER INFO*

*Paper history:*
Received 05 August 2022
Received in revised form 05 October 2022
Accepted 14 October 2022

*Keywords*:
*Alkaline Proteases*
*Bacillus subtilis*
*Low-Cost Substrate*
*Starchy Wastes*
*Kinetic Model*

*ABSTRACT*

Alkaline proteases are widely used in industrial processes due to their high pH tolerance and thermal stability. In present work, the protease producing ability of *Bacillus* strains (*Bacillus subtilis* PTCC 1254, *B. subtilis* PTCC 1156 and *B. subtilis* PTCC 1715) was studied. *B. subtilis* PTCC 1254 showed the highest proteolytic activity and therefore, the strain was selected as the biological agent in the submerged fermentation. Cell growth kinetic model was investigated using Malthus and Logistic equations, which were relatively well fitted to the experimental data. The maximum specific growth rate for Malthus and Logistic models were 0.187 and 0.377 $h^{-1}$, respectively. The optimum culture conditions were defined as follows: pH 9, temperature 37°C, fermentation time 72 h, agitation speed 150 rpm and 4% inoculum with medium contained 1 g/l $CaCl_2$, 0.6 g/l $K_2HPO_4$, 1 g/l $KH_2PO_4$, 0.2 g/l $MgSO_4.7H_2O$, 2 g/l sugarcane bagasse and 4 g/l corn bran as carbon and nitrogen sources. A 25% v/v industrial wastewater containing starchy waste was used as main substrate. Under optimum conditions, maximum alkaline protease activity of 117.43 U/ml was achieved. Also, the obtained protease was able to remove blood stain from cotton fabric and hydrolyze gelatin of X-ray film. Thus, this protease showed potential applications in detergent and photographic industries.

***doi***: *10.5829/ije.2023.36.03c.11*

## 1. INTRODUCTION

Enzymes as biocatalysts are used in biochemical reactions. Enzymes are also commercially used in number of industrial processes [1]. Among various enzymes, about 60% of total enzyme marketplace are devoted to protease which are the most important group of industrial enzymes [2, 3]. Protease catalyze the hydrolysis of peptide bonds linking amino acids in the polypeptide chain of the protein molecule [4]. Enzymes are specifically classified based on enzyme structure and properties of enzyme active site. Proteases are categorized based on their activities with special functional group such as carboxyl, serine, metallo, neutral, acidic and alkaline proteases [5]. The most important group of enzymes so far used are the alkaline serine proteases [6]. Alkaline proteases as additives are extensively used in pharmaceuticals, dehairing of leather, textile, food and detergent industries [7, 8]. The major sources of alkaline proteases consist of plants, animal organs and microorganisms. The microorganisms including bacteria, molds and yeasts can produce alkaline proteases [5, 9, 10]. Presently, *Bacillus* species are commercially used to obtain alkaline proteases due to their high pH and temperature tolerances [11]. Selection of the right microorganism is very important in production of high yield of the desirable enzymes. Furthermore, protease production by microorganisms is affected by the medium composition; the nitrogen and carbon sources and process parameters such as pH, temperature, agitation speed, incubation time and inoculum size [12, 13]. Achieving high enzyme productivity significantly depends on selection of suitable fermentation technique and optimization of

*Corresponding Author Institutional Email: Najafpour@nit.ac.ir
(G. Najafpour Darzi)

Please cite this article as: Z. Jafari, G. D. Najafpour, H. Zare, Growth Media Optimization for Production of Alkaline Protease from Industrial Wastewater using *Bacillus subtilis* PTCC 1254, ***International Journal of Engineering, Transactions C: Aspects,*** Vol. 36, No. 03, (2023) 513-522

media composition [14, 15]. Proteases and other enzymes are often produced by submerged and solid state fermentation techniques [16, 17]. Currently, more than 90% of the commercial enzymes are produced through implication of submerged culture due to its obvious advantages in consistent enzyme production characteristics with defined medium, process conditions and advantages in downstream despite of the cost-intensiveness for medium components [18, 19]. The cost of enzyme production is the most important factor which effects on process economics. The most important factor in the cost of enzyme production in submerged fermentation is devoted to the growth medium [20]. One of the environmental problems in recent years is the treatment and release of industrial wastewater. Certainly, special wastewater, in particular those collected from food factories can be used for production of value-added products. Through, specific process and recyclable materials can be utilized for production of protein, enzyme and etc. [21, 22]. Another low-cost substrate that can be used for enzyme production is agricultural waste. The cost of enzyme production is reduced by utilization of agro-waste like rice bran, wheat bran and corn bran [23, 24]. In this study, specific strain of bacterial strains with high proteolytic activity was selected. In addition, considering the economic aspect of enzyme production, low-cost substrate was used for enzyme production. The purpose of present work was to demonstrate a thermal tolerant species of bacteria for the production of protease by means of media and process parameters optimization in order to maximize enzyme productivities.

## 2. MATERIALS AND METHODS

**2. 1. Organisms and Media** *B. subtilis* PTCC 1254, *B. subtilis* PTCC 1156, *B. subtilis* PTCC 1715 were supplied by the Iranian Research Organization for Science and Technology, Iran. These microorganisms were cultivated in a medium containing 4 g/l glucose, 2 g/l peptone, 2 g/l yeast extract, 1 g/l $KH_2PO_4$ and 0.2 g/l $MgSO_4.7H_2O$, and were incubated in an incubator-shaker (IKA KS 4000 ic Control) at 33°C and 110 rpm for 24 h. The stock cultures of all strains were maintained on culture tubes and stored at -4°C for long term preservation. To prepare solid phase media for culture studies, 2% agar was added to the liquid media. The microorganisms were cultured for purity and stock cultures were regenerated in every month on a fresh plate.

**2. 2. Materials** Industrial wastewater was collected from the starch manufacturing plant (Mahshad, Yazd, Iran). The wastewater consisted: starch (3.65 g/l), glucose (3.321 g/l), total nitrogen (8.8 mg/l N), $NH_4$ (11.7 mg/l), $NH_3$ (10.7 mg/l), total phosphate (52.48 mg/l P), amount of ash (0.2%), total suspended solid (1.06%). The substrates screened were sugarcane bagasse, rice bran, wheat bran as carbon supplements; corn bran and soybean meal as nitrogen sources. All substrates were washed with distilled water and dried at 60°C for 48 h to remove undesired debris. In order to obtain proper powder, dried substrate was milled and kept in a dry place. All substrates were purchased from local market.

**2. 3. Screening for Alkaline Protease Activity** Casein-agar medium consisted 10 g/l casein, 5 g/l NaCl, 12 g/l agar, 5 g/l beef extract and 5 g/l peptone. The respective strains were inoculated on the plates as a single line and incubated at 37°C for 48 h. The production of alkaline protease was proved by the formation of clear zones surrounding the colonies [25]. The microorganism with maximum zone formation was selected for further analysis.

**2. 4. Inoculum Preparation and Production of Enzyme** A loop-full of the agar culture of each strain was added into 50 ml of the medium containing 10 g/l glucose, 5 g/l peptone, 5 g/l yeast extract, 0.2 g/l $MgSO_4.7H_2O$ and 1 g/l $KH_2PO_4$, and were incubated at 37°C for 24 h. This formulation is known as modified Horikoshii medium [26]. The inoculum was prepared by inoculating 5% of the prepared solution into prior medium and incubated for 16 h. Then 5% of the inoculum was added into medium containing (g/l): peptone 5, $KH_2PO_4$ 1, $K_2HPO_4$ 0.6, and 25% (v/v) starchy waste. Submerged fermentation was carried out at 37°C and 130 rpm for 72 h. The fermentation residue was centrifuged at 8000 rpm and kept at 4°C for 10 min. The supernatants were used to measure protease activity.

**2. 5. Growth Kinetics** The culture containing 10 g/l glucose, 5 g/l peptone, 5 g/l yeast extract, 0.2 g/l $MgSO_4.7H_2O$ and 1 g/l $KH_2PO_4$ was inoculated with 5% (v/v) inoculum and incubated in a shaking incubator at 37°C for 24 h. Samples were taken at certain time intervals and the sugar concentration and cell density were determined. Cell dry weight was determined using a 0.25 µm filter by drying biomass at 60 °C for 24 h. 3,5-dinitrosalicylic acid (DNS) method was used to determine reduced sugar concentration [27].

Malthus and logistic equations are known as unstructured kinetics models that are used for investigation of kinetic growth of *B. subtilis* PTCC 1254. Malthus rate model is defined as the changes of biomass concentration which is proportional to the cell growth:

$$\frac{dx}{dt} = \mu x \quad (1)$$

where x is cell dry weight (g/l) and µ is specific growth rate ($h^{-1}$). Apply separation of variables then integration with initial condition, the above equation is simplified as:

$$\ln\left(\frac{x}{x_0}\right) = \mu t \quad (2)$$

where $x_0$ is the initial cell dry weight (g/l) and t is the incubation time (h). Logistic equation is derived by the following equation:

$$\mu = \mu_m(1 - \frac{x}{x_m}) \quad (3)$$

where $\mu_m$ and $x_m$ are the maximum specific growth rate ($h^{-1}$) and the maximum cell concentration (g/l), respectively. By substitution of the above equation into the Malthus equation and performing integration, cell dry weight can be expressed as the following equation [28]:

$$x = \frac{x_0 \exp(\mu_m t)}{1-(\frac{x_0}{x_m})(1-\exp(\mu_m t))} \quad (4)$$

**2. 6. Assay for Proteolytic Activity** Alkaline protease activity was assayed by the suggested method of Sigma-Aldrich. 5 ml casein solution (0.65%, w/v casein in 50 mM potassium phosphate buffer, pH 7.4) was placed at the water bath at 37°C until equilibrium was achieved. One ml of the enzyme solution was poured to the mixture and allowed to react for 10 minutes. Then the reaction was stopped with 5 ml TCA solution (0.11 M trichloroacetic acid). After 30 min the sample was centrifuged at 8000 rpm for 10 min. A 2 ml of the supernatant was mixed with 5 ml sodium carbonate solution (0.5 M) and 1 ml Folin-Ciocalteu's phenol solution and the mixture was incubated at water bath at 37°C for 30 min. The amount of tyrosine released was determined using a UV-VIS spectrophotometer (UNICO, 2100 series, USA) at 660 nm against the blank. The concentration of tyrosine released was obtained by a spectrophotometer at a wavelength of 660 nm. One unit of protease activity is equivalent to the protease required to release 1 µg tyrosine under standard conditions in 1 min.

**2. 7. Optimized Culture Conditions for the Growth of *B. Subtilis* PTCC 1254** The basal media with 25% (v/v) starchy waste as a carbon source was used for production of alkaline protease by *B. subtilis* PTCC 1254. Initial experiments showed that optimum percent of waste for production of protease was 25% (v/v). Several nitrogen sources such as 5 (g/l) yeast extract, casein, potassium nitrate, ammonium chloride, sodium nitrate, soybean meal, corn bran and corn flour were replaced instead of peptone. The basal medium was supplemented with various carbon sources such as 5 (g/l) glucose, fructose, lactose, arabinose, starch, sugarcane bagasse, rice bran and wheat bran. Effect of different parameters such as temperature (30, 35, 37, 40 and 45°C), pH (5, 6, 7, 8, 9, 10, 11 and 12), $CaCl_2$ concentration (0.5, 1, 1.5 and 2 g/l), inoculum concentration %v/v (1, 2, 3, 4, 5 and 10), agitation speed (110, 130, 150, 180 and 200 rpm) and incubation time (24, 48, 72, and 96 h) were studied. All the experiments were carried out in triplicates.

**2. 8. Cell Growth and Protease Production** The *B. subtilis* PTCC 1254 culture was inoculated once in the basal medium (pH 7, agitation rate 130 rpm) and once in the optimal medium under optimal conditions. Samples were aseptically taken at different time intervals and cell density along with enzyme activity was determined.

**2. 9. Applications of Alkaline Protease from *B. Subtilis* PTCC 1254** For assessing blood stain removing ability, human blood 100 µl was injected on 100% cotton fabric, then was placed at oven for 5 min (95–100 °C). The alkaline protease (10 ml, 117.43 U/ml) was applied to the stain. The removal of blood stain was investigated at room temperature. Ability of gelatin hydrolysis from X-ray films was also investigated. The X-ray films were washed with double distilled water and dried with ethanol; then were placed in an oven at 40°C for 30 min. X-ray films were placed in the enzyme solutions and incubated in a shaking incubator. Finality, the effect of enzyme activity on the X-ray film was investigated after 10, 20, 30 and 40 minutes. Also, the turbidity of reaction mixture was determined at 660 nm.

## 3. RESULTS AND DISCUSSION

**3. 1. Screening for Alkaline Protease Activity** Protease production ability of all three bacterial samples cultured on casein-agar medium was investigated. Figure 1 shows colonies and the clear zone created by each one of the bacterial colonies. All strains showed a positive result for protease production on casein-agar medium, but the best protease producer displayed the highest clear zone of inhibition was *B. subtilis* PTCC 1254. Several studies have demonstrated that the formation of clear zone on casein-agar or skim milk agar by a bacterial colony is an indication of alkaline protease production [29, 30]. The results showed that all three strains can produce alkaline proteases.

**3. 2. *B. Subtilis* PTCC 1254 Growth Kinetic** Figure 2 shows the changes of sugar concentration and cell growth during the fermentation time. The growth curve showed that *B. subtilis* PTCC 1254 had a short lag phase. Exponential growth phase was extended from 2 to 16 h of incubation time; while after 16 h, the substrate concentration was reduced by 70%.

Based on obtained data, Malthus and Logistic kinetic growth rate modes are illustrated in Figures 3a and 3b, respectively. The data were relatively well fitted with a regression of 0.94 and 0.97 for Malthus and Logistic models, respectively. The maximum specific growth rate for Malthus and Logistic models were 0.187 and 0.377 $h^{-1}$, respectively. Malthus model is based on simple exponential growth while Logistic model can project the


**Figure 1.** Bacteria cultured on casein-agar medium, (A) *B. subtilis* PTCC 1156, (B) *B. subtilis* PTCC 1715 and (C) *B. subtilis* PTCC 1254

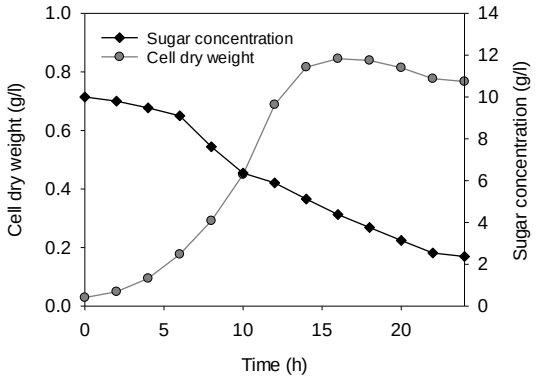


**Figure 2.** Cell dry weight and sugar concentration profiles

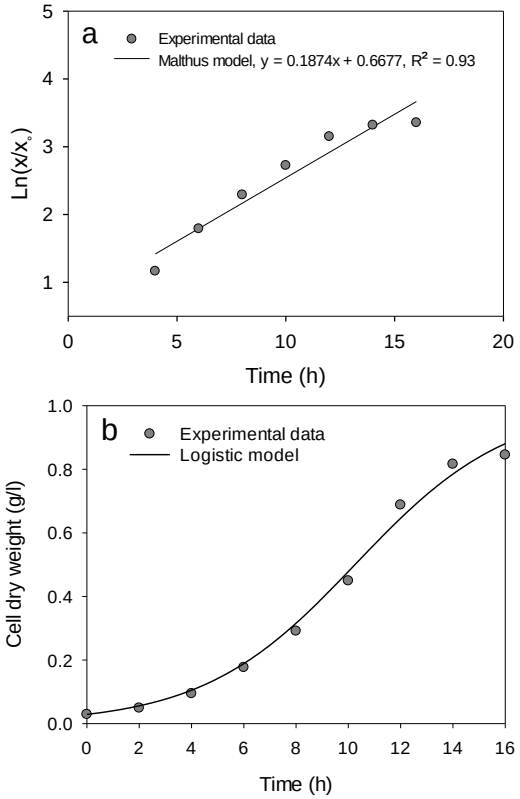


**Figure 3.** Fitting the experimental data to (a) Malthus kinetic model and (b) Logistic kinetic model

growth curve while considering any growth inhibition term. Based on obtained $\mu_{max}$ Logistic rate model was able to describe cell growth and kinetic rate of *B. subtilis* PTCC 1254 in submerged fermentation. Batch kinetics and modeling of alkaline protease production by isolated *Bacillus* sp. was also reported by other researcher using Moser -Boulton kinetic model [31].

### 3. 3. Production and Enzymatic Activity of Strains

Temperature, agitation and incubation time for the production of alkaline protease by *Bacillus* species were 30-37°C, 100-200 rpm and 24-120 h, respectively [32]. Accordingly, 37°C temperature, 130 rpm and 72 h were selected for incubation of all samples and then bacteria were cultivated in the basal medium. Enzyme activity in each strain was considered with respect to the above-mentioned method. Table 1 summarized the results of enzyme production for each bacterium. The obtained results showed that the unit activity of enzyme production by *B. subtilis* PTCC 1254 was more than other two samples, so the specified strain was selected for further study.

### 3. 4. Effect of Nitrogen Sources

In primary production of amino acids, nucleic acids, protein and cell wall components are metabolized via utilization of desired nitrogen source. The regulatory effect of these nitrogen sources on the enzyme synthesis was investigated. Presence of both carbon and nitrogen sources in the medium should highly be affected on production of enzyme protease [33]. By evaluating the effect of different nitrogen sources on protease production, it was determined that corn flour and corn bran resulted in the highest enzyme activity (73.20 and

**TABLE 1.** Enzyme activity of different strains of bacteria

| Sample of bacteria | Enzyme activity (U/ml) |
|---|---|
| *B. subtilis* PTCC 1254 | 29.55 |
| *B. subtilis* PTCC 1715 | 6.7 |
| *B. subtilis* PTCC 1156 | 1.44 |

72.07 U/ml). Organic nitrogen sources had significant effect on enzyme production, whereas simple inorganic nitrogen sources showed reduced alkaline protease production (see Table 2). Present study is in agreement with previous research as reported that inorganic nitrogen sources significantly reduced protease production in compare to organic nitrogen sources [12, 34, 35]. Use of low-cost feedstock and optimizing the media composition with minimum requirements for maximum enzyme production has a critical role in industrial scale enzyme production. Since corn bran is by-product of the corn industry, it was preferred over corn flour due to its low cost. The advantage of corn bran could be because the organism prefers proteins with slow metabolism or partially hydrolyzed. In many microorganisms, accumulated amino acids that may be produced by highly metabolized nitrogen substrates, repress production of protease [36]. Based on obtained results, it was obtained that the best nitrogen source for enzyme production may be quite different which is depended on selection of suitable microorganism.

**3. 5. Effect of Carbon Supplementation** In general, it is clearly projected that the desired medium composition for different microorganisms may significantly influence on production of alkaline proteases. Availability of both the carbon and nitrogen sources within the medium had significant effect on protease production and both of these parameters applied regulatory affecting on enzyme production. In this study, complex and simple carbon sources were investigated. Protease production was decreased when simple carbon sources were used in the culture medium, that is most probably caused by the catabolite repression of the enzyme. Unlike simple carbon sources, complex carbon sources were desired substrates for protease production by *B. subtilis* PTCC 1254. The obtained result is in agreement with previous reported data regarding protease production [37-39]. The amount of proteolytic enzyme reached to the maximum in the presence of sugarcane bagasse. Enzyme activity was enhanced by addition of 2 (g/l) sugarcane bagasse (82.09 U/ml) when compared to a basal medium without sugarcane bagasse (see Table 3). A decrease in enzyme production was observed at low and high concentrations of sugarcane. The results suggested that proper concentration level of sugarcane bagasse played a significant role in enhancing the production of alkaline protease. Catabolic repression or substrate inhibition resulted in repressed enzyme production at high substrate concentrations.

**3. 6. Effect of Incubation Time** A 50 ml of optimized medium was incubated at 37°C (130 rpm) for duration of 24, 48, 72 and 96 hours. Figure 4 presents the effect of incubation time on protease activity. The optimum enzyme production of 81.44 U/ml was observed after 48 h; However, numerically, the highest production of protease was observed at 72 hours (82.09 U/ml). It should be noted that whether increase in fermentation time and hence increase in operational cost can be compensated by extra enzyme production. According to the findings in our experiments, a short fermentation time would be more cost effective compare to the extra enzyme production. A decrease in enzyme units was

**TABLE 2.** Effect of nitrogen sources on the protease production in basal medium

| Nitrogen Sources | Concentration (g/l) | Enzyme activity (U/ml) |
|---|---|---|
| **Blank** | 0 | 29.55 |
| **Soybean meal** | 5 | 63.71 |
| **Corn flour** | 5 | 73.20 |
| **Corn bran** | 2 | 72.07 |
| | 4 | 78 |
| | 5 | 72.03 |
| | 6 | 67.27 |
| | 8 | 64.96 |
| | 10 | 56.48 |
| **Yeast extract** | 5 | 50.49 |
| **Casein** | 5 | 61.34 |
| **Potassium nitrate** | 5 | 11.58 |
| **Sodium nitrate** | 5 | 23.74 |
| **Ammonium chloride** | 5 | 25.58 |

**TABLE 3.** Effect of carbon sources on protease production in basal medium containing 0.4% corn bran and supplemented with carbon source

| Carbon Sources | Concentration (g/l) | Enzyme activity (U/ml) |
|---|---|---|
| **Blank** | 0 | 78 |
| **Starch** | 5 | 66.68 |
| **Wheat bran** | 5 | 70.53 |
| **Rice bran** | 5 | 73.20 |
| **Sugarcane bagasse** | 1 | 72.01 |
| | 2 | 82.09 |
| | 3 | 79.78 |
| | 4 | 79.13 |
| | 5 | 78.66 |
| **Glucose** | 5 | 48.41 |
| **Fructose** | 5 | 51.79 |
| **Lactose** | 5 | 46.75 |
| **Arabinose** | 5 | 42.54 |

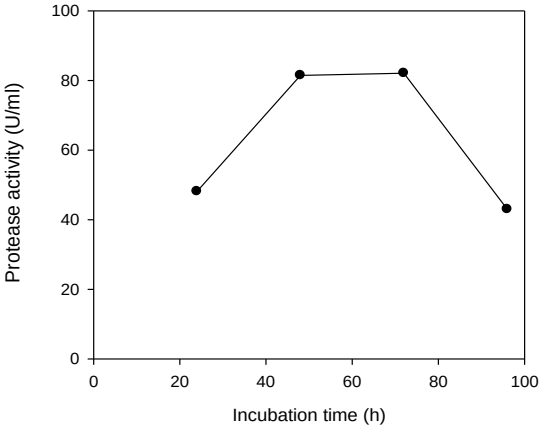


**Figure 4.** Effect of incubation time on protease activity

observed with increasing incubation time, which could be due to hydrolysis of the protease.

**3. 7. Effect of Medium Initial pH** In general, the morphological and physiological characteristics of an organism are affected by pH of culture medium. In addition, pH affects many enzymatic processes and the Transport of compounds through the cell membrane [40]. The effect of initial pH for *B. subtilis* PTCC 1254 was obtained by adjusting the culture medium at different initial pH. A 5% (v/v) inoculum was added to the culture medium and incubated at 37°C and 130 rpm for 48 hours.

The protease activity profile at different pH values are shown in Figure 5. This strain produced alkaline protease enzyme in pH wide range from 5 to 9; maximum protease production was found at pH 9 (88.14 U/ml).

**3. 8. Effect of Temperature** Temperature is the major rolling parameter in growth of microorganism, and it regulates the synthesis and excretion of the enzyme through changes of the physical properties of the cell membrane for extracellular enzymes. One temperature can inhibit the growth of microorganisms while another temperature can activate it. Therefore, in order to obtain an maximum protease production, incubation temperature should be controlled as a critical parameter [41]. The effect of incubation temperature on proteolytic activity was determined by inoculation of 5% inoculum. The effect of temperature on the enzyme activity was obtained by inoculating 5% inoculum into 50 ml of medium at 30, 33, 37, 40 and 45°C for 48 h (Figure 6). Maximum protease activity of 88.14 U/ml was found at 37°C. The reduced enzyme activity at any temperature higher than 37°C might be due to enzyme configuration changes or degradation at high temperature [40, 42].

**3. 9. Effect of Agitation Speed** Agitation is an influential parameter for mass transfer for the oxygen requirement of microorganisms. Particularly, to make energy for cellular activities, $O_2$ plays the role of a terminal electron acceptor for oxidative reactions. It has been found that the variation in agitation speed affects the intensity of mixing in shake flasks and nutrient availability [43]. Protease activity was investigated at the agitation speed of 110, 130, 150, 180 and 200 rpm. The effect of the agitation speed on the enzyme production is depicted in Figure 7.

Agitation speed below 150 rpm caused low protease activity caused by limitation not maintaining enough dissolved oxygen for cell growth. Enzyme activity increased with increasing agitation speed, and maximum protease activity was found at 150 rpm. However, keeping the agitation speed at 200 rpm, the enzyme activity (54.82 U/ml) was decreased due to disturbance created at high shear forces. Based on cultivation of the organism, the desired agitation rate was defined at 150 rpm.

**3. 10. Effect of Inoculum Size** Determining inoculum size with regard to microbial fermentation processes is important since lag phase is eliminated. Increasing in the inoculum size up to 4 v/v% (113.11 U/ml) at which enzyme activity achieved maximum

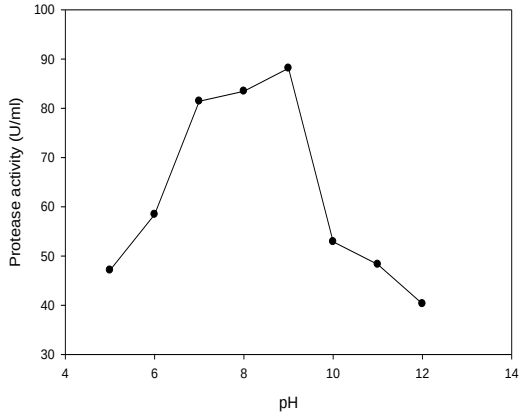


**Figure 5.** Effect of media pH on production of protease

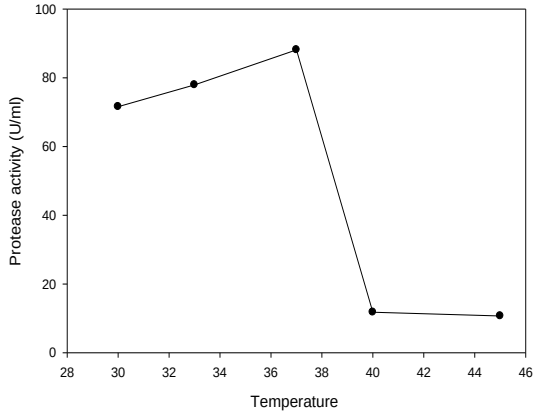


**Figure 6.** Effect of temperature on production of protease

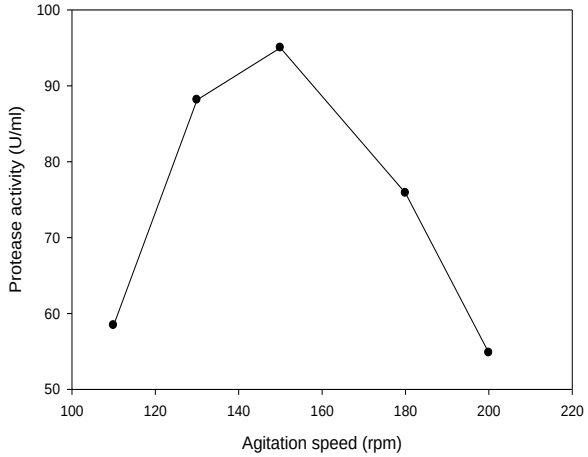


**Figure 7.** Effect of Agitation Speed on Production of Protease

levels, protease production increased steadily. Thereafter (4%), enzyme activity did not change significantly. Suitable inoculum size can balance between the biomass and available, which improve optimal protease production. [44].

**3. 11. Effect of $CaCl_2$ Concentration** $CaCl_2$ was used in the composition of the medium to help stabilize the protease secreted by *B. subtilis* PTCC 1254. Addition of $CaCl_2$ also enhanced and maintained the enzyme activity. Regarding protease activities, $CaCl_2$ showed an enhanced effect at a concentration of 1 g/l. Concentrations higher than 1 g/L of $CaCl_2$ had an inhibitory effect which caused decreased in protease activity to 33.05 U/ml.

**3. 12. Cell Growth and Protease Production** By studying the cell growth of *B. subtilis* PTTC 1254, it was found that in both of medium, the microorganism showed a lag phase of about 4 h. The growth phase was exponential until about 18 h, then it entered the stationary phase. Protease production almost corresponded with cell growth and the maximum value was obtained in the stationary phase (Figure 8). The relationship between growth and enzyme production with different organisms has been reported. Maximum protease production by *Pseudoalteromonas* was achieved at the end of the exponential phase. Whereas, maximal alkaline protease production with *Bacillus* sp VE1 occurred during the early stationary phase [45]. Comparing the production of alkaline protease in basal and optimal medium showed that growth trends were quite similar in both media; however, the amount of enzyme production extensively varied. Maximum alkaline protease was 29.55 U/ml in the basal medium (72 h), while the maximum production of enzyme was achieved after 48 h of fermentation (117.43 U/ml) which is much shorter incubation time in compare to basal medium.

**3. 13. Applications of Alkaline Protease from *B. Subtilis* PTCC 1254** The ability of gelatin hydrolysis of X-ray film by the protease obtained from *B. subtilis* PTCC 1254 was investigated. As shown in Figure 9, the enzyme treatment time increased, the gelatin layer was more hydrolyzed and the X-ray films became brighter. The turbidity of reaction mixture was gradually increased with respect to time. In this way, the turbidity was 0.327, 0.926, 1.539 and 1.924 after 10, 20, 30 and 40 min, respectively. Also, alkaline protease from *B. subtilis* PTCC 1254 was able to remove blood stain from cotton fabric (Figure 10). Therefore, the produced protease is suitable for the use in detergent and photographic industries.

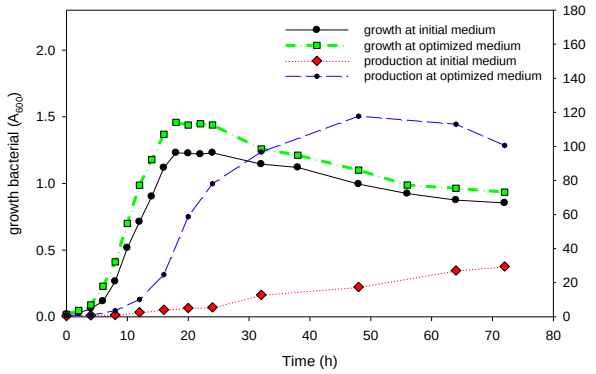


**Figure 8.** Cell growth and protease production in the basal medium and optimal medium

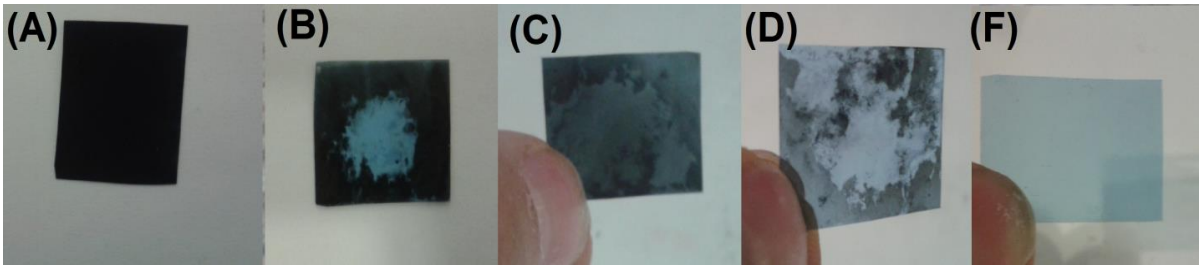


**Figure 9.** Application of *B. subtilis* PTCC 1254 protease for gelatin hydrolysis of X-ray film, (X-ray film before enzyme treatment (A), X-ray film after 10 min (B), 20 min (C), 30 min (D) and 40 min (F) of enzyme treatment)

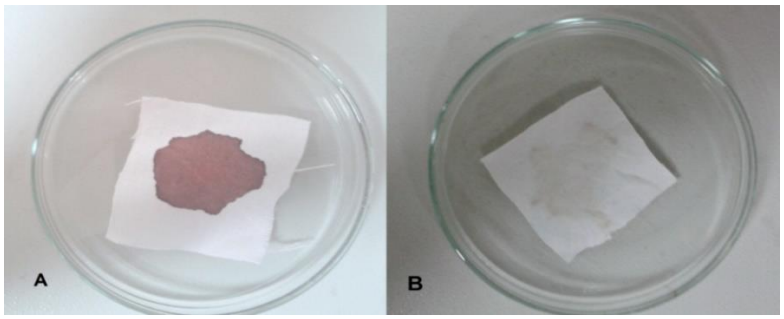


**Figure 10.** Application of *B. subtilis* PTCC 1254 protease in removing blood from cotton fabric, ((A) bloody cotton fabric before enzyme treatment and (B) cotton fabric after 10 min of enzyme treatment)

## 4. CONCLUSION

The most important factor affecting on wide application of alkaline proteases for desired use is enzyme cost. In submerged fermentation, a significant part of the total production cost of enzymes is related to the cost of substrate for the cell growth. Under submerged fermentation, the use of organic-based industrial wastewater and agricultural waste such as corn bran and sugarcane bagasse can reduce the cost of producing enzymes. Achievement of high enzyme productivity significantly depends on selection of suitable fermentation technique and optimization of media composition. Malthus and Logistic equations, known as unstructured kinetic models, were used to investigate the growth kinetics of *B. subtilis* PTCC 1254. The data were relatively well fitted with a regression of 0.94 and 0.97 for Malthus and Logistic models, respectively. The maximum specific growth rate for Malthus and Logistic models were 0.187 and 0.377 $h^{-1}$, respectively. The highest level of protease activity was achieved with the optimized media composition and culture cultivation conditions: industrial starchy wastewater 25% (v/v), sugarcane bagasse concentration 2 g/l, corn bran concentration 4 g/l, $CaCl_2$ 1 g/l, $MgSO_4.7H_2O$ 0.2 g/l, $KH_2PO_4$ 1 g/l, $K_2HPO_4$ 0.6 g/l, pH 9, temperature 37°C, inoculum concentration 4% v/v, agitation speed 150 rpm and fermentation time 48 h. At the optimum condition, alkaline protease production by *B. subtilis* PTCC 1254 increased from 29.55 to 117.43 U/ml. The selected strain showed significant enhancement in protease production under optimized conditions. In addition, the protease produced by *B. subtilis* PTCC 1254 successfully removed the blood stain from cotton fabric and hydrolyzed the gelatin of X-ray film. Thus, the obtained protease found having high potential for applications in detergent and photographic industries.

## 5. ACKNOWLEDGMENT

The authors would like to thank Biotechnology Research Center, Noshirvani University of Technology, Babol, Iran, for the facilities provided to carry out present research work.

## 6. REFERENCES

1. Meghwanshi, G.K., Kaur, N., Verma, S., Dabi, N.K., Vashishtha, A., Charan, P., Purohit, P., Bhandari, H., Bhojak, N. and Kumar, R., "Enzymes for pharmaceutical and therapeutic applications", ***Biotechnology and Applied Biochemistry***, Vol. 67, No. 4, (2020), 586-601. doi: 10.1016/j.desal.2011.06.034
2. Naveed, M., Nadeem, F., Mehmood, T., Bilal, M., Anwar, Z. and Amjad, F., "Protease-a versatile and ecofriendly biocatalyst with multi-industrial applications: An updated review", ***Catalysis Letters***, Vol. 151, No. 2, (2021), 307-323. doi: 10.1007/s10562-020-03316-7
3. Pouryafar, F., Najafpour, G., Noshadi, N. and Jahanshahi, M., "Thermostable alkaline protease production via solid state fermentation in a tray bioreactor using *bacillus licheniformis* ATCC 21424", ***International Journal of Environmental Research***, Vol. 9, No. 4, (2015), 1127-1134. doi: 10.22059/IJER.2015.1001
4. Quanten, T., Savić, N.D. and Parac-Vogt, T.N., "Hydrolysis of peptide bonds in protein micelles promoted by a zirconium (iv)-substituted polyoxometalate as an artificial protease", ***Chemistry–A European Journal***, Vol. 26, No. 49, (2020), 11170-11179. doi: 10.1002/chem.202001920
5. Vinoth, J., Murugan, S. and Stalin, C., "Optimization of alkaline protease production and its fibrinolytic activity from the bacterium *Pseudomonas fluorescens* isolated from fish waste discharged soil", ***African Journal of Biotechnology***, Vol. 13, No. 30, (2014), 3052-3060. doi: 10.5897/AJB2014.13863
6. Matkawala, F., Nighojkar, S., Kumar, A. and Nighojkar, A., "Microbial alkaline serine proteases: Production, properties and applications", ***World Journal of Microbiology and Biotechnology***, Vol. 37, No. 4, (2021), 1-12. doi: 10.1007/s11274-021-03036-z
7. Gemechu, G., Masi, C., Tafesse, M. and Kebede, G., "A review on the bacterial alkaline proteases", ***Journal of Xidian University***, Vol. 14, No. 11, (2020), 632-634. doi: 10.37896/jxu14.11/022
8. Hashmi, S., Iqbal, S., Ahmed, I. and Janjua, H.A., "Production, optimization, and partial purification of alkali-thermotolerant proteases from newly isolated *Bacillus subtilis* S1 and *Bacillus amyloliquefaciens* KSM12", ***Processes***, Vol. 10, No. 6, (2022), 1050. doi: 10.3390/pr10061050
9. Arya, P., Jani, S.A., Rajput, K.N. and Raval, V., "Thermostable alkaline proteases from bacteria: A review", ***National Conference on Innovations in Biological Sciences***, 2020. doi: 10.2139/ssrn.3562387

10. Noshadi, N., Mohammadi, M., Najafpour, G. and Pouryafar, F., "Thermostable α-amylase from lignocellulosic residues using *bacillus amyloliquefaciens*", ***International Journal of Engineering, Transactions B: Applications,*** Vol. 30, No. 8, (2017), 1110-1117. doi: 10.5829/ije.2017.30.08b.01
11. Varia, A.D., Shukla, V.Y. and Tipre, D.R., "Alkaline protease-a versatile enzyme", ***International Journal of Research and Analytical Reviews***, Vol. 6, No. 2, (2019), 208-219. doi: http://doi.one/10.1729/Journal.20854
12. Haddar, A., Fakhfakh-Zouari, N., Hmidet, N., Frikha, F., Nasri, M. and Kamoun, A.S., "Low-cost fermentation medium for alkaline protease production by *Bacillus mojavensis* A21 using hulled grain of wheat and sardinella peptone", ***Journal of Bioscience and Bioengineering***, Vol. 110, No. 3, (2010), 288-294. doi: 10.1016/j.jbiosc.2010.03.015
13. Elgammal, E.W., El-Khonezy, M.I., Ahmed, E.F. and Abd-Elaziz, A.M., "Enhanced production, partial purification, and characterization of alkaline thermophilic protease from the endophytic fungus *Aspergillus ochraceus* BT21", ***Egyptian Pharmaceutical Journal***, Vol. 19, No. 4, (2020), 338-349. doi: 10.4103/epj.epj_31_20
14. dos Santos Aguilar, J.G. and Sato, H.H., "Microbial proteases: Production and application in obtaining protein hydrolysates", ***Food Research International***, Vol. 103, No., (2018), 253-262. doi: 10.1016/j.foodres.2017.10.044
15. Gaddad, S.M., "Enhanced production of extracellular alkaline protease by *Bacillus cereus* GVK21 by optimized formulations", ***International Journal of Pharmacy and Biological Sciences, Transactions B: Applications***, Vol. 9, No. 1, (2019), 1103-1113. doi: 10.21276/ijpbs.2019.9.1.141
16. Vaseghi, Z. and Najafpour, G., "A comparison on lipase production from soybean meal and sugarcane bagasse in solid state fermentation using *rhizopus oryzae*", ***International Journal of Engineering, Transactions B: Applications,*** Vol. 27, No. 2, (2014), 171-176. doi: 10.5829/idosi.ije.2014.27.02b.01
17. Hosseinpour, M., Najafpour, G., Younesi, H., Khorrami, M. and Vaseghi, Z., "Lipase production in solid state fermentation using *aspergillus niger*: Response surface methodology", ***International Journal of Engineering, Transactions B: Applications,*** Vol. 25, No. 3, (2012), 151-159. doi: 10.5829/idosi.ije.2012.25.03b.01.
18. Krishnaveni, K., DJ M, B.M., Ramesh, S. and Kalaichelvan, P., "Production and optimization of extracellular alkaline protease from *Bacillus subtilis* isolated from dairy effluent", ***Der Pharmacia Lettre***, Vol. 4, No. 1, (2012), 98-109.
19. López-Gómez, J.P. and Venus, J., "Potential role of sequential solid-state and submerged-liquid fermentations in a circular bioeconomy", ***Fermentation***, Vol. 7, No. 2, (2021), 76. doi: 10.3390/fermentation7020076
20. Alarid-García, C., Hernández-Calderón, O.M., Rios-Iribe, E.Y., González-Llanes, M.D. and Escamilla-Silva, E.M., "Production of β-glucosidase by *Aspergillus niger* CDBB-H-175 on submerged fermentation", ***The Canadian Journal of Chemical Engineering***, Vol. 100, No. 7, (2022), 1489-1501. doi: 10.1002/cjce.24236
21. Zhu, X., Qi, J., Cheng, L., Zhen, G., Lu, X. and Zhang, X., "Depolymerization and conversion of waste-activated sludge to value-added bioproducts by fungi", ***Fuel***, Vol. 320, No., (2022), 123890. doi: 10.1016/j.fuel.2022.123890
22. Tropea, A., "Food waste valorization", ***Fermentation***, Vol. 8, No. 4, (2022), 168. doi: 10.3390/fermentation8040168
23. Singh, R.S., Chauhan, K. and Jindal, A., "Response surface optimization of solid state fermentation for inulinase production from *Penicillium oxalicum* using corn bran", ***Journal of Food Science and Technology***, Vol. 55, No. 7, (2018), 2533-2540. doi: 10.1007/s13197-018-3173-3
24. Espoui, A.H., Larimi, S.G. and Najafpour, G.D., "Optimization of protease production process using bran waste using *Bacillus licheniformis*", ***Korean Journal of Chemical Engineering***, Vol. 39, No. 3, (2022), 674-683. doi: 10.1007/s11814-021-0965-3
25. Li, S., He, B., Bai, Z. and Ouyang, P., "A novel organic solvent-stable alkaline protease from organic solvent–tolerant bacillus licheniformis yp1a", ***Journal of Molecular Catalysis B: Enzymatic***, Vol. 56, No. 2-3, (2009), 85-88. doi: 10.1016/j.molcatb.2008.08.001
26. Horikoshi, K., "Alkaliphiles: Some applications of their products for biotechnology", ***Microbiology and Molecular Biology Reviews***, Vol. 63, No. 4, (1999), 735-750. doi: 10.1128/MMBR.63.4.735-750.1999
27. Najafpour, G., Younesi, H. and Ismail, K.S.K., "Ethanol fermentation in an immobilized cell reactor using saccharomyces cerevisiae", ***Bioresource Technology***, Vol. 92, No. 3, (2004), 251-260. doi: 10.1016/j.biortech.2003.09.009
28. Najafpour, G., "Biochemical Engineering and Biotechnology, Elsevier, (2015). doi: 10.1016/C2013-0-09819-2
29. Abou-Elela, G.M., Ibrahim, H.A., Hassan, S.W., Abd-Elnaby, H. and El-Toukhy, N.M., "Alkaline protease production by alkaliphilic marine bacteria isolated from marsa-matrouh (egypt) with special emphasis on *Bacillus cereus* purified protease", ***African Journal of Biotechnology***, Vol. 10, No. 22, (2013), 4631-4642. doi: 10.5897/AJB10.2111
30. Bajaj, B.K., Sharma, N. and Singh, S., "Enhanced production of fibrinolytic protease from *Bacillus cereus* NS-2 using cotton seed cake as nitrogen source", ***Biocatalysis and Agricultural Biotechnology***, Vol. 2, No. 3, (2013), 204-209. doi: 10.1016/j.bcab.2013.04.003
31. Zamani, M. and Khayati, G., "Batch kinetics and modeling of alkaline protease production by isolated *bacillus* sp.(research note)", ***International Journal of Engineering; Transactions C: Aspects***, Vol. 28, No. 6, (2015), 841-847. doi: 10.5829/idosi.ije.2015.28.06c.03
32. Aehle, W., "Enzymes in Industry: Products and Applications, John Wiley & Sons, (2006).
33. Blieva, R., Mustafin, K., Akhmetsadykov, N., Suleimenova, Z., Saduyeva, Z., Zhakipbekova, A., Tapenbayeva, I., Kalieva, A. and Narmuratova, Z., "Optimization of culture medium for enhanced protease biosynthesis in *Streptomyces globisporus*", ***Rasayan Journal of Chemistry***, Vol. 14, No. 1, (2021), 270-275. doi: 10.31788/ RJC.2021.1416123
34. Gnanadoss, J.J. and Devi, S.K., "Optimization of nutritional and culture conditions for improved protease production by *Aspergillus nidulans* and *Aspergillus flavus*", ***Journal of Microbiology, Biotechnology and Food Sciences***, Vol. 4, No. 6, (2015), 518-523. doi: 10.15414/jmbfs.2015.4.6.518-523
35. Murthy, P.S. and Naidu, M.M., "Protease production by *Aspergillus oryzae* in solid-state fermentation utilizing coffee by-products", ***World Applied Sciences Journal***, Vol. 8, No. 2, (2010), 199-205.
36. Degering, C., Eggert, T., Puls, M., Bongaerts, J., Evers, S., Maurer, K.-H. and Jaeger, K.-E., "Optimization of protease secretion in *Bacillus subtilis* and *Bacillus licheniformis* by screening of homologous and heterologous signal peptides", ***Applied and Environmental Microbiology***, Vol. 76, No. 19, (2010), 6370-6376. doi: 10.1128/AEM.01146-10
37. Al-Harbi, N.A., "Production and physical characterization of thermo-stable and organic solvents-tolerant protease from mesophilic *Bacillus sp.* NASK P6", ***Biosciences Biotechnology Research Asia***, Vol. 9, No. 1, (2016), 157-164.
38. Reddy, L., Wee, Y.-J., Yun, J.-S. and Ryu, H.-W., "Optimization of alkaline protease production by batch culture of *Bacillus sp.* RKY3 through plackett–burman and response surface

methodological approaches", ***Bioresource Technology***, Vol. 99, No. 7, (2008), 2242-2249. doi: 10.1016/j.biortech.2007.05.006

39. Zare, H., Meiguni, F. and D Najafpour, G., "Production of alkaline protease using industrial waste effluent as low-cost fermentation substrate", ***Iranian Journal of Energy and Environment***, Vol. 12, No. 3, (2021), 264-272. doi: 10.5829/ijee.2021.12.03.11
40. George-Okafor, U. and Mike-Anosike, E., "Screening and optimal protease production by *Bacillus sp*. SW-2 using low cost substrate medium", ***Research Journal of Microbiology***, Vol. 7, No. 7, (2012), 327-336. doi: 10.17311/jm.2012.327.336
41. Balaji, N., Rajasekaran, K., Kanipandian, N., Vignesh, V. and Thirumurugan, R., "Isolation and screening of proteolytic bacteria from freshwater fish cyprinus carpio", ***International Multidisciplinary Research Journal***, Vol. 2, No. 6, (2012), 56-59.
42. Genckal, H. and Tari, C., "Alkaline protease production from alkalophilic *Bacillus sp*. Isolated from natural habitats", ***Enzyme and Microbial Technology***, Vol. 39, No. 4, (2006), 703-710. doi: 10.1016/j.enzmictec.2005.12.004
43. Nascimento, W.C.A.d. and Martins, M.L.L., "Production and properties of an extracellular protease from thermophilic *Bacillus sp*", ***Brazilian Journal of Microbiology***, Vol. 35, No. 1-2, (2004), 91-96. doi: 10.1590/S1517-83822004000100015
44. Sandhya, C., Sumantha, A., Szakacs, G. and Pandey, A., "Comparative evaluation of neutral protease production by *Aspergillus oryzae* in submerged and solid-state fermentation", ***Process Biochemistry***, Vol. 40, No. 8, (2005), 2689-2694. doi: 10.1016/j.procbio.2004.12.001
45. Sanchez-Porro, C., Mellado, E., Bertoldo, C., Antranikian, G. and Ventosa, A., "Screening and characterization of the protease cp1 produced by the moderately halophilic bacterium *Pseudoalteromonas sp*. Strain CP76", ***Extremophiles***, Vol. 7, No. 3, (2003), 221-228. doi: 10.1007/s00792-003-0316-9

## Persian Abstract

**چکیده**

پروتئازهای قلیایی به دلیل تحمل pH بالا و پایداری حرارتی به طور گسترده در فرآیندهای صنعتی استفاده می‌شوند. در کار حاضر، توانایی تولید پروتئاز سویه‌های *باسیلوس* (PTCC 1254، PTCC 1156 و PTCC 1715) بررسی شد. *باسیلوس سوبتیلیس* PTCC 1254 بالاترین فعالیت پروتئولیتیک را نشان داد و بنابراین به عنوان عامل بیولوژیکی در تخمیر غوطه‌وری انتخاب شد. سینتیک رشد سلولی با استفاده از مدل‌های مالتوس و لجستیک مورد بررسی قرار گرفت، که به خوبی با داده‌های تجربی برازش شدند. حداکثر نرخ رشد ویژه برای مدل های مالتوس و لجستیک به ترتیب ۰/۱۸۷ و ۰/۳۷۷ بر ساعت بود. شرایط کشت بهینه به این صورت تعریف شد: pH ۹ ، دمای ۳۷ درجه سانتی‌گراد، زمان تخمیر ۷۲ ساعت، سرعت هم زدن ۱۵۰ دور در دقیقه و ٤ درصد مایه تلقیح با ۱ گرم در لیتر $CaCl_2$، ۰/٦ گرم در لیتر $K_2HPO_4$، ۱ گرم در لیتر $KH_2PO_4$، ۰/۲ گرم در لیتر $MgSO_4.7H_2O$، ۲ گرم در لیتر باگاس نیشکر و ٤ گرم در لیتر سبوس ذرت به عنوان منابع کربن و نیتروژن. پساب صنعتی ۲۵ درصد وزنی حاوی پسماند نشاسته‌ای به عنوان سوبسترای اصلی استفاده شد. در شرایط بهینه، حداکثر فعالیت پروتئاز قلیایی ۱۱۷/٤۳ U/ml به دست آمد. همچنین، پروتئاز به‌دست‌آمده قادر به حذف لکه خون از پارچه کتان و هیدرولیز ژلاتین فیلم اشعه ایکس بود. بنابراین، این پروتئاز کاربردهای بالقوه‌ای در صنایع شوینده و عکاسی نشان داد.

International Journal of Engineering

Journal Homepage: www.ije.ir

# Fabrication of Aluminum 5083/SiC Surface Composite on Tungsten Inert Gas Weld Joint by Novel Direct Friction Stir Processing Technique

K. D. Tandel*, J. V. Menghani

*Sardar Vallabhbhai National Institute of Technology, Surat, India*

*P A P E R I N F O*

*Paper history:*
Received 25 November 2022
Received in revised form19 December 2022
Accepted 20 December 2022

*Keywords*:
*Autogenous Tungsten Inert Gas Welding*
*Direct Friction Stir Processing*
*Hollow Tool*
*Surface Modification*

*A B S T R A C T*

For the creation of surface reinforcement particles in the metal matrix, friction stir processing is frequently utilized. Formation of aluminum/SiC surface composite on tungsten inert gas (TIG) butt weld of Al5083 by a novel technique of direct friction stir processing (DFSP) using a hollow tool is successfully demonstrated in this work. Deposition of SiC in the stir zone of DFSP was confirmed by X-ray diffraction (XRD) method. Micro analysis of weld joint was achieved using metallographic microscope and scanning electron microscope (SEM). Microstructure of stir zone of DFSP shows finely distributed SiC reinforcement particles in aluminum matrix. Absence of detrimental intermetallics was confirmed by energy dispersive spectroscopy (EDS) analysis. Tensile strength of DFSPed specimen was found to be 227.3 MPa which is 19.5% lower than UTS of autogenous TIG weld specimen. Microhardness of SZ of DFSP was found to be increased from TIG weld microhardness of 86 Hv to 107 Hv due to presence of SiC particles.

***doi**: 10.5829/ije.2023.36.03c.12*

## 1. INTRODUCTION

Aluminum alloys are incredibly superior material for space, marine and automobile applications due to their specific properties like good low temperature ductility, high strength to weight ratio, good weldability and good corrosion resistance. Al 5083 is a non-heat treatable aluminum alloy having excellent sea water and industrial chemical corrosion resistance and possesses maximum strength among all non-heat treatable aluminum alloys. However, their mechanical properties like wear resistance and hardness are not very promising. The mechanical properties of Al 5083 can only be enhanced in a few ways [1].

The continuous pursuit of lightweight materials with tailored properties to meet the increasing need for energy efficient and tenable structure resulted in the creation of composite materials. Two or more components with different physical and chemical properties are combined to form a composite material. When they are united, they produce a material which is having desirable characteristics that are superior than individual components. The composite materials are unique and distinguishable in the final product [2]. One of the most extensively utilized approaches for improving the mechanical characteristics of aluminum alloys is metal matrix composite (MMC) technology, in which particles are reinforced across the entire volume. In MMCs, secondary phase reinforcements are combined with a metal matrix that is rather light. For composites to function as the primary load-bearing element, reinforcements are mostly in the form of granules, whiskers, or fibres. Ceramics, carbides, nanotubes, and oxides such as $Al_2O_3$, $B_4C$, TiC, $SiO_2$, TiN, SiC and carbon nanotubes are some of the most often utilized reinforcements in MMCs [3]. MMCs strengthened with ceramic particles have better strength, elasticity, and resilience to wear, fatigue, and creep than unreinforced metals, making them ideal structural materials for the automobile and aerospace sectors. Major drawback of

*Corresponding Author Email: kdtandel.gecd@gmail.com
(K. D. Tandel)

Please cite this article as: K. D. Tandel, J. V. Menghani, Fabrication of Aluminum 5083/SiC Surface Composite on Tungsten Inert Gas Weld Joint by Novel Direct Friction Stir Processing Technique, ***International Journal of Engineering, Transactions C: Aspects,*** Vol. 36, No. 03, (2023) 523-531

these composites is deterioration of ductility and impact strength because of inclusion of strong, hard to deform ceramic particles, this, to some extent, restricts their vast range of uses.

For numerous applications, where corrosion and wear resistant characteristics is required in the component, the service life of the component is mostly determined by their surface characteristics. In these cases, it is preferable to reinforce only the top layer of the material with ceramic particles, while the remaining bulk of the material keep their original structure and composition with higher ductility and toughness, referred to as surface composites (SC) [4].

Aluminum matrix composites are fabricated by numerous methods which can be broadly categorized in to liquid state, and solid state deposition process. In recent times, many surface modification techniques which calls for processing of liquid phase at elevated temperature, such as laser melt treatment [5], plasma spraying [6], high-energy electron beam irradiation [7], and casting [8], are evolved to create MMCs. In this situation, it is difficult to avert reaction between the surface reinforcement and the metal matrix and thus emergence of unfavorable brittle phases is inevitable. Above mentioned difficulty can be averted by processing SC below melting point temperature of the metal matrix. A solid state technique such as Friction Stir Processing (FSP) is the best suited to avoid reaction between reinforcement particle and metal matrix and to maintain the elemental state of the metallic particle [4]. FSP was invented and evolved by Mishra et al. [9], which works on the principle of Friction Stir Welding (FSW). FSW is a revolutionary solid state joining process, invented and patented by the Welding Institute, UK in the year 1991 (G.B. Patent 9125978.8, Int. Patent PCT/GB92/02203, 1991) [10]. In the FSP technique, a non-consumable tool having a shoulder and a probe of specific design is used. Probe height is kept as per targeted processing depth. Tool is rotated at certain RPM and plunged into the base metal until its shoulder is rubbing against the base metal surface. After an appropriate dwell time, the tool is then traversed along the desired processing path at definite feed rate. Due to the frictional heating caused by the tool rubbing on the base metal, the material around the tool probe softens. The combined effect of tool rotation and transverse movement results in severe plastic deformation and plastic material glide all around the tool probe [11, 12].

Amount of heat input into the base metal depends upon tool RPM and feed rate. Higher tool RPM and lower feed rate will increase the heat generated during the process. Higher heat input parameters during FSP will tend to produce coarse grain structure in the stir zone (SZ) whereas, low heat input parameters will lead to formation of tunnel defect in the SZ. Hence, optimum set of FSP parameters are required which produces fine grain defect free structure in the SZ [13]. Tool geometry also as a great impact on amount of frictional heat generation and plastic flow of material during FSP [14]. During the process, there is a chance to integrate second phase particles and create composites because of the high material flow. Therefore, to achieve both a flawless SZ and a uniform dispersion of the particles, the FSP parameters must be optimized [15].

Fabrication of surface composites (SCs) on aluminum alloy matrix using FSP technique was first exercised by Mishra et al [4]. SiC powder mixed with small amount of methanol was applied on the Al 5083 surface. FSP was performed on the preplaced SiC layer after drying in air. Tool having pin height of 1mm was used for FSP. Uniformly distributed particles having satisfactory bonding in surface Al-SiC composite layer ranging from 50 µm to 200 µm was produced by FSP technique. Increase in SC's microhardness by twice as that of base metal was reported. Since then, SC fabrication by the novel technique of FSP had motivated significant research work on this subject. Successful formation of aluminum based MMCs reinforced with particles like SiC [16-19], $Al_2O_3$ [20], [21], $TiO_2$ [22], $B_4C$ [23-25], NiTi [26] and $Si_3N_4$ [27] have been reported.

Different techniques of incorporating surface MMCs by FSP have been adopted by researchers. Reinforcement particles are prefilled in groove cut or blind holes drilled on the parent metal surface [28, 29]. FSP is performed later on to mix the reinforcement with the metal matrix. Loss of reinforcement particles during FSP had been a prime concern as exact targeted proportion of reinforcement particles deposition is difficult to achieve. In order to reduce loss of reinforcement particles during FSP, they are blended with methanol before prefilling in the groove or hole and then dried in the air so that they stick together and with the metal surface during FSP being performed [4, 30]. To further reduce loss of reinforcement particles, a capping pass is performed utilizing a pinless tool before final FSP using a usual tool having a pin [24, 31]. A thin plate was used to cover the groove in a different method adopted by Mahmoud et al. [32] and Lim et al. [33]. FSP was then applied to the plate along the groove. This technique successfully avoids material loss, but it still has problems with bonding the original plate to the "cover plate", which necessitates specialized tool design and meticulous control over other process variables. To produce surface reinforcement particles on AZ31 material, Huang et al. [34] adopted a direct-FSP approach with a hollow pin-less tool pre-filled with SiC powder. SiC powder is deposited during FSP through a hollow pin-less tool carrying a centrally drilled hole of 8mm. Under the optimum process parameters of the direct-FSP, an unvarying composite layer up to depth of 150 µm was constructed.

FSP tool configuration and process parameters are the two main characteristics which can be varied to achieve homogenous particle distribution. Low axial force and lesser processing depth will not be effective in uniform dispersion of reinforcement particles whereas higher axial force for deeper processing target depth will expel

surface reinforcement particles from the surface [4, 34]. Higher tool feed rate will lead to decrease in heat input during FSP. This can result in the lack of the necessary plastic martial flow for particle dispersal. Multi pass FSP technique may therefore be adopted to improve reinforcement particle distribution [35-37]. By and large it is observed that increasing tool rotation speed and decreasing too feed rate will improve reinforcement particle dispersion [38]. Greater heat input associated with multi-pass FSP causes improved stirring and mixing [39]. Influence of tool pin geometry on reinforcement element distribution has been studied by many researchers. Mahmoud et al. [32] had studied effect of tool probe size and shape on SiC dispersion in A1050-H24 aluminum metal matrix by FSP. They have discovered that the tool having square probe had uniformly disseminated the SiC particles in the stir zone compared to other tool probe profile irrespective of tool rotation speed. However, the uniformity of the SiC particle distribution in the nugget zone was not significantly affected by the probe size. Azizieh et al. [38] had compared nanoparticle distribution using columnar probe with and without thread, and thread with three flutes by FSP method. The results of their experiments demonstrated that homogeneous nanoparticle dispersion was obtained using a tool probe with a thread without flutes. Threads promote downward motion of material flow along the thread during FSP.

In the present investigation, surface reinforcement of Al 5083 TIG butt weld surface by SiC composite fabrication via direct friction stir processing (DFSP) method is proposed. FSP tool used in this work is a hollow tool having a cylindrical pin. Homogenous dispersion of SiC particles in aluminum matrix was achieved in single pass of DFSP. This new approach is based on direct particle injection technique during performing FSP. Therefore, objective of this work is to eliminate pre-FSP operations performed on the plate surface such as groove cutting or hole drilling and achieve homogenous SiC distribution in single pass FSP.

## 2. MATERIAL AND METHOD

Cold rolled aluminum alloy 5083 sheet of 6mm thickness was used in this work. Weight % composition of Al 5083 according to ASTM B209/B928M is 5% Mg, 0.15% Si, 0.35% Fe, 0.05% Cr, 0.05% Cu, 0.02% Zn and rest is Al. To produce surface composite layer, commercially available SiC powder of 400 mesh size was used as reinforcement element. 75mm x 150mm size plate was cut using abrasive cutting disc and faying surface was made flat grounded to produce zero root gap setup for Tungsten Inert Gas (TIG) welding which is shown in Figure 1.

Faying surfaces and nearby region of welding was rubbed by polish paper followed by acetone cleaning to remove aluminum oxide, oil and dirt prior to TIG welding. Butt joint of Al 5083, 6mm thick plate was produced by TIG welding without adding filler wire. Welding was performed on machine welding station where torch travel was controlled by machine. Therefore, constant TIG welding torch travel speed was achieved by maintaining constant arc length. TIG welding was performed using Lincoln Electric made Aspect 300 welding machine. Welding parameters were 150 Amp current, 16 V voltage, 120 mm/min travel speed, 13-15 lpm shielding gas flow rate. Argon gas having 99.95% purity was used as shielding gas. Two autogenous TIG welding passes, one each on either side, were deposited to produce full fusion butt joint of Al 5083, 6mm thick plate.

After TIG welded plate cooled down to room temperature, it was mounted on a milling machine table for performing Direct Friction Stir Processing (DFSP) on it. Geeta Engineering Pvt. Ltd. made milling machine was used for performing DFSP. Specially designed non-consumable hollow tool was used to direct implant SiC surface composite simultaneously during performing FSP as illustrated in Figure 2. The FSP tool was manufactured from the tool steel followed by hardening (heating in the range of 840 °C to 870 °C and oil quenching) and tempering (heating in the range of 500 °C to 650 °C and oil quenching). The targeted depth for surface processing was up to 2mm. Therefore, hollow FSP tool is also having cylindrical probe of 5mm dimeter and 1.8mm length. Known quantity of SiC powder was prefilled in the hollow FSP tool. After completion of one FSP pass, remaining SiC powder was collected and weighed to get

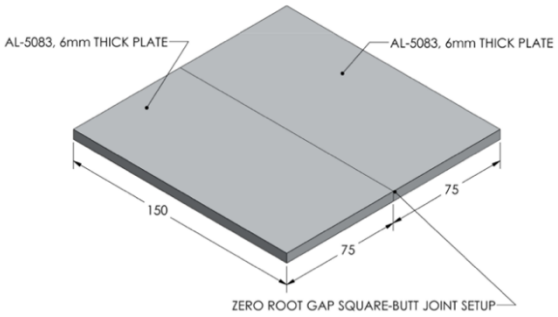


**Figure 1.** Square Butt Joint Set-up

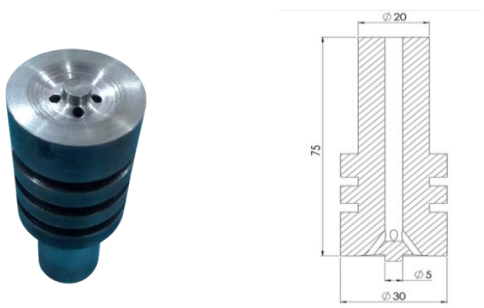


**Figure 2.** Hollow Tool for DFSP (Dimensions shown are in mm)

the SiC consumption value during FSP by weight difference. Weight measurement was taken on analytical balance (Ana Matrix Instrument Technologies Pvt. Ltd., HZK-FA210) having maximum capacity of 210 gm and readability 0.1 mg sensitivity. After cooling to room temperature, DFSP on other side of the plate was performed. DFSP was performed at three different tool rotational speed to find out effect of frictional heat input on the SiC particle distribution and mechanical characteristics of the weld joint. Different set of DFSP parameters are shown in Table 1.

Macro examination of weld cross section was performed to evaluate processing depth and to ensure absence of macro defects. Microstructural evaluation of Direct Friction Stir Processed (DFSPed) specimen was performed on Carl Zeiss, Jena, Model-EPY Type-2 optical microscope. Specimen for macro and micro examination was sectioned perpendicular to the weld seam and they were etched with Keller's reagent. ImageJ software was used to digitally measure the grain size (diameter).

To reveal the mechanical properties of the weld joint after performing FSP on it, tensile test and microhardness tests were performed. Sub sized specimens, according to ASTM B557 were prepared for tensile test and test was performed on computer controlled tensometer having 2 Ton load capacity. Microhardness was measured using diamond indenter by applying 200gm force for 20 seconds dwell time. Microhardness measurement was carried out starting from the weld center to going away from the weld center to cover all regions of the weldment.

Scanning Electron Microscopy (SEM) analysis of as-processed specimen on top surface and on cross-section was performed to evaluate presence and dispersion of SiC particles. EDS was used for qualitative analysis of DFSPed specimens. Chemical analysis of both TIG welded specimen and DFSPed specimen were evaluated by EDS method. SEM and EDS were performed on Hitachi made, Model - S-3400N machine. X-Ray Diffraction (XRD) scan was also performed on the DFSPed specimen to identify the crystalline phases and compound types present in the material.

## 3. RESULT AND DISCUSSION

### 3. 1. Macro and Micro Examinations

Figure 3 shows cross-sectional macrograph of Autogenous TIG welding followed by FSPed specimen. Macrograph reveals complete overlapping of both Autogenous TIG welding passes to produce full fusion weld joint. No traces of lack of fusion, macro pores, undercut and crack in the weldment were observed in the macro examination. Figure 4 shows microstructures of autogenous TIG welded plate at various locations viz. weld metal, HAZ and unaffected base metal. Due to the fact that, aluminium 5xxx series is a non-heat treatable and work hardenable alloys, the base metal microstructure is observed similar to that of rolling work hardening microstructure as shown in Figure 5(c). Microstructure of uninfluenced parent metal reveals un-recrystallized, and elongated grain in aluminum solid solution. It is evident that in case of fusion welding process such as TIG welding process, a wide HAZ arises as a result of material fusion and high temperatures experienced by nearby base material. The HAZ microstructure, as shown in Figure 5(b) reveals fine intermetallic particles distributed in coarse recrystallised grains of average grain size of 35 $\mu m$ in aluminum solid solution. No cracks or porosities were observed in the HAZ region. The weld metal microstructure shows fine columnar-dendritic, epitaxial grains having average grain size of 22 $\mu m$ in aluminum solid solution that has inter-dendritic eutectic constituents primarily $Al_3Mg_2$. The HAZ area, on the other hand, lacks columnar grain structure. Some traces of micro-pores were observed in the weld metal microstructure shown in Figure 5(a). The novel approach of using DFSP on autogenous TIG welded joint showed significant improvement in weld zone microstructure and resulted in improvement of mechanical properties. Figure 6 shows microstructures of TIG + DFSP welded joint with addition of SiC surface reinforcement particles. Microstructure reveals that previous coarse grain dendritic TIG welded structure is crushed by strong stirring effect produced by FSP tool. Temperature in the stir zone was lower than melting point of the base metal

**TABLE 1.** DFSP Parameters and Tensile Test Results

| Sample ID | Tool RPM | Feed Rate, mm/min | UTS, MPa | % Elongation |
|---|---|---|---|---|
| B1 | - | - | 299.67 | 22 |
| T1 | - | - | 282.5 | 20 |
| TFH1 | 545 | 31.5 | 213.6 | 17 |
| TFH2 | 765 | 31.5 | 227.3 | 18.75 |
| TFH3 | 380 | 31.5 | 189.3 | 9.37 |

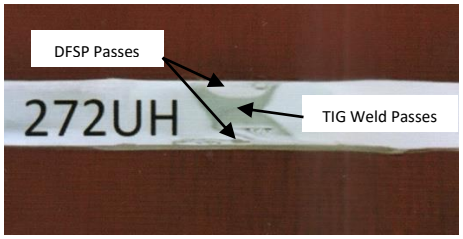


**Figure 3.** Macrograph of Autogenous TIG + FSP Specimen

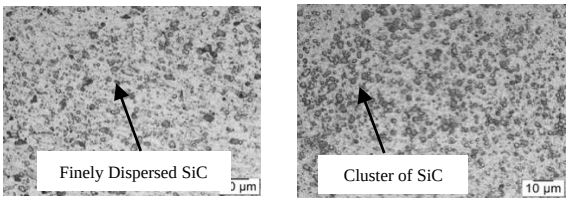


(a) DFSP at 765 RPM (b) DFSP at 545 RPM

**Figure 4.** Comparison of DFSP Microstructure at Tool Rotation Speed of (a) 765 rpm and (b) 545 rpm

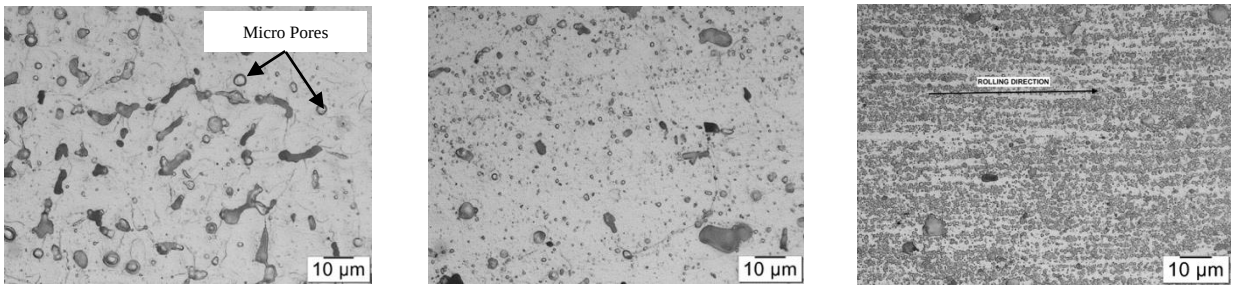


(a) TIG Weld (b) TIG HAZ (c) Base Metal

**Figure 5.** Autogenous TIG Weld Microstructure, Magnification 500x

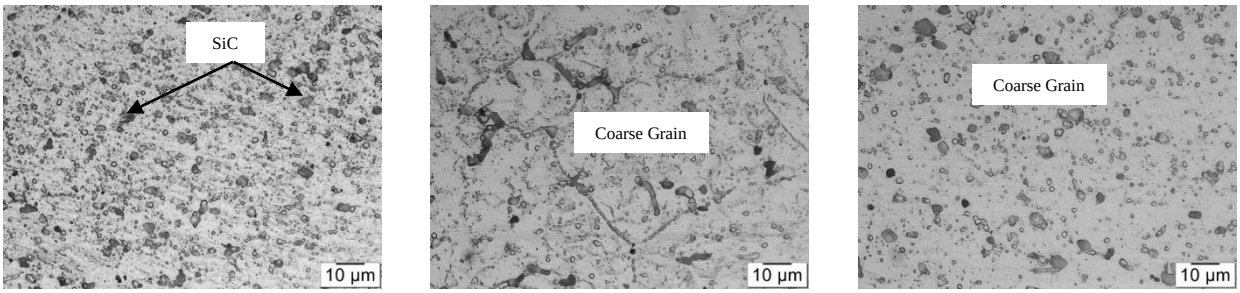


(a) At Top of Specimen FSPed Region (SiC addition) (b) At Center of Specimen TIG Weld Region (c) TMAZ

**Figure 6.** Autogenous TIG Weld + DFSP Microstructure, Tool Rotation at 765 RPM, Magnification 500x

but high enough to promote recrystallisation and produces fine grained equiaxed structure (average grain size of 4.6 $\mu m$) in the SZ of TIG + DFSPed specimens. Microstructural evaluation reveals fine dispersion of SiC particles (dark regions) in the fine grain crystallized structure of Aluminium solid solution. The particles were pushed and churned into the TIG weld metal as they release out of the through hole into the confined area between the incurved shoulder and workpiece during DFSP. As a result, the particles dispersed in the SZ in a homogenous and distributed manner after only single pass operation. However, dispersion of SiC particles was finer at higher tool rotation speed of 765 rpm compared to tool rotation speed of 545 rpm as shown in Figure 4. Significant amount of micro pores were seen in the microstructure of stir zone of TIG + DFSPed weldment, which resulted in drop in UTS of the weld joint. These pores are the result of hydrogen entrapment during DFSP method in which SiC powder is used to deposit on the surface of the TIG weldment. SiC powder may be the primary source of hydrogen in the weldment which is trapped during cooling of the stir zone. Comparison of microstructures of the weld center shown in Figures 5(a) and 6(b) discovers that core microstructure of unprocessed TIG weld metal of FSPed specimen shows grain growth due to added heat of FSP (average grain size of 57 $\mu m$).

Subsequent grain coarsening was also observed in the TMAZ of DFSPed specimen (average grain size of 30 $\mu m$) as shown in Figure 6(c). Figure 7 shows XRD images of TIG welded aluminum 5083 alloy (T) and SiC reinforced aluminum 5083 alloy (THF) subjected to single pass of DFSP. Clear peak of Al was seen in both the cases where as marginal peak of SiC was also observed in TIG+DFSP specimen. Since the volume fraction of Al is higher than that of SiC, SiC peaks seems to be week in Al/SiC composite. Another interesting information was revealed during XRD was no traces of γ phase ($Mg_{17}Al_{12}$) was reported in both TIG and TIG+DFSP specimens. Some researchers have discovered the formation of this phase in the weld zone of Al5XXX, however the existence of phase is not seen in our work. As γ phase ($Mg_{17}Al_{12}$) is rich in Mg and time required for diffusion of Mg is not sufficient to form this phase [40]. It is also evident from the XRD analysis that no intermetallic phases were formed after performing DFSP. SEM images of TIG welded specimen and TIG + DFSP specimens are shown in Figure 8. SEM scan of TIG weld region in the centre shows no clear indication of

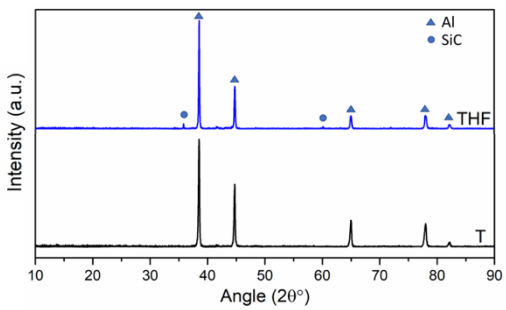


**Figure 7.** XRD Image of TIG + DFSP Specimen

micro pores (Figure 8b) whereas, SEM scan of SZ of DFSP at the top and at the cross section shows uniform dispersion of SiC particles in aluminum matrix. No clustering of SiC particles were observed even after single pass of DFSP (Figures 8c and 8d). Differences in size of SiC particles were observed in the SEM analysis. Extreme plastic deformation and shearing effect caused by FSP tool leads to reduction in the SiC particle size [31]. EDS result shown in Figure 8e reveals significant amount of Si and C along with parent element Al which confirms uniform distribution and presence of SiC particles in the SZ of DFSP. No sign of any detrimental inter-metallics were reported in EDS analysis of SZ of DFSPed region.

**3. 2. Mechanical Properties** The Ultimate Tensile Strength (UTS) of Autogenous TIG and Autogenous TIG + DFSP (Hollow Tool, addition of SiC) weld specimens are presented in Table 1. Tensile test result shows that UTS of TIG welded specimen (282.5 MPa) is 5.7% lower than base metal UTS (299.67 MPa). UTS of a specimen after depositing SiC on TIG weld through DFSP is found to be 227.3 MPa which is 19.5% lower than UTS of TIG weld. Comparing UTS values of DFSPed specimens at different tool rotation speed, better tensile strength is reported for tool rotation speed of 765 RPM whereas least tensile strength is reported for lowest tool RPM of 380 RPM. Low tool rpm is responsible for insufficient churning action of base metal for better grain refinement. Better dispersion of SiC particles in aluminium matrix can be achieved using higher tool rotation speed even in single pass [41]. Marginal loss in ductility of weld metal is observed after Autogenous TIG welding due to formation of dendritic structure and intermetallic compounds in the weld metal. However, in DFSP weld specimen, further reduction in ductility of weldment is observed due to deposition of SiC reinforcements in stir zone. HAZ damage in non-heat treatable alloys is limited

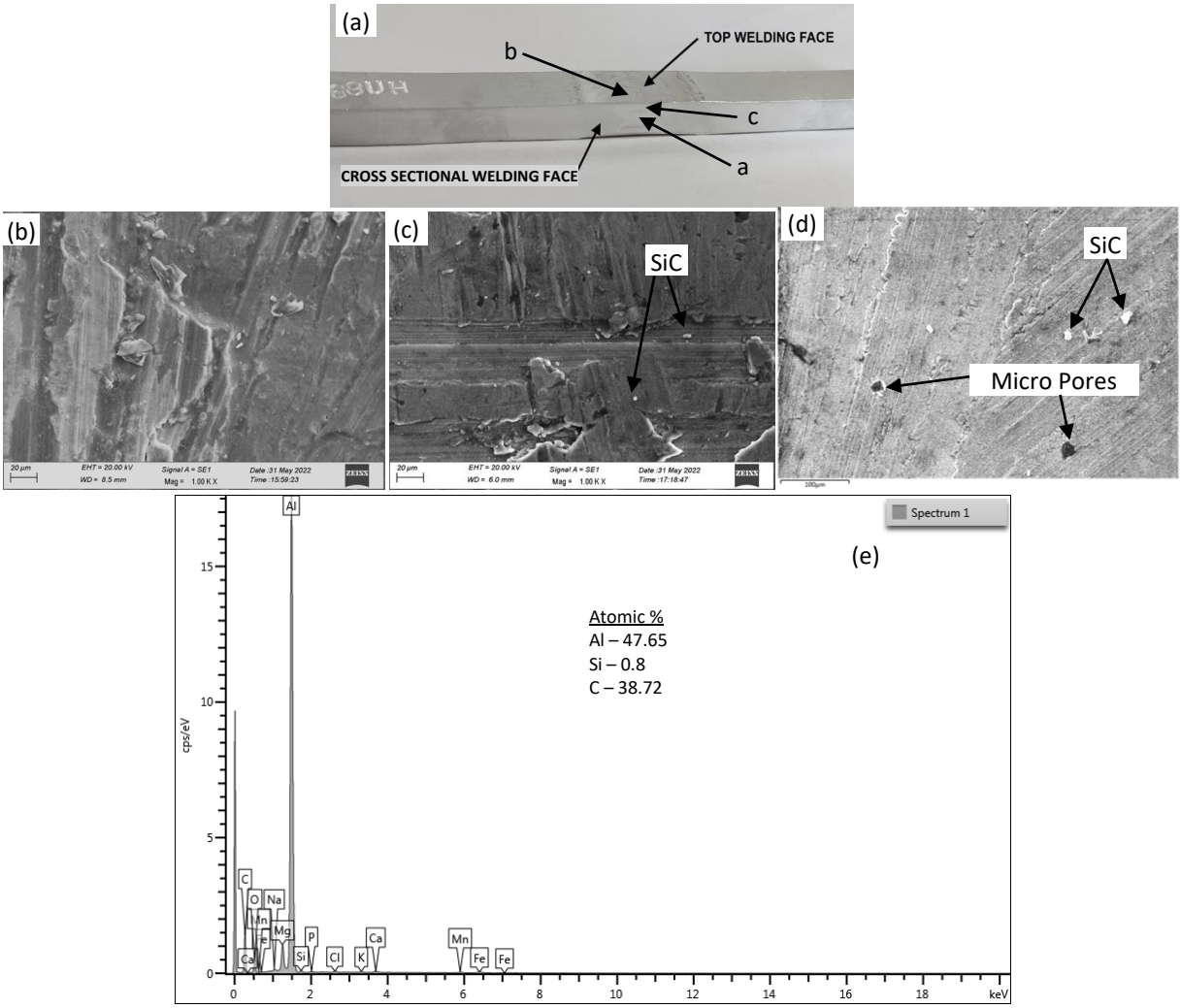


**Figure 8.** (a) Weld cross section macro image showing location of SEM spots; SEM Images of (b) TIG Weld at cross section; (c) SZ of DFSP at top face; (d) SZ of DFSP at cross section, (e) EDS Result of Shown Area in image C; Magnification 1000 X

to grain coarsening, recrystallization, and recovery, as opposed to heat treatable alloys, where strengthening precipitates may dissolve or coarsen. As a result, the HAZ strength loss is not nearly as severe as it is in heat treatable alloys. Dendritic microstructure of the TIG weld metal lowers tensile strength of the weld joint whereas, fine grain equiaxed microstructure in the SZ of the DFSPed region tends to increase tensile strength.

Figure 9 shows microhardness mapping of Autogenous TIG and Autogenous TIG + DFSP (Hollow Tool, addition of SiC surface reinforcement) weld specimens across the weld seam. Maximum hardness value of average 107 Hv is reported in the weld area for all the specimens. Maximum micro hardness value in the stir zone of DFSP specimen is observed due to presence of SiC particles. The results of micro hardness tests range between 80 and 110 HV, indicating softening in the HAZ region. This is mostly due to recrystallisation in the weld and HAZ that occurred during welding. The hardness of TMAZ of DFSP region reduced somewhat (average 93.3 Hv) compared to SZ because of second phase particle disintegration and coarsening produced by thermo-mechanical effect.

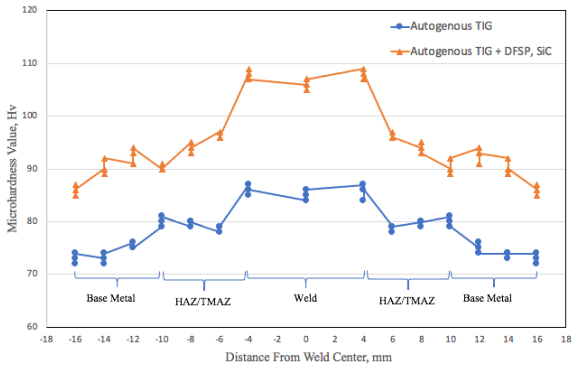


**Figure 9.** Microhardness Mapping of Autogenous TIG Weld and DFSP Specimen

## 4. CONCLUSION

Al-SiC surface composites are successfully fabricated through Direct Friction Stir Processing (DFSP) technique using hollow tool without forming any macro welding defects in stir zone. The conclusions from the test results are summarized as below:

The welding parametes, 150 Amp current, 16 V voltage, and 120 mm/min travel speed are capable of producing full fusion weld joint by autogenous TIG welding process.

Novel approach of directly depositing SiC reinforcement particles in aluminum metal metrix is successfully demonstrated by using DFSP technique with the help of hollow tool having a pin. SEM and XRD analysis confirm presence of SiC particles in SZ of DFSP. EDS scan reveals uniform dispersion of reinforcement particles even after single pass of DFSP.

Study of microstructures and SEM images reveals micro porosities in Autogenous TIG weld metal and in SZ of DFSP after depositing SiC surface reinforcement. Considerable Grain coarsening in weld metal and HAZ is observed after Autogenous TIG weld. Whereas evenly distributed SiC particles in fine grain recrystallized structure is observed in SZ of DFSP specimen.

Maximum UTS of DFSP specimen (227.3 MPa) is reported for the tool rotation speed of 765 RPM and travel speed of 31.5 mm/min. UTS of DFSPed specimen was 19.5% lower than Autogenous TIG weld UTS of 282.5 MPa. From the measurement of percentage elongation, loss of ductility of TIG weld is also reported after performing DFSP on it. However, microhardness value of SZ of DFSP is increased by 25.5% due to presence of SiC particles.

## 5. REFERENCES

1. Bauri, R., Ram, G.J., Yadav, D. and Kumar, C.S., "Effect of process parameters and tool geometry on fabrication of Ni particles reinforced 5083 Al composite by friction stir processing," ***Materials Today: Proceedings***, Vol. 2, No. 4-5, (2015), 3203-3211, doi: 10.1016/j.matpr.2015.07.115.
2. Sharma, D.K., Mahant, D. and Upadhyay, G., "Manufacturing of metal matrix composites: A state of review," ***Materials Today: Proceedings***, Vol. 26, (2020), 506-519, doi: 10.1016/j.matpr.2019.12.128.
3. Nguyen-Dinh, N., Hejjaji, A., Zitoune, R., Bouvet, C. and Crouzeix, L., "Nguyen-Dinh, N., et al. "Machining of FRP composites: surface quality, damage, and material integrity: critical review and analysis", ***Futuristic Composites***, Springer Singapore, (2018), 1-35.
4. Mishra, R.S., Ma, Z.Y. and Charit, I., "Friction stir processing: a novel technique for fabrication of surface composite," ***Materials Science and Engineering: A***, Vol. 341, No. 1, (2003), 307-310, doi: https://doi.org/10.1016/S0921-5093(02)00199-5.
5. Pantelis, D., Tissandier, A., Manolatos, P. and Ponthiaux, P., "Formation of wear resistant Al-SiC surface composite by laser melt-particle injection process," ***Materials Science and Technology***, Vol. 11, No. 3, (1995), 299-303, doi: 10.1179/mst.1995.11.3.299.
6. Tailor, S., Mohanty, R.M., Sharma, V.K. and Soni, P.R., "Fabrication and Wear Behavior of Nanostructured Plasma-Sprayed 6061Al-SiCp Composite Coating," ***Journal of Thermal Spray Technology***, Vol. 23, No. 7, (2014), 1081-1088, doi: 10.1007/s11666-014-0065-6.
7. Choo, S.H., Lee, S. and Kwon, S.J., "Effect of flux addition on the microstructure and hardness of TiC-reinforced ferrous surface composite layers fabricated by high-energy electron beam irradiation," ***Metallurgical and Materials Transactions A***, vol. 30, No. 12, (1999), 3131-3141, doi: 10.1007/s11661-999-0224-4.
8. Attia, A.N., "New phase reinforcement for composite materials," ***Materials & Design***, Vol. 22, No. 6, (2001), 459-466, doi: 10.1016/s0261-3069(00)00080-7.
9. Mishra, R.S., Mahoney, M.W., McFadden, S.X., Mara, N.A. and Mukherjee, A.K., "High strain rate superplasticity in a friction stir

processed 7075 Al alloy," ***Scripta Materialia***, Vol. 42, No. 2, (1999), 163-168, doi: 10.1016/S1359-6462(99)00329-2.

10. Thomas, W. M., "Friction stir welding and related friction process characteristics," Proc. 7th International Conference Joints in Aluminium (INALCO'98), *(*1998), 1-18.
11. Mehdi, H. and Mishra, R.S., "Effect of friction stir processing on mechanical properties and heat transfer of TIG welded joint of AA6061 and AA7075," ***Defence Technology***, Vol. 17, No. 10 (2021), 715-727, doi: 10.1016/j.dt.2020.04.014.
12. Mishra, R.S. and Ma, Z.Y., "Friction stir welding and processing," ***Materials Science and Engineering: R: reports***, Vol. 50, No.1, (2005), 1-78, doi: https://doi.org/10.1016/j.mser.2005.07.001.
13. Tandel, K.D. and Menghani, J.V., "Effect of Friction Stir Processing on Fusion Welded Joint of Al-5083," ***International Journal of Engineering, Transactions C: Aspects***, Vol. 35, No. 9 (2022), 1735-1743, doi: 10.5829/IJE.2022.35.09C.09.
14. Aval, H.J., "Influences of pin profile on the mechanical and microstructural behaviors in dissimilar friction stir welded AA6082--AA7075 butt Joint," ***Materials & Design***, Vol. 67, (2015), 413-421, doi: https://doi.org/10.1016/j.matdes.2014.11.055.
15. Sudhakar, M., Rao, C.S. and Saheb, K.M., "Production of Surface Composites by Friction Stir Processing-A Review," ***Materials Today: Proceedings***, Vol. 5, No. 1, Part 1, (2018), 929-935, doi: https://doi.org/10.1016/j.matpr.2017.11.167.
16. Sharma, A., Sharma, V.M., Mewar, S., Pal, S.K. and Paul, J., "Friction stir processing of Al6061-SiC-graphite hybrid surface composites," ***Materials and Manufacturing Processes***, Vol. 33, No. 7, (2018), 795-804, doi: 10.1080/10426914.2017.1401726.
17. Salehi, M., Saadatmand, M. and Mohandesi, J.A., "Optimization of process parameters for producing AA6061/SiC nanocomposites by friction stir processing," ***Transactions of Nonferrous Metals Society of China***, Vol. 22, No. 5, (2012), 1055-1063, doi: https://doi.org/10.1016/S1003-6326(11)61283-1.
18. Dolatkhah, A., Golbabaei, P., Givi, M.B. and Molaiekiya, F., "Investigating effects of process parameters on microstructural and mechanical properties of Al5052/SiC metal matrix composite fabricated via friction stir processing," ***Materials & Design***, Vol. 37, (2012), 458-464, doi: https://doi.org/10.1016/j.matdes.2011.09.035.
19. Jain, S. and Mishra, R.S., "Microstructural and mechanical behavior of micro-sized SiC particles reinforced friction stir processed/welded AA7075 and AA6061," ***Silicon***, (2022), doi: 10.1007/s12633-022-01716-5.
20. Mehdi, H., Mehmood, A., Chinchkar, A., Hashmi, A.W., Malla, C. and Mohapatra, P., "Optimization of process parameters on the mechanical properties of AA6061/Al2O3 nanocomposites fabricated by multi-pass friction stir processing," ***Materials Today: Proceedings***, Vol. 56, (2022), 1995-2003, doi: https://doi.org/10.1016/j.matpr.2021.11.333.
21. Kianezhad, M. and Raouf, A.H., "Effect of nano-Al2O3 particles and friction stir processing on 5083 TIG welding properties," ***Journal of Materials Processing Technology***, Vol. 263, (2019), 356-365, doi: https://doi.org/10.1016/j.jmatprotec.2018.08.010.
22. Khodabakhshi, F., Simchi, A., Kokabi, A.H., Nosko, M., Simanĉik, F. and Švec, P., "Microstructure and texture development during friction stir processing of Al-Mg alloy sheets with TiO2 nanoparticles," ***Materials Science and Engineering: A***, Vol. 605, (2014), 108-118, doi: 10.1016/j.msea.2014.03.008.
23. Rejil, C.M., Dinaharan, I., Vijay, S.J. and Murugan, N., "Microstructure and sliding wear behavior of AA6360/(TiC+B 4C) hybrid surface composite layer synthesized by friction stir processing on aluminum substrate," ***Materials Science and Engineering: A***, Vol. 552, (2012), 336-344, doi: 10.1016/j.msea.2012.05.049.
24. Rana, H.G., Badheka, V.J. and Kumar, A., "Fabrication of Al7075/B4C surface composite by novel Friction Stir Processing (FSP) and investigation on wear properties," ***Procedia Technology***, Vol. 23, (2016), 519-528.
25. Boopathi, S., Thillaivanan, A., Pandian, M., Subbiah, R. and Shanmugam, P., "Friction stir processing of boron carbide reinforced aluminium surface (Al-B4C) composite: Mechanical characteristics analysis," ***Materials Today: Proceedings***, Vol. 50, (2022), 2430-2435, doi: https://doi.org/10.1016/j.matpr.2021.10.261.
26. Dixit, M., Newkirk, J.W. and Mishra, R.S., "Properties of friction stir-processed Al 1100-NiTi composite," ***Scripta Materialia***, Vol. 56, No. 6, (2007), 541-544, doi: 10.1016/j.scriptamat.2006.11.006.
27. Moghaddas, M.A. and Kashani-Bozorg, S.F., "Effects of thermal conditions on microstructure in nanocomposite of Al/Si 3N 4 produced by friction stir processing," ***Materials Science and Engineering: A***, Vol. 559, (2013), 187-193, doi: 10.1016/j.msea.2012.08.073.
28. Akinlabi, E.T., Mahamood, R.M., Akinlabi, S.A. and Ogunmuyiwa, E., "Processing parameters influence on wear resistance behaviour of friction stir processed Al-TiC composites," ***Advances in Materials Science and Engineering***, (2014).
29. Akramifard, H.R., Shamanian, M., Sabbaghian, M. and Esmailzadeh, M., "Microstructure and mechanical properties of Cu/SiC metal matrix composite fabricated via friction stir processing," ***Materials & Design***, Vol. 54, (2014), 838-844, doi: https://doi.org/10.1016/j.matdes.2013.08.107.
30. Mazaheri, Y., Karimzadeh, F. and Enayati, M.H., "A novel technique for development of A356/Al2O3 surface nanocomposite by friction stir processing," ***Journal of Materials Processing Technology***, Vol. 211, No. 10, (2011), 1614-1619, doi: 10.1016/j.jmatprotec.2011.04.015.
31. Rathee, S., Maheshwari, S., Siddiquee, A.N. and Srivastava, M., "Distribution of reinforcement particles in surface composite fabrication via friction stir processing: Suitable strategy," ***Materials and Manufacturing Processes***, Vol. 33, No. 3, (2018), 262-269, doi: 10.1080/10426914.2017.1303147.
32. Mahmoud, E.R.I., Takahashi, M., Shibayanagi, T. and Ikeuchi, K., "Effect of friction stir processing tool probe on fabrication of SiC particle reinforced composite on aluminium surface," ***Science and Technology of Welding and Joining***, Vol. 14, No. 5, (2009), 413-425, doi: 10.1179/136217109X406974.
33. Lim, D.K., Shibayanagi, T. and Gerlich, A.P., "Synthesis of multi-walled CNT reinforced aluminium alloy composite via friction stir processing," ***Materials Science and Engineering: A***, Vol. 507, No. 1-2, (2009), 194-199, doi: 10.1016/j.msea.2008.11.067.
34. Huang, Y., Wang, T., Guo, W., Wan, L. and Lv, S., "Microstructure and surface mechanical property of AZ31 Mg/SiCp surface composite fabricated by Direct Friction Stir Processing," ***Materials & Design***, Vol. 59, (2014), 274-278, doi: https://doi.org/10.1016/j.matdes.2014.02.067.
35. Mahmoud, E.R.I., Ikeuchi, K. and Takahashi, M., "Fabrication of SiC particle reinforced composite on aluminium surface by friction stir processing," ***Science and Technology of Welding and Joining***, Vol. 13, No. 7, (2008), 607-618, doi: 10.1179/136217108X333327.
36. Yang, R., Zhang, Z., Zhao, Y., Chen, G., Guo, Y., Liu, M. and Zhang, J., "Effect of multi-pass friction stir processing on microstructure and mechanical properties of Al3Ti/A356 composites," ***Materials Characterization***, Vol. 106, (2015), 62-69, doi: 10.1016/j.matchar.2015.05.019.
37. Surekha, K., Murty, B.S. and Rao, K.P., "Microstructural characterization and corrosion behavior of multipass friction stir processed AA2219 aluminium alloy," ***Surface and Coatings Technology***, Vol. 202, No. 17, (2008), 4057-4068, doi: 10.1016/j.surfcoat.2008.02.001.

38. Azizieh, M., Kokabi, A.H. and Abachi, P., "Effect of rotational speed and probe profile on microstructure and hardness of AZ31/$Al_2O_3$ nanocomposites fabricated by friction stir processing," ***Materials & Design***, Vol. 32, No. 4, (2011), 2034-2041, doi: 10.1016/j.matdes.2010.11.055.

39. Sharma, V., Gupta, Y., Kumar, B.M. and Prakash, U., "Friction Stir Processing Strategies for Uniform Distribution of Reinforcement in a Surface Composite," ***Materials and Manufacturing Processes***, Vol. 31, No. 10, (2016), 1384-1392, doi: 10.1080/10426914.2015.1103869.

40. Heirani, F., Abbasi, A. and Ardestani, M., "Effects of processing parameters on microstructure and mechanical behaviors of underwater friction stir welding of Al5083 alloy," ***Journal of Manufacturing Processes***, Vol. 25, (2017), 77-84, doi: https://doi.org/10.1016/j.jmapro.2016.11.002.

41. Singh, R., Rizvi, S.A. and Tewari, S.P., "Effect of friction stir welding on the tensile properties of aa6063 under different conditions," ***International Journal of Engineering, Transactions A: Basics***, Vol. 30, No. 4, (2017), 597-603, doi: 10.5829/idosi.ije.2017.30.04a.19.

## Persian Abstract

**چکیده**

برای ایجاد ذرات تقویت کننده سطح در ماتریس فلزی، پردازش اغتشاشی اصطکاکی اغلب مورد استفاده قرار می گیرد. تشکیل کامپوزیت سطح آلومینیوم/SiC بر روی گاز خنثی تنگستن (TIG) جوش لب به لب Al5083 توسط یک تکنیک جدید پردازش اغتشاش اصطکاکی مستقیم (DFSP) با استفاده از یک ابزار توخالی با موفقیت در این کار نشان داده شده است. رسوب SiC در منطقه اغتشاشی DFSP با روش پراش اشعه ایکس (XRD) تایید شد. تجزیه و تحلیل میکرو اتصال جوش با استفاده از میکروسکوپ متالوگرافی و میکروسکوپ الکترونی روبشی (SEM) به دست آمد. ریزساختار منطقه هم‌زن DFSP ذرات تقویت‌کننده SiC ریز توزیع شده را در ماتریس آلومینیوم نشان می‌دهد. عدم وجود مواد بین فلزی مضر با تجزیه و تحلیل طیف‌سنجی پراکنده انرژی (EDS) تایید شد. استحکام کششی نمونه DFSPed 227.3 مگاپاسکال است که ۱۹.۵٪ کمتر از UTS نمونه جوش TIG خودزا است. ریزسختی SZ از DFSP به دلیل وجود ذرات SiC از ریزسختی جوش TIG 86 Hv به ۱۰۷ Hv افزایش یافته است.

International Journal of Engineering

Journal Homepage: www.ije.ir

# Synthesis of Hard Layer by Titanium Addition During Welding Process and Quenched Directly

S. Syaripuddin*[a], S. Sopiyan[a], S. Aditya[a], S. D. Yudanto[b], F. B. Susetyo[a]

[a] *Department of Mechanical Engineering, Universitas Negeri Jakarta, Jakarta, Indonesia*
[b] *Research Center for Metallurgy - National Research and Innovation Agency, Serpong, Indonesia*

*PAPER INFO*

*Paper history:*
Received 02 December 2022
Received in revised form 31 December 2022
Accepted 01 January 2023

*Keywords*:
*Hardfacing*
*Ti*
*Welding*
*Hardness*
*Quenching Oil*

*ABSTRACT*

Enhance the surface hardness of materials usually conducted through a hardfacing technique. Hardfacing is popular, whereby materials with better properties are deposited over cheaper bulk material. This work fabricated hard layers by adding titanium (Ti) wire during the welding process. This research used low-carbon steel as the base material, wire optime Ti grade 1 for Ti addition, and an HV 600 electrode with a diameter of 3.2 mm for filler metal. A single-layer weld was conducted with SMAW (positive polarity and 90 A). The samples were directly quenched in a different solution after welding. The properties of the weld layer were examined phase, structure, microstructure, macrostructure, and hardness using optical emission spectroscopy (OES), x-ray diffraction (XRD), an optical microscope, a digital camera, and a hardness device, respectively. Adding titanium (Ti) to the weld layer and quenching the samples after welding in the solution enhances the hardness. This phenomenon is attributed to different phase compositions, oxides, and microstructures. A fine dispersion of small particles and oxide amount is important in increasing hardness. There is no cracking in the weld and base metal. In conclusion, samples BNTiO and BNTiM are recommended for lathe-cutting tools.

***doi**: 10.5829/ije.2023.36.03c.13*

## 1. INTRODUCTION

High Speed Steel (HSS) is a commonly used cutting tool in the lathe. For dry-cutting operational conditions, four factors need consideration: pressure, temperature, sliding speed, and the interface. Thus, factors could affect high wear rate, heat, and short tool life [1]. These conditions could be reduced by increasing the hardness. HSS commercial lathe-cutting tool hardness is around 765.68 HV [2].

Enhance the surface hardness of materials usually conducted through a hardfacing technique. Hardfacing is popular, whereby materials with better properties are deposited over cheaper bulk material [3]. Furthermore, hardfacing is one of the most economical techniques to mitigate the wear of tools and components of a machine [4]. By increased the hardness on the surface of the metal with less hardness is the cheapest than using a bulk metal with high hardness. Hardfacing applies a hard surface layer on the base material to resist abrasion, impact, and erosion.

Welding is one technique for fusion between two materials [5]. The welding process also could be conducted to reach the hard layer. Therefore, a hard layer could result from welding processes such as shielded metal arc welding (SMAW) [6, 7], Flux core arc welding (FCAW) [6], plasma transferred arc welding (PTA) [8], electro-slag welding (ESW) [9], and gas tungsten arc welding (GTAW) [10]. The SMAW technique is more flexible and easy to operate than others.

Commonly filler metals used for hardfacing are iron (Fe)-based alloys, cobalt (Co)-based alloys, and nickel (Ni)-based alloys. Singh [11] has reported hardfacing single layers through various hard alloy filler metals (iron (Fe)-based alloys), resulting in hardness between 375 and 543 HV. A different electrode composition has resulted in different hardness. A filler metal with a high carbon (C), Manganese (Mn), and chromium (Cr) has a resulting

*Corresponding Author Institutional Email: *Syaripuddin_andre@unj.ac.id* (S. Syaripuddin)

Please cite this article as: S. Syaripuddin, S. Sopiyan, S. Aditya, S. D. Yudanto, F. B. Susetyo, Synthesis of Hard Layer by Titanium Addition During Welding Process and Quenched Directly, ***International Journal of Engineering, Transactions C: Aspects,*** Vol. 36, No. 03, (2023) 532-539

high hardness. Deng et al. [12] reported that hardfacing by cobalt (Co)-based alloys resulted in different hardness for different thicknesses. Less thickness is resulting high hardness. This phenomena is caused by the absence of the fine grain when the thickness is decreased. Kesavan and Kamaraj [8] have found that aging treatment of a nickel-based hardfacing has reduced the hardness when treatment time increased.

Titanium (Ti) and Ti-alloys are widely applied in marine, petrochemical, chemical, aerospace, and biomedical industries because promising high specific strength and high corrosion resistance [13, 14]. Furthermore, Ti also promises good hardness and erosion resistance [15]. Therefore adding a Ti into the weld layer could increase the hardness. Zhou et al. [16] have added 0.263 wt% Ti in the flux of the SMAW filler metal (Fe-Cr13-C-Nb). Exhibit Ti leads to a decreasing hardness from 46.2 to 45.2 HRC. Ti could be aglomerated perfectly between filler and based metal because the flux is changed into gasses as shielding for molten metal when the SMAW process is performed. Zhou et al. [16] found that the hardness of the layer increased from 56 to 61 HRC with titanium content from 0 to 0.63 wt%. Increased Ti content to 1.17 wt% could form TiC carbide because too much carbon is consumed by titanium. It led to a change in the microstructure to a hypereutectoid one and caused a decrease in the hardness. Moreover, the exhibit Ti content in the layer also increases the hardness than Zr addition by approximately 603 and 584 HV, respectively [17].

In addition, increasing the hardness of a material can also be conducted by quenching techniques in various solutions such as oil [18, 19]. Vegetables and engine oil were used for quenching operations to avoid undesirable microstructure [18, 20]. Dauda et al. [20] quenched carbon steel in engine oil, and Totten et al. [21] also quenched steel in vegetable oil which could increase the hardness. Various oils for quenching solution would be resulting different microstructures due to different cooling rates. Engine oil and vegetable oil at 40 ºC have a cooling rate of 64.4 and 71.9 K/s, respectively [21]. The cooling rate decreases as the viscosity of the solution increases [22].

Before quenching, the sample was heated in a muffle furnace. Commonly, the muffle furnace temperature is set to > 800ºC, and the specimen was heated 0.5 until 1 hour [18]. For cost efficiency, the sample quench after the welding process is similar to when the sample heating with a muffle furnace and then rapidly quenching because the temperature during the welding process is around 1200 ºC, which is similar to heating with a muffle furnace [23].

In this research, the hardfacing by the commercial electrode and adding Ti during welding on the low-carbon steel was conducted. Moreover, after welding, each sample was directly quenched in vegetable oil and engine oil. It is worth to be mentioned and to highlight the major concern about properties and hardness result by adding Ti in the weld layer and directly quenching method after weld. This method is more cost-effective than heating the sample with a muffle furnace. The application of this research is for lathe cutting tools application.

## 2. MATERIALS AND METHODS

This research used low-carbon steel (150×10×10 mm) as the base material. The composition of the base material is 0.128 wt% C, 0.359 wt% Si, 0.996 wt% Mn, 0.225 wt% Cr, 0.167 wt% Cu, and Fe balance (see Figure 1). Wire optime Ti grade 1 with a diameter of 0.65 mm (from the USA) was used for Ti addition. The weight of each Ti wire used is 0.225 g. HV 600 electrode (typical composition: 0.6 wt% C, 1 wt% Mn, 0.4 wt% Si, 4wt% Cr, and Fe balance) with a diameter of 3.2 mm (from Nikko Steel Manufacturer) was used for filler metal.

Prior welding process, the based material surface was cleaned by hand grinder. HV 600 electrode was dried for 1 hour (150 ºC). Three pieces of Ti wire (150×∅ 0.65mm) were placed on the surface of low carbon steel and welded single layer with SMAW (Fro BF 443, positive polarity, and 90 A).

This research was resulting three different samples that were welded using an HV 600 electrode without Ti addition and directly cooled in the natural air, quenched in 1L of engine oil (SAE 20-50), and 1 L of palm oil, namely BNU, BNO, BNM, respectively. Afterward, three samples were welded using an HV 600 with Ti addition. They directly cooled in the natural air, quenched in 1 L of palm oil, and 1L of engine oil (SAE 20-50) were BNTiU, BNTiO, and BNTiU, respectively. The sample after the weld is shown in Figure 2.

The samples were checked with Was Foundry Master-Optical Emission Spectroscopy (OES) according to ASTM E415. X-ray diffraction (XRD) PANalytical Aeris with CoK=1.789 Å and step size 0.0217° was used to analyze the phase composition and crystal structure. The Rietveld method was used to calculate the lattice parameters [24]. Furthermore, the sample was mounted in the epoxy resin, grinding, polishing, etching in 3%

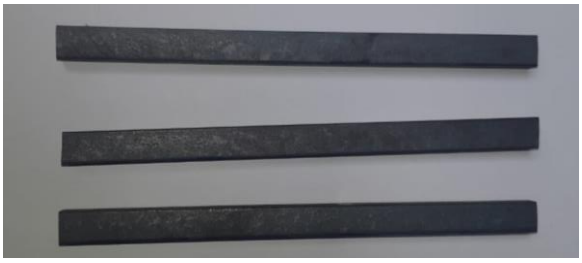

**Figure 1.** Base material

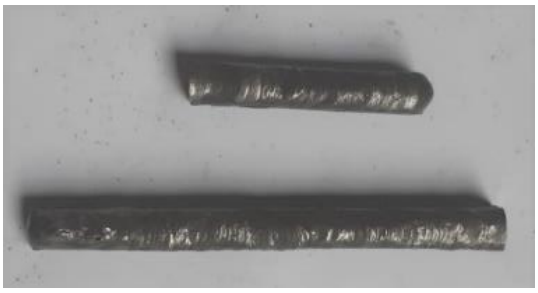

**Figure 2.** Weld samples

Nital, and captured by a digital camera for macrostructure. It was also checked by an inverted optical metallurgy microscope Olympus BX41M – LED for microstructure investigation (ASTM E407). Afterward, samples were hardness measured by Vickers hardness tester FV-300e (5$kg_f$ of load). Five readings were collected to have average hardness.

## 3. RESULT AND DISCUSSION

**3. 1. OES** Based on the OES result, the base material was welded with HV 600 electrodes, resulting welded layer in the composition: 0.342 wt%C, 0.182 wt%Si, 0.608 wt%Mn, 2.09 wt%Cr, 0.139 wt%Cu, and Fe balance. The 0.342 wt%C in the steel is close to medium carbon steel [25].

The base material was welded with HV 600 electrode and added a Ti wire resulting welded layer in the composition: 0.443 wt%C, 0.366 wt%Si, 0.923 wt%Mn, 2.19 wt%Cr, 0.144 wt%Cu, 0.147 wt% Ti, and Fe balance. Ti was perfect adding in the weld layer, as proved by the OES result.

**3. 2. XRD** Figure 3 shows the diffraction pattern of the various samples. The plane peaks (110) and (211) are reflections of the α-iron (ferrite) phase. These α-iron phase plane peaks are in good agreement with the results of other studies [26-28]. The peak magnification of 110 plane diffraction patterns in the inset of Figure 3 (2θ = 50-53°) shows an asymmetric peak shape. According to Han et al. [28], this asymmetrical peak denotes the presence of an α'-iron (martensite) phase. The peak at an angle of 2θ = 41.3°, identified as the $Fe_3O_4$ phase, illustrates how the welding process used results in the oxidation of the steel.

Different intensity values can be seen in the diffraction patterns of the four samples. This intensity value can be connected to the full width at half maximum (FWHM) value of each sample. The BNTiO sample has the smallest crystallite size, according to the qualitative analysis of the FWHM values of the α-iron and α'-iron phases in the (110) and (211) planes, as summarized in Table 1.

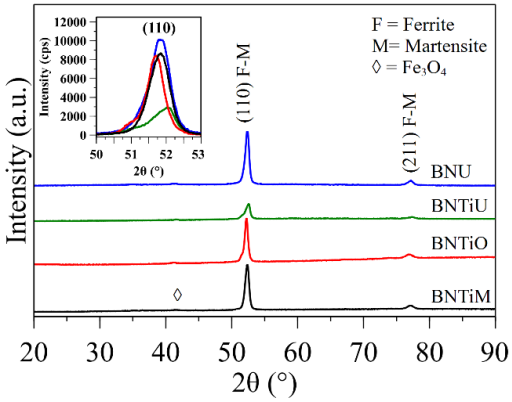


**Figure 3.** XRD various samples

**TABLE 1.** Quantitative analysis of diffraction patterns for various samples

| Source | BNU | BNTiU | BNTiO | BNTiM |
|---|---|---|---|---|
| **Ferrite phase** | | | | |
| Crystal system: Body Center Cubic (BCC) | | | | |
| Space group: Im-3m | | | | |
| Lattice a (nm) | 0.2878 | 0.2867 | 0.2881 | 0.2875 |
| **Martensite phase** | | | | |
| Crystal system: Body Center Tetragonal (BCT) | | | | |
| Space group: I4/mmm | | | | |
| Lattice a (nm) | 0.2855 | 0.2857 | 0.2859 | 0.2821 |
| Lattice c (nm) | 0.2935 | 0.2958 | 0.2931 | 0.2876 |
| α-Fe (wt.%) | 81.24 | 60.35 | 72.75 | 85.41 |
| α'-Fe (wt.%) | 15.99 | 32.30 | 23.86 | 13.02 |
| $Fe_3O_4$ (wt.%) | 2.77 | 7.35 | 3.39 | 1.57 |
| FWHM (110) (°) | 0.695 | 0.858 | 0.548 | 0.680 |
| FWHM (211) (°) | 0.980 | 1.090 | 1.030 | 1.120 |
| Rwp (%) | 3.30 | 5.31 | 3.46 | 3.52 |
| $\chi^2$ | 1.360 | 1.369 | 1.662 | 1.268 |

The composition of the phase formed and lattice constants were determined through the quantitative analysis of the diffraction patterns. Figure 4 compares the results of the calculated and observed diffraction patterns for the BNTiM sample. This study uses the Rietveld method to analyze diffraction patterns quantitatively. The overlapping peak (110) of the ferrite and martensite phase fractions were calculated using the Rietveld method in order to determine its composition. The ferrite and martensite phase fractions for the BNTiM sample were 85.41 wt.% and 13.02 wt.%, respectively (see Table 1). The sample with the greatest α-iron phase content out of the other three is the BNTiM sample.

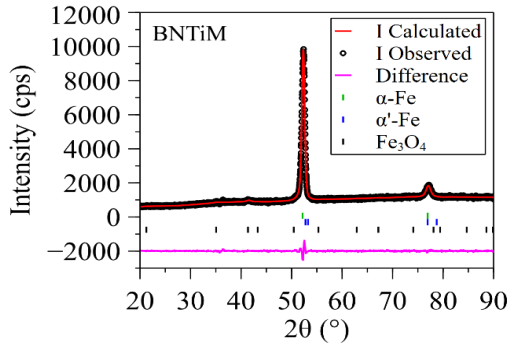


**Figure 4.** Diffraction patterns for the BNTiM sample calculated with the Rietveld method

The BNTiM sample, which has a body center cubic (BCC) structure with the space group Im-3m, has a lattice constant value (a=b=c) of 0.2875 nm. Table 1 shows the lattice constants for the four samples. These constant lattice values are identical to those previously reported [29-31].

**3. 3. Microstructure** Microstructure observation for the samples with an optical microscope was conducted as shown in Figure 5.

Based on Figure 5, we can observe different microstructures were formed. Samples with air cooling have similar characteristics for Ti addition and without Ti addition. It seems 0.147 wt% Ti addition does not influence the microstructure. This phenomenon is due to

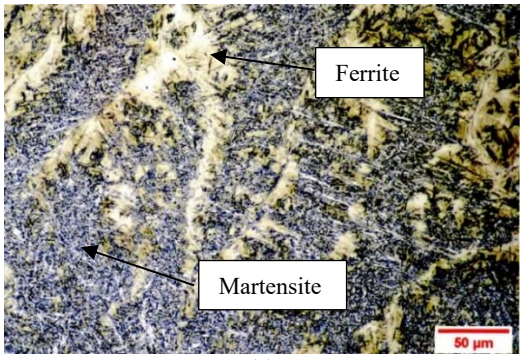


(a)

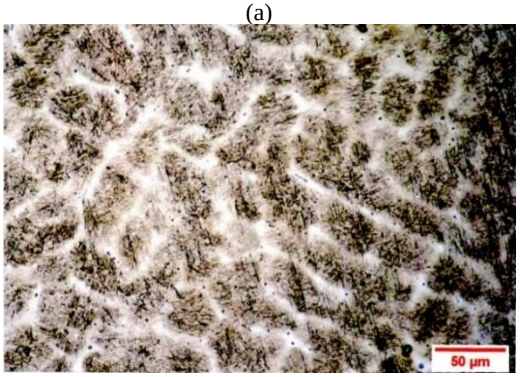


(b)

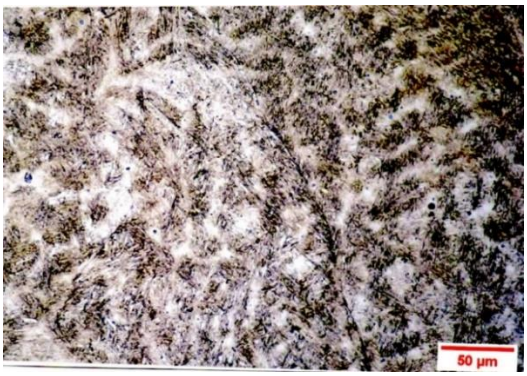


(c)

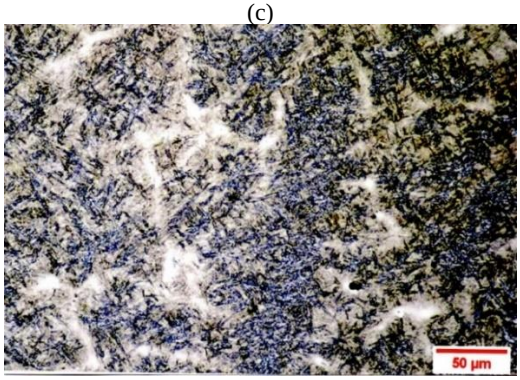


(d)

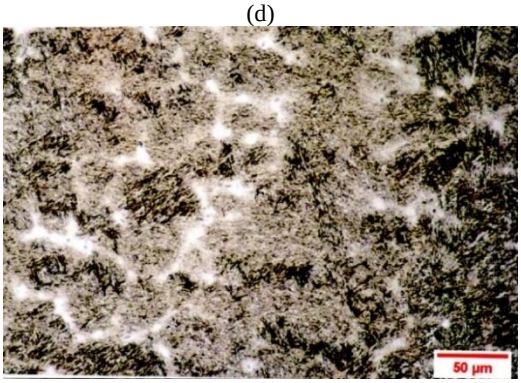


(e)

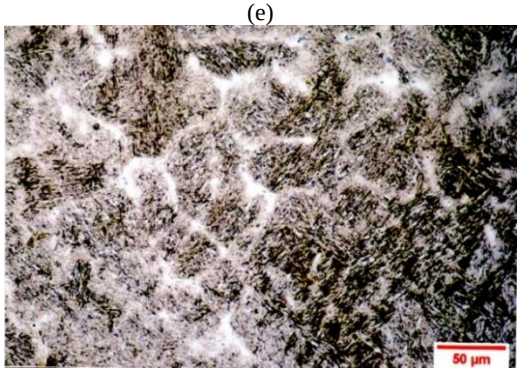


(f)

**Figure 5.** Microstructure result (a) BNU, (b) BNO, (c) BNM, (d) BNTiU, (e) BNTiO, and (f) BNTiM

only 0.147 wt% Ti being formed in the welded layer based on the OES result. Zhou et al. [16] have reported 0.28 wt%Ti could change the microstructure. When the

Ti composition of Ti raised to 1.17 wt%, the microstructure significantly changed.

From Figures 5(a) and 5(d), we can see a un uniform distribution of ferrite (white region) and martensite (dark area). This behavior was confirmed with the XRD result, where 81.24 wt % ferrite and 15.99 wt % martensite were in the BNU. Moreover, 60.35 wt % ferrite and 32.30 wt % martensite were realized in the BNTiU. The distribution and compositions formed between martensite and ferrite could avoid cracking [32]. It has been no cracking seen in the samples based on microstructure observation.

Quenching in palm oil and engine oil significantly influences the microstructure, similar to other cases reported in literature [20]. Figure 5 shows the martensitic phase and perfect agreement with different research results [33]. Quenching the samples in the solution led to uniformly changing ferrite (α-Fe) distribution between martensite (α'-Fe). Randomly martensite structure is distributed in a ferrite matrix after quenching [34]. This phenomenon is due to the oil's rapid cooling; hence, conducted ferrite becomes finer and does not grow more [35]. The quench heat treatment would be resulting smooth distribution of ferrite and martensite [36].

**3. 4. Macrostructure** The samples were compared to evaluate the effect of the quenching solution and Ti addition to the macrostructure. Macrostructure observation with a digital camera is shown in Figure 6.

Based on Figure 6, we can see different macrostructures were formed. Fusion between the base metal and weld metal is shown for various samples.

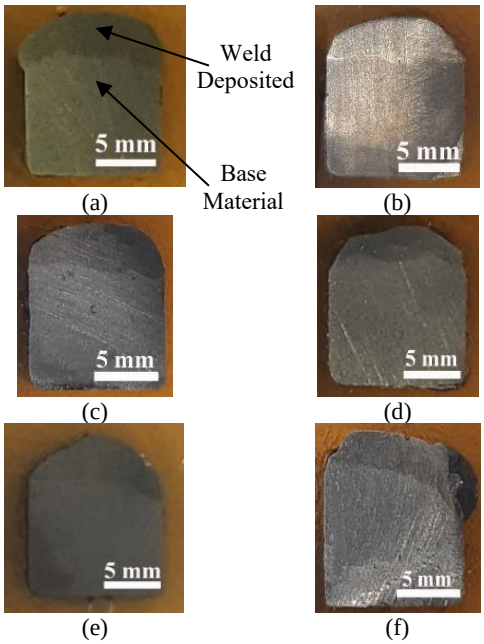


**Figure 6.** Macrostructure result (a) BNU, (b) BNO, (c) BNM, (d) BNTiU, (e) BNTiO, and (f) BNTiM

There are no visible cracks on the macrostructure. Commonly, this occurs influenced by welding conditions, mechanical restraint, and hydrogen trapping [37, 38]. It means the welding condition in this research could avoid this, and no hydrogen trapping appears in the weld metal.

The penetration of the weld layer would increase by raising the current of welding. Shukla et al. [39] showed 1.2 mm deep penetration when welding using 90 A and positive polarity. Rising to 120 A, reach a deep penetration of around 1.75 mm. The negative polarity and 90º of the electrode angle with a current at 120 A revealed full penetration because of more heat to the weld region [35, 39]. Moreover, a higher current for positive polarity is needed to get full penetration than negative polarity [40]. Plate thickness also influences penetration. Shifting to more thicknesses could increase penetration [35]. In this research, a single layer of weld penetrates approximately 3 mm for various samples. It shows perfect agglomeration between the base material and weld metal. Adding Ti in the weld layer is not influence the penetration. This result differs from others because welding parameters such as an electrode, current, and electrode are different. Commonly penetration of the weld layer is affected by the polarity, current, and angle of the electrode for the SMAW process [39].

**3. 5. Hardness Distributions** A comparison of the sample hardness was carried out in Figure 7.

Many factors influence hardness were formed. Khamari et al. [35] found that increasing the current would increase the hardness. Dauda et al. [20] found various oil for quenching media resulting in differences in hardness. An exhibit of a fine dispersion of small particles of ferrite and martensite also contributed to higher hardness [20].

Based on Figure 7, we can see that quenching the sample increased the hardness. BNU sample was resulting an average hardness of 503.48 HV. This hardness agrees with the manufacturer of a diverse range of advanced welding consumable HV 600 for single-layer welding, resulting in hardness between 440 – 540 HV [41]. Quench the sample into oils significantly increase the hardness [20].

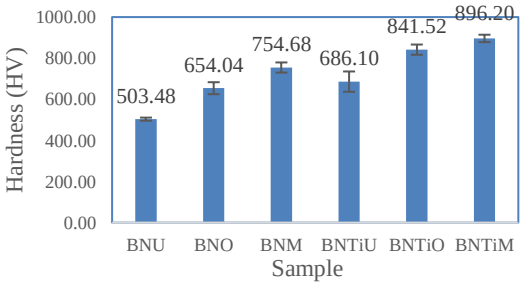


**Figure 7.** Hardness Vickers of the different specimens

Its seem samples where quenching in oils has higher hardness than air cooling. Air and oil cooling could increase the hardness by around 4.5% and 40%, respectively [42]. Sample where quenching in palm oil has a higher hardness than engine oil. This value is attributed to palm oil having less viscosity than engine oil and thus affecting the higher cooling rate. As we know, engine oil has 64.4 and vegetable oil has 71.9 K/s of viscosity at 40º C [20, 21]. A shift to a higher cooling rate led to higher hardness [43]. For this study, we found that palm oil is the best quenching solution to increase the hardness.

Adding Ti also increases the hardness of the sample when quenching in a different solution. This result perfectly agrees with other research where adding Ti improves the hardness, whereas adding 0.63 wt% Ti could increase the hardness from 56 to 61 HRC [16]. Increasing the Ti from 0.63 to 1.17 wt% could decrease the hardness because too much carbon is consumed when titanium content is 1.17 wt% [16]. Therefore, there is a limitation contained in the layer when Ti is added. Moreover, 0.147 wt% Ti in the weld layer increases hardness by around 0.2% for a sample with and without the quenching process.

Based on Table 1, we can realize that the quenched sample with Ti addition in the engine oil and palm oil led to a decrease in the oxide ($Fe_3O_4$). This phenomenon may be attributed to the solution cooling rate that increased sample hardness. Iron oxide could affect the strength of the material [44].

Compared to Table 1, an increase in the hardness linearly within increase in the ferrite for a sample with Ti addition. Adding Ti could increase in the hardness of the ferrite matrix [45]. The ferrite phase is the main factor in increasing the hardness in this research. A shift to higher ferrite composition (see Table 1) and fine dispersion of small ferrite particles could enhance the hardness.

Based on the hardness test result, BNTiO, and BNTiM have more hardness than the HSS commercial for a lathe-cutting tool [2]. This value means the samples are recommended for the cutting tool. But this needs deep further investigation.

## 4. CONCLUSIONS

The effect of Ti addition and quenching of the samples is summarized as follows:

1. Adding titanium (Ti) to the weld layer and quenching the samples after welding in the solution enhances the hardness. This phenomenon is attributed to different phase compositions, oxides, and microstructures.
2. A fine dispersion of small ferrite particles and oxide amount is important in increasing the hardness.
3. Adding Ti in the weld layer did not influence the penetration. Therefore, there is no cracking in the weld and base metal.
4. BNTiO, and BNTiM samples are recommended for cutting tools.

## 5. ACKNOWLEDGMENT

This research was funded by Engineering Faculty, Universitas Negeri Jakarta (Contract No. 017/UN39.5.FT/PP/IV/2022).

## 5. REFERENCES

1. Jesudass Thomas, S., and Kalaichelvan, K. "Comparative study of the effect of surface texturing on cutting tool in dry cutting." ***Materials and Manufacturing Processes***, Vol. 33, No. 6, (2018), 683-694. https://doi.org/10.1080/10426914.2017.1376070
2. Susetyo, F. B., Dwiyati, S. T., and Hutomo, M. B. P. "Fabrikasi Lapisan Pada Baja 0 , 192 % C Sebagai Alternatif Pahat Bubut." ***Jurnal kajian Teknik Mesin***, Vol. 5, No. 1, (2020), 42-47.
3. Asad, S., Dilawary, A., Motallebzadeh, A., Atar, E., and Cimenoglu, H. "Influence of Mo on the high temperature wear performance of NiCrBSi hardfacings." ***Tribology International***, Vol. 127, (2018), 288-295. https://doi.org/10.1016/j.triboint.2018.06.022
4. Wang, Y., Gou, J., Chu, R., Zhen, D., and Liu, S. "The effect of nano-additives containing rare earth oxides on sliding wear behavior of high chromium cast iron hardfacing alloys." ***Tribology International***, Vol. 103, (2016), 102-112. https://doi.org/10.1016/j.triboint.2016.06.041
5. Jabbar Hassan, A., Boukharouba, T., Miroud, D., Titouche, N., and Ramtani, S. "Experimental investigation of friction pressure influence on the characterizations of friction welding joint for aisi 316." ***International Journal of Engineering Transactions C: Aspects***, Vol. 33, No. 12, (2020), 2514-2520. https://doi.org/10.5829/ije.2020.33.12c.12
6. Chaidemenopoulos, N. G., Psyllaki, P. P., Pavlidou, E., and Vourlias, G. "Aspects on carbides transformations of Fe-based hardfacing deposits." ***Surface and Coatings Technology***, Vol. 357, (2019), 651-661. https://doi.org/10.1016/j.surfcoat.2018.10.061
7. Yang, K., Gao, Y., Yang, K., Bao, Y., and Jiang, Y. "Microstructure and wear resistance of Fe-Cr13-C-Nb hardfacing alloy with Ti addition." ***Wear***, Vol. 376-377, , (2017), 1091-1096. https://doi.org/10.1016/j.wear.2016.12.062
8. Kesavan, D., and Kamaraj, M. "Influence of aging treatment on microstructure, wear and corrosion behavior of a nickel base hardfaced coating." ***Wear***, Vol. 272, No. 1, (2011), 7-17. https://doi.org/10.1016/j.wear.2011.05.041
9. Wang, H., and Yu, S. "Influence of heat treatment on microstructure and sliding wear resistance of high chromium cast iron electroslag hardfacing layer." ***Surface & Coatings Technology***, Vol. 319, (2017), 182-190. https://doi.org/10.1016/j.surfcoat.2017.04.013
10. Sadeghi, F., Naja, H., and Abbasi, A. "Technology The effect of Ta substitution for Nb on the microstructure and wear resistance of an Fe-Cr-C hardfacing alloy." ***Surface & Coatings Technology***, Vol. 324, (2017), 85-91. https://doi.org/10.1016/j.surfcoat.2017.05.067

11. Singh, H. "Studies the Effect of Iron Based Hardfacing Electrodes on Stainless Steel Properties Using Shielded Metal Arc Welding Process." ***International Journal of Research in Advent Technology***, Vol. 2, No. 4, (2014), 2321-963.
12. Deng, H., Shi, H., and Tsuruoka, S. "Influence of coating thickness and temperature on mechanical properties of steel deposited with Co-based alloy hardfacing coating." ***Surface and Coatings Technology***, Vol. 204, No. 23, (2010), 3927-3934. https://doi.org/10.1016/j.surfcoat.2010.05.013
13. Tavoosi, M., Arjmand, S., and Adelimoghaddam, B. "Surface & Coatings Technology Surface alloying of commercially pure titanium with aluminium and nitrogen using GTAW processing." ***Surface & Coatings Technology***, Vol. 311, (2017), 314-320. https://doi.org/10.1016/j.surfcoat.2016.12.115
14. Ebrahimi, N., Hosseinzadeh, A. S. A., Vaezi, M., and Mozafari, M. "Evaluation of Corrosion Resistance of Bi-layered Plasma-sprayed Coating on Titanium Implants." ***International Journal of Engineering, Transactions A: Basics***, Vol. 35, No. 4, (2022), 635-643. https://doi.org/10.5829/ije.2022.35.04a.03
15. More, S. R., Bhatt, D. V., Menghani, J. V., Paul, C. P., and Desale, G. R. "Laser cladding of pac 718, tribaloy T-700 and METCO 41 C hard facing powders on AISI SS 304L substrate." ***International Journal of Engineering, Transactions B: Applications***, Vol. 34, No. 2, (2021), 480-486. https://doi.org/10.5829/IJE.2021.34.02B.20
16. Zhou, Y. F., Yang, Y. L., Li, D., Yang, J., Jiang, Y. W., Ren, X. J., and Yang, Q. X. "Effect of titanium content on microstructure and wear resistance of Fe-Cr-C hardfacing layers." ***Welding Journal***, Vol. 91, No. 8, (2012), 229-236.
17. Yung, D., Zikin, A., Hussainova, I., Danninger, H., Badisch, E., and Gavrilovic, A. "Tribological performances of ZrC-Ni and TiC-Ni cermet reinforced PTA hardfacings at elevated temperatures." ***Surface and Coatings Technology***, Vol. 309, , (2017), 497-505. https://doi.org/10.1016/j.surfcoat.2016.11.099
18. Faria, D., Brito, P., Ramos, P. A., Resende, L. P., and Ant, D. "Experimental investigation of cooling behavior and residual stresses for quenching with vegetable oils at different bath temperatures." ***Journal of Cleaner Production***, Vol. 216, (2019), 230-238. https://doi.org/10.1016/j.jclepro.2019.01.194
19. Mohmmed, A. A., N Y, Z., and J H, M. "The effect of polymeric quenching media on mechanical properties of medium carbon steel." In IOP Conf. Series: Materials Science and Engineering 1-6. https://doi.org/10.1088/1757-899X/454/1/012053
20. Dauda, M., Kuburi, L. S., and Obada, D. O. "Effects of Various Quenching Media On Mechanical Properties of Annealed 0.509Wt%C -0.178Wt%Mn Steel." ***Nigerian Journal of Technology***, Vol. 34, No. 3, (2015), 506-512.
21. Totten, G. E., Tensi, H. M., and Lainer, K. "Performance of vegetable oils as a cooling medium in comparison to a standard mineral oil." ***Journal of Materials Engineering and Performance***, Vol. 8, No. 4, (1999), 409-416. https://doi.org/10.1361/105994999770346693
22. Dodo, R. M., Ause, T., Shehu, U., Abdulhamid, S., and Onoja, K. K. "Study Of Maize Starch Solution As Quenching Media For 0 62 % C High Carbon Steel." ***International Journal of Engineering***, Vol. XV, No. 4, (2017), 63-68.
23. García-García, V., Mejía, I., and Reyes-Calderón, F. "Experimental and FEM study of Ti-containing TWIP steel weldability." ***Journal of Materials Processing Technology***, Vol. 261, (2018), 107-122. https://doi.org/10.1016/j.jmatprotec.2018.05.028
24. Larson, A. C., and Dreele, R. B. Von. General Structure Analysis System (GSAS) (Vol. 748).
25. Ikubanni, P. P., Agboola, O. O., Adediran, A. A., and Adeleke, A. A. "Experimental data on mechanical properties evaluation of medium carbon steel quenched in different waste media." ***Data in Brief***, Vol. 20, (2018), 1224-1228. https://doi.org/10.1016/j.dib.2018.08.185
26. Tomota, Y., Wang, Y. X., Ohmura, T., Sekido, N., Harjo, S., Kawasaki, T., Gong, W., and Taniyama, A. "In situ neutron diffraction study on ferrite and pearlite transformations for a 1.5Mn-1.5Si-0.2C steel." ***ISIJ International***, Vol. 58, No. 11, (2018), 2125-2132. https://doi.org/10.2355/isijinternational.ISIJINT-2018-336
27. Dalshad Omar, H. "Investigation the Structure and Morphology of Iron Metallic by Difference Techniques." ***Journal of Nanotechnology and Advanced Materials,*** Vol. 3, No. 2, (2015), 57-61. Retrieved from http://dx.doi.org/10.12785/jnam/030201
28. Han, R., Li, W., Pan, W., Zhu, M., Zhou, D., and Li, F. S. "1D magnetic materials of Fe3O4 and Fe with high performance of microwave absorption fabricated by electrospinning method." ***Scientific Reports***, Vol. 4, (2014), 1-5. https://doi.org/10.1038/srep07493
29. Zhou, D. S., and Shiflet, G. J. "Ferrite: Cementite crystallography in pearlite." ***Metallurgical Transactions A***, Vol. 23, No. 4, (1992), 1259-1269. https://doi.org/10.1007/BF02665057
30. Balasubramaniam, R., Ramesh Kumar, A. V., and Dillmann, P. "Characterization of rust on ancient Indian iron." ***Current Science***, Vol. 85, No. 11, (2003), 1546-1555.
31. Lawrynowicz, Z. "Bainite Transformation in Experimental Fe-Cr-Mo-V-Ti-C Steel." ***Advance in Materials Sciences***, Vol. 13, No. 2, (2003), 12-18. https://doi.org/10.2478/adms-2013-0005 Z.
32. Brykov, M. N., Petryshynets, I., Džupon, M., Kalinin, Y. A., Efremenko, V. G., Makarenko, N. A., Pimenov, D. Y., and Kováč, F. "Microstructure and properties of heat affected zone in high-carbon steel after welding with fast cooling in water." ***Materials***, Vol. 13, No. 22, (2020), 1-13. https://doi.org/10.3390/ma13225059
33. Srikarun, B., and Muangjunburee, P. "The effect of iron-based hardfacing with chromium powder addition onto low carbon steel." ***Materials Today: Proceedings***, Vol. 5, No. 3, (2018), 9272-9280. https://doi.org/10.1016/j.matpr.2017.10.100
34. Joshua, T. O., Alao, O. A., and Oluyori, R. T. "Effects of Various Quenching Media on the Mechanical Properties of Inter - Critically Annealed 0.267 % C - 0.83 % Mn Steel." ***International Journal of Engineering and Advanced Technology***, Vol. 3, No. 6, (2014), 121-127.
35. Khamari, B. K., Dash, S. S., Karak, S. K., and Biswal, B. B. "Effect of welding parameters on mechanical and microstructural properties of GMAW and SMAW mild steel joints." ***Iron making and Steel making***, Vol. 47, No. 8, (2019), 844-851. https://doi.org/10.1080/03019233.2019.1623592
36. Bello, K. A., Hassan, S. B., Abdulwahab, M., and Shehu, U. "Effect of Ferrite-Martensite Microstructural Evolution on Hardness and Impact Toughness Behaviour of High Martensite Dual Phase Steel." ***Australian Journal of Basic and Applied Sciences***, Vol. 1, No. 4, (2007), 407-414.
37. Zacharia, T. "Dynamic stresses in weld metal hot cracking." ***Welding Journal***, No. July, (1994), 164-172.
38. Gan, L., Huang, F., Zhao, X., Liu, J., and Cheng, Y. F. "Hydrogen trapping and hydrogen induced cracking of welded X100 pipeline steel in H2S environments." ***International Journal of Hydrogen Energy***, Vol. 43, No. 4, (2018), 2293-2306. https://doi.org/10.1016/j.ijhydene.2017.11.155
39. Shukla, A. A., Joshi, V. S., Chel, A., and Shukla, B. A. "Analysis of Shielded metal arc welding parameter on Depth of Penetration on AISI 1020 plates using Response surface methodology." ***Procedia Manufacturing***, Vol. 20, (2018), 239-246. https://doi.org/10.1016/j.promfg.2018.02.035
40. Wu, D., Chen, H., Huang, Y., He, Y., Hu, M., and Chen, S. "Monitoring of weld joint penetration during variable polarity

plasma arc welding based on the keyhole characteristics and PSO-ANFIS." ***Journal of Materials Processing Technology***, Vol. 239, (2017), 113-124. https://doi.org/10.1016/j.jmatprotec.2016.07.021

41. Nikko, S. *Manufacturers of a Diverse Range of Advance Welding Consumables HV 600*.
42. Dewangan, S., Singhal, P., Selvaraj, S. K., Dev, S. J., and Swathish, R. S. "Analysing strength , hardness and grain-structure of 0.2 %-C steel specimens processed through an identical heating period with different continuous transformation rates specimens processed through an identical heating period with different continuous." In ***Materials Research***, 1-14.
43. Chen, Z., Nash, P., and Zhang, Y. "Correlation of Cooling Rate, Microstructure and Hardness of S34MnV Steel." ***Metallurgical and Materials Transactions B: Process Metallurgy and Materials Processing Science***, Vol. 50, No. 4, (2019), 1718-1728. https://doi.org/10.1007/s11663-019-01621-0
44. Huang, Z., Yi, L., and Jiang, T. "Mechanisms of strength decrease in the initial reduction of iron ore oxide pellets." ***Powder Technology***, Vol. 221, (2012), 284-291. https://doi.org/10.1016/j.powtec.2012.01.013
45. Moon, J., Kim, S., Jang, J. il, Lee, J., and Lee, C. "Orowan strengthening effect on the nanoindentation hardness of the ferrite matrix in microalloyed steels." ***Materials Science and Engineering A***, Vol. 487, No. 1-2, (2008), 552-557. https://doi.org/10.1016/j.msea.2007.10.046

## Persian Abstract

**چکیده**

سختی سطح مواد را که معمولاً از طریق تکنیک هارد فاسینگ انجام می شود، افزایش دهید. Hard facing رایج است، به طوری که مواد با خواص بهتر بر روی مواد فله ارزان‌تر رسوب می‌کنند. این کار با افزودن سیم تیتانیوم (Ti) در طول فرآیند جوشکاری، لایه‌های سختی را ساخت. این تحقیق از فولاد کم کربن به عنوان ماده پایه، سیم بهینه Ti با درجه ۱ برای افزودن Ti، و یک الکترود HV 600 با قطر ۳.۲ میلی متر برای فلز پرکننده استفاده کرد. یک جوش تک لایه با SMAW (قطب مثبت و ۹۰ A) انجام شد. نمونه ها به طور مستقیم پس از جوشکاری در محلول دیگری خاموش شدند. خواص لایه جوش به ترتیب فاز، ساختار، ریزساختار، درشت ساختار و سختی با استفاده از طیف‌سنجی انتشار نوری (OES)، پراش اشعه ایکس (XRD)، میکروسکوپ نوری، دوربین دیجیتال و دستگاه سختی مورد بررسی قرار گرفت. افزودن تیتانیوم (Ti) به لایه جوش و کوئنچ کردن نمونه ها پس از جوشکاری در محلول باعث افزایش سختی می شود. این پدیده به ترکیبات فازی، اکسیدها و ریزساختارهای مختلف نسبت داده می شود. پراکندگی ریز ذرات کوچک و مقدار اکسید در افزایش سختی مهم است. هیچ ترک خوردگی در جوش و فلز پایه وجود ندارد. در نتیجه، نمونه‌های BNTiO و BNTiM برای ابزارهای تراشکاری توصیه می‌شوند.

International Journal of Engineering

Journal Homepage: www.ije.ir

# Numerical Analysis on Flow Characteristics of Gas-liquid Two-phase Flow in a Vertical Pipe with Downward Stream

S. Hasanpour, I. Mirzaee, M. Khalilian*

*Mechanical Engineering Department, Faculty of Engineering, Urmia University, Urmia, Iran*

*P A P E R I N F O*

*Paper history:*
Received 19 November 2022
Received in revised form 17 December 2022
Accepted 24 December 2022

*Keywords*:
*Two-phase Flow*
*Downward Flow*
*Numerical Simulation*
*Level Set Method*

*A B S T R A C T*

Through this paper, a 3D simulation together with experimental observation was conducted to study two-phase flow in a vertical tube. OpenFOAM software was employed to analyze air and water. Main flow stream was downward which was considered to be within a vertical pipe of 10 mm in diameter. Study included two inputs for flows: upper input for water and side input for air. Several states with various mass fluxes for both water and air were studied. Based on physics of the issue, numerical simulation was considered to be time-dependent. Obtained results showed that when air velocity occupied lower values, air momentum cannot overcome water momentum leading in small slugs. When airflow velocity was more than water flow rate, it dominated water flow and consequently could affect mainstream direction. Also, velocity graphs on centerline represented that going forward in time, velocity magnitude experiences a significant value of fluctuations and large oscillations occur next to outlet. Comparing experimental and numerical results, approximately 9% differences can be found which showed suitable agreement. Results showed that at initial steps, void fraction faces a significant jump in values. Intensity of this change in void fraction values was higher in lower water velocity. Indeed, by increment of water velocity, inertial forces associated with liquid phase find a dominant role in overall hydrodynamics of the gas-liquid flow. Also, it is obvious that flowing manner in cases 1, 2, and 3 are similar but after case 4, flow pattern varies. These changes are more considerable in cases 5 and 6.

***doi**: 10.5829/ije.2023.36.03c.14*

**NOMENCLATURE**

| | |
|---|---|
| D | Pipe diameter, m |
| $F$ | Force, kg m/s$^2$ |
| g | Gravitational acceleration, m$^2$ |
| $h$ | Enthalpy |
| k | Turbulence kinetic energy, m$^2$/s$^2$ |
| p | Static pressure, pa |
| Q | Volume flow rate, m$^3$/s |
| $q$ | Generation term |
| $T$ | Turbulent viscosity tensor |
| Re | Reynolds number |
| $t$ | Time, s |
| $u$ | Velocity, m/s |

| **Greek Symbols** | |
|---|---|
| $\alpha$ | Void fraction |
| $\rho$ | Density, kg/m$^3$ |
| $\mu$ | Dynamic viscosity, Pa.s |
| $\omega$ | Specific dissipation rate, kg/m$^2$s |
| **Subscript** | |
| i | Interaction |
| int | Initial |
| G,g | Gas phase |
| L,l | Liquid phase |
| c | Continues phase |
| d | Dispersed phase |
| k | Phase k |
| s | Surface |

## 1. INTRODUCTION

The multiphase flow is named for the stream of two substances that are in different phases from the viewpoint of physics. Through the last decades, it was revealed that multiphase flows (especially the application is gas\liquid two-phase flow) could occur within a variety of industrial applications. The industrial applications that included the gas-liquid two-phase flow included power plants, fuel refinery systems, drug production processes, and so on.

*Corresponding Author Institutional Email: m.khalilian@urmia.ac.ir (M. Khalilian)

Please cite this article as: S. Hasanpour, I. Mirzaee, M. Khalilian, Numerical Analysis on Flow Characteristics of Gas-liquid Two-phase Flow in a Vertical Pipe with Downward Stream, ***International Journal of Engineering, Transactions C: Aspects,*** Vol. 36, No. 03, (2023) 540-547

These high technological applications urge the investigations to better understanding of the nature of the multiphase flows [1, 2].

A type of multiphase flow named the gas-liquid two-phase flow is one of the major types of multiphase flow that widely exists in natural and industrial applications. The complexity of the nature of these types of streams makes them very interesting for researchers of this field. This complexity is based on the nature of two different phases and could be intensified by the variations in the orientation, shape, and form of the flowing path. Findings have presented that the gas-liquid two-phase flow could present different thermal and hydraulic behavior in different flow patterns [3]. They represented that the centrifugal forces influence the flow pattern in helical tubes. Golan [4] implemented an experimental investigation within a 0.038 m diameter round tube that the air-water two-phase flow was considered as the working fluids. Through their investigation, the flow patterns of bubbly, slug, oscillatory, and annular flow patterns were observed. The hydrodynamic behavior of the flow around a Taylor ascending bubble using the VOF model was numerically studied by Taha and Cui [5]. The results represented that the movement of this bubble creates a very thin layer of film on the sides of the bubble and in contact with the wall. Hossain et al. [6] employed the VOF model to study the oscillating behavior of slug flow. They utilized the k-ε model for turbulence flow simulation. An empirical investigation of the mixing of gas-liquid flow within horizontal pipes was conducted by Akhlaghi et al. [7]. They performed a numerical analysis to compare the results with the experimental ones. Their results showed that when the surface velocity of the gas phase is enhanced at a constant surface velocity of the liquid, the fraction of the gas slug length to that of the liquid slug goes up significantly. Yu et al. [8] worked on the thermal and hydrodynamic features of slug flow in a microchannel. In their study, they also utilized the VOF model to simulate this flow. Gupta et al. [9] experimentally studied the thermal and hydrodynamic characteristics of two-phase flows including the Taylor bubble employing a fluid volume model. The results reported that the Nusselt number of two-phase flows is up to 2.5 times higher than single-phase. Newtonian and non-Newtonian fluids including two phases examined by Ratkovich et al. [10]. They provided a relationship to predict the volume fraction values. Zheng et al. [11] numerically investigated the features of the Taylor bubble in the ascending flow in the vertical tube. The results of their study represented that in the flow where the inertial force is predominant, the shear stress of the wall enhances with an increase in velocity of the Taylor bubble. Abdulkadir et al. [12] compared the experimental and numerical results of the Taylor bubble studying. The results of their study represented that the use of the VOF model can provide an acceptable result for studying the features of two-phase flow models.

An investigation conducted by Adegoke and Oyediran [13] included the nonlinear dynamics behavior of cantilevered pipes that included the gas-liquid two-phase flow. Through their studies, they applied different scales of methods to provide the axial and transverse vibrations. Furthermore, the influence of Poisson's ratio and the pressurization on the dynamic response of the pipe were probed through their results. Wang et al. [14] represented a dynamic configuration of a horizontal pipe that consisted of slug flow. They applied the finite element method for solving the governing equation associated with the motion of gas liquid two phase flow. Their results presented a good agreement between the results of the simulation and the empirical results. Their results presented a significant impact of the slug transition velocity on the main features of the system as like to damping. Mimouni et al. [15] reported that the changes in the values of the flow rates of both phases in the inlet section of the horizontal pipes results in the presence of various flow patterns. They reported that the flow patterns may consist of slug, plug and intermittent flow patterns. Also, it was found that the intermitted nature of the gas-liquid flow interrupts the ordinary performance of the instruments associated with the oil and gas refinery systems [16] and may cause some very significant damages to the pipelines [17]. An investigation implemented by Montgomery [18] focused on the flow properties within an S-shaped riser. They probed the feaures of flow patterns associated with various separator pressures and developed a stability criterion to observe the stable and unstable flow. Malekzadeh et al. [19] performed some experiments associated with long pipeline-riser systems. They tried to focus in the features of the gas-liquid two-phase flow in these systems. Xie et al. [20] studied the influence of backpressure on severe slugging characteristics in a large flow loop with a total pipeline length of 405 m. Assari et al. [21] utilized the mixture method to simulate the gas-liquid two-phase flow inside an air-water ejector. Their results revealed a deviation of 7% between the simulation results and the existing empirical data. Han et al. [22] tried to propose and develop a new technology to determine the void fraction which was based on an artificial neural network.

Based on the literature reviewed, there are limited numerical works on the downward air-water two-phase flow in detail. Also, some papers showed the results without any comparison with experimental data which is done in this work. Therefore, herein, this kind of flow is studied numerically in a 3D vertical pipe through various mass fluxes. The present study includes several sections. The first section is an introduction and literature review of the proposed issue. The next part has essential definitions of numerical methodology. Then, the result

and discussion part is discussed. Finally, the conclusion and studied references, specific parts are shown, respectively.

## 2. METHODOLOGY and VERIFICATION

The geometric configuration was developed and meshed in Gambit software. Then, the desired model is exported to OpenFOAM software and the simulation steps in this software are continued.

Six balance equations are defined in an overall two-fluid model. However, seven different dependent flow factors of $\alpha_g$, $u_g.u_l.h_g.h_l.p_g$ and $p_l$ play their roles which brings a kind of complexity to solving the mentioned equations. There are two individual methods to get a complete set of equations. The first is the definition of more simplifications to diminish the number of dependent parameters. The second one is to develop further differential equations to get an equilibrium condition between the number of dependent parameters and equations. Thus, usually, the assumption of equal local pressure $p_g = p_l = p$ are stated because the variation in local pressure among the individual phases was considered to be slight and could be considered negligible for various applications. Supposing a unique local pressure amount, the below mass, momentum, and energy conservation equations could be extracted:

Conservation of mass equation:

$$\frac{\partial}{\partial t}\alpha_k\rho_k + \nabla(\alpha_k\rho_k\boldsymbol{u}_k) = \Gamma_k \quad (1)$$

Momentum balance equation:

$$\frac{\partial}{\partial t}\alpha_k\rho_k\boldsymbol{u}_k + \nabla(\alpha_k\rho_k\boldsymbol{u}_k \otimes \boldsymbol{u}_k) + \alpha_k\nabla p + (p - p_k^{int})\nabla\alpha_k = \alpha_k\rho_k g + F_k^{int} + \Gamma_k u^{int} - \nabla.(\alpha_k T_k) \quad (2)$$

Energy balance equation:

$$\frac{\partial}{\partial t}\alpha_k\rho_k h_k + \nabla(\alpha_k\rho_k h_k\boldsymbol{u}_k) - \alpha_k\frac{D_k p}{Dt} = \Gamma_k h_k^{int} + q_k^{ext} \quad (3)$$

Through which the term k equals g for gas or vapor. Furthermore, the k equals l for the liquid phase. $\frac{D_k}{Dt}$ stands for the material derivative and $T_k$ stands for the turbulent viscosity tensor [23]. The main configuration is a three-dimensional pipe of 10 mm in diameter with a side input at the head. To do the numerical evaluation, three different mass fluxes of 0.75, 1.5, and 2 l/min were considered for the water flow rate. Simultaneously, five mass fluxes of 0.01, 0.2, 1, 3, and 5 l/min were considered for air flow rate. Table 1 shows the related velocities for all mass fluxes.

Level-Set Method (LSM) was employed to simulate the problem. The level-set method is a popular interface-tracking method for computing two-phase flows with topologically complex interfaces. In the level-set method, the interface is captured and tracked by the level-set function, defined as a signed distance from the interface. Assuming the curve of Γ is perpendicular to the speed of v, then the level-set function $\varphi$ could easily satisfy the level-set equation:

**TABLE 1.** Various velocity values for water and airflow

| Cases | Water vel. [m/s] | Air vel. [m/s] |
|---|---|---|
| Case 1 (based case) | 0.01 | 0.005 |
| Case 2 | 0.02 | 0.005 |
| Case 3 | 0.01 | 0.008 |
| Case 4 | 0.0265 | 0.053 |
| Case 5 | 0.0265 | 0.159 |
| Case 6 | 0.0265 | 0.265 |

$$\frac{\partial\varphi}{\partial t} = v|\nabla\varphi| \quad (4)$$

The solution $\varphi$ of Equation (4) describes the time-dependent position of the interface Γ(t), implicitly as its zero level, i.e.

$$\Gamma(t) = \{x\epsilon\Omega: \varphi(x,t) = 0\} \quad (5)$$

This approach renders the method robust with respect to topological changes of the interface. For instance, a collision of two droplets can be handled easily. Figure 1 shows the main flow domain. As it is observed, water is fed to the pipe from the head and the air enters from the side input. In both inlets, the velocity value is known as previously mentioned and the outlet consists of specified relative pressure equal to zero.

The mesh independency, herein, is the first step. Figure 2 shows that the unstructured meshes are used in this simulation.

In this study, firstly, five different cell numbers are investigated. To assess solution mesh independence, Figure 3 is extracted. This figure shows that the magnitude of outlet velocity varies by changing cell numbers. It is clear that after 350,000 cells, the changes

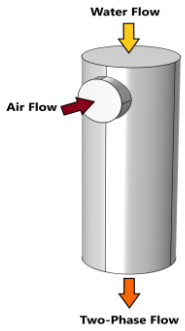


**Figure 1.** Main simulated domain

**Figure 1.** Unstructured used meshes

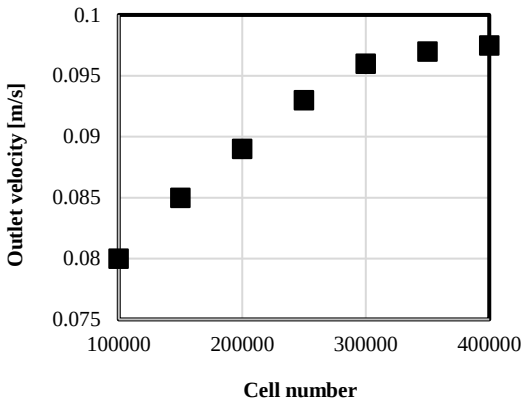


**Figure 3.** Solution mesh independence based on outlet velocity for 1s

in velocity magnetite is negligible. Therefore, to reduce computation cost, this number of cell is selected to fulfill the numerical procedure.

The most important part of the numerical investigations is the reliability checking of the results. To this aim and for the validation of the simulation results, the results of the flow map were compared with those obtained with Oshinowo [24]. Figure 4 depicts the flow map results of the present simulation in comparison with the results of Oshinowo [24]. Looking at the mentioned figure, it could be concluded that the flow transition points between the flow patterns of bubbly-slug, slug-froth, and froth-falling film of the simulation results are in good agreement with those associated with the results of Oshinowo [24]. Although there is a minor deviation between the results of the present simulation and the results of the Oshinowo [24], this difference can be explained based on the differences in the description of the physical structure of the flow patterns defined by individual investigators.

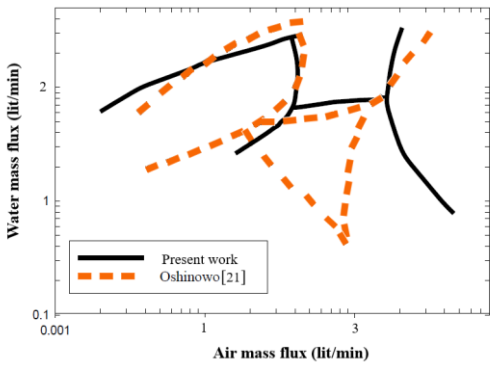


**Figure 2.** Flow pattern comparison for present work vs. Oshinowo [24].

## 3. EXPERIMENTAL SETUP

The setup consisted of two main streams including the airlines and waterline. For the water line, a tank was used as water storage and a drain was fabricated to exit the extra water. A pump supplied the water from this tank. It is worth to be mentioned that the tank was filled with tape water. A mixer was located in the next step that combined the airflow with water flow to generate the two-phase flow. It should be noted that the airflow was produced by employing a compressor with suitable pressure to feed the mixer. Furthermore, three individual rotameters (KHL-08A01M-V mode) were utilized to sense the volumetric flow rates of each stream. The test section included a 4 m pipeline through which a camera was located in the last 1 m for capturing the flow structure. A schematic depiction of the experimental setup is shown in Figure 5.

## 4. RESULTS and DISCUSSION

Firstly, according to Table 1, case 1 is the base case for this simulation. Thus massive data are extracted for this case to show the flow dynamics in the investigated domain then the results of other cases were compared to each other briefly. The previous findings have revealed that the void fraction is a function of some different factors as the mass flow rate of the individual mass flow rates of each phase and also the flow patterns. Through the dominant flow patterns that are observed in

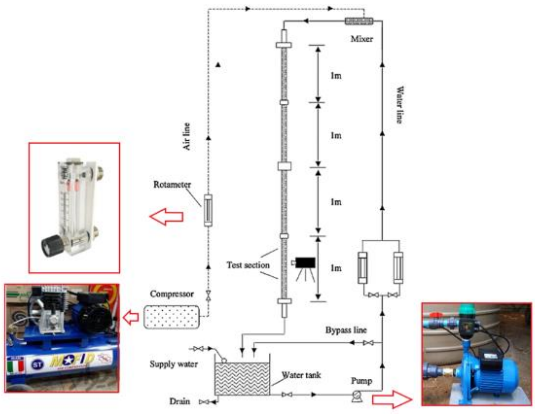


**Figure 5.** Schematic of the experimental setup

downward flows the minimum values of void fraction were found to be associated with the bubbly flow, whereas the maximum values were always relevant to the annular flow patterns. Through Figure 6, the variation of void fraction in terms of the variation of air flow rate and for different water flow rates are depicted. It was found that at the initial steps the void fraction faces a significant jump in the values. The intensity of this rapid change in the values of the void fraction was higher in the lower values of the water velocity. Indeed, by the increment of water velocity, the inertial forces associated with the liquid phase find a dominant role in the overall hydrodynamics of the gas-liquid two-phase flow. Looking at Figure 6, it could be concluded that after a certain value of the air velocity the void fraction curves face an almost constant slope. It should be noted that the above-mentioned statement is in good agreement with previously presented findings of some other investigations, from which their work were published by Jiang and Rezkallah [25], Usui and Sato [26], Nguyen [27] and Vatani and Domiri-Ganji [28] could be named.

Since the solution domain is 3D so to deduce understandable results, it is essential to specify a certain line to extract data on which. Figure 7 shows this centerline. Also, it is worth mentioning that to reduce solution time, the simulation is run out up to 5s.

The first parameter studied on the centerline is velocity magnitude. Figure 8 represents this parameter for different periods. This figure shows that by going forward in time, the centerline velocity oscillation is larger. Furthermore, it is obvious that near the outlet, the fluctuations bigger. According to the geometry and base case parameters, water flow is dominant initially while time spending, and air volume fraction increase, and these phenomenon cause fluctuations in the mainstream. Figures 9 and 10 demonstrate such facts.

Figure 11 shows velocity contours to clarify the happened physical phenomena in the studied domain.

Figure 12 is a comparison among velocity contours for all cases at plane x=0.0 mm in 5s. As shown, when air velocity is less, airflow cannot overcome the mainstream of water while when air has a higher velocity value, it can dominate water momentum and can cause direction change for the mainstream. To show slug or bubble flow, it is recommended to represent the air volume fraction on the XZ plane. Therefore, Figure 13 is extracted.

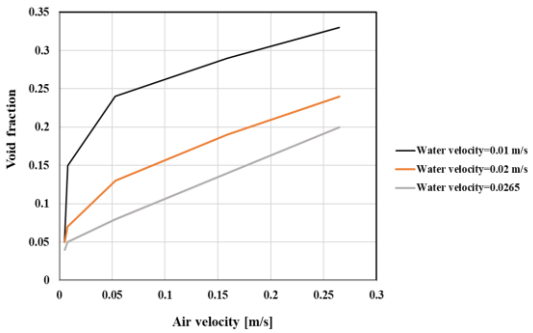


**Figure 6.** The void fraction for different water and air velocities

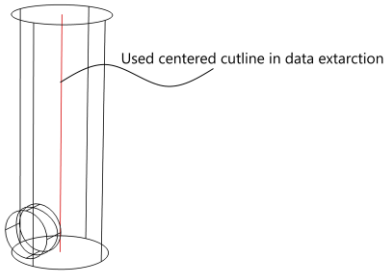


**Figure 7.** Specified centerline in the studied domain

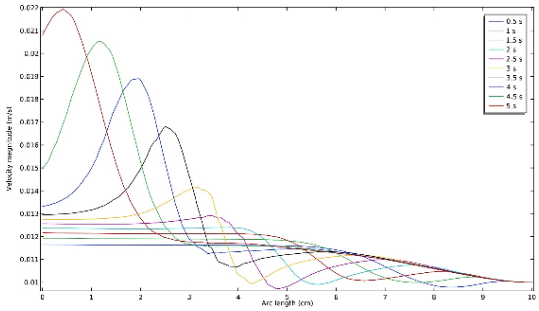


**Figure 8.** Velocity magnitude for base case on the centerline via time

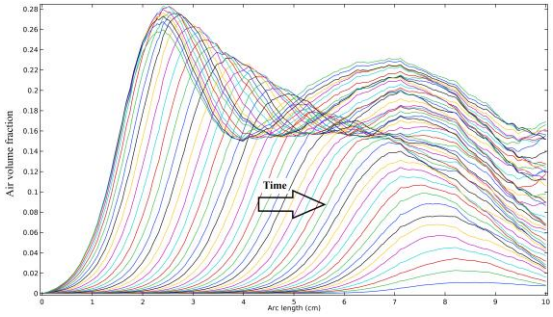


**Figure 9.** Air volume fraction during the time for the base case

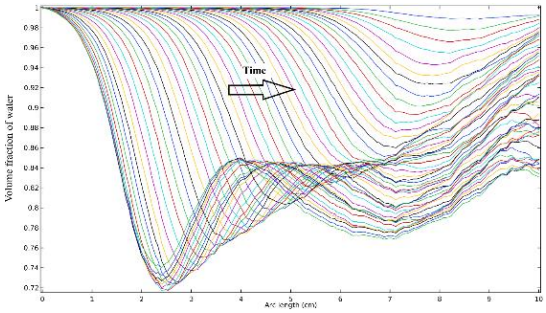


**Figure 10**. Water volume fraction during the time for the base case

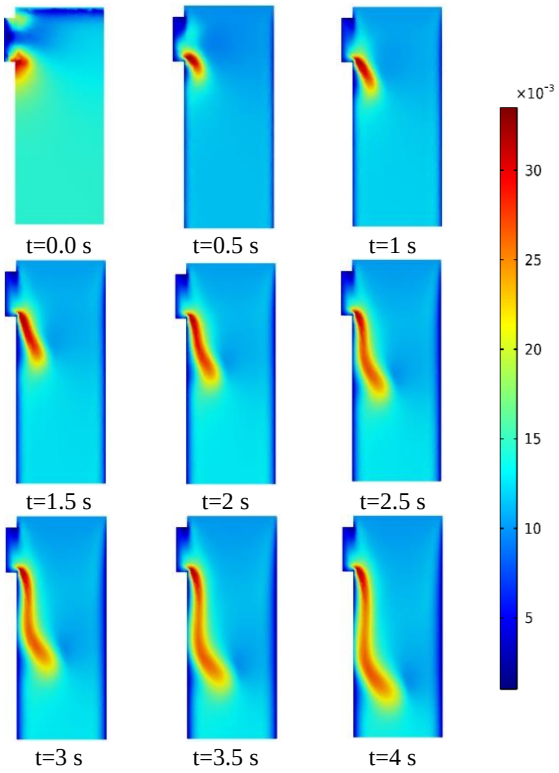


**Figure 11.** Velocity contours for the base case at x=0.0 mm

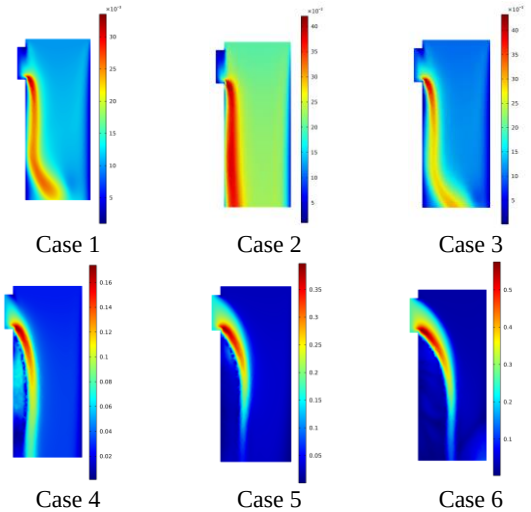


**Figure 12.** Comparison of velocity contours for all cases in 5s at x=0.0

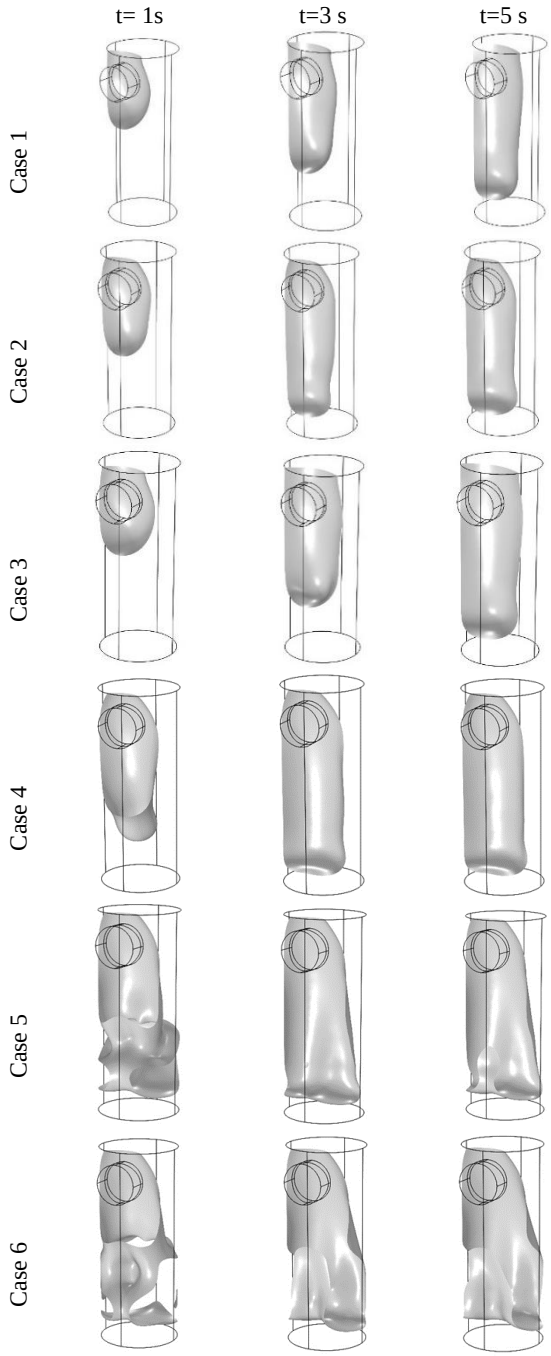


**Figure 13.** 3D void fraction for All cases at 1, 3, and 5s

Figure 13 is the 3D void fraction for all cases. It is clear that the flowing manner in cases 1, 2, and 3 are somewhat similar but after case 4, the flow pattern varies. These changes are more considerable in cases 5 and 6. In fact, with specified water influx and increased air flow rate this happens. To compare the numerical results with the achieved experimental ones, Figure 14 is extracted as follows:

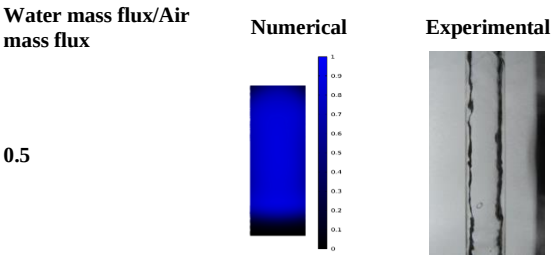

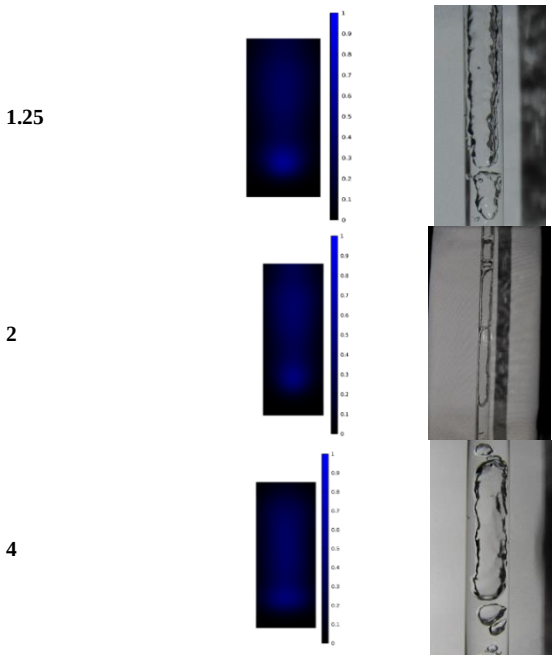


**Figure 14.** Comparison of experimental and numerical results for various ratios of water and air mass flux

## 5. CONCLUSION

The present work included a numerical simulation and an experimental study of downward gas-liquid two-phase flows within a pipe with 10 mm of diameter. The main domain consisted of two inputs for flows. The head input was for water as the liquid phase and the side input was for air as the gaseous phase. In the first step of the numerical investigation, solution mesh independence is investigated then six cases with different mass fluxes were studied. The simulation was transient modeling. To reduce the computation time, just 5 seconds was considered for extracting data. The level set method was utilized to model two-phase interactions. The verification process showed there was a minor deviation between the results of the present simulation and the results of the reported data by others. The achieved results demonstrated that when airflow velocity was low, air momentum could not overcome water momentum so small slugs or massive bubbles were observed but when airflow velocity is more than water one, it can dominate water flow and consequently can affect the mainstream direction. In such cases actually, airflow is dominant and covers almost all core of the pipe. Comparing experimental and numerical results, approximately 9% differences can be found so it shows suitable agreement.

## 6. REFERENCES

1. Jafarmadar, S., "The effects of pressure difference in nozzle's two phase flow on the quality of exhaust mixture", ***International Journal of Engineering, Transactions B: Applications***, Vol. 26, No. 5, (2013), 553-562. doi: 10.5829/idosi.ije.2013.26.05b.12.
2. Tayari, E., Torkzadeh, L., Domiri Ganji, D. and Nouri, K., "Analytical solution of electromagnetic force on nanofluid flow with brownian motion effects between parallel disks", ***International Journal of Engineering, Transactions B: Applications***, Vol. 35, No. 8, (2022), 1651-1661. doi: 10.5829/IJE.2022.35.08B.21.
3. Murai, Y., Inaba, K., Takeda, Y. and Yamamoto, F., "Backlight imaging tomography for slug flows in straight and helical tubes", ***Flow Measurement and Instrumentation***, Vol. 18, No. 5-6, (2007), 223-229. https://doi.org/10.1016/j.flowmeasinst.2007.07.001
4. Golan, L.P., "An air-water study of vertical upward and downward two-phase flow", (1969).
5. Taha, T. and Cui, Z.F., "Cfd modelling of slug flow in vertical tubes", ***Chemical Engineering Science***, Vol. 61, No. 2, (2006), 676-687. https://doi.org/10.1016/j.ces.2005.07.022
6. Hossain, M., Chinenye-Kanu, N.M., Droubi, G.M. and Islam, S.Z., "Investigation of slug-churn flow induced transient excitation forces at pipe bend", ***Journal of Fluids and Structures***, Vol. 91, (2019), 102733. https://doi.org/10.1016/j.jfluidstructs.2019.102733
7. Akhlaghi, M., Mohammadi, V., Nouri, N.M., Taherkhani, M. and Karimi, M., "Multi-fluid vof model assessment to simulate the horizontal air–water intermittent flow", ***Chemical Engineering Research and Design***, Vol. 152, (2019), 48-59. https://doi.org/10.1016/j.cherd.2019.09.031
8. Yue, C., Zhang, Q., Zhai, Z. and Ling, L., "Cfd simulation on the heat transfer and flow characteristics of a microchannel separate heat pipe under different filling ratios", ***Applied Thermal Engineering***, Vol. 139, (2018), 25-34. https://doi.org/10.1016/j.applthermaleng.2018.01.011
9. Gupta, R., Fletcher, D.F. and Haynes, B.S., "Cfd modelling of flow and heat transfer in the taylor flow regime", ***Chemical Engineering Science***, Vol. 65, No. 6, (2010), 2094-2107. https://doi.org/10.1016/j.ces.2009.12.008
10. Ratkovich, N., Majumder, S. and Bentzen, T.R., "Empirical correlations and cfd simulations of vertical two-phase gas–liquid (newtonian and non-newtonian) slug flow compared against experimental data of void fraction", ***Chemical Engineering Research and Design***, Vol. 91, No. 6, (2013), 988-998. https://doi.org/10.1016/j.cherd.2012.11.002
11. Zheng, D., He, X. and Che, D., "Cfd simulations of hydrodynamic characteristics in a gas–liquid vertical upward slug flow", ***International Journal of Heat and Mass Transfer***, Vol. 50, No. 21-22, (2007), 4151-4165. https://doi.org/10.1016/j.ijheatmasstransfer.2007.02.041
12. Abdulkadir, M., Hernandez-Perez, V., Lo, S., Lowndes, I. and Azzopardi, B.J., "Comparison of experimental and computational fluid dynamics (CFD) studies of slug flow in a vertical riser", ***Experimental Thermal and Fluid Science***, Vol. 68, (2015), 468-483. https://doi.org/10.1016/j.expthermflusci.2015.06.004
13. Adegoke, A.S. and Oyediran, A.A., "The analysis of nonlinear vibrations of top-tensioned cantilever pipes conveying pressurized steady two-phase flow under thermal loading", ***Mathematical and Computational Applications***, Vol. 22, No. 4, (2017), 44. https://doi.org/10.3390/mca22040044
14. Wang, L., Yang, Y., Li, Y. and Wang, Y., "Dynamic behaviours of horizontal gas-liquid pipes subjected to hydrodynamic slug flow: Modelling and experiments", ***International Journal of Pressure Vessels and Piping***, Vol. 161, (2018), 50-57. dhttps://doi.org/10.1016/j.ijpvp.2018.02.005
15. Mimouni, S., Fleau, S. and Vincent, S., "Cfd calculations of flow pattern maps and les of multiphase flows", ***Nuclear Engineering***

***and Design***, Vol. 321, (2017), 118-131. https://doi.org/10.1016/j.nucengdes.2016.12.009

16. Zhou, H., Guo, L., Yan, H. and Kuang, S., "Investigation and prediction of severe slugging frequency in pipeline-riser systems", ***Chemical Engineering Science***, Vol. 184, (2018), 72-84. https://doi.org/10.1016/j.ces.2018.03.050
17. Tay, B.L. and Thorpe, R.B., "Hydrodynamic forces acting on pipe bends in gas–liquid slug flow", ***Chemical Engineering Research and Design***, Vol. 92, No. 5, (2014), 812-825. https://doi.org/10.1016/j.cherd.2013.08.012
18. Montgomery, J., "Severe slugging and unstable flows in an s-shaped riser", (2002).
19. Malekzadeh, R., Henkes, R. and Mudde, R., "Severe slugging in a long pipeline–riser system: Experiments and predictions", ***International Journal of Multiphase Flow***, Vol. 46, (2012), 9-21.
20. Xie, C., Guo, L., Li, W., Zhou, H. and Zou, S., "The influence of backpressure on severe slugging in multiphase flow pipeline-riser systems", ***Chemical Engineering Science***, Vol. 163, (2017), 68-82. https://doi.org/10.1016/j.ces.2017.01.028
21. Assari, M., Basirat Tabrizi, H., Jafar Gholi Beik, A. and Shamesri, K., "Numerical study of water-air ejector using mixture and two-phase models", ***International Journal of Engineering, Transactions B: Applications***, Vol. 35, No. 2, (2022), 307-318. doi: 10.5829/ije.2022.35.02b.06.
22. Han, B., Ge, B., Wang, F., Gao, Q., Li, Z. and Fang, L., "Void fraction detection technology of gas-liquid two-phase bubbly flow based on convolutional neural network", ***Experimental Thermal and Fluid Science***, Vol. 142, (2023), 110804. https://doi.org/10.1016/j.expthermflusci.2022.110804
23. Graf, U. and Papadimitriou, P., "Simulation of two-phase flows in vertical tubes with the ctfd code flubox", ***Nuclear Engineering and Design***, Vol. 237, No. 20-21, (2007), 2120-2125. https://doi.org/10.1016/j.nucengdes.2007.02.011
24. Oshinowo, O., "Two-phase flow in a vertical tube coil", University of Toronto, (1971),
25. Jiang, Y. and Rezkallah, K.S., "A study on void fraction in vertical co-current upward and downward two-phase gas-liquid flow—i: Experimental results", ***Chemical Engineering Communications***, Vol. 126, No. 1, (1993), 221-243. https://doi.org/10.1080/00986449308936220
26. Usui, K. and Sato, K., "Vertically downward two-phase flow,(i) void distribution and average void fraction", ***Journal of Nuclear Science and Technology***, Vol. 26, No. 7, (1989), 670-680. https://doi.org/10.1080/18811248.1989.9734366
27. Nguyen, V.T., "Two-phase, gas-liquid concurrent flow: An investigation of holdup, pressure drop and flow pattern in a pipe at various inclinations", ResearchSpace@ Auckland, (1975),
28. Vatani, M. and Domiri-Ganji, D., "Experimental examination of gas-liquid two-phase flow patterns in an inclined rectangular channel with 90 bend for various vertical lengths", ***International Journal of Engineering, Transactions A: Basics***, Vol. 35, No. 4, (2022), 685-691. doi: 10.5829/IJE.2022.35.04A.07.

## Persian Abstract

**چکیده**

در این مقاله، شبیه‌سازی سه‌بعدی همراه با مشاهدات تجربی برای مطالعه جریان دو فازی در یک لوله عمودی انجام گرفت. برای تجزیه و تحلیل هوا و آب از نرم افزار Open FOAMاستفاده شد. جریان اصلی رو به پایین که در داخل یک لوله عمودی به قطر ۱۰ میلی متر بود در نظر گرفته شد. مطالعه شامل دو ورودی برای جریان بود: ورودی بالایی برای آب و ورودی جانبی برای هوا. چندین حالت با شار جرمی مختلف برای آب و هوا مورد مطالعه قرار گرفت. بر اساس فیزیک موضوع، شبیه سازی عددی وابسته به زمان در نظر گرفته شد. نتایج به‌دست‌آمده نشان داد که وقتی سرعت هوا دارای مقادیر کمتری است ، تکانه هوا نمی‌تواند بر تکانه آب که منجر به اسلاگ های کوچک می شود غلبه کند. هنگامی که سرعت جریان هوا بیشتر از آب بود، بر جریان آب تسلط داشت و در نتیجه می‌توانست جهت جریان اصلی را تحت تأثیر قرار دهد. همچنین نمودارهای سرعت روی خط مرکزی نشان می‌دهند که هر چه زمان پیش می رود، بزرگی سرعت مقدار قابل توجهی از نوسانات را تجربه می‌کند و نوسانات بزرگ در نزدیک خروجی رخ می‌دهد. مقایسه نتایج تجربی و عددی، با تقریباً ۹ درصد اختلاف، تطابق قابل قبولی را نشان داد. نتایج نشان داد که در مراحل اولیه، تخلخل با افزایش مقدار قابل توجهی همراه است. شدت این تغییر در مقادیر تخلخل در سرعت کمتر آب بیشتر بود. در واقع، با افزایش سرعت آب، نیروهای اینرسی مرتبط با فاز مایع نقش غالبی در هیدرودینامیک کلی جریان گاز– مایع پیدا می‌کنند. همچنین بدیهی است که نحوه جریان در موارد ۱، ۲ و ۳ مشابه است اما پس از مورد ٤، الگوی جریان متفاوت است. این تغییرات در موارد ۵ و ٦ بیشتر قابل توجه است.

International Journal of Engineering

Journal Homepage: www.ije.ir

# Experimental Analysis and Physical Mechanism Investigation of $Al_2O_3$ Effect on New and Aged Transformer Oil Properties

A. H. Mashhadzadeh[a], S. M. Seyyedbarzegar[*b], A. Samani[c]

[a] *Department of Electrical Engineering, Gorgan Branch, Islamic Azad University, Gorgan, Iran*
[b] *Department of Electrical Engineering, Shahrood University of Technology, Shahrood, Iran*
[c] *Department of Electrical Engineering, Islamic Azad University, Science and Research Branch, Tehran, Iran*

*PAPER INFO*

*Paper history:*
Received 21 October 2022
Received in revised form 24 Desember 2022
Accepted 01 January 2023

*Keywords*:
*Transformer Oil*
*Breakdown Voltage*
*Partial Discharge*
*Thermal Aging*
*Physical Mechanism*

*ABSTRACT*

$Al_2O_3$ nanoparticles were used to improve the performance of the vital properties of transformer oil (TO) under normal operating conditions and when subjected to thermal aging. Different weight percentages of $Al_2O_3$ in the TO were considered to maximize the breakdown voltage (BDV). $Al_2O_3$ nanofluid (NF) increases the BDV by 116% (31.1 kV to 67.4 kV) and the heat transfer by 33.4%, and also minimizes partial discharge (PD) by 66%. The reduction of PD is also related to the ability of $Al_2O_3$ to adsorb hydrogen and acetylene, two oil-soluble gases that are effective in PD. Even $Al_2O_3$NF was more resistant to water content in TO. BDV for TO and $Al_2O_3$NF, when water content increased to more than 30 ppm, were reduced by 57% and 19%, respectively. According to Arrhenius equation, both samples were placed at 120°C for 29 days to age samples (equivalent to about 30 years). Aged $Al_2O_3$NF has continued its exceptional performance and improved BDV by 121% compared to aged TO, and also $Al_2O_3$NF showed its capacity well and improved PD compared to aged TO by 71%. All the favorable properties of $Al_2O_3$NF are conditional on the stability of $Al_2O_3$. FESEM confirms the stability of $Al_2O_3$.

***doi***: *10.5829/ije.2023.36.03c.15*

## 1. INTRODUCTION

Transformers, which account for almost 60% [1] of the network cost, provide the connection between production and consumption due to changes in voltage level [2]. Transformer oil acts as a very important insulating part of the transformer. It plays a decisive role in its life [3].

The oil that is inside the transformers and is moving between the various internal components. It is like blood ins human body [4]. Examination of oil-soluble gases, such as a blood test or a scan of the human body, can warn about the internal failers of the transformer and an increase in the probability of its proper function [5].

During normal and electrical faults (breakdowns, partial discharges (PDs)) operation, the oil in power transformer ages and decompositions, breaking specific C-C and C-H bonds in the oil molecules. These conditions lead to the release of gases in the oil [6, 7]. Acetylene, carbon dioxide, methane, ethylene, carbon monoxide and hydrogen are the six main defective gases that dissolve in transformer oil (TO) [8]. Soluble gases in the oil cause a PD, which should not be underestimated. Among the mentioned gases, hydrogen and acetylene have the most severe damages and are also the most critical factors in the formation of PD [9, 10].

In general, oil performs two basic functions, cooling and insulation. It has been used for more than a century to insulate the electrical components of transformers and to transfer the heat generated in the transformer winding [11]. The two inhibiting factors for maximum power transfer and reducing the size of the transformer are the thermal and insulating properties of the oil [12]. The thermal conductivity of the oil in the transformer is usually not high, which weakens its cooling performance and ultimately reduces the life of the transformer [13, 14]. In addition, transformer operation and the aging of the

*Corresponding Author Instutional Email: seyyedbarzegar@shahroodut.ac.ir (S. M. Seyyedbarzegar)

Please cite this article as: A. H. Mashhadzadeh, S. M. Seyyedbarzegar, A. Samani, Experimental Analysis and Physical Mechanism Investigation of $Al_2O_3$ Effect on New and Aged Transformer Oil Properties, ***International Journal of Engineering, Transactions C: Aspects,*** Vol. 36, No. 03, (2023) 548-557

oil, the breakdown voltage (BDV) is significantly reduced. One of the ways to improve the properties of oil is to use nanoparticles (NPs) and make a nanofluids (NFs) based on oil. NPs generally have a higher thermal conductivity. NPs help to increase the thermal conductivity of pure oil and even increase the BDV in some cases [15].

The experimental investigation has showed that the thermal conductivity of nanofluids is characterized by several dynamics such as volume or mass fraction of NPs, NPs type, NPs shape and size. Thermal conductivity mineral oil-based nanofluids with various volume concentrations suspended with $Al_2O_3$ (with 20 nm diameter) NPs has been examined by Timofeeva et al. [16]. About 4% of Nps was noted for the maximum improvement in thermal conductivity. Also, the investigation of the thermal conductivity of NFs with a rise in NPs concentrations has been reported by Jin [17] and Ilyas et al. [18]. In this study, a maximum enhancement about 16% in thermal conductivity at three wt% NPs concentrations has been achived. The thermal conductivity of MWCNT NPs based NFs has been investigaion for NPs effects on TO by Aberoumand and Jafarimoghaddam [19]. The results embodied an improvement of 160%. The author revealed that attributes of NPs cause this vast increase. They experimentally performed $Ag/WO_3$ hybrid NF in TO in three different weight fractions of 1, 2, and 4%. According to obtained results, the hybrid NFs used at a higher weight fraction and a temperature at100 ° C have increased the thermal conductivity by 41% [19]. Bhunia et al. [20] improve that $TiO_2$ (50–70 nm) with weight fractions (0.005 wt%) provide almost 13–23% thermal conductivity enhancement. Mansour et al. [21] showed barium titanate (BTO) NPs were inserted into the base TO by a concentration of 0.005 g/L. This insertion enhances the heat transfer coefficient by 33%. Parvar et al. [22] showed that the thermal conductivity of ZnO nanoparticles is higher than pure TO at 25°C. By adding this NPs to TO, it has shown that the thermal conductivity of NF increased by increasing NPs concentration in TO. Under these conditions, at volume fractions of 0.05% and 1% NPs in TO, the thermal conductivity increased approximately by 4.61% and 11.53%, respectively.

Babu and Babu [23] used nanocrystal nickel-manganese ferrite at different concentrations. In their article, the effect of increasing concentrations on the increase of dielectric strength was investigated. As a result, the concentration of 0.04 g/L showed a great increase in breakdown of voltage, about 42.3% [23]. Electrical strength and stability of $SiO_2$, $Al_2O_3$ and $TiO_2$ based NFs at different concentrations were investigated by Paul et al. [24] for TO. The reported data showed the highest breakdown of voltage for $Al_2O_3$ at a concentration of 0.06 g/L [23]. Oparanti et al. [25] utilized $TiO_2$, $Al_2O_3$, and $MoS_2$ NPs in TO and showed that the dielectric strength of $TiO_2$ was higher than the other samples. Electrical BDV in TO NFs with NPs such as ZnO, MgO, $Al_2O_3$, $TiO_2$, $SiO_2$, graphite, $LiTaO_3$ and $Fe_3O_4$ was investigated by Moghadassi et al. [26]. Electrical breakdown was studied for NFs based on ester oil at 0.2 to 1 weight percentage of $Al_2O_3$ nanoparticles. They observed that $Al_2O_3$ (at 0.6wt%) NPs improve the BDV of ester oil to 29kV [25]. As you can see, various valuable studies have been done on the effect of NPs on the improvement of BDV and thermal properties. However, as far as the author's knowledge, less research has been done on reducing the PD (as one of the essential properties of TO) in oil using NPs as well as improving the BDV and heat transfer simultaneously. Failure to consider PD in applying NPs in TO is a vast and severe gap in research on this subject. Also, one of the other issues is the stability of nanomaterials in the oil, which can be said that almost less attention has been paid. This lack of awareness and research has been done while all the properties of NPs in oil (and their function) have a natural and extraordinary relationship to stability. On the other hand, in normal operating conditions of the transformer, it is often subjected to different stress conditions and causes the oil to move towards aging. So, the function and stability of NPs inside the oil should not be neglected when aging occurs.

In this paper, $Al_2O_3$ was used to reduce the partial discharge, improving the BDV and TO heat transfer under normal and thermal aging conditions. Another fundamental goal that has been studied in this research is to provide an obvious and accurate sight of the relationship between PD and gas-soluble bubbles, as well as the physical mechanism of $Al_2O_3$NPs in oil. $Al_2O_3$ and a two-stage method have been used to make the NF. Several samples of NF were prepared by considering different amounts of NPs. NF was regarded as the primary sample whose BDV was maximized. Stability is the fundamental problem in using NPs in oil, which were photographed FESEM to prove the stability of $Al_2O_3$NPs. In the next step, laboratory tests (BDV, gas Chromatography, moister effect on BVD, heat transfer, total acid number (TAN), PD) were performed on the samples. In the last stage of the laboratory test, to comprehensively evaluate the performance and stability of $Al_2O_3$ in the TO, the oil is thermally aged using the Arrhenius equation and examined (BDV, TAN, PD). Finally, the physical mechanism of $Al_2O_3$NP function was investigated.

## 2. MATERIALS AND METHODS

**2. 1. Materials** Table 1 summarizes the specifications of NP that was purchased from US Research Nanomaterials, Inc. (USA). As can be seen, $Al_2O_3$ has a purity of more than 99% and a heat transfer

**TABLE 1.** NP specifications

| Nano particle | Purity | Color | Specific heat capacity | Density |
|---|---|---|---|---|
| $Al_2O_3$ (20 nm) | 99+% | White | 880 J/(kg-K) | 3890 kg/m$^3$ |

coefficient of 880 J/(kg-K), which indicates a relatively high power to improve the thermal transfer coefficient of the final nano oil. The average particle size (APS) is 20 nm.

**2. 2. NF Prepration Methods** Single-step and two-step designs are usually used for preparation of NF. The single-phase method involves the simultaneous development and dispersion of particles in the fluid. Drying, storage, transfer, and dispersion of NPs are avoided in single-phase process. Therefore, the accumulation of NPs is limited and fluid stability has increased [26]. Single-phase systems have the ability to produce nanoparticles with homogeneous distribution. Based on this, particles can be placed in a liquid at stable condition. This process has advantages due to the control of NP size, reduction of NP aggregation, and development of NFs including metal NPs. In addition to being expensive, this method is not able to produce NFs on a large scale. Another major drawback associated with the single-phase process is that the development of NFs with high volume loadings of NPs is very challenging.

The two step process is commonly used to synthesize NFs by stirring NPs in the base fluids. Typically, two steps are involved in this technique. NPs are commercially available and are produced using physical, chemical and mechanical methods at the first step. The most important physical, chemical and mechanical methods are crushing, grinding, sol-gel. Then, in the second phase the dry NPs are dispersed in the base liquids using ultrasound, magnetic mixing, and high shear agitation. During this phase, some activities, for example, the incorporation of scattered materials or ultrasound, are usually performed to improve the stability of the derived NFs [27].

The two-step process is usually used to prepare $Al_2O_3$NF [28]. By using this method, it has been shown that $Al_2O_3$ has excellent stability [23]. As shown in Figure 1, $Al_2O_3$ and mineral oil are first throughly mixed in a magnetic stirrer for 30 minutes. In the next step, the sample is placed in a sonic device for 30 minutes to obtain a homogeneous mixture. In the last stage, to achieve high accuracy in the test results and complete removal of oil-soluble gases (which occurs in the previous steps), the solution is kept at a pressure of less than 1 kPa for 48 hours. It is very important to mention two points. First, the initial moisture content of the NPs has been tried to be very low so as not to aberration the test results (for 10 h at 160 °C), and second, all the above steps have been performed at environment temperature.

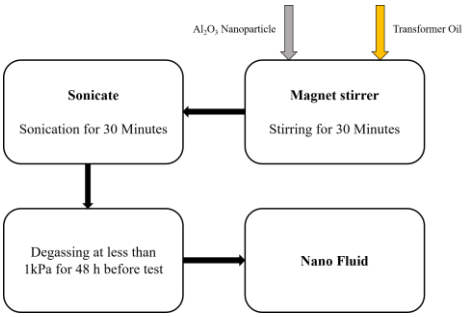


**Figure 1.** Two steps method for $Al_2O_3$NF preparation

One way to prove the uniform distribution of NPs in oil is to use field emission scanning electron microscopy (FESEM). FESEM is used to visualize tiny topographic details on the surface. This technique is used to observe structures with several nanometers in size. FESEM is consequential in two ways: 1) Evidence of homogeneous dispersion of NPs in the oil 2) Displacement of APS. FESEM photo of NF can be seen in Figure 2. As it turns out, 1) NPs are well dispersed and stabled; 2) APS of $Al_2O_3$ is 20 nm. The importance of NP stability is analyzed in section 5.

## 3. EXPERIMENTAL TEST

As mentioned above, TO as a liquid insulator is a type of insulating oil with suitable electrical and thermal insulating properties. Two functions of TO that are related to the life of the transformer are cooling and electrical insulation. The TO deteriorates over time due to operating conditions. These conditions affect the performance of the transformer. Therefore, checking the status of the TO during the operation period is vital. For this purpose, testing sequences and procedures are defined by different international standards. In this section, some critical electrical tests on oil insulation are evaluated.

**3. 1. Breakdown Voltage** The insulating strength of TO is considered one of its electrical properties in oil testing. The BDV test is introduced in this regard. BDV

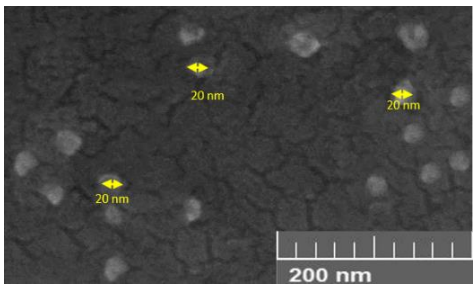


**Figure 2.** FESEM micrographs provided from $Al_2O_3$ NP

is determined based on the voltage level that flashover occurs between two electrodes at a certain distance. BAUR PGO S-3 device was used for this test and the procedure is described in Standard Method ASTM D1816. According to the standard, two electrodes are fixed with a gap of 2.5 mm, and voltage is applied to them. The rate of rising of the applied voltage is controlled at 2 kV/s. As the voltage increases, the amount of voltage is recorded when the first discharge occurs between electrodes. After pouring the oil into the test vessel, it is rested for 10 minutes, and then the voltage is applied. This test is performed six times with an interval of 1 minute, and at the end, the average of the obtained results is considered BDV. All experiments were conducted at room temperature and power frequency (50 Hz).

**3. 2. Gas Chromatography** To obtain the number of dissolved gases in TO, gas chromatography method has been used. Acetylene, carbon dioxide, methane, ethylene, carbon monoxide and hydrogen are the six main defective gases that dissolved in TO. Determining the amount of $H_2$ and $C_2H_2$ in base oil and NF is crucial to investigate and prove the performance of $Al_2O_3$NF in the PD process.

**3. 3. Water Content** Water, as a destructive factor, reduces the boiling point of TO, premature aging of TO, and degrades the insulating properties of paper insulation. The moisture in the paper insulation has the ability to transfer to the oil, which increases the oxidation level, which will increase the water and acid content in the oil. Therefore, it is necessary to always control the water content of TO, which has been carried out using the necessary tests by the METHROM 831 device under ASTM D877 standard.

**3. 4. Heat Transfer Test** The use of nanoparticles in TO has been investigated as a new method to improve heat transfer. In general, the goal is to increase the thermal conductivity and reduce the heat produced. One of the most practical ways to measure heat transfer is to use the immerse heating method [29]. The selected sample must first be placed in a particular container to use this method. Then, to increase the temperature inside the oil, an element must be placed inside it. To monitor the temperature inside the sample, place a thermometer at a fixed distance from the element. The element must be connected to a constant voltage source in the next step. In order to ensure equal conditions of the element in experimental samples, its voltage and current are monitored. In the final stage, to check the temperature transfer, temperature changes are recorded in seconds.

**3. 5. Total Acid Number** The acid concentration in TO is defined as the oil's TAN. The standard unit for measuring TAN is mg KOH/g. Generally, it refers to the milligrams of potassium hydroxide (KOH) necessary to countract free acids in 1 gram of oil. Based on ASTM D974 standard, transformer oil TAN has been measured. The main source of acid production in TO is oil decay/oxidation. The TAN in the oil detriment the structure of insulation and can raise the corrosion intensity of inside parts of transformer in the existence of moisture.

**3. 6. Partial Discharges** According to Standard IEC 60343, PD in TO is localized insulating discharge in a limited volume of liquid insulation when subjected to high voltage electrical stress. According to mentioned standard, the distance between the needle and plane electrode was set to 1 mm. PD is one of the sources of deterioration of TO, which can even lead to electrical discharge in the oil. The PD apparent charge quantity is measured and recorded to measure PD. In this regard, the base charge is significant in measuring PD and must be present in minimal amounts. PD pulses created in the oil were conditioned in the electronic coupling device, connected to a coupling capacitor, and processed in the measuring instrument. Due to the very high sensitivity of PD measurements to noise, it is necessary to calibrate the measuring device to achieve high accuracy. A JDEVS-PDMA 300 was utilized for PD test. PD signals were sense by the PD detector device at a voltage of approximately 32% of each sample's BDV. This voltage was considered as the PD initial voltage. This experiment aimed to decrease the quantity of PD in the TO by NPs; the applied voltage was approximately 40% of that of the BDV of each sample to ensure the conditions of PD [30].

**3. 7. Thermal Aging** Destruction of electrical insulation plays an important role in the aging of the transformer and reducing its life. Increasing heat in the insulation can lead to its decomposition, which can intensify this process. The losses of Core and coil in operating transformers cause considerable internal heat. If it does not transfer out quickly, it can increase the insulation system's aging rate and shorten the unit's life. In addition to what was said about aging, humidity is another important factor. In fact, the creation of oxygen in the transformer oil along with other gases in it leads to the production of water [31]. Figure 3 represents a superficial schematic of the decomposition mechanism of transformer insulation. Aluminum and iron are the main components of the body and winding of transformers, and nothing can be done to remove them. Still, moisture and $O_2$ play a significant role in transformer oil degradation. Therefore, in examining the aging process of oil, moisture and $O_2$ must be monitored.

Arrhenius equation has been used for the thermal aging of oil. Pure oil and $Al_2O_3$NF were placed at 120°C for 29 days for accelerating aging. By increasing the

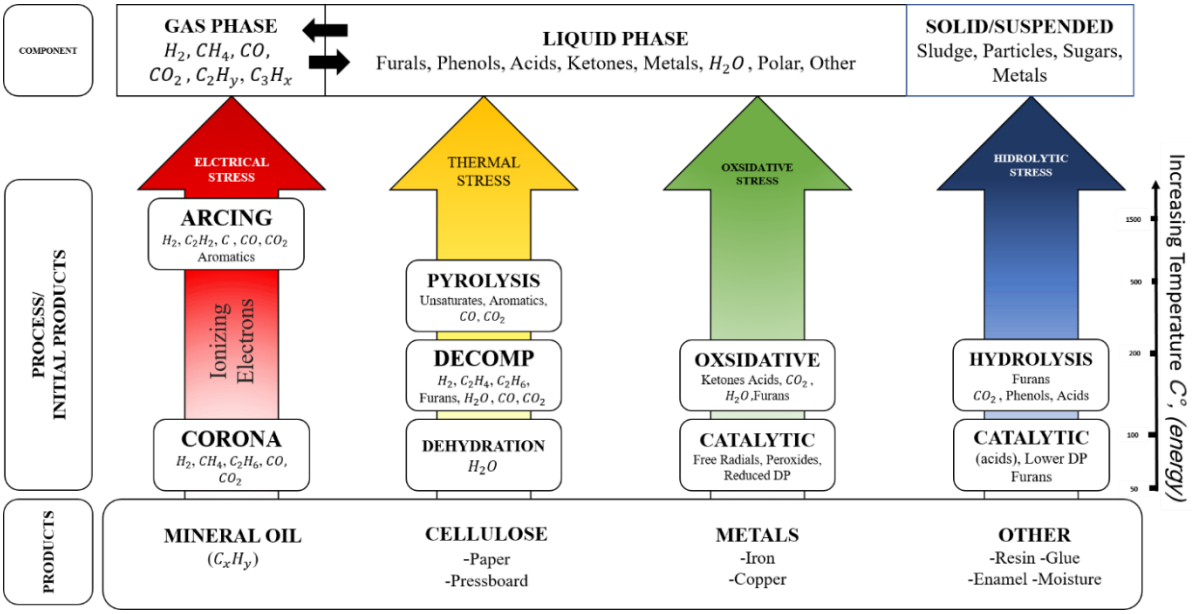


**Figure 3.** schematic of the decomposition mechanism of transformer insulation

temperature by 7°C from the reference temperature (60°C), it is possible to halve the lifetime of the insulating material. Hence, accelerated thermal aging for 29 days at 120°C approximates 30 years [32]. Both aged samples were taken out periodically for BDV and TAN tests during this process.

## 4. RESULTS AND DISCUSSION

**4. 1. Pure Oil and $Al_2O_3$ NF Test Results** The amount of BDV is one of the essential factors in TO. To improve the properties of the oil using NPs, the BDV should be increased as much as possible. For this purpose and to achieve the maximum BDV, five samples of NFs with values of 0.01, 0.05, 0.1, 0.02, and 0.3 g/L of $Al_2O_3$ NPs were considered. The point to pay special attention is that the water content is less than 10 ppm in all samples, and all tests are performed at room temperature.

The BDV diagram for the base oil and the other five NFs is shown in Figure 4. As can be seen, for TO and NFs with concentration of 0.01, 0.05, 0.1, 0.02, and 0.3 g/L, the BDVs are 31.1, 60.9, 67.4, 62.6, 56.7 and 50.1 kV, respectively. The BDV is maximized for 0.05 g / l. NF, in this case, has been able to improve the BDV by about 116%, which is very impressive. For all NFs, the BDV is greater than pure oil. Because the BDV is one of the essential properties of TO, to maximize the BDV, 0.05 g/L of $Al_2O_3$ is used to achieve the desired $Al_2O_3$NF. The results obtained up to 0.05 g/L can be justified: By increasing NP concentration up to 0.05 g/L, the amount of charge traps and as a result BDV increases. Meanwhile, for concentrations higher than 0.05 g/L,

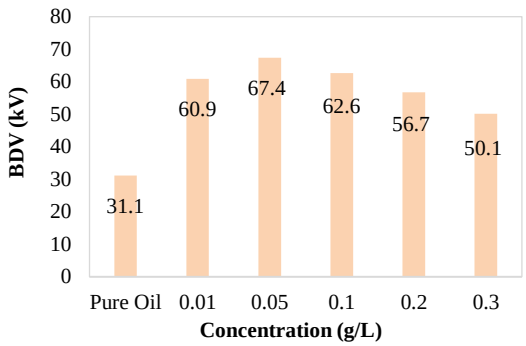


**Figure 4.** The BDV of TO/$Al_2O_3$ NFs

BDV decreases due to the accumulation of nanoparticles. However, the reversible NP aggregation caused by the electric field improves the BDV due to the catch of free electrons.

The presence of acid content in transformer oil is unavoidable due to its operating conditions. The TO and NF TAN values are 0.03 and 0.01, respectively. These values indicate that the TAN value was within the allowable range for both samples, and the NF (albeit a small one) was even able to reduce it. Table 2 shows the amount of $H_2$ and $C_2H_2$ gases in the TO and $Al_2O_3$NF samples. As can be seen, $Al_2O_3$NF reduced the amount of $H_2$ from 67 to 9 ppm (86% reduction) and the amount of $C_2H_2$ from 198 to 53ppm (73% reduction).

The water content must be low and equal in range to perform a BDV test. Otherwise, the values obtained for the BDV will not be valid. The water content test results prove that water content is less than 10 ppm for both

**TABLE 2.** Amount of $H_2$ and $C_2H_2$ after GC test, TAN for samples

| $H_2$ (ppm) | TO | $Al_2O_3NF$ |
|---|---|---|
| | 67 | 9 |
| $C_2H_2$ (ppm) | 198 | 53 |
| TAN (mg KOH/g) | 0.03 | 0.01 |

samples. An experiment was designed to demonstrate the destructive effect of moisture inside TO. Thus, four samples of TO and four $Al_2O_3NF$ with different water content were provided. The moisture effect on the BDV of TO and $Al_2O_3NF$ is shown in Figure 5. It is pretty evident that the BDV decreases from 31.1 kV to 13.2 kV by increasing the amount of moisture in the oil from less than 10 to more than 30 ppm, which indicates a 57% decrease in the BDV. For the same moisture inside the $Al_2O_3NF$, the BDV decreases from 67.4 to 54.5 kV, representing a 19.1% reduction. As can be seen, as the water content increases, the $Al_2O_3NF$ experiences a smaller percentage reduction in the amount of BDV than the MO. One of the reasons for this is the ability of $Al_2O_3$ to absorb $H_2$ as one of the constituents of water in MO.

Figure 6 illustrates the results obtained from the immerse heating method. Both samples' temperature changes were recorded from ambient temperature (25 °C) to 80 °C. As can be seen, the oil has risen from 25 to 80 °C in 560 seconds. On the other hand, Nano oil only needs 373 seconds to cross the same path. This result shows that the temperature in nano oil is transferred to the base oil 33.4% faster, and in the transformer operation, it can transfer heat from the warmer part of the transformer to the lower temperature parts in less time. There are many cases of transformer explosions. Increasing the thermal conductivity of TO reduces the flammability of TO and expands the safety point of view.

One of the tests that show the effect of NPs on oil performance is the PD test. Parameters such as the number of charges and the phase angle can be achieved using this test. The number of charges of TO is equal to 1373. The phase angle variations of PD based on

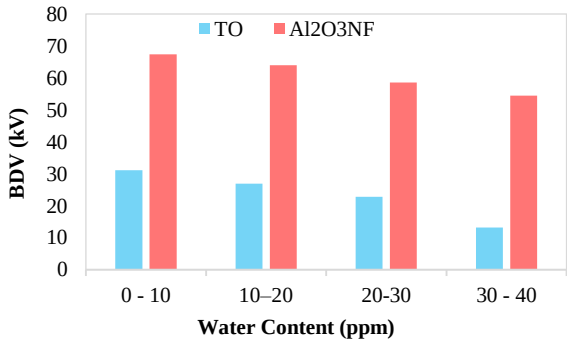


**Figure 5.** Effect of moisture on the BDV

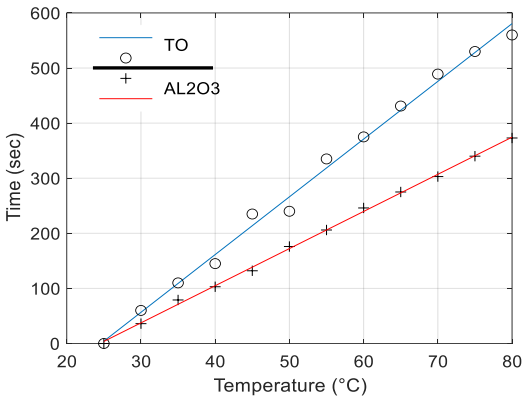


**Figure 6.** The time required to increase the temperatures

reference sinusoidal voltage waveform is shown in Figure 7(a). Based on the presented result for TO, the PD has occurred between $45 < \varphi < 135$ at positive or negative cycle of the reference waveform. However, most PD with larger amplitudes are seen at angles less than 90 degrees.

Using the $Al_2O_3$, the number of charges in $Al_2O_3NF$ sample has reduced by 66%. The number of charges in $Al_2O_3NF$ is equal to 461. As shown in Figure 7(b), the trend of phase angle variation of $Al_2O_3NF$ is similar to TO. The comparison of TO and $Al_2O_3NF$ at the same phase angles shows a decrease in the PD number and amplitude. The change of phase angle in the positive

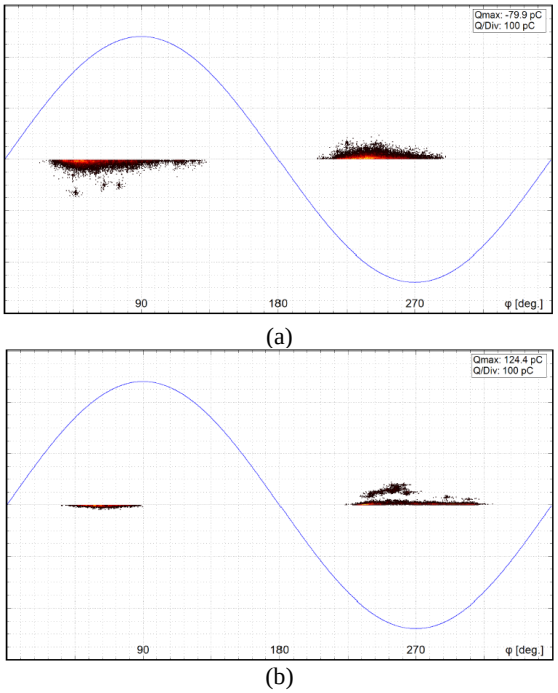


**Figure7.** The phase angle variations of PD based on reference sinusoidal voltage waveform (a) for TO; (b) for $Al_2O_3NF$

cycle to less than 90 degrees indicates the proper performance of the $Al_2O_3$ to control the PD in the oil. The oil insulation performance against PD activity is improved via the NPs proposed in this paper.

**4. 2. Aged Oil and $Al_2O_3$ NF Test Results** Three essential properties of the TO, which are very important and decisive in its performance in aging, are BDV, PD and TAN. Figure 8 shows the average value of TO and $Al_2O_3$NF BDV in the aging state. As you can see, the BDV for TO starts at 31.1 kV and decreases to 20.4 kV after 29 days, which is a 34% reduction. The decreasing trend of oil BDV is due to oil aging. This reduction for NF also remains strong. The BDV for the $Al_2O_3$NF starts at 67.4 kV and decreases after 29 days to 45.2 kV (33% reduction).

Figure 9 shows the TAN for aged TO (ATO) and NF samples. The point to note is that according to ASTM D974, the maximum number of acids is 1.2 mg KOH/g. As the aging process begins and MO's ages increases, the amount of TAN also increases so that the TAN of the ATO at the end of 29 days is more than the allowable limit and has a value of 1.4 mg KOH/g. This result indicates a very unsatisfactory condition of the ATO load after the aging process. The situation does not change much for $Al_2O_3$NF, and the TAN for $Al_2O_3$NF increases with an increase in thermal aging of the NF. But the exciting point is that the $Al_2O_3$NF has been able to comply with the permissible limit and maintain the oil condition better.

PD is one of the things that changes due to the aging of the oil. Based on the aging process used in this paper, the parameters used for PD were investigated. The number of charges in ATO has increased to 2781. This amount has increased by 102% compared to TO. Under these conditions, the angle of occurrence of PD has increased and, according to Figure 10, the angle is approximately between $45 < \varphi < 135$ . These conditions are different from the performance of TO and indicate variations in the oil's PD.

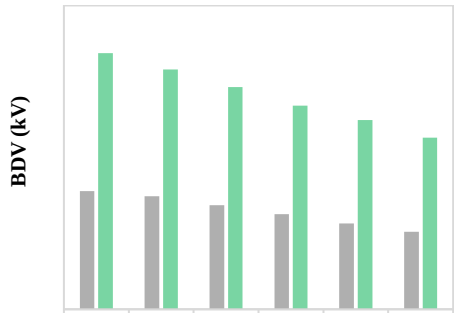


| Days | 0 | 6 | 12 | 18 | 24 | 29 |
|---|---|---|---|---|---|---|
| TO | 31.1 | 29.8 | 27.4 | 25 | 22.6 | 20.4 |
| Al2O3NF | 67.4 | 63.1 | 58.5 | 53.6 | 49.8 | 45.2 |

**Figure 8.** Mean BDV for aged TO and NF

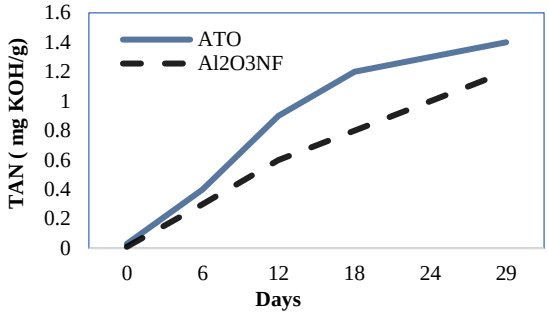


**Figure 9.** TAN values for ATO and $Al_2O_3$NF

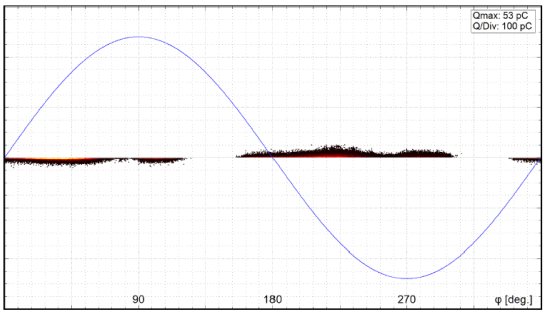


**Figure 10.** The phase angle variations of PD based on reference sinusoidal voltage waveform for ATO

The result presented in Figure 11 shows that the repetition of the oil aging process with the $Al_2O_3$NF has caused variations in the PD parameters. Based on this, it is possible to improve the oil properties of TO and aged ones. The reduction in the number of charges is significant. PD reduced to 801, which shows the addition of $Al_2O_3$ prevents the occurrence of PD in the aged oil by about 71%. A significant result of the suitable performance of the NP is the change in PD's angle, which is between 45 and 135 degrees. These situations, along with reducing the number of charges, indicate the improved ATO performance in combination with the $Al_2O_3$.

Figure 12 presents the immerse heating method for both samples after thermal aging. Both samples' temperature changes were recorded from ambient temperature (25 °C) to 80 °C. As can be seen, the ATO temperature has risen from 25 to 80 °C in 631 seconds. Aged-NF needs 398 seconds to reach 80°C. This result shows that the temperature in Aged NF transferred 36.9% faster than ATO. Also, transformer oil is about 13% less capable of moving heat in the aging state than before.This is about 7% for nanofluids.

## 5. PHYSICAL MECHANISM

The performance of NPs in this work can be split into two general aims: improving electrical and thermal

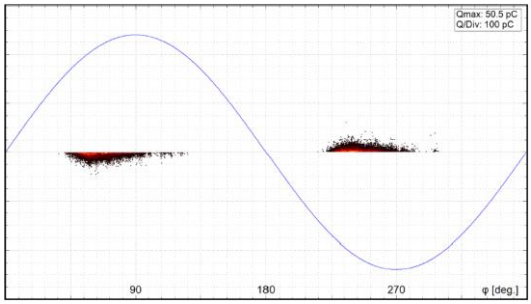


**Figure 11.** The phase angle variations of PD based on reference sinusoidal voltage waveform for aged $Al_2O_3$NF

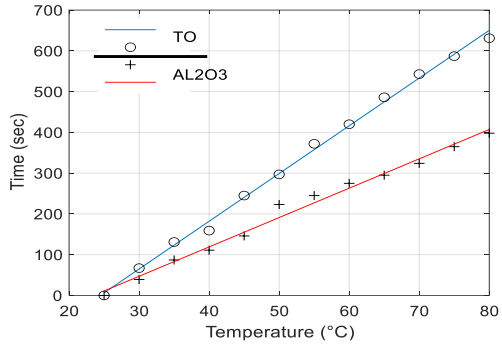


**Figure 12.** The time required to increase the temperatures for both samples in aging mode

properties. The mechanism of NPs action in improving the BDV is that the NPs trap and absorb electrons. In other words, this NP acts as an electron absorber in NFs, which reduces the streamer propagation and increases the BDV compared to TO. On the other hand, another critical reason for NPs to help improve the BDV is the low conductivity of NPs.

The same factors used to improve the BDV also apply to PDs. PD inside the oil is a localized dielectric breakdown (DB) in such a way that it does not entirely bridge the space between the two conductors (electrical breakdown does not occur). When free electrons are absorbed and trapped, the conditions for PD become much more difficult. This factor causes a PD to happen later. On the other hand, the PD is due to the presence of soluble gas bubbles inside the oil and the difference between its dielectric coefficient and the oil. As observed, when the NPs were added to the base oil, the number of soluble gases inside the oil dramatically decreased. These two factors can be mentioned as the main reasons for reducing PD for $Al_2O_3$NF.

One of the important factors in heat transfer, which plays a decisive role in determining the insulation system, is thermal conductivity, which must be high for TO. Transformer oil must have good heat transfer and low viscosity. However, the thermal conductivity of TO is usually low, which causes damage to the transformer in overload conditions. Therefore, it is important to increase the thermal conductivity of the transformer in order to increase its lifespan. Ideally, transformer oil should have good heat transfer and low viscosity in addition to proper insulating properties. Various methods have been used to increase TO thermal conductivity and heat transfer.

The method used to improve heat transfer is a suspension of convenient NPs into the TO. Nano-materials have a significant and, at the same time, unique property: improved surface-to-volume ratio or aspect ratio. This feature increases the effect of cooling in the transformer. The heat produced in the transformer is absorbed by nano materials. In this regard, the strength and melting point of these materials can be improved by changing their dimensions. The heat generated in the transformer is transferred due to the structure and molecular motion of the oil and is transferred from the hot point to the cold point according to the principle of thermodynamics. By adding NPs to the oil, its performance in heat transfer can be increased.

The main challenge in producing a NFs is the homogeneous dispersion of NPs. In fact, NPs tend to aggregate under the influence of Van der Waal's forces. Meanwhile, long-term dispersion is considered as a primary requirement in practical applications. Also, thermal conductivity as another parameter is affected by the stability of NF, which has the ability to improve thermal conductivity if stability is provided. To solve this challenge, physical and chemical methods such as adding surfactants and using different surface modifications for nanoparticles have been used.

FESEM clearly shows that $Al_2O_3$ has very good stability. As long as the NPs have a uniform distribution and do not stick to each other; They have a higher surface-to-volume ratio (aspect ratio) and further improve thermal conductivity.

In aging mode, the physical mechanism performance of NPs is highly dependent on how they interact with $O_2$ and moisture as the two main factors in accelerating aging (aging catalysts). An effect to consider is that it is two unpaired electrons in the ground state for $O_2$. One or both of the two unpaired electrons of $O_2$ molecules can be coupled with the unpaired electron of paramagnetic free radicals. The diradical aspect of the $O_2$ molecule is considered as a favorable factor for creating an effective reaction with weak hydrocarbon. Under this reaction, hydroperoxide is created, which changes the color of the oil from bright yellow to amber. In this regard, The presence of copper increases redox reactions. This condition leads to an increase in oil dissipation factor due to the production of load carriers. Due to the weakness of the peroxide bond, it is possible to break it. Based on this, the absorption of the thermal energy of the chain reaction by two new free radicals leads to the strengthening of

oxidation. Also, insoluble colloidal suspensions are created from the combination of free radicals. In general, increasing the concentration of free radicals increases random chemical reactions between them. Eventually, the soluble and insoluble oil-borne decomposition products are the result.

As can be seen, in the aging state, the conditions for $Al_2O_3$ become much more complex, and they have to deal with the more threatening factors of the oil properties. The function of $O_2$ in oil was discussed above. $O_2$ is a massive threat for two reasons: a) free electrons, b) accelerated oxidation and aging. It was seen that the NP could trap the free electrons of $O_2$ to some extent and reduce its movement speed. On the other hand, absorbing $O_2$ reduces the aging process of the oil, and oil conditions remain at an acceptable level.

## 6. CONCLUSION

A noteworthy point in the results is the effect of water content on the samples and the much better reaction of the NF against it compared to TO. In such a way, NF has withstood a higher voltage against moisture and has been able to have a much lower BDV reduction percentage (19.1% vs 57%) than oil. This behavior of NPs regarding water dissolved in oil can occur for two main reasons:

a) Dissolved water bound to the surface of $Al_2O_3$, which has the property of reducing the BDV of liquid insulation, can be the cause of this condition. The breaking of multi-molecular water clusters attached to the surface of some $Al_2O_3$ into single water molecules can increase the BDV in these conditions.
b) As you can see in the gas chromatography results, the amount of $H_2$ dissolved in the oil has decreased by about 86%. Since oil-soluble $H_2$ is one of the factors in the formation of water in oil, when the amount of hydrogen can be reduced, the amount of water can also be reduced. As the amount of water in the oil decreases, it can be expected that (because one of the causes of oil aging has decreased) the oil will show better properties than pure aging oil as it ages.

## 7. REFERENCES


1. M. M. Islam, G. Lee, and S. N. Hettiwatte, "A review of condition monitoring techniques and diagnostic tests for lifetime estimation of power transformers," ***Electrical Engineering***, Vol. 100, No. 2, (2018), 581-605, https://doi.org/10.1007/s00202-017-0532-4
2. A. A. Taheri, A. Abdali, M. Taghilou, H. H. Alhelou, and K. Mazlumi, "Investigation of Mineral Oil-Based Nanofluids Effect on Oil Temperature Reduction and Loading Capacity Increment of Distribution Transformers," ***Energy Reports***, Vol. 7, (2021) 4325-4334, DOI:10.1016/j.egyr.2021.07.018
3. M. Hussain, F. A. Mir, and M. Ansari, "Nanofluid transformer oil for cooling and insulating applications: A brief review," ***Applied Surface Science Advances***, Vol. 8, (2022), 100223, DOI: 10.1016/j.apsadv.2022.100223
4. M. R. Meshkatoddini and S. Abbospour, "Aging study and lifetime estimation of transformer mineral oil," American J. of ***Engineering and Applied Sciences,*** Vol. 1, No. 4, (2008), 384-388, DOI: 10.3844/ajeassp.2008.384.388
5. M. Duval, "Dissolved gas analysis: It can save your transformer," ***IEEE Electrical Insulation Magazine***, Vol. 5, No. 6, (1989), 22-27. DOI: 10.1109/57.44605.
6. J. Faiz and M. Soleimani, "Dissolved gas analysis evaluation in electric power transformers using conventional methods a review," ***IEEE Transactions on Dielectrics and Electrical Insulation***, Vol. 24, No. 2, (2017), 1239-1248, DOI: 10.1109/TDEI.2017.005959
7. J. Dai, H. Song, G. Sheng, and X. Jiang, "Dissolved gas analysis of insulating oil for power transformer fault diagnosis with deep belief network," ***IEEE Transactions on Dielectrics and Electrical Insulation***, Vol. 24, No. 5, (2017), 2828-2835, DOI: 10.1109/TDEI.2017.005959
8. D.-E. A. Mansour, "Development of a new graphical technique for dissolved gas analysis in power transformers based on the five combustible gases," ***IEEE Transactions on Dielectrics and Electrical Insulation***, Vol. 22, No. 5, (2015), 2507-2512, DOI: 10.1109/TDEI.2015.004999
9. J. Weesmaa, M. Sterner, B. Pahlavanpour, L. Bergeld, J. Nunes, and K. Sundkvist, "Study of stray gassing measurements by different methods," in Electrical Insulation and Dielectric Phenomena (CEIDP), 2013 IEEE Conference on, (2013), 184-189.DOI: 10.1109/CEIDP.2013.6748192.
10. G. Xiao, W. Chen, C. Yu, and L. Jin, "Study on ZnO-based gas sensor for detection of acetylene dissolved in transformer oil," in 2018 IEEE International Instrumentation and Measurement Technology Conference (I2MTC), (2018), 1-6, DOI: 10.1109/I2MTC.2018.8409830
11. M. Rafiq, Y. Lv, and C. Li, "A review on properties, opportunities, and challenges of transformer oil-based nanofluids," ***Journal of Nanomaterials***, Vol. 2016, (2016), Article ID 8371560, http://dx.doi.org/10.1155/2016/8371560.
12. R. E. Hebner, "Measurement of electrical breakdown in liquids," ***in The liquid state and its electrical properties: Springer,*** pp. 519-537, (1988).
13. M. Chiesa and S. K. Das, "Experimental investigation of the dielectric and cooling performance of colloidal suspensions in insulating media," ***Colloids and Surfaces A: Physicochemical and Engineering Aspects***, Vol. 335, No. 1-3, (2009), 88-97, DOI: 10.1016/j.colsurfa.2008.10.044
14. Asefi M., Molavi H., Shariaty-Niassar M., Babaee Darband J., Nemati N., Yavari M., Akbari M, "An investigation on stability, electrical and thermal characteristics of transformer insulting oil nanofluids", ***International Journal of Engineering, Transactions A: Basics***, Vol. 29, No. 10, (2016), 1332-1340, DOI: 10.5829/idosi.ije.2016.29.10a.02
15. M. Yang, C. Li, L. Luo, R. Li, and Y. Long, "Predictive model of convective heat transfer coefficient in bone micro-grinding using nanofluid aerosol cooling," ***International Communications in Heat and Mass Transfer***, Vol. 125, (2021), 105317, DOI: 10.1016/j.icheatmasstransfer.2021.105317
16. E. V. Timofeeva, J. L. Routbort, and D. Singh, "Particle shape effects on thermophysical properties of alumina nanofluids," ***Journal of Applied Physics***, Vol. 106, No. 1, (2009), 014304, DOI: 10.1063/1.3155999
17. H. Jin, "Dielectric strength and thermal conductivity of mineral oil based nanofluids," Doctoral Thesis, (2015), https://doi.org/10.4233/uuid:10d18961-a23f-478e-b6e2-181d897d8541

18. S. U. Ilyas, R. Pendyala, M. Narahari, and L. Susin, "Stability, rheology and thermal analysis of functionalized alumina-thermal oil-based nanofluids for advanced cooling systems," ***Energy Conversion and Management***, Vol. 142, (2017), 215-229, http://dx.doi.org/10.1016/j.enconman.2017.01.079
19. S. Aberoumand and A. Jafarimoghaddam, "Experimental study on synthesis, stability, thermal conductivity and viscosity of Cu–engine oil nanofluid," ***Journal of the Taiwan Institute of Chemical Engineers***, Vol. 71, (2017), 315-322, DOI: 10.1016/j.jtice.2016.12.035
20. M. M. Bhunia, K. Panigrahi, C. B. Naskar, S. Bhattacharjee, K. K. Chattopadhyay, and P. Chattopadhyay, "2D square nanosheets of Anatase $TiO_2$: A surfactant free nanofiller for transformer oil nanofluids," ***Journal of Molecular Liquids***, Vol. 325, (2021), 115000, DOI: 10.1016/j.molliq.2020.115000
21. D.-E. A. Mansour, E. M. Shaalan, S. A. Ward, A. Z. El Dein, H. S. Karaman, and H. M. Ahmed, "Multiple nanoparticles for improvement of thermal and dielectric properties of oil nanofluids," ***IET Science, Measurement & Technology***, Vol. 13, No. 7, (2019), 968-974, DOI: 10.1049/iet-smt.2018.5015
22. M. Parvar, S. Saedodin, and S. H. Rostamian, "Experimental study on the thermal conductivity and viscosity of transformer oil-based nanofluid containing ZnO nanoparticles," ***Journal of Heat and Mass Transfer Research***, Vol. 7, No. 1, (2020), 77-84, DOI : 10.22075/JHMTR.2020.19303.1267
23. S. R. Babu and P. R. Babu, "Comparative Analysis Of Stability And Dielectric Break Down Strength of Transformer Oil Based Nanofluids." ***International Journal of Electrical Engineering and Technology***, Vol. 11, No. 5, (2020), 113-119, DOI: 10.34218/IJEET.11.5.2020.013.
24. G. Paul, M. Chopkar, I. Manna, and P. Das, "Techniques for measuring the thermal conductivity of nanofluids: a review," ***Renewable and Sustainable Energy Reviews***, Vol. 14, No. 7, (2010), 1913-1924, DOI: 10.1016/j.rser.2010.03.017
25. S. Oparanti, A. Khaleed, A. Abdelmalik, and N. Chalashkanov, "Dielectric characterization of palm kernel oil ester-based insulating nanofluid," in 2020 IEEE Conference on Electrical Insulation and Dielectric Phenomena (CEIDP), (2020), 211-214. DOI: 10.1109/CEIDP49254.2020.9437477
26. A. Moghadassi, E. Ghomi, and F. Parvizian, "A numerical study of water based $Al_2O_3$ and $Al_2O_3$–Cu hybrid nanofluid effect on forced convective heat transfer," ***International Journal of Thermal Sciences***, Vol. 92, (2015), 50-57, DOI: 10.1016/j.ijthermalsci.2015.01.025
27. M. Rafiq, M. Shafique, A. Azam, and M. Ateeq, "Transformer oil-based nanofluid: The application of nanomaterials on thermal, electrical and physicochemical properties of liquid insulation-A review," ***Ain Shams Engineering Journa***l, Vol. 12, No. 1, (2021), 555-576, DOI: 10.1016/j.asej.2020.08.010
28. Koutras, K.N.; Naxakis, I.A.; Pyrgioti, E.C.; Charalampakos, V.P.; Gonos, I.F.; Antonelou, A.E.; Yannopoulos, S.N. The Influence of Nanoparticles, "The Influence of Nanoparticles' Conductivity and Charging on Dielectric Properties of Ester Oil Based Nanofluid," ***Energies***, Vol. 13, No. 24, (2020), 6540. https://doi.org/10.3390/en13246540
29. X. Wang, Z. Wang, Q. Liu, and P. Dyer, "Dissolved gas analysis of thermal faults in transformer liquids simulated using immersed heating method," ***IEEE Transactions on Dielectrics and Electrical Insulation***, Vol. 25, No. 5, (2018), 1749-1757, DOI: 10.1109/TDEI.2018.007158
30. Y. Du, Y. Lv, C. Li, M. Chen, Y. Zhong, J. Zhou, X. Li, Y. Zhou, "Effect of semiconductive nanoparticles on insulating performances of transformer oil," ***IEEE Transactions on Dielectrics and Electrical Insulation***, Vol. 19, No. 3, (2012), 770-776, DOI: 10.1109/TDEI.2012.6215079
31. L. Loiselle, I. Fofana, J. Sabau, S. Magdaleno-Adame, and J. C. Olivares-Galvan, "Comparative studies of the stability of various fluids under electrical discharge and thermal stresses," ***IEEE Transactions on Dielectrics and Electrical Insulation***, Vol. 22, No. 5, (2015), 2491-2499, DOI: 10.1109/TDEI.2015.7311022
32. T. Tsuboi, J. Takami, S. Okabe, K. Inami, and K. Aono, "Aging effect on insulation reliability evaluation with weibull distribution for oil-immersed transformers," ***IEEE Transactions on Dielectrics and Electrical Insulation***, Vol. 17, No. 6, (2010), 1869-1876. DOI: 10.1109/TDEI.2010.5658240


## Persian Abstract


**چکیده**

نانوذرات $Al_2O_3$ برای بهبود عملکرد خواص ذاتی روغن ترانسفورماتور (TO) در شرایط بهره‌برداری پایدار و در معرض پیری حرارتی استفاده شد. درصدهای وزنی مختلف $Al_2O_3$ در TO برای به حداکثر رساندن ولتاژ شکست (BDV) در نظر گرفته شد. نانوسیال $Al_2O_3$ (NF) ولتاژ شکست را ۱۱۶٪ (۳۱.۱ کیلوولت به ٦٧.٤ کیلوولت) و انتقال حرارت را تا ۳۳.٤٪ افزایش می دهد و همچنین تخلیه جزئی (PD) را تا ٦٦٪ به حداقل می‌رساند. کاهش PD همچنین به توانایی $Al_2O_3$ برای جذب هیدروژن و استیلن، دو گاز محلول در روغن که در PD موثر هستند، مرتبط است. حتی $Al_2O_3NF$ نسبت به محتوای آب در TO مقاوم‌تر است. ولتاژ شکست برای TO و $Al_2O_3NF$، زمانی که محتوای آب به بیش از ۳۰ ppm افزایش یابد، به ترتیب ۵۷٪ و ۱۹٪ کاهش یافته است. طبق معادله آرنیوس، هر دو نمونه به مدت ۲۹ روز در دمای ۱۲۰ درجه سانتیگراد قرار گرفتند تا نمونه‌ها پیر شوند (معادل حدود ۳۰ سال). $Al_2O_3NF$ پیرشده BDV را ۱۲۱٪ نسبت به TO پیرشده و همچنین PD را نسبت به TO پیر شده تا ۷۱٪ بهبود داده است. تمام خواص مطلوب $Al_2O_3NF$ مشروط به پایداری $Al_2O_3$ است. FESEM پایداری $Al_2O_3$ را تایید می کند.

International Journal of Engineering

Journal Homepage: www.ije.ir

# Comparative Analysis of Web Hosting Server Performance

E. B. Setiawan*, A. Setiyadi

*Faculty of Engineering and Computer Science, Universitas Komputer Indonesia, Bandung, Indonesia*

*PAPER INFO*

*Paper history:*
Received 11 December 2022
Received in revised form 15 January 2023
Accepted 16 January 2023

*Keywords*:
*Web Hosting*
*Server*
*Performance*
*Analysis*
*Website*

*ABSTRACT*

This research discusses the comparison performance of different hosting servers. The hosting server that is used as a comparison consists of four types. Namely, Indonesian shared hosting servers, foreign shared hosting servers, Indonesian virtual private servers, and foreign virtual private servers. The parameters tested in this study are load time, domain name system, connection, and secure socket layer. The tools used for testing the performance comparison of the hosting server are Dotcom-Tools, Pingdom.com, Webpage Test, and sitespeed. The results of this comparison can be an input for potential users who have plans to online their applications using a hosting server. The total value of web server hosting Indonesian shared hosting servers (SH I) is 28.975 milliseconds (ms), foreign shared hosting servers (SH LN) are 8.267 ms, Indonesian virtual private servers (VPS I) are 14.195 ms, Foreign virtual private servers (VPS LN) are 11.835 ms. This research concludes that foreign shared hosting servers (SH LN) are the best web hosting servers because, on some of the parameters tested, this server has the best value because it gets the lowest value with 8.267 ms.

***doi**: 10.5829/ije.2023.36.03c.16*

## 1. INTRODUCTION

Internet technology and online applications continue to evolve all the time. For example, online technology is used for the education process [1], teaching evaluation process [2], meeting [3], electronic commerce [4], and online banking transaction processing [5]. Millions of websites and online-based applications have been created with various types and functions to meet the needs and support human life. Hosting is an internet service that provides resources in the form of servers [6] and services [7] that can make websites or applications accessible to the public online.

Web hosting is a service that provides a data storage server for website placement [8] which the public can access through a connection to the internet network from personal computers in all corners of the world. Web hosting provides various technologies and features that can provide effective web service and security mechanisms [9]. Currently, there are many web hosting service providers, especially in Indonesia. The packages offered are diverse, ranging from affordable to costly prices. There are several types of web hosting today, including shared hosting, reseller hosting, VPS, and cloud hosting [10]. Some types have different architectures [11], performance [12], and features. When choosing the hosting service, of course, prospective users will pay attention to the things needed [13], starting from the specifications needed to match the website to be hosted, such as the hosting server capacity, bandwidth provided, processor, RAM, and the number of domains that can be used.

The web hosting server can be interpreted as the centre, both the database centre and the system centre. The server is a computer in charge of serving every request made by the client computer [14], which returns the results of the request to the client computer. A server is a particular device in a computer network that is a place to allow resource sharing [15]. Several types of servers can be tailored to the client's needs to assist the client in doing his job. The type of server can be physical or virtual machine (VM) [16]. Preparing a hosting server requires excessive time and effort [17].

*Corresponding Author Institutional Email: eko@email.unikom.ac.id
(E. B. Setiawan)

Please cite this article as: E. B. Setiawan, A. Setiyadi, Comparative Analysis of Web Hosting Server Performance, ***International Journal of Engineering, Transactions C: Aspects,*** Vol. 36, No. 03, (2023) 558-564

Shared hosting is web hosting that uses the same web server computer for several hosting users simultaneously[18]. The advantage of shared hosting is that the price is relatively low. The disadvantage of shared hosting is that if there is a problem with one of the web hosting users, it will affect all web hosting users [19]. Therefore, shared hosting is the most popular type of hosting. Usually, web hosting providers offer many attractive packages for this type of web hosting.

A virtual private server (VPS) is a server that uses virtualization [20], which is a strategy to reduce data centre power consumption. By doing virtualization, one physical server host has many virtual servers. Therefore, in addition to better use of hardware, server virtualization can reduce data centre space, making computing with efficiency server usage [21] and reducing energy requirements in the data centre [22].

With so many types of web hosting servers available today, of course, users want to use the most suitable web hosting. Web hosting service providers most widely used and provided are shared hosting services [23] and virtual private servers [24]. Therefore, this research conducted a performance test of the types of web hosting, namely shared hosting and virtual private servers. Thus, the purpose of this research can be formulated to assist hosting users in determining the type of web hosting to be used.

## 2. RESEARCH METHOD

The research method carried out consists of six stages. The first stage is the determination of the hosting server, the second stage is the determination of the website, the third stage is the determination of the assessment parameters, and the fourth stage is the determination of tools to conduct performance assessments. Finally, the analysis process is the fifth stage carried out so that the conclusions are obtained from the research, which is the final stage. In general, the stages of the research carried out can be seen in Figure 1.

**2. 1. Determining the Hosting Server** Hosting comes from the world host. Computers connected to the network can take advantage of the facilities available on a computer that is the host connected to the network. Hosting provides server resources for rent [25], thus enabling organizations and individuals to place information on the internet. Server hosting consists of a combination of servers or servers connected to a high-speed internet network. For effective utilization, load must be balanced among all resources server[26]. Hosting can be used by organizations and individuals to store web page files that have been created so that they can be accessed online.

A virtual private server divides a physical server into several virtual private servers [27] so that each VPS looks and works like a standalone server. Each VPS has full root access, an operating system, and its settings for scripts, users, processing, filesystems, and server resource management such as standalone CPU and RAM. In contrast to share hosting, which uses server resources and influences each other. VPS allows multiple operating systems to run simultaneously on a single physical server machine. Using a virtual private server can improve the server's performance, but the costs involved when renting a VPS are more expensive than shared hosting.

Several hosting servers are determined at this stage, which will be analyzed for performance comparisons.

The public, namely, often uses four hosting servers:

a. Indonesian shared hosting servers (SH I)
b. Foreign shared hosting servers (SH LN)
c. Indonesian virtual private servers (VPS I)
d. Foreign virtual private servers (VPS LN)

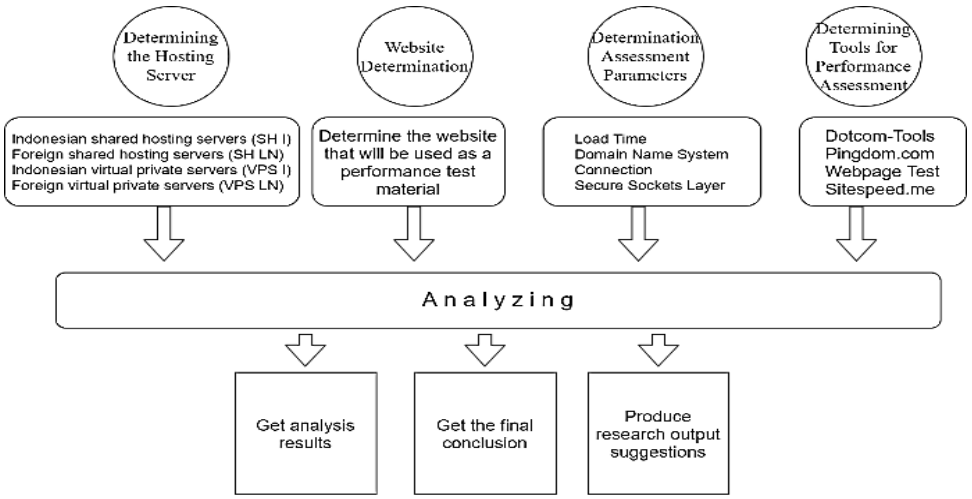


**Figure 1.** Stages of the research conducted

**2. 2. Website Determination** At this stage, a website determined to be stored on the four servers. The online website is the same website on each server. The selected website only consists of a few pages and only displays information. A website is a collection of pages that convey information that contains text, still or moving images, animation, sound, and a combination of all of them, both static and dynamic. The website forms a series of interconnected buildings from these pages. The relationship of these pages is called a hyperlink, while the text used as a connecting medium is called hypertext. Things that must be prepared to build a website are a domain name, website hosting and content management system (CMS). In this study, one website was hosted on four different servers.

**2. 3. Determination of Assessment Parameters** Tests are carried out to find out which type of hosting is better, carried out with the same internet connection conditions and website page loads so that it is expected to get precise and accurate results. The test in determining which type of hosting is better in this study is to use a comparison method.

The parameters to be tested in this study are as follows:

1). Load Time

Load time is the time it takes for a website to display a website page to completion [28]. Long load times can lead to poor service experiences [29]. The amount of multimedia content contained in a website can aggravate the load time of a website [30].

2). Domain Name System

A Domain Name System (DNS) is a service application on the internet that translates a domain name into an IP address [31]. DNS helps map a computer's hostname to an IP address. DNS can have an effect on web performance [32].

3). Connection

A server is a particular computer with a socket connected to a unique port number. The server waits for the socket to accept a connection request (request) from a client (passive open). The connection parameter is the speed of the server and client to communicate and make requests-responses [33]. Average server connection time can be used to determine the performance of a website and web hosting server [34].

4). Secure Socket Layer

Secure Socket Layer (SSL) is a protocol used for secure web browsing [35]. SSL is designed to protect data on the Internet. In general, the function of SSL is to secure personal data, such as names, addresses, or credit card numbers, from cybercriminals. The workings of SSL is to lock the cryptographic key into the information to be identified. The data will also be well encrypted during the transfer process so that third parties will not be able to enter and steal sensitive information. SSL has significant impact on the web hosting performance [36].

**2. 4. Determining Tools for Performance Assessment** Several supporting tools are used to determine the performance of various parameters. The assessment tools used are Dotcom Tools, Pingdom.com, Webpage test and sitespeed. Dotcom-Tools is a free website speed and performance testing and tools and used to determine the loading time of a web hosting server [37]. Pingdom is a website performance and availability monitoring [38]. A webpage test is a website performance and optimization test [39]. Finally, Sitespeed is an open-source tool that helps analyze and optimize the website speed and web performance [40] based on best practices.

**2. 5. Comparative Result Analysis** This stage analyses the results of the performance comparison of the four hosting servers where the test website is stored. The analysis process is carried out by comparing the values and numbers of the assessment results from each tool and parameter used.

**2. 6. Getting a Conclusion** The comparisons made in the previous stage are used to conclude the research conducted. However, the research results depend on other parameters that will change in the future.

## 3. RESULT AND DISCUSSION

Tests conducted in this study have limitations, namely:

1. There are four types of hosting servers to be tested, namely: Indonesian shared hosting servers (SH I), foreign shared hosting servers (SH LN), Indonesian virtual private servers (VPS I), Foreign virtual private servers (VPS LN).
2. Tests on four types of hosting servers are carried out on one computer with the same internet connection and the same website.
3. Testing using four tools, namely: dotcom-tools, pingdom.com, webpage test, and sitespeed
4. The test uses load time, Domain Name System, connection and Secure Socket Layer criteria.
5. The internet connection used for testing is a data package from same internet service provider.
6. Testing using the same website.
7. The browser used for testing is Google Chrome.

The testing process carried out using the dotcom-tools tools can be seen in Figure 2, the pingdom.com tools can be seen in Figure 3, the webpage-test tools can be seen in Figure 4, and the testing process using sitespeed can be seen in Figure 5.

| | |
|---|---|
| Sum of DNS times in ms | 0.04 |
| Sum of Connection times in ms | 1.57 |
| Sum of SSL times in ms | 1.62 |
| Sum of Request times in ms | 0.01 |
| Sum of FirstPacket times in ms | 18.06 |
| Sum of Download times in ms | 4.76 |

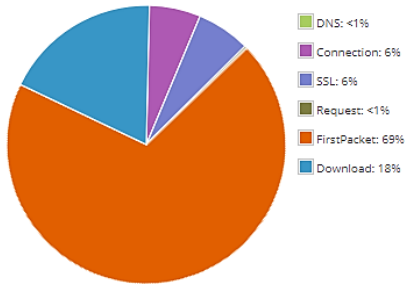


**Figure 2.** Testing process using Dotcom-tools

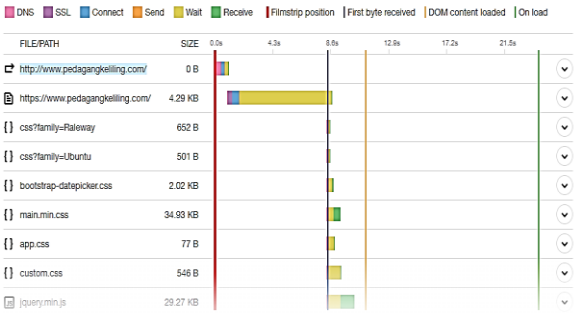


**Figure 3.** Testing process using Pingdom.com

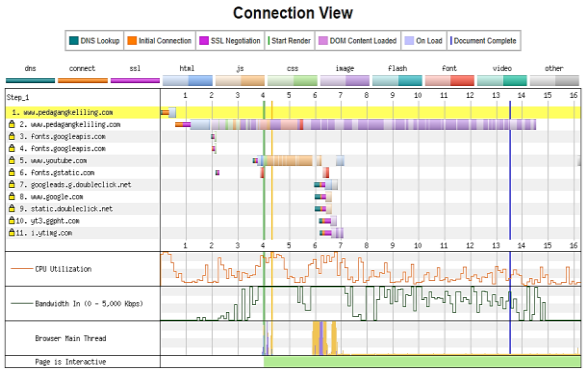


**Figure 4.** Testing process using Webpage-test

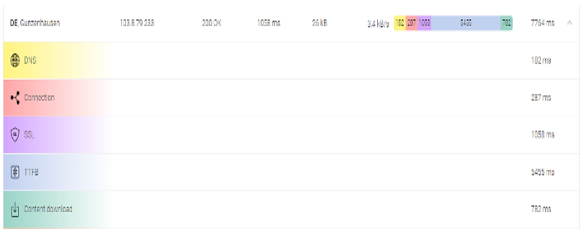

**Figure 5.** Testing process using Sitespeed

From the tests carried out in this research on four types of hosting servers using four web performance measuring tools and a website for testing, the following results were obtained for the test material parameters. The smaller the value obtained from these parameters, the better the hosting server. In presenting the test results, milliseconds are used. The test results for the load time parameters can be seen in Table 1 and Figure 6. It can see that foreign shared hosting has the best load time performance with total value 4977 milliseconds.

Based on the results of testing the DNS parameters as shown in Table 2 and Figure 7, Indonesia's shared hosting server (SH I) has better DNS performance compared to other types of hosting servers with 276 milliseconds.

The test results for the connection parameter can be seen in Table 3 and Figure 8. It can see that foreign shared hosting has the best connection performance with 1081 milliseconds.

The test results for SSL parameters can be seen in Table 4 and Figure 9. It can see that Foreign Virtual

**TABLE 1.** Load Time Parameter Test Results

| Server | Dotcom-tools | Pingdom.com | Webpage test | Sitespeed | Total |
|---|---|---|---|---|---|
| SH I | 6410 | 7830 | 737 | 7764 | 22741 |
| SH LN | 3660 | 883 | 187 | 247 | 4977 |
| VPS I | 4420 | 1350 | 316 | 1096 | 7182 |
| VPS LN | 5280 | 613 | 542 | 935 | 7370 |

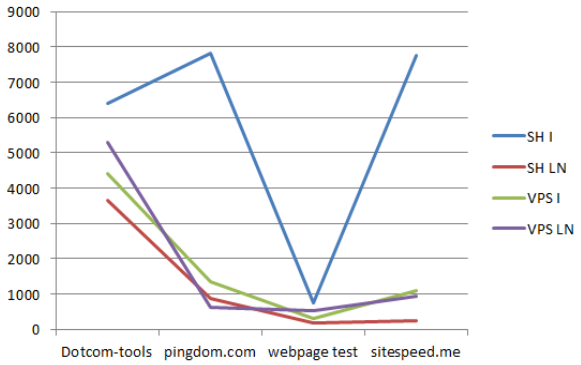


**Figure 6.** Graph of Load Time Test Results

**TABLE 2.** DNS Parameter Test Result

| Server | Dotcom-tools | Pingdom.com | Webpage test | Sitespeed | Total |
|---|---|---|---|---|---|
| SH I | 40 | 27 | 27 | 182 | 276 |
| SH LN | 310 | 731 | 28 | 5 | 1074 |
| VPS I | 880 | 495 | 28 | 536 | 1939 |
| VPS LN | 250 | 312 | 27 | 186 | 775 |

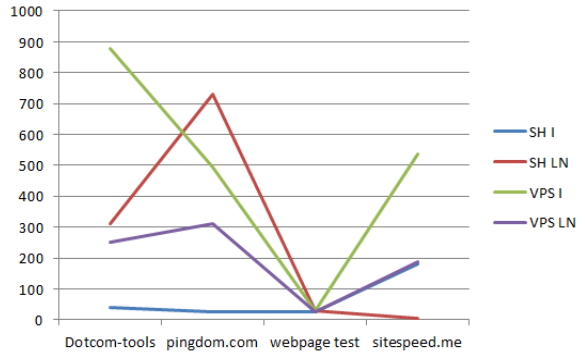


**Figure 7.** Graph of DNS Test Results

**TABLE 3.** Connection Parameter Test Result

| Server | Dotcom-tools | Pingdom .com | Webpage test | Sitespeed | Total |
|---|---|---|---|---|---|
| SH I | 1570 | 559 | 263 | 287 | 2679 |
| SH LN | 800 | 158 | 110 | 13 | 1081 |
| VPS I | 1740 | 273 | 282 | 171 | 2466 |
| VPS LN | 3320 | 7 | 37 | 82 | 3446 |

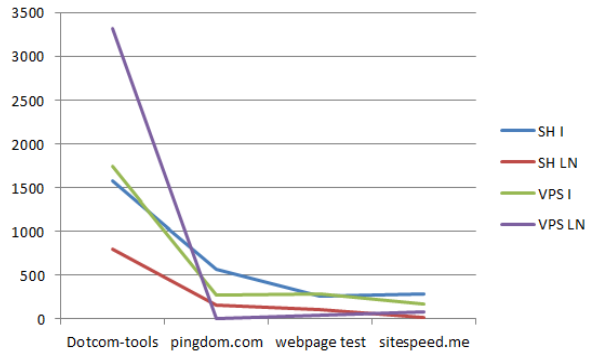


**Figure 8.** Graph of Connection Test Results

**TABLE 4.** SSL Test Result

| Server | Dotcom-tools | Pingdom. com | Webpage test | Sitespeed | Total |
|---|---|---|---|---|---|
| SH I | 1620 | 301 | 300 | 1058 | 3279 |
| SH LN | 850 | 82 | 132 | 71 | 1135 |
| VPS I | 2270 | 19 | 57 | 262 | 2608 |
| VPS LN | 50 | 24 | 90 | 80 | 244 |

Private Server has the best SSL performance compared to other types of server hosting with 244 milliseconds.

After testing, the values for each type of hosting server can be obtained which can see in Table 5.

The test results on four parameters to measure the performance of four types of hosting servers can see in Figure 10.

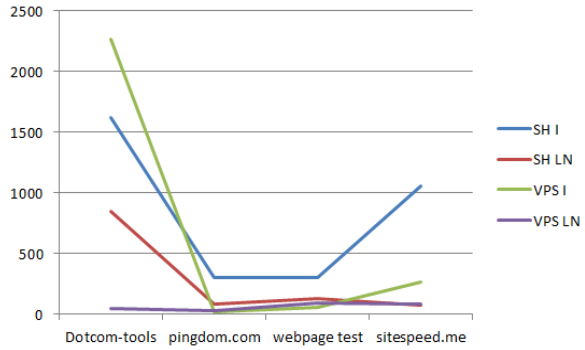


**Figure 9.** Graph of SSL Test Results

**TABLE 5.** Total Value of Server Hosting Type

| Server Hosting | Total Value |
|---|---|
| SH I | 28975 |
| SH LN | 8267 |
| VPS I | 14195 |
| VPS LN | 11835 |

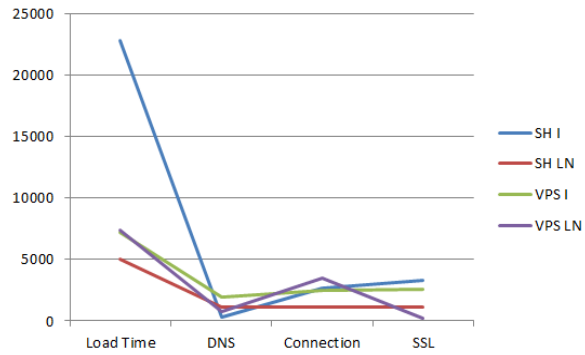


**Figure 10.** Hosting server test results

The total value of the hosting server type is obtained to see which hosting server is the best. After testing the four types of hosting servers using 4 tools to measure web performance against the following four measurement parameters, a list of the best hosting server sequences is made:

1. Foreign shared hosting server, total 8.267 ms
2. Foreign virtual private server, total 11.835 ms
3. Indonesian virtual private server, total 14.195 ms
4. Indonesian shared hosting server, total 28.975 ms

Foreign shared hosting server is the best hosting server because on several parameters tested, this type of server is superior to other servers and has the smallest (best) value with total 8.267 milliseconds. With the smaller the total value obtained, the performance of the web hosting is faster so that it has better performance. The results obtained can be used as a reference for choosing the hosting server, but many performance

measurement parameters were still not tested in this study.

## 4. CONCLUSION

Based on the results of the research that has been done, it is concluded that foreign shared hosting server is the best hosting server several tools and parameters can be used to test the performance of the types of web hosting. This test will be significantly influenced by various factors that can make different results. The results of this study will vary with different infrastructure conditions.

## 5. ACKNOWLEDGEMENTS

Authors wishing acknowledge to Universitas Komputer Indonesia and Direktorat Riset, Teknologi dan Pengabdian Kepada Masyarakat, Direktorat Jenderal Pendidikan Tinggi, Riset dan Teknologi for help and support this research using grant Penelitian Riset Terapan Kompetitif Nasional 2022-2024 with master contract number 156/E5/PG.02.00.PT/2022 and derivative contract number 96/SP2H/RT-MONO/LL4/2022, 004/SP/DP3M/UNIKOM/VI/2022.

## 6. REFERENCES

1. Khatser, G., Khatser, M., Bukharina, L., Dybchynska, Y., and Lysenko, M. "Transformation of the Educational Process within Online Technologies Implementation in the Period of the Global Crisis." ***International Journal of Emerging Technologies in Learning***, Vol. 16, No. 11, (2021). https://doi.org/10.3991/ijet.v16i11.21265
2. Xu, X., and Liu, F. "Optimization of Online Education and Teaching Evaluation System Based on GA-BP Neural Network." ***Computational Intelligence and Neuroscience***, Vol. 2021, (2021). https://doi.org/10.1155/2021/8785127
3. Pratama, H., Azman, M. N. A., Kassymova, G. K., and Duisenbayeva, S. S. "The Trend in Using Online Meeting Applications for Learning During the Period of Pandemic COVID-19: A Literature Review." ***Journal of Innovation in Educational and Cultural Research***, Vol. 1, No. 2, (2020). https://doi.org/10.46843/jiecr.v1i2.15
4. Khan, M. M., Shams-E-Mofiz, M., and Sharmin, Z. A. "Development of E-Commerce-Based Online Web Application for COVID-19 Pandemic." ***iBusiness***, Vol. 12, No. 04, (2020). https://doi.org/10.4236/ib.2020.124008
5. Naruetharadhol, P., Ketkaew, C., Hongkanchanapong, N., Thaniswannasri, P., Uengkusolmongkol, T., Prasomthong, S., and Gebsombut, N. "Factors Affecting Sustainable Intention to Use Mobile Banking Services." ***SAGE Open***, Vol. 11, No. 3, (2021). https://doi.org/10.1177/21582440211029925
6. Iqbal Kurniansyah, M., and Sinurat, S. "Sistem Pendukung Keputusan Pemilihan Server Hosting dan Domain Terbaik untuk WEB Server Menerapkan Metode VIKOR." ***Jurnal Sistem Komputer dan Informatika***, Vol. 2, No. 1, (2020).
7. Ezhilchelvan, P., and Mitrani, I. "Optimal provisioning of servers for hosting services of multiple types." ***Simulation Modelling Practice and Theory***, Vol. 75, (2017). https://doi.org/10.1016/j.simpat.2017.03.011
8. Ramamurthy, A., Saurabh, S., Gharote, M., and Lodha, S. "Selection of cloud service providers for hosting web applications in a multi-cloud environment." In Proceedings - 2020 IEEE 13th International Conference on Services Computing, SCC 2020. https://doi.org/10.1109/SCC49832.2020.00034
9. Huynh, T. T., Nguyen, T. D., Nguyen, N. T. H., and Tan, H. "Privacy-Preserving for Web Hosting." In ***Lecture Notes of the Institute for Computer Sciences, Social-Informatics and Telecommunications Engineering, LNICST***, Vol. 334. https://doi.org/10.1007/978-3-030-63083-6_24
10. Held, G. "Web-Hosting Options." In A Practical Guide to Content Delivery Networks. https://doi.org/10.1201/ebk1439835883-10
11. Shabani, I., Mëziu, E., Berisha, B., and Biba, T. "Design of Modern Distributed Systems based on Microservices Architecture." ***International Journal of Advanced Computer Science and Applications***, Vol. 12, No. 2, (2021). https://doi.org/10.14569/IJACSA.2021.0120220
12. Bommannavar, P. A., Shah, A., Singh, A., and Krishnan, R. "Analyzing Performance Parameters for Cloud Service Selection usingAHP." In 2021 6th International Conference for Convergence in Technology, I2CT 2021. https://doi.org/10.1109/I2CT51068.2021.9418148
13. Husain, A., Zaki, M. H., and Islam, S. "Performance Evaluation of Private Clouds : OpenStack vs Eucalyptus." ***International Journal of Distributed and Cloud Computing***, Vol. 6, No. 1, (2018).
14. Mardianto, I., Sugiarto, D., and Ashari, K. A. "The Elastic Stack Ability Test To Monitor Slowloris Attack on Digital Ocean Server." ***Ultimatics : Jurnal Teknik Informatika***, Vol. 13, No. 2, (2022). https://doi.org/10.31937/ti.v13i2.2209
15. Antal Horváth, I., Scully, Z., and Van Houdt, B. "Mean Field Analysis of Join-Below-Threshold Load Balancing for Resource Sharing Servers." ***Performance Evaluation Review***, Vol. 48, No. 1, (2020). https://doi.org/10.1145/3393691.3394199
16. Bermejo, B., and Juiz, C. "A general method for evaluating the overhead when consolidating servers: performance degradation in virtual machines and containers." ***Journal of Supercomputing***, Vol. 78, No. 9, (2022). https://doi.org/10.1007/s11227-022-04318-5
17. Lee, S. "Reducing complexity of server configuration through public cloud storage." ***Electronics (Switzerland)***, Vol. 10, No. 11, (2021). https://doi.org/10.3390/electronics10111277
18. Sunny, M., Shaji, S., Sabu, S., Uthaman, U., and George, G. "Deploy—Web Hosting Using Docker Container." In ***Lecture Notes in Electrical Engineering*** (Vol. 735 LNEE, 335-345). Springer Science and Business Media Deutschland GmbH. https://doi.org/10.1007/978-981-33-6977-1_26
19. Sheela, T., Akila, V., Sravya, B., and Harshitha, T. "Secure Online Examination System on Azure Cloud with Load Balancer." In Proceedings of the 2021 4th International Conference on Computing and Communications Technologies, ICCCT 2021. https://doi.org/10.1109/ICCCT53315.2021.9711889
20. Cohen, A., and Nissim, N. "Trusted detection of ransomware in a private cloud using machine learning methods leveraging meta-features from volatile memory." ***Expert Systems with Applications***, Vol. 102, (2018). https://doi.org/10.1016/j.eswa.2018.02.039
21. Yousefipour, A., Rahmani, A. M., and Jahanshahi, M. "Improving the load balancing and dynamic placement of virtual machines in cloud computing using particle swarm optimization algorithm." ***International Journal of Engineering Transactions C: Aspects***, Vol. 34, No. 6, (2021). https://doi.org/10.5829/ije.2021.34.06c.05

22. Rezai, H., and Speily, O. R. B. "Energy aware resource management of cloud data centers." ***International Journal of Engineering, Transactions B: Applications***, Vol. 30, No. 11, (2017). https://doi.org/10.5829/ije.2017.30.11b.14
23. Pham, N. M. N., Le, V. S., and Nguyen, H. H. C. "Energy efficient resource allocation for virtual services based on heterogeneous shared hosting platforms in cloud computing." ***Cybernetics and Information Technologies***, Vol. 17, No. 3, (2017). https://doi.org/10.1515/cait-2017-0029
24. Balen, J., Vajak, D., and Salah, K. "Comparative performance evaluation of popular virtual private servers." ***Journal of Internet Technology***, Vol. 21, No. 2, (2020). https://doi.org/10.3966/160792642020032102003
25. Jain, P., Munjal, Y., Gera, J., and Gupta, P. "Performance Analysis of Various Server Hosting Techniques." In ***Procedia Computer Science***, Vol. 173. https://doi.org/10.1016/j.procs.2020.06.010
26. Shukla, A., Kumar, S., and Singh, H. "Load balancing approaches for web servers: A survey of recent trends." ***International Journal of Engineering, Transactions B: Applications***, Vol. 31, No. 2, (2018). https://doi.org/10.5829/ije.2018.31.02b.09
27. Putra, A. A., Kusrini, K., and Pramono, E. "Sistem Pendukung Keputusan Dalam Pemilihan Control Panel Virtual Private Server Menggunakan Metode Ahp Dan Saw." ***Creative Information Technology Journal***, Vol. 5, No. 1, (2019). https://doi.org/10.24076/citec.2017v5i1.116
28. Pratama, F. "Analisis Performa Load Time Sister Menggunakan Layanan KampusGoPublic." ***Syntax Idea***, Vol. 4, No. 1, (2022). https://doi.org/10.36418/syntax-idea.v4i1.1736
29. Stringam, B., and Gerdes, J. "Service gap in hotel website load performance." ***International Hospitality Review***, Vol. 33, No. 1, (2019), 16-29. https://doi.org/10.1108/ihr-09-2018-0012
30. Mjelde, E., and Opdahl, A. L. "Load-time reduction techniques for device-agnostic web sites." ***Journal of Web Engineering***, Vol. 16, No. 3-4, (2017), 312-347.
31. Novianto, D. "Optimasi Waktu Query Dan Filtering Nama Domain Pada Dns Server Lokal Menggunakan Bind 9." ***Jurnal Ilmiah Informatika Global***, Vol. 8, No. 1, (2017).
32. Hounsel, A., Borgolte, K., Schmitt, P., Holland, J., and Feamster, N. "Comparing the Effects of DNS, DoT, and DoH on Web Performance." In The Web Conference 2020 - Proceedings of the World Wide Web Conference, WWW 2020, 562-572. Association for Computing Machinery, Inc. https://doi.org/10.1145/3366423.3380139
33. Maulana, A. R., and Rahmatulloh, A. "Websocket untuk Optimasi Kecepatan Data Transfer pada Real Time Chatting." ***Innovation in Research of Informatics***, Vol. 1, No. 1, (2019). https://doi.org/10.37058/innovatics.v1i1.667
34. Mittal, M., and Dhari, S. V. "A regression model for analysis of bounce rate using web analytics." ***International Journal of Innovative Technology and Exploring Engineering***, Vol. 8, No. 9 Special Issue, (2019), 646-649. https://doi.org/10.35940/ijitee.I1103.0789S19
35. Hussain, M. A., Jin, H., Hussien, Z. A., Abduljabbar, Z. A., Abbdal, S. H., and Ibrahim, A. "Enc-DNS-HTTP: Utilising DNS infrastructure to secure web browsing." ***Security and Communication Networks***, Vol. 2017, (2017). https://doi.org/10.1155/2017/9479476
36. Alnatheer, M. A. "Secure Socket Layer (SSL) Impact on Web Server Performance." ***Journal of Advances in Computer Networks***, Vol. 2, No. 3, (2014), 211-217. https://doi.org/10.7763/jacn.2014.v2.114
37. Meister, V. G., Hu, W., Arkan, E., and Günther, H. "Multi-component Infrastructure for e-Lectures: A Viable Solution for Small and Medium-Sized Organizations." In ***Lecture Notes in Business Information Processing***, Vol. 365, 119-134. Springer. https://doi.org/10.1007/978-3-030-31143-8_9
38. Jun, T. W., Xiang, L. Z., Ismail, N. A., Goy, W., and Yi, R. "Usability Evaluation of Social Media Websites." ***Modernization in Engineering Technology and Science***, Vol. 03, No. 01, (2021).
39. Tutul Hossain, M., Hassan, R., Amjad, M., and Rahman, M. A. "Web Performance Analysis: An Empirical Analysis of E-Commerce Sites in Bangladesh." ***International Journal of Information Engineering and Electronic Business***, Vol. 13, No. 4, (2021), 47-54. https://doi.org/10.5815/ijieeb.2021.04.04
40. Borzemski, L., and Kędras, M. "Measured vs. Perceived Web Performance." In ***Advances in Intelligent Systems and Computing***, Vol. 1050. https://doi.org/10.1007/978-3-030-30440-9_27


## Persian Abstract


**چکیده**

این تحقیق عملکرد مقایسه سرورهای میزبانی مختلف را مورد بحث قرار می دهد .سرور میزبانی که به عنوان مقایسه استفاده می شود از چهار نوع تشکیل شده است .یعنی سرورهای میزبانی مشترک اندونزیایی، سرورهای میزبانی مشترک خارجی، سرورهای خصوصی مجازی اندونزیایی و سرورهای خصوصی مجازی خارجی .پارامترهای تست شده در این مطالعه زمان بارگذاری، سیستم نام دامنه، اتصال و لایه سوکت امن است .ابزارهای مورد استفاده برای آزمایش مقایسه عملکرد سرور میزبانیDotcom-Tools ، Pingdom.com، Webpage Testو Sitespeed هستند .نتایج این مقایسه می تواند ورودی برای کاربران بالقوه ای باشد که قصد دارند برنامه های خود را با استفاده از یک سرور میزبان آنلاین آنلاین کنند .ارزش کل وب سرورهای میزبانی وب سرورهای میزبانی مشترک اندونزی 28.975 (SH I) میلی ثانیه(ms) ، سرورهای میزبانی مشترک خارجی 8.267 (SH LN) میلی‌ثانیه، سرورهای خصوصی مجازی اندونزیایی 14.195 (VPS I) میلی‌ثانیه، سرورهای خصوصی مجازی خارجی هستند (VPS LN) . 11.835میلی‌ثانیه است .این تحقیق نتیجه می‌گیرد که سرورهای میزبانی مشترک خارجی (SH LN) بهترین سرورهای میزبانی وب هستند، زیرا در برخی از پارامترهای آزمایش شده، این سرور بهترین مقدار را دارد زیرا کمترین مقدار را با ۸.۲۶۷ میلی‌ثانیه دریافت می‌کند.

International Journal of Engineering

Journal Homepage: www.ije.ir

# Equilibrium of Ammonia ($NH_3$) and Ammonium ($NH_4^+$) during Microalgae Harvesting using Electrocoagulation

P. Purwono*[a], H. Hadiyanto[a,b], M. A. Budihardjo[c]

[a] *Doctoral Program of Environmental Sciences, School of Postgraduate Studies, Diponegoro University, Semarang, Indonesia*
[b] *Center of Biomass and Renewable Energy (CBIORE), Chemical Engineering Department, Diponegoro University, Semarang, Indonesia*
[c] *Department of Environmental Engineering, Faculty of Engineering, Diponegoro University, Semarang, Indonesia*

*PAPER INFO*

*Paper history:*
Received 11 November 2022
Received in revised form 13 January 2023
Accepted 28 January 2023

*Keywords*:
*Equilibrium*
*Dunaliella Salina*
*Electrocoagulation*
*Ammonia*
*Ammonium*
*Harvesting*

*ABSTRACT*

Harvesting microalgae is an important process in gaining biomass while the remaining water is still rich in nutrients. These nutrients, mainly nitrogen and phosphorous, could cause eutrophication of water bodies (rivers, lakes, and oceans) and ecosystem degradation if discharged directly without proper treatment. Electrocoagulation (EC) is one of the harvesting methods and has several advantages: ease of operation, fast harvesting, adaptability, environmental friendliness, and low footprint. However, EC method for harvesting microalgae has the potential in producing ammonia, which is undesirable due to its threat to the environment. The purpose of this study is to establish the equilibrium of ammonium ($NH_4^+$) and ammonia ($NH_3$) during *Dunaliella salina* harvesting. The harvesting was conducted using EC with a variation of 20 volts, 30 min, and 400 rpm. The result shows that the harvesting efficiency can reach 93.72% after 5 min of processing, decreasing the concentration of inorganic nitrogen compounds in total ammonia nitrogen (TAN) to 98.80%.

***doi**: 10.5829/ije.2023.36.03c.17*

## 1. INTRODUCTION

Climate change mitigation, environmental deterioration, and energy scarcity are society's greatest concerns in the 21st century [1]. Biofuels derived from microalgae have become one of the most popular used renewable energy sources. Currently, the focus of efforts to reduce climate-altering $CO_2$ emissions is shifting from fossil fuels to ones based on biological materials [2]. Microalgae are a biological resource that can be used for many things, such as making food, medicine, animal feed, biofertilizers, cosmetics, fuels, treating wastewater, and making bioplastics [3].

Microalgae produce wastewater containing additional nutrients such as nitrogen and phosphorus immediately after harvest. If these pollutants are not handled carefully, they can cause eutrophication of water bodies (like rivers, lakes, and oceans) and damage to ecosystems [4, 5]. One of the things that contributes to ecosystem degradation is water pollution. Therefore, appropriate solutions are needed to reduce the impact of environmental damage as soon as possible. The harmful effects of ammonia nitrogen on the aquatic environment are attracting global attention [6]. Untreated microalgae effluent containing nutrients (nitrogen and phosphorus) has the potential to pollute aquatic bodies. Instead of treating microalgae effluent before disposal, water dilution may be used [7], but water is a scarce resource [8].

The hardest part of any microalgae-based activity is harvesting the algae. Consquently, the harvesting process is an interesting subject to study so that it can be used in the field. Centrifugation and membrane filtration are the usual methods for large-scale harvesting cultures of microalgae [9]. However, require complex maintenance. Therefore, new methods must be developed to make maintenance easier and lower harvesting costs without slowing down harvesting or making the biomass less pure [10]. EC is a microalgae harvesting method that needs to be explored because of its ease of operation, fast harvesting, adaptability, environmental friendliness, and low footprint [11]. When compared to centrifugation alone, the usage of EC can save up to 89% of energy [12].

*Corresponding Author Institutional Email: purwonopurwono@students.undip.ac.id (P. Purwono)

Please cite this article as: P. Purwono, H. Hadiyanto, M. A. Budihardjo, Equilibrium of Ammonia ($NH_3$) and Ammonium ($NH_4^+$) during Microalgae Harvesting using Electrocoagulation, ***International Journal of Engineering, Transactions C: Aspects,*** Vol. 36, No. 03, (2023) 565-572

After harvesting microalgae using EC, wastewater with extra nutrients such as nitrogen will be produced. The wastewater contains ammonium and ammonia, which can be quantified as total ammonia nitrogen [13]. In wastewater, ammonium and ammonia are all in equilibrium. Their relative concentrations depend on pH and temperature, at high pH and temperature values promoting the production of ammonia molecules [14].

Producing microalgae and harvesting employing EC (Al electrodes) can remove 75% of the total nitrogen in 5 hours [15]. Similar results were obtained by Liu and Liu [16], which integrated *Chlorella vulgaris* cultivation and EC pretreatment with iron electrodes that removed 88% of total nitrogen from anaerobic digestion wastewater in 40 min. The anode chamber of the biocathode-coupled electrocoagulation cell (bio-ECC) achieved nitrogen removal rates of 7.28 $mg.L^{-1}.h^{-1}$, while the cathode chamber achieved nitrogen removal rates of 6.77 $mg.L^{-1}.h^{-1}$ [17]. However, the previous studies focused on the decrease in nitrogen ($NH_4^+$-N and total nitrogen), neglecting the equilibrium between ammonium and ammonia. Actually, ammonia production is undesirable due to its toxicity to aquatic biota [6]. According to Meetiyagoda and Fujino [18], wastewater from microalgae harvesting should be introduced into water budies because of contaminants. The novelty of this research includes a high microalgae harvesting efficiency, a quick harvesting time, and a non-toxic microalgae culture wastewater effluent for aquatic biota.The purpose of this research is to investigate the equilibrium between ammonium and ammonia during microalgae harvesting. This study harvested *D. salina* utilizing EC with a voltage of 20 volts, a duration of 30 min, using stainless steel and iron electrodes.

## 2. MATERIALS AND METHODS

**2. 1. The Substrate of *D. salina*** This research was conducted using an experimental laboratory method. Cultures of *D. salina* were obtained from UgoPlankton, Jepara Regency and cultured at UPT C-BIORE Laboratory, Diponegoro University, Semarang, Indonesia. Testing of the total ammonia nitrogen, pH, and temperature was carried out at the Environmental Laboratory, Faculty of Engineering, Diponegoro University and UPT Laboratory C-BIORE. The sampling method used was SNI 6989.59:2008 [19]. The parameters observed were pH, temperature (°C), ammonia, ammonium, and total ammonia nitrogen.

**2. 2. EC Experiment** The harvesting of *D. salina* using EC wais carried out under fixed conditions, which means researchers did not modify any parameters, including pH, initial concentration, room temperature, etc. The stirring speed and substrate volume refer to previous research conducted by Lucakova et al. [20] with a stirring speed of 400 rpm using a magnetic stirrer and a culture volume of 500 mL. The operational details of the research are shown in Table 1. The stainless steel cathode and iron anode are completely submerged in *D. salina* culture. Coating the cathode with a circular insulator (0.5 cm) and inserting it into the anode prevents the cathode and anode from binding together. The experiment was conducted utilizing direct current (DC) electricity with a constant voltage of 20 volts. Using an AC-DC adapter, a 220 volt AC supply was transformed into DC (Sunshine 30V 5A, P-3005D, China). Electrocoagulation times ranging from 0 to 30 min were varied to assess the harvesting efficiency and TAN from the culture of *D. salina.* The settling time was set for 60 min. At a depth of 2 cm, samples were taken from the supernatant to check the optical density (OD), the harvesting efficiency of *D. salina* (%), the total alkalinity (TAN), pH, and temperature.

**2. 3. Sample Analysis and Concentration Calculation** The pH and temperature measurement refers to standard methods for the examination of water and wastewater [21]. pH was measured using a pH meter WalkLAB TL9000 (TransInstruments, Singapore). TAN analysis was performed using the phenate method [20] by adding 1 mL of phenol, 1 mL of sodium nitroprusside,

**TABLE 1.** Details of harvesting operations *D. salina* using EC

| Indicator | Unit | Note |
|---|---|---|
| Temperature | °C | The temperature according to laboratory conditions |
| pH | - | pH according to the conditions of the microalgae to be harvested (initial pH is 8.72) |
| Glass beaker volume | mL | 600 |
| Types of microalgae | - | *D. salina* |
| Microalgae culture vol | mL | 500 |
| Stirrer/magnet | mm | 25 x 8 |
| Anode material | - | stainless steel 304 |
| Anode shape/geometry | - | spiral/ helix |
| Anode length | cm | 10 |
| Anode diameter | cm | 5 |
| Cathode material | - | iron S45C |
| Cathode shape/geometry | - | solid |
| Cathode length | cm | 10 |
| Cathode diameter | cm | 2 |
| Stirring speed | rpm | 400 |
| Settling time | min | 60 |

and 2.5 mL of oxidizing solution to 25 mL of sample in a 50 mL Erlenmeyer flask. Plastic or paraffin wrap covered the sample.

The color requires at least an hour to develop at room temperature (22-27°C) and under dark , and it is stable for 24 hours. Spectrophotometric measurement of color absorption was at 640 nm wavelength (UV-Vis Genesys 150 Spectrophotometer, Thermo Scientific, USA). The stock ammonia solution was diluted to create standard and blank solutions. A standard curve plotted standard absorbance versus standard ammonia concentration. Sample absorbance was compared to a standard curve to calculate concentration. Ammonium concentration was then calculated using equation (2) [22]. Removal efficiency was calculated using equation (3). A spectrophotometer (Spectroquant®Prove 100, Merck KGaA, Darmstadt, Germany) adjusted to a wavelength of 442 nm was used to measure the optical density (OD) of *D. salina* culture, which allowed for the calculation of the percentage of harvesting efficiency (%).

Lie and Liu [23] stated that optical density is an accurate and efficient approach for measuring microalgal biomass (OD). A spectrophotometer was utilized to scan the maximum wavelength automatically [24].

$$Ammonia = \frac{\text{TAN X } 10^{pH}}{e^{\left(\frac{6344}{273+oC}\right)} + 10^{pH}} \quad (1)$$

where Ammonia is the concentration of ammonia as nitrogen (mg/L), TAN is the concentration of total ammonia nitrogen (mg/L), pH and temperature (°C).
Ammonium calculation:

$$\text{Ammonium} = \text{TAN} - \text{ammonia} \quad (2)$$

where: Ammonium is the concentration of ammonium as nitrogen (mg/L), Ammonia is the concentration of ammonia as nitrogen (mg/L), TAN is the concentration of total ammonia nitrogen (mg/L).

$$\text{Removal efficiency (\%)} = [1-(X_{out}/X_{in})]*100 \quad (3)$$

Where: Removal efficiency is the removal efficiency of *D. salina* culture (%), $X_{in}$ is the initial concentration (mg/L), $X_{out}$ is the final concentration (mg/L).

The statistical significance of the research findings was determined using analysis of variance (ANOVA) (Origin 2022 software) at a 95% confidence level (p value 0.05).

## 3. RESULT AND DISCUSSION

### 3. 1. Harvesting Efficiency of *D. salina* Culture

The harvesting efficiency of *D. salina* was evaluated based on differences in optical density (OD) at wavelength 442 nm between the initial and harvested samples. This comparison was made in order to determine how successfully the microalgae were harvested [25].

What stands out in Figure 1 is the harvesting efficiency of *D. salina* culture in 2 min of 56.33%. It is interesting to observe that the harvesting efficiency can reach 93.72% after 5 min of electrocoagulation. The harvesting efficiency reaches a maximum of 98.43% when the electrolysis time is as long as 30 min. In applying electrocoagulation to harvest *D.* salina, $Fe^{3+}$ ions react with *D. salina* and cause coagulation [26]. This harvesting efficiency value is higher than the research conducted by Lucakova et al. [27], where the harvesting efficiency of *Chlorella vulgaris* is 85%. Parmentier [28] harvested *Chlorella* in continuous mode using an electrocoagulation-flotation tubular reactor and successfully harvested 88%. The harvesting efficiency of this study is higher than that of Mixson et al. [29], who applied EC using Al anodes for harvesting *D. viridis*. After 24 hours of EC, more than 95% of the biomass was harvested. The analysis of variance and harvesting time of *D. salina* using EC had no significant effect on harvesting efficiency; at the 0.05 level, the slope was significantly different from zero. This shows that harvesting for more than 5 min does not significantly increase the efficiency of the harvest.

The type of algae can affect the harvesting process due to autoflocculation [30]. *Scenedesmus quadricauda* produces extracellular polymeric substances (EPS) that stimulate efficient self-flocculation. If the pH drops, the negatively charged functional groups in EPS or microalgae cell walls will accept protons. The surface charge of the cell would then be neutralized in the culture media to produce a floc [31].

**3. 2. pH** Figure 2 shows the change in the pH value of *D. salina* culture during harvesting using the EC. The pH value of *D. salina* culture wastewater was as required in government regulation. Government regulations are decisions made by the government in the form of regulations that apply to all regions of the country. We

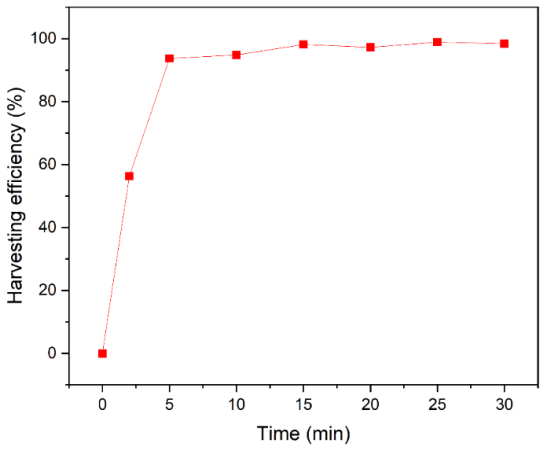


**Figure 1.** Graphics of harvesting efficiency (%) of *D. salina* culture when harvested using EC for 30 min

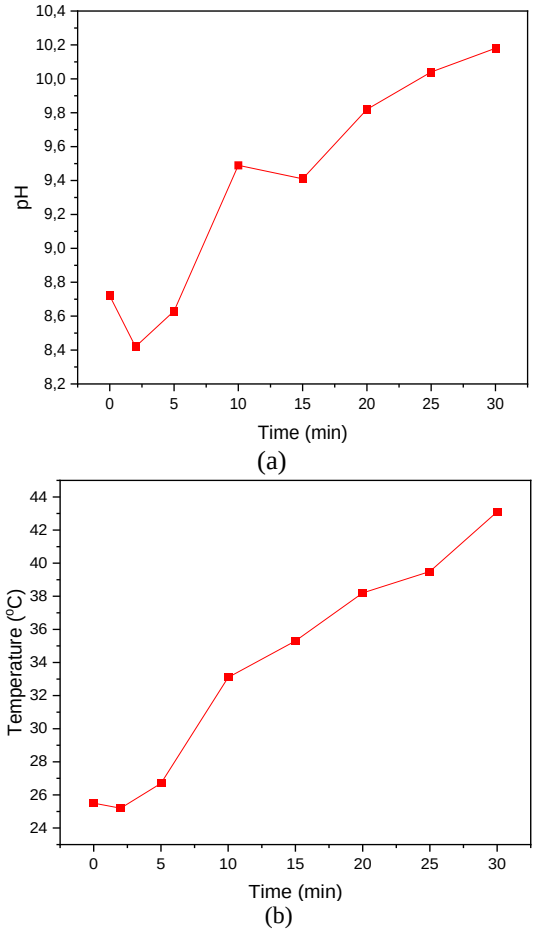


**Figure 2.** Graph of *D. salina* culture pH and temperature when harvested using EC for 30 min

used Government Regulation Number 22 of 2021 concerning the Implementation of Environmental Protection and Management of Class II Rivers, which states that a safe pH for the environment is between 6-9.

What stands out in Figure 2 is that the initial pH of *D. salina culture* was 8.72; after EC was carried out in an effort to harvest microalgae, the pH decreased in 2 min and 5 min by 8.42 and 8.63, respectively. However, at 10 min, the pH increased to 9.49, and at 30 min the pH increased to 10.18. The analysis of variance and harvesting time of *D. salina* using EC has a significant effect on temperature increase; at the 0.05 level, the slope is significantly different from zero. Based on this study, the pH of *D. salina* culture wastewater was safe for the environment when the harvesting process was carried out for 5 min.

As a result of oxidation processes at the anode, $Fe^{2+}$ ions will be produced if iron is used [32], as in the reaction Equation (4). Meanwhile, a reduction of water at the cathode creates hydroxide ions and $H_2$ gas (5).

$$Fe \rightarrow Fe^{2+} + 2e^- \quad (4)$$

$$2\ H_2O + 2e^- \rightarrow 2\ OH^- + H_2 \quad (5)$$

The pH of a solution increases as a result of the hydroxide ions produced through Equation (5). The longer the electrolysis process is conducted, the more $OH^-$ ions are produced at the cathode, resulting in a higher pH of the solution [33]. In this study, the pH during the harvesting of microalgae was alkaline. At this pH, it has the potential to shift ammonium equilibrium to ammonia, which is toxic to aquatic biota (Equation (6)) [34].

$$NH_4^+ + OH^- \leftrightarrow NH_3.H_2O \leftrightarrow NH_3 + H_2O \quad (6)$$

**3. 3. Temperature** Temperature measurements were carried out in situ in the laboratory at around 8 AM and 4 PM. Temperature affects certain chemical and biological reactions that occur in water and the organisms that live in it [35]. Temperature also affects other water quality indicators, such as dissolved oxygen (DO) and the power of hydrogen (pH) [36].

Figure 2 shows the change in *D. salina* culture temperature during harvesting using the EC process for 30 min. The temperature value of *D. salina* culture wastewater, as required in government regulation number 22 of 2021 concerning the Implementation of Environmental Protection and Management of class II rivers, is three deviations from the room temperature of the study site. During the research, the laboratory room temperature was 26°C, so the maximum temperature required was 29°C (26°C+3°C = 29°C).

What stands out in Figure 2 is that the initial *D. salina* culture temperature was 25.5°C; after EC was carried out in an effort to harvest microalgae, the temperature increased to 26.7°C at 5 min. The temperature s increased to 33.1°C at 10 min and 43.1°C at 30 min. Based on the ANOVA test, the harvesting time of *D. salina* using EC had a significant effect on the temperature increase; at the 0.05 level, the slope was significantly different from zero.

In this study, the wastewater temperature exceeds the limits of standards after the harvesting of *D. salina* for 30 min. The temperature of wastewater is safe for water bodies when the harvesting process using EC is carried out for 5 min. This increase in temperature has the potential to shift the balance of $NH_4^+$ to $NH_3$ [14], which is toxic to aquatic biota.

**3. 4. Removal Efficiency of Total Ammonia Nitrogen (TAN)** Total Ammonia Nitrogen (TAN) is the sum of ammonium and ammonia present in the water sample [13]. Figure 3(a) shows the TAN removal (%) and TAN concentration on *D. salina* culture during harvesting using EC for 30 min. Although the concentration of TAN is not required in government regulation number 22 of 2021 regarding the

Implementation of Environmental Protection and Management, TAN needs to be analyzed because it can be used to determine the concentration of ammonium and ammonia. Ammonia has attracted high global attention because its presence in surface water has a highly toxic effect on aquatic biota [6]. *D. salina* culture wastewater containing TAN has the potential to contaminate water bodies if disposed of directly without treatment. In addition to treating *D. salina* culture wastewater, efforts that can be made when disposing of microalgae culture wastewater include dilution by water [7], but water is a scarce resource [8].

What stands out in Figure 3 is that the concentration of TAN in the initial *D. salina culture* was 0.98 mg/L; after EC was carried out in an effort to harvest microalgae, TAN decreased to 0.87mg/L in the 2nd min. The concentration of TAN decreased continuously at 5, 10, 15, 20, 25, and 30 min, respectively, by 0.70 mg/L, 0.63 mg/L, 0.61 mg/L, 0.50 mg/L, 0.46 mg/L, and 0.27 mg/L. Based on the ANOVA test, the harvesting time of *D. salina* using EC had a significant effect on the decrease in TAN; at the 0.05 level, the slope was significantly different from zero.

In this study, maximum TAN removal of 72.49% resulted from the EC process for 30 min, 20 volts of electric power, stainless steel and iron electrodes. TAN removal was as low as 11.25% when using an electrolysis time of 2 min. This TAN removal is slightly lower than the results of a study conducted by Saavedra et al. [15], where the process of cultivating microalgae and harvesting using EC (Al electrodes) can remove 75% of total nitrogen and 5 hours of electrolysis time. Similar results were found by Liu and Liu [16], who integrated *Chlorella vulgaris* cultivation and EC pretreatment with iron electrodes capable of removing 88% of total nitrogen from anaerobic digestion wastewater for 40 min. Although the results of this study are lower, the TAN process only takes 2 min, while the study of Saavedra et al. [15] takes 5 hours and Liu and Liu [16] had 40 min of treatment.

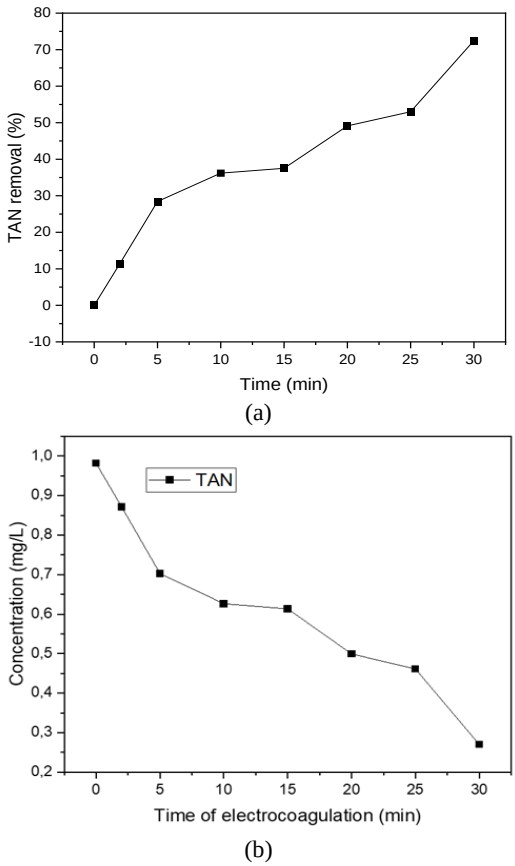


**Figure 3.** Graph of (a) TAN removal (%) and (b) TAN concentration of *D. salina* culture when harvested using EC

### 3. 5. The Equilibrium of Ammonia and Ammonium

Ammonia is an inorganic non-metallic component present in water [37]. The results of changes in ammonia and ammonium concentrations on *D. salina* culture during harvesting using the EC process for 30 min are shown in Figure 4. The ammonia concentration required in government regulation number 22 of 2021 for the Implementation of Environmental Protection and Management of Class II rivers is 0.2 mg/ L.

What stands out in Figure 4 is that the ammonia concentration in the initial *D. salina* culture was 0.23 mg/L, and ammonia decreased to 0.15 mg/L after EC for 5 min. Ammonia concentration for 10 min, 15 min, 20 min, and 25 min increased to 0.47 mg/L, 0.46 mg/L, 0.45 mg/L, and 0.44 mg/L, respectively. In this study, the concentration of ammonia in wastewater after harvesting *D. salina* for 30 min exceeds the limits of standards. Based on the ANOVA test, the harvesting time of *D. salina* using EC had no significant effect on the reduction of ammonia; at the 0.05 level, the slope was not significantly different from zero.

Temperature and pH might have had an effect on the amount of ammonia. The increase in ammonia may be due to the effect of increasing temperature and pH when harvesting using EC. When the pH increases, the reaction equilibrium tends to form $NH_3$ [14], as shown in Equation (6).

According to the equilibrium reaction, if the pH is high, the reaction equilibrium will shift toward $NH_3$. This is in accordance with the findings of Liu and Liu [16], which state that, when the pH of the solution is basic, the reaction equilibrium will shift to the right, thus inducing the formation of ammonia. Hydrogen and oxygen gases increase when water is electrolyzed, and nitrate is converted to nitrogen gas, but $NH_3$ is usually formed as well [38]. Othmani et al. [34] state that the pH of the solution increases after the EC process. The wastewater pH and temperature influence the relative concentrations of ammonia gas and ammonium ions [40].

The initial ammonium concentration of *the D. salina culture* was 0.75mg/L. After EC was carried out in an effort to harvest microalgae, ammonium decreased to 0.55mg/L at 5 min. Ammonium concentration decreased by 0.15 mg/L, 0.05 mg/L, 0.03 mg/L, and 0.01 mg/L after 10, 15, 20, 25, and 30 min, respectively. In this study, the maximum ammonium removal of 98.80 % resulted from the EC treatment for 30 min, 20 volts, stainless steel electrodes and iron. Wastewater treatment using electrochemistry previously reported was able to convert $NH_4^+$ into $NO_3$ and $N_2$ gas through the oxidation process [41]. Based on the ANOVA test, the harvesting time of *D. salina* using EC had a significant effect on ammonium reduction; at the 0.05 level, the slope was significantly different from zero.

Overall, the harvesting time of *D. salina* using EC had no significant effect on the reduction of ammonia but had a significant effect on the reduction of ammonium. Based on this study, it can be concluded that pH harvesting of *D. salina* using EC for 30 min actually increased the concentration of ammonia, which is toxic to aquatic biota. Overall, there was a decrease in the concentration of inorganic nitrogen compounds in the form of TAN. This was due to there being a general decrease in the concentration of ammonium.

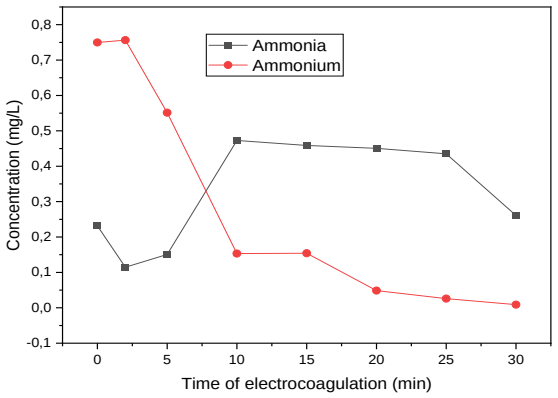


(a)

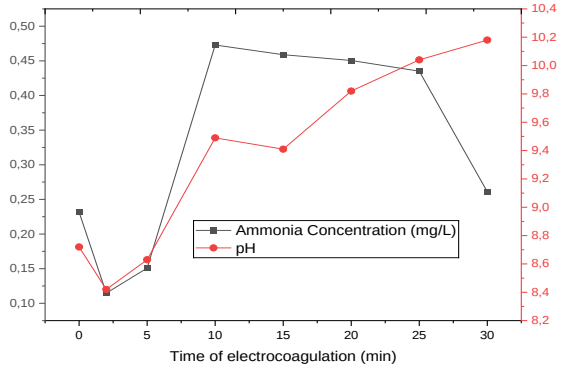


(b)

**Figure 4.** Equilibrium graph (a) concentrations of ammonia and ammonium; (b) pH and concentration of ammonia in *D. salina* culture when harvested using EC for 30 min

## 4. CONCLUSION

The harvesting efficiency reached 93.72 % after 5 min of electrocoagulation, which is a remarkable result. When the electrolysis time is as long as 30 min, the harvesting efficiency reaches its most significant point, which is 98.43%. *D. salina* culture wastewater that complies with regulatory standards in terms of temperature and pH may only be harvested for a maximum of 5 min. Overall, inorganic nitrogen compounds in the form of TAN decreased, which was dominated by a decrease in ammonium. Harvesting *D. salina* using EC was found to increase the concentration of ammonia, which is toxic to aquatic biota. Therefore, additional wastewater treatment is required so that the wastewater from microalgae harvesting is non-toxic to aquatic biota. In addition to the treatment of microalgae culture wastewater, efforts that can be made when disposing of microalgae culture wastewater are by reusing microalgae culture wastewater as a culture medium for these microalgae or other species.

## 5. ACKNOWLEDGMENT

The authors would like to acknowledge Wahyu from C-BIORE Laboratory, Diponegoro University and Marcelinus Christwardana, Chemistry Department of Diponegoro University, for their collaborative efforts in data collection and analysis.

## 6. REFERENCES

1. Cvetković, S. M., Radoičić, T. K., Novaković, J. G., Kovačević, V., Lopičić, Z. R., Adamović, V., and Kijevčanin, M. L. "Renewable hydrogen production perspective in Serbia via biogas generated from food processing wastewaters." ***Journal of Cleaner Production***, Vol. 363, (2022), 132142. https://doi.org/10.1016/j.jclepro.2022.132142
2. Hadiyanto, H., Widayat, W., Christwardana, M., and Pratiwi, M. E. "The flocculation process of Chlorella sp. using chitosan as a bio-flocculant: Optimization of operating conditions by response surface methodology." ***Current Research in Green and Sustainable Chemistry***, Vol. 5, (2022), 100291. https://doi.org/10.1016/j.crgsc.2022.100291
3. Figueiredo, D., Ferreira, A., Quelhas, P., Schulze, P. S. C., and Gouveia, L. "Nannochloropsis oceanica harvested using electrocoagulation with alternative electrodes – An innovative approach on potential biomass applications." ***Bioresource Technology***, Vol. 344, (2022). https://doi.org/10.1016/j.biortech.2021.126222
4. Xu, Z., Wang, H., Cheng, P., Chang, T., Chen, P., Zhou, C., and Ruan, R. "Development of integrated culture systems and harvesting methods for improved algal biomass productivity and wastewater resource recovery – A review." ***Science of The Total Environment***, Vol. 746, (2020), 141039. https://doi.org/https://doi.org/10.1016/j.scitotenv.2020.141039
5. Khan, S., Anjum, R., Raza, S. T., Ahmed Bazai, N., and Ihtisham, M. "Technologies for municipal solid waste management:

Current status, challenges, and future perspectives." ***Chemosphere***, Vol. 288, (2022), 132403. https://doi.org/https://doi.org/10.1016/j.chemosphere.2021.132403

6. Wang, X., Li, J., Chen, J., Cui, L., Li, W., Gao, X., and Liu, Z. "Water quality criteria of total ammonia nitrogen (TAN) and un-ionized ammonia (NH3-N) and their ecological risk in the Liao River, China." ***Chemosphere***, Vol. 243, (2020). https://doi.org/10.1016/j.chemosphere.2019.125328
7. Sounni, F., Elgnaoui, Y., El Bari, H., Merzouki, M., and Benlemlih, M. "Effect of mixture ratio and organic loading rate during anaerobic co-digestion of olive mill wastewater and agro-industrial wastes." ***Biomass Conversion and Biorefinery***, (2021). https://doi.org/10.1007/s13399-021-01463-4
8. Ferreira, A., Figueiredo, D., Cardeiras, R., Nabais, R., Ferreira, F., Ribeiro, B., Cordovil, C. M. D. S., Acién, F. G., and Gouveia, L. "Exploring Different Pretreatment Methodologies for Allowing Microalgae Growth in Undiluted Piggery Wastewater." ***Agronomy***, Vol. 12, No. 3, (2022). https://doi.org/10.3390/agronomy12030580
9. Nguyen, T. D. P., Le, T. V. A., Show, P. L., Nguyen, T. T., Tran, M. H., Tran, T. N. T., and Lee, S. Y. "Bioflocculation formation of microalgae-bacteria in enhancing microalgae harvesting and nutrient removal from wastewater effluent." ***Bioresource Technology***, Vol. 272, (2019), 34-39. https://doi.org/10.1016/j.biortech.2018.09.146
10. Guldhe, A., Misra, R., Singh, P., Rawat, I., and Bux, F. "An innovative electrochemical process to alleviate the challenges for harvesting of small size microalgae by using non-sacrificial carbon electrodes." ***Algal Research***, Vol. 19, (2016), 292-298. https://doi.org/https://doi.org/10.1016/j.algal.2015.08.014
11. Das, P. P., Sharma, M., and Purkait, M. K. "Recent progress on electrocoagulation process for wastewater treatment: A review." ***Separation and Purification Technology***, Vol. 292, (2022), 121058. https://doi.org/10.1016/j.seppur.2022.121058
12. Fayad, N., Yehya, T., Audonnet, F., and Vial, C. "Harvesting of microalgae Chlorella vulgaris using electro-coagulation-flocculation in the batch mode." ***Algal Research***, Vol. 25, (2017), 1-11. https://doi.org/https://doi.org/10.1016/j.algal.2017.03.015
13. Caicedo, J. R., Van Der Steen, N. P., Arce, O., and Gijzen, H. J. "Effect of total ammonia nitrogen concentration and pH on growth rates of duckweed (Spirodela polyrrhiza)." ***Water Research***, Vol. 34, No. 15, (2000), 3829-3835. https://doi.org/10.1016/S0043-1354(00)00128-7
14. Purwono, P., Hibbaan, M., Rezagama, A., and Budihardjo, M. A. "Ammonia-nitrogen ($NH3^{-}N$) and ammonium-nitrogen ($NH4^{+-}N$) equilibrium on the process of removing nitrogen by using tubular plastic media." ***Journal of Materials and Environmental Sciences,*** Vol. 8, No. S, (2017), 4915-4922.
15. Saavedra, M. D. M., Bissoto, F. P., de Souza, R. A., Concha, V. O. C., and Bastos, R. G. "Growth of desmodesmus subspicatus green microalgae and nutrient removal from sugarcane vinasse clarified by electrocoagulation using aluminum or iron electrodes." ***DYNA (Colombia)***, Vol. 86, No. 211, (2019), 225-232. https://doi.org/10.15446/dyna.v86n211.72379
16. Liu, Z., and Liu, Y. "Synergistic integration of electrocoagulation and algal cultivation to treat liquid anaerobic digestion effluent and accumulate algal biomass." ***Process Biochemistry***, Vol. 51, No. 1, (2016), 89-94. https://doi.org/https://doi.org/10.1016/j.procbio.2015.11.003
17. Dong, Y., Qu, Y., Li, C., Han, X., Ambuchi, J. J., Liu, J., Yu, Y., and Feng, Y. "Simultaneous algae-polluted water treatment and electricity generation using a biocathode-coupled electrocoagulation cell (bio-ECC)." ***Journal of Hazardous Materials***, Vol. 340, (2017), 104-112. https://doi.org/https://doi.org/10.1016/j.jhazmat.2017.06.055
18. Meetiyagoda, T. A. O. K., and Fujino, T. "Optimization of electrocoagulation–flotation treatment with an aluminum anode to enhance Microcystis aeruginosa cell removal efficiency." ***Journal of Water Process Engineering***, Vol. 48, (2022), 102871. https://doi.org/10.1016/j.jwpe.2022.102871
19. Indonesia, S. N. "Air dan Air Limbah-Bagian 59: Metode Pengambilan Contoh Air Limbah." ***SNI***, Vol. 6989, (2008), 2008.
20. Lucakova, S., Branyikova, I., Kovacikova, S., Pivokonsky, M., Filipenska, M., Branyik, T., and Ruzicka, M. C. "Electrocoagulation reduces harvesting costs for microalgae." ***Bioresource Technology***, Vol. 323, (2021), 124606. https://doi.org/10.1016/j.biortech.2020.124606
21. APHA. Standard Methods for the Examination of Water and Wastewater (23rd ed.). Washington.
22. Anthonisen, A. C., Loehr, R. C., Prakasam, T. B. S., and Srinath, E. G. "Inhibition of nitrification by ammonia and nitrous acid." ***Journal (Water Pollution Control Federation)***, (1976), 835-852.
23. Lu, L., Yang, G., Zhu, B., and Pan, K. "A comparative study on three quantitating methods of microalgal biomass." ***Indian Journal of Geo-Marine Sciences***, Vol. 46, No. 11, (2017), 2265-2272.
24. Wellburn, A. R. "The Spectral Determination of Chlorophylls a and b, as well as Total Carotenoids, Using Various Solvents with Spectrophotometers of Different Resolution." ***Journal of Plant Physiology***, Vol. 144, No. 3, (1994), 307-313. https://doi.org/https://doi.org/10.1016/S0176-1617(11)81192-2
25. Mussa, A., Hafiz, M. A., Das, P., and Hawari, A. H. "Harvesting of Chlorella sp. microalgae by dielectrophoretic force using titanium dioxide ($TiO_2$) insulated electrodes." ***Algal Research***, Vol. 65, (2022). https://doi.org/10.1016/j.algal.2022.102730
26. Bunce, J. T., Ndam, E., Ofiteru, I. D., Moore, A., and Graham, D. W. "A review of phosphorus removal technologies and their applicability to small-scale domestic wastewater treatment systems." ***Frontiers in Environmental Science***, Vol. 6, No. FEB, (2018), 1-15. https://doi.org/10.3389/fenvs.2018.00008
27. Lucakova, S., Branyikova, I., Kovacikova, S., Masojidek, J., Ranglova, K., Branyik, T., and Ruzicka, M. C. "Continuous electrocoagulation of Chlorella vulgaris in a novel channel-flow reactor: A pilot-scale harvesting study." ***Bioresource Technology***, Vol. 351, (2022). https://doi.org/10.1016/j.biortech.2022.126996
28. Parmentier, D., Manhaeghe, D., Baccini, L., Van Meirhaeghe, R., Rousseau, D. P. L., and Van Hulle, S. "A new reactor design for harvesting algae through electrocoagulation-flotation in a continuous mode." ***Algal Research***, Vol. 47, (2020). https://doi.org/10.1016/j.algal.2020.101828
29. Mixson, S. M., Stikeleather, L. F., Simmons, O. D., Wilson, C. W., and Burkholder, J. A. M. "pH-induced flocculation, indirect electrocoagulation, and hollow fiber filtration techniques for harvesting the saltwater microalga Dunaliella." ***Journal of Applied Phycology***, Vol. 26, No. 4, (2014), 1701-1709. https://doi.org/10.1007/s10811-013-0232-z
30. Ummalyma, S. B., Mathew, A. K., Pandey, A., and Sukumaran, R. K. "Harvesting of microalgal biomass: Efficient method for flocculation through pH modulation." ***Bioresource Technology***, Vol. 213, (2016), 216-221. https://doi.org/https://doi.org/10.1016/j.biortech.2016.03.114
31. Aljuboori, A. H. R., Uemura, Y., and Thanh, N. T. "Flocculation and mechanism of self-flocculating lipid producer microalga Scenedesmus quadricauda for biomass harvesting." ***Biomass and Bioenergy***, Vol. 93, (2016), 38-42. https://doi.org/https://doi.org/10.1016/j.biombioe.2016.06.013
32. Garcia-Segura, S., Eiband, M. M. S. G., de Melo, J. V., and Martínez-Huitle, C. A. "Electrocoagulation and advanced electrocoagulation processes: A general review about the fundamentals, emerging applications and its association with

other technologies." ***Journal of Electroanalytical Chemistry***, Vol. 801, (2017), 267-299. https://doi.org/https://doi.org/10.1016/j.jelechem.2017.07.047

33. Tahreen, A., Jami, M. S., and Ali, F. "Journal of Water Process Engineering Role of electrocoagulation in wastewater treatment : A developmental review." ***Journal of Water Process Engineering***, Vol. 37, (2020), 101440. https://doi.org/10.1016/j.jwpe.2020.101440
34. Purwono, Rezagama, A., Hibbaan, M., and Arief Budihardjo, M. "Ammonia-Nitrogen (NH3¯N) and Ammonium-Nitrogen (NH4+¯N) equilibrium on the process of removing Nitrogen by using tubular plastic media." ***Journal of Materials and Environmental Sciences,*** Vol. 8, No. S, (2017), 4915-4922.
35. Tibebe, D., Negash, A., Mulugeta, M., Kassa, Y., Moges, Z., and Yenealem, D. "Investigation of selected physico-chemical quality parameters in industrial wastewater by electrocoagulation process, Ethiopia." ***BMC Chemistry***, Vol. 16, No. 1, (2022), 1-9. https://doi.org/10.1186/s13065-022-00865-3
36. Haymanot, A., Heluf, G., and Molla, A. "Effects of municipal and industrial discharges on the quality of Beressa river water, Debre Berhan, Ethiopia." ***Journal of Ecology and The Natural Environment***, Vol. 7, (2015), 23-28. https://doi.org/10.5897/JENE2015.0495
37. Al-Othman, A. A., Kaur, P., Imteaz, M. A., Hashem Ibrahim, M. E., Sillanpää, M., and Mohamed Kamal, M. A. "Modified bio-electrocoagulation system to treat the municipal wastewater for irrigation purposes." ***Chemosphere***, Vol. 307, (2022). https://doi.org/10.1016/j.chemosphere.2022.135746
38. Mook, W. T., Chakrabarti, M. H., Aroua, M. K., Khan, G. M. A., Ali, B. S., Islam, M. S., and Abu Hassan, M. A. "Removal of total ammonia nitrogen (TAN), nitrate and total organic carbon (TOC) from aquaculture wastewater using electrochemical technology: A review." ***Desalination***, Vol. 285, (2012), 1-13. https://doi.org/10.1016/j.desal.2011.09.029
39. Othmani, A., Kadier, A., Singh, R., Igwegbe, C. A., Bouzid, M., Aquatar, M. O., Khanday, W. A., Bote, M. E., Damiri, F., Gökkuş, Ö., and Sher, F. "A comprehensive review on green perspectives of electrocoagulation integrated with advanced processes for effective pollutants removal from water environment." ***Environmental Research***, Vol. 215, (2022). https://doi.org/10.1016/j.envres.2022.114294
40. Wang, L. K., Hung, Y.-T., and Shammas, N. K. Advanced Physicochemical Treatment Technologies. ***Advanced Physicochemical Treatment Technologies*** (Vol. 5). Springer. https://doi.org/10.1007/978-1-59745-173-4
41. Reilly, M., Cooley, A. P., Richardson, B., Tito, D., and Theodorou, M. K. "Electrocoagulation of food waste digestate and the suitability of recovered solids for application to agricultural land." ***Journal of Water Process Engineering***, Vol. 42, (2021), 102121. https://doi.org/https://doi.org/10.1016/j.jwpe.2021.102121

## Persian Abstract

**چکیده**

برداشت ریزجلبک ها یک فرآیند مهم در به دست آوردن زیست توده است در حالی که آب باقیمانده هنوز غنی از مواد مغذی است. این مواد مغذی، عمدتاً نیتروژن و فسفر، در صورت تخلیه مستقیم و بدون تصفیه مناسب، می‌توانند باعث اتروفیکاسیون بدنه‌های آبی (رودخانه‌ها، دریاچه‌ها و اقیانوس‌ها) و تخریب اکوسیستم شوند. انعقاد الکتریکی (EC)یکی از روش‌های برداشت است و دارای چندین مزیت است: سهولت در عملیات، برداشت سریع، سازگاری، سازگاری با محیط زیست و ردپای کم. با این حال، روش EC برای برداشت ریزجلبک‌ها پتانسیل تولید آمونیاک را دارد که به دلیل تهدید محیط زیست نامطلوب است. هدف از این مطالعه ایجاد تعادل آمونیوم ($NH_4^+$)و آمونیاک ($NH_3$)در طول برداشت *Dunaliella salina* است. برداشت با استفاده از EC با تغییرات ۲۰ ولت، ۳۰ دقیقه و ۴۰۰ دور در دقیقه انجام شد. نتیجه نشان می دهد که راندمان برداشت می تواند پس از ۵ دقیقه پردازش به ۹۳.۷۲ درصد برسد و غلظت ترکیبات نیتروژن معدنی در نیتروژن کل آمونیاک (TAN)را به ۹۸.۸۰ درصد کاهش دهد.

International Journal of Engineering

Journal Homepage: www.ije.ir

# A Hybrid Approach to Sentiment Analysis of Iranian Stock Market User's Opinions

M. Ahangari, A. Sebti*

*Department of Computer Engineering, Faculty of Engineering, Golestan University, Gorgan, Iran*

*P A P E R I N F O*

*Paper history:*
Received 14 December 2022
Received in revised form 22 January 2023
Accepted 24 Januray 2023

*Keywords*:
*Sentiment Analysis*
*Opinion Mining*
*Lexicon Creation*
*Persian Lexicon*
*Support Vector Machine*

*A B S T R A C T*

With the significant growth of social media, individuals and organizations are increasingly using public opinion in these media to make their own decisions. The purpose of sentiment analysis is to automatically extract people's sentiments from those social networks. Social networks related to financial markets, including stock markets, have recently attracted the attention of many individuals and organizations. people in these networks share their opinions and ideas about each share in the form of a post or tweet. In fact, sentiment analysis in this field is the assessment of people's attitude towards each share. There are different approaches in sentiment analysis, in this article, a hybrid approach is proposed for sentiment analysis. In this way the feature vector used in machine learning is obtained from a lexicon that is automatically extracted from user's tweets. This lexicon is made by using stock price information related to user's opinion. Also, by using the next day's price information of each share, amendments were suggested to this lexicon. Therefore, the lexicon generated for the feature vector was constructed in three ways, and all three methods reported about an 8% improvement over the baseline method in terms of F-score. The baseline method that is considered for this work, is the Persian version of SentiStrength lexicon which is designed for general purpose.

***doi**: 10.5829/ije.2023.36.03c.18*

**NOMENCLATURE**

| | | | |
|---|---|---|---|
| $BR$ | $v$ | $P_{Min}$ | Share minimum price in day |
| $P_{Close}$ | Share closing price | $P_{Max}$ | Share maximum price in day |
| $P_{PrevClose}$ | Yesterday close price | | |

## 1. INTRODUCTION

What others think is always an important piece of information in the decision-making process for most people. The internet and the web now (among other things) make it possible for us to use the opinions and experiences of a wide range of people who are neither our personal acquaintances nor recognized professional critics in our everyday decisions [1]. With the dramatic growth of social media (e.g., reviews, forum discussions, blog and social networks) on the web, individuals and organizations increasingly use public opinion in these media for their decision-making process. However, finding and monitoring tweets on forums and reviewing the information contained in them, still remains a difficult task due to wide variety of sites. A mature reader will have difficulty in identifying relevant sites and accurately summarizing the information and opinions contained in them [2]. Today, customers and business owners use these opinions to identify the strengths and weaknesses of their products, but due to an increase in the volume of tweets, this no longer possible to study them case by case and draw a final conclusion and as a result, the need for a system to acquire knowledge automatically under the title of sentiment analysis (also known as opinion mining) emerged.

The sentiment analysis or opinion mining has many applications, in politics (elections, predicting political developments, the degree of unity of people or society in a case, etc.), social sciences and psychology (analysis of social and cultural issues, analysis of the impact of various events on people's behavior, etc.), management

*Corresponding Author Institutional Email: a.sebti@gu.ac.ir (A.Sebti)

Please cite this article as: M. Ahangari, A. Sebti, A Hybrid Approach to Sentiment Analysis of Iranian Stock Market User's Opinions, ***International Journal of Engineering, Transactions C: Aspects,*** Vol. 36, No. 03, (2023) 573-584

and leadership (assistance in decision-making, awareness of the level of satisfaction of customers or subscribers or a group of contacts, etc.).

So far, a lot of researches has been done in the field of opinion mining and sentiment analysis in English, Chinese and Russian languages. Despite the fact that Persian is the main language of Iran, Afghanistan and Tajikistan, and more than 110 million people around the world speak this language, very little researches have been done on the analysis of sentiments in Persian texts and there are still many complications and challenges in the analysis of sentiments and feelings in Persian language. Today, sentiment analysis can be used in various applications. Part of which includes the recognition of feelings towards specific issues in the field of product review, customer relationship management, financial markets and politics [3].

Financial markets, including stock markets, are markets that have always attracted the attention of many people. As a result, social networks that are related to these markets have been given much attention. In these social networks, users publish their opinions in the form of a post or tweet based on the state of shares or the market as a whole. User's opinions can be a reflection of the Functionality, news or price value of companies and based on the analysis that exists about a share or even they could be without any analysis and support, completely emotional and non-technical. Hence, it can be said that these comments contain positive or negative emotions.

Sentiment analysis in this field is the evaluation of people's attitude towards each share. which can be used for senior managers in various organizations, companies for whom the satisfaction or dissatisfaction of shareholders is important, or to predict the future trend of a stock.

A unique feature of these networks is that the price information of each share is available on the day of comment for that share. Since shares are growing or falling every day. Opinions or comments that shareholders or analysts publish every day are affected by this share growth and decline. In this research, we proved that the sentiment hidden in the comments or tweets posted on the days when the stock is falling or growing are correlated with the price information of that stock. In the proposed system, we used this topic to extract words automatically, to improve the quality of opinion mining in these networks.

In general, there are two main methods of sentiment analysis. Lexicon based method and machine learning based method [4]. Machine learning methods work to predict the polarity of sentiments based on training and testing data sets. And they can use supervised learning methods (they use labeled data for text classification) and unsupervised learning methods (they use raw data for text classification). While the Lexicon based approach does not require initial training to extract data. In these methods, a predefined list of words is used. So that each word is associated with a specific feeling. For our work, we first created a dictionary of the stock market corpus and then using this dictionary along with support vector machine (SVM), we evaluated our approach.

There are three general techniques for building sentimental lexicon. Manual technique, where each word is labeled by an expert according to the polarity of that word, which is time-consuming and costly. Creating emotional lexicon based on a dictionary, such as WordNet [5], which contains synonyms and antonyms of words and creating sentimental lexicon using corpus, this method is usually used to create sentimental lexicon for certain fields. The construction of sentimental lexicon in this way can be created by using the occurrence of words with each other, for example, if a word comes with words with positive polarity, it can be said that word also has positive polarity, or it is possible to match the polarity of the words of an already existing dictionary with that corpus by using a corpus in a certain area.

In our work, we use corpus-based method to build our proposed lexicon. The corpus used in this method is in the field of financial markets, which we extracted them from the , which includes 1,100,000 comments from the shareholders of the stock markets. In the proposed method, words and their polarity are extracted automatically.

In this article, a hybrid method is introduced that uses a lexicon and SVM algorithm to present a new model for sentiment analysis. In this way, the feature vector used in model learning is calculated from the constructed lexicon. In order to categorize the comments of each user, we used a 3-class classification, which includes three classes: positive, negative, and neutral. Also, using the generated dictionary in the feature vector has been done and compared in three ways. The conducted tests show that the use of the proposed method in all three modes has an improvement of about 8% in F-Score compared to the baseline method.

The rest of this article deals with the following topics: In section two, some of the most important researches related to the development of sentimental vocabulary for the Persian language are discussed. In the third section, the process of creating sentimental lexicon and the proposed model for sentiments analysis are described in detail. Evaluation and testing of the proposed model was done in the fourth section. And in the fifth section, we presented our conclusion.

## 2. RELATED WORKS

The most important and main step in the process of obtaining customer satisfaction is to identify the expectations, demands and possibly the requirements proposed by the consumer. Keeping in mind that not all customers are available in person or people who have

important comments about the product do not share it with the producers, it is possible to use social networks and taking into account the fact that people in this network share their opinions with others, get the information they need without the presence of the customer. Applications of sentiment analysis are examined at three levels: document level, sentence and aspect level [6]. Our work focuses on sentiment prediction at the document level in which we assign a positive, negative or neutral label to each document.

User comments are subjective documents that are rapidly being produced in virtual worlds. Therefore, they have a large volume. And it is not possible to review comments manually. Therefore, we need to use and choose appropriate techniques and methods to check opinions automatically. In general, the available techniques for sentiment analysis are divided into two categories; Techniques based on machine learning and techniques based on lexicon. Until now, most of the studies in the field of sentiment analysis have used machine learning techniques [7, 8]. Most of these works used SVM and Naïve Bayes algorithm for their work. They can use supervised or unsupervised learning methods. Supervised methods use labeled data for text classification, while unsupervised methods only use raw data [9]. Lexicon-based techniques use a dictionary to detect the sentiments of a text and determine the polarity of the given text with statistical calculations on positive and negative words. One of the most important advantages of this technique is that it is fast and does not require training data. And the main disadvantage of this method is its lack of scalability [10]. In the rest of this section, we will discuss some of the presented methods based on machine learning and based on lexicon.

**2. 1. Machine Learning Based Method** Turney [11] presented a simple unsupervised learning algorithm to classify reviews as recommended (thumbs up) or not recommended (thumbs down). in which the classification of a review is predicted by the average semantic tendency of the phrases in the review, which contain adjectives or adverbs. His proposed algorithm reaches an average accuracy of 74% when evaluated on 410 reviews from the site, opinions, sampling from four different domains (car reviews, banks, movies, and travel destinations). Rani and Kumar [12] conducted sentiment analysis on movie review data, which is in Hindi. They did this using different configurations of Convolutional Neural Network (CNN) configurations. They compared the results given by their Convolutional Neural Network model with the most advanced results of classic machine learning algorithms. The results of their work showed that their proposed model is able to achieve better performance than classical machine learning approaches and reached 95% accuracy. To overcome the shortcomings of current sentiment analysis methods, a sentiment analysis method based on Recurrent Neural Network (RNN) called Bidirectional Long Short-Term Memory (BiLSTM) [13]. After embedding the words using the Word2vec model and calculating the weight of the words using the TF_IDF algorithm, they converted their data, which includes 15,000 hotel review texts, into a weighted vector and then applied it to a BiLSTM network. Their experiments showed that their proposed model has higher accuracy and F1-Score than CNN, RNN, long short-term memory (LSTM) and Naïve Bayes algorithm. The accuracy and F1-Score obtained in their workwere about 91 and 92%, respectively. In a similar work conducted by Rhanoui et al. [14], they used Doc2vec model instead of Word2vec for word embedding, and also used CNN along with LSTM network to extract features as best as possible. They showed with experiments that their proposed method has higher accuracy compared to CNN, LSTM, BiLSTM and CNN-LSTM. The accuracy obtained for their proposed method, on their dataset, which is French articles obtained from national and international newspapers, is around 91%. So far, many works have been done using Support Vector Machine and Naïve Bayes algorithm for sentiment analysis [15-19]. The first work that has been done in the field of sentiment analysis in Persian language is the use of two standard methods of Support Vector Machine and Naïve Bayes in the field of movie review [20]. Also, the characteristics of the presence and Frequency of Unigrams, Bigrams and Trigrams for displaying documents were compared. According to the evaluations they made, they realized that in their work, the SVM algorithm performed better than Naïve Bayes. Also, using the Unigram feature improves the efficiency of the classifier compared to Bigram and Trigram. Also, considering only the presence of a feature has a better result than repeating it. In a similar work conducted by Saraee and Bagheri et al. [21], by examining four different information criteria, including Document Frequency (DF), Term Frequency Variance (TFV), Mutual Information (MI), and Modified Mutual Information (MMI), which were proposed by them, they found that the proposed method has a relatively better performance than the approaches of DF, TFV, and MI. The corrected mutual information can generally reach 85% of the F-Score criterion.

Another version of support vector machine used with particle swarm optimization algorithm for movie review data on Twitter [22]. It shows that using the particle swarm optimization algorithm to determine the parameters of the support vector machine, as well as using the features of n-grams and especially Unigrams can improve the accuracy by 4%. This improvement can be increased to about 2% more by cleaning the data. The first dataset called Pars-ABSA, which is completely based on aspects in Persian language, was presented by Ataei et al. [23]. To test the dataset, 6 models that have recently been used for the sentiment analysis based on aspects, in different fields in English, and their focus is

on deep learning methods, were used. Among the results of all models on their proposed work, the TD-LSTM model has had surprising results, because this model had poorer results compared to other models in English datasets, but in their work [24], it has better results than other models. In another work, two deep learning models (automatic encoders and complex neural networks) were used in the Persian movie review data set. The results obtained from these two models were compared with multilayer perceptron, the results showed that automatic encoders have higher accuracy than multilayer perceptron, and the proposed complex neural network model also performs better than automatic encoders with an accuracy of 82.6%.

Also, in some works, sentiment analysis is used to make predictions for other topics. Derakhshan et al. [25], used sentiment analysis to predict share price movement in stock markets. They proposed a new method that incorporates part-of-speech tags into topic modeling methods and called their method "LDA-POS" method. The average accuracy of the results for this method on quite large datasets in both English and Persian languages reach promising results of 56.24% and 55.33%, respectively, and they outperformed better than the related work that used its English dataset. Also, they produced a dataset for Persian language including five stocks, user opinions and their price movements, which is a valuable resource and they claim that this dataset is the first dataset of Persian stocks which containing quite a protracted time. In a similar work by Li et al. [26], they build a stock prediction system and propose an approach that 1) converts historical prices into technical indicators that summarize aspects of the price information, and models news sentiments by using different sentiment dictionaries and represents textual news articles by sentiment vectors, 2) constructs a two-layer LSTM neural network to learn the sequential information within market snapshots series, 3) constructs a fully connected neural network to make stock predictions. Experiments have been conducted on more than five years of real Hong Kong stock market data using four different sentiment dictionaries. Two baseline models, i.e. MKL and SVM, are employed as benchmarks to compare the performances of their proposed approach. They found from the results that, 1. Based on both information sources, the LSTM outperforms the MKL and the SVM in both prediction accuracy and F1 score. 2. The LSTM incorporating both information sources outperform the models that only use either technical indicators or news sentiments. 3. Among the four sentiment dictionaries, finance domain-specific sentiment dictionary models the new sentiments better, which brings at most 120% prediction performance improvement, compared with the other three dictionaries (at most 50%).

**2. 2. Lexicon-Based Methods** Most people working in the field of sentiment analysis have focused on machine learning-based methods, and few of them have turned their attention to vocabulary-based methods. Until now, a lot of good lexicon has been produced for English-language works [27-30], but the production of lexicon for the sentiment analysis in Persian language has not been given much attention.

One of the known polarity lexicon for English is SentiWordNet [31], In SentiWordNet, three points are assigned to each of the sets of synonyms in WordNet, which shows how positive, negative and neutral these sets are. This resource contains more than 117,000 sets of synonyms. The main idea of building SentiWordNet is to classify WordNet synonym sets using vocabularies of synonym sets. The important thing to consider about the scores assigned to each set of synonyms is that these scores do not indicate the strength of the polarity. They only indicate how positive, negative or neutral a set of synonyms is. As a result, the sum of these three scores for each set is equal to one. Another vocabulary of general polarity known for the English language is NRC lexicon [32]. This lexicon assigns tags to each word such as emotional, anger, fear, expectation, disgust, . as well as positive and negative tags, which is about 15,000 words and was manually created through Amazon's Mechanical Turk. The first approach of sentiment analysis in Persian [33], which is based on lexicon, was done by providing a framework for sentiment analysis. They introduced 2 sources for sentiment analysis in Persian language: 1. A Persian vocabulary that is related to Persian sentimental words along with its polarity. 2. A dataset that is manually collected and labeled by an expert. They used the Dempster-Shafer theory to determine the polarity of each document. The results of their work show that their proposed method gets a higher F-Score rating of about 90% compared to the methods based on machine learning. In another work by Basiri and Kabiri [34], help to solve the problem of lack of resources for sentiment analysis in Persian language, they present two new resources named SPerSent and CNRC for sentiment analysis in Persian language. SPerSent is a sentence-level dataset where each sentence is associated with two labels, a binary label for determining polarity and a 5-star rating label. CNRC is a Persian lexicon, which was created using the NRC [35] lexicon along with three steps of processing. To evaluate the CNRC lexicon, they compared it with the Persian version of the NRC and Senti_Str [36] lexicons on the SPerSent dataset by the Naïve Bayes machine learning algorithm. The results showed that the CNRC vocabulary has higher efficiency and accuracy than the other two lexicons. In a work similar to the method discussed by Basiri and Kabiri [37], they compared four vocabularies to prove that the direct translation of an English vocabulary into Farsi does not have the right quality in sentiment analysis, which includes the Persian version of Adjectives, CNRC, SentiStrength, NRC. The results showed that the direct translation used in NRC has the weakest performance,

while the pre-processing and lexicon refinement used in SentiStrength and CNRC improved the performance. Also, the results showed that using only adjectives leads to better results compared to using NRC.

Sabeti et al. [38] have proposed a new graph-based method for selecting and expanding seeds to generate general polarity vocabulary, called LexiPers, which includes more than 6000 words.

Amiri et al. [39] presented another method for lexicon-based sentiment analysis. They collected a Persian vocabulary that consists of adjectives, words and expressions considered in two formal and informal categories. Also, the collected vocabulary corresponds to standard Persian or obsolete Persian used by a certain number of native speakers. They also created a web interface that enables native speakers to manually assign a score to vocabulary words. Following the creation of an annotated Persian emotion vocabulary, they designed and developed a 3-language pipeline based on the GATE framework. Its components included a Persian tokenizer, Sentence Splitter, Part of Speech Tags and Gazetteer. As a result, they reported an accuracy of about 65%, which was considered an improvement compared to similar vocabulary-based approaches.

Dehkharghani [40] proposed a new translation-based method for creating polarity vocabulary in languages where there are few lexical resources for sentiment analysis, and applies it to Persian language. Their proposed method is done in four steps, first the words are translated into Farsi, then the translated words are manually labeled as positive, negative and neutral. The next step is feature extraction by English polarity vocabulary, and then, classification is done by Logistic Classifier. This is done by learning the mapping between the inputs described by the extracted features, and the three class labels (positive, negative and neutral). Finally, after the experiments, it was able to reach 92.95% accuracy by considering all four mentioned English vocabularies to extract features.

## 3. THE PROPOSED SYSTEM

Our work is divided into two phases, the first phase shows the lexicon building process and the second phase shows the process of classification tweets using the generated lexicon.

**3. 1. Lexicon Creation** As mentioned earlier, due to the importance of financial markets, we automatically created a lexicon for sentiment analysis in the stock market. This work was done in several steps, which are shown in Figure 1. The data or tweets intended for this purpose, and also used for evaluation and testing, were extracted from the site sahamyab.com and stored in our database. Also, we extracted the price value of each share from the official website of Iran Stock Exchange[1] and stored it in a separate table from the database. Table 1 summarized the information of shares stored in the database.

According to the proposed system for lexicon creation in Figure 1, after data collection, pre-processing is done on them. In the following, we will review and explain each of these pre-processing.

**3. 1. 1. Remove Unnecessary Tweets** Unfortunately, the daily price information of shares is not

**TABLE 1.** Information of selected shares

| Share | Frequency | year |
|---|---|---|
| Dey | 85461 | 1392-1399 |
| Fmeli | 43054 | 1392-1399 |
| Folad | 35978 | 1392-1399 |
| Haffari | 8917 | 1392-1399 |
| Hkashti | 30907 | 1392-1399 |
| Khodro | 162371 | 1392-1399 |
| Khsapa | 157308 | 1392-1399 |
| Satran | 31383 | 1392-1399 |
| Shabendar | 147451 | 1392-1399 |
| Shapna | 88118 | 1391-1399 |
| Shatran | 22605 | 1392-1399 |
| Tapico | 51276 | 1392-1399 |
| VTejarat | 50341 | 1392-1399 |
| VBMellat | 77265 | 1392-1399 |
| VBSader | 107565 | 1392-1399 |

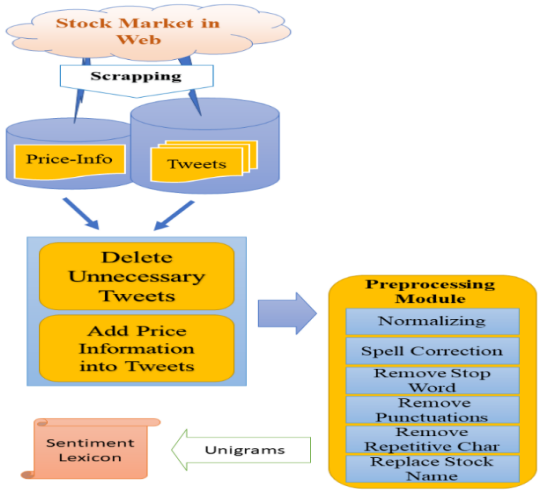


**Figure 1.** Proposed method for lexicon creation

[1] http://www.tsetmc.com/

available for all the days of posting comments. Since we needed this price information to automatically create the desired lexicon, we had to remove this category of tweets. The number of these tweets decreased to 900,000 tweets after this stage. Some examples of this price information along with time and stock name are given in Table 2.

### 3. 1. 2. Adding Share Price Information To Tweets

After removing unnecessary tweets, price information was added for each tweet. This information, which part of it is given in Table 2, has been used to determine the weight and polarity of the words of the final lexicon. Table 3 shows some of the tweets along with their price information.

**3. 1. 3. Preprocessing** One of the important steps in sentiment analysis is data pre-processing, choosing appropriate pre-processing methods can improve the correct classification of data [41]. Therefore, we perform data preprocessing in six steps:

**TABLE 2.** Some information for each share

| Share | Date | Maximum Price | Close price | Yseterday Price |
|---|---|---|---|---|
| Dey | 1399/12/25 | 18813 | 19486 | 19941 |
| Khodro | 1399/02/27 | 587 | 1174 | 1174 |
| Haffari | 1397/11/29 | 4121 | 4072 | 4116 |
| Hkashti | 1393/07/30 | 5607 | 5605 | 5687 |
| Folad | 1388/03/04 | 1884 | 1865 | 1900 |

**TABLE 3.** Example of Price information for each share

| Price Information | Tweets |
|---|---|
| ‘Share symbol’: ‘خودرو’, ‘date’: 1392/08/26, ‘maximum price’: 3150, ‘minimum price’: 3070, ‘close price’: 3090, ‘yesterday price’: 3075, … | #خودرو #حکشتی امروز هر دو صف می‌شوند. خوشبین |
| ‘Share symbol’: ‘شبندر’, ‘date’: 1393/01/26, ‘maximum price’: 2900, ‘minimum price’: 2854, ‘close price’: 2871, ‘yesterday price’: 11566, … | #شبندر سال ۹۴ تا سال ۹۶ شبندر بازم بهتر می‌شود. |
| ‘Share symbol’: ‘خودرو’, ‘date’: 1396/09/27, ‘maximum price’: 3150, ‘minimum price’: 3070, ‘close price’: 3090, ‘yesterday price’: 2850, … | #فولاد سلام خدمت دوستان فولادی با توجه به رشد خوب فولاد که نوش همه سهامدارن آن باشد، متاسفانه واگرائی منفی را نشان می‌دهد. احتیاط بیشتر پیشنهاد می‌شود. الهی همه پر سود باشند. |

[1] https://www.sobhe.ir/hazm/
[2] is negative
[3] prices

### Step 1: Normalization

For data normalization, we used the HAZM tool[1], which is a library for the Python language. This tool consists of different modules. that we used its normalization module for our work. Some words in Farsi consist of several parts. These words are usually separated from each other by a semi-space. But usually, people do not follow this point in the tweets they post on social networks. For example, the word "آن‌ها" is also incorrectly written as "آن ها". One of the tasks that this module does for us is to convert these types of spaces into thin spaces. Also, some letters in Farsi have different Unicode. In particular, the letters "ی" and "ک" which are sometimes written as "ي" and "ك" respectively. These letters are also converted into their standard form by this module. In fact, in this section, we converted the non-standard words into standard form.

### Step 2: Correcting Words

In most informal texts of Persian websites, users write the words as they use them in daily conversations. For this reason, these texts contain a large number of words with non-standard spelling. Therefore, checking the spelling of words in Persian is more challenging than in English [33]. To solve this problem, a list of words along with the number of their occurrences was extracted from the tweets stored in the database. Then the size of this list was reduced in two steps. In the first step, we used the known corpus of Hamshahri [42] in order to match each word from the obtained list with it. In the second step, with the assumption that the words whose frequency is less than ten times in the whole data will have a small effect on the estimation of the sentimental polarity of the sentences, these words were removed from the list, That left 2782 words from the list. Table 4 shows some of the words in this list along with their correct equivalents. Finally, the correct equivalent of each of these words was manually entered and applied to the entire database.

### Step 3: Removing Stop Words

To reduce the size of the data and improve the accuracy of sentiment analysis, we removed the stop words that do

**TABLE 4.** Part of the list of informal Persian words with its formal equivalent

| Incorrectly Spelled Words | The Correction Equivalent |
|---|---|
| منفیه | منفی است[2] |
| قیمتا | قیمت‌ها[3] |
| میریزه | می‌ریزد[4] |
| میگرده | می‌گردد[5] |
| نشن | نشوند[6] |

[4] decant
[5] turn
[6] don’t be

not have a significant impact on sentiment recognition and are frequently repeated in our dataset. For this purpose, unlike other works that use the list of known stop words for recognition, we created a Unigrams of words in the dataset, along with the frequency of each of them, to identify stop words. Assuming that the frequency of stop words in the data set will have a significant difference with other words. With this method, effective words in the dataset, which may be recognized as a stop word by the existing stop word lists, remain in the dataset.

**Step 4: Removing Punctuation Marks**
All punctuation marks except "#" and "." were removed from the dataset.

**Step 5: Removing Duplicate Letters**
Sometimes, among tweets, people write some words by repeating one letter to emphasize a topic, for example, they use "نههههههه" to emphasize the word "نه". In this module, the repetition of these letters was removed.

**Step 6: Changing The Share Name**
Since the name of the share does not affect the process of recognizing sentiments and causes redundancy in our lexicon, in this section we changed the name of shares to a special noun (#سهم), in order to prevent redundancy in the dataset, and to improve the word matching process.

**3. 1. 4. Building Lexicon** As mentioned in section 1, there are 3 general ways to build lexicon. that our job is to build lexicon based on corpus. The approach of the proposed system to build lexicon is to use n-grams features (especially Unigram and Bigram) in tweet data. Also, price information corresponding to each tweet is calculated to calculate the growth rate of each share at the time of sending tweet. The reason for calculating the growth rate is that we assume that when the growth rate of a stock is positive, people who tweet about that stock in these social networks will use more positive words in their tweets due to their sense of satisfaction. Also, if the share growth rate is negative, more negative words are used in the tweets that these people publish, due to their feeling of discomfort. Based on this, for each tweet, the growth rate was calculated according to the time of posting and which share this tweet is related to. To calculate the growth rate, we used Equation (1).

$$\text{Growth Rate} = \begin{cases} \frac{P_{Close}-P_{Min}}{P_{Min}} & , P_{Close} - P_{PrevClose} > 0 \\ \frac{P_{Close}-P_{Max}}{P_{Max}} & , P_{Close} - P_{PrevClose} < 0 \\ 0 & , P_{Close} - P_{PrevClose} = 0 \end{cases} \quad (1)$$

In our data, the "closing price" is available for each stock on each day. The reason for this is that if a share starts with a high value at the beginning of the trading hours and faces a significant decrease at the end of the trading hours, the comments or tweets that users publish for that share are very important and significant in terms of sentiments .The opposite is also true, i.e. if a share starts trading with a low value at the beginning of the market trading hours, and this value increases during the trading hours, the comments published by users are often associated with positive feelings. Therefore, using the lowest price and the highest price makes a better distinction for calculating the growth rate. Better distinction means that if the mentioned conditions happen, the growth rate for those tweets will be more positive or negative. For this purpose, to calculate the growth rate, we first check whether that share has increased or decreased compared to the previous day, if there is an increase, we calculate the growth rate from the first rule of formula, and if there is a decrease, we use the second rule of the formula.

As mentioned, the extraction of lexicon words was done by the feature of n-grams, and we entered the growth rate and frequency of these words along with it. The calculation of the growth rate of each of these lexicon words is that first, when these words are selected from tweets by the n-gram feature, the growth rate of each of the tweets in which that word is located is considered in a list for that word and after scanning all the tweets, the average of these growth rates for each word is considered as the growth rate of each word. For example, if the word "فروش" is present in 1000 tweets, the average growth rate of these tweets is considered as the growth rate of this word. As mentioned, we used unigram feature as n-gram feature. The details of which are mentioned below.

- **Building ParsStock-v1 Lexicon**

A part of the lexicon created using the Unigram feature is given in Table 5.

As mentioned before, our lexicon is automatically extracted and its size is 11422. After extracting words, these words were sorted and stored based on the absolute value of frequency multiplication in growth. Our purpose of doing this sorting is to show the impact of the growth rate on the feelings of shareholders or people who are active in social media related to the stock market and

**TABLE 5.** Part of the Lexicon obtained with Unigram feature

| Words | Frequency | Mean of Grow Rate (%) |
|---|---|---|
| فروش[1] | 89179 | -0.533 |
| خرید[2] | 128991 | 0.051 |
| خوشبین[3] | 161192 | 0.266 |
| حمایت[4] | 30432 | -0.604 |

[1] sale
[2] buy
[3] optimist
[4] support

share their opinions in these networks. Also, this sorting helps to reduce the feature vector dimension and its more effective conclusion, so that the words that have a greater impact on the sentiment analysis process are placed at the top of the lexicon.

After sorting, these words were used to form a feature vector for the comments, and for this we considered 11 different cases, which actually differ in the length of the vector for each comment. These 11 cases include vectors with dimensions of 11000, 10000, 9000, 8000, 7000, 6000, ..., 1000, the length of each vector is based on the number of the first N words of each list, which means that a vector with a length of 11000 is the same as the first 11000 words of the arranged lexicon. Since we used SVM for classification in our work, these feature vectors were used for SVM inputs. To build these feature vectors, we tried 3 different methods and compared the results of each of them. In the following, we will consider each of these methods.

**Method 1: Constructing the Feature Vector using the Presence and Absence of Words**

In this method, the numbers 1 and 0 are respectively assigned to the presence and absence of tweet's words in the feature vector and then given as input to SVM.

**Mehtod 2: Feature Vector Construction using Growth Rate**

In this method, for the presence of tweet words in the feature vector, the growth rate of that word is used, and if it is not present, the value is considered zero.

**Method 3: Feature Vector Construction using Modified Growth Rate**

This method is the same as the previous method, but the amount of growth rate has been modified. The reason for these adjustments is that although some lexicon words express a positive feeling in nature, the growth rate for them has become negative. The reason why the value of the growth rate in these words has become negative is that despite the promising tweets in which these words were seen, they were tweeted on the days in which the growth rate was negative. In order to recognize and correct some of these words in the lexicon and change their growth rate from negative to positive, we used the following method.

By looking carefully at the posted tweets, we will find that some of the comments posted by analysts are actually analysis or predictions of the future state of the share. In other words, the analyst observes the trading status of the stock on the current day, which is a negative day, and sees signs of the stock's return, and as a result, posts a positive tweet about the stock. It should be noted that the mentioned symptoms do not lead to a positive growth rate and are only discovered by a sharp analyst. With this argument, examining the tweets that were posted on negative days with a positive tomorrow can lead us to those words. Therefore, we selected tweets whose growth rate was negative on that day and positive on the next day, and among these selected tweets, we finally selected those whose growth rate changes from negative to positive were significant. In such a way that the growth rate on the day of tweet publication is less than -2 and on the day after the tweet publication, this growth rate is more than 2. After selecting tweets, Bigram words were extracted from these tweets. The reason for this is that we assumed that if the words that are extracted in this condition express a positive feeling, their frequency number will be higher compared to the case where only the growth rate on the day of the tweet is negative and the growth rate on the next day is not important. Therefore, we calculated the frequency of each bigram in the case where the growth rate becomes positive the next day, compared to the case where the growth rate is negative only at the time the tweet was sent and among these bigrams, we selected those whose ratio was greater than 1 and we saved it in a list called GrowRateChangeList.

After this, according to the previous method, we scored each of the feature vector values for each tweet. With the difference that, in addition to calculating the unigram for each tweet and checking its presence or absence in the feature vector, the Bigram values of that tweet are also calculated, and if these Bigrams exist in the GrowRateChangeList, the feature vector values for those words in the tweet, which is the growth rate here, are changed to positive if they are negative. And then they are considered as the input of the SVM.

**3. 2. Classification** After the comments were placed in the vector space, we used the SVM for classification. Then, all the states obtained by the three mentioned methods were given as input to the SVM to build the model and were evaluated and compared.

Figure 2 shows the proposed model for building the final model.

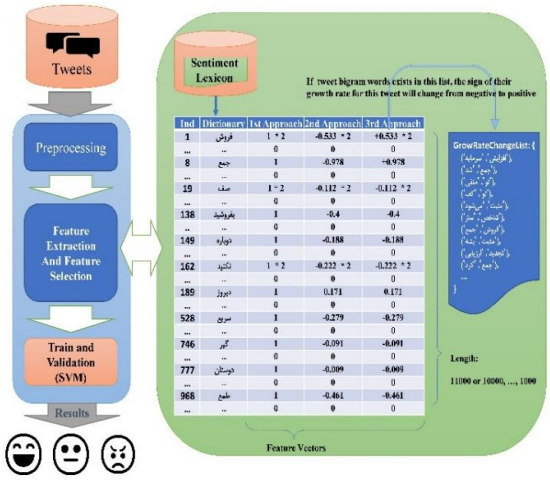


**Figure 2.** Proposed model for building the final model

## 4. EVALUATION

As mentioned, using the lexicons we generated, we performed three different methods to construct the feature vector for each tweet, and for each of these methods, 11 different cases are considered, which differ in the length of their feature vector. In order to compare, in our work we calculated all these states for each method and compared their results. Also, in order to show the efficiency of this method and compare it with other lexicons, we used a general lexicon that was used in the work of Basiri et al. [33], to calculate sentiments in our work. And we compared the obtained results with the results obtained from the proposed lexicon**.** For comparison, we randomly selected 1000 tweets from our database, and manually determined the polarity of each of them. In order to select the polarity, we used three classes: positive, negative and neutral. Table 6 shows the characteristics of our dataset.

**4. 1. SentiStrength Lexicon** An accessible library that is used to detect the polarity and strength of short and informal social texts [43]. Basiri et al. [33] used this library to analyze sentiments on their work. Since this software was designed and created for the English language, Basiri et al. [33] first manually translated the main list of words into Persian. And after removing the repeated words, they used them in their work.

**4. 2. Assessment Steps** In order to determine the polarity of each tweet in the dataset, we used machine learning methods in our work, and for this purpose, the SVM algorithm was used for classification. In the training and validation phase, 10-fold cross validation was used to make the process independent of the training data. In order to evaluate the classification model, since our data is unbalanced, we used three common evaluation criteria namely Precision, recall, and F1-score. Also we used Python to implement the proposed method. To use SVM, we used the Scikit-Learn library of Python. Scikit-Learn contains the svm library, which contains built-in classes for different SVM algorithms. Since our task is a classification task, we used the support vector classifier class written as SVC in Scikit-Learn's SVM library. This class has one parameter which is the kernel type. In the case of a simple SVM, we simply set this parameter as "linear" because simple SVMs can only classify linearly separable data.

**TABLE 6.** Dataset specifications

| Label | Frequency |
|---|---|
| Positive | 500 |
| Negative | 166 |
| Neutral | 334 |

**4. 3. Final Evaluation** In Tables 7, 8 and 9, the evaluation results for all cases obtained by different methods are summarized. Also, the best result obtained by the feature vector construction method using the modified growth rate is highlighted. As can be seen in Tables 7, 8 and 9, in general, the results obtained from the feature vector construction method using the modified growth rate are better than the results obtained by other methods in terms of the F1-score measure.

This improvement is tangible in two aspects, first in terms of the F1-score measure, in 9 out of 11 different cases, the mentioned method is better than other methods. As well as, the highest F1-score value is when the length of the vector is equal to 6000, which also belongs to the feature vector construction method using the modified growth rate. In Figure 3, a graph is shown

**TABLE 7.** Results of the evaluation of the proposed lexicons based on feature vector constructed using the presence and absence of words

| Cases | Precision | Recall | F-Score |
|---|---|---|---|
| Feature vector length 11000 | 57.6 | 56.0 | 56.5 |
| Feature vector length 10000 | 57.7 | 55.9 | 56.5 |
| Feature vector length 9000 | 57.6 | 55.8 | 56.4 |
| Feature vector length 8000 | 57.3 | 55.4 | 56.1 |
| Feature vector length 7000 | 57.6 | 55.8 | 56.4 |
| Feature vector length 6000 | 57.3 | 55.5 | 56.1 |
| Feature vector length 5000 | 57.9 | 56.4 | 56.8 |
| Feature vector length 4000 | 57.6 | 55.7 | 56.3 |
| Feature vector length 3000 | 57.3 | 55.7 | 56.2 |
| Feature vector length 2000 | 56.9 | 55.0 | 55.6 |
| Feature vector length 1000 | 56.9 | 54.0 | 55.1 |

**TABLE 8.** Results of the evaluation of the proposed lexicons based on feature vector constructed using growth rate

| Cases | Precision | Recall | F-Score |
|---|---|---|---|
| Feature vector length 11000 | 56.9 | 57.7 | 56.9 |
| Feature vector length 10000 | 57.1 | 57.8 | 57.0 |
| Feature vector length 9000 | 57.2 | 57.8 | 57.1 |
| Feature vector length 8000 | 56.9 | 57.5 | 56.8 |
| Feature vector length 7000 | 57.4 | 57.9 | 57.3 |
| Feature vector length 6000 | 56.8 | 57.5 | 56.8 |
| Feature vector length 5000 | 57.1 | 57.7 | 57.1 |
| Feature vector length 4000 | 56.5 | 57.0 | 56.4 |
| Feature vector length 3000 | 56.1 | 56.5 | 56.0 |
| Feature vector length 2000 | 56.8 | 56.9 | 56.6 |
| Feature vector length 1000 | 55.4 | 55.7 | 55.3 |

**TABLE 9.** Results of the evaluation of the proposed lexicons and SentiStrength using modified growth rate

| Cases | Precision | Recall | F-Score |
|---|---|---|---|
| Feature vector length 11000 | 57.5 | 58.4 | 57.5 |
| Feature vector length 10000 | 57.5 | 58.4 | 57.6 |
| Feature vector length 9000 | 57.8 | 58.6 | 57.8 |
| Feature vector length 8000 | 57.6 | 58.3 | 57.5 |
| Feature vector length 7000 | 57.4 | 58.1 | 57.4 |
| **Feature vector length 6000** | **57.8** | **58.6** | **57.9** |
| Feature vector length 5000 | 57.8 | 58.6 | 57.8 |
| Feature vector length 4000 | 57.4 | 58.0 | 57.4 |
| Feature vector length 3000 | 56.4 | 56.8 | 56.3 |
| Feature vector length 2000 | 55.0 | 55.7 | 55.1 |
| Feature vector length 1000 | 54.8 | 54.8 | 54.6 |

that draws the F1-score measure for each of the proposed methods.

In Figure 3, the effect of the growth rate in the calculation of emotions as well as the polarity of the sentences was well shown. As can be seen in the figure, correcting the growth rate made the results better in 9 out of 11 cases. Also, in order to compare the lexicon obtained in our work with other works, we used SentiStrength lexicon which is created for general usage and compared the results of this lexicon with our work in Table 10.

In Table 10, the best result of the proposed method is compared with the result obtained from SentiStrength lexicon. According to Table 10, the task of polarity detection using SentiStrength lexicon, which was created for general purpose, has the least accuracy in stock market data. The reason for this low accuracy is that the words in the data of the stock market are specific to the stock market and are not widely used in other fields. Therefore, SentiStrength lexicon among other lexicons obtained the lowest accuracy in all states.

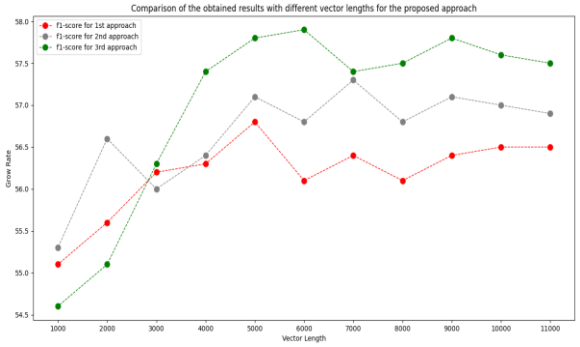


**Figure 3.** Comparing the results obtained from different cases that exist for the proposed lexicons

**TABLE 10.** Best result of the evaluation of the proposed lexicons and SentiStrength

| Approach | Precision | Recall | F-Score |
|---|---|---|---|
| **Feature vector construction using modified growth rate with vector length 6000** | **57.8** | **58.6** | **57.9** |
| Feature vector construction using SentiStrength lexicon | 51.2 | 49 | 49.8 |

## 5. CONCLUSION AND SUGGESTION

The purpose of sentiment analysis is to automatically extract people's opinions on various topics on the web**.** Social networks are an environment where people discuss and exchange opinions every day. One of these networks, which is always the focus of society, is the social networks related to the financial market. The stock market is one of these financial markets where people buy and sell shares. In these networks, people express their opinions about stocks. In our work, we performed opinion mining on tweets that are published daily in the stock market. The unique feature of these networks is the presence of price information for each share every day. We used this to automatically extract lexicon from 900,000 tweets available in these networks. In fact, these features were used to calculate the growth rate of each share at the time of tweeting, and the scores of obtained words for lexicon were determined with the help of these growth rates. To evaluate the proposed method for lexicon generation and feature vector construction based on it, the generated lexicon was compared with the Persian version of SentiStrength lexicon, which is designed for general use, and the results were evaluated. The results showed that their lexicon is less efficient than the lexicon produced by the proposed method in the field of stock exchange. Also, on our dataset, the best F-Score obtained by the proposed method is equal to 57.9%, which is 8% more than the value obtained for SentiStrength lexicon. In addition, after the investigations carried out in the feature selection, we were able to slightly improve the F-Score in our work by creating a new solution to modify the growth rate values that are used to score the feature vectors.

In the price analysis that was performed, the share price analysis of the day of posting tweets and the days before and after that was used. And it was shown that the state of the share in the coming days can help us to identify sentiments. Because many of the comments posted by users, are actually a reflection of the share's status in the upcoming days.

## 6. REFERENCES

1. Pang, B. and Lee, L., "Opinion mining and sentiment analysis", ***Foundations and Trends in Information Retrieval***, Vol. 2, No. 1-2, (2008), 1-135. doi: 10.1561/9781601981516

2. Liu, B. and Zhang, L., A survey of opinion mining and sentiment analysis, ***Mining Text Data***. 2012, Springer.415-463. doi: 10.1007/978-1-4614-3223-4_13
3. Chaturvedi, I., Cambria, E., Welsch, R.E. and Herrera, F., "Distinguishing between facts and opinions for sentiment analysis: Survey and challenges", ***Information Fusion***, Vol. 44, (2018), 65-77. doi: 10.1016/j.inffus.2017.12. 006
4. Taboada, M., Brooke, J., Tofiloski, M., Voll, K. and Stede, M., "Lexicon-based methods for sentiment analysis", ***Computational Linguistics***, Vol. 37, No. 2, (2011), 267-307. doi: 10.1162/COLI_a_00049
5. Miller, G.A., "Wordnet: An electronic lexical database", ***MIT press***, (1998). doi: 10.7551/mitpress/7287.001.0001
6. Liu, B., "Sentiment analysis and opinion mining", ***Synthesis Lectures on Human Language Technologies***, Vol. 5, No. 1, (2012), 1-167. doi: 10.1007/978-3-031-02145-9
7. Li, S., "Sentiment classification using subjective and objective views", ***International Journal of Computer Applications***, Vol. 80, No. 7, (2013). doi: 10.5120/13875-1749
8. Jo, Y. and Oh, A.H., "Aspect and sentiment unification model for online review analysis", in Proceedings of the fourth ACM International Conference On Web search and Data Mining. (2011), 815-824. doi: 10.1145/1935826 .1935932
9. Maynard, D. and Funk, A., "Automatic detection of political opinions in tweets", in Extended semantic web conference, Springer. (2011), 88-99. doi: 10.1007/978-3-642-25953-1_8
10. Dashtipour, K., Hussain, A., Zhou, Q., Gelbukh, A., Hawalah, A.Y. and Cambria, E., "Persent: A freely available persian sentiment lexicon", in International conference on brain inspired cognitive systems, Springer. (2016), 310-320. doi: 10.1007/978-3-319-49685-6_28
11. Turney, P.D., "Thumbs up or thumbs down? Semantic orientation applied to unsupervised classification of reviews", arXiv preprint cs/0212032, (2002).
12. Rani, S. and Kumar, P., "Deep learning based sentiment analysis using convolution neural network", ***Arabian Journal for Science and Engineering***, Vol. 44, No. 4, (2019), 3305-3314. doi: 10.1007/s13369-018-3500-z
13. Xu, G., Meng, Y., Qiu, X., Yu, Z. and Wu, X., "Sentiment analysis of comment texts based on bilstm", ***Ieee Access***, Vol. 7, No., (2019), 51522-51532. doi: 10.1109/ACCESS.2019.2909919
14. Rhanoui, M., Mikram, M., Yousfi, S. and Barzali, S., "A cnn-bilstm model for document-level sentiment analysis", ***Machine Learning and Knowledge Extraction***, Vol. 1, No. 3, (2019), 832-847. doi: 10.3390/make1030048
15. Ahmad, M., Aftab, S. and Ali, I., "Sentiment analysis of tweets using svm", ***International Journal of Computer Applications***, Vol. 177, No. 5, (2017), 25-29. doi: 10.5120/ijca2017915758
16. Ahmad, M., Aftab, S., Bashir, M.S., Hameed, N., Ali, I. and Nawaz, Z., "Svm optimization for sentiment analysis", ***International Journal of Advanced Computer Science and Applications***, Vol. 9, No. 4, (2018). doi: 10.14569/IJACSA.2018.090455
17. Korovkinas, K., Danėnas, P. and Garšva, G., "Svm and k-means hybrid method for textual data sentiment analysis", ***Baltic Journal of Modern Computing***, Vol. 7, No. 1, (2019), 47-60. doi: 10.22364/bjmc.2019.7.1.04
18. Dey, L., Chakraborty, S., Biswas, A., Bose, B. and Tiwari, S., "Sentiment analysis of review datasets using naive bayes and k-nn classifier", arXiv preprint arXiv:1610.09982, (2016).
19. Narayanan, V., Arora, I. and Bhatia, A., "Fast and accurate sentiment classification using an enhanced naive bayes model", in International Conference on Intelligent Data Engineering and Automated Learning, Springer. (2013), 194-201. doi: 10.1007/978-3-642-41278-3_24
20. Hajmohammadi, M.S. and Ibrahim, R., "A svm-based method for sentiment analysis in persian language", in International conference on graphic and image processing (ICGIP 2012), SPIE. Vol. 8768, (2013), 697-701. doi: 10.1117/12.2010940
21. Saraee, M. and Bagheri, A., "Feature selection methods in persian sentiment analysis", in International conference on application of natural language to information systems, Springer. (2013), 303-308. doi: 10.1007/978-3-642-38824-8_29
22. Basari, A.S.H., Hussin, B., Ananta, I.G.P. and Zeniarja, J., "Opinion mining of movie review using hybrid method of support vector machine and particle swarm optimization", ***Procedia Engineering***, Vol. 53, (2013), 453-462. doi: 10.1016/j.proeng.2013.02.059
23. Ataei, T.S., Darvishi, K., Javdan, S., Minaei-Bidgoli, B. and Eetemadi, S., "Pars-absa: An aspect-based sentiment analysis dataset for persian", arXiv preprint arXiv:1908.01815, (2019).
24. Dashtipour, K., Gogate, M., Adeel, A., Ieracitano, C., Larijani, H. and Hussain, A., "Exploiting deep learning for persian sentiment analysis", in International conference on brain inspired cognitive systems, Springer. (2018), 597-604. doi: 10.1007/978-3-030-00563-4_58
25. Derakhshan, A. and Beigy, H., "Sentiment analysis on stock social media for stock price movement prediction", ***Engineering Applications of Artificial Intelligence***, Vol. 85, (2019), 569-578. doi: 10.1016/j.engappai.2019.07 .002
26. Li, X., Wu, P. and Wang, W., "Incorporating stock prices and news sentiments for stock market prediction: A case of hong kong", ***Information Processing & Management***, Vol. 57, No. 5, (2020), 102212. doi: 10.1016/j.ipm.2020.102212
27. Cambria, E., Olsher, D. and Rajagopal, D., "Senticnet 3: A common and common-sense knowledge base for cognition-driven sentiment analysis", in Twenty-eighth AAAI conference on artificial intelligence. (2014). doi: 10.1609/aaai.v28i1.8928
28. Hu, M. and Liu, B., "Mining and summarizing customer reviews", in Proceedings of the tenth ACM SIGKDD international conference on Knowledge discovery and data mining. (2004), 168-177. doi: 10.1145/1014052.1014073
29. Deng, L. and Wiebe, J., "Mpqa 3.0: An entity/event-level sentiment corpus", in Proceedings of the 2015 conference of the North American chapter of the association for computational linguistics: ***Human Language Technologies.*** (2015), 1323-1328. doi: 10.3115/v1/N15-1146
30. Neviarouskaya, A., Prendinger, H. and Ishizuka, M., "Sentiful: A lexicon for sentiment analysis", ***IEEE Transactions on Affective Computing***, Vol. 2, No. 1, (2011), 22-36. doi: 10.1109/T-AFFC.2011.1
31. Esuli, A. and Sebastiani, F., "Sentiwordnet: A publicly available lexical resource for opinion mining", in Proceedings of the Fifth International Conference on Language Resources and Evaluation (LREC'06), (2006).
32. Mohammad, S.M. and Turney, P.D., "Crowdsourcing a word–emotion association lexicon", ***Computational Intelligence***, Vol. 29, No. 3, (2013), 436-465. doi: 10.1111/j.1467-8640.2012.00460.x
33. Basiri, M.E., Naghsh-Nilchi, A.R. and Ghassem-Aghaee, N., "A framework for sentiment analysis in persian", ***Open Transactions on Information Processing***, Vol. 1, No. 3, (2014), 1-14. doi: 10.15764/OTIP.2014.03001
34. Basiri, M.E. and Kabiri, A., "Sentence-level sentiment analysis in persian", in 2017 3rd International Conference on Pattern Recognition and Image Analysis (IPRIA), IEEE. (2017), 84-89. doi: 10.1109/PRIA.2017.7983023
35. Mohammad, S.M., Kiritchenko, S. and Zhu, X., "Nrc-canada: Building the state-of-the-art in sentiment analysis of tweets", arXiv preprint arXiv:1308.6242, (2013).

36. Thelwall, M., Buckley, K. and Paltoglou, G., "Sentiment strength detection for the social web", ***Journal of the American Society for Information Science and Technology***, Vol. 63, No. 1, (2012), 163-173. doi: 10.1002/asi.21662

37. Basiri, M.E. and Kabiri, A., "Translation is not enough: Comparing lexicon-based methods for sentiment analysis in persian", in 2017 International Symposium on Computer Science and Software Engineering Conference (CSSE), IEEE. (2017), 36-41. doi: 10.1109/CSICSSE .2017.8320114

38. Sabeti, B., Hosseini, P., Ghassem-Sani, G. and Mirroshandel, S.A., "Lexipers: An ontology based sentiment lexicon for persian", arXiv preprint arXiv:1911.05263, (2019).

39. Amiri, F., Scerri, S. and Khodashahi, M., "Lexicon-based sentiment analysis for persian text, In Proceedings of the International Conference Recent Advances in Natural Language Processing, (2015), 9-16.

40. Dehkharghani, R., "Sentifars: A persian polarity lexicon for sentiment analysis", ***ACM Transactions on Asian and Low-Resource Language Information Processing***, Vol. 19, No. 2, (2019), 1-12. doi: 10.1145/3345627

41. Haddi, E., Liu, X. and Shi, Y., "The role of text pre-processing in sentiment analysis", ***Procedia Computer Science***, Vol. 17, (2013), 26-32. doi: 10.1016/j.procs.2013 .05.005

42. AleAhmad, A., Amiri, H., Darrudi, E., Rahgozar, M. and Oroumchian, F., "Hamshahri: A standard persian text collection", ***Knowledge-Based Systems***, Vol. 22, No. 5, (2009), 382-387. doi: 10.1016/j.knosys.2009.05.002

43. Thelwall, M., Buckley, K., Paltoglou, G., Cai, D. and Kappas, A., "Sentiment strength detection in short informal text", ***Journal of the American Society for Information Science and Technology***, Vol. 61, No. 12, (2010), 2544-2558. doi: 10.1002/asi.21416

## Persian Abstract

**چکیده**

با رشد چشمگیر رسانه‌های اجتماعی، افراد و سازمان‌ها به طور فزاینده ای از افکار عمومی در این رسانه‌ها برای تصمیم گیری خود استفاده می کنند. هدف از تحلیل احساسات استخراج خودکار احساسات افراد از آن شبکه‌های اجتماعی است. شبکه‌های اجتماعی مرتبط با بازارهای مالی، از جمله بازار سهام، اخیرا مورد توجه افراد و سازمان‌های بسیاری قرار گرفته است. افراد در این شبکه‌ها نظرات و ایده‌های خود را در مورد هر سهم در قالب یک پست یا توییت به اشتراک می گذارند. در واقع تحلیل احساسات در این زمینه، ارزیابی نگرش افراد نسبت به هر سهم است. رویکردهای مختلفی در تحلیل احساسات وجود دارد، در این مقاله یک رویکرد ترکیبی برای تجزیه و تحلیل احساسات پیشنهاد شده است. در رویکرد پیشنهادی بردار ویژگی مورد استفاده در یادگیری ماشین از واژگانی که به طور خودکار از توییت‌های کاربر استخراج می شود، به دست می آید. این واژگان با استفاده از اطلاعات قیمت سهام مربوط به نظر کاربر ساخته شده است. همچنین با استفاده از اطلاعات قیمت روز بعد هر سهم، اصلاحاتی در این واژگان پیشنهاد شده است. این واژگان برای بردار ویژگی به سه روش ایجاد شده که در هر سه روش حدود ۸ درصد بهبود نسبت به روش پایه از نظر امتیاز F گزارش شده است. روش پایه ای که برای مقایسات در نظر گرفته شده است، نسخه فارسی واژه نامه SentiStrength است که برای اهداف عمومی طراحی شده است.

International Journal of Engineering

Journal Homepage: www.ije.ir

# An Enhanced McCormick Envelopes to Represent Kron's Loss Formula

H. Sharifzadeh*

*Department of Electrical and Computer Engineering, Hakim Sabzevari University, Sabzevar, Iran*

*P A P E R I N F O*

*Paper history:*
Received 28 January 2022
Received in revised form 18 January 2023
Accepted 02 February 2023

*Keywords*:
*Kron's Loss Formula*
*McCormick Envelopes*
*Tight Relaxations*

*A B S T R A C T*

Recently, some researchers have employed the McCormick envelopes method to convexify some NP-hard optimization problems with bilinear terms. However, few publications concentrate on its variants to derive a more tight convex relaxation for practical applications. This paper proposes a new viewpoint on Kron's loss formula, also known as the B-matrix formula, as an equation having bilinear terms. Relying on the perspective, we transform the loss equation to some linear constraints using an enhanced McCormick relaxation. In the technique, the domain of bilinear variables is divided into some smaller parts to improve the relaxation tightness. Some case studies with different nonconvex terms are considered to verify the effectiveness of the enhanced envelopes for capturing Kron's loss formula. The findings from the numerical simulations suggest that the proposed approach can represent Kron's loss equation precisely. Moreover, the method performs more effectively than the other methods available in the literature as it usually converges to more optimal solutions.

***doi**: 10.5829/ije.2023.36.03c.19*

**Graphical Abstract**

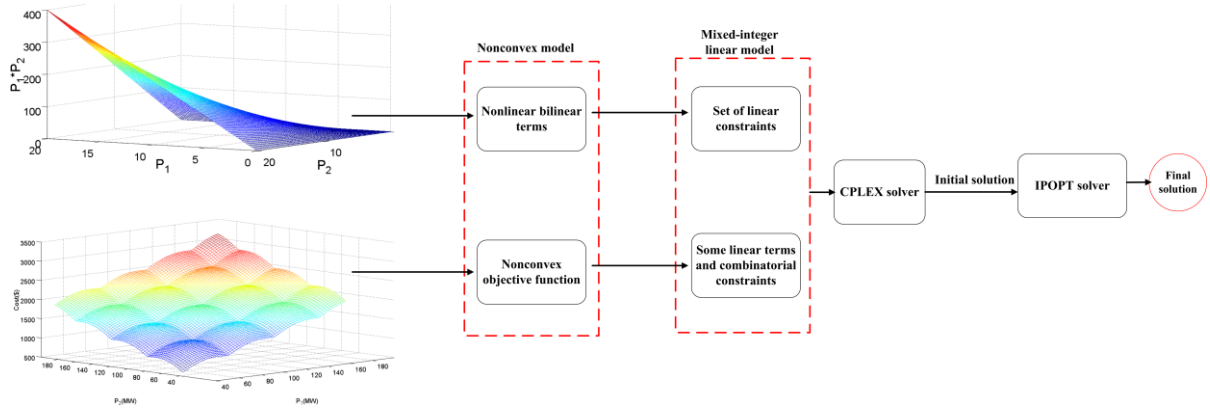


## NOMENCLATURE

| **Indices** | | | |
|---|---|---|---|
| $h$ | Breakpoint indices of cost functions | $D$ | Demand |
| $k, j$ | Generating unit indices | $e_{Max}^{k,j}$ | The maximum distance in McCormick envelopes |
| $n$ | Subinterval indices of Partitioned McCormick | $M^{k,j,n}$ | Big-M for constraint relaxation |
| $x$ | POZ indices | $P_k^L, P_k^U$ | Lower and upper bounds of generation in unit $k$ |
| **Sets** | | $P_k^{pozd^x}, P_k^{pozu^x}$ | Lower and upper bounds of x$^{th}$ POZ in unit $k$ |
| | | $P_k^0$ | Initial generation levels obtained from previous hour ED solution |

*Corresponding Author Institutional Email: h.sharifzade@hsu.ac.ir
(H. Sharifzadeh)

Please cite this article as: H. Sharifzadeh, An Enhanced McCormick Envelopes to Represent Kron's Loss Formula, ***International Journal of Engineering, Transactions C: Aspects,*** Vol. 36, No. 03, (2023) 585-593

| | | | |
|---|---|---|---|
| $H_k$ | Set of breakpoint indices of cost functions | $P_k^{L,n}, P_k^{U,n}$ | New lower and upper bounds of generation for unit *k* in subinterval *n* for partitioned McCormick |
| $K$ | Set of generating units | $\bar{p}_{h,k}$ | Generation in breakpoint *h* for unit *k* |
| $N$ | Set of Subinterval indices of Partitioned McCormick | $UR_k/DR_k$ | Ramp up/down limit for unit *k* |
| $X = \{1,2,\ldots,q\}$ | Set of POZ indices | **Variables** | |
| **Parameters** | | $P_k$ | Generation level of unit *k* |
| $c_k, b_k, a_k, e_k, f_k$ | Coefficients of cost function. characteristics | $\tilde{p}_{h,k}$ | Generation level of unit *k* in segment h for piecewise linear approximation of cost. function |
| $B_{00}, B_{k0}, B_{kj}$ | Loss coefficients in Kron's formula | $P_{losses}$ | Transmission losses |
| $v_{k,j}$ | Auxiliary continuous variables in the McCormick relaxation | **Functions** | |
| $v_{k,j}^n$ | Auxiliary continuous variables in the partitioned McCormick relaxation | $O(P)$ | The total cost of generating units |
| $z_R^{k,n}$ | Binary variables in the McCormick relaxation | $\tilde{O}(P)$ | The approximated total cost of generating units |
| $z_{h,k}$ | Binary variables in the partitioned McCormick relaxation | $PC_k$ | Generation cost of unit *k* |

## 1. INTRODUCTION

The increasing pressure on enhancing power systems' economic and environmental performance requires more efficient tools for electrical network management. However, most current tools, such as market-clearing models, usually ignore the transmission losses due to emerging complex optimization problems [1-4]. Nevertheless, this simplification leads to inefficient and imprecise modeling.

One can directly incorporate the physic of the problem to model the losses as accurately as possible using the AC power flow equations. Nonetheless, the accurate model creates highly nonlinear nonconvex equations constituting an NP-hard problem. On the other hand, one can use the DC power flow model as an alternative approach, which is the current practice of some electricity markets [5]. Although the DC power flow equations build a linear model, they do not consider the losses and, as a result, can not capture the network behavior accurately.

An intermediate technique can include one or some equations solely to approximate the transmission losses as the network effect model. The most well-known technique for approximating the losses is Kron's equation employing a nonlinear equation to represent the network losses [6].

Kron's formula yields a more straightforward loss computation approach than the complex nonlinear AC power equations. Kron's formula yields a more simple loss computation approach than the complex nonlinear AC power equations. However, it also questions the efficacy of the conventional optimization algorithms to solve the constructed model even in a relatively simple economic dispatch (ED) problem, especially when a model includes some other practical constraints such as wire drawing effects.

The ED problem involving the loss formula as a constraint can be solved using traditional nonlinear programming techniques such as the interior-point method or sequential quadratic programming (SQP) [7]. The techniques exhibit reliable behavior to solve nonlinear problems in general. Nevertheless, as a weakness, these solution algorithms naturally converge to local solutions rather than the global ones, which is problematic in multimodal problems.

In the past decade, some researchers have used newly emerged artificial intelligence (AI) algorithms to solve the complex problem [8]. In the area of the nonconvex ED, to name a few, differential evolution [9], teaching-learning algorithm [10], hybrid particle swarm optimization [11], chameleon swarm [12], artificial bee colony [13], peafowl optimization [14], hybridization of ETLBO and IPSO [15], Hybrid Multi-Verse Optimizer [16], ray optimization algorithm [17], particle swarm [18-20], GA–API [21], shuffled differential evolution [22], quasi-oppositional teaching learning [23], oppositional real coded chemical reaction [24], and krill herd algorithm [25] have been employed to solve the ED.

The algorithm utilizing stochastic parallel search mechanisms can solve the problem more effectively than the nonlinear programming methods and find the global solution. Moreover, they do not rely on objective function/constraint gradients to search the feasible space. However, they lack compelling evidence for convergence. Moreover, one generally can find some discrepancies in their identified solutions in different algorithm runs in practice. Although a deterministic technique has been previously presented [26], it does not consider trnamission losses in its ED model.

On the other side, relatively new deterministic global optimization methods usually utilize the convex relaxation of the nonconvex region to solve the nonconvex problems. McCormick envelopes have been introduced to relax generally nonconvex bilinear terms to one convex region [27]. A bilinear term is defined as the product of two different variables, i.e., the 'x×y' term. The nonlinear

parts of Kron's equation are bilinear terms in $P_k \times P_j$ form, where $P_k$ and $P_j$ represent the generation level of generating units $k$ and $j$, respectively.

In the literature, the transmission losses usually are ignored or managed heuristically, which usually leads to infeasibility. To the best of our knowledge, this work, for the first paper, calculates the losses using a robust deterministic technique known as the McCormick relaxation. Moreover, we utilize an enhanced version of the relaxation to improve the solution optimality. As the distinct advantage, the proposed method reliably converges to the optimal solution while the convergence is guaranteed.

We propose an enhanced McCormick technique to relax the unit generation product expressions in this work. The enhanced envelopes leverage deterministic approaches rather than stochastic searches used in AI algorithms, thereby presenting a robust and stable convergence behavior.

In summary, the contribution of this paper include the following:

1) We proposed a new viewpoint on Kron's formula as an equation having bilinear terms. Relying on the viewpoint, we transform the loss equation to some linear constraints that can be solved efficiently using available optimization software.

2) The presented enhanced version of the McCormick formulation provides a tight linear problem. Moreover, we linearized the nonconvexity terms due to wire drawing effects, and thereby we transformed the nonlinear nonconvex ED model to a fully tight linear model.

3) We also proposed a new mixed-integer technique to enforce prohibited operating zones (POZs) of the generating units having nonconvex space due to disjoint feasible space rather than nonconvex functions.

The rest of the paper organizes as follows: Firstly, in section 2, we formulate an ED model with the transmission losses. In the next section, we formulate the enhanced McCormick relaxation to recast Kron's formula as linear constraints. To verify the effectiveness of the proposed approach, we use two case studies having multimodal objective functions. The simulation results obtained from applying the solution method in the case studies are reported in section 4. Section 5 concludes the paper.

## 2. PROBLEM STATEMENT

The ED problem includes the sum of the generation costs as the objective function and a set of equality and inequality constraints describing the physical and technical limits of the power system [18]. The details of the considered ED formulation are provided below.

*Objective function:* Traditionally, the production costs of the generating units are shown by quadratic expressions. The objective function of the ED problem usually is defined as the sum of the generating unit production cost. Mathematically, the ED objective function can be computed as follows:

$$Min \sum_{k\in K} PC_k(P_k) = \sum_{k\in K}\left(c_k P_k^2 + b_k P_k + a_k\right) \quad (1a)$$

The representation of the cost functions in Equation (1a) makes the implicit assumption that a thermal unit has only one steam valve. However, the current modern units with multiple steam valves have more complex cost functions. For these modern units, the cost functions usually include sinusoidal terms, modeling the wire drawing effects, in addition to the quadratic expressions. Therefore, a more general objective function with the complex cost function can be expressed as follows:

$$MinO(P) = \sum_{k\in K} PC_k(P_k) = \sum_{k\in K}\begin{pmatrix} c_k P_k^2 + b_k P_k + a_k \\ +e_k\left|sin(f_k \times (P_k^L - P_k))\right| \end{pmatrix} \quad (1b)$$

The surface of the objective function, considering only two generating units, is shown in Figure 1. As can be seen, it forms a nonconvex space with many local minimal challenging optimization algorithms.

*Equality constraints:* Here, we represent the transmission network losses using well-known Kron's formula. Accordingly, the generating units should meet the total system load as well as the transmission losses. The requirement usually is called the power balance equation and can be written as follows:

$$\sum_{k\in K} P_k = D + P_{losses} \quad (2)$$

The $P_{losses}$ denotes the transmission losses and can be computed using Kron's formula by the following equation:

$$P_{losses} = B_{00} + \sum_{k\in K} P_k B_{k0} + \sum_{k\in K} \sum_{j\in K} P_k B_{kj} P_j \quad (3)$$

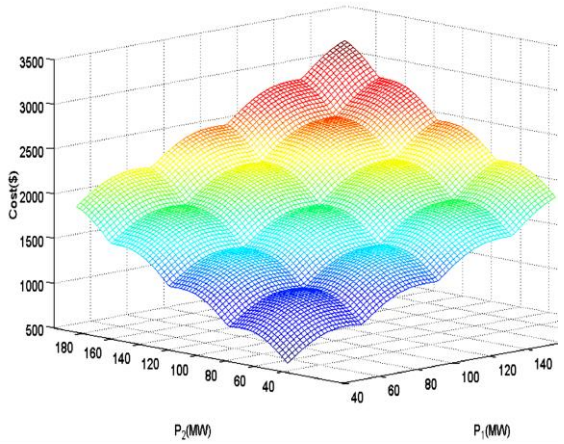


**Figure 1.** Nonconvex space of the objective function considering two generating units

$P_k B_{kj} P_j$, shown in red in Equation (3), are bilinear terms that are highly nonlinear and nonconvex in general.

Figure 2 illustrates the complex structure of the bilinear term. Next, we attempt to relax the bilinear terms tightly using the enhanced McCormick envelopes.

*Inequality constraints:* The technical limits of the generating units require that the units should be operated within the feasible range of generation:

$$P_k^L \le P_k \le P_k^U \forall k \in K \tag{4}$$

Furthermore, some units have prohibited operating zone (POZ), namely $P_k \notin \left[P_k^{pozd^x}, P_k^{pozu^x}\right]$. The generation limits considering the POZ can be described as follows:

$$\begin{aligned} &P_k^L \le P_k \le P_k^{pozd^1} \forall k \in K \; P_k^{pozu^x} \le P_k \le \\ &P_k^{pozd^{x+1}} \forall k \in K, \forall x \in X = \{1,2,\dots,q\} \; P_k^{pozu^q} \le \\ &P_k \le P_k^U \forall k \in K \end{aligned} \tag{5}$$

Finally, the ramp rate limits of the generation units for a single period ED problem can be modeled by the following constraints:

$$P_k \le P_k^0 + UR_k \forall k \in K \tag{6a}$$

$$P_k \ge P_k^0 - DR_k \forall k \in K \tag{6b}$$

In the next section, we reformulate the bilinear terms ($P_k P_j$) of Kron's equation in Equation (3) as well as the rectified sinusoidal terms ($|sin(f_k \times (P_k^L - P_k))|$) in Equation (1b) to achieve a (mixed-integer) linear model.

## 3. PROPOSED METHOD

The McCormick relaxation forming the convex hull of the bilinear term $P_k P_j$using two underestimators and two overestimators can be computed as follows [27]:

$$v_{k,j} \ge P_k^L P_j + P_k P_j^L - P_k^L P_j^L \tag{7a}$$

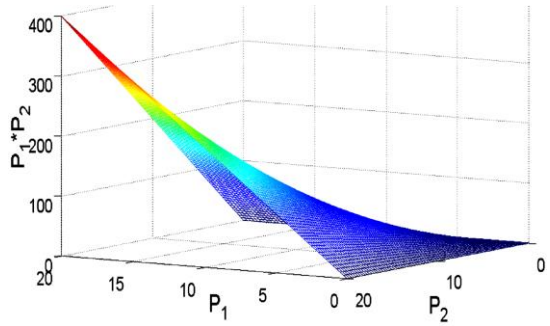


**Figure 2.** The complex surface of the bilinear expression

$$v_{k,j} \ge P_k^U P_j + P_k P_j^U - P_k^U P_j^U \tag{7b}$$

$$v_{k,j} \le P_k^U P_j + P_k P_j^L - P_k^U P_j^L \tag{7c}$$

$$v_{k,j} \le P_k P_k^U + P_k^L P_j - P_k^L P_j^U \tag{7d}$$

The new variable $v_{kj}$, together with the four additional linear constraints (7a)-(7d), replaces the bilinear nonconvex space with a convex one. As an advantage, the constructed constraints are linear, and as a result, one can solve the new problem using matured linear programming (LP) solvers.

As can be seen, the built constraints depend on the variable bounds, namely $[P_k^L, P_k^U]$ and $[P_j^L, P_j^U]$. It can be shown that the maximum distance of the relaxed space from the bilinear surfaces can be computed by the following equation [27]:

$$e_{Max}^{k,j} = \frac{(P_k^U - P_k^L)(P_j^U, P_j^L)}{4} \tag{8}$$

The expression in Equation (8) demonstrates that the maximum distance is proportional to the variable ranges: as the variable ranges widen, the relaxation performance weakens. Thus, one can divide the ranges into smaller parts and formulate the relaxation based on the new bounds to improve the relaxation tightness [28]. In this way, the McCormick relaxation is constructed for each sub-interval separately. Figure 3 illustrates the idea behind the partitioning mechanism more clearly [29]. As the number of partitions (N) increases, the envelopes build a set of tighter relaxations.

In this paper, we divide the generation bounds to N smaller subintervals and apply the McCormick envelopes for each of the subintervals separately. To this end, consider a unit whose generation level is denoted by $P_k^n$. The new generation variable in smaller subinterval has the following bounds:

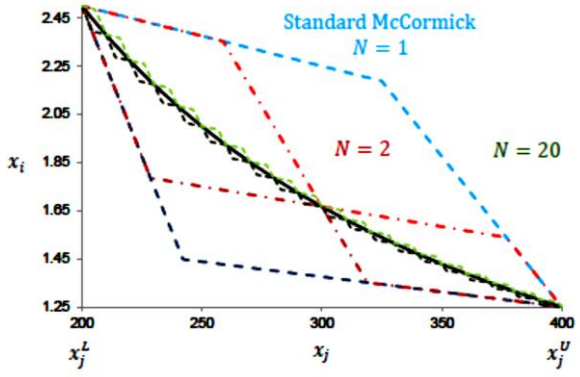


**Figure 3.** Tightening the McCormick relaxation by increasing the number of partitions [29]

$$P_k^{L,n} \le P_k^n \le P_k^{U,n} \quad (9)$$

Therefore, the original generation level variables and subinterval generation variables have the following relationships:

$$P_k = \sum_{\forall n \in N} P_k^n \quad (10)$$

$$P_k^n \le z_R^{k,n} P_k^{U,n} \forall n \in N, \forall k \in K \quad (11)$$

$$\sum_{\forall n \in N} z_R^{k,n} = 1 \forall k \in K \quad (12)$$

Constraint (12) requires only one subinterval can be selected at the same time, and other subinterval generations are enforced to be zero using constraint (11). To avoid introducing too many partitions and binary variables, we build the McCormick relaxation using one variable partitioning rather than two variables partitioning. Thus, the enhanced McCormick for the new generation variables with the novel bounds can be expressed as follows:

$$v_{k,j}^n \ge P_k^{L,n} P_j + P_k^n P_j^L - P_k^{L,n} P_j^L - M^{k,j,n} \times (1 - z_R^{k,n}) \quad (13a)$$

$$v_{k,j}^n \ge P_k^{U,n} P_j + P_k^n P_j^U - P_k^{U,n} P_j^U - M^{k,j,n} \times (1 - z_R^{k,n}) \quad (13b)$$

$$v_{k,j}^n \le P_k^{U,n} P_j + P_k^n P_j^L - P_k^{U,n} P_j^L - M^{k,j,n} \times (1 - z_R^{k,n}) \quad (13c)$$

$$v_{k,j}^n \le P_j P_k^{U,n} + P_j^L P_k^n - P_k^{L,n} P_j^U - M^{k,j,n} \times (1 - z_R^{k,n}) \quad (13d)$$

(13a)-(13d): $\forall n \in N, \forall k, j \in K$

$$v_{k,j}^n \le P_k^{U,n} P_j^U z_R^{k,n} \forall n \in N, \forall k, j \in K \quad (14)$$

$$P_{losses} = B_{00} + \sum_{k \in K} P_k B_{k0} + \sum_{n \in N} \sum_{j \in K} \sum_{k \in K} B_{kj} \times v_{k,j}^n \quad (15)$$

The Nonconvex cost functions also pose a challenge for the solution of the ED problem. Based on a technique that has been proposed by sharifzadeh [4]. We represent the nonconvex cost functions Equation (1b) through piecewise linear approximation rendering mixed-integer linear programming (MILP):

$$Min\tilde{O}(P) = \sum_{k \in K} \sum_{h \in H_k} \left(\alpha_{h,k} \tilde{p}_{h,k} + \beta_{h,k} z_{h,k}\right) \quad (16)$$

$$P_k = \sum_{h \in H_k} \tilde{p}_{h,k} \, \forall k \in K \quad (17)$$

$$\tilde{p}_{h-1,k} z_{h,k} \le \tilde{p}_{h,k} \le \tilde{p}_{h,k} z_{h,k} \forall k \in K, \forall h \in H_k \quad (18)$$

$$\sum_{h \in H_k} z_{h,k} = 1 \, \forall k \in K \quad (19)$$

Moreover, relying on the MILP representation, we propose a new technique to handle POZ restrictions. We can include the POZ segment bounds as the pairs of breakpoints in the piecewise linear approximation and, thereby, POZ segments can be avoided by imposing the pertained integer variables to become zero, namely:

$$\tilde{p}_{h,k} \in \left[P_k^{pozd^x}, P_k^{pozu^x}\right] \rightarrow z_{x,k} = 0 \forall k \in K, \forall x \in X \quad (20)$$

To summarize, the Mixed Integer-McCormick envelopes (MI-ME) model can be expressed as follows:
*Objective function:* Equation (16)
*Constraints:* (2), (5), (6a), (6b), (9)-(15) and (17) - (20)

As the solution obtained by the MI-ME model may contain error because of the approximations, we use its optimal solution as the initial solution of the original NLP model. The goal is to obtain a more accurate solution without approximation error. Clearly, the NLP model objective function is Equation (1b), and its constraints include Equations (2), (3), (5), (6a), and (6b). It is noted as the NLP model is a nonconvex problem, the pertained NLP solver converges to the nearest point to MI-ME optimal solution. Later in the numerical result section, we analyze the MI-ME and NLP roles to enhance the quality of obtained solutions.

## 4. NUMERICAL RESULTS

To show the effectiveness of the proposed solution method, we adopt two case studies, including 6-unit and 40-unit test systems modeling the transmission losses using Kron's formula. We draw required data for the 6-unit and 40-unit case studies from [18]. The case studies also include the sinusoidal cost functions stemmed from the wire drawing effects. The generation ranges of the 6-unit case study also contain POZs complicating the solution space. Therefore, the ED feasible spaces of both case studies make a complex nonconvex problem. As a result, they need particular solution techniques with global search ability rather than locally based solvers .

We use GAMS 24.1.3 to implement our solution approach and CPLEX 12 to solve the constructed ED model[1]. The absolute optimality gap is set to 0. Moreover, IPOPT as the NLP solver is employed to refine the final solution. We perform all simulations in a laptop with 8 GB RAM and 2.7 GHz Core i7 processors .

Table 1 displays the solutions of the ED problem reported in earlier works as well as the proposed method results for 6-unit case study. The first column in the tables shows the different ED solution methods that can be found in earlier works as well as the solution obtained by the

[1] http://www.gams.com

proposed method. The next three columns (columns two, three, and four) exhibit the reported optimal costs, i.e., objective function in Equation (1b). As the AI-based algorithms use random search mechanisms, they usually converge to different solutions in each algorithm application. The algorithms generally run several times, for example, 50 times. Then, the best and worst identified solutions, as well as the average of the identified solutions among all trial runs, are recorded. However, note that the proposed approach always converges to a unique solution in different runs as it relies on deterministic mechanisms to find the optimal solution. In other words, we solely write down the obtained solution of the proposed method three times in the pertained three columns of Tables 1 and 3.

Consider the second column of Table 1, which shows the best cost, among some conducted experiments as reported in the corresponding study, of the solution methods in case study I. As can be seen, the MI-ME identifies a more optimal solution compared with the other techniques. A couple of the meta-heuristic algorithms randomly obtain some optimal points close the MI-ME solution as shown in the second column of the table; however, the poor performance of their average and especially the worst solutions, in columns three and four of Table 1, respectively, suggests they exhibit unacceptable behavior in different trial runs, as they statistically converge to a weaker solution compared with their own best solution.

Table 2 shows the optimal scheduling of the generating units in case I, based on the proposed method, leading to \$15449.89, as the considered objective function in Equation (1b).

Table 3 shows the solutions of earlier studies and the proposed method result for case II, namely 40-unit case study. Case study II with a larger and more complex feasible space reasonably reveals the efficacy of the solution methods more clearly. From the viewpoint of the best solutions, rarely the previous studies have found the solutions close to the proposed Mi-ME solution, as can be seen in the second column of Table 3. More importantly, the result reported in columns three and four of Table 3 shows that the earlier works have low success rates. Namely, a large discrepancy can be seen between their identified solutions in different trial runs.

Apart from the discrepancy drawback, the AI techniques heavily rely on their parameters to search the solution space. In other words, their obtained solutions change depending on their parameter values. For example, the different versions of Particle swarm optimization (PSO) in Table 1, such as PSO, NPSO, NPSO-LRS, RDPSO, and IRDPSO, have parameters such as cognitive coefficient and social coefficient, number of iterations, and number of particles that need to be tuned beforehand. In other words, the results of the AI algorithms are sensitive to their parameter setup. The sensitivity challenges the application of these algorithms in practice, as a new difficult problem arises on how to tune the parameters effectively, which is an unsolved problem in general.

**TABLE 1.** Comparison of the solution method results in the 6-unit case study

| Method | Cost($) | | |
|---|---|---|---|
| | **Best** | **Average** | **Worst** |
| SA [17] | 15545.5 | 15488.98 | 15461.1 |
| GA [17] | 15524.69 | 15477.71 | 15457.96 |
| TS [17] | 15498.05 | 15472.56 | 15454.89 |
| PSO [17] | 15491.71 | 15465.83 | 15450.14 |
| GA [18] | 15459 | 15469 | 15524 |
| MTS [17] | 15453.64 | 15451.17 | 15450.06 |
| NPSO [19] | 15450 | 15452 | 15454 |
| NPSO-LRS [19] | 15450 | 15450.5 | 15452 |
| PSO [18] | 15450 | 15454 | 15492 |
| RDPSO [19] | 15449.89 | 15458.01 | NA[a] |
| IRDPSO [19] | 15449.89 | 15456.55 | NA |
| Proposed | 15449.89 | 15449.89 | 15449.89 |

a: Not available

**TABLE 2.** The optimal generation scheduling of the proposed method in case I

| Units | Generation (MW) |
|---|---|
| P1 | 447.5038 |
| P2 | 173.3182 |
| P3 | 263.4628 |
| P4 | 139.0653 |
| P5 | 165.4734 |
| P6 | 87.1347 |
| The objective function($) | **15449.89** |

**TABLE 3.** Comparison of the solution method results in the 40-unit case study

| Method | Cost($) | | |
|---|---|---|---|
| | **Best** | **Average** | **Worst** |
| GA-API [21] | 139864.96 | NA | NA |
| SDE [22] | 138157.46 | NA | NA |
| QOTLBO [23] | 137329.86 | NA | NA |
| BBO [24] | 137026.82 | 137116.58 | 137587.82 |
| DE/BBO [24] | 136950.77 | 136966.77 | 137150.77 |
| ORCCRO [24] | 136855.19 | 136855.19 | 136855.19 |
| KHA [25] | 136670.37 | 136671.24 | 136671.86 |
| Proposed | 136450.21 | 136450.21 | 136450.21 |

As a significant advantage, we design the MI-ME leveraging advanced deterministic modeling techniques as well as standardized off-the-shelf solvers. On the other side, AI algorithms are mainly devised based on some 'heuristics' and personal experiences. To the best of our knowledge, the algorithms lack compelling evidence for convergence. The large discrepancies between the obtained solutions of the algorithms also suggest their weakness in finding a unique solution and lack of reliable convergence. However, the proposed model and the employed solvers have solid evidence to prove their reliable convergence, as the achieved result confirms the advantage as well.

The optimal scheduling of the generating units in case II, obtained by the proposed method, is illustrated in Table 4. The scheduling results in \$136450.21, as the operation cost.

As noted earlier, we also used an NLP solver to refine the solution of the MI-ME. To analyze the share of the MI-ME and the NLP solvers in the improvement of the obtained solutions, we separately reported the solutions obtained in the models in Table 5. Moreover, we also shown the change in the solutions of the MI-ME model after the application of the NLP solver in percentage terms. Mathematically, the change can be computed as follows:

$$Difference(\%) = \frac{Cost_{MI-ME} - Cost_{NLP}}{Cost_{MI-ME}} \times 100 \quad (21)$$

Comparison of the results of MI-ME and NLP models, in columns two and three of Table 5 in both cases, indicates that the obtained objective functions are close to each other. To put it simply, the difference, as defined in Equation (21), between the obtained objective functions is less than 0.1%, as can be seen from column four of Table 5. Therefore, the MI-ME model converges to one point quite close to the final solution, and then, the NLP solver solely takes a small step forward to improve the solution locally.

To illustrate the change more clearly, we display the generation levels in the obtained solutions of the MI-ME and NLP models for case study I in Figure 4. As the figure shows, the change in generation levels in the MI-ME solution after the application of the NLP solver is negligible, suggesting that the MI-ME solution is placed very close to the final solution.

To show the power of the MI-ME in finding the optimal solution of the problem, the convergence characteristic of the incumbent value in case study II is illustrated in Figure 5. The 40-unit case includes many local minimal complicating finding the globally optimal solution. However, as the figure reveals, it only takes 6 steps to find the optimal solution.

Finally, to demonstrate the effectiveness of the proposed partitioned McCormick againts the classical McCormick, the case studies are also solved using the classical one. Table 6 compares the derived solution of the two McCormick types.

The table shows that in small-sized problems, such as 6-unit case, the classical McCormick performs satisfactory, as it also may find the optimal solution. Nonetheless, as the problem size increases, the classical one fails to find the optimal solution. On the other side, the proposed partitioned McCormick presents a tighter relaxation and can obtain the more optimal solutions consequently.

**TABLE 4.** The optimal generation scheduling of the proposed method in case II

| Units | Generation (MW) | Units | Generation (MW) |
|---|---|---|---|
| P1 | 114 | **P21** | 523.2794 |
| P2 | 114 | **P22** | 550 |
| P3 | 120 | **P23** | 523.2794 |
| P4 | 179.7331 | **P24** | 523.2794 |
| P5 | 87.7999 | **P25** | 523.2794 |
| P6 | 140 | **P26** | 523.2794 |
| P7 | 300 | **P27** | 10 |
| P8 | 300 | **P28** | 10 |
| P9 | 290.4802 | **P29** | 10 |
| P10 | 279.5997 | **P30** | 87.7999 |
| P11 | 243.5997 | **P31** | 190 |
| P12 | 94 | **P32** | 190 |
| P13 | 484.0392 | **P33** | 190 |
| P14 | 484.0392 | **P34** | 200 |
| P15 | 484.0392 | **P35** | 164.7998 |
| P16 | 484.0392 | **P36** | 164.7998 |
| P17 | 489.2794 | **P37** | 110 |
| P18 | 489.2794 | **P38** | 110 |
| P19 | 511.2794 | **P39** | 110 |
| P20 | 511.2794 | **P40** | 550 |
| The objective function(\$) | | **136450.21** | |

**TABLE 5.** cost obtained in the MI-ME model compared with the NLP model

| Case study | Cost (\$) | | |
|---|---|---|---|
| | MI-ME | NLP | Difference (%) |
| 6-unit | 15443.64 | 15449.89 | 0.04 |
| 40-units | 136311.371 | 136450.21 | 0.10 |

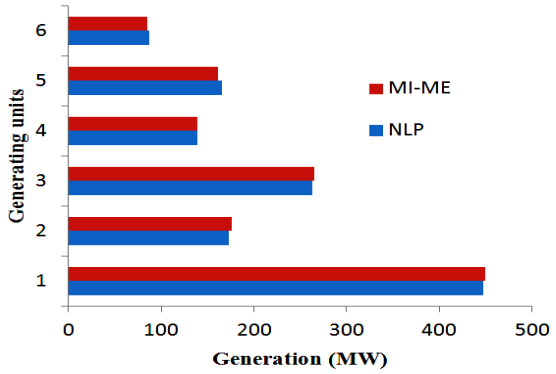


**Figure 4.** Generation levels in solutions of MI-ME and NLP models

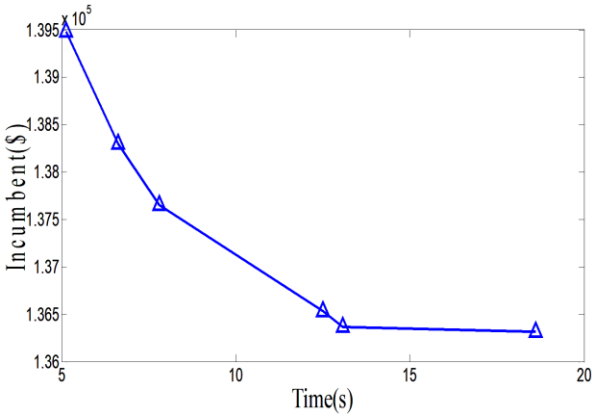


**Figure 5.** The convergence characteristic of the incumbent value in 40-unit case

**TABLE 6.** Comparison of the classical and partitioned McCormick relaxations in the considered case studies

| McCormick type | Case study | |
|---|---|---|
| | 6-unit | 40-units |
| The classical McCormick | 15449.89 | 136617.10 |
| The proposed partitioned McCormick | 15449.89 | 136450.21 |

## 5. CONCLUSION

To represent a tractable formulation of Kron's formula for transmission loss computation, we have proposed a novel viewpoint on the problem based on the McCormick relaxation of bilinear terms. To this end, we employ an enhanced McCormick envelope that tightly captures the loss equation. Comparison of the obtained solutions of the MI-ME model with the earlier work results on the adopted case studies shows the advantage of the proposed method to find the more optimal solutions. Furthermore, as the presented model relies on deterministic mechanisms for searching the solution space using matured solvers, it exhibits a highly reliable convergence behavior. Finally, the presented model can easily be employed without difficult trial and error procedures usually used to tune the parameters in AI algorithms.

## 6. REFERENCES


1. Valinejad, J., Oladi, Z., Barforoushi, T. and Parvania, M., "Stochastic unit commitment in the presence of demand response program under uncertainties", ***International Journal of Engineering, Transactions B: Applications***, Vol. 30, No. 8, (2017), 1134-1143. doi: 10.5829/ije.2017.30.08b.04.
2. Lotfi, M.M., "Short-term price-based unit commitment of hydrothermal gencos: A pre-emptive goal programming approach", ***International Journal of Engineering, Transactions C: Aspects***, Vol. 26, No. 9, (2013), 1017-1030. doi: 10.5829/idosi.ije.2013.26.09c.09.
3. Shakouri G, H., Amin Naseri, M. and Neshat, N., "A game theoretic approach for sustainable power systems planning in transition", ***International Journal of Engineering, Transactions C: Aspects***, Vol. 30, No. 3, (2017), 393-402. doi: 10.5829/idosi.ije.2017.30.03c.09.
4. Sharifzadeh, H., "Sharp formulations of nonconvex piecewise linear functions to solve the economic dispatch problem with valve-point effects", ***International Journal of Electrical Power & Energy Systems***, Vol. 127, (2021), 106603. doi: 10.1016/j.ijepes.2020.106603.
5. Bhattiprolu, P.A. and Conejo, A.J., "Multi-period ac/dc transmission expansion planning including shunt compensation", ***IEEE Transactions on Power Systems***, Vol. 37, No. 3, (2021), 2164-2176. doi: 10.1109/TPWRS.2021.3118704.
6. Saleh, S.A. and Chowdhury, M.R., "Survivability analysis of impacts of load-side activities on power systems", ***IEEE Transactions on Industry Applications***, Vol. 58, No. 2, (2022), 1869-1878. doi: 10.1109/TIA.2022.3146102.
7. Su, W., Yu, S.S., Li, H., Iu, H.H.-C. and Fernando, T., "An mpc-based dual-solver optimization method for dc microgrids with simultaneous consideration of operation cost and power loss", ***IEEE Transactions on Power Systems***, Vol. 36, No. 2, (2020), 936-947. doi: 10.1109/TPWRS.2020.3011038.
8. Sharifzadeh, H. and Amjady, N., "A review of metaheuristic algorithms in optimization", ***Journal of Modeling in Engineering***, Vol. 12, No. 38, (2014), 27-43. doi: 10.22075/JME.2017.1677.
9. Zou, D. and Gong, D., "Differential evolution based on migrating variables for the combined heat and power dynamic economic dispatch", ***Energy***, Vol. 238, (2022), 121664. https://doi.org/10.1016/j.energy.2021.121664
10. Niknam, T., Azizipanah-Abarghooee, R. and Aghaei, J., "A new modified teaching-learning algorithm for reserve constrained dynamic economic dispatch", ***IEEE Transactions on Power Systems***, Vol. 28, No. 2, (2012), 749-763. doi: 10.1109/TPWRS.2012.2208273.
11. Ellahi, M., Abbas, G., Satrya, G.B., Usman, M.R. and Gu, J., "A modified hybrid particle swarm optimization with bat algorithm parameter inspired acceleration coefficients for solving eco-friendly and economic dispatch problems", ***IEEE Access***, Vol. 9, No., (2021), 82169-82187. doi: 10.1109/ACCESS.2021.3085819.
12. Braik, M.S., Awadallah, M.A., Al-Betar, M.A., Hammouri, A.I. and Zitar, R.A., "A non-convex economic load dispatch problem using chameleon swarm algorithm with roulette wheel and levy flight methods", ***Applied Intelligence***, (2023), 1-40. https://doi.org/10.1007/s10489-022-04363-w
13. Sutar, M. and Jadhav, H., "An economic/emission dispatch based on a new multi-objective artificial bee colony optimization

algorithm and nsga-ii", ***Evolutionary Intelligence***, (2022), 1-36. https://doi.org/10.1007/s12065-022-00796-x

14. Ali, M.H., El-Rifaie, A.M., Youssef, A.A., Tulsky, V.N. and Tolba, M.A., "Techno-economic strategy for the load dispatch and power flow in power grids using peafowl optimization algorithm", ***Energies***, Vol. 16, No. 2, (2023), 846. https://doi.org/10.3390/en16020846
15. Goudarzi, A., Fahad, S., Ni, J., Ghayoor, F., Siano, P. and Haes Alhelou, H., "A sequential hybridization of etlbo and ipso for solving reserve-constrained combined heat, power and economic dispatch problem", ***IET Generation, Transmission & Distribution***, Vol. 16, No. 10, (2022), 1930-1949. https://doi.org/10.1049/gtd2.12404
16. Iqbal, M.N., Bhatti, A.R., Butt, A.D., Sheikh, Y.A., Paracha, K.N. and Ashique, R.H., "Solution of economic dispatch problem using hybrid multi-verse optimizer", ***Electric Power Systems Research***, Vol. 208, (2022), 107912. doi. https://doi.org/10.1016/j.epsr.2022.107912
17. Beirami, A., Vahidinasab, V., Shafie-khah, M. and Catalão, J.P., "Multiobjective ray optimization algorithm as a solution strategy for solving non-convex problems: A power generation scheduling case study", ***International Journal of Electrical Power & Energy Systems***, Vol. 119, (2020), 105967. https://doi.org/10.1016/j.ijepes.2020.105967
18. Gaing, Z.-L., "Particle swarm optimization to solving the economic dispatch considering the generator constraints", ***IEEE Transactions on Power Systems***, Vol. 18, No. 3, (2003), 1187-1195. doi: 10.1109/TPWRS.2003.814889.
19. Selvakumar, A.I. and Thanushkodi, K., "A new particle swarm optimization solution to nonconvex economic dispatch problems", ***IEEE Transactions on Power Systems***, Vol. 22, No. 1, (2007), 42-51. doi: 10.1109/TPWRS.2006.889132.
20. Elsayed, W.T., Hegazy, Y.G., El-bages, M.S. and Bendary, F.M., "Improved random drift particle swarm optimization with self-adaptive mechanism for solving the power economic dispatch problem", ***IEEE Transactions on Industrial Informatics***, Vol. 13, No. 3, (2017), 1017-1026. doi: 10.1109/TII.2017.2695122.
21. Ciornei, I. and Kyriakides, E., "A ga-api solution for the economic dispatch of generation in power system operation", ***IEEE Transactions on Power Systems***, Vol. 27, No. 1, (2011), 233-242. doi: 10.1109/TPWRS.2011.2168833.
22. Reddy, A.S. and Vaisakh, K., "Shuffled differential evolution for large scale economic dispatch", ***Electric Power Systems Research***, Vol. 96, (2013), 237-245. https://doi.org/10.1016/j.epsr.2012.11.010
23. Roy, P.K. and Bhui, S., "Multi-objective quasi-oppositional teaching learning based optimization for economic emission load dispatch problem", ***International Journal of Electrical Power & Energy Systems***, Vol. 53, (2013), 937-948. https://doi.org/10.1016/j.ijepes.2013.06.015
24. Bhattacharjee, K., Bhattacharya, A. and nee Dey, S.H., "Oppositional real coded chemical reaction optimization for different economic dispatch problems", ***International Journal of Electrical Power & Energy Systems***, Vol. 55, (2014), 378-391. doi. https://doi.org/10.1016/j.ijepes.2013.09.033
25. Mandal, B., Roy, P.K. and Mandal, S., "Economic load dispatch using krill herd algorithm", ***International Journal of Electrical Power & Energy Systems***, Vol. 57, (2014), 1-10. doi. https://doi.org/10.1016/j.ijepes.2013.11.016
26. Sharifzadeh, H., "Solving economic load dispatch by a new hybrid optimization method", ***International Journal of Industrial Electronics Control and Optimization***, Vol. 3, No. 4, (2020), 469-474. https://doi.org/10.22111/ieco.2020.32914.1239
27. Floudas, C.A., "Deterministic global optimization: Theory, methods and applications, Springer Science & Business Media, Vol. 37, (2013).
28. Bergamini, M.L., Aguirre, P. and Grossmann, I., "Logic-based outer approximation for globally optimal synthesis of process networks", ***Computers & Chemical Engineering***, Vol. 29, No. 9, (2005), 1914-1933. https://doi.org/10.1016/j.compchemeng.2005.04.003
29. Castro, P.M., "Tightening piecewise mccormick relaxations for bilinear problems", ***Computers & Chemical Engineering***, Vol. 72, (2015), 300-311. https://doi.org/10.1016/j.compchemeng.2014.03.025

## Persian Abstract

**چکیده**

در سالهای اخیر بعضی محققان از پوش‌های مک‌کرمیخ برای محدب‌سازی بعضی مسائل بهینه‌سازیِ NP-hard دارای عبارات دوسویه استفاده کرده اند. با این حال، تعداد بسیار معدودی از تحقیقات، بر دیگر انواع این پوش جهت بدست آوردن یک ریلکس محدب چفت‌تر بویژه برای کاربردهای عملی تمرکز کرده‌اند. این مقاله یک دیدگاه جدید از رابطه تلفات Kron، با نام رابطه B-matrix نیز شناخته می‌شود، به‌عنوان یک معادله که دارای عبارات دوسویه است ارائه می‌کند. براساس این نگاه، ما رابطه تلفات مذکور را با استفاده از یک ریلکس توسعه‌یافته مک‌کرمیخ به تعدادی قیود خطی تبدیل می‌کنیم. در روش مذکور، دامنه متغیرهای دوسویه به بخش‌های کوچکتری تقسیم می‌شود تا چفتی ریلکس‌سازی بهبود یابد. برای ارزیابی کارایی پوش‌های توسعه‌یافته در توصیف رابطه تلفات Kron، چند سیستم مطالعاتی با عبارات نامحدب مختلف با استفاده از رهیافت مذکور بررسی می‌شوند. یافته‌های شبیه‌سازی‌های عددی حاکی از آن هستند که روش پیشنهادی قادر به نمایش دقیق رابطه تلفات Kron است. همچنین، این روش نسبت به دیگر روش‌های ارائه‌شده در این زمینه موثرتر عمل می‌کند چراکه معمولا به جواب‌های بهینه‌تری همگرا می‌شود.

International Journal of Engineering

Journal Homepage: www.ije.ir

# Application of a Novel Optimization Algorithm in Design of Lead Rubber Bearing Isolation Systems for Seismic Rehabilitation of Building Structures

F. Mehri[a], S. Mollaei*[a], E. Noroozinejad Farsangi*[b], M. Babaei[a], F. Ghahramani[c]

[a] *Department of Civil Engineering, University of Bonab, Bonab, East Azerbaijan, Iran*
[b] *Faculty of Civil and Surveying Engineering, Graduate University of Advanced Technology, Kerman, Iran*
[c] *Department of Civil Engineering, Urmia University, Urmia, Iran*

*PAPER INFO*

*Paper history:*
Received 03 January 2023
Received in revised form 26 January 2023
Accepted 28 January 2023

*Keywords*:
*Lead Rubber Bearing Isolator*
*Optimization*
*Mass Irregularity*
*Near-Fault Earthquake*

*ABSTRACT*

Various mechanical and geometrical parameters have different effects on the isolation system's performance. Thus, a sensitivity study of the isolated structures' behavior is an essential matter. In this regard, the isolation systems should be designed using optimization approaches to consider the effects of the different factors. In this study, the optimal design of the lead rubber bearing (LRB) seismic isolation was conducted by considering mass irregularity and near-fault seismic excitation effects. Also, sensitivity analysis of the behavior of the considered isolated buildings was implemented concerning the mechanical parameters of the LRB system. A nonlinear time history dynamic analysis was used here, and the design optimization of the LRB isolator was programmed using the newly introduced grasshopper optimization algorithm (GOA). The main purpose was to investigate the ability of the GOA to optimize the design parameters of the LRB-isolated frames. The results proved the desirable ability of the GOA to solve optimal design problems for isolation systems. Also, the sensitivity analysis of the seismic behavior of LRB base-isolated structures showed that the yield base shear index had the most important effects. Also, the mass irregularity parameter showed a negligible influence.

***doi**: 10.5829/ije.2023.36.03c.20*

## 1. INTRODUCTION

During ground motions, structures vibrate, and if the structures have weak energy dissipation, they will be damaged, and in more severe cases, the structures will be collapsed. In recent decades, extensive studies have been conducted on developing structural control systems for the robust design of structures under seismic excitations [1-5]. In structural control systems, the mechanism of control devices has a significant role in the energy dissipation caused by earthquakes. A seismic isolation system with suitable force-displacement hysteresis properties can have the desired characteristics, such as optimum flexibility, high damping, and reduction of horizontal earthquake forces [6]. The primary purpose of the seismic isolation method is to prevent the transfer of horizontal ground motions and seismic forces to the superstructure. The reduction of transmitted seismic force to the superstructure is achieved by increasing the natural period of the structure and energy dissipation at the isolation level [7]. One of the most common types of isolation systems is the lead rubber bearing (LRB).

The seismic behavior of isolated structures is affected by different parameters. Various studies have been conducted to evaluate the behavior of the isolation system. In some studies, the impact of the type and mechanical parameters of the isolator has been assessed [8, 9]. Also, the effect of soil interaction on the isolation system [10, 11], isolation in tall buildings [12], evaluation of fragility curves in system isolation [13], reliability analysis [14], and reliability-based design [15] in isolated systems, semi-active isolation systems [16], hybrid control strategies for the isolated structures [17, 18], optimization of the shape memory alloy based friction pendulum system [19], and the cost benefits of isolations in the seismic design of structures [20] have

*Corresponding Authors Institutional Emails: s.mollaei@ubonab.ac.ir (S. Mollaei) & noroozinejad@kgut.ac.ir (E. Noroozinejad)

Please cite this article as: F. Mehri, S. Mollaei, E. Noroozinejad Farsangi, M. Babaei, F. Ghahramani, Application of a Novel Optimization Algorithm in Design of Lead Rubber Bearing Isolation Systems for Seismic Rehabilitation of Building Structures, ***International Journal of Engineering, Transactions C: Aspects,*** Vol. 36, No. 03, (2023) 594-603

been studied. Shaking table experiments have been carried out on base-isolated building systems [21]. Recently, the Telescopic Column (TC) system was proposed as a novel rocking-isolation method by Farsangi et al. [22].

Also, some studies showed that the performance of the isolation systems can be affected by factors such as geometric conditions, the irregularity of the structure, and seismic excitation characteristics. The damage caused by earthquakes depends on many factors, such as failure mechanism, site location, soil type, and earthquake record characteristics, including frequency content, duration, and amplitude [23]. Some researchers have studied the effects of ground motion [24], the impact of horizontal and vertical components [25], and the effect of earthquake frequency content [26] on the performance of isolated systems. The effects of near-fault and far-fault earthquakes have also been considered in some other studies [27-29]. In several studies, the effects of asymmetry in structure [30], the presence of soft stories [31], and eccentricity [32] on isolated structures have been studied. An isolated building with LRB isolators was analyzed using a series of real near-fault earthquake ground accelerations [33].

Determining the mechanical parameters of isolator devices to achieve efficient performance for the isolation system is a complex process. However, studies have shown that the behavior of these systems can be influenced by various conditions. Therefore, the design of isolation systems is defined in the framework of design optimization problems. One of the efficient methods in solving engineering optimization problems is meta-heuristic algorithms [34, 35]. So far, several metaheuristic algorithms have been introduced, such as charged system search (CSS), colliding bodies optimization (CBO), vibrating particle system (VPS) [34], ant colony optimization (ACO) [36], grasshopper optimization algorithm (GOA) [37], and so on. Recently, the particle swarm optimization algorithm was used to optimize the magneto-rheological (MR) damper parameters [38].

The literature review proved that more investigation is necessary for the optimization of the base isolation design process, especially when using novel optimization algorithms. In this study, the optimum design of a seismic isolation system with LRB isolators is solved using the newly introduced method of GOA while considering the mass irregularity and near-fault earthquake effects. The main purpose here is to evaluate the GOA method for optimizing the design of the LRB-isolated system.

## 2. MATERIALS AND METHODS

**2. 1. Seismic Isolation Systems** Rubber supports can provide the flexibility and deformation required for vibration isolation. If these supports are combined with a lead core to dissipate input energy, the necessary damping is also offered for the system. The shear deformation of the lead core in rubber supports can be controlled by using steel plates in the system. So, the lead core deforms against shear forces and causes a bilinear hysteresis behavior in the device [39]. Also, the rubber part of this isolation system is responsible for providing the restoration force (Figure 1 (a)).

In practice, all LRB isolation systems are simulated with a bilinear hysteresis model based on the three parameters of elastic stiffness ($K_1$), post-yield stiffness ($K_2$), and specified yield strength ($Q_y$), as shown in Figure 1 (b). The post-yield stiffness is obtained from the desired period of the structural system. For lead rubber bearing (LRB) and frictional pendulum systems (FPS), elastic stiffness is a coefficient of post-yield stiffness [28].

Initially, a time period is selected for the isolated structure ($T_2$) at the design displacement level, usually between 2 and 3 seconds. Then the post-yield stiffness of the isolated system for the selected period can be calculated using Equation (1):

$$K_2 = M \times \left(\frac{2\pi}{T_2}\right)^2 \quad (1)$$

In this relationship, M is the total mass of the whole structure isolated at the base. Also, the yield shear strength at the isolation level ($Q_y$) can be defined using Equation (2):

$$Q_y = \alpha M g \quad (2)$$

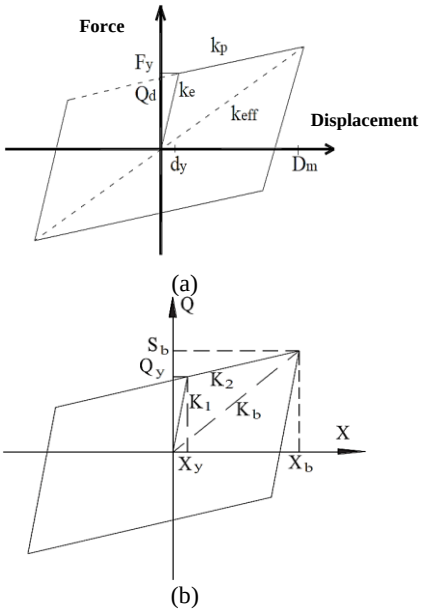


**Figure 1.** (a) Hysteretic loops parameters [40]; and (b) A bilinear behavioral model the LRB isolation used in this study [28]

In this relationship, α is the yield shear coefficient. Assuming a value between 0 and 1, the effective shear force on the structure can be determined. In the bilinear behavioral model, the value of the elastic stiffness of the system ($K_1$) can be determined by selecting the yield deformation component ($X_y$) as the elastic behavior limit.

$$K_1 = \frac{Q_y}{X_y} \tag{3}$$

Therefore, the ratio of initial stiffness to post-yield stiffness is defined as the parameter $\alpha_k$ in relation (4):

$$\alpha_k = \frac{K_1}{K_2} \tag{4}$$

Also, the damping of the isolation system ($c_b$) in terms of the effective damping ratio ($\xi_b$), which represents the dissipated energy, is equal to Equation (5):

$$c_b = 2\xi_b\sqrt{K_2 \times M} \tag{5}$$

**2. 2. Nonlinear Dynamic Analysis** The dynamic response of a structural system beyond its linear elastic range can usually not be calculated by an analytical solution. Even if the excitation changes are described by a simple function. Therefore, using numerical methods in the analysis of nonlinear systems is necessary. The Newmark method with a modified Newton-Raphson iteration approach is generally used for nonlinear dynamic equation solutions [41].

The dynamic equation of a structure with nonlinear behavior is written as Equation (6):

$$M\ddot{U}(t) + C\dot{U}(t) + F_S(t) = P(t) \tag{6}$$

where $t$ is the time; $U$, $\dot{U}$ and $\ddot{U}$, are displacements, velocities, and acceleration vectors relative to the ground, respectively; M is the mass matrix; C is the damping matrix; $F_S$ is the vector of resisting forces, which is a function of displacement and P(t) is the applied force, which for the seismic case is given by ground acceleration time history. Also, the initial condition is $U(0) = U_0$ and $\dot{U}(0) = \dot{U}_0$. According to the equilibrium conditions in each time interval, the equation of motion during the time step $t_{i+1}$ can be written as follows:

$$M\ddot{U}_{i+1} + C\dot{U}_{i+1} + F_{s_{i+1}} = P_{i+1} \tag{7}$$

In this paper, the constant average acceleration method with Newton–Raphson iterations has been used to analyze the nonlinear MDOF structures. At first, the initial state of the structural system is determined ($K_{T0}$ and $F_{s0}$). Then, also, the initial acceleration is calculated:

$$\ddot{U}_0 = M^{-1}\left(P_0 - C\dot{U}_0 - F_{s0}\right) \tag{8}$$

then for each time step:

$$\bar{P}_{i+1} = P_{i+1} + a_1U_i + a_2\dot{U}_i + a_3\ddot{U}_i \quad , \quad i = 0.1.2.\ldots \tag{9}$$

where:

$$a_1 = \left(\frac{1}{\beta(\Delta t)^2}\right)M + \left(\frac{\gamma}{\beta\Delta t}\right)C \tag{10}$$

$$a_2 = \left(\frac{1}{\beta\Delta t}\right)M + \left(\frac{\gamma}{\beta} - 1\right)C \tag{11}$$

$$a_3 = \left(\frac{1}{2\beta} - 1\right)M + \Delta t\left(\frac{\gamma}{2\beta} - 1\right)C \tag{12}$$

If the resisting forces are not equal to the applied force, a residual force vector is defined as:

$$\bar{R}_{i+1} = \bar{P}_{i+1} - (F_s)_{i+1} - a_1U_{i+1} \tag{13}$$

By using the Newton–Raphson iteration method, the additional displacement due to this residual force is determined by solving:

$$\Delta U = (\bar{K}_T)_{i+1}{}^{-1} \times \bar{R}_{i+1} \tag{14}$$

where $\bar{K}_T$ is the tangent stiffness that can be considered as follows:

$$(\bar{K}_T)_{i+1} = (K_T)_{i+1} + a_1 \tag{15}$$

The responses of a nonlinear structure can be obtained as follows:

$$U_{i+1} = U_i + \Delta U \tag{16}$$

$$\dot{U}_{i+1} = \left(\frac{\gamma}{\beta\Delta t}\right)\Delta U + \left(1 - \frac{\gamma}{\beta}\right)\dot{U}_i - \Delta t\left(1 - \frac{\gamma}{2\beta}\right)\ddot{U}_i \tag{17}$$

$$\ddot{U}_{i+1} = \left(\frac{1}{\beta(\Delta t)^2}\right)\Delta U - \left(\frac{1}{\beta\Delta t}\right)\dot{U}_i + \left(1 - \frac{1}{2\beta}\right)\ddot{U}_i \tag{18}$$

where $\gamma$ and $\delta$ are Newmark parameters, in this study, $\gamma = 0.5$ and $\delta = 0.25$ have been used for nonlinear analysis of the structure.

**2. 3. Grasshopper Optimization Algorithm** Optimization methods in their classical form use the derivation information of the objective function to find the optimal solution. These methods fall into the locale optimum points for complex problems, and cannot be used for underivable functions. Another type of optimization methods are stochastic methods, such as meta-heuristic algorithms. These methods are generally population-based algorithms inspired by nature. One of the evolutionary algorithms is the grasshopper optimization algorithm (GOA) which is inspired by the grasshopper lifecycle [37]. Most of the nature-inspired algorithms divide the search area into exploration and exploitation parts. In the exploration step, search agents are driven by random movements, while, in the exploitation phase, they tend to move locally around their place.

The theoretical model used to simulate grasshoppers' behavior was initially in the form of Equation (19):

$$X_i = S_i + G_i + A_i \tag{19}$$

where $X_i$ indicates the position of the grasshopper *i*, $S_i$ is the social interaction, $G_i$ is the force of gravity applied to the grasshopper *i*, and $A_i$ represents the direction of the wind. The value of $S_i$, that is, the social interaction for grasshopper *i*, is calculated by Equation (20):

$$S_i = \sum_{j=1}^{N} S(d_{ij})\widehat{d_{ij}} \quad (20)$$

where $d_{ij}$ indicates the distance between grasshoppers *i* and *j* and is calculated as Equation (21):

$$d_{ij} = |x_i - x_j| \quad (21)$$

as shown in Equation (20), $\widehat{d_{ij}}$ is a unit vector from the *i*th to the *j*th grasshopper. *S* is also a function for defining social force. The function *S*, which defines a social force, is calculated as in Equation (22):

$$S(r) = fe^{\frac{-r}{l}} - e^{-r} \quad (22)$$

where $f$ represents the intensity of gravity, and $I$ represents the length of the gravity scale. Parameters $I$ and $f$ significantly change the comfort zone, attraction, and repulsion.

Research has shown that the initial grasshopper motion relationship cannot be used in swarm simulation and optimization algorithms since this relationship prevents exploration and exploitation in the search space around a solution. The model is used for outdoor crowding. Therefore, Equation (23) has been used and can simulate the interaction between the grasshoppers in the swarm.

$$x_i^d = c\left(\sum_{j=1}^{N} c\frac{ub_d - lb_d}{2} s(|x_j^d - x_i^d|)\frac{x_j - x_i}{d_{ij}}\right) + \widehat{T_d} \quad (23)$$

Where $ub_d$ is the upper bound in the *d*-th dimension, and $lb_d$ is the lower bound in the *d*-th dimension. $\widehat{T_d}$ is the value of the *d*-th dimension in the target (the best solution ever seen), and *c* is a decreasing constant to reduce the area of comfort, repulsion, and attraction.

In Equation (23), *S* is obtained from Equation (19), and the parameters of gravity (*G*) and wind direction (*A*) are not considered. Based on this equation, the next position of a grasshopper can be defined using its current position, the target position, and the positions of all other grasshoppers. To maintain a balance between exploration and exploitation, parameter *c* needs to decrease with increasing repetition times during the algorithm. The coefficient *c* reduces the comfort zone in proportion to the number of repetitions (Equation (24)):

$$c = c_{max} - i\frac{C_{max} - C_{min}}{l} \quad (24)$$

where $C_{max}$ is the maximum value, $C_{min}$ is the minimum value, $i$ represents the current iteration number, and $l$ is the maximum number of algorithm iterations. In the simulations, the value of $C_{max}$ is 1 and the value of $C_{min}$ is 0.00001.

**2. 4. Design Formulation** Design variables are a set of parameters that affect design details and design results. Different parameters affect the design of base isolation systems in building structures. Parameters that are independently involved in the behavior mechanism of Lead Rubber Bearings are selected as design variables. The behavioral model of any Lead Rubber Bearing is influenced by independent factors such as yield displacement ($X_y$), secondary time period ($T_2$), base shear yield coefficient (α), damping ratio ($\xi_b$), etc., that parameters such as initial hardness ($K_1$), Secondary stiffness ($K_2$), yield shear strength ($Q_y$) and damping coefficient ($c_b$) are functions of these changes. In the optimum design of a Lead Rubber Bearing, these parameters are selected as the design variables. Constraints on the optimum design of isolations apply to the design variables due to physical limitations and acceptable results. According to the above, the optimum design of Lead Rubber Bearing for building structures is formulated as Equation (25):

$$Find: Design\ Variables\ X = \begin{Bmatrix} X_y \\ T_2 \\ \alpha \\ \xi_b \end{Bmatrix}$$

$$which\ minimizes\ Objective\ Function: f(X) \quad (25)$$

$$Subject\ to: \begin{cases} X_{y_{min}} \le X_y \le X_{y_{max}} \\ T_{2_{min}} \le T_2 \le T_{2_{max}} \\ \alpha_{min} \le \alpha \le \alpha_{max} \\ \xi_{b_{min}} \le \xi_b \le \xi_{b_{max}} \end{cases}$$

In this paper, the objective function for the optimization problem is defined based on performance indices for inter-story drift. This index shows the effect of control devices on system performance and is expressed based on the ratio of controlled maximum drift response to uncontrolled maximum response:

$$Objective\ Function = f(\mathrm{X}) = \left|\frac{Max(drift_{i,Controlled})}{Max(drift_{i,Uncontrolled})}\right| \quad (26)$$

where $drift_i$ is the inter-story drift of the *i*-th story.

The iteration process of the proposed algorithm has been summarized in Table 1 for steps i to i + 1. Also, the procedure of finding the displacement, velocity, and acceleration responses for the next steps are summarized in Table 2.

**2. 5. Numerical Case Studies** In this article, the numerical studies include three cases:

**Case 1:** In the first case, the seismic behavior of the base-isolated building structure with LRB is analyzed for sensitivity to evaluate the effect of LRB mechanical parameters and the mass irregularity of the structure.

**TABLE 1.** Summary of the steps of Newton-Raphson method used here

| |
|---|
| 1) Data definition: $u_{i+1}^{(0)} = u_i$ , $f_S^{(0)} = (f_S)_i$, $\Delta R^{(1)} = \Delta\hat{p}_i$, $\hat{K}_T = \hat{K}_i$ |
| 2) Iterative calculations (j=1,2, …): $\hat{K}_T \Delta u^{(j)} = \Delta R^{(j)} \rightarrow \Delta u^{(j)}$ , $u_{i+1}^{(j)} = u_{i+1}^{(j-1)} + \Delta u^{(j)}$ $\Delta f^{(j)} = f_S^{(j)} - f_S^{(j-1)} + (\hat{K}_T - K_T)\Delta u^{(j)}$, $\Delta R^{(j+1)} = \Delta R^{(j)} - \Delta f^{(j)}$ |
| 3) Repeating (j→j+1) |

**TABLE 2.** Steps of the Newmark method used here

| |
|---|
| Average acceleration method $\beta = \frac{1}{4}, \gamma = \frac{1}{2}$ |
| 1) Initial calculations: $\ddot{u}_0 = \frac{p_0 - c\dot{u}_0 - (f_s)_0}{m}$ |
| 1-2) Determination of the $\Delta t$ : $a = \frac{1}{\beta \Delta t} m + \frac{\gamma}{\beta} c$ , $b = \frac{1}{2\beta} m + \Delta t \left(\frac{\gamma}{2\beta} - 1\right) c$ |
| 2) Iterative calculations: $\Delta\hat{p}_i = \Delta p_i + a\dot{u}_i + b\ddot{u}_i$ |
| 2-1) Determination of the tangential stiffness $(K_i)$ : $\hat{k} = k + \frac{\gamma}{\beta \Delta t} c + \frac{1}{\beta (\Delta t)^2} m$ |
| 2-2) Determination of the $\Delta u$ using the updated Newton-Raphson method and Table 1: $\Delta\dot{u}_i = \frac{\gamma}{\beta \Delta t}(\Delta u_i) + -\frac{\gamma}{\beta}\dot{u}_i + \Delta t \left(1 - \frac{\gamma}{2\beta}\right)\ddot{u}_i$ , $\Delta\ddot{u}_i = \frac{1}{\beta (\Delta t)^2}(\Delta u_i) - \frac{1}{\beta \Delta t}\dot{u}_i - \frac{1}{2\beta}\ddot{u}_i$ $\ddot{u}_{i+1} = \ddot{u}_i + \Delta\ddot{u}_i$ , $\dot{u}_{i+1} = \dot{u}_i + \Delta\dot{u}_i$ , $u_{i+1} = u_i + \Delta u_i$ |
| 3) Repeating (i→i+1) |

**Case 2:** In the second case, the LRB isolation system is designed using the GOA meta-heuristic optimization method. To have a comprehensive comparison of GOA algorithm performance, some of the well-known metaheuristic algorithms, such as Particle Swarm Optimization (PSO), Harmony Search (HS), and Colliding Body Optimization (CBO), are selected to solve the optimum design of LRB.

**Case 3:** Finally, in the third case, the seismic behavior of isolated building structures with optimized LRB isolators using GOA with the best solution is evaluated under near-fault earthquakes and mass irregularities, and the performance of LRB isolators is compared in different conditions.

For numerical studies, benchmark structural models are used. These structural models include two models of 5-story (Example 1) and 10-story (Example 2) building structures. These structures have a two-dimensional lumped mass shear building system. The mechanical properties of the considered structures, such as mass, stiffness, and damping, are assumed to be the same for all the stories. The mass and stiffness of each story are respectively 445 ton and 448 $MN/m$ for 5-story models; those values are respectively 252.1 ton and 354.2 $MN/m$ in the 10-story models. For these models, the damping ratio ($\xi_s$) is assumed to be 0.02 and the damping coefficient (c) for each story can be calculated using Riley method. Also, the reference structural models are drawn in Figure 2.

To calculate the seismic responses and optimize the design of the LRB isolator, the generated Gaussian random white noise with a duration of 40 seconds and a maximum acceleration of 0.35 g is used as ground motion acceleration (Figure 3). Also, the ground acceleration of near-fault earthquakes is used to study the seismic behavior of isolated building structures with the optimal LRB system. According to many of the past studies [42-44] and seismic design guidelines, the recordings of three real earthquakes were utilized in this research. The Imperial Valley, the Northridge, and the Chi-Chi earthquakes were used here. The details of the considered earthquakes are presented in Table 3, which are selected from the Pacific earthquake Engineering Research Center (PEER). Irregular conditions for building models are defined based on mass irregularities in the height of the

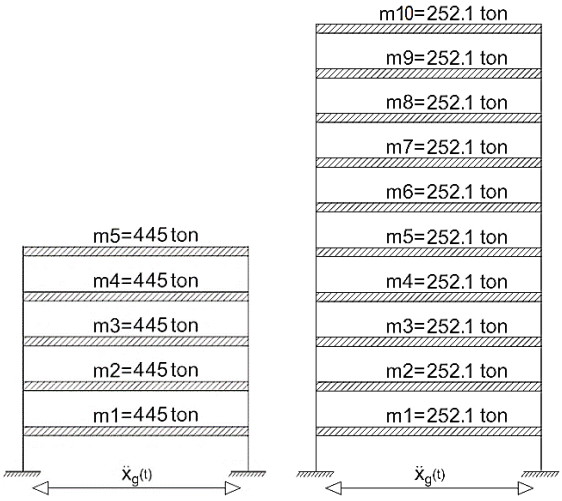


**Figure 2.** Reference structural models considered here

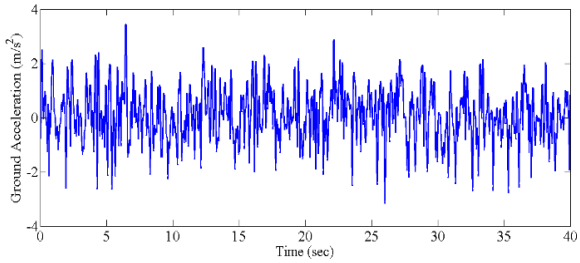


**Figure 3.** Time history of ground acceleration in random white noise (W(t))

**TABLE 3.** Details of earthquakes used in this study [28]

| Event | Station | Magnitude | Distance (km) | PGA ($\frac{m}{s^2}$) | $\frac{PGV}{PGA}$ |
|---|---|---|---|---|---|
| Imperial Valley | El Centro | 6.5 | 1.35 | 4.40 | 0.26 |
| Northridge | NWH-360 | 6.7 | 6.8 | 5.79 | 0.17 |
| Chi-Chi | TCU-052 | 7.6 | 1.84 | 3.56 | 0.52 |

structure. Irregularity for this building model is defined as a 50% variation in the mass of successive stories.

## 3. RESULTS AND DISCUSSION

To show the effect of each parameter of the isolator on system performance, the sensitivity analysis is used here. To achieve this aim, the sensitivity of the seismic responses of isolated structures with LRB is evaluated in relation to changes in the values of the yield base shear coefficient, secondary period, yield displacement, damping coefficient, and mass irregularity. Every parameter changes incrementally in the allowable range of parameters. The changes in maximum inter-story drift responses for each component are shown in Figures 4 and 5 for 5 and 10- story building models, respectively. As shown in Figures 4 and 5, the structural drift response has a high sensitivity to the yield base shear ratio. Also, the mass irregularity does not have a considerable effect on the performance of isolated structures.

In the second part, the results obtained from solving the optimization problem in the design of isolation systems with LRB isolators are presented. The outputs of

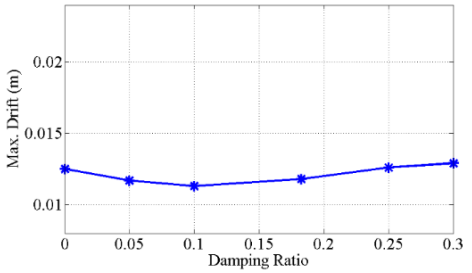


(c)

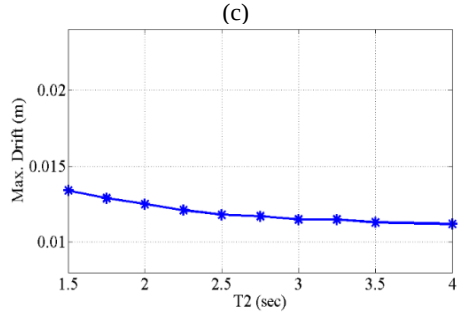


(d)

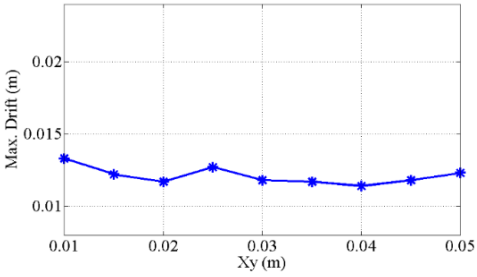


(e)

**Figure 4.** The variation of maximum drift response in a 5-story isolated building structure relative to: (a) mass irregularity; (b) base shear ratio; (c) Damping; (d) secondary time period; (e) yield displacement

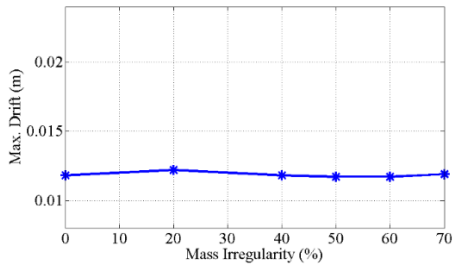


(a)

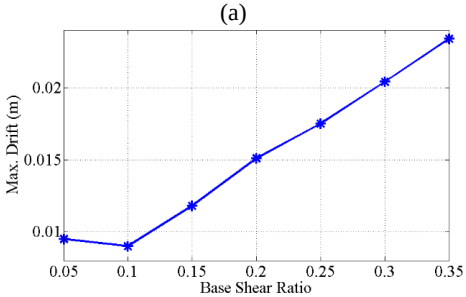


(b)

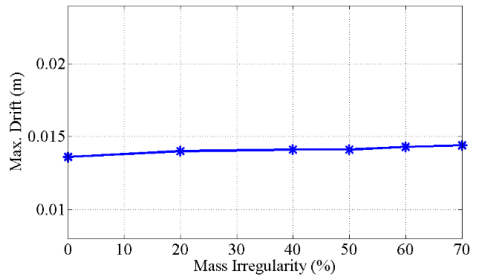


(a)

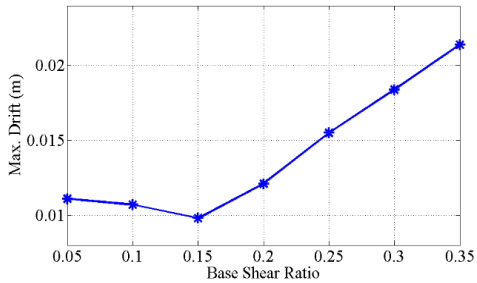


(b)

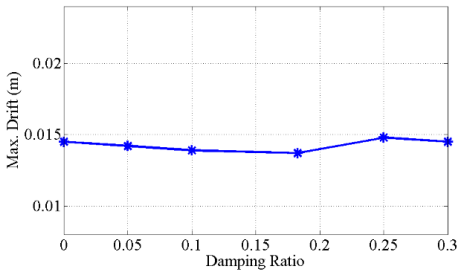


(c)

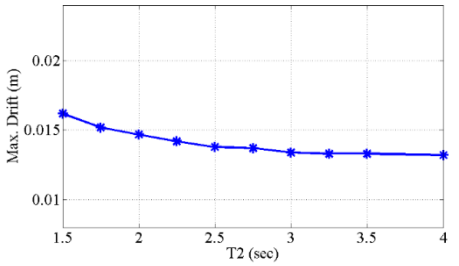


(d)

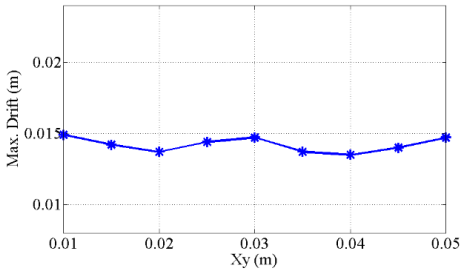


(e)

**Figure 5.** The variation of maximum drift response in a 10-story isolated building structure relative to: (a) mass irregularity; (b) base shear ratio; (c) Damping; (d) secondary time period; (e) yield displacement

this problem include the convergence history of the objective function, the minimum value calculated for the objective function, and the optimal values of design variables. Figure 6 shows the convergence history diagram for the defined objective function based on controlled seismic responses in the isolated building with LRB isolators for the GOA. According to this method, the minimum value for the ratio of maximum controlled responses to uncontrolled responses for the 5-story structural models is 0.19995, and for 10-story structural models, it is 0.4058.

In order to perform a comprehensive evaluation of the performance of the algorithms, a statistical test was performed based on the best solution, the mean, and the standard deviation of the solutions. The results of statistical tests for the GOA algorithm compared to PSO, HS, and CBO algorithms to solve the optimum design of the base isolation system are presented in Table 4. This statistical test was performed for each 5 and 10-story building structure case study based on 30 independent runs. According to the results of this test, in Table 4, the GOA algorithm shows its stability and robustness for solving the LRB design problem. Table 5 shows the results obtained from the optimal design of LRB isolators using GOA, including design variables and constraints for 5 and 10-story structural models.

Finally, the seismic behavior of isolated building structures using optimized LRB isolators is evaluated in both regular and mass irregularity cases under near-fault earthquakes. In this regard, the time history of seismic inter-story drift response at the maximum level is compared to the near-fault records of the Imperial Valley, Northridge, and Chi-Chi. Figures 7 to 9 show the drift time history of a 5-story structure for each earthquake. Under the Imperial Valley earthquake, the maximum drift is 0.95 cm for the regular 5-story structural model and 0.99 cm for the irregular 5-story structural model. For the Northridge earthquake, the maximum drift is 0.72 cm for the regular 5-story structural model and 0.70 cm for the irregular 5-story structural model. Also, under the Chi-Chi earthquake, the maximum drift value is 1.10 cm for the regular 5-story structural model and 1.05 cm for the irregular 5-story structural model.

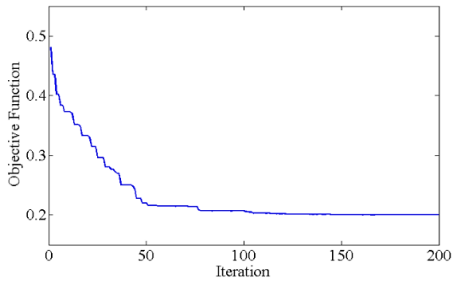


(a)

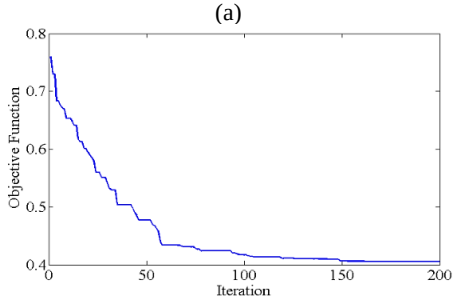


(b)

**Figure 6.** Convergence history of the objective function for the design of LRB with the GOA (a) 5-story (b) 10-story

**TABLE 4.** Statistical test for the optimization problem

| Model | Test | PSO | HS | CBO | GOA |
|---|---|---|---|---|---|
| 5-story | Best | 0.21754 | 0.25736 | 0.24328 | 0.19995 |
| | Mean | 0.25641 | 0.29768 | 0.27585 | 0.22584 |
| | STD | 0.04743 | 0.05303 | 0.04538 | 0.02461 |
| 10-story | Best | 0.41886 | 0.46629 | 0.45043 | 0.40579 |
| | Mean | 0.45718 | 0.50906 | 0.48452 | 0.43041 |
| | STD | 0.04938 | 0.05954 | 0.04489 | 0.03615 |

**TABLE 5.** Optimal design results for the LRB isolator with GOA algorithm

| Set | Parameter | Dimension | Value | |
|---|---|---|---|---|
| | | | 5- Story | 10- Story |
| Objective Function | Controlled Responses | - | 0.19995 | 0.40579 |
| Design Variables | Yield Base Shear Ratio ($\alpha$) | - | 0.055024 | 0.058653 |
| | Yield Deformation ($X_y$) | cm | 0.019219 | 0.038141 |
| | Secondary Period ($T_2$) | s | 2.9937 | 3.9946 |
| | Damping Ratio ($\zeta_b$) | % | 0.20751 | 0.13873 |
| Constraints | Stiffness Ratio ($\alpha_k$) | - | 0.1569 | 0.16407 |
| | Isolator Deformation | cm | 0.20127 | 0.3849 |

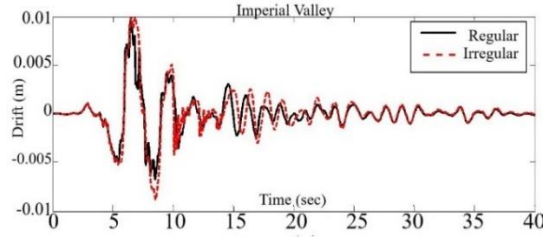


**Figure 7.** Time history of maximum drift for the 5-story model under Imperial Valley earthquake

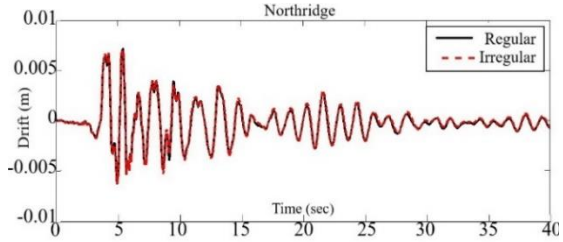


**Figure 8.** Time history of maximum drift for the 5-story model under Northridge earthquake

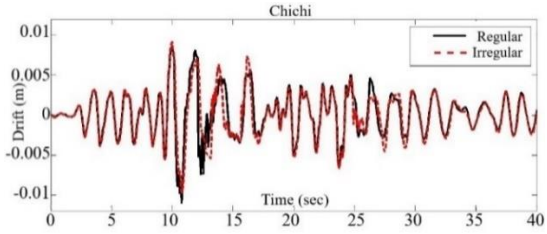


**Figure 9.** Time history of maximum drift for the 5-story model under the Chi-Chi earthquake

Figures 10 to 12 show the time history of maximum drift for a 10-story structure under each earthquake. Under the Imperial Valley earthquake, the maximum drift is 1.53 cm and 1.60 cm for the regular and irregular 10-story structural models, respectively. For the

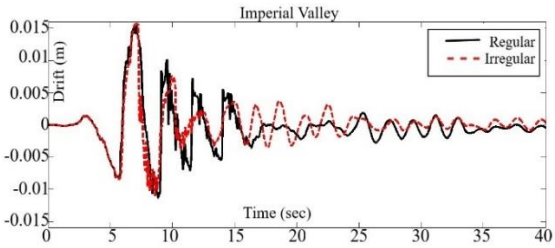


**Figure 10.** Time history of maximum drift for the 10-story model under Imperial Valley earthquake

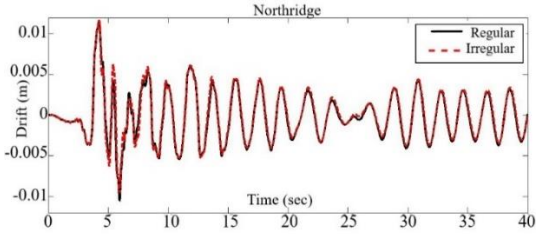


**Figure 11.** Time history of maximum drift for the10-story model under Northridge earthquake

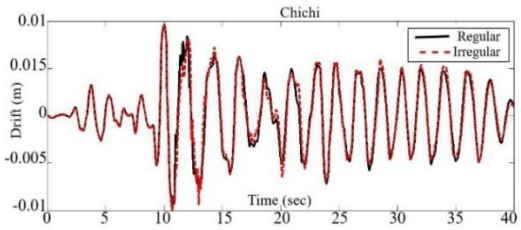


**Figure 12.** Time history of maximum drift for the 10-story model under the Chi-Chi earthquake

Northridge earthquake, the maximum drift for a 10-story structural model in both regular and irregular modes is 1.16 cm. Also, under the Chi-Chi earthquake, the maximum drift value for a model of 10-story structures in both regular and irregular modes is 1.00 cm. As can be seen, the presence of irregularities in the isolated structure does not affect the drift response of the structure under near-fault earthquakes. The existence of mass irregularity in the structure can lead to a change in the main period time of the structure and, consequently, a change in the seismic behavior of the structure. However, the use of seismic isolators at the base of building structures increases the main period of the structure. And it creates distance from the dominant frequencies of ground motion.

## 4. CONCLUSIONS

The primary purpose of this study was to optimum design a lead rubber-bearing seismic isolation system and evaluate the effects of mass irregularity and near-fault

seismic excitation on the seismic responses of buildings. Also, the sensitivity analysis of the isolated structures to the mechanical parameters of the lead-rubber bearing system and the mass irregularity was conducted here.

For numerical studies, two models of 5- and 10-story building structures with lumped mass shear frame systems were selected. The seismic behavior of these structures was studied under regularity and irregularity of mass conditions and in two fixed base and isolated cases with the LRB isolator. The LRB system's characteristics were optimally designed using GOA.

The sensitivity analysis of the seismic behavior of the LRB-isolated structures showed that the yield base shear ratio is the most influential parameter. According to the results of statistical tests comparing the GOA algorithm to the PSO, HS, and CBO algorithms to solve the optimum design of the base isolation system, the GOA has an excellent ability to solve the optimization problem of the isolation system design for building structures. The seismic performance of LRB isolation systems, which were optimally designed for regular structures, was not affected by mass irregularities in the structure. Also, the LRB isolation system had the identical performance in controlling the seismic responses of structures in the presence of mass irregularity under near faults earthquakes for both 5- and 10-story models. In other words, the performance of LRB isolators was not degraded by changes in the height of building structures.

## 5. REFERENCES


1. Spencer Jr, B. and Soong, T., "New applications and development of active, semi-active and hybrid control techniques for seismic and non-seismic vibration in the USA", in Proceedings of international post-SMiRT conference seminar on seismic isolation, passive energy dissipation and active control of vibration of structures, Cheju, Korea., (1999), 23-25.
2. Farsangi, E.N., Takewaki, I., Yang, T.Y., Astaneh-Asl, A. and Gardoni, P., "Resilient structures and infrastructure, Springer, (2019).
3. Pal, S., Roy, B. and Choudhury, S., "Comparative performance study of tuned liquid column ball damper for excessive liquid displacement on response reduction of structure", ***International Journal of Engineering, Transactions B: Applications,*** Vol. 33, No. 5, (2020), 753-759. https://doi.org/10.5829/ije.2020.33.05b.06
4. Barkhordari, M. and Tehranizadeh, M., "Ranking passive seismic control systems by their effectiveness in reducing responses of high-rise buildings with concrete shear walls using multiple-criteria decision making", ***International Journal of Engineering***, ***Transactions B: Applications,*** Vol. 33, No. 8, (2020), 1479-1490. http://dx.doi.org/10.5829/ije.2020.33.08b.06
5. Basu, B., Bursi, O.S., Casciati, F., Casciati, S., Del Grosso, A.E., Domaneschi, M., Faravelli, L., Holnicki-Szulc, J., Irschik, H. and Krommer, M., "A european association for the control of structures joint perspective. Recent studies in civil structural control across europe", ***Structural Control and Health Monitoring***, Vol. 21, No. 12, (2014), 1414-1436. http://dx.doi.org/10.1002/stc.1652
6. Soong, T. and Spencer Jr, B., "Supplemental energy dissipation: State-of-the-art and state-of-the-practice", ***Engineering Structures***, Vol. 24, No. 3, (2002), 243-259. https://doi.org/10.1016/S0141-0296(01)00092-X
7. Cheng, F.Y., "Smart structures: Innovative systems for seismic response control, CRC press, (2008).
8. Matsagar, V.A. and Jangid, R., "Influence of isolator characteristics on the response of base-isolated structures", ***Engineering Structures***, Vol. 26, No. 12, (2004), 1735-1749. http://dx.doi.org/10.1016/j.engstruct.2004.06.011
9. Tamim Tanwer, M., Kazi, T.A. and Desai, M., "A study on different types of base isolation system over fixed based", in Information and Communication Technology for Intelligent Systems: Proceedings of ICTIS 2018, Volume 1, Springer., (2019), 725-734.
10. Spyrakos, C., Koutromanos, I. and Maniatakis, C.A., "Seismic response of base-isolated buildings including soil–structure interaction", ***Soil Dynamics and Earthquake Engineering***, Vol. 29, No. 4, (2009), 658-668. https://doi.org/10.1016/j.soildyn.2008.07.002
11. Aydin, E., Ozturk, B., Bogdanovic, A. and Farsangi, E.N., "Influence of soil-structure interaction (ssi) on optimal design of passive damping devices", in Structures, Elsevier. Vol. 28, (2020), 847-862.
12. El-Bayoumi, K., Naguib, M. and Salem, F.A., "Dynamic analysis of high rise seismically isolated buildings", ***American Journal of Civil Engineering***, Vol. 3, No. 2, (2015), 43-50. doi: 10.11648/j.ajce.20150302.13
13. Flora, A., Perrone, G. and Cardone, D., "Evaluating collapse fragility curves for existing buildings retrofitted using seismic isolation", ***Applied Sciences***, Vol. 10, No. 8, (2020), 2844. https://doi.org/10.3390/app10082844
14. Castaldo, P., Palazzo, B. and Della Vecchia, P., "Seismic reliability of base-isolated structures with friction pendulum bearings", ***Engineering Structures***, Vol. 95, (2015), 80-93. https://doi.org/10.1016/j.soildyn.2019.105930
15. Peng, Y., Ma, Y., Huang, T. and De Domenico, D., "Reliability-based design optimization of adaptive sliding base isolation system for improving seismic performance of structures", ***Reliability Engineering & System Safety***, Vol. 205, (2021), 107167. https://doi.org/10.1016/j.ress.2020.107167
16. Barrera-Vargas, C.A., Díaz, I.M., Soria, J.M. and García-Palacios, J.H., "Enhancing friction pendulum isolation systems using passive and semi-active dampers", ***Applied Sciences***, Vol. 10, No. 16, (2020), 5621. https://doi.org/10.3390/app10165621
17. Hessabi, R.M., Mercan, O. and Ozturk, B., "Exploring the effects of tuned mass dampers on the seismic performance of structures with nonlinear base isolation systems", ***Earthquakes and Structures***, Vol. 12, No. 3, (2017), 285-296. http://dx.doi.org/10.12989/eas.2017.12.3.285
18. Ozturk, B., Cetin, H., Dutkiewicz, M., Aydin, E. and Noroozinejad Farsangi, E., "On the efficacy of a novel optimized tuned mass damper for minimizing dynamic responses of cantilever beams", ***Applied Sciences***, Vol. 12, No. 15, (2022), 7878. http://dx.doi.org/10.3390/app12157878
19. Sreeman, D. and Kumar Roy, B., "Optimization study of isolated building using shape memory alloy with friction pendulum system under near-fault excitations", ***International Journal of Engineering, Transactions B: Applications*** Vol. 35, No. 11, (2022), 2176-2185. http://dx.doi.org/10.5829/IJE.2022.35.11B.12
20. Yurdakul, M. and Yıldız, M.B., "A study on seismic isolation of building used lrb", ***Challenge***, Vol. 6, No. 2, (2020), 52-60. http://dx.doi.org/10.20528/cjsmec.2020.02.001
21. Rakicevic, Z., Bogdanovic, A., Farsangi, E.N. and Sivandi-Pour, A., "A hybrid seismic isolation system toward more resilient structures: Shaking table experiment and fragility analysis", ***Journal of Building Engineering***, Vol. 38, (2021), 102194. http://dx.doi.org/10.1016/j.jobe.2021.102194

22. Noroozinejad Farsangi, E., Tasnimi, A.A., Yang, T., Takewaki, I. and Mohammadhasani, M., "Seismic performance of base-isolated buildings under multi-directional earthquake excitations", ***Smart Struct. Syst***, Vol. 22, No. 4, (2018), 383-397. https://cir.nii.ac.jp/crid/1050282677492590720
23. Hayden, C.P., Bray, J.D. and Abrahamson, N.A., "Selection of near-fault pulse motions", ***Journal of Geotechnical and Geoenvironmental Engineering***, Vol. 140, No. 7, (2014), 04014030. http://dx.doi.org/10.1061/(ASCE)GT.1943-5606.0001129
24. Mavronicola, E.A., Polycarpou, P.C. and Komodromos, P., "Effect of ground motion directionality on the seismic response of base isolated buildings pounding against adjacent structures", ***Engineering Structures***, Vol. 207, (2020), 110202. https://doi.org/10.1016/j.engstruct.2020.110202
25. Jamalzadeh, A. and Barghian, M., "Dynamic response of a pendulum isolator system under vertical and horizontal earthquake excitation", ***Periodica Polytechnica Civil Engineering***, Vol. 59, No. 3, (2015), 433-440. https://doi.org/10.3311/PPci.7848
26. Cancellara, D. and De Angelis, F., "A base isolation system for structures subject to extreme seismic events characterized by anomalous values of intensity and frequency content", ***Composite Structures***, Vol. 157, (2016), 285-302. https://doi.org/10.1016/j.compstruct.2016.09.002
27. Providakis, C., "Effect of supplemental damping on lrb and fps seismic isolators under near-fault ground motions", ***Soil Dynamics and Earthquake Engineering***, Vol. 29, No. 1, (2009), 80-90. https://doi.org/10.1016/j.soildyn.2008.01.012
28. Rong, Q., "Optimum parameters of a five-story building supported by lead-rubber bearings under near-fault ground motions", ***Journal of Low Frequency Noise, Vibration and Active Control***, Vol. 39, No. 1, (2020), 98-113. http://dx.doi.org/10.1177/1461348419845829
29. Anajafi, H., Poursadr, K., Roohi, M. and Santini-Bell, E., "Effectiveness of seismic isolation for long-period structures subject to far-field and near-field excitations", ***Frontiers in Built Environment***, Vol. 6, (2020), 24. https://doi.org/10.3389/fbuil.2020.00024
30. Kilar, V. and Koren, D., "Seismic behaviour of asymmetric base isolated structures with various distributions of isolators", ***Engineering Structures***, Vol. 31, No. 4, (2009), 910-921. https://doi.org/10.1016/j.engstruct.2008.12.006
31. Choudhury, S.S. and Patro, S.K., Seismic control of soft storey buildings using lrb isolation system, in Recent developments in sustainable infrastructure: Select proceedings of icrdsi 2019. 2020, Springer.301-309.
32. Tena-Colunga, A. and Zambrana-Rojas, C., "Dynamic torsional amplifications of base-isolated structures with an eccentric isolation system", ***Engineering Structures***, Vol. 28, No. 1, (2006), 72-83. https://doi.org/10.1016/j.engstruct.2005.07.003
33. Özuygur, A.R. and Noroozinejad Farsangi, E., "Influence of pulse-like near-fault ground motions on the base-isolated buildings with lrb devices", ***Practice Periodical on Structural Design and Construction***, Vol. 26, No. 4, (2021), 04021027. http://dx.doi.org/10.1061/(ASCE)SC.1943-5576.0000603
34. Kaveh, A., "Advances in metaheuristic algorithms for optimal design of structures, Springer, (2014).
35. Danesh, M., "Evaluation of seismic performance of pbd optimized steel moment frames by means of neural network", ***Jordan Journal of Civil Engineering***, Vol. 13, No. 3, (2019). doi. https://jjce.just.edu.jo/issues/paper.php?p=4774.pdf
36. Dorigo, M. and Di Caro, G., "Ant colony optimization: A new meta-heuristic", in Proceedings of the 1999 congress on evolutionary computation-CEC99 (Cat. No. 99TH8406), IEEE. Vol. 2, (1999), 1470-1477.
37. Saremi, S., Mirjalili, S. and Lewis, A., "Grasshopper optimisation algorithm: Theory and application", ***Advances in Engineering Software***, Vol. 105, (2017), 30-47. https://doi.org/10.1016/j.advengsoft.2017.01.004
38. Abdeddaim, M., Djerouni, S., Ounis, A., Athamnia, B. and Farsangi, E.N., "Optimal design of magnetorheological damper for seismic response reduction of base-isolated structures considering soil-structure interaction", in Structures, Elsevier. Vol. 38, (2022), 733-752.
39. Naeim, F. and Kelly, J.M., "Design of seismic isolated structures: From theory to practice, John Wiley & Sons, (1999).
40. Code, I.H.G.D., "Vice presidency for strategic planning and supervision", ***Tehran, Iran: Ministry of Roads and Urban Development***, (2012). https://www.bhrc.ac.ir/Portals/8/PropertyAgent/1567/Files/1894/Code523.pdf
41. Newmark, N.M., "A method of computation for structural dynamics", ***Journal of the Engineering Mechanics Division***, Vol. 85, No. 3, (1959), 67-94. https://doi.org/10.1061/JMCEA3.0000098
42. Stanikzai, M.H., Elias, S., Matsagar, V.A. and Jain, A.K., "Seismic response control of base-isolated buildings using tuned mass damper", ***Australian Journal of Structural Engineering***, Vol. 21, No. 1, (2020), 310-321. https://doi.org/10.3390/app10041230
43. Ariga, T., Kanno, Y. and Takewaki, I., "Resonant behaviour of base-isolated high-rise buildings under long-period ground motions", ***The Structural Design of Tall and Special Buildings***, Vol. 15, No. 3, (2006), 325-338. http://dx.doi.org/10.1002/tal.298
44. Furukawa, T., Ito, M., Izawa, K. and Noori, M.N., "System identification of base-isolated building using seismic response data", ***Journal of Engineering Mechanics***, Vol. 131, No. 3, (2005), 268-275. http://dx.doi.org/10.1061/(ASCE)0733-9399(2005)131:3(268)


## Persian Abstract


**چکیده**

پارامترهای مکانیکی و هندسی مختلف می‌توانند بر روی رفتار سیستم جداسازی پایه اثر داشته باشند. بنابراین، انجام تحلیل حساسیت رفتار سازه‌ی جداسازی شده یک امر ضروری است. در نتیجه، سیستم‌های جداسازی باید با روش‌های بهینه‌سازی طراحی شوند تا اثرات عوامل مختلف در آنها لحاظ گردد. در این مطالعه، کاربرد یک الگوریتم بهینه‌سازی جدید در طراحی سیستم‌های جداساز لاستیکی با هسته‌ی سربی (LRB) برای مقاوم‌سازی لرزه‌ای سازه‌های ساختمانی بررسی شد. تحلیل حساسیت رفتار ساختمان جداسازی شده با درنظر گرفتن خصوصیات مکانیکی سیستم جداساز و نامنظمی جرمی انجام گردید. در اینجا، تحلیل تاریخچه- زمان غیرخطی جهت تعیین پاسخ‌ها به کار رفت و همچنین طراحی بهینه‌ی جداساز در برنامه‌ی MATLAB با استفاده از الگوریتم جدید بهینه‌سازی ملخ (GOA) تهیه شد. اهداف اصلی بررسی قابلیت الگوریتم بهینه‌سازی ملخ در طراحی بهینه‌ی پارامترهای قاب‌های جداسازی شده با سیستم LRB بود. نتایج نشان دهنده‌ی قابلیت مطلوب این الگوریتم در طراحی این نوع سیستم جداساز بود. همچنین، تحلیل حساسیت پاسخ سازه‌ی جداسازی شده نشان داد که شاخص برش پایه‌ی تسلیم دارای بیشترین اثر روی پاسخ‌ها بود. نامنظمی جرمی نیز اثر ناچیزی در تحلیل حساسیت نشان داد.

## AIMS AND SCOPE

The objective of the International Journal of Engineering is to provide a forum for communication of information among the world's scientific and technological community and Iranian scientists and engineers. This journal intends to be of interest and utility to researchers and practitioners in the academic, industrial and governmental sectors. All original research contributions of significant value focused on basics, applications and aspects areas of engineering discipline are welcome.

This journal is published in three quarterly transactions: Transactions A (Basics) deal with the engineering fundamentals, Transactions B (Applications) are concerned with the application of the engineering knowledge in the daily life of the human being and Transactions C (Aspects) - starting from January 2012 - emphasize on the main engineering aspects whose elaboration can yield knowledge and expertise that can equally serve all branches of engineering discipline.

This journal will publish authoritative papers on theoretical and experimental researches and advanced applications embodying the results of extensive field, plant, laboratory or theoretical investigation or new interpretations of existing problems. It may also feature - when appropriate - research notes, technical notes, state-of-the-art survey type papers, short communications, letters to the editor, meeting schedules and conference announcements. The language of publication is English. Each paper should contain an abstract both in English and in Persian. However, for the authors who are not familiar with Persian, the publisher will prepare the latter. The abstracts should not exceed 250 words.

All manuscripts will be peer-reviewed by qualified reviewers. The material should be presented clearly and concisely:

- *Full papers* must be based on completed original works of significant novelty. The papers are not strictly limited in length. However, lengthy contributions may be delayed due to limited space. It is advised to keep papers limited to 7500 words.
- *Research* notes are considered as short items that include theoretical or experimental results of immediate current interest.
- *Technical notes* are also considered as short items of enough technical acceptability with more rapid publication appeal. The length of a research or technical note is recommended not to exceed 2500 words or 4 journal pages (including figures and tables).

*Review papers* are only considered from highly qualified well-known authors generally assigned by the editorial board or editor in chief. Short communications and letters to the editor should contain a text of about 1000 words and whatever figures and tables that may be required to support the text. They include discussion of full papers and short items and should contribute to the original article by providing confirmation or additional interpretation. Discussion of papers will be referred to author(s) for reply and will concurrently be published with reply of author(s).

## INSTRUCTIONS FOR AUTHORS

Submission of a manuscript represents that it has neither been published nor submitted for publication elsewhere and is result of research carried out by author(s). Presentation in a conference and appearance in a symposium proceeding is not considered prior publication.

Authors are required to include a list describing all the symbols and abbreviations in the paper. Use of the international system of measurement units is mandatory.

- On-line submission of manuscripts results in faster publication process and is recommended. Instructions are given in the IJE web sites: www.ije.ir-www.ijeir.info
- Hardcopy submissions must include MS Word and jpg files.
- Manuscripts should be typewritten on one side of A4 paper, double-spaced, with adequate margins.
- References should be numbered in brackets and appear in sequence through the text. List of references should be given at the end of the paper.
- Figure captions are to be indicated under the illustrations. They should sufficiently explain the figures.
- Illustrations should appear in their appropriate places in the text.
- Tables and diagrams should be submitted in a form suitable for reproduction.
- Photographs should be of high quality saved as jpg files.
- Tables, Illustrations, Figures and Diagrams will be normally printed in single column width (8cm). Exceptionally large ones may be printed across two columns (17cm).

## PAGE CHARGES AND REPRINTS

The papers are strictly limited in length, maximum 8 journal pages (including figures and tables). For the additional to 8 journal pages, there will be page charges. It is advised to keep papers limited to 3500 words.

| **Page Charges for Papers More Than 8 Pages (Including Abstract)** | |
|---|---|
| For International Author *** | **$55 / per page** |
| For Local Author | **100,000 Toman / per page** |

## AUTHOR CHECKLIST

- Author(s), bio-data including affiliation(s) and mail and e-mail addresses).
- Manuscript including abstracts, key words, illustrations, tables, figures with figure captions and list of references.
- MS Word files of the paper.

**I**nternational **J**ournal of **E**ngineering, P.O. Box 13145-1659, Tehran, I.R. Iran
Materials and Energy Research Center, 5 Ahuramazda St., Alvand Ave., Argentina Sq., Tehran, Islamic Republic of Iran
www.merc.ac.ir - www.emerc.ac.ir


THOMSON REUTERS

WEB OF SCIENCE


Scopus®

CAS®
A DIVISION OF THE
AMERICAN CHEMICAL SOCIETY




Google
Scholar